# TRACE ELEMENT PARTITIONING BETWEEN COEXISTING METAMORPHIC MINERALS AND TRACE ELEMENT ZONING IN METAMORPHIC MINERALS FROM GAGNON TERRANE, WESTERN LABRADOR

CENTRE FOR NEWFOUNDLAND STUDIES

TOTAL OF 10 PAGES ONLY
MAY BE XEROXED

(Without Author's Permission)

PANSEOK YANG

National Library
of Canada

Acquisitions and
Bibliographic Services

395 Wellington Street
Ottawa ON K1A 0N4
Canada

Biblioth□que nationale
du Canada

Acquisisitons et
services bibliographiques

395, rue Wellington
Ottawa ON K1A 0N4
Canada

*Your file Votre r□f□rence*
*ISBN: 0-612-84076-X*
*Our file Notre r□f□rence*
*ISBN: 0-612-84076-X*

The author has granted a non-exclusive licence allowing the National Library of Canada to reproduce, loan, distribute or sell copies of this thesis in microform, paper or electronic formats.

The author retains ownership of the copyright in this thesis. Neither the thesis nor substantial extracts from it may be printed or otherwise reproduced without the author's permission.

L'auteur a accord□ une licence non exclusive permettant □ la Biblioth□que nationale du Canada de reproduire, pr□ter, distribuer ou vendre des copies de cette th□se sous la forme de microfiche/film, de reproduction sur papier ou sur format □lectronique.

L'auteur conserve la propri□t□ du droit d'auteur qui prot□ge cette th□se. Ni la th□se ni des extraits substantiels de celle-ci ne doivent □tre imprim□s ou aturement reproduits sans son autorisation.

**Canada**

# Trace element partitioning between coexisting metamorphic minerals and trace element zoning in metamorphic minerals from Gagnon Terrane, western Labrador

by

Panseok Yang B.Sc (Hons)., M.Sc.

A thesis submitted to the School of Graduate Studies in partial fulfilment of the requirements for the degree of Doctoral of Philosophy.

Department of Earth Sciences

Memorial University of Newfoundland

December, 2001

St. John's Newfoundland

# Abstract

Because of their wide-range in chemical properties, trace element partitioning and zoning in metamorphic systems provides valuable information on various metamorphic processes which are not recorded or preserved by major elements. Trace element partitioning between coexisting minerals and major and trace element zoning patterns were investigated using an electron microprobe and a laser ablation microprobe - inductively coupled plasma - mass spectrometry for pelites in Gagnon terrane, western Labrador.

Large variations in the partitioning of Sc and Cr between coexisting garnet and biotite indicate lost or modification of equilibrium compositions by garnet resorption and disquilibrium, respectively. Crystal lattice strain of garnet controls trace element partitioning, so that the distribution of elements occupying each cation site in the garnet structure shows parabolic relations with ionic radius. Sc and Ti partitioning are controlled by Al contents in biotite and Ca in garnet, respectively. Weak to moderate thermal dependence of Co, Zn and Zr partitioning maybe related to increases in thermal expansivities with metamorphic grade.

Similar to garnet and biotite pairs, trace element partitioning between biotite and muscovite shows controls of crystal lattice strain. The distributions of Li, Sc, Sr and Ba show dependence on both temperature and major element compositions. V and Zr partitioning is moderately dependent on temperature.

For garnets with spiral internal fabrics, growth zoning for some major and trace elements exhibits a spiral pattern *(spiral zoning)*, implying that incorporation of these

elements was mainly restricted to discrete growth regions of the crystal at any one time. Low amphibolite-facies garnets show Cr zoning parallel to foliation, indicating that the garnet overprinted a matrix fabric with a heterogeneous Cr distribution during growth *(overprint zoning)*. In contrast, in mid/upper amphibolite-facies garnet porphyroblasts, Cr zoning becomes concentric, indicating an enhanced diffusion rate.

Various Mn concentrations in the same annulus from garnet porphyroblasts in a thin-section suggests that Mn did not achieve thin-section scale equilibrium during the annulus formation, raising questions concerning the use of Mn concentration as a time marker. The origins of Y-annuli are suggested in this study: (1) Y-annuli produced by garnet resorption and regrowth characterized by an irregular and discontinuous annulus with a steeper slope on the inner side of the annulus, (2) Y-annuli produced by discontinuous breakdown of Y- and REE-rich minerals characterized by euhedral annuli and (3) Y-annuli produced by changes in garnet growth speed. Trace minerals responsible for the formation of Y-annuli are identified using REE ratios on small intervals on the annuli.

Phosphorus and Y concentrations in garnet and apatite coexisting with apatite and xenotime, respectively, vary systematically with metamorphic grade. This study demonstrate that trace element zoning combined with partitioning data provides valuable information on *P-T*, reaction histories, scale of equilibrium and kinetics.

# Acknowledgements

Firstly, I would like to thank my supervisor, Toby Rivers, for his guidance, support, hospitality and patience throughout the course of the study. I also wish to thank my former co-supervisor, Simon Jackson who now is in Macquarie University, Australia, for providing me incisive and thought provoking comments on all matters scientific for the first two years of my study. I have greatly benefited from discussions with many people on aspects of the project: Henry Longerich, Aprodite Indares, Roger Mason, Thomas Zack, Richard Cox, Ingo Horn, Lance Forthyder and Calorine Pettibon. Jeroen van Gool at the Geological Survey of Denmark kindly provided me the samples, maps and thin-sections used in the study. Frank Spear, George Jenner and Greg Dunning thoroughly read early versions of the thesis. Thanks also to staff at the Department of Earth Sciences, Memorial University of Newfoundland, especially Mike Tubrett and Maggie Piranian for their help with LAM-ICP-MS and electron microprobe, respectively. The study was financed by a graduate fellowship from the School of Graduate Studies, Memorial University of Newfoundland (1995-2000).

I am also grateful to a number of friends with whom I have shared enjoyable and unforgettable hours in Newfoundland. Finally, I would like to thank my mother and wife. The former for encouraging me in my education, the latter for providing emotional support and love.

# Table of Contents

# List of Tables

# Lists of Figures

# Lists of Appendices

# Chapter 1: General introduction

## 1.1 Introduction

An important goal of metamorphic petrologists is to understand the dynamics of metamorphic processes during the development of metamorphic terranes. To achieve this, it is necessary to characterize the changes in pressure (P), temperature (T), mineral reactions, reaction rates, and the duration of metamorphic processes, as well as the chemical environment, the distance over which chemical equilibrium took place, and the role of deformation that occurred during a particular metamorphic event. Significant progress on several of these topics has been made using phase relations, geothermobarometry, and the distribution of inclusions and zoning in metamorphic porphyroblasts (*e.g.*, Tracy et al., 1976; Thompson et al., 1977; Spear and Selverstone, 1983; Selverstone et al., 1984; Spear et al., 1984; Spear and Rumble, 1986, St-Onge, 1987; Tuccillo et al., 1990; Kohn et al., 1992; Menard and Spear, 1994). Uplift, heating, and cooling histories have been determined through kinetic modelling (*e.g.*, Lasaga et al., 1977; Tracy and Dietsch, 1982; Ehlers et al., 1994; Spear and Parrish, 1996), $Ar^{40}/Ar^{39}$ geochronology (*e.g.*, Harrison et al., 1979; Cliff and Droop, 1985), and integrated petrologic and geochronologic investigations (*e.g.*, Hollister, 1982; Selverstone, 1985; Kohn et al., 1995). Changes in deformation histories have been studied using relationships between porphyroblasts and the overprinted and matrix foliations (*e.g.*, Rosenfeld, 1970; Bell, 1985; Bell et al., 1992; Williams and Jiang, 1999). However, other

aspects of the dynamics of metamorphism, such as changes in the rates of mineral growth and nucleation, the degree of equilibrium or overstepping, and metasomatism have not been quantitatively addressed in detail.

Thus far, metamorphic petrologists have essentially limited their attention to major elements in their studies of element partitioning between coexisting metamorphic minerals and zoning in metamorphic porphyroblasts, largely because of the analytical difficulty of obtaining spatially resolved trace element concentrations from within microdomains of individual crystals. However, trace elements have advantages over major elements in petrogenetic studies because of the wide-range in chemical properties they exhibit. Ion size, charge, degree of formation of ionic bonds, crystal field stabilization energy and other chemical properties all vary significantly among trace elements. Therefore, the distribution and zoning of trace elements of varying chemical properties has the potential to elucidate a range of different processes during metamorphism. The recent development of several microprobe techniques with a spatial resolution of a few microns or tens of microns, and with lower limits of detection in the ppm to ppb range, has placed the goal of spatially resolved trace element analyses in metamorphic rocks within reach, and this study represents an attempt to exploit this new capability.

In this study, trace element distributions between coexisting metamorphic minerals from greenschist- to upper amphibolite-facies pelites and quartzofeldspathic rocks were investigated using a laser ablation system coupled to an VG PQII ICP-MS (LAM-ICP-MS). The knowledge of *trace element partitioning* among coexisting metamorphic

minerals is necessary for more realistic quantitative modelling of metamorphic processes, and to provide important constraints on pressure and temperature estimation. *Trace element zoning* combined with major element zoning in metamorphic minerals has the potential to provide important insights into metamorphic processes such as: (1) elemental fractionation caused by mineral growth or breakdown; (2) changes in *P-T* conditions; (3) the operation of disequilibrium processes and (4) open system behaviour (Hickmott and Spear, 1992; Lanzirotti, 1995). In conjunction with the study of major elements, studies of trace element distribution between coexisting metamorphic minerals and trace element zoning in metamorphic minerals should provide a more complete understanding of the metamorphic processes.

## 1.2 Literature review

### 1.2.1 Trace element distribution between coexisting metamorphic minerals

Studies of trace element distribution between coexisting minerals in metapelitic and metabasic rocks were undertaken in the 1950's through to the late 1960's (Nickel, 1954; DeVore, 1955; Kretz, 1959; Engel and Engel, 1960; Turekian and Phinney, 1962; Albee, 1965; Moxham, 1965; Schwarcz, 1967; Hietanan, 1969). Nickel (1954) reported trace element data for coexisting hornblende, biotite and chlorite and interpreted the data in terms of the relative electronegativities of the major and trace elements involved. DeVore (1955) examined a large number of mineral analyses from the literature and explained trace element distributions in terms of ionic properties and bonding mechanisms. Kretz

(1959) presented trace element data for coexisting biotite, hornblende, and garnet in amphibolite facies gneisses. He evaluated the distributions of trace elements in terms of chemical phase theory. Moxham (1965) interpreted the trace element distributions between hornblende and biotite in terms of the structures of the two minerals and of the ionic properties of the trace and major elements involved. All of the above studies were based on mineral separates analyzed by absorption spectrographic or emission spectrographic methods. However, with the widespread availability of the electron microprobe in the 1960's, it soon became apparent that many metamorphic minerals exhibit significant major element zoning, and the significance of spatially unresolved, bulk trace element analysis of these minerals began to be questioned. As a result, the topic fell into disrepute among petrologists for about 20 years, until the advent of more appropriate analytical techniques.

With the introduction of ICP-MS, studies on the behaviour and distribution of elements present in much lower concentrations (down to sub ppb level) became possible, although the analytical technique is not completely free from zoning and contamination from micro-inclusions in host minerals. Lonergan and Dahl (1989) calculated partition coefficients between garnet and biotite from lower sillimanite and migmatite zones pelitic schists using mineral separates analyzed by ICP spectromety. Their findings led them to suggest that trace element partitioning is thermally sensitive and could be used for formulate a range of geothermometers. Dahl et al. (1993) presented analyses of trace element partitioning between biotite and muscovite using an ICP spectrometry. They investigated the effects of crystal chemistry, crystal field stabilization, and temperature

on the distribution of 18 elements between biotite and muscovite occurring from the staurolite to the sillimanite zones.

Recently, Pyle and Spear (1999b) reported trace element distribution coefficients between garnet and biotite and biotite and muscovite, from pelites ranging from garnet to migmatite zone using laser ablation - inductively coupled plasma - mass spectrometry (LA-ICP-MS). This micro-beam technique can effectively reduce or remove the zoning and contamination problems. They found a thermal dependence of Sc and Cr partitioning between garnet and biotite and crystal chemical effects on trace element substitution in alkali sites in micas. Kretz et al. (1999) used X-ray fluorescence, instrumental neutron activation, and particle-induced X-ray emission (PIXE) methods to determine distribution of trace elements among garnet, Ca-pyroxene, hornblende, biotite, plagioclase and K-feldspar in a granulite. They attributed significant variation in distribution coefficients to differences from place to place in the magnitude of deformation and recrystallization, combined with rates of lattice and crystal-boundary diffusion rate that are unique for the various elements.

Although most data from the above studies are inaccurate and/or variable to permit determination of the controls on the variability of partition coefficients, selected trace element data are summarized in terms of garnet to give a general background for the trace element partitioning study undertaken in this thesis (Fig. 1.1). The sources of data used in Fig. 1.1 are presented in Table 1.1. The partition coefficient (D) is defined as ppm element in garnet/ppm element in other mineral. A few first order conclusions are apparent from the data in Table 1.1. First, it is difficult to determine the relative

partitioning order among minerals because of a lack of data for some minerals and severe overlap in partitioning data for others. Most partition coefficients obtained by micro-sampling techniques overlap with those obtained from bulk-mineral analyses, except for the V partition coefficient between garnet and ilmenite. It appears that Sc is preferentially substituted into garnet compared to all coexisting minerals, except hornblende and chlorite for which the distribution is about 1 (Fig. 1.1a). In contrast, V garnet/mineral partition coefficients for chlorite and hornblende (Fig. 1.1b) overlap over a wide range with an average partition coefficient of less than one. In general, vanadium can be classified as garnet-incompatible element. A SIMS analysis indicates that V is more enriched in ilmenite than garnet (Hickmott and Spear, 1992). Cr partitioning between garnets and other minerals suggests that Cr is incompatible in garnet (Fig. 1.1c). Garnet/mineral partition coefficients for Co are generally less than 1, implying it is also an incompatible element in garnet (Fig. 1.1d). Ni can also be regarded as a garnet-incompatible element based on all measured distributions (Fig. 1.1e). Yttrium garnet/mineral distributions are shown in Fig. 1.1f. Yttrium is a strongly incorporated into garnet relative to the other common metamorphic silicates.

Most of the studies on which Fig. 1.1 is based were initiated with a goal of using the pressure and temperature dependence of partition coefficients for geothermobarometry. This goal was occasionally achieved. For example, Kretz (1959) demonstrated the thermal dependence of V and Ti between hornblende and biotite. Krylova et al. (1970) suggested that partition coefficients of Sc between garnet and biotite generally increase from the epidote-amphibolite facies to the granulite facies, which was also confirmed by

Pyle and Spear (1999b). Comparison of the Engel and Engel's (1960) V partitioning data between garnet and biotite with other lower temperature data sets (Devore, 1955; Albee, 1965; Hietanan, 1969) shows that V partitioning between garnet and biotite decreases with increasing temperature. However, this thermal dependence is complicated by the distinct correlation between the Ca content in garnet and the V partition coefficient between garnet and biotite (Kretz, 1959). These results provided tantalizing insights into the potential use of trace element partitioning for geothermobarometery, but its widespread application has so far not been realized.

The irregular mineral/mineral trace element distributions that appeared in most of the previous studies may have been produced by: (1) poor data quality, (2) impurities in the analysed mineral separates, (3) trace element zoning in metamorphic phases especially for bulk-mineral analyses, (4) selection of non-equilibrium mineral pairs in the case of micro-beam techniques, and (5) disequilibrium partitioning of trace elements. The third possibility is supported by the fairly systematic mineral/mineral partitioning observed in upper-amphibolite to granulite facies terrains (Kretz, 1959; Engel and Engel, 1960; Korsman, 1975), where homogeneous minerals predominate as a result of rapid intracrystalline diffusion at high temperatures. The last possibility was suggested by Kretz et al. (1999) on the basis of variation in the distribution of a particular trace element between two mineral phases that could not be explained by variations in temperature, major element phase composition and analytical imprecision. The analytical problems mentioned above can be effectively minimized when the *in situ* analytical capability of an instrument such as a LAM-ICP-MS is employed with X-ray mapping.

### 1.2.2 Trace element zoning in metamorphic minerals

Recent studies have shown that trace element zoning, combined with major element zoning in garnet and other minerals, can provide important insights into the dynamics of metamorphism (Hickmott et al., 1987; Hickmott and Shimizu, 1989; Hickmott and Spear, 1992; Ayres and Vance, 1994; De Lima et al., 1995; Lanzirotti, 1995; Schwandt et al., 1996; Spear and Kohn, 1996; Bea et al., 1997; Chernoff and Carlson, 1999; Pyle and Spear, 1999a). Hickmott and others (1987, 1989, 1992) are pioneers in the study of trace element zoning in garnets in pelitic rocks. They measured trace element zoning in garnet from a variety of metamorphic environments using an ion microprobe. Hickmott et al. (1987) suggested that disturbances in the garnet zonation of trace elements from the western Tauern Window, Austria, could be a result of external or internal metasomatism, representing an open-system behaviour. Hickmott and Shimizu (1989), who studied trace element partitioning in garnets from the contact metamorphic terrane of the Kwoiek area, British Columbia, suggested that the irregular behaviour of some trace elements (Ti, Cr, and V) indicates disequilibrium during garnet growth, perhaps due to solute trapping of surface-segregated trace elements during rapid garnet growth. Hickmott and Spear (1992) used phase equilibria, inclusion relations, and major and trace element zoning in garnets to investigate reactions histories in a suite of calc- pelites from the NW Shelburne Falls quadrangle of western Massachusetts. They suggested several characteristic trace element patterns for deciphering metamorphic reactions during garnet growth, including: (1) Sc, Y, Zr, and HREE increases as a result of breakdown of clinozosite, (2) increases in

MREE by breakdown of amphibole, (3) Co increases in garnet by consumption of magnetite during garnet growth, (4) decreases in Y, Zr, and HREE in garnet implying that of clinozosite growth in equilibrium with garnet. They also suggested that zoning of trace elements whose activities in the rocks are buffered, such as Na and Ti in certain assemblages, have the potential to be useful geothermobarometers.

Spear and Kohn (1996) showed that trace element zoning in garnet can be used to decipher metamorphic reactions and *P-T* histories during garnet growth. Pyle and Spear (1999a) used the electron microprobe, X-ray mapping and backscattered electron imaging (BSE) to study the distribution of Y in pelitic garnets as a function of the metamorphic grade. They demonstrated that trace minerals such as xenotime take part in garnet-forming reactions and that Y activity in garnet is buffered by coexisting xenotime. Using the thermal dependence of Y activity in garnet coexisting with xenotime, Pyle and Spear (2000) calibrated an empirical YAG (yttrium aluminum garnet) - xenotime geothermometer. Lanzirotti (1995), Chernoff and Carlson (1999), and Pyle and Spear (1999a) reported an interesting Y zoning pattern in garnet characterized by extreme oscillatory zoning that they explained as due to one or more of kinetic factors, breakdown of accessory minerals, and resorption during garnet growth. The interpretation of the origin of Y annuli in garnet remains a controversial subject.

### 1.2.3 Trace element geothermobarometers

Some of the proposed trace element geothermobarometers applicable to crustal conditions are briefly summarized below.

***YAG-xenotime thermometer (Pyle and Spear, 2000)***: This thermometer is based on a negative correlation between Y concentration in garnet and temperature observed in xenotime-bearing metapelites. Y concentration decreases from ~5,500 ppm to less than 100 ppm over a 150 °C interval. An empirical calibration between Y concentration in garnet coexisting with xenotime and temperature estimated by the garnet-biotite Fe-Mg exchange geothermometer is

$$\ln(ppm\ Y\ in\ garnet) = \frac{16031(\pm 862)}{T} - 13.25(\pm 1.12) \qquad (1.1)$$

where $T$ is the equilibration temperature in K. This geothermometer is most sensitive over the garnet and staurolite zones (450-550°C).

***Monazite-xenotime thermometer (Andrehs and Heinrich, 1998)***: A limited solid solution exists between the rare-earth phosphates monazite and xenotime. Experimental and empirical studies show that the equilibrium partitioning of the rare-earth elements and Y between coexisting monazite and xenotime is both pressure and temperature dependent (Gratz and Heinrich, 1997; Heinrich et al., 1997; Andrehs and Heinrich, 1998; Gratz and Heinrich, 1998). In particular, the partitioning of Y has been calibrated as a geothermometer by Gratz and Heinrich (1997) through experiments on the $CePO_4$-$YPO_4$ binary. Their thermometer can be expressed as:

$$T = \frac{\ln(100 X^{Y}_{monazite} / 1.459 + 0.0852 \times P)}{2.2745 \times 10^{-3}} \qquad (1.2)$$

where $T$ is the equilibration temperature in °C, $X^{Y}_{monazite}$ is the mole fraction of Y in monazite, and $P$ is the pressure in kbar. The thermometer has been calibrated on natural monazite-xenotime pairs between 400 and 700°C and experimentally between 450 and 800°C. Calculation of a temperature using Eq. (1.2) requires an independent estimate of pressure, but the pressure dependence of the reaction is weak. A more important concern is whether or not coexisting monazite and xenotime in the samples were, in fact, in chemical equilibrium at the time of their crystallization, particularly given the persistence of both minerals through high-grade metamorphism and melting at crustal pressure and temperature conditions. The advantages of the thermometer are that coexisitng monazite and xenotime may occur over a wide range of metamorphic temperatures, and that a direct link between temperature and age determinations can be made by U-Pb and Sm-Nd dating of monazite and xenotime (*e.g.* Visupic and Hodges, 2001).

***REE in garnet barometer (Bea et al., 1997):*** This barometer is based on the progressive uptake of $REE^{3+}$ by garnet with increasing pressure. It has been empirically calibrated against garnet-kyanite-plagioclase-quartz barometer and the proposed barometric equation is

$$P\ (\text{kbar}) = 3.6 + 5.6\ (\text{Gd/Dy})^{\text{Grt}} \qquad (1.3)$$

The barometer is strongly influenced by whole-rock composition (mineral assemblages) and major element compositions and may be used to estimate pressure within a range of 4-9 kbar for rocks in which garnet coexists with monazite and where garnets have unit cell dimensions of less than 11.46 Å. The proposed REE substitution into garnet is

$3R^{2+}=2REE^{3+} + \square$, which produces a decrease in dimensions of the unit cell in garnet with the incorporation of $REE^{3+}$. In accordance with the suggested substitution, high-pressure garnets in their study show a negative Eu anomaly because $Eu^{2+}$ does not take part in the substitution.

However, the proposed REE substitution scheme involving site vacancies would enhance the defect structure, which in turn, may increase the rate of diffusion of the REE relative to that of the divalent cations. Sharp peaks in $REE^{3+}$ zoning are preserved in the rims of garnets from greenschist to granulite facies metamorphic rocks where divalent elements do not show discontinuities in zoning (*e.g.* Hickmott et al., 1987; Hickmott and Shimizu, 1990; Hickmott and Spear, 1993; Spear and Kohn, 1996; Chernoff and Carlson, 1999), a result that is not compatible with the proposed REE substitution.

***Zr in garnet (Keane and Essene, 1996)***: This thermobarometer was calibrated based on variation of Zr concentration in garnet coexisting with zircon and quartz. The Zr concentration in garnet (Zr garnet) is buffered by the presence of zircon and quartz by the reaction

$$Fe_3AlZrSi_2AlO_{12} + 2SiO_2 = Fe_3Al_2Si_3O_{12} + ZrSiO_4. \quad (1.4)$$

This reaction proceeds to the right with increasing pressure and temperature. The calibrated *P-T* slopes of the isopleths are somewhat steeper than that of the kyanite = sillimanite reaction. This geothermobarometer may be particularly important in high-grade metamorphic terranes where most conventional thermobarometers have been reset. At low metamorphic grade, however, Zr activity in garnet may not buffered because of

limited diffusion of Zr, as suggested by Hickmott and Spear (1992), who have noted that Zr zoning in garnet coexisting with zircon varies with breakdown of clinozoisite.

## 1.3 Geology of Gagnon terrane, northern Grenville Province

The study area consists of three distinct lithotectonic terranes: the Superior Province foreland, and the parautochthonous Gagnon terrane, and the overlying Molson Lake terrane (Fig. 1.2). Metasediments in the Gagnon terrane are part of the Paleoproterozoic Knob Lake Group that was deposited on the passive continental margin of the Superior Craton (Rivers, 1980). Rocks of Superior Province and Molson Lake terrane were not considered in this study. This section contains a summary of the geological history of the Gagnon terrane based on the work of Rivers (1983a, 1983b) and van Gool (1992).

### 1.3.1 Lithologic Units

The crystalline basement on which the Knob Lake Group sediments were deposited consists of Archean mafic and quartzo-feldspathic gneisses and migmatites, all with granulites facies mineralogies, and late granitoids which were not deformed prior to the Grenvillian Orogeny. The Knob Lake Group sediments were deposited unconformably on the Archean basement. The Knob Lake Group stratigraphy in the area consists from bottom to top of the following formations (Fig. 1.2).

The *Attikamagen Formation* consists of quartzo-feldspathic gneisses, interleaved with garnet-biotite or aluminous schists and gneisses. Thin intercalations of dolomitic

marble, calc-silicate and metavolcanic amphibolites occur locally. The protoliths of these rocks are interpreted to be greywackes that were deposited at shallow to moderate depths on the continental slope. The *Denault Formation* forms a pure, massive, coarse-crystalline dolomitic marble, which locally contains calc-silicates. It is interpreted to have formed a reef on the edge of the continental shelf. The *Wishart Formation* is a mature quartzite, representing a proximal (beach) depositional environment. The majority of these rocks are pure, massive, coarse-grained, recrystallized quartzites. The *Sokoman Formation* is a banded iron formation containing a carbonate-quartzite member, a chert-oxide member and a carbonate-silicate member. The *McKay River Formation* forms lenses (< 20 m thick) of amphibolite that are interpreted to be derived from mafic volcaniclastics. The *Menihek Formation* forms the top of the Knob Lake Group sequence in the area. In the western part of the area it is a pelitic schist, rich in graphite and biotite, with a dark-grey to black appearance. The southeastern occurrences of the Menihek Formation are more rich in quartz and feldspar and generally contain garnet and kyanite, which makes these rocks quite similar in appearance to the Attikamagen Formation. The Knob Lake Group and its basement were intruded by the Mesoproterozoic Shabogamo Gabbro.

### 1.3.2 Deformation history

Gagnon terrane is a foreland-directed, metamorphic fold-thrust belt (Rivers, 1983b) that carried Paleoproterozoic metasediments and part of their Archean crystalline basement in a north-northwest-directed thrust movement onto the Superior Province

foreland. Deformation and metamorphism in Gagnon terrane resulted from the emplacement of Molson Lake terrane as a thick thrust wedge over Gagnon terrane along a major ductile shear zone, and the subsequent accretion of rocks of Gagnon terrane into the base of the thrust wedge during its emplacement (van Gool, 1992; Rivers et al., 1993).

Gagnon terrane in the area consists of two thrust systems, an upper, metasediment-dominated system and a lower, basement-dominated system (van Gool, 1992). A pervasive southeast-dipping foliation ($S_1$) and south-southeast-plunging stretching lineation (Ls) characterize the main fabric in the upper thrust system and in the shear zone of the lower thrust system. $F_1$ fold axes are generally oriented sub-parallel to the stretching lineation, plunging south-southeast. Thrusts in both systems are southeast-dipping ductile shear zones. During progressive thrusting, $D_1$ structures were folded into northwest-verging $F_2$ folds and were locally affected by north-west-directed, out-of-sequence thrusts.

Two trends can be seen in the microstructures from west to east. First, in the lowest thrust sheets most garnets have spiral inclusion trails, suggesting syn-kinematic growth. Towards the higher thrust sheets the rotational component decreases. This is interpreted to be a result of the increasing thickness of the sedimentary cover to the southeast in which local shearing accommodated the movement of the overriding Molson Lake terrane. A second trend shows that towards the higher thrust sheets in the southeast, the amount of deformation post-dating peak metamorphism increases. The rocks in these higher thrust sheets experienced a longer deformation history than those near the front of

the belt because they were incorporated in the thrust belt earlier and were forming second and third generation structures at the same time that the lower thrust sheets were being incorporated in the belt and developing their $D_1$ structures (van Gool, 1992).

## 1.4 Metamorphism in Gagnon terrane

Metamorphic zonation in the area was documented in detail by Rivers (1983b) and van Gool (1992), based on diagnostic mineral assemblages and the presence or absence of migmatite in pelitic and quartzo-feldspathic rocks. The metamorphic zones and isograds trend north-northeast and metamorphic grade in Gagnon terrane increases from lower greenschist facies at the Grenville Front in the northwest to upper amphibolite facies in the southeast near Molson Lake terrane across a distance of 30 km (Fig. 1.3). Metamorphic grade also increases along the strike of the belt towards the southwest. The metamorphic field gradient in the area characterizes the thrust belt as a medium pressure facies series with increasing $P$ and $T$ towards the southeast. Thrusting in Gagnon terrane caused a telescoping and inversion of the metamorphic gradient, with discontinuities in the metamorphic field gradient across some of the thrusts (Fig. 1.3).

### 1.4.1 Mineral assemblages and metamorphic reactions

Five metamorphic zones are defined in the area, each with its own diagnostic mineral assemblage (Rivers, 1983b). With metamorphic grade increasing from lower greenschist to upper amphibolite facies these zones are biotite-muscovite-chlorite (zone 1), garnet-

biotite (zone 2), staurolite-kyanite (zone 3), garnet-biotite-kyanite (zone 4), and migmatite zones (zone 5). Representative metamorphic mineral assemblages occurring in the area are given in Table 1.2 with metamorphic reactions accounting for the change of the mineral assemblages. Besides the reactions shown in Table 1.2 many more continuous reactions are expected to have taken place, but only the reaction isograds that separate the mineral assemblage zones are reported here. A detailed discussion of the assemblages and reactions was given by Rivers (1983b) and van Gool (1992), of which the following is a summary with minor modifications.

*Zone 1* is characterized by the occurrence of biotite-muscovite-chlorite in pelites and biotite, muscovite, and epidote in calc-pelites with depletion of chlorite. *Zone 2* is characterized by the presence of garnet and the absence of primary chlorite with biotite and muscovite. The boundaries of this zone are poorly defined, partly a result of the bulk composition of the rocks in the zone and partly because of poor coverage in the field of the southwestern and northeastern parts of the zone. The garnet-in isograd locally cuts across several major thrusts sheets, but seems to be offsets by the thrust faults (Fig. 1.3). Two garnet-producing reactions are proposed for pelitic (R1) and calc-pelitic rocks (R2) (Table 1.2). *Zone 3* is characterized by the occurrence of staurolite + kyanite and is considered to mark the onset of amphibolite-facies or medium-grade metamorphism in the area (Winkler, 1979).

The transition from zone 2 to zone 3 coincides with thrusts, suggesting a metamorphic jump across these tectonic boundaries. This explains why staurolite and kyanite appear at the same isograd, even though they are interpreted to have formed by

different reactions, R3 and R4, respectively (Table 1.2). Other reactions for the formation of kyanite and staurolite are possible, but evidence for them was not found in this study, possibly because part of the metamorphic gradient was removed by thrusting. Possibly for the same reason, there is no zone in which primary chloritoid is stable, which elsewhere has commonly been reported as a precursor to staurolite in pelitic rocks. Chloritoid occurs locally as a retrograde mineral replacing staurolite.

In *zone 4* the products of staurolite-terminal reaction, Grt + Bt + Ky, form the diagnostic assemblage. Many samples from zone 4 contain two morphologically different species of kyanite, an early coarse-grained $Ky_1$ and a younger fine-grained $Ky_2$. $Ky_1$ appears to be similar to the kyanite occurring in zone 3, which suggests that $Ky_2$, which only appears in zone 4, is formed by the staurolite-breakdown reaction R5. The melt isograd defines the western boundary of *zone 5*. This zone is characterized by the occurrence of migmatite in rocks of semi-pelite composition. Deformation of the leucosomes gives the rocks a gneissic banding, parallel to the regional foliation. Melting is restricted to the quartzo-feldspathic rocks, in which R6 is responsible for the formation of granitic melt. The upper limit of metamorphic grade is the vapour absent reaction R8, since in zone 5 the assemblage Ms + Bt + Ab + Qtz is still stable and the assemblage Ky + Kfs has not been observed within Gagnon terrane. This indicates that either the temperature did not attain the level of the reaction curve or the reaction is not consistent with the compositions of the phases involved.

Graphite, pyrite, ilmenite, rutile, magnetite, apatite, xenotime, monazite, tourmaline, zircon and carbonate occur as accessory minerals. Chlorite occurs as a late retrograde

phase locally in most zones, overgrowing or replacing pre-existing minerals. Breakdown of garnet, commonly to form biotite and plagioclase, and late growth of muscovite, locally replacing kyanite or biotite, are also retrograde features. Late muscovite and chlorite generally lack a preferred orientation and overgrow the $S_1$ foliation.

### 1.4.2 Intensive variables of metamorphism

Although pelitic and calc-pelitic samples from Gagnon terrane contain appropriate assemblages (Grt-Bt-Ms-Ky-Qtz-Pl-Ilm-Rt) for *P-T* estimation, the compositions of the minerals are often outside accepted ranges for mineral solution models. For example, many garnets show $X_{grs}$ larger than 0.20, which cannot be modeled adequately by garnet solution models such as these of Hodges and Spear (1982) and Ganguly and Saxena (1984). It was also sometimes difficult to determine the equilibrium composition of garnet due to the extensive mineral retrogradation and resorption, especially from the Grt-Bt-Ky and migmatite zones. With these considerations in mind, the results of thermobarometric analysis from van Gool (1992) are summarized below.

Among various garnet-biotite thermometers available at the time, van Gool (1992) found that the Ferry and Spear (1978) calibration, assuming ideal mixing, gave the most reasonable temperature estimation. For pressure estimates, the Grt-Ms-Pl-Bt barometer of Ghent and Stout (1981, calibration of Hodges and Crowley, 1985), the Pl-Ky-Grt-Qtz barometer of Ghent (1976, calibration of Hodges and Royden, 1984), and the Ms-Grt-Bt-Pl-Qtz barometer of Hodges and Crowley (1985) were used. Garnet compositions along the profiles were used in combination with the compositions of matrix minerals to

estimate the P-T paths by simultaneous solution of the thermometer-barometer pair, assuming an infinite reservoir of the matrix minerals with respect to the garnet.

Temperatures calculated from the garnet-biotite geothermometer range between 450-750°C (Fig. 1.3). Temperature estimations for high grade rocks show a large scatter probably due to the variable retrogradation of both garnet rims and matrix biotites and garnet resorption in the samples. Estimated metamorphic pressures in the area range from 6 kbar in the Grt-Bt zone to 11 kbar in the migmatite zone. The *P-T* paths show a hairpin-shaped path (not shown), indicating that the garnets grew under increasing *P* and *T* (van Gool, 1992; Indares, 1995). The hairpin shape of the *P-T* path has a peak at 700 to 750°C and 10 to 11 kbar near the eastern boundary of Gagnon terrane, indicating that when the peak of metamorphism was reached, cooling and decompression followed immediately, without any time for thermal relaxation between the prograde and retrograde parts of the paths. Preservation of growth zoning profiles in garnets that were heated up to approximately 750°C indicates that, in spite of the increased diffusion rates at these temperature, there was not enough time for the garnets to homogenize, compatible with the hairpin-shaped *P-T* path. Garnet commonly experiences complete homogenization between 600 and 750°C depending on grain size and the duration of residence under high-temperature conditions (Spear, 1988).

The metamorphic rocks in Gagnon terrane show little evidence of textural disequilibrium features such as pseudomorphs, reaction textures, and sector zoning in staurolite. The compatibility between estimated *P-T* conditions and coexisting mineral assemblages provides another piece of evidence suggesting that equilibrium at the major

element level was achieved. In addition, a systematic increase in both metamorphic temperature and pressure towards the southeastern part of the area indicates that the metamorphic rocks attained regional equilibrium.

### 1.4.3 Age of metamorphism

The upper age limit for metamorphism in Gagnon terrane is constrained by the emplacement age of the Shabogamo gabbro (1459+23/-22 Ma, U/Pb zircon, Connelly and Heaman, 1993). $^{40}Ar/^{39}Ar$ determinations on hornblende from the amphibolite facies part of the Gagnon terrane, which have yielded apparent ages of 968 to 925 Ma (Dallmeyer and Rivers, 1983), are interpreted to record the time of cooling through the closure temperature of argon in hornblende. In addition, several U/Pb zircon lower intercepts of about 1000 Ma have been interpreted to indicate that metamorphism in Gagnon terrane took place at about this time (Connelly and Heaman, 1993, Connelly et al., 1995). However, a recent LAM-ICP-MS U/Pb study by Cox et al. (2001) has cast some doubt on this interpretation. They analysed zircon and monazite from an Archean metadiorite and metagabbro reworked under upper amphibolite facies in Gagnon terrane and a Paleoproterozoic pelite (Attikamagen Formation) metamorphosed under mid-amphibolite facies conditions (both from southwest of the area shown in Fig. 1.2). Meamorphic zircons from the diorite and gabbro yielded ages of 1124 ± 19 and 1147 ± 11 Ma respectively, which overlap within error, whereas the monazites yielded three distinct ages of 1131 ± 9, 1082 ± 8 and 1017 ± 21 Ma. These results suggest that there may have been three periods of metamorphism in Gagnon terrane, with the earliest at

about 1130 Ma being previously unknown in this part of the Grenville Province. Further work is required to understand the significance of this result.

## 1.5 Aims and Objectives

The aim of this study is to investigate the distribution and behaviour of trace elements during greenschist to amphibolite facies metamorphism by applying a number of techniques to the pelitic and calc-pelitic rocks of the area. In detail, the objectives of the study are as follows:

(1) To determine factors controlling trace element distribution among coexisting metamorphic minerals. The LAM-ICP-MS is used to analyse trace element concentration in metamorphic minerals. This technique provides the required spatial resolution and analytical detection limits for the *in situ* determination of trace elements. Distribution of trace elements between coexisting minerals is investigated in terms of major element composition, crystal structure and metamorphic temperature and pressure.

(2) To characterize the zoning patterns of refractory minerals such as garnet, kyanite, staurolite, epidote and apatite, which can provide constraints on *P-T* changes, reaction histories and growth mechanisms during metamorphism. This was achieved by quantitative EMP spot analyses, qualitative EMP line profiles, X-ray mapping, SEM analyses, and LAM-ICP-MS spot analyses. The trace element partitioning data, textural relationships, inclusion relationships, and major element zoning patterns are

all combined to interpret the patterns of trace element zoning in the minerals.

## 1.6 Thesis Outline

This thesis consists of eight chapters. The principles of trace element partitioning, analytical techniques and a summary of distribution coefficients among coexisting metamorphic minerals in Gagnon terrane are given in Chapter 2. Details of trace element partitioning between coexisting garnet and biotite, and biotite and muscovite, are provided in Chapters 3 and 4, respectively. The controlling factors in trace element partitioning between coexisting minerals are sought in terms of major element composition, crystal-chemical and *P-T-X* factors. The established partitioning coefficients among coexisting metamorphic minerals are then used to interpret trace element zoning in later chapters. Chapter 5 describes the principles and mechanisms of growth zoning and the analytical techniques employed. Chapter 6 is devoted to major and trace element zoning in garnet and kyanite. The patterns of garnet growth zoning and the mobility of Cr during metamorphism are examined in this chapter. Chapter 7 deals with trace element zoning in garnet, apatite and epidote group minerals with emphasis on the involvement of accessory minerals during the growth of garnet. The origin of Y annuli and the petrologic implications of phosphorus zoning in garnet, Y zoning in apatite, and the scale of equilibrium are investigated in this chapter. The final chapter summarizes the general conclusions from the previous chapters. This thesis also includes appendixes containing all the collected LAM-ICP-MS data and the X-ray mapping code for Cameca SX-50

electron microprobe that was developed in this study. A slightly modified version of chapters 3, 4 and 6 were published as individual papers: Chapter 3 (Yang, P., Rivers, T., and Jackson, S., 1999. Crystal-chemical and thermal controls on trace-element partitioning between coexisting garnet and biotite in metamorphic rocks from western Labrador. Canadian Mineralogist, 37, 43-468), Chapter 4 (Yang, P. and Rivers T., 2000. Trace element partitioning between coexisting biotite and muscovite from metamorphic rocks, western Labrador: Structural, compositional and thermal controls. Geochimica et Cosmochimica Acta, 64, 1451-1472), and Chapter 6 (Yang, P. and Rivers, T., 2001. Chromium and manganese zoning in pelitic garnet and kyanite: Spiral, overprint and oscillatory (?) patterns and the role of garnet growth. Journal of Metamorphic Geology). Chapter 7 has been submitted to the Journal of Geological Materials Research for publication.

Table 1.1. Sources of the data presented in Fig 1.1.

| References | Methods | Minerals analyzed | Metamorphic grades |
|---|---|---|---|
| DeVore (1955a) | Spectrographic | Grt, Chl, Bt, Amp, Ms | Amphibolite |
| Kretz (1959) | Spectrographic | Grt, Amp, Bt | Granulite |
| Engel & Engel (1960) | Emission Spec. | Grt, Bt, Pl | Amphibolite-granulite |
| Turekian & Phinney (1962) | Spectrographic | Grt, Bt | Amphibolite |
| Albee (1965) | Emission Spec. | Grt, Bt, Chl, Cld, Ilm | Amphibolite |
| Hietenan (1969) | Spectrographic | Grt, Bt, Ms, St | Amphibolite |
| Krylova et al. (1970) | Spectrographic | Grt, Bt | Amphibolite - granulite |
| Bollinberg & Bryhni (1972) | Spectrographic | Grt, Amp | Eclogite |
| Korsman (1975) | Emission Spec. | Grt, Bt | Granulite |
| Pride & Mueke (1981) | INAA | Grt, Amp, Pl | Granulite |
| Hickmott & Spear (1992) | Ion microprobe | Grt, Bt, Ms, Pl, Czo, Ilm, Mag, Chl | Amphibolite |
| Pyle & Spear (1999) | LA-ICP-MS | Grt, Bt, Ms | Amphibolite |
| Kretz et al. (1999) | XRF, INAA, PIXE | Grt, Cpx, Hbl, Bt, Pl, Kf | Upper Amphibolite |

Table 1.2. Diagnostic mineral assemblages in metamorphic zones and model reactions that occur at zone boundaries (modified from Rivers, 1983b).

| Zones | Mineral assemblages | Reactions | |
|---|---|---|---|
| 1 | Qtz+Bt+Kfs±Ms | | |
| | Qtz+Chl+Bt±Ms±Ep | | |
| | | $Chl+Qtz+Ms=Grt+Bt+Pl+H_2O$ | (R1) |
| | | $Chl+Ep+Qtz+Ms=Grt+Bt+H_2O$ | (R2) |
| 2 | Qtz+Chl+Bt+Grt±Ms | | |
| | Qtz+Bt+Grt±Kfs±Ms | | |
| | | $Chl+Ms+Grt=St+Bt+Qtz+H_2O$ | (R3) |
| | | $St+Qtz=Grt+Ky+H_2O$ | (R4) |
| 3 | Qtz+St+Grt+Ky±Ms | | |
| | Qtz+St+Grt±Bt±Ms | | |
| | | $St+Ms+Qtz=Grt+Bt+Ky+H_2O$ | (R5) |
| 4 | Qtz+Grt+Ky+Bt±Ms | | |
| | | $Bt+Ms+Kfs+Ab+Qtz+H_2O=Liq$ | (R6) |
| 5 | Qtz+Ky+Bt+Grt+Liq±Ms | | |
| | | $Bt+Ms+Ab+Qtz+H_2O=Ky+Liq$ | (R7) |
| | | $Bt+Ms+Ab+Qtz=Kfs+Ky+Liq$ | (R8) |

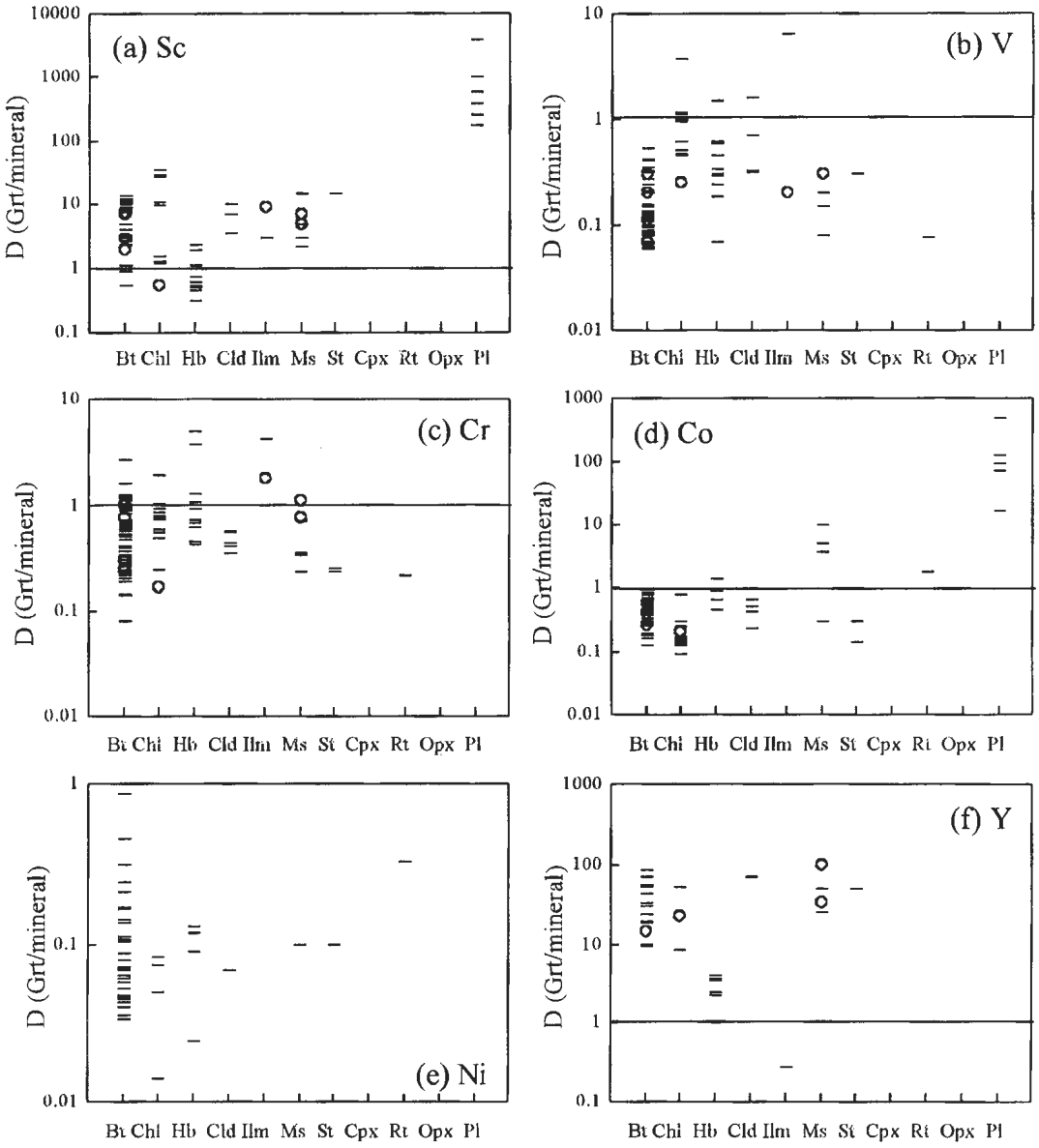


Fig. 1.1. Representative garnet/mineral partition coefficients from literature data. The sources of data used for the plots are given in Table 1.1. Horizontal bars represent partitioning data from mineral separates and open circles represent partitioning data acquired by micro-beam techniques. Mineral abbreviation after Kretz (1983).

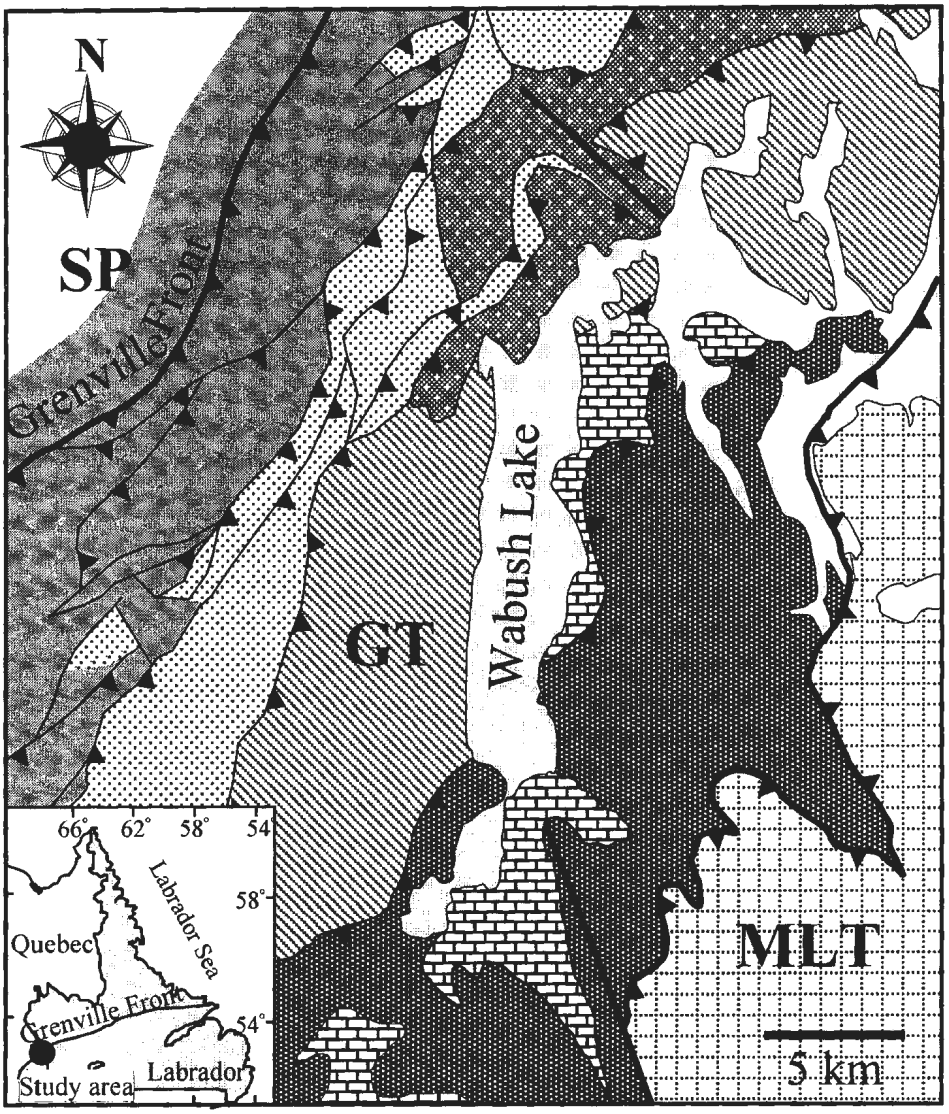


Fig. 1.2 Lithotectonic map of the Grenville Province in southwestern Labrador. SP-Superior Province, GT-Gagnon terrane, and MLT-Molson lake terrane.

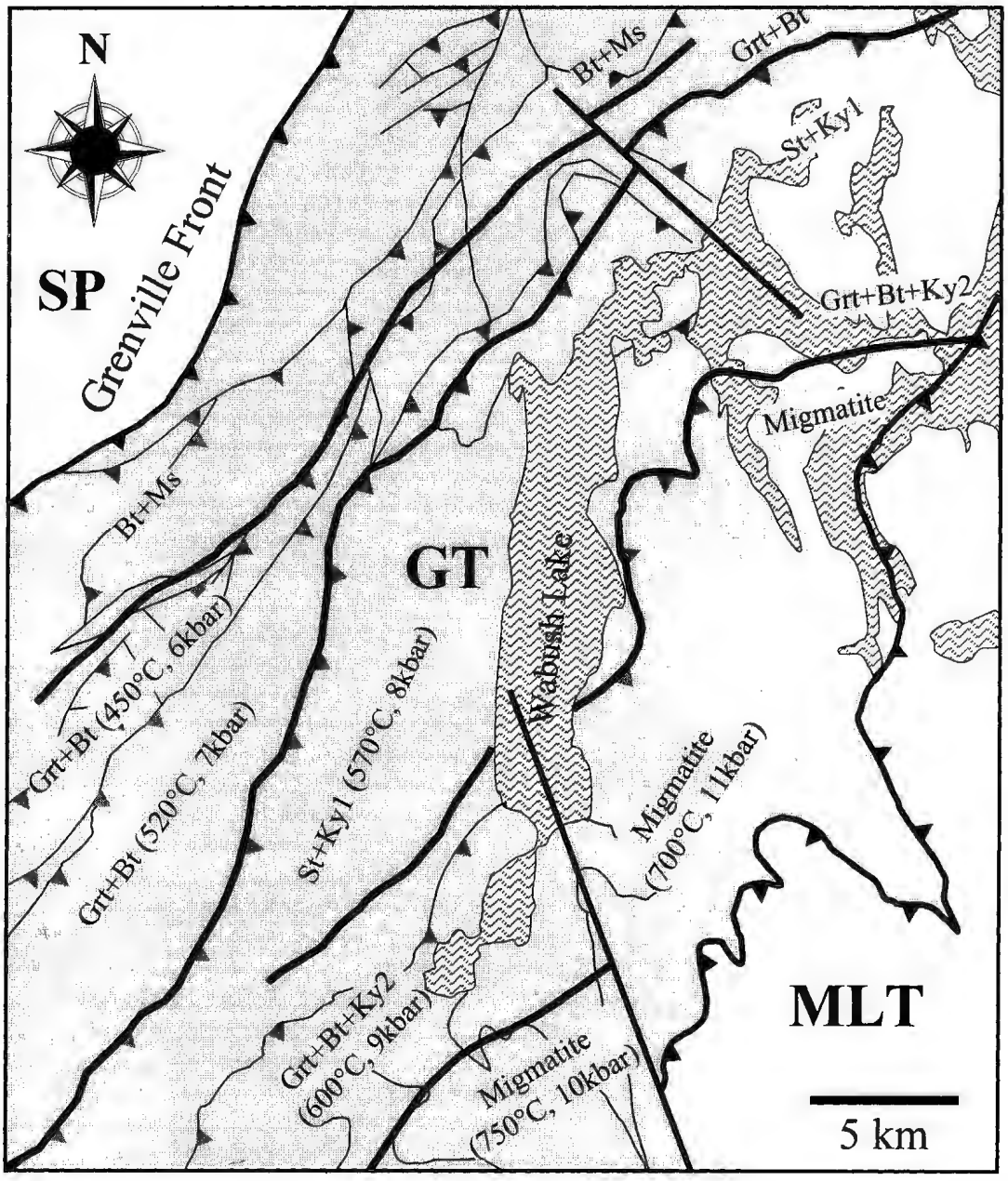


Fig. 1.3. Map of metamorphic zoning based on mineral assemblages in metapelitic and quartzo-feldspathic rocks. Estimated peak metamorphic pressures and temperatures from van Gool (1992). SP - Superior Province, GT - Gagnon terrane and MLT - Molson Lake terrane.

# Chapter 2: Trace element partitioning between coexisting metamorphic minerals

## 2.1 Introduction

Knowledge of the distribution of trace elements in minerals is important in order to understand and quantitatively model the behaviour of these elements during geological processes. Distributions of trace elements among coexisting minerals are also potentially very useful, particularly if they are simple functions of pressure ($P$), temperature ($T$) and major element composition ($X$) (e.g. Kretz, 1959). However, despite their potential importance, the number of trace element partitioning studies in metamorphic petrology declined sharply after the late 1960's due to the small amount of useful petrogenetic information derived up to that time, and the apparently non-systematic trace element partitioning with metamorphic grade. These unfruitful results were, to some extent, a result of the bulk mineral analysis methods employed, in which contamination by micro-inclusions in mineral separates and chemical zoning in refractory minerals could not be completely avoided. Thus, there is a strong need to reinvestigate trace element partitioning in metamorphic rocks using a modern micro-beam technique such the LAM-ICP-MS.

An accurate knowledge of the partition coefficients between coexisting metamorphic minerals for a wide range of trace elements is essential if useful petrogenetic information is to be extracted from trace element concentrations measured in metamorphic minerals.

The controls of *P-T-X* in trace element partitioning in metamorphic systems are widely recognized and yet the quantitative links between them and partition coefficients are poorly understood. Consequently, although most processes of chemical differentiation occur under conditions of varying *P*, *T* and *X*, a lack of understanding of their effects obliges geochemists to adopt a largely empirical approach using constant average distribution values in modeling (e.g., Haack *et al.*, 1984). In this chapter, the principles of trace element partitioning, the analytical techniques employed and the trace element analyses of 10 minerals from 20 samples examined in this study are summarized.

## 2.2 The principles of trace element partitioning

### 2.2.1 Thermodynamics of trace element distribution

The thermodynamics underlying the partitioning of trace elements are discussed thoroughly in papers by Kretz (1959 and 1961) and McIntire (1962) and are reviewed briefly below. The distribution of a trace element can be viewed as a simple exchange reaction for which the thermodynamic basis is well established (e.g., Kretz, 1961). For example, the partitioning of trace element *i* and major element *j* between coexisting minerals *A* and *B* can be expressed by the exchange reaction:

$$iA + jB = jA + iB \tag{2.1}$$

At equilibrium,

$$\mu_{iA} + \mu_{jB} = \mu_{jA} + \mu_{iB} \tag{2.2}$$

where $\mu_{iA}$ is the chemical potential of *i* in *A*, which is related to concentration by

$$\mu_{iA} = G_{iA} + RT \ln X_{iA}\gamma_{iA} \tag{2.3}$$

Here $G_{iA}$ is the molar Gibbs energy of pure *iA*, R is the gas constant, $\gamma_{iA}$ is an activity coefficient, and $X_{iA}$ is the mole fraction *i/(i+j)*. By introducing three additional equations of the kind (2.3) and substituting into (2.2) we obtain

$$\frac{X_{jA}}{X_{iA}} \times \frac{X_{iB}}{X_{jB}} = \left[\frac{\gamma_{jB}}{\gamma_{jA}}\right]\left[\frac{\gamma_{iA}}{\gamma_{iB}}\right]\left[\exp(-\Delta G^{\circ}/RT)\right] \tag{2.4}$$

The quotient on the left is the distribution coefficient ($K_D$). Because $X_{jA}$ and $X_{jB}$ are very nearly 1.0, the distribution coefficient on the left may be written as $X_{iB}/X_{iA}$.

At low concentrations, the second quotient on the right $\left(\left[\frac{\gamma_{iA}}{\gamma_{iB}}\right]\right)$ is expected to remain independent of trace element concentration (Henry's Law) and may change with temperature. Therefore, the first quotient on the right will also remain constant by the Gibbs-Duhem equation. $\Delta G^{\circ}$ is the Gibbs energy difference in Eq. 2.1 with all components pure, and is a function of temperature, pressure, and major element composition. The effects of *P* are predicted to be small owing to the small changes in the volume of the exchange reactions. The results of trace element partitioning are most readily examined by a plot of $X_{iB}$ against $X_{iA}$, which is expected to produce a straight line of slope $K_D$, passing through the origin.

In this study, two partition coefficients are defined. A single element, mass fraction, partition coefficient of trace element *i* between minerals A and B is defined by:

$$D_i = \frac{ppm\ i\ in\ A}{ppm\ i\ in\ B} \tag{2.5}$$

Although most geochemical models adopt a $D_i$, from thermodynamic and mineralogical stand-points it is more meaningful to calculate the proportion of atomic sites in the lattice filled by the trace element, out of the number of sites available to that element. This molar partition coefficient, $D_i^*$ is defined by:

$$D_i^* = \frac{X_i^A / n}{X_i^B / n} \tag{2.6}$$

where $n$ represents sum of the cations for the site assumed to contain element $i$. A and B again represent coexisting minerals. This approach produces a more realistic estimate of partitioning between phases, but loses validity outside the Henry's law region. For many trace elements and mineral phases, the position occupied by the atoms is not known, although site occupancies of metamorphic minerals may be made approximately on the basis of ionic radius and charge, because trace elements are presumed as a first approximation to fit into sites which most closely resemble their ionic radius and charge requirements (e.g., Dahl *et al.*, 1993). It is also difficult to define solution components, and to express concentration in terms of molar fraction. Thus, it is common practice to examine trace element distributions in terms of a mass fraction (ppm).

### 2.2.2 *P-T* effects on trace element distribution

The thermal dependence of the partition coefficient can be expressed by holding pressure and composition constant and assuming $\Delta H^\circ$ to be independent of temperature and pressure:

$$\left(\frac{\partial \ln K_D}{\partial 1/T}\right)_{P,X} = \frac{-\Delta H^o}{R} \tag{2.7}$$

where $\Delta H^o$ is enthalpy. A plot of $lnK_D$ versus $1/T$ is therefore linear, if the change of heat capacity, $\Delta C_p = 0$. However, the contribution to the $K_D$ of the excess chemical potential of $iA$ and $iB$ at an infinite dilution may be more important than that of $\Delta G^o$ for some trace elements. The situation is more comprehensible if we consider that substitution of a trace element in a crystal structure is commonly accompanied by local lattice deformation, the degree of which depends strongly on the amplitude of the thermal agitation of atoms in the immediate vicinity (Blundy and Wood, 1991 and 1994). Thus, it is expected that elements similar in size to the optimum ionic radius of the site will satisfy the relation (2.7), whereas those with markedly different ionic radii and charge will result in deviations from it.

Positive slopes on $lnK_D$ vs $1/T$ diagrams imply that the heat of reaction ($\Delta H_r$) is negative, but for incompatible elements it would seem to make more sense for this enthalpy to be positive. This is because if mineral A routinely rejects element $i$ from its structure, positive work must be expended to incorporate $i$ into A. If the heat of formation is treated as a Born-Haber sum, i.e.,

$$\Delta H_r = \Delta H_m + \Delta H_f \tag{2.8}$$

where $\Delta H_m$ is the heat of mixing (i.e., the change in enthalpy due to the change of chemical environment) and $\Delta H_f$ is the heat of formation. These are the only possible contributions to the heat of reaction, and in a system where both solid solutions are ideal, the heat of reaction will simply equal the heat of formation. For compatible elements,

$\Delta H_m$ may be negative; for incompatible elements $\Delta H_m$ is possibly positive. $\Delta H_f$ is negative and $\Delta H_r$ will be negative in all cases for compatible elements and it will be negative for incompatible elements if $\Delta H_f > |\Delta H_M|$. Thus, positive slopes on $lnK_D$ vs. $1/T$ diagrams for incompatible elements may indicate the control of element partitioning by the heat of formation.

The effects of temperature on trace element partitioning are difficult to predict because enthalpy changes for trace element exchange reactions are not available or cannot be calculated with sufficient precision using calorimetric data. However, the effects of temperature can be evaluated empirically if the temperature of equilibration can be determined for mineral pairs with known trace element contents. This exercise is carried out in Chapters 3 and 4 for garnet-biotite and biotite-muscovite pairs. The evaluation of thermal dependence of trace element partitioning can be difficult because: (1) there is no guarantee that trace element equilibration occurred at the same time and at the same temperature as that for the major elements, and (2) from a crystal-chemical point of view, $P$-$T$ would be a dependent variable if the major element partitioning on which temperatures are based affects the size and other properties of crystallographic sites available to the trace elements in ways that may or may not be similar to the effects of $P$-$T$ itself.

Pressure effects on trace element partitioning can be expressed as:

$$\left(\frac{\partial lnK_D}{\partial P}\right)_{T,X} = \frac{\Delta V}{RT} \tag{2.9}$$

Since trace elements usually substitute for host cations of similar ionic radius, the

difference between the volume terms on the right-hand side of Eq. 2.9 is generally small. It might be expected, therefore, that for many systems the partition coefficient will not vary appreciably with moderate changes of pressure (McIntire, 1962). However, there are examples of the pressure effects on trace element partitioning in both igneous and metamorphic systems. For example, Zn partitioning between clinopyroxene and olivine in igneous system is reported to change by 10-20% for a 5 kbar change in crystallization pressure (Johnson, 1994). In another example from igneous rocks, Liu *et al.* (1992) suggested that the optimum radius of the M2 site in clinopyroxene from basaltic melt was a function of pressure in the REE substitution and attributed the reason to decreasing M2-O interatomic distance in pyroxenes with increasing pressure. An example in metamorphic rocks is given by Enami *et al.* (1995), who suggested that increasing pressure favours incorporation of Na with Y and Yb into eclogitic garnets by a substitution $Na^{+}(Y,Yb)^{3+}(Ca,Mn)^{2+}_{-2}$.

### 2.2.3 Compositional effects on trace element distribution

If a solid solution is not ideal and there are interactions between the constituent molecules, the excess chemical potentials of these molecules contribute to the $K_D$. Examples of major element effects on trace element partitioning in metamorphic rocks include the increasing partition coefficient of V between garnet and biotite with increasing Ca content in garnet (Kretz, 1959), and the decreasing partition coefficients of Cr between garnet and biotite with decrease in the Mg/Fe+Mg+Mn in garnet (Korsman, 1975). Hendricks and Dahl (1987) also reported that $D_i$ values for $Fe^{3+}$, $Cr^{3+}$, and $V^{3+}$

between garnet and biotite increase from 7.7 to 12.7, 0.9 to 4.7, and 0.7 to 2.0, respectively, as the grossular component increases from 0.2 to 0.5. They attributed the reason to localized structural expansion accompanying increase in the grossular component of garnet.

### 2.2.4 Crystal chemical effects

It has been known for a long time that mineral-melt and mineral-fluid partition coefficients for series of isovalent cations show a near-parabolic dependence on cation radius (e.g. Onuma, 1968), indicating the controls of ionic radius, charge and crystal structure on the partitioning of trace elements. This has been shown for plagioclase (Blundy and Wood, 1991), amphibole (Liu *et al.*, 1992; LaTourrette *et al.*, 1995; Brenan *et al.*, 1995), clinopyroxene (Blundy *et al.*, 1995; Wood and Blundy, 1997), olivine (Beattie, 1994), and garnet (Liu *et al.*, 1992; van Westrenen *et al.*, 1999). Beattie (1994) explained these observations using lattice-strain models, based on the work of Nagasawa (1966) and Brice (1975). In the model of Blundy and Wood (1994), trace element partitioning on a given structural site is characterized by the site radius ($r_i$), its Young's modulus ($E$), and the strain-free partition coefficient $D_o$ for an element with ideal radius $r_o$:

$$\log D = \log D_0 - \frac{4\pi N_A E}{2.303RT}\left[\frac{r_0}{2}(r_i - r_0)^2 + \frac{1}{3}(r_i - r_0)^3\right] \qquad (2.10)$$

where $N_A$ is Avogadro's number, $R$ is the gas constant, and $T$ is in $K$. The apex of a peak in a distribution vs. ionic radius diagram (Onuma diagram) was assumed to be the optimum ionic radius for a cation in a given structural site, while the width of the peak

was interpreted as the ability of the lattice to adapt to non-ideal cations in that position, implying elasticity of the crystal lattice (Blundy and Wood, 1994). The peak position in an Onuma diagram can be shifted by major element composition (van Westrenen *et al.*, 1999) and pressure (Liu *et al.*, 1992).

One of the problems with Onuma diagrams is that they are made using a single coordination number, even if a mineral has two possible cation positions of different coordination number, because the relative distribution of an element between two such positions is seldom known. In addition, the ionic radii determined from the distances between ions in crystals depend on the structure of the crystal, and trace cations usually occur in distorted coordination sites where bond distance varies widely. Thus, careful interpretation will be required for ions displaying small differences in ionic radius.

The lattice-strain theory has rarely been applied to mineral-mineral systems. Reitan *et al.* (1980) reported that the REE distribution between coexisting clinopyroxene and orthopyroxene showed a parabolic curve on an Onuma diagram. Mason (1982) used similar approach to document the control of ionic radius on trace element distribution between K-feldspar and albite from a pegmatite. Unlike mineral-melt and mineral-fluid systems, where the bulk modulus is assumed to be dominated by minerals only, trace element partitioning in mineral-mineral systems is probably a more complicated function of ionic radius and charges because crystal structures and bulk-moduli in both minerals are important, resulting in various different shapes of curves in the Onuma diagram. However, the shapes of curves should vary systematically and continuously.

### 2.2.5 Crystal lattice strain and crystal field effects

Ionic size and charge of trace element has long been recognized that ionic size and charge have major effects on element substitution in crystals. The diagrams of the logarithm of partition coefficient *vs.* ionic radius (Onuma diagrams) provide an insight into the lattice control of trace element distributions in silicate mineral-melt systems (Onuma *et al.*, 1968; Jensen, 1973; Philpotts, 1978; Beattie, 1994; Blundy and Wood, 1994) and in mineral-mineral systems (Reitan *et al.*, 1980; Mason, 1982; and Liu *et al.*, 1992). In this diagram, all elements of the same valency give relatively smooth curves. These patterns suggest that ionic radius and crystal structure strongly influence the partitioning of trace elements. The apex of a peak in an Onuma diagram was assumed to be the optimum ionic radius for a cation in a given structural site, while the width of the peak was interpreted as the ability of the lattice to adapt to non-ideal cations in that position, implying elasticity of the crystal lattice (*e.g.*, Jensen, 1973). One of the problems of Onuma diagrams is that the diagrams are made using just one coordination number, even if a mineral has two cation positions of different coordination number, because the relative distribution of an element between two such positions is seldom known. In addition, the ionic radii determined from the distances between ions in crystals depend on the structure of the crystal, and cations usually occur in distorted coordination sites where bond distance varies widely. Thus, careful interpretation will be required for ions displaying small differences in ionic radius.

Site occupancies of metamorphic minerals can be made approximately on the basis of ionic radius and charge because trace elements are presumed as a first approximation

to fit into sites which most closely resemble their ionic radius and charge requirements. In garnet, it is to be expected that Ni, Co, Cu, Cr, Sr and Ba should be found in the X site of garnet in terms of ionic radius. However, Cr may occur in 6 coordination site as well as 8 coordination site in garnet (Meagher, 1982). The compatibility for the HREEs in garnet is a result of the dominance of Fe, Mg, and Ca in a small eight-fold coordination site which is ideally suited for the HREEs (Deer *et al.*, 1982). In biotite, the 6 coordination site is occupied by Mg and Fe and presumably also by the Mn, Cr, Ni, Co, and REE. The Ti may either be in this site or in the tetrahedral site.

Distribution of trace elements between coexisting metamorphic minerals can be greatly influenced by the nature of the structure of the minerals involved. One of the well-known structural controls on trace element distribution are crystal-field effects (*e.g.*, Schwarcz, 1967). When a transition metal ion is in a crystal structure, the effects of a non-spherical electrostatic field on the five degenerate orbitals is to lower the degeneracy by splitting the d-orbitals into different energies (Burns, 1993). The net stabilization energy is termed the crystal field stabilization energy (CFSE). The change in CFSE, $\Delta_{CFSE}$, for a transition metal ion depends on the ionic charge ($Q$), d-orbital radius ($r$), identity and symmetry of coordinated ligands, and interatomic distance ($R$) between metal ion and ligand, as indicated by

$$\Delta_{CFSE} = Q(r^4/R^5) \qquad (2.11)$$

(Burns, 1993). The inverse fifth-power relationship indicates that $\Delta_{CFSE}$ changes rapidly with variations of metal-ligand distances. The $\Delta_{CFSE}$ is also a function of both temperature and pressure. Pressure effects on $\Delta_{CFSE}$ are known to be negligible, but the temperature

effects are not well defined in metamorphic environments (Burns, 1993).

Transition metals will be preferentially concentrated in the phase in which they experience the largest $\Delta_{CFSE}$, assuming other free-energy changes associated with the substitution of the trace elements are negligible compared to $\Delta_{CFSE}$. Thus, the larger the $\Delta_{CFSE}$ for the ion, the more the ion will be fractionated into a given crystal site. Relative octahedral crystal field splitting parameters, $\Delta_o$, from Burns (1993), predict the following order of $D_i$ values for divalent cations in a mineral, if there is no further splitting of d orbitals,

Ni $(6/5\Delta_o)$ > Co $(4/5\Delta_o)$ > Cu $(3/5\Delta_o)$ > Mn $(0\Delta_o)$ = Zn $(0\Delta_o)$;

and for trivalent cations,

Cr $(6/5\Delta_o)$ > V $(4/5\Delta_o)$ > Sc $(0\Delta_o)$.

$Mn^{2+}$, $Fe^{3+}$, and $Sc^{3+}$ which do not undergo crystal field splitting, should experience no fractionation due to crystal field effects, but may be fractionated by differences in charge, size and covalency.

Schwarcz (1967) demonstrated that crystal-field stabilization is more important than ionic radius in accounting for the distributions of certain transition-metal ions among coexisting metamorphic minerals, a conclusion confirmed by other workers (e.g., Annersten and Ekström, 1971; Dupuy *et al.*, 1980; Hendricks and Dahl, 1987; and Dahl *et al.*, 1993). Dahl *et al.* (1993) demonstrated the crystal-field effects on trace element partitioning between muscovite and biotite based on the fact that the biotite cation-ligand distance of the octahedral site is shorter than that of muscovite. However, Cr distributions among coexisting metamorphic minerals shown by Sánchez-Vizcaíno *et al.* (1995) did

not follow the patterns predicted by $\Delta_{CFSE}$.

## 2.3 Analytical Techniques

Twenty samples from the Gagnon terrane were selected for bulk major and trace element determination, electron microprobe (EMP) analyses, and LAM-ICP-MS analyses. Whole-rock major and trace element compositions were determined by x-ray fluorescence (XRF) and solution ICP-MS, respectively.

### 2.3.1 EMP analyses

Major and minor element analyses were performed on the Cameca® SX-50 electron microprobe at Memorial University of Newfoundland using simultaneous energy dispersive (ED) and wavelength dispersive (WD). An accelerating voltage of 15 kV, a beam current of 20 nA and a beam diameter of 1-3 μm were used for most mineral analyses except for plagioclase and mica analyses. ED analyses used a cobalt gain calibration. Natural and synthetic standards were used for the calibration of WD analyses, with data reduction of raw counts performed with a Link® ZAF matrix-correction program.

Mica and plagioclase analyses were carried out using a 15 kV accelerating voltage, 10 nA current and a 5 μm beam diameter. Ti, F and Cl in micas were determined by WD analysis using ilmenite, apatite and tugtupite ($Na_4AlBeSi_4O_{12}Cl$) as standards, respectively. Precision at the 1σ level for Ti (used for calibration of LAM-ICP-MS

results, see below) was better than 6 relative % in both biotite and muscovite.

In each thin section two or three garnet/matrix pairs were analysed. Analyses by back-scattered electron (BSE) image analysis and spot WD X-ray analysis of all garnet grains were carried out as preliminary step to determine the equilibrium composition of garnet. If possible, rims of minerals in contact were analysed and the electron beam was placed about 15 μm in from the grain boundary to give the same analysis position as the laser analysis. The electron microprobe data were used for phase equilibria, to estimate metamorphic temperature and pressure, and as internal standards for LAM-ICP-MS data calculations (see below).

### 2.3.2 LAM-ICP-MS

Mineral separate analyses average the chemistry of zoned minerals, thereby losing the equilibrium compositions necessary for investigation of element partitioning. The micro-beam technique that is employed to overcome this limitation must have detection limits that are low enough for trace element investigation. The technique must also possess reasonable spatial resolution. LAM-ICP-MS meets these requirements (Jackson *et al.*, 1992; Jenner *et al.*, 1993; Bea *et al.*, 1994; Günther *et al.*, 1995; Fryer *et al.*, 1995; Fedorowich *et al.*, 1995). Concentrations of rare earth elements (REE) and selected transition trace elements (Sc, Ti, V, Cr, Mn, Co, Ni, Y, Zr, and Ba) were determined by LAM-ICP-MS at Memorial University of Newfoundland. REE are well known for their systematic variation in chemical properties, which provide an opportunity to examine crystal chemical effects on trace element partitioning. Metals of the transition groups

were selected because they substitute readily for iron and magnesium in the common ferromagnesian minerals such as garnet, staurolite and biotite.

Samples were chosen on the basis of petrographic and preliminary EMP studies, with maximum effort focused on garnet-bearing, low-variance assemblages in metapelitic and quartzo-feldspathic rocks. Polished thick sections (~100 μm) of samples were examined with optical and EMP methods before laser ablation to avoid mineral inclusions on the surface of laser analysis spots.

A laser sampler utilizing a frequency-quadrupled Nd:YAG laser source with a wavelength of 266 nm was coupled to a Fisons ®-VG PQII+"S" ICP-MS. The details of this system are described in Jackson *et al.* (1992), Jenner *et al.* (1994), and Taylor *et al.* (1997), and here we only present information pertinent to this study.

The laser was operated in Q-switched mode, with pulse energy optically attenuated to between 0.2 and 1 mJ and a pulse-repetition rate of 10 Hz. Data acquisition was performed by peak jumping in pulse counting mode, acquiring individual intensity data for each analyte isotope during each mass spectrometer sweep (~ 1 sec). A total of about 480 sweeps, comprising a gas background interval of about 200 sweeps followed by an ablation interval of about 280 sweeps was performed for each analysis. The laser pit sizes were generally about 30-60 μm in diameter, depending on target material, length of ablation, pulse energy and degree of defocusing.

Calibrations were made against the National Institute of Science and Technology (NIST) standard reference material (SRM) 610, which has a nominal abundance of 500 ppm of the trace elements concerned (Pearce *et al.* 1997). Calcium (for garnet, epidote,

plagioclase, apatite), Ti (for biotite, muscovite, ilmenite, rutile,), and Si (kyanite, chlorite), whose concentrations were previously determined by EMP analyses, were used as internal standards to correct for differences in ablation yield between samples and the calibration standard. Data reduction followed the protocol outlined by Longerich *et al.* (1996a). Concentrations and detection limits were calculated using algorithms derived by Longerich *et al.* (1996b).

The limit of detection, as defined by $3\sigma$ counting statistic errors, for BCR-2, a glass reference material, for a ~50 μm beam size and ~0.5 mJ/pulse, was typically in the range 3-35 ppb for most high-mass elements (Rb to Ta), and between 68 and 6000 ppb for lower-mass elements (Li to Zn) (Table 2.1). However, detection limits for samples are different from the glass standard because of different beam diameters, counting times and ablation energy used for each single analysis. Cr, Mn, Co, and Ni show systematically high backgrounds and low sensitivities compared to the other elements in every specimen, as also indicated by others (e. g., Horn *et al.*, 1994). These high backgrounds result in high detection limits for these elements.

Given the inherent heterogeneity of minerals and the impossibility of doing repeated measurements on the same spot, it is not possible to calculate the precision of the LAM-ICP-MS technique on natural samples. Instead, precision was estimated by repeated analyses of BCR-2 using operating conditions similar to those applied during routine analyses (Table 2.1). Repeated measurements of the BCR-2 glass at the same ablation conditions yielded precisions ($1\sigma$) of better than 5 and 10 % relative for absolute concentrations above and below 1 ppm, respectively, except for Cr and Ni. The poor

precision obtained for Cr and Ni is attributed to their concentrations approaching detection limits.

Potential sources of error in addition to counting statistic of laser signals include: (1) inaccuracies in the determination of the normalizing elements such as Ca, Si and Ti by EMP and mismatch between electron microprobe and laser spots; (2) analytical errors in the determination of calibration standard, (3) contamination from previously ablated grains or micro-inclusions within grains; and (4) fractionation of chalcophile elements such as Zn and Cu during sample ablation and plasma transportation. Great efforts were made to spatially match the LAM-ICP-MS and EMP analysis spots to reduce the first error, especially for garnet. However, because of the different sampling resolutions of the two techniques (μm for EMP *vs.* tens of μm for LAM-ICP-MS), accuracy can be degraded for minerals that possess significant fine-scale zoning in the normalizing elements. To reduce within-run fractionation, the laser was operated in defocused mode (*i.e.*, focused ~100 μm above the sample surface), thereby reducing the relative amount of defocusing of the laser beam during ablation. Despite these efforts, Zn and Cu display strong fractionation effects as indicated by invariably higher concentrations compared to the literature values (Table 2.1) and by increasing signals over time.

The time-resolved analysis of the LAM-ICP-MS allows detection of zoning and inclusions in the analyzed mineral grain during ablation, which is a great advantage over other microbeam techniques such as PIXE and SIMS. Detection of inclusions of minerals very different in composition from the host (*e.g.*, apatite or zircon in a silicate) was easily done by examination of the time-resolved signals. However, where micro-inclusions with

similar concentrations of trace elements are included in host minerals, detection of inclusions in the ablated spot is not easy, the only way being the internal consistency of the results. P, Si, Zr, Ba, and HREE were used as indicators of contamination in analyzed minerals by micro-inclusions and adjacent minerals. $ThO^+/Th^+$ was maintained below 0.5% to minimize molecular and doubly charged species production.

### 2.3.3 Whole-rock analyses

For ten representative pelite and calc-pelite samples, whole-rock determinations of major and trace element abundance were made by XRF and solution ICP-MS at the Department of Earth Sciences, Memorial University of Newfoundland (MUN). Samples were slabbed, examined to ensure that clean unaltered chunks were analyzed, crushed to pea-size using a jaw-crusher, and ground to powder in a tungsten-carbide puck mill.

***X-ray fluorescence:*** A Fisons/ARL® model 8420+ sequential wavelength-dispersion X-ray fluorescence spectrometer was used to analyze whole-rock major element concentrations. The details of XRF procedure for whole-rock samples analyzed at MUN are given in Longerich (1995). Samples were prepared as pressed pellets using 5 g of rock powder mixed with 0.7 g of BRP-5933 Bakelite® phenolic resin. Accuracy of the XRF data is evaluated by comparing the values determined for a standard rock. Relative precisions are approximately 2% for CaO, MgO, and $Al_2O_3$, and 5% for $SiO_2$, $TiO_2$ and $K_2O$.

***ICP-MS:*** Whole-rock concentrations of 14 rare-earth elements (REE) and six other trace-elements (Y, Zr, Nb, Ba, Hf, and Ta) were determined by solution inductively coupled plasma-mass spectrometry (ICP-MS; Perkin Elmer Sciex Elan® model 250), following acid digestion and sodium peroxide ($Na_2O_2$) sinter digestion procedures.

The analytical procedure for the acid digestion was as follows: (1) a $HF/HNO_3$ (+ boric and oxalic acids) digestion of a 0.1 g sample aliquot, (2) analysis of the solution by inductively coupled plasma mass spectrometry using the method of standard addition to correct for matrix effects. Details of the procedure are given in Jenner *et al.* (1990).

Acid resistant phases such as zircon, graphite, ilmenite and other oxides may not always dissolve completely even after multi-acid attack. A sodium peroxide sinter digestion method (Longerich *et al.*, 1990), was used for the analysis of Y, the REE and Th in these rocks. The analytical procedure was as follows: (1) sintering of a 0.2 g sample aliquot with sodium peroxide, (2) dissolution of the sinter cake, separation and dissolution of REE hydroxide-bearing precipitate, (3) analysis by ICP-MS using the method of internal standardisation to correct for matrix and drift effects. The advantage of the sintering technique is that it practically ensures complete digestion of resistant REE-bearing accessory phases (e.g. zircon, fluorite). Full details of the procedure are given in Longerich *et al.* (1990).

For quality control, one or more geological reference material standards were prepared and analyzed with samples, together with a reagent blank. Sample detection limits in ppm are generally about 10% of chondritic values. For most elements, the precision of the method, determined from multiple analyses of several international

reference standards, is 3-7%.

Synthetic solutions were used to calibrate the ICP-MS. Standard reference materials, MRG-1 and BR-688, and reagent blanks were analyzed for quality-control purposes.

## 2.4 Textures and mineral chemistry

Representative analyses of 10 minerals from the 20 samples are presented in Table 2.3. Details of major and trace element chemistries of garnet, biotite and muscovite are provided in Chapters 3 and 4.

### 2.4.1 Garnet

Garnet porphyroblasts displaying features indicative of growth in a static environment, such as concentric bands of ilmenite and quartz inclusions, coexist with garnet porphyroblasts showing rotational fabrics in their cores in the same thin-section. In the garnets with rotational fabrics, the rims are post-kinematic and asymmetric pressure shadows are associated with the external $S_2$ foliation. Garnets in the garnet+biotite zone are small (less than a few mm) euhedral porphyroblasts. In contrast, garnets above the garnet+biotite zone are large (up to a few cm) and occur as irregular anhedral porphyroblasts that are commonly rich in inclusions. Most of the garnets are differentially resorbed, with their irregular habits due to both prograde and retrograde stages of metamorphism. The inclusions in garnet are used to evaluate phase relations early in the history of the samples and the reactions involved in garnet growth.

The garnet crystals consist of variably zoned, spessartine-rich (up to 6.5 wt%),

almandine garnets with Mg-rich rims, and Fe- and Mn-rich cores. In keeping with their more Ca-rich bulk compositions, the garnets from calc-pelites are more Ca-enriched (up to 8.9 wt%) than garnets from typical pelites. The abundance and zoning of Ca in garnet in calc-pelites in Gagnon terrane is similar to that reported in garnets from calc-pelites in the Strafford Dome, Vermont (Menard and Spear, 1993).

Gagnon terrane garnets have high abundances of Li, Sc, V, Cr, Co, Zn, Y, MREE and HREE, but have extremely low concentrations of Ni, Rb, Sr, Nb, Cs, Ba, LREE, Hf and Ta (Table 2.3 and Fig. 2.2a). Chondrite-normalized REE patterns of representative garnet rims (Fig. 2.3a) show irregular profiles in the REE from La to Nd due to high analytical errors involved, small negative Eu anomalies and a strong, progressive increase from Sm to Dy. However, the patterns of chondrite-normalized REE between Dy and Lu vary significantly from sample to sample and are not related to metamorphic grade. The variable degree of HREE fractionation may reflect differences in mineral assemblages and reaction history (see Chapter 7). The details of trace element zoning in garnets are provided in Chapters 6 and 7.

### 2.4.2 Biotite

Analyzed biotite crystals are all of intermediate $X_{Fe}$ (0.36-0.58) and moderate $TiO_2$ content (0.8-2.13 wt%; Table 2.3). Biotite adjacent to the retrograded rims of garnets are more Fe-rich and Ti-poor than matrix biotite. Biotite inclusions in garnet are more Fe-rich than matrix biotites. The F content of biotite is up to 0.6 wt% and Cl contents are low.

Biotite crystals are rich in Li, Rb, Nb, Cs and Ba as well as in first-row transition elements, but have extremely low concentrations of Y and REE (Table 2.3 and Fig. 2.2). The chondrite-normalized REE diagram for biotite (Fig. 2.3b) shows enrichment of LREE over HREE with a small negative Eu anomaly regardless of the total REE abundance in the biotite. This pattern is similar to that of biotite from a migmatite analyzed by the LAM-ICP-MS technique (Bea *et al.*, 1994), but different from flat or HREE-enriched, chondrite-normalized REE profiles from biotite mineral separates (Roaldset, 1975; van Breemen, 1980; Gromet and Silver, 1983). Invariably high REE contents from the bulk analyses of biotite separates point to contamination from REE-rich micro-inclusions in biotite. Partitioning of selected trace elements between garnet and biotite is discussed in detail in Chapter 3.

### 2.4.3 Muscovite

Muscovite is the predominant matrix phase in several samples and occurs in three habits: (1) elongate foliation-defining grains; (2) reaction product after garnet; and (3) inclusions in garnet. Muscovite compositions are moderately phengite-rich (Si/22 oxygens = 6.18-6.28); these Si contents are higher than low-pressure facies series micas of amphibolite grade (Guidotti, 1978; Miyashiro and Shido, 1985). Muscovite becomes more Si-rich at higher pressures in K-buffered assemblages (Massone and Schreyer, 1987). $X_{Na}$ (=Na/Na+K) values are below 0.19. Retrograde muscovite crystals developed around garnet porphyroblasts differ from normal prograde muscovite crystals in their higher Fe/Mg ratios and Ti contents. F and Cl contents of muscovite are low.

Muscovite contains significant concentrations of Li, Sc, V, Cr, Zn, Rb, Sr, and Ba (Table 2.3 and Fig. 2.2c). In contrast, Y, Zr, REE, Hf and Ta are extremely low in muscovite. Chondrite-normalized REE patterns (Fig. 2.3c) show a weak LREE/HREE fractionation or flat profiles with strong positive Eu anomalies. In comparison, mineral separate analyses of muscovite from greenschist-amphibolite facies transition (Roaldset, 1975) show flat chondrite-normalized REE patterns with a large variation in the average normalized values (20 to 100), which are much greater than those from Gagnon terrane (< 10), implying bulk muscovite analyses of mineral separates were also contaminated by REE-rich micro-inclusions. Partitioning of selected trace elements between biotite and muscovite is discussed in detail in Chapter 4.

### 2.4.4 Staurolite

Staurolite is mainly found in low-Ca, high-Fe pelites. Sector zoning is not observed in staurolite porphyroblasts in Gagnon terrane. Staurolite is a late-stage mineral invariably overgrowing the $S_2$ foliation and locally retrograded to sericite. Staurolite crystals have high Fe/Fe+Mg ratios (0.67~0.88).

Li and Zn contents are high (up to 1152 and 1060 ppm, respectively) and V, Cr, Co and Ni abundances are moderate (Table 2.3 and Fig. 2.2d). High Li and Zn contents in staurolite are known to exist (e.g. Dutrow, 1986), but we were unable to find any mention in the literature of the concentrations of transition elements in staurolite. REE in staurolite are below LAM-ICP-MS detection limits.

### 2.4.5 Kyanite

Kyanite is found in two habits, large ($Ky_1$) and small ($Ky_2$) grains (van Gool, 1992), implying two different generations of kyanite. Kyanite crystals display oscillatory zoning defined by Cr under cathode luminescence. Up to three rings were observed, mainly in $Ky_1$. The numbers of rings are not related to metamorphic grade. Kyanite contains no detectable trace impurities at high concentrations except for Fe, Li, V and Cr (Table 2.3 and Fig. 2.2e). Trace element zoning in kyanite is discussed in detail in Chapter 6.

### 2.4.6 Epidote

Epidote is included in many garnets and is also found as a matrix phase in a few calc-pelite samples. In several samples, epidote inclusions are restricted to the cores of garnet where they do not exist rimward of a textural unconformity defined by a decrease in the abundance of inclusions. The small grain-size of these epidote inclusions precludes investigation of trace element zoning in many individual grains. One large epidote inclusion in garnet that was analyzed by LAM-ICP-MS shows strong enrichments in Sc, V, Cr, Sr and Y and moderate enrichments in Ni and Zn (Table 2.3 and Fig. 2.2f).

Epidote is commonly enriched in LREE over HREE (Grauch, 1989; Sorensen and Grossman, 1989; Pan and Fleet, 1996; Finger *et al.*, 1998) because of the larger A2 site in epidote which is suitable for the incorporation of LREE. However, the epidote inclusion in garnet from sample P-11 shows a marked enrichment in chondrite-normalized MREE over LREE and HREE, with a positive Eu anomaly (Fig. 2.3d), which is similar to epidote crystals from eclogitic gabbro (Tribuzio *et al.* 1996). Pan and Fleet (1996)

suggested that the pattern of REE in epidote can be controlled by both crystal chemical factors and external factors such as the composition of metasomatic REE-rich fluids. For example, they reported epidote and clinozoisite enriched in HREE over LREE from hydrothermal veins. The MREE-enriched, chondrite-normalized pattern in the Gagnon epidote in Fig. 2.3d may have been produced by growth of LREE-enriched minerals such as monazite, titanite and allanite during epidote growth if metasomatic infiltration of MREE-rich fluid can be excluded. This topic is discussed further in Chapter 7.

### 2.4.7 Plagioclase

Plagioclase recrystallized throughout the thermal history of the region; it is included in garnets, and yet is also a late mineral, overgrowing the $S_2$ foliation. However, it occurs primarily as porphyroblasts (1-3 mm in size). Zoning in the porphyroblasts is pronounced. The majority of grains have sodic cores and calcic rims. Plagioclase inclusions in garnet are commonly more sodic than matrix grains.

Plagioclase is rich in Sr, has moderate concentrations of Ba and REE, and extremely low concentrations of Li, Rb, Cs, and the transition metals (mostly below detection limits, Table 2.3 and Fig. 2.2g). Ca contents are correlated with Sr ($r = 0.81$) and also have some positive correlation with Ba. The correlation between Sr and Eu is excellent. Chondrite-normalized patterns (Fig. 2.3e) show moderate LREE/HREE fractionation (La/Lu=50-180) and a strong positive Eu anomaly (Eu/Eu*=15-30).

2.4.8 Fe-Ti-oxides and apatite

Ilmenite predominates over rutile in Fe-rich, staurolite-bearing pelites and in low grade rocks. Rutile is the predominant Ti-oxide in high grade rocks and commonly overgrows early ilmenite. Ilmenite and rutile occur as inclusions in virtually every porphyroblast and matrix mineral. Ilmenite is strongly enriched in Zn and Nb and moderately enriched in V, Cr and Co (Table 2.3 and Fig. 2.2h). Rutile is strongly enriched in V, Cr, Ni, Zr and Nb (Table 2.3 and Fig. 2.2i). The concentrations of REE in ilmenite and rutile are negligible. Magnetite is found only as inclusions in garnet in Fe-rich rocks and was not analysed in this study.

Apatite has high Sr, Y and REE contents (Table 2.3 and Fig. 2.2j). Chondrite-normalized REE patterns of apatite are provided in Fig. 2.3f. Apatite is known to be commonly enriched in LREE (Gromet and Silver, 1983; Finger *et al.*, 1998; Gulii and Jarvis, 1998). The chondrite-normalized REE pattern of apatite 88-32 (Fig. 2.3f) shows the typical pattern characterized by slight depletion from La to Nd, a negative Eu anomaly, and HREE depletion. Relative to the apatite from samples 88-32, the remaining four apatites show more marked depletions in LREE and HREE. This pattern is similar to apatite from metasomatized, migmatitic garnet amphibolite (Sorensen and Grossman, 1989) and eclogitic gabbro (Tribuzio *et al.*, 1996). As in the case of epidote, REE patterns in apatite are also controlled by coexisting REE-rich minerals or metamorphic fluids.

Pyrrhotite, tourmaline, zircon, xenotime, allanite, barite, and thorite also occur as accessory minerals in the analyzed samples. Due to their small grain size, analysis of

trace element concentrations for these minerals was not attempted.

## 2.5 Distribution of trace elements in coexisting metamorphic minerals

The average partitioning data for all trace elements analyzed between the ten coexisting minerals are presented in Table 2.4 and distribution matrices for selected elements between these phases are summarized for twenty samples in Fig. 2.4. Na, P, Ca and Ti are not considered because their chemical potentials are defined by equilibria between Na-, P-, Ca-, and Ti-bearing silicates, phosphates and oxides, and hence are not amenable to treatment by using a partition coefficient approach.

Forty-five distribution coefficients must be specified to fully describe the distribution of a trace element among the ten mineral phases. Only nine of these distribution coefficients are independent provided they are chosen to include every mineral at least once, i.e., a specification of any nine will determine the remaining thirty-six, which are referred to as dependent ratios (see Kretz *et al.*, 1999). Approximate relative orders of trace element enrichment among the analyzed minerals are provided in Fig. 2.4 for selected elements. The sources of variation in average distribution coefficients include: change in *P-T* ranging from greenschist to upper amphibolite facies, compositional zoning in refractory minerals, major element phase composition, and possibly disequilibrium partitioning, especially for slow diffusing elements such as Cr (see chapter 6). With all these caveats in mind, the general patterns of trace element distribution between minerals analyzed in this study are described below.

Scandium and Y are slightly enriched in epidote compared to coexisting garnet; the

relative order of enrichment of Sc and Y is Ep > Grt > Rt > Ms ≈ Ilm ≈ Bt > Pl > Ap > Ky and Ep > Grt > Ap > Ilm > Pl ≈ Bt > Ms > Ky, respectively (Figs. 2.4 a, f). Garnet is expected to take up the majority of the Sc and Y released by the breakdown of epidote. Concentrations of Sc in kyanite are the lowest compared to garnet among the investigated minerals, resulting in distribution coefficients (Grt/Ky) as high as 986. Distribution of LREE is mainly controlled by apatite (Table 2.4), whereas MREE are nearly equally shared by apatite and epidote (Fig. 2.4h). In contrast, HREE show a preference for garnet (Table 2.4), indicating garnet incorporates increasing amounts of the smaller REE relative to coexisting minerals.

Lithium, Cr, Co and Zn are strongly enriched in staurolite; $D_{Li}$ (Grt/St) is 0.29 (Table 2.4) and the relative order of Zn enrichment is St > Bt ≈ Ilm > Ms > Grt > Rt > Ap ≈ Ep (Fig. 2.4e). Li and Zn released by breakdown of staurolite are mainly incorporated by biotite and muscovite, and biotite and ilmenite, respectively. Consideration of Fig. 2.4c suggests that Cr is incorporated into metamorphic minerals in approximately the following order: St ≈ Ky ≈ Bt ≈ Ms ≈ Grt ≈ Ep > Rt > Ilm > Ap. Chromium is nearly equally shared by staurolite and kyanite. After breakdown of staurolite and kyanite, Cr will be mainly incorporated into micas.

Nickel, Rb and Cs are highly concentrated in biotite (Table 2.4). In contrast to the preliminary study of Hickmott and Spear (1992), V is not enriched in ilmenite compared to other minerals in Gagnon terrane. Vanadium is most strongly enriched in epidote with the following order of enrichment; Ep > Rt ≈ Ms > Bt ≈ St > Ky > Ilm ≈ Grt > Ap (Fig. 2.4b). Strontium is strongly enriched in plagioclase and muscovite, with epidote and

apatite containing similar amounts of Sr. Niobium, Zr, Hf and Ta are strongly enriched in rutile. However, the compositions of rutile inclusions in garnet may not represent equilibrium compositions with other matrix minerals. Strong enrichment of Nb and Zr in rutile from eclogites is reported by Sassi *et al.* (2000) and Zack *et al.* (in press). Relative Zr partitioning is apparently: Rt > Grt ≈ Ep > Ilm > Ms > Bt > Ap > St ≈ Pl (Fig. 2.4g). Zr is nearly equally partitioned between epidote and garnet. The data presented show that, at least for the rocks we have analyzed, garnets in the pelitic rocks, and both garnet and epidote in the calc-pelites, represent significant repositories of the whole-rock Zr budget because no other major phases contain comparable amounts of Zr. It follows from these observations that breakdown of either garnet or epidote in rocks such as these will release Zr.

Table 2.1. Precision and mean values for a glass standard BCR-2 determined by LAM-ICP-MS.

| Elements | AVG | STD | RSD | DL | No | Known | AVG/Known |
|---|---|---|---|---|---|---|---|
| Li | 8.4 | | | 5.95 | 1 | 9.98 | 0.84 |
| Sc | 31 | 0.8 | 2% | 0.65 | 5 | 32.6 | 0.96 |
| $TiO_2$ | 2.05 | 0.04 | 2% | 0.000 | 10 | 2.24 | 0.91 |
| V | 402 | 11 | 3% | 0.06 | 7 | 407 | 0.99 |
| Cr | 15 | 2.5 | 16% | 2.50 | 6 | 16 | 0.94 |
| MnO | 0.18 | 0.01 | 4% | 0.000 | 7 | 0.177 | 1.03 |
| Co | 36 | 1.7 | 5% | 0.32 | 7 | 37 | 0.98 |
| Ni | 11 | 1.4 | 12% | 1.04 | 7 | 13 | 0.87 |
| Zn | 173 | 12 | 7% | 0.58 | 5 | 129.5 | 1.33 |
| Cu | 20 | 1.0 | 5% | 0.35 | 5 | 19 | 1.08 |
| Rb | 54 | | | 0.01 | 2 | 47.51 | 1.14 |
| Sr | 337 | 7.6 | 2% | 0.00 | 5 | 337 | 1.00 |
| Y | 31 | 1.7 | 5% | 0.00 | 7 | 32.51 | 0.98 |
| Zr | 170 | 6.3 | 4% | 0.02 | 10 | 184.4 | 0.92 |
| Nb | 10 | 1.0 | 9% | 0.00 | 5 | 13.14 | 0.82 |
| Cs | 1.3 | | | 0.01 | 2 | 1.19 | 1.09 |
| Ba | 644 | 21 | 3% | 0.03 | 10 | 681 | 0.95 |
| La | 25 | 1.1 | 4% | 0.00 | 7 | 25.3 | 1.01 |
| Ce | 54 | 1.7 | 3% | 0.00 | 9 | 53.6 | 1.01 |
| Hf | 4.8 | 0.3 | 5% | 0.02 | 7 | 5.17 | 0.94 |
| Ta | 0.6 | 0.1 | 9% | 0.00 | 7 | 0.78 | 0.77 |

Based on 10 determinations over the period March 19, 1996 to April 5, 1997. AVG=average; STD=standard deviation; RSD=relative standard deviation; DL=detection limits; No=number of observations; and Known=literature values from Govindaraju (1994).

Table 2.2. Bulk-rock compositions of selected metapelites from Gagnon terrane determined by XRF and ICP-MS.

| Element | 87-279* | 87-283* | 87-51 | 87-86 | 88-45 | 88-57* | 88-74 | 88-85 |
|---|---|---|---|---|---|---|---|---|
| (wt %) | | | | | | | | |
| $SiO_2$ | 51 | 47 | 57 | 60 | 55 | 55 | 54 | 55 |
| $TiO_2$ | 0.0154 | 0.027 | 0.0084 | 0.0085 | 0.009 | 0.0087 | 0.0082 | 0.0086 |
| $Al_2O_3$ | 0.15 | 0.14 | 0.19 | 0.22 | 0.20 | 0.15 | 0.23 | 0.22 |
| $FeO^{\#}$ | 0.1163 | 0.1333 | 0.0693 | 0.0484 | 0.081 | 0.0853 | 0.0784 | 0.0747 |
| MgO | 6.65 | 7.47 | 4.99 | 3.71 | 3.71 | 7.35 | 5.40 | 4.15 |
| MnO | 0.0022 | 0.0018 | 0.001 | 0.0009 | 0.0003 | 0.0008 | 0.0008 | 0.0005 |
| CaO | 1.34 | 2.83 | 1.01 | 0.70 | 0.52 | 1.81 | 0.49 | 0.32 |
| NaO | 0.01 | 0.02 | 0.03 | 0.01 | 0.01 | 0.03 | 0.02 | 0.01 |
| $K_2O$ | 0.04 | 0.04 | 0.05 | 0.06 | 0.04 | 0.04 | 0.05 | 0.05 |
| | | | | | | | | |
| (ppm) | | | | | | | | |
| Sc | 19 | 21 | 14 | 22 | 15 | 17 | 16 | 19 |
| V | 363 | 250 | 122 | 97 | 129 | 149 | 139 | 152 |
| Cr | 154 | 119 | 134 | 120 | 227 | 339 | 243 | 232 |
| Ni | 25 | 34 | 10 | 18 | 0 | 58 | 74 | 35 |
| Cu | 38 | 52 | 25 | 15 | 16 | 36 | 20 | 37 |
| Zn | 104 | 146 | 52 | 38 | 49 | 60 | 55 | 86 |
| Sr | 82 | 169 | 151 | 76 | 102 | 313 | 36 | 71 |
| Y | 25 | 31 | 11 | 21 | 17 | 2 | 16 | 20 |
| Zr | 251 | 321 | 246 | 282 | 141 | 213 | 90 | 119 |
| Nb | 27 | 21 | 19 | 19 | 15 | 12 | 7 | 16 |
| Ba | 536 | 587 | 951 | 1367 | 463 | 558 | 338 | 634 |
| La | 30 | 35 | 7 | 32 | 34 | 17 | 46 | 29 |
| Ce | 69 | 81 | 21 | 94 | 67 | 40 | 93 | 56 |
| Pr | 8 | 9 | 2 | 8 | 8 | 4 | 10 | 6 |
| Nd | 31 | 36 | 8 | 26 | 28 | 12 | 38 | 21 |
| Sm | 5.95 | 6.92 | 1.71 | 5.35 | 4.64 | 1.61 | 6.58 | 3.95 |
| Eu | 1.15 | 1.72 | 0.37 | 0.94 | 1.07 | 0.52 | 1.14 | 0.80 |
| Gd | 5.06 | 6.47 | 1.40 | 3.87 | 3.64 | 0.89 | 4.73 | 3.75 |
| Tb | 0.78 | 0.93 | 0.24 | 0.62 | 0.55 | 0.11 | 0.60 | 0.69 |
| Dy | 4.74 | 5.56 | 1.77 | 3.85 | 3.28 | 0.50 | 3.26 | 4.03 |
| Ho | 1.00 | 1.14 | 0.43 | 0.81 | 0.62 | 0.09 | 0.63 | 0.77 |
| Er | 3.07 | 3.51 | 1.55 | 2.50 | 1.70 | 0.26 | 1.69 | 2.14 |
| Tm | 0.47 | 0.58 | 0.27 | 0.39 | 0.22 | 0.05 | 0.22 | 0.30 |
| Yb | 3.12 | 3.81 | 1.97 | 2.82 | 1.41 | 0.34 | 1.49 | 1.91 |
| Lu | 0.49 | 0.59 | 0.33 | 0.42 | 0.20 | 0.07 | 0.17 | 0.27 |
| Hf | 5.67 | 6.60 | 5.50 | 6.84 | 3.31 | 5.49 | 2.24 | 2.91 |
| Ta | 2.01 | 1.57 | 2.15 | 2.58 | 2.14 | 1.68 | 1.44 | 1.77 |
| | | | | | | | | |
| La/Sc | 1.60 | 1.68 | 0.53 | 1.44 | 1.87 | 1.26 | 2.42 | 1.53 |

Notes: * Calc-pelites (epidote-bearing); # Total Fe as FeO.

Table 2.3 Mineral compositions determined by EMP and LAM-ICP-MS.

| | 87-255 | | | 87-271 | | 87-279D | | | 87-283E | |
|---|---|---|---|---|---|---|---|---|---|---|
| | Grt | St | Ilm | Grt | Bt | Grt | Bt | Ms | Grt | Bt |
| $SiO_2$ | 37.70 | 28.80 | 0.17 | 37.30 | 36.90 | 37.80 | 37.16 | 46.92 | 37.20 | 36.00 |
| $TiO_2$ | | 0.52 | 52.06 | | 0.80 | | 1.65 | 0.74 | | 1.70 |
| $Al_2O_3$ | 21.10 | 54.00 | | 20.80 | 18.30 | 21.00 | 17.64 | 33.53 | 21.00 | 16.90 |
| FeO | 38.70 | 14.60 | 49.08 | 29.10 | 24.00 | 30.30 | 17.93 | 1.59 | 27.40 | 18.90 |
| MgO | 2.20 | 1.10 | 0.15 | 0.90 | 7.90 | 2.40 | 11.25 | 1.29 | 1.80 | 10.30 |
| MnO | 0.70 | | | 6.50 | 0.30 | 2.90 | 0.18 | 0.01 | 4.20 | 0.20 |
| CaO | 1.30 | | | 6.50 | | 6.70 | | | 8.90 | |
| $Na_2O$ | 0.02 | | | | | | | 0.90 | | 0.30 |
| $K_2O$ | | | | | 9.40 | | 9.94 | 10.19 | | 9.20 |
| F | | | | | | | 0.59 | 0.11 | | |
| Cl | | | | | | | 0.07 | | | |
| Total | 101.72 | 99.02 | 101.47 | 101.10 | 97.60 | 101.10 | 96.41 | 95.27 | 100.50 | 93.50 |
| | | | | | | | | | | |
| Li | | 1152 | | | 156 | | 121 | 73 | | 146 |
| Na | 35 | 217 | | | | | | | | |
| $P_2O_5$ | 0.09 | | | | | | | | | |
| CaO | 0.29 | | | 7.40 | | 6.70 | | | 8.90 | |
| Sc | 38 | | | 70 | 13 | 61 | 14 | 51 | 81 | 18 |
| $TiO_2$ | 0.01 | 0.53 | 50.98 | 0.04 | 0.80 | 0.03 | 1.65 | 0.74 | 0.04 | 1.78 |
| V | 20 | 128 | 63 | 62 | 168 | 130 | 636 | 1262 | 116 | 544 |
| Cr | 110 | 462 | 62 | 316 | 298 | 110 | 192 | 354 | 59 | 215 |
| MnO | | | | | | 2.90 | 0.17 | 0.01 | 3.90 | 0.10 |
| Co | 33 | 126 | 62 | 6.2 | 42 | 6.4 | 19 | | 9.0 | 43 |
| Ni | | | | | 70 | | 38 | | | 86 |
| Cu | | | | | | 10 | 15 | | | 15 |
| Zn | 24 | 1069 | 235 | | 178 | 73 | 628 | 33 | 63 | |
| Rb | | | 0.67 | | 488 | | | | | |
| Sr | | | 2.3 | | 2.3 | | 1.9 | 165 | | 1.2 |
| Y | 15 | | 0.13 | 147 | 0.22 | 257 | 1.9 | 0.26 | 258 | 0.78 |
| Zr | | | | 1.2 | 0.15 | 0.95 | 0.22 | 0.59 | 1.1 | 0.68 |
| Nb | | | | | 11 | | 34 | 13 | | 26 |
| Cs | | | | | 12 | | | | | |
| Ba | | | 2.4 | 0.07 | 1489 | | 1264 | 4804 | | 2027 |
| La | | 0.01 | 0.04 | | 5.7 | 0.01 | 3.4 | 0.13 | | 1.2 |
| Ce | | | | | | | 8.5 | 0.55 | | 2.4 |
| Pr | | | | | 1.3 | | 1.4 | 0.10 | 0.01 | 0.29 |
| Nd | | | | | | | 6.2 | 0.34 | | 1.3 |
| Sm | 0.10 | | | 0.79 | 0.74 | 0.32 | 1.2 | 0.11 | | |
| Eu | 0.07 | | | 1.7 | 0.19 | 0.24 | 0.16 | 0.08 | 0.08 | |
| Gd | | | | 6.9 | | 4.2 | 0.76 | 0.10 | 0.57 | |
| Tb | 0.30 | | 0.01 | 2.4 | 0.02 | 3.2 | 0.08 | 0.01 | 0.84 | |
| Dy | | | | | | 46 | 0.47 | 0.09 | 19 | 0.15 |
| Ho | 0.66 | | | 4.2 | 0.02 | 12 | 0.08 | 0.01 | 10 | |
| Er | | | | | | 28 | 0.20 | 0.03 | 54 | |
| Tm | 0.27 | | | 1.5 | | 3.1 | 0.03 | | 8.4 | 0.01 |
| Yb | | | | | | 15 | 0.13 | | 52 | |
| Lu | 0.27 | | | 1.4 | | 1.7 | 0.04 | | 6.7 | 0.01 |
| Hf | | | | 0.06 | | 0.02 | 0.02 | 0.10 | 0.05 | 0.08 |
| Ta | | | | 0.01 | 0.75 | | 2.3 | 0.19 | | 1.2 |

Note: Oxides are in wt%, elements are in ppm.

Table 2.3 Continued.

| | 87-283E | 87-287 | | 87-81A | | | | | | 87-83C |
|---|---|---|---|---|---|---|---|---|---|---|
| | Ilm | Grt | Ap | Grt | Grt | Bt | Ms | Pl | Ap | Grt |
| $SiO_2$ | 0.10 | 39.50 | 3.00 | 37.30 | 37.50 | 36.93 | 47.02 | 67.80 | | 37.30 |
| $TiO_2$ | 50.20 | 0.02 | | | | 1.56 | 0.39 | | | |
| $Al_2O_3$ | | 22.00 | | 20.80 | 20.80 | 17.35 | 34.44 | 19.80 | | 20.80 |
| FeO | 44.50 | 28.80 | | 31.70 | 31.60 | 19.92 | 1.76 | | | 30.00 |
| MgO | 0.20 | 4.60 | | 1.90 | 1.90 | 10.08 | 1.09 | | | 1.80 |
| MnO | 2.10 | 0.80 | | 2.40 | 2.70 | 0.20 | 0.01 | | | 3.70 |
| CaO | | 7.80 | 55.50 | 6.50 | 6.80 | | | 2.30 | 56.20 | 7.00 |
| $Na_2O$ | | 0.03 | 0.03 | | | | 0.88 | 9.80 | | |
| $K_2O$ | | | | | | 9.26 | 10.07 | | | |
| F | | | | | | 0.36 | 0.09 | | | |
| Cl | | | | | | 0.14 | | | | |
| Total | 97.10 | 103.55 | 58.53 | 100.60 | 101.30 | 95.81 | 95.75 | 99.70 | 56.20 | 100.60 |
| | | | | | | | | | | |
| Li | | | | | | 659 | | | | |
| Na | | | | | | | | | | |
| $P_2O_5$ | | | | | | | | | 42 | |
| CaO | | 7.50 | 56.04 | 6.50 | 6.80 | | 0.10 | 2.30 | 56.10 | 7.00 |
| Sc | 13 | 78 | | | 102 | 18 | 41 | | | 65 |
| $TiO_2$ | 50.30 | 0.04 | | 0.03 | 0.05 | 1.56 | 0.39 | | | 0.05 |
| V | 129 | 50 | 1.3 | 36 | 45 | 165 | 243 | | | 69 |
| Cr | | 58 | | 134 | 33 | 155 | 89 | | | 33 |
| MnO | 2.13 | 0.79 | 0.03 | 2.16 | 2.26 | 0.16 | 0.01 | | 0.05 | 4.05 |
| Co | 26 | 19 | | 9.5 | 10 | 40 | | | | 17 |
| Ni | | | | | | 95 | | | | |
| Cu | | | | | | 6.7 | | | | |
| Zn | 415 | 61 | | 38 | 32 | 282 | 17 | | | 61 |
| Rb | | | | | | | | | | |
| Sr | 5.6 | | | | | 1.7 | 69 | | 133 | |
| Y | 0.49 | 152 | 217 | 458 | 357 | 0.95 | | | 161 | 15 |
| Zr | 0.69 | 2.9 | 0.39 | 0.97 | 1.9 | 1.8 | 0.12 | | | 1.9 |
| Nb | 158 | | | | | 39 | 18 | | | |
| Cs | | | | | | | | | | |
| Ba | | | | 0.40 | | 857 | 3794 | 12 | | |
| La | | | 6.8 | | | 1.4 | 0.02 | 0.03 | | |
| Ce | | | 20 | | 0.07 | 4.5 | 0.14 | 0.15 | | 0.02 |
| Pr | | | 3.3 | | | 0.53 | | | | |
| Nd | | | 19 | | | 2.1 | | | | |
| Sm | | 0.61 | 9.5 | | | 0.43 | | | | 0.18 |
| Eu | | 0.75 | 1.5 | | 0.16 | 0.08 | | | | 0.18 |
| Gd | | 5.2 | 19 | | 1.6 | 0.19 | | | | 3.0 |
| Tb | | 2.5 | 5.0 | | 1.2 | 0.03 | | | | 1.7 |
| Dy | | 23 | 33 | | 34 | 0.19 | | | | 20 |
| Ho | | 5.2 | 7.9 | | 17 | 0.04 | | 0.01 | | 4.7 |
| Er | | 12 | 18 | | 84 | 0.14 | | | | 13 |
| Tm | | 1.6 | 2.9 | | 18 | | | | | 1.7 |
| Yb | | 8.5 | 17 | 111 | 128 | 0.12 | | | | 9.7 |
| Lu | | 1.3 | 2.3 | | 18 | 0.01 | | | | 1.2 |
| Hf | | | | | | 0.08 | 0.04 | 0.08 | | |
| Ta | | | | | | 2.5 | 0.49 | | | 0.02 |

Note: Oxides are in wt%, elements are in ppm.

Table 2.3 Continued.

| | 87-83C | | | 87-86C | | | | | 88-32B | |
|---|---|---|---|---|---|---|---|---|---|---|
| | Bt | Ms | Ilm | Grt | Bt | Ms | Pl | Ap | Grt | Bt |
| $SiO_2$ | 36.98 | 46.47 | 0.20 | 37.2 | 37.23 | 47.17 | 62.30 | | 37.60 | 35.92 |
| $TiO_2$ | 1.57 | 0.38 | 51.40 | | 1.62 | 0.45 | | | | 1.54 |
| $Al_2O_3$ | 17.67 | 34.14 | | 20.7 | 17.75 | 33.85 | 22.80 | | 21.20 | 17.58 |
| FeO | 19.57 | 1.67 | 43.70 | 30.1 | 19.23 | 1.79 | | | 35.30 | 21.91 |
| MgO | 10.58 | 1.14 | | 1.70 | 10.74 | 1.26 | | | 1.60 | 8.97 |
| MnO | 0.13 | 0.01 | 4.20 | 4.30 | 0.12 | 0.01 | | | 2.10 | 0.07 |
| CaO | | | | 6.50 | | | 4.40 | 57.20 | 5.20 | |
| $Na_2O$ | 0.35 | 0.96 | | | | 0.89 | 8.00 | | | |
| $K_2O$ | 9.61 | 10.05 | | | 9.64 | 10.14 | | | | 9.24 |
| F | 0.51 | 0.14 | | | 0.54 | 0.13 | | | | 0.50 |
| Cl | 0.06 | | | | 0.06 | 0.03 | | | | 0.11 |
| Total | 97.03 | 94.97 | 99.50 | 100.5 | 96.92 | 95.71 | 97.50 | 57.20 | 103.00 | 95.83 |
| | | | | | | | | | | |
| Li | 149 | 41 | | 45 | 165 | 78 | | 109 | | 64 |
| Na | | | | | | | | | | |
| $P_2O_5$ | | | | | | | | 43 | | |
| CaO | | | 0.73 | 6.50 | | 0.07 | 4.40 | 57.00 | 5.20 | 2.18 |
| Sc | 13 | 24 | 13 | 64 | 16 | 48 | | 1.3 | 43 | 37 |
| $TiO_2$ | 1.57 | 0.38 | 51.00 | 0.03 | 1.62 | 0.45 | | 0.001 | 0.09 | 0.66 |
| V | 158 | 237 | 46 | 36 | 186 | 230 | | | 53 | 127 |
| Cr | 192 | 108 | | 22 | 172 | 97 | | 5.2 | | 69 |
| MnO | 0.14 | 0.004 | 2.36 | 4.40 | 0.13 | 0.005 | | 0.03 | 1.62 | 1.51 |
| Co | 55 | 2.0 | 26 | 14 | 55 | 2.0 | | 2.2 | 8.2 | 21 |
| Ni | 179 | 8.6 | | 0. | 126 | 7.1 | | 6.9 | | 53 |
| Cu | 7.5 | | | 0. | 5.9 | 2.1 | | 4.1 | | 3.1 |
| Zn | 475 | 17 | 117 | 55 | 597 | 29 | | 8.2 | 104 | 144 |
| Rb | | | | | | | | | | 386 |
| Sr | 1.2 | 114 | | 0.02 | 1.4 | 105 | 477 | 222 | | 48 |
| Y | 0.72 | 0.20 | 0.65 | 707 | 0.25 | 0.70 | | 129 | 150 | 236 |
| Zr | 0.68 | 0.55 | 16 | 1. | 0.06 | 0.02 | | 0.26 | 3.4 | 0.77 |
| Nb | 42 | 20 | 491 | 0.08 | 43 | 25 | | 0.16 | | 29 |
| Cs | | | | | | | | | | 16 |
| Ba | 1146 | 3829 | | 0.03 | 1061 | 4750 | 23 | 1.3 | | 1829 |
| La | 1.1 | 0.20 | | | 0.66 | | | 4.8 | | 2.2 |
| Ce | 2.1 | 0.66 | | | 1.1 | | | 17 | | 7.0 |
| Pr | 0.32 | 0.06 | | | 0.20 | | | 2.1 | | 0.81 |
| Nd | 1.1 | 0.23 | | 0.03 | | | | 19 | | 4.8 |
| Sm | 0.37 | | | 0.21 | 0.14 | | | 9.9 | | 0.67 |
| Eu | 0.03 | 0.05 | | 0.28 | | | | 2.8 | 0.58 | 0.21 |
| Gd | 0.18 | | | 3. | | | | 15 | | |
| Tb | | | | 2. | | | | 4.3 | 2.2 | |
| Dy | 0.12 | 0.05 | | 59 | | | | 31 | | |
| Ho | | 0.02 | | 25 | | | | 5.6 | 5.3 | |
| Er | | 0.07 | | 97 | | 0.04 | | 12 | | |
| Tm | | | | 16 | | | | 0.72 | | |
| Yb | | | | 100 | | | | 3.4 | 8.2 | |
| Lu | | | | 15 | | | | 0.37 | 0.96 | |
| Hf | | | | | | 0.11 | | | | 0.06 |
| Ta | 2.9 | 0.70 | | | 2.6 | 0.94 | | | | 1.7 |

Note: Oxides are in wt%, elements are in ppm.

Table 2.3 Continued.

| | 88-32B | | 88-45D | | | 88-48C | | | 88-49A | |
|---|---|---|---|---|---|---|---|---|---|---|
| | Ms | Ap | Grt | Bt | Ms | Grt | Bt | Ms | Grt | Bt |
| $SiO_2$ | 46.83 | | 37.90 | 37.58 | 47.02 | 38.00 | 37.81 | 46.56 | 38.59 | 38.20 |
| $TiO_2$ | 0.37 | | | 1.68 | 0.78 | | 1.21 | 0.38 | 0.00 | 1.10 |
| $Al_2O_3$ | 33.87 | | 21.30 | 18.58 | 34.84 | 21.30 | 19.09 | 34.68 | 22.18 | 17.20 |
| FeO | 2.10 | | 35.20 | 16.27 | 1.24 | 35.50 | 14.57 | 1.56 | 32.18 | 11.20 |
| MgO | 1.16 | | 4.20 | 12.01 | 1.13 | 5.10 | 13.89 | 1.16 | 8.70 | 16.40 |
| MnO | 0.00 | | 0.40 | 0.00 | 0.00 | | 0.00 | 0.00 | 0.00 | |
| CaO | | 57.20 | 3.30 | | | 1.40 | | | 0.58 | |
| $Na_2O$ | 0.66 | | | 0.41 | 1.38 | | 0.48 | 1.21 | 0.03 | 0.90 |
| $K_2O$ | 10.71 | | | 7.70 | 8.94 | | 9.45 | 9.89 | | 8.00 |
| F | 0.11 | | | 0.37 | 0.10 | | 0.26 | | | |
| Cl | | | | | | | 0.02 | 0.01 | | |
| Total | 95.84 | 57.20 | 102.30 | 94.61 | 95.42 | 101.30 | 96.80 | 95.44 | 102.25 | 93.00 |
| | | | | | | | | | | |
| Li | - | | | 296 | 74 | | | | | |
| Na | | | | | | | | | | |
| $P_2O_5$ | | 43 | | | | | | | | |
| CaO | | 57.00 | 3.30 | 0.04 | 0.05 | 1.40 | | | | |
| Sc | 26 | | 70 | 6 | 19 | 24 | 8.0 | 15 | | 6.6 |
| $TiO_2$ | 0.33 | | 0.01 | 1.68 | 0.78 | 0.04 | 1.21 | 0.38 | 0.02 | 1.10 |
| V | 205 | 13 | 23 | 201 | 24 | 32 | 124 | 162 | 31 | 252 |
| Cr | 103 | | 191 | 366 | 14 | 116 | 201 | 252 | 146 | 252 |
| MnO | 0.002 | 0.02 | 0.32 | 0.004 | | 0.10 | 0.003 | | 0.03 | 0.001 |
| Co | | | 13 | 24 | 0.7 | 19 | 39 | | 26 | 65 |
| Ni | | | | 60 | | | 83 | | | 312 |
| Cu | | | | 8.4 | 2.7 | | 2.7 | | | |
| Zn | 14 | | 125 | 567 | 21 | 16 | | | 41 | 17 |
| Rb | | | | 684 | 24 | | | | | 244 |
| Sr | | | | 2.3 | 21 | | 1.6 | 481 | | 17 |
| Y | 0.11 | 900 | 172 | 0.08 | 0.07 | 13 | | | 4.9 | |
| Zr | 0.24 | | 2.4 | 0.16 | 1.2 | 9.0 | 0.36 | 0.19 | 3.1 | 0.17 |
| Nb | | | | 1.0 | 1.7 | | 12 | 12 | | |
| Cs | | | | 37 | 2.2 | | | | | |
| Ba | 2765 | | | 796 | 1896 | 0.35 | 320 | 703 | | 266 |
| La | 0.08 | 248 | | 0.25 | 0.88 | | 0.82 | 0.82 | | 0.04 |
| Ce | 0.12 | 865 | | 0.82 | 0.97 | 0.03 | 1.95 | 2.22 | | 0.06 |
| Pr | 0.04 | 142 | 0.01 | 0.11 | 0.06 | | 0.19 | 0.22 | | 0.01 |
| Nd | | 680 | 0.09 | 0.36 | 0.06 | 0.15 | 0.51 | 0.58 | | 0.24 |
| Sm | | 169 | 1.4 | | | 0.88 | | 0.05 | 0.11 | |
| Eu | 0.04 | 27 | 1.6 | | 1.0 | 0.40 | 0.03 | 0.07 | 0.10 | 0.02 |
| Gd | 0.11 | 161 | 20 | | | 3.1 | | | 0.76 | |
| Tb | | 25 | 8.7 | | | 0.61 | | | 0.16 | |
| Dy | 0.05 | 160 | 57 | | | 3.3 | 0.03 | | 1.2 | |
| Ho | 0.01 | 35 | 8.2 | | | 0.62 | | | 0.20 | |
| Er | | 108 | 13 | | | 1.3 | | 0.02 | 0.26 | |
| Tm | | 15 | 1.1 | | | 0.12 | | | 0.03 | |
| Yb | | 90 | 4.5 | | | 0.55 | | | 0.11 | |
| Lu | 0.01 | 12 | 0.42 | | | 0.06 | | | 0.02 | 0.02 |
| Hf | | | | 0.03 | | 0.09 | | 0.05 | | |
| Ta | | | | 0.06 | 0.07 | 0.00 | 0.65 | 0.29 | | |

Note: Oxides are in wt%, elements are in ppm.

Table 2.3 Continued.

| | 88-49A | 88-57A | | | 88-58A | | | 88-74D | | |
|---|---|---|---|---|---|---|---|---|---|---|
| | St | Grt | Bt | Pl | Grt | Bt | Ms | Ky | Grt | Bt |
| $SiO_2$ | 28.03 | 38.50 | 37.57 | 61.50 | 37.90 | 36.38 | 47.30 | 37.00 | 37.70 | 37.08 |
| $TiO_2$ | 0.65 | | 1.90 | | | 2.13 | 0.91 | | | 2.12 |
| $Al_2O_3$ | 52.67 | 21.30 | 17.67 | 24.70 | 21.40 | 18.01 | 33.06 | 62.40 | 21.40 | 18.34 |
| FeO | 13.17 | 27.20 | 18.20 | | 38.10 | 20.87 | 1.63 | 0.60 | 35.30 | 17.27 |
| MgO | 3.10 | 3.40 | 11.60 | | 3.7 | 9.54 | 1.42 | | 4.70 | 11.83 |
| MnO | 0.00 | 3.60 | | | 0.4 | 0.02 | 0.00 | | 1.70 | 0.03 |
| CaO | 0.00 | 8.40 | | 6.20 | 1.4 | | | | 1.50 | |
| $Na_2O$ | 0.10 | | 0.20 | 8.20 | | 0.40 | 0.70 | | | 0.54 |
| $K_2O$ | | | 8.00 | | | 9.73 | 10.46 | | | 9.29 |
| F | | | | | | 0.35 | 0.15 | | | 0.21 |
| Cl | | | | | | 0.03 | | | | |
| Total | 97.72 | 102.40 | 95.13 | 100.60 | 102.90 | 97.46 | 95.64 | 100.00 | 102.30 | 96.71 |
| | | | | | | | | | | |
| Li | | | | | | 189 | 28 | 415 | 31 | 212 |
| Na | | | | | | | | | | |
| $P_2O_5$ | | | | | | | | | | |
| CaO | | 8.40 | | 6.20 | 1.4 | 0.04 | 0.04 | | 1.44 | 0.03 |
| Sc | | 118 | 36 | | 11 | 13 | 7.7 | | 77 | 13 |
| $TiO_2$ | 0.65 | 0.04 | 2.08 | | 0.005 | 2.13 | 0.91 | 0.01 | 0.01 | 2.12 |
| V | 170 | 61 | 342 | | 18 | 131 | 119 | 76 | 12 | 249 |
| Cr | 679 | 638 | 605 | | 18 | 178 | 66 | 437 | 12 | 257 |
| MnO | 0.01 | 1.38 | 0.10 | | 0.5 | 0.02 | | | 1.33 | 0.03 |
| Co | 104 | 19 | 28 | | 24 | 53 | 2.5 | | 44 | 106 |
| Ni | 95 | | 208 | | | 109 | 5.7 | | | 280 |
| Cu | | | 5.1 | | | 5.9 | 1.0 | | | 7.0 |
| Zn | 414 | 67 | 796 | | 25 | 481 | 23 | | 75 | 290 |
| Rb | | | | | | 461 | 193 | | | 481 |
| Sr | 0.07 | | 2.6 | | 0.1 | 4.8 | 108 | | | 2.1 |
| Y | | 21 | 0.07 | | 13 | 0.25 | 0.02 | | 28 | 0.06 |
| Zr | | 3.4 | 0.10 | | 1.4 | 0.12 | 1.8 | | 5.7 | 0.13 |
| Nb | | | | | | 24 | 14 | | | 19 |
| Cs | | | | | | 27 | 5.3 | | | 8.6 |
| Ba | | 0.50 | 1347 | 46 | | 392 | 451 | 0.56 | | 598 |
| La | | 0.01 | 0.91 | 0.25 | 0.0 | 0.23 | | | | 0.02 |
| Ce | | | | 0.57 | | 0.45 | | 0.00 | | 0.04 |
| Pr | | 0.01 | 0.14 | 0.04 | | 0.04 | | | 0.01 | 0.01 |
| Nd | 0.05 | | 0.70 | | | 0.09 | 0.01 | | 0.13 | |
| Sm | | 0.84 | | | | | | | 0.82 | |
| Eu | | 0.69 | 0.01 | 0.24 | 0.4 | | 0.09 | | 0.71 | |
| Gd | | 4.5 | | 0.08 | | | | | 6.3 | |
| Tb | 0.01 | 1.0 | | | 2.4 | | | | 1.7 | |
| Dy | | 6.2 | | | | | | | 8.9 | |
| Ho | | 0.76 | | | 3.9 | | | | 1.6 | |
| Er | | 2.0 | | | | | | | 6.7 | |
| Tm | | 0.37 | | | | | | | 1.3 | |
| Yb | 0.06 | 2.4 | | | 10 | | | | 10 | |
| Lu | 0.01 | 0.49 | | | 1.2 | | | | 1.6 | |
| Hf | | | | | | | 0.09 | | 0.08 | 0.01 |
| Ta | | | | | | 2.4 | 0.73 | | | 1.1 |

Note: Oxides are in wt%, elements are in ppm.

Table 2.3 Continued.

| | 88-74E | 88-80C | | | | 88-85C | | | 88-87 | |
|---|---|---|---|---|---|---|---|---|---|---|
| | Ms | Bt | Ky | Pl | Ap | Grt | Bt | Ms | Gt | Bt |
| $SiO_2$ | 46.73 | 38.50 | 37.10 | 65.10 | | 38.10 | 37.40 | 47.04 | 38.61 | 36.40 |
| $TiO_2$ | 0.75 | 1.40 | | | | | 1.71 | 0.92 | 0.0 | 1.90 |
| $Al_2O_3$ | 33.57 | 19.10 | 62.40 | 23.60 | | 21.30 | 18.92 | 33.87 | 22.08 | 18.90 |
| FeO | 2.53 | 12.40 | 0.7 | | | 34.90 | 16.40 | 1.27 | 33.54 | 6.90 |
| MgO | 1.06 | 15.70 | | 0.60 | | 4.40 | 12.49 | 1.25 | 4.7 | 12.20 |
| MnO | 0.00 | 0.20 | | | | 0.40 | 0.01 | 0.00 | 0.8 | 0.30 |
| CaO | | | | 2.30 | 56.80 | 3.00 | | | 1.8 | 1.00 |
| $Na_2O$ | 1.18 | 0.40 | | 9.30 | | | 0.41 | 1.21 | 0.0 | 1.30 |
| $K_2O$ | 8.69 | 9.00 | | | | | 8.50 | 9.26 | | 6.90 |
| F | 0.07 | 0.20 | | | | | 0.43 | 0.13 | | |
| Cl | 0.01 | 0.01 | | | | | 0.01 | 0.01 | | |
| Total | 94.59 | 96.91 | 100.20 | 100.90 | 56.80 | 102.10 | 96.28 | 94.96 | 101.65 | 85.80 |
| | | | | | | | | | | |
| Li | 43 | 86 | | | | | 372 | 80 | | |
| Na | | | | | | | | | | |
| $P_2O_5$ | | | | 218 | 43 | | | | | |
| CaO | 0.05 | 0.01 | | 2.60 | 56.80 | 3.00 | 0.03 | 0.07 | 1.3 | |
| Sc | 16 | 70 | | | | 83 | 4.6 | 12 | 66 | 10 |
| $TiO_2$ | 0.75 | 1.32 | 0.005 | | | 0.01 | 1.71 | 0.92 | 0.0 | 1.90 |
| V | 217 | 238 | 73 | | | 22 | 248 | 301 | 22 | 161 |
| Cr | 104 | 473 | 388 | | | 111 | 345 | 239 | 104 | 250 |
| MnO | 0.001 | | | | | 0.41 | 0.01 | | 0.6 | 0.01 |
| Co | 4.1 | 32 | | | | 20 | 30 | 1.7 | 16 | 39 |
| Ni | 9.5 | 233 | | | | | 40 | 2.9 | | 115 |
| Cu | 0.8 | | | | | | 7.8 | 1.5 | | |
| Zn | 16 | 277 | | | | 109 | 475 | 34 | 69 | 415 |
| Rb | 208 | 393 | | | 0.57 | | 679 | 367 | | 439 |
| Sr | 63 | 4.4 | 0.0 | 629 | 480 | | 4.5 | 279 | | 8.5 |
| Y | 0.06 | 0.68 | 0.1 | 0.71 | 948 | 90 | 0.07 | 0.22 | 43 | |
| Zr | 1.7 | 0.16 | | 0.10 | 0.23 | 2.9 | 0.17 | 1.4 | 3.3 | 0.18 |
| Nb | 14 | 14 | 0.0 | | | | 1.3 | 3.7 | | |
| Cs | 0.9 | 3.6 | | | | | 31 | 5.3 | | |
| Ba | 1045 | 2634 | | 39 | | 1.0 | 1073 | 1969 | 2.2 | 1244 |
| La | | 0.02 | | 0.63 | 34 | | 0.15 | 2.5 | | |
| Ce | | | | | | 0.01 | 0.36 | 2.84 | | |
| Pr | | | | 0.12 | 55 | 0.10 | 0.04 | 0.14 | | |
| Nd | | | | | | 0.22 | 0.13 | 0.20 | | |
| Sm | | | | 0.06 | 206 | 1.2 | | | 0.6 | |
| Eu | 0.22 | 0.01 | | 0.53 | 52 | 1.0 | 0.01 | 1.1 | 0.5 | 0.05 |
| Gd | 0.03 | 0.06 | | | 269 | 10 | 0.02 | 0.01 | 4.6 | 0.02 |
| Tb | | 0.01 | | | 45 | 2.7 | | | 1.4 | |
| Dy | | | | | | 13 | | | 8.4 | |
| Ho | | 0.02 | 0.0 | | 41 | 1.8 | | | 1.4 | |
| Er | | | | | | 3.0 | | | 3.4 | |
| Tm | | 0.04 | | | 7.76 | 0.43 | | | 0.6 | |
| Yb | | | | | | 2.5 | | | 4.4 | |
| Lu | | 0.03 | | 0.02 | 4.7 | 0.35 | | | 0.8 | |
| Hf | 0.13 | 0.06 | | | | | | 0.15 | | |
| Ta | 0.53 | 0.40 | | | | | 0.05 | 0.15 | | |

Note: Oxides are in wt%, elements are in ppm.

Table 2.3 Continued.

| | 88-87 | 88-88 | | | | P-11A | | | | | |
|---|---|---|---|---|---|---|---|---|---|---|---|
| | Ms | Gt | Bt | Ms | Ky | Grt | Bt | Ep | Pl | Ap | Rt |
| $SiO_2$ | 48.40 | 38.11 | 36.76 | 47.00 | 36.41 | 38.32 | 37.26 | 37.33 | 64.60 | 0.10 | |
| $TiO_2$ | 0.90 | 0.00 | 2.10 | 0.80 | | | 1.57 | | | 95.90 | |
| $Al_2O_3$ | 35.40 | 21.88 | 19.08 | 36.00 | 62.10 | 21.84 | 17.22 | 26.92 | 24.20 | | |
| FeO | 0.60 | 32.40 | 15.38 | 0.50 | 0.20 | 28.00 | 12.58 | 7.64 | | 0.70 | |
| MgO | 2.70 | 4.85 | 12.28 | 2.40 | | 7.58 | 14.99 | | 0.70 | | |
| MnO | | 0.86 | | | | 0.63 | 0.00 | | | | |
| CaO | 1.00 | 4.07 | | 1.00 | | 4.01 | 0.00 | 23.93 | 3.10 | | 56.60 |
| $Na_2O$ | 1.20 | 0.00 | 0.49 | 1.10 | | | 0.50 | | 8.00 | | |
| $K_2O$ | 6.30 | | 9.46 | 6.30 | | | 8.88 | | | | |
| F | | | | | | | | | | | |
| Cl | | | | | | | | | | | |
| Total | 96.50 | 102.18 | 95.55 | 95.10 | 98.71 | 100.38 | 93.01 | 95.82 | 100.60 | 96.70 | 56.60 |
| | | | | | | | | | | | |
| Li | | | | | | 4.8 | 93 | | | | |
| Na | | | 38 | 73 | 162 | | | | | | |
| $P_2O_5$ | | | | | | 0.03 | 0.01 | 0.09 | | | 28 |
| CaO | | 2.95 | | | | 3.48 | | 24.55 | 6.73 | | 57.15 |
| Sc | 17 | 35 | | | | 77 | 25 | 176 | 5.3 | 36 | |
| $TiO_2$ | 0.90 | 0.02 | 2.16 | 0.90 | | 0.02 | 1.67 | 0.09 | 0.002 | 96.00 | |
| V | 195 | 24 | 151 | 176 | 43 | 28 | 332 | 352 | | 792 | 0.6 |
| Cr | 154 | 142 | 176 | 325 | 396 | 238 | 944 | 1263 | | 1053 | |
| MnO | 0.001 | 0.55 | | | | | | | | | |
| Co | 3.3 | 44 | 110 | | | 25 | 63 | 1.0 | | 5.4 | |
| Ni | 15 | | | | | 1.2 | 270 | 19 | | 97 | 1.5 |
| Cu | | | | | | | | | | | |
| Zn | 57 | 166 | 895 | 54 | | 49 | 314 | 7.9 | | 29 | |
| Rb | 299 | | 504 | 295 | | | 418 | | | | |
| Sr | 178 | | 2.0 | 52 | | 0.02 | 4.4 | 241 | 1273 | | 328 |
| Y | | 27 | | | | 52 | 0.17 | 225 | 0.06 | | 253 |
| Zr | 1.7 | 3.4 | | 1.6 | | 6.7 | 0.15 | 11 | | 154 | 0.02 |
| Nb | | | | | | | 4 | 0.06 | | 2777 | 0.01 |
| Cs | | | | | | | 5.3 | 0.04 | | | |
| Ba | 1979 | | 1163 | 2576 | 0.01 | | 1576 | 2.4 | 32 | | 0.23 |
| La | | | 1.1 | 0.02 | | | 3.1 | 10 | 0.86 | | 2.3 |
| Ce | | | | | | | | | | | |
| Pr | | | 0.34 | | | 0.01 | 0.58 | 4.1 | 0.10 | | 5.3 |
| Nd | 0.03 | 0.02 | | | | | | | | | |
| Sm | | 0.88 | 0.23 | 0.06 | | 1.3 | 0.32 | 24 | 0.21 | | 36 |
| Eu | 0.34 | 0.48 | 0.03 | 0.31 | | 0.98 | 0.06 | 16 | 0.40 | | 12 |
| Gd | | 3.2 | | | | 7.7 | 0.17 | 50 | 0.13 | | 67 |
| Tb | | 0.83 | | | | 1.9 | 0.02 | 12 | | | 9.2 |
| Dy | | 4.4 | | | | | | | | | |
| Ho | | 0.81 | | 0.01 | | 2.1 | | 8.7 | | | 7.8 |
| Er | | 2.2 | | | | | | | | | |
| Tm | | 0.34 | | | | 0.50 | | 0.95 | | | 1.6 |
| Yb | | 2.6 | | | | | | | | | |
| Lu | | 0.16 | | | | 0.42 | | 0.29 | | | 0.94 |
| Hf | | | | | | 0.09 | 0.08 | 0.28 | | 9.8 | |
| Ta | | | | | | | 0.34 | 0.01 | | 89 | |

Note: Oxides are in wt%, elements are in ppm.

Table 2.4 Average distribution coefficients between coexisting minerals from greenschist to upper amphibolite facies metapelites and quartzofeldspathic rocks, Gagnon terrane.

| $D_i$ | Bt/Ap | | | Bt/Ep | | | Bt/Ilm | | | Bt/Ky | | |
|---|---|---|---|---|---|---|---|---|---|---|---|---|
| | AVG | STD | N | AVG | STD | N | AVG | STD | N | AVG | STD | N |
| Li | 1.5E+00 | | 1 | | | | | | | 5.3E-01 | | |
| Sc | 1.3E+01 | | 1 | 1.4E-01 | | 1 | 1.2E+00 | | 2 | 1.5E+02 | | |
| V | 4.3E+03 | | 2 | 9.4E-01 | | 1 | 3.8E+00 | | 2 | 3.9E+00 | 1.1E+00 | 4 |
| Cr | 3.3E+01 | | 1 | 7.5E-01 | | 1 | | | | 1.1E+00 | 5.2E-01 | 4 |
| Co | 2.5E+01 | | 1 | 6.5E+01 | | 1 | 1.9E+00 | | 2 | | | |
| Ni | 9.8E+01 | | 2 | 1.4E+01 | | 1 | | | | | | |
| Cu | 1.4E+00 | | 1 | | | | | | | | | |
| Zn | 7.3E+01 | | 1 | 4.0E+01 | | 1 | 4.1E+00 | | 1 | | | |
| Rb | 6.9E+02 | | 1 | | | | | | | | | |
| Sr | 1.0E-02 | 3.3E-03 | 4 | 1.8E-02 | | 1 | 2.1E-01 | | 1 | 3.6E+02 | | 1 |
| Y | 2.3E-03 | 2.5E-03 | 4 | 7.5E-04 | | 1 | 1.4E+00 | | 2 | 6.0E+00 | | 1 |
| Zr | 4.6E-01 | | 2 | 1.4E-02 | | 1 | 5.2E-01 | | 2 | | | |
| Nb | 4.7E+02 | | 2 | 6.9E+01 | | 1 | 1.2E-01 | | 2 | 8.2E+02 | | 1 |
| Cs | | | | 1.2E+02 | | 1 | | | | | | |
| Ba | 3.8E+03 | | 2 | 6.6E+02 | | 1 | | | | 4.6E+04 | | 2 |
| La | 4.8E-01 | 7.2E-01 | 3 | 3.0E-01 | | 1 | | | | | | |
| Ce | 6.7E-02 | | 1 | | | | | | | 2.9E+00 | | 1 |
| Pr | 6.8E-02 | 5.9E-02 | 3 | 1.4E-01 | | 1 | | | | 3.3E+03 | | 1 |
| Nd | | | | | | | | | | 1.7E+00 | | 1 |
| Sm | 1.2E-02 | | 2 | 1.4E-02 | | 1 | | | | | | |
| Eu | 2.4E-03 | | 2 | 3.6E-03 | | 1 | | | | 6.8E+01 | | 1 |
| Gd | 1.4E-03 | | 2 | 3.5E-03 | | 1 | | | | | | |
| Tb | 9.4E-04 | | 2 | 1.4E-03 | | 1 | | | | | | |
| Dy | | | | | | | | | | | | |
| Ho | 3.4E-04 | 2.5E-04 | 2 | 1.5E-04 | | 1 | | | | 2.0E+00 | | 2 |
| Er | | | | | | | | | | | | |
| Tm | 2.7E-03 | 3.0E-03 | 2 | 9.7E-04 | | 1 | | | | | | |
| Yb | | | | | | | | | | | | |
| Lu | 5.3E-03 | 1.8E-03 | 2 | 1.3E-02 | | 1 | | | | | | |
| Hf | | | | 2.8E-01 | | 1 | | | | | | |
| Ta | | | | 3.5E+01 | | 1 | | | | | | |

Notes: $D_i$, (ppm i in mineral A)/(ppm i in mineral B); AVG, average of distribution coefficients; STD, standard deviation at 1$\sigma$; and N, number of measurements.

Table 2.4 Continued.

| $D_i$ | Bt/Ms | | | Bt/Pl | | | Bt/Rt | | | Bt/St | | |
|---|---|---|---|---|---|---|---|---|---|---|---|---|
| | AVG | STD | N | AVG | STD | N | AVG | STD | N | AVG | STD | N |
| Li | 3.8E+00 | 1.9E+00 | 18 | | | | | | | 1.9E-01 | | 1 |
| Sc | 6.1E-01 | 3.6E-01 | 24 | 4.7E+00 | | 1 | 7.0E-01 | | 1 | | | |
| V | 8.1E-01 | 2.3E-01 | 25 | | | | 4.2E-01 | | 1 | 1.5E+00 | | 2 |
| Cr | 1.4E+00 | 6.6E-01 | 25 | | | | 9.0E-01 | | 1 | 3.7E-01 | | 2 |
| Co | 2.2E+01 | 1.1E+01 | 21 | | | | 1.2E+01 | | 1 | 6.4E-01 | | 2 |
| Ni | 1.7E+01 | 8.3E+00 | 18 | | | | 2.8E+00 | | 1 | 3.2E+00 | | 2 |
| Cu | 6.3E+00 | 4.4E+00 | 15 | | | | | | | | | |
| Zn | 1.9E+01 | 1.0E+01 | 24 | | | | 1.1E+01 | | 1 | 3.7E-02 | | 2 |
| Rb | 2.3E+00 | 6.3E-01 | 17 | | | | | | | | | |
| Sr | 2.4E-02 | 1.5E-02 | 25 | 4.8E-03 | 1.9E-03 | 4 | | | | 2.3E+02 | | 1 |
| Y | 3.5E+00 | 3.2E+00 | 16 | 1.8E+00 | | 2 | | | | | | |
| Zr | 2.3E-01 | 2.7E-01 | 16 | 2.7E+01 | | 2 | 9.9E-04 | | 1 | 1.3E+01 | | 1 |
| Nb | 1.6E+00 | 7.1E-01 | 21 | | | | 1.4E-03 | | 1 | 2.5E+00 | | 1 |
| Cs | 1.4E+01 | 8.5E+00 | 15 | | | | | | | | | |
| Ba | 4.4E-01 | 2.0E-01 | 25 | 5.1E+01 | 1.6E+01 | 6 | | | | | | |
| La | 2.4E+02 | 5.3E+02 | 14 | 9.6E+00 | 1.7E+01 | 5 | | | | | | |
| Ce | 2.4E+01 | 3.5E+01 | 13 | 1.5E+01 | | 2 | | | | | | |
| Pr | 3.3E+01 | 5.3E+01 | 12 | 2.4E+00 | 2.9E+00 | 4 | | | | | | |
| Nd | 1.3E+01 | 9.5E+00 | 6 | 1.5E-01 | | 1 | | | | 4.3E+00 | | 1 |
| Sm | 9.6E+00 | 6.9E+00 | 6 | 1.6E+00 | | 1 | | | | | | |
| Eu | 2.0E+00 | 4.6E+00 | 14 | 6.5E-02 | 6.4E-02 | 3 | | | | | | |
| Gd | 7.6E+00 | 5.9E+00 | 3 | 1.3E+00 | | 1 | | | | | | |
| Tb | 1.2E+01 | | 2 | 6.2E+00 | | 1 | | | | | | |
| Dy | 3.7E+00 | | 2 | | | | | | | | | |
| Ho | 4.4E+00 | | 2 | 2.0E+00 | | 2 | | | | | | |
| Er | 6.7E+00 | | 1 | | | | | | | | | |
| Tm | 2.2E+00 | | 1 | | | | | | | | | |
| Yb | 5.3E+00 | | 1 | | | | | | | | | |
| Lu | 1.1E+00 | | 1 | 1.9E+00 | | 1 | | | | 2.2E+00 | | 1 |
| Hf | 8.1E-01 | 6.1E-01 | 10 | 1.0E+00 | | 1 | 7.9E-03 | | 1 | | | |
| Ta | 4.1E+00 | 2.6E+00 | 18 | 6.8E+02 | | 2 | 3.8E-03 | | 1 | 1.8E+00 | | 1 |

Notes: $D_i$, (ppm i in mineral A)/(ppm i in mineral B); AVG, average of distribution coefficients; STD, standard deviation at 1σ; and N, number of measurements.

Table 2.4 Continued.

| $D_i$ | Ep/Ap | | | Ep/Pl | | | Ep/Rt | | | Grt/Ap | | |
|---|---|---|---|---|---|---|---|---|---|---|---|---|
| | AVG | STD | N | AVG | STD | N | AVG | STD | N | AVG | STD | N |
| Li | | | | | | | | | | 4.2E-01 | | 1 |
| Sc | | | | 3.3E+01 | | 1 | 4.9E+00 | | 1 | 5.0E+01 | | 1 |
| V | 603.8 | | 1 | | | | 4.4E-01 | | 1 | 4.4E+02 | 7.5E+02 | 4 |
| Cr | | | | | | | 1.2E+00 | | 1 | 4.3E+00 | | 1 |
| Co | | | | | | | 1.8E-01 | | 1 | 6.4E+00 | | 1 |
| Ni | 12.3 | | 1 | | | | 1.9E-01 | | 1 | 1.0E-02 | | 1 |
| Cu | | | | | | | | | | 2.0E-02 | | 1 |
| Zn | | | | | | | 2.7E-01 | | 1 | 6.7E+00 | | 1 |
| Rb | | | | | | | | | | | | |
| Sr | 0.7 | | 1 | 1.9E-01 | | 1 | | | | 7.5E-05 | | 1 |
| Y | 0.9 | | 1 | 3.5E+03 | | 1 | | | | 1.8E+00 | 2.2E+00 | 5 |
| Zr | 576.2 | | 1 | | | | 6.9E-02 | | 1 | 2.6E+02 | 4.4E+02 | 3 |
| Nb | 9.8 | | 1 | | | | 2.0E-05 | | 1 | 5.2E-01 | | 1 |
| Cs | | | | | | | | | | | | |
| Ba | 10.2 | | 1 | 7.5E-02 | | 1 | | | | 1.4E-01 | | 2 |
| La | 4.4 | | 1 | 1.2E+01 | | 1 | | | | 3.8E-03 | | 1 |
| Ce | | | | | | | | | | | | |
| Pr | 0.8 | | 1 | 4.2E+01 | | 1 | | | | | | |
| Nd | | | | | | | | | | 1.6E-03 | | 1 |
| Sm | 0.7 | | 1 | 1.2E+02 | | 1 | | | | 4.0E-02 | 2.2E-02 | 3 |
| Eu | 1.3 | | 1 | 3.9E+01 | | 1 | | | | 1.8E-01 | 2.1E-01 | 4 |
| Gd | 0.7 | | 1 | 3.8E+02 | | 1 | | | | 2.5E-01 | | 2 |
| Tb | 1.2 | | 1 | 4.4E+03 | | 1 | | | | 3.7E-01 | 2.7E-01 | 4 |
| Dy | | | | | | | | | | 1.3E+00 | | 2 |
| Ho | 1.1 | | 1 | | | | | | | 1.4E+00 | 2.0E+00 | 4 |
| Er | | | | | | | | | | 4.5E+00 | | 2 |
| Tm | 0.6 | | 1 | | | | | | | 7.6E+00 | 1.2E+01 | 3 |
| Yb | | | | | | | | | | 1.0E+01 | 1.7E+01 | 3 |
| Lu | 0.3 | | 1 | | | | | | | 1.1E+01 | 2.0E+01 | 4 |
| Hf | | | | | | | 2.8E-02 | | 1 | | | |
| Ta | | | | | | | 1.1E-04 | | 1 | | | |

Notes: $D_i$, (ppm i in mineral A)/(ppm i in mineral B); AVG, average of distribution coefficients; STD, standard deviation at 1σ; and N, number of measurements.

Table 2.4 Continued.

| $D_i$ | Grt/Bt | | | Grt/Ep | | | Grt/Ilm | | | Grt/Ky | | |
|---|---|---|---|---|---|---|---|---|---|---|---|---|
| | AVG | STD | N | AVG | STD | N | AVG | STD | N | AVG | STD | N |
| Li | 5.7E-01 | 6.1E-01 | 7 | | | | | | | | | |
| Sc | 6.6E+00 | 4.9E+00 | 28 | 8.1E-01 | | 1 | 5.7E+00 | | 2 | | | |
| V | 1.9E-01 | 8.7E-02 | 32 | 2.6E-01 | | 1 | 9.0E-01 | 5.8E-01 | 3 | 5.8E-01 | | 1 |
| Cr | 5.9E-01 | 3.0E-01 | 32 | 1.3E+00 | | 1 | 1.8E+00 | | 1 | 3.6E-01 | | 1 |
| Co | 3.9E-01 | 1.4E-01 | 32 | 2.7E+01 | | 1 | 5.0E-01 | 1.5E-01 | 3 | | | |
| Ni | 1.2E-03 | 2.1E-03 | 4 | | | | | | | | | |
| Cu | 5.2E-01 | 3.4E-01 | 4 | | | | | | | | | |
| Zn | 2.0E-01 | 1.5E-01 | 28 | 6.8E+00 | | 1 | 2.6E-01 | 2.3E-01 | 3 | | | |
| Rb | 3.7E-03 | | 1 | | | | | | | | | |
| Sr | 5.3E-02 | 8.7E-02 | 5 | | | | | | | | | |
| Y | 8.4E+02 | 8.0E+02 | 25 | 2.2E-01 | | 1 | 2.9E+02 | 2.1E+02 | 3 | | | |
| Zr | 1.7E+01 | 1.5E+01 | 29 | 1.3E+00 | | 1 | 1.6E+00 | | 1 | | | |
| Nb | 1.6E-02 | | 2 | | | | | | | | | |
| Cs | | | | | | | | | | | | |
| Ba | 1.7E-03 | 3.0E-03 | 11 | 2.5E-02 | | 1 | | | | | | |
| La | 7.2E-02 | 1.2E-01 | 6 | 8.8E-04 | | 1 | | | | | | |
| Ce | 3.6E-02 | 4.8E-02 | 7 | | | | | | | | | |
| Pr | 3.6E-01 | 7.4E-01 | 13 | | | | | | | | | |
| Nd | 2.0E-01 | 1.4E-01 | 3 | | | | | | | | | |
| Sm | 4.1E+01 | 9.9E+01 | 13 | 5.3E-02 | | 1 | | | | | | |
| Eu | 2.0E+01 | 3.1E+01 | 17 | 6.9E-02 | | 1 | | | | 1.2E+03 | | 1 |
| Gd | 1.0E+02 | 1.7E+02 | 9 | | | | | | | | | |
| Tb | 8.6E+01 | 6.4E+01 | 9 | 1.8E-01 | | 1 | 5.3E+01 | | 1 | | | |
| Dy | 1.6E+02 | 1.1E+02 | 9 | | | | | | | | | |
| Ho | 4.3E+02 | 5.0E+02 | 8 | 2.9E-01 | | 1 | 1.4E+02 | | 1 | | | |
| Er | 3.8E+02 | 3.4E+02 | 5 | | | | | | | | | |
| Tm | 1.1E+03 | 1.7E+03 | 7 | 8.1E-01 | | 1 | | | | | | |
| Yb | 3.1E+02 | 4.0E+02 | 6 | | | | | | | | | |
| Lu | 3.7E+02 | 5.8E+02 | 10 | 2.1E+00 | | 1 | | | | | | |
| Hf | 1.7E+00 | 2.1E+00 | 6 | | | | | | | | | |
| Ta | 3.4E-02 | 3.7E-02 | 6 | | | | | | | | | |

Notes: $D_i$, (ppm i in mineral A)/(ppm i in mineral B); AVG, average of distribution coefficients; STD, standard deviation at 1σ; and N, number of measurements.

Table 2.4 Continued.

| $D_i$ | Grt/Ms | | | Grt/Pl | | | Grt/Rt | | | Grt/St | | |
|---|---|---|---|---|---|---|---|---|---|---|---|---|
| | AVG | STD | N | AVG | STD | N | AVG | STD | N | AVG | STD | N |
| Li | 3.2E+00 | 3.6E+00 | 3 | | | | | | | 2.6E-01 | | 1 |
| Sc | 4.9E+00 | 4.3E+00 | 18 | 1.5E+01 | | 1 | 4.0E+00 | | 1 | | | |
| V | 1.6E-01 | 6.4E-02 | 20 | | | | 1.2E-01 | | 1 | 2.0E-01 | 5.0E-02 | 3 |
| Cr | 8.3E-01 | 6.3E-01 | 19 | | | | 1.6E+00 | | 1 | 2.7E-01 | 7.1E-02 | 3 |
| Co | 9.2E+00 | 4.3E+00 | 15 | | | | 4.8E+00 | | 1 | 2.7E-01 | 2.7E-02 | 3 |
| Ni | | | | | | | | | | | | |
| Cu | | | | | | | | | | | | |
| Zn | 4.8E+00 | 3.8E+00 | 19 | | | | 1.8E+00 | | 1 | 4.8E-02 | 4.5E-02 | 3 |
| Rb | 9.2E-03 | | 1 | | | | | | | | | |
| Sr | 1.7E-03 | 1.6E-03 | 3 | 2.5E-05 | | 2 | | | | | | |
| Y | 2.1E+03 | 2.1E+03 | 15 | 8.0E+02 | | 1 | | | | | | |
| Zr | 5.1E+00 | 5.1E+00 | 14 | | | | 9.2E-02 | | 1 | 4.6E+02 | | 1 |
| Nb | 3.2E-03 | | 1 | | | | | | | | | |
| Cs | | | | | | | | | | | | |
| Ba | 9.3E-04 | 1.1E-03 | 7 | 6.1E-03 | | 2 | | | | | | |
| La | 1.1E+01 | | 2 | 2.8E-02 | | 1 | | | | | | |
| Ce | 2.0E-01 | 2.6E-01 | 5 | 4.8E-01 | | 1 | | | | | | |
| Pr | 1.3E+00 | 2.0E+00 | 4 | 2.3E-01 | | 2 | | | | | | |
| Nd | 9.9E-01 | 6.7E-01 | 3 | | | | | | | | | |
| Sm | 1.3E+01 | 6.9E+00 | 4 | 6.2E+00 | | 1 | | | | 2.6E+01 | | 1 |
| Eu | 3.7E+00 | 3.3E+00 | 16 | 2.7E+00 | 3.7E-01 | 2 | | | | | | |
| Gd | 3.5E+02 | 3.8E+02 | 3 | 5.6E+01 | 4.0E+00 | 2 | | | | | | |
| Tb | 4.7E+02 | | 2 | 7.3E+02 | | 1 | | | | 2.4E+01 | | 1 |
| Dy | 4.5E+02 | | 2 | | | | | | | | | |
| Ho | 5.4E+02 | 4.6E+02 | 5 | 1.5E+03 | | 1 | | | | | | |
| Er | 9.5E+02 | 1.2E+03 | 4 | | | | | | | | | |
| Tm | 2.0E+02 | | 1 | | | | | | | 3.9E+02 | | 1 |
| Yb | | | | | | | | | | 2.0E+00 | | 1 |
| Lu | 2.8E+02 | | 2 | | | | | | | 2.9E+00 | | 1 |
| Hf | 4.0E-01 | | 2 | | | | | | | | | |
| Ta | 1.9E-02 | | 2 | | | | | | | 1.7E-01 | | 1 |

Notes: $D_i$, (ppm i in mineral A)/(ppm i in mineral B); AVG, average of distribution coefficients; STD, standard deviation at 1σ; and N, number of measurements.

Table 2.4 Continued.

| $D_i$ | Ky/Ap | | | Ky/Pl | | | Ms/Ap | | | Ms/Ilm | | |
|---|---|---|---|---|---|---|---|---|---|---|---|---|
| | AVG | STD | N | AVG | STD | N | AVG | STD | N | AVG | STD | N |
| Li | | | | | | | 7.2E-01 | | 1 | | | |
| Sc | | | | | | | 3.7E+01 | | 1 | 1.8E+00 | | 1 |
| V | | | | | | | 4.9E+03 | | 2 | 5.1E+00 | | 1 |
| Cr | | | | | | | 1.9E+01 | | 1 | | | |
| Co | | | | | | | 9.3E-01 | | 1 | 7.6E-02 | | 1 |
| Ni | | | | | | | 1.0E+00 | | 1 | | | |
| Cu | | | | | | | 5.1E-01 | | 1 | | | |
| Zn | | | | | | | 3.5E+00 | | 1 | 1.4E-01 | | 1 |
| Rb | | | | | | | | | | | | |
| Sr | 2.5E-05 | | 1 | | | | 5.0E-01 | | 2 | | | |
| Y | 1.2E-04 | | 1 | | | | 2.8E-03 | | 2 | 3.2E-01 | | 1 |
| Zr | | | | | | | 8.2E-02 | | 1 | 3.5E-02 | | 1 |
| Nb | | | | | | | 1.6E+02 | | 1 | 4.1E-02 | | 1 |
| Cs | | | | | | | | | | | | |
| Ba | | | | | | | 3.7E+03 | | 1 | | | |
| La | | | | | | | 3.2E-04 | | 1 | | | |
| Ce | | | | 3.2E-03 | | 1 | 1.3E-04 | | 1 | | | |
| Pr | | | | | | | 2.9E-04 | | 1 | | | |
| Nd | | | | 9.0E-02 | | 1 | | | | | | |
| Sm | | | | | | | | | | | | |
| Eu | | | | | | | 1.6E-03 | | 1 | | | |
| Gd | | | | | | | 6.6E-04 | | 1 | | | |
| Tb | | | | | | | | | | | | |
| Dy | | | | | | | 2.9E-04 | | 1 | | | |
| Ho | 1.7E-04 | | 1 | 5.6E-01 | | 1 | 3.3E-04 | | 1 | | | |
| Er | | | | | | | 3.3E-03 | | 1 | | | |
| Tm | | | | | | | 2.1E-04 | | 1 | | | |
| Yb | | | | | | | | | | | | |
| Lu | | | | | | | 6.2E-04 | | 1 | | | |
| Hf | | | | | | | | | | | | |
| Ta | | | | | | | | | | | | |

Notes: $D_i$, (ppm i in mineral A)/(ppm i in mineral B); AVG, average of distribution coefficients; STD, standard deviation at 1σ; and N, number of measurements.

Table 2.4 Continued.

| $D_i$ | Ms/Ky | | | Ms/Pl | | | Pl/Ap | | | Pl/Rt | | |
|---|---|---|---|---|---|---|---|---|---|---|---|---|
| | AVG | STD | N | AVG | STD | N | AVG | STD | N | AVG | STD | N |
| Li | 1.0E-01 | | 1 | | | | | | | | | |
| Sc | | | | | | | | | | 1.5E-01 | | 1 |
| V | 3.7E+00 | | 2 | | | | | | | | | |
| Cr | 7.3E-01 | | 2 | | | | | | | | | |
| Co | | | | | | | | | | | | |
| Ni | | | | | | | | | | | | |
| Cu | | | | | | | | | | | | |
| Zn | | | | | | | | | | | | |
| Rb | | | | | | | | | | | | |
| Sr | | | | 2.2E-01 | | 1 | 2.4E+00 | 1.3E+00 | 3 | | | |
| Y | | | | | | | 5.0E-04 | | 2 | | | |
| Zr | | | | | | | 4.6E-01 | | 1 | | | |
| Nb | | | | | | | | | | | | |
| Cs | | | | | | | | | | | | |
| Ba | 1.0E+05 | | 2 | 2.6E+02 | | 2 | 7.7E+01 | | 2 | | | |
| La | | | | 6.9E-01 | | 1 | 1.9E-01 | | 2 | | | |
| Ce | | | | 9.4E-01 | | 1 | | | | | | |
| Pr | | | | | | | 1.0E-02 | | 2 | | | |
| Nd | | | | | | | | | | | | |
| Sm | | | | | | | 3.0E-03 | | 2 | | | |
| Eu | 7.5E+02 | | 1 | | | | 2.2E-02 | | 2 | | | |
| Gd | | | | | | | 2.0E-03 | | 1 | | | |
| Tb | | | | | | | 2.8E-04 | | 1 | | | |
| Dy | | | | | | | | | | | | |
| Ho | | | | | | | | | | | | |
| Er | | | | | | | | | | | | |
| Tm | | | | | | | | | | | | |
| Yb | | | | | | | | | | | | |
| Lu | | | | | | | 3.4E-03 | | 1 | | | |
| Hf | | | | 5.9E-01 | | 1 | | | | | | |
| Ta | | | | 2.6E+02 | | 1 | | | | | | |

Notes: $D_i$, (ppm i in mineral A)/(ppm i in mineral B); AVG, average of distribution coefficients; STD, standard deviation at 1$\sigma$; and N, number of measurements.

Table 2.4 Continued.

| $D_i$ | Rt/Ap | | | St/Ilm | | |
|---|---|---|---|---|---|---|
| | AVG | STD | N | AVG | STD | N |
| Li | | | | | | |
| Sc | | | | | | |
| V | 1.4E+03 | | 1 | 2.0E+00 | | 1 |
| Cr | | | | 7.5E+00 | | 1 |
| Co | | | | 2.0E+00 | | 1 |
| Ni | 6.4E+01 | | 1 | | | |
| Cu | | | | | | |
| Zn | | | | 4.6E+00 | | 1 |
| Rb | | | | | | |
| Sr | | | | | | |
| Y | | | | | | |
| Zr | 8.4E+03 | | 1 | | | |
| Nb | 4.8E+05 | | 1 | | | |
| Cs | | | | | | |
| Ba | | | | 9.2E-04 | | 1 |
| La | | | | 2.4E-01 | | 1 |
| Ce | | | | | | |
| Pr | | | | | | |
| Nd | | | | | | |
| Sm | | | | | | |
| Eu | | | | | | |
| Gd | | | | | | |
| Tb | | | | | | |
| Dy | | | | | | |
| Ho | | | | | | |
| Er | | | | | | |
| Tm | | | | | | |
| Yb | | | | | | |
| Lu | | | | | | |
| Hf | | | | | | |
| Ta | | | | | | |

Notes: $D_i$, (ppm i in mineral A)/(ppm i in mineral B); AVG, average of distribution coefficients; STD, standard deviation at 1σ; and N, number of measurements.

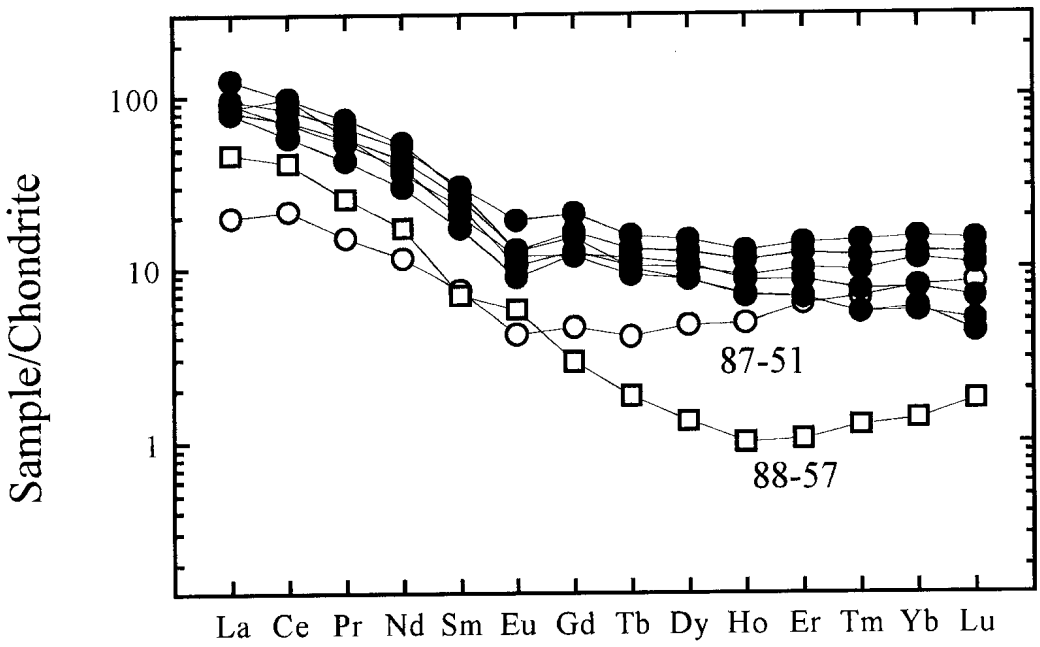


Fig. 2.1. Chondrite normalized bulk-rock compositions of selected metapelites from Gagnon terrane. Most samples (●) behave as a coherent group, but two (○ and □) display different trends (see text for discussion).

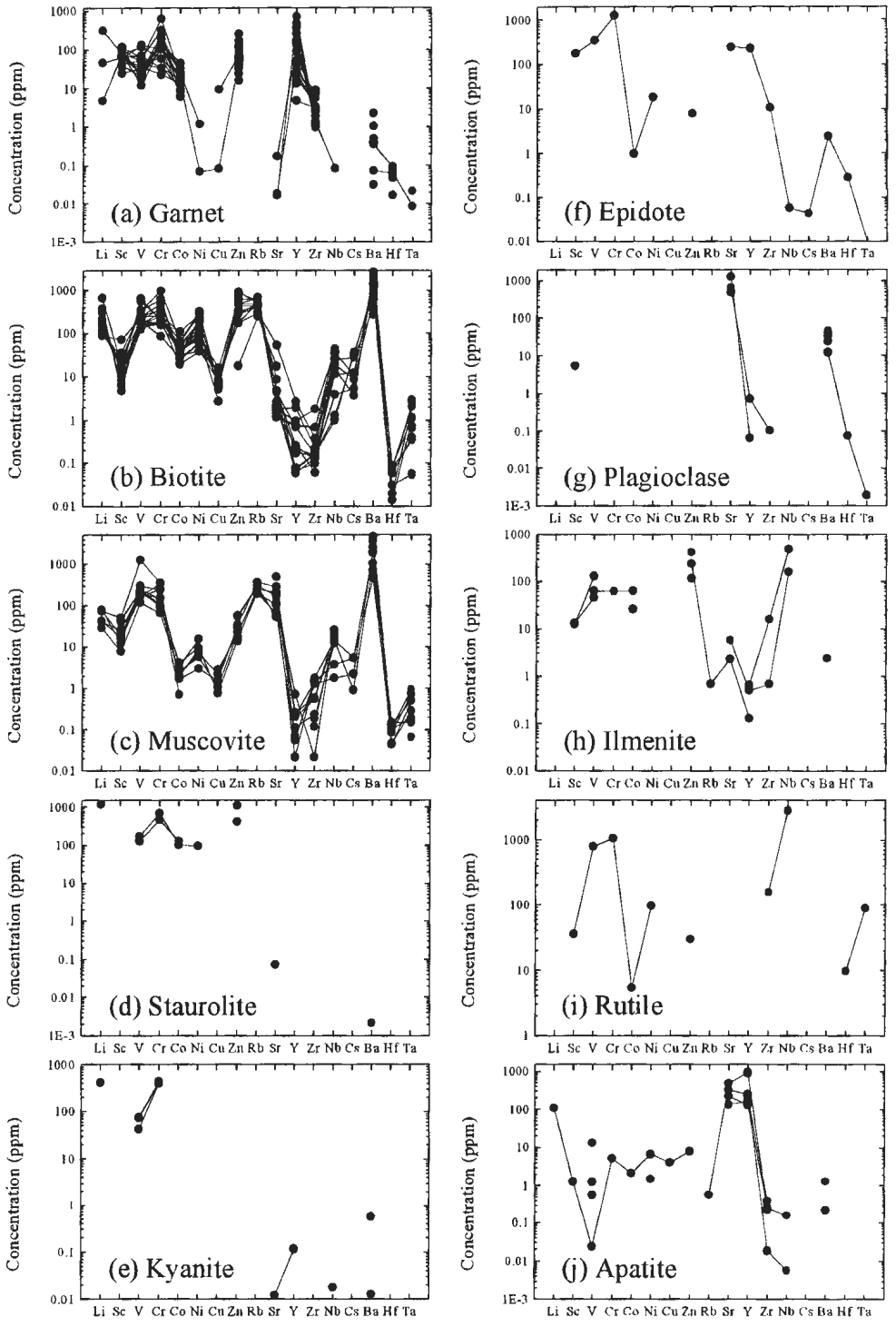


Fig. 2.2. Absolute abundance plots of trace elements other than REE in minerals from Gagnon terrane pelites analyzed by LAM-ICP-MS.

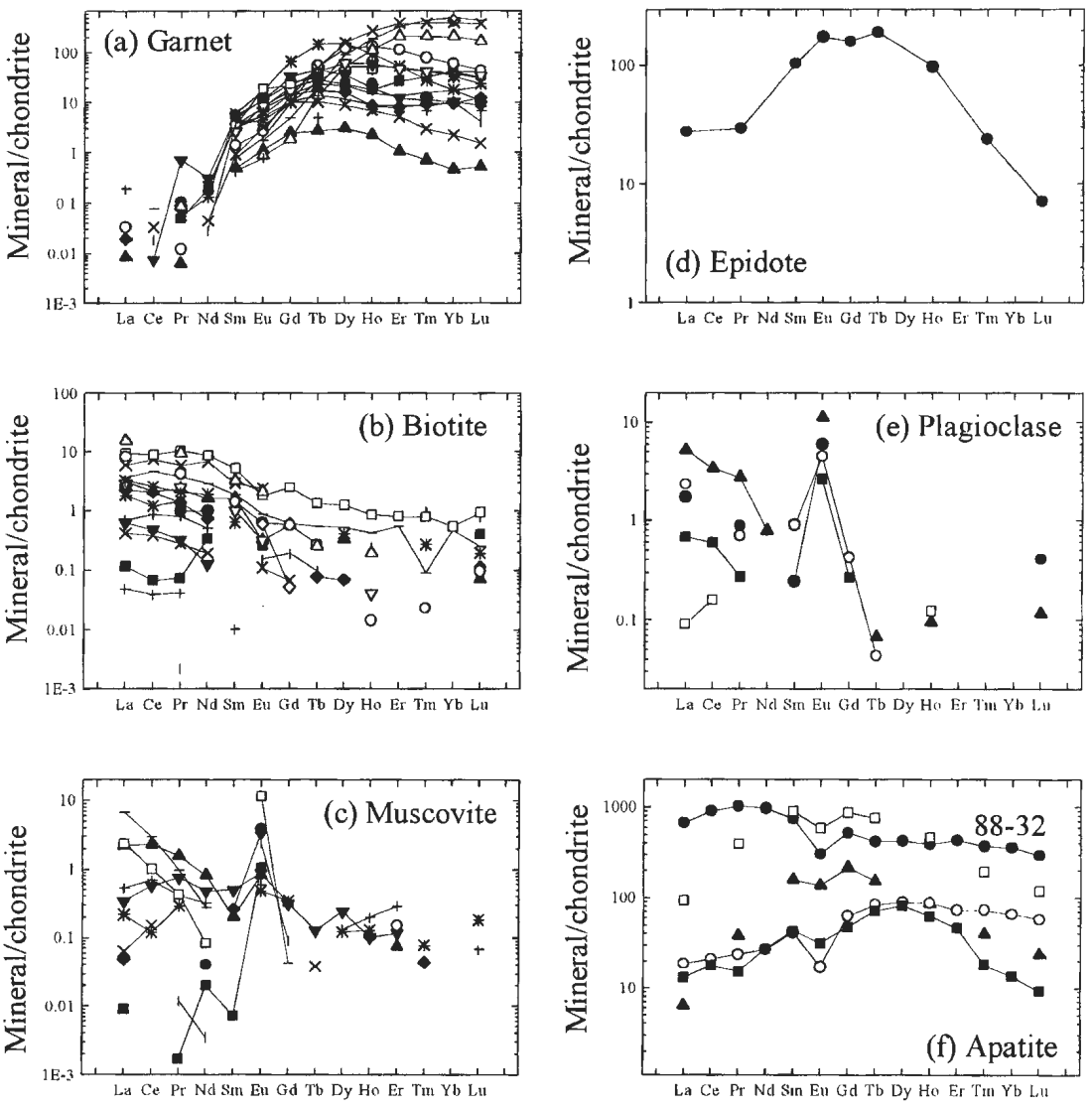


Fig. 2.3. Chondrite-normalized REE patterns of analyzed minerals. Chondrite values are from Taylor and McLennan (1985).

(a)

| Sc | Grt | Bt | Ms | St | Ky | Ep | Pl | Ilm | Rt | Ap |
|---|---|---|---|---|---|---|---|---|---|---|
| Grt | | | | | | | | | | |
| Bt | $6.62\pm 4.95^{28}$ | | | | | | | | | |
| Ms | $4.92\pm 4.30^{18}$ | $0.61\pm 0.36^{24}$ | | | | | | | | |
| St | | | | | | | | | | |
| Ky | *986* | 149 | *244* | | | | | | | |
| Ep | 0.81 | 0.14 | *0.16* | | *0.0009* | | | | | |
| Pl | 15 | 4.72 | *7.74* | | *0.032* | 33 | | | | |
| Ilm | $5.67\pm 1.11^{2}$ | $1.20\pm 0.34^{2}$ | *1.97* | | *0.0081* | *8.57* | *0.25* | | | |
| Rt | 4 | 0.70 | *1.15* | | *0.0047* | 4.92 | 0.15 | *0.58* | | |
| Ap | 50 | 12.82 | 37 | | *0.086* | *92* | *2.72* | *11* | *18* | |

$D_{Sc}$: Ep > Grt > Bt > Ms ≈ Ilm ≈ Rt > Pl > Ap > Ky

(b)

| V | Grt | Bt | Ms | St | Ky | Ep | Pl | Ilm | Rt | Ap |
|---|---|---|---|---|---|---|---|---|---|---|
| Grt | | | | | | | | | | |
| Bt | $0.19\pm 0.087^{32}$ | | | | | | | | | |
| Ms | $0.16\pm 0.064^{20}$ | $0.81\pm 0.23^{25}$ | | | | | | | | |
| St | $0.20\pm 0.050^{3}$ | $1.55\pm 0.088^{2}$ | *1.91* | | | | | | | |
| Ky | 0.58 | $3.87\pm 1.11^{4}$ | $3.67\pm 0.67^{2}$ | *2.50* | | | | | | |
| Ep | 0.026 | 0.95 | *0.012* | *0.61* | *0.25* | | | | | |
| Pl | | | | | | | | | | |
| Ilm | $0.90\pm 0.58^{3}$ | $3.82\pm 0.58^{2}$ | 5.13 | 2.04 | *0.99* | *4.02* | | | | |
| Rt | 0.12 | 0.42 | *0.52* | *0.27* | *0.11* | 0.44 | | *0.11* | | |
| Ap | 440 | 4279 | 4943 | *2761* | *1106* | 604 | | *1120* | 1360 | |

$D_{V}$: Ep > Rt ≈ Ms > Bt ≈ St > Ky > Ilm ≈ Grt > Ap

Fig. 2.4 Distribution matrix (column minerals/row minerals) for Sc, V, Cr, Co, Zn, Y, Zr and Gd. Superscript is the number of measurements. Italicized numbers are dependent ratios, obtained from independent ratios.

(c)

| Cr | Grt | Bt | Ms | St | Ky | Ep | Pl | Ilm | Rt | Ap |
|---|---|---|---|---|---|---|---|---|---|---|
| Grt | | | | | | | | | | |
| Bt | $0.59\pm 0.30^{32}$ | | | | | | | | | |
| Ms | $0.83\pm 0.63^{19}$ | $1.45\pm 0.66^{25}$ | | | | | | | | |
| St | $0.27\pm 0.071^{3}$ | $0.37\pm 0.002^{2}$ | *0.26* | | | | | | | |
| Ky | 0.36 | $1.06\pm 0.52^{4}$ | $0.73\pm 0.12^{2}$ | *2.86* | | | | | | |
| Ep | 1.33 | 0.75 | *0.52* | *2.03* | *0.71* | | | | | |
| Pl | | | | | | | | | | |
| Ilm | 1.78 | *3.02* | *2.14* | 7.47 | *4.94* | *1.34* | | | | |
| Rt | 1.59 | 0.90 | *0.62* | *2.43* | *0.85* | 1.20 | | *0.89* | | |
| Ap | 4.30 | 33 | *2.28* | *89* | *31* | *44* | | *2.42* | *37* | |

$D_{Cr}$: St ≈ Ky ≈ Bt ≈ Ms ≈ Grt ≈ Ep > Rt > Ilm > Ap

(d)

| Co | Grt | Bt | Ms | St | Ky | Ep | Pl | Ilm | Rt | Ap |
|---|---|---|---|---|---|---|---|---|---|---|
| Grt | | | | | | | | | | |
| Bt | $0.39\pm 0.14^{32}$ | | | | | | | | | |
| Ms | $9.24\pm 4.26^{15}$ | $21.78\pm 10.62^{21}$ | | | | | | | | |
| St | $0.27\pm 0.027^{3}$ | $0.64\pm 0.018^{2}$ | *0.030* | | | | | | | |
| Ky | | | | | | | | | | |
| Ep | 27 | 65.21 | *3.00* | *102* | | | | | | |
| Pl | | | | | | | | | | |
| Ilm | $0.50\pm 0.15^{3}$ | $1.87\pm 0.35^{2}$ | 0.076 | 2.03 | | *0.029* | | | | |
| Rt | 4.79 | 11.63 | *0.53* | *18* | | 0.18 | | *6.22* | | |
| Ap | 6.41 | 25.38 | 0.93 | *40* | | *0.39* | | *14* | *2.18* | |

$D_{Co}$: St > Bt ≈ Ilm > Grt > Rt ≈ Ap ≈ Ms > Ep

Fig. 2.4 Continued.

(e)

| **Zn** | Grt | Bt | Ms | St | Ky | Ep | Pl | Ilm | Rt | Ap |
|---|---|---|---|---|---|---|---|---|---|---|
| Grt | | | | | | | | | | |
| Bt | $0.20\pm 0.15^{28}$ | | | | | | | | | |
| Ms | $4.82\pm 3.77^{19}$ | $19\pm 10^{24}$ | | | | | | | | |
| St | $0.048\pm 0.044^{3}$ | $0.037\pm 0.007^{2}$ | *0.0019* | | | | | | | |
| Ky | | | | | | | | | | |
| Ep | 6.77 | 40 | *2.11* | *1081* | | | | | | |
| Pl | | | | | | | | | | |
| Ilm | $0.26\pm 0.23^{3}$ | 4.08 | 0.14 | 4.56 | | | | | | |
| Rt | 1.81 | 11 | *0.58* | *297* | | 0.27 | | *2.70* | | |
| Ap | 6.74 | 73 | 3.52 | *1973* | | *1.83* | | *18* | *6.64* | |

$D_{Zn}$: St > Bt ≈ Ilm > Ms ≈ Rt > Grt > Ap ≈ Ep

(f)

| **Y** | Grt | Bt | Ms | St | Ky | Ep | Pl | Ilm | Rt | Ap |
|---|---|---|---|---|---|---|---|---|---|---|
| Grt | | | | | | | | | | |
| Bt | $836\pm 804^{25}$ | | | | | | | | | |
| Ms | 2051 | $3.53\pm 3.19^{16}$ | | | | | | | | |
| St | | | | | | | | | | |
| Ky | *4999* | 5.98 | *2.44* | | | | | | | |
| Ep | 0.22 | 0.0008 | *.00011* | | *.00004* | | | | | |
| Pl | 802 | $1.79\pm 1.16^{2}$ | *0.39* | | 0.16 | 3496 | | | | |
| Ilm | $292\pm 212^{3}$ | $1.36\pm 0.34^{2}$ | 0.32 | | *0.058* | *1327* | *0.36* | | | |
| Rt | | | | | | | | | | |
| Ap | $1.75\pm 2.25^{5}$ | $.0024\pm .0023^{4}$ | 0.0028 | | 0.0012 | 0.89 | $.0005\pm .0004^{2}$ | *0.0060* | | |

$D_{Y}$: Ep > Grt > Ap > Ilm > Pl ≈ Bt > Ms > Ky

Fig. 2.4 Continued.

(g)

| **Zr** | Grt | Bt | Ms | St | Ky | Ep | Pl | Ilm | Rt | Ap |
|---|---|---|---|---|---|---|---|---|---|---|
| Grt | | | | | | | | | | |
| Bt | 17± 15[29] | | | | | | | | | |
| Ms | 5.09± 5.09[14] | 0.23 | | | | | | | | |
| St | 457 | 13 | *90* | | | | | | | |
| Ky | | | | | | | | | | |
| Ep | 1.34 | 0.014 | *0.26* | *0.0029* | | | | | | |
| Pl | *459* | 27 | *117* | *2.08* | | *1929* | | | | |
| Ilm | 1.58 | 0.52 | 0.35 | *0.0035* | | *1.18* | *0.019* | | | |
| Rt | 0.092 | .00099 | *0.0043* | .00008 | | 0.069 | *.00004* | *0.0019* | | |
| Ap | 262 | 0.46± 0.32[2] | 0.082 | *0.57* | | 576 | 0.46 | *166* | | |

$D_{Zr}$: Rt > Grt ≈ Ep > Ilm > Ms > Bt > Ap > St ≈ Pl

(h)

| **Gd** | Grt | Bt | Ms | St | Ky | Ep | Pl | Ilm | Rt | Ap |
|---|---|---|---|---|---|---|---|---|---|---|
| Grt | | | | | | | | | | |
| Bt | 103 | | | | | | | | | |
| Ms | 348 | 7.63± 5.94[3] | | | | | | | | |
| St | | | | | | | | | | |
| Ky | | | | | | | | | | |
| Ep | *0.36* | 0.0035 | *.00046* | | | | | | | |
| Pl | 56±4[2] | 1.34 | *0.16* | | | 380 | | | | |
| Ilm | | | | | | | | | | |
| Rt | | | | | | | | | | |
| Ap | 0.25± 0.033[2] | .0014± .0019[2] | 0.0066 | | | 0.75 | 0.0020 | | | |

$D_{Gd}$: Ap ≈ Ep > Grt > Pl > Bt > Ms

Fig. 2.4 Continued.

# Chapter3: Crystal chemical and thermal controls on trace-element partitioning between coexisting garnet and biotite in metamorphic rocks from western Labrador

## 3.1 Introduction

Trace element distributions have great potential in the study of metamorphic assemblages and the *P-T-X* conditions of metamorphism because they are usually more sensitive to metamorphic reactions and the local chemical environments than major elements (Hickmott and Shimizu, 1990; Hickmott and Spear, 1992; Lanzirotti, 1995; Schwandt *et al.*, 1996). For example, trace element zoning is known to be a useful monitor of metamorphic reaction history where trace element-enriched refractory minerals are involved in the reactions (Hickmott and Spear, 1992). In addition, in a classic study, Kretz (1959) showed that equilibrium trace element partitioning among coexisting metamorphic minerals has the potential to reflect metamorphic grade. On the basis of his and other data, Kretz (1961) developed the thermodynamic theory for the equilibrium distribution of trace elements between coexisting metamorphic minerals, and in so doing demonstrated quantitatively the potential of trace element thermometry. However, apart from the studies of Kretz (1959), Engel and Engel (1960), Krylova *et al.*

(1970) and Dahl *et al.* (1993), trace element thermometry utilizing trace element partitioning between coexisting metamorphic minerals has not been widely tested or applied.

As a result, quantitative understanding of trace element partitioning and the relative roles of temperature and the major element composition/crystal structure in determining the distribution coefficients remain rudimentary in metamorphic systems. Available trace element partitioning data from natural systems are both scarce and/or of questionable quality (*e.g.* DeVore, 1955; Turekian and Phinney, 1962; Engel and Engel; 1960), and experimental data are virtually non-existent because of difficulties in attaining equilibrium. Many of the studies noted above were unable to document systematic trace-element distributions between coexisting metamorphic minerals, possibly because of poor data quality as well as zoning within one or more of the phases analysed (especially garnet, *e.g.* Hickmott *et al.,* 1987). The laser ablation microprobe coupled to an ICP-MS (LAM-ICP-MS) holds the promise of changing this situation decisively (Jackson *et al.*, 1992; Jenner *et al.,* 1993; Fryer *et al.,* 1995; Taylor *et al.,* 1997) by eliminating uncertainty related to compositional zoning and contamination by solid or fluid microinclusions that arise by analyzing mineral separates. However, no applications of the technique to garnet-biotite pairs have yet been attempted.

In this paper, we provide trace element data (Sc, Ti, V, Cr, Mn, Co, Ni, Cu, Zn, Nd, Y, Ba, Sr, Zr, Hf, Ta and REE) on garnet and biotite from metamorphic rocks equilibrated under greenschist to upper amphibolite facies conditions. Garnet-biotite pairs were chosen for this study because of their widespread coexistence in metapelitic and related

rocks, their wide stability range from greenschist to granulite facies and their overall utility in petrogenetic studies. In addition, coexisting garnet and biotite provide an independent estimation of metamorphic temperature using conventional major element thermometry. On the basis of our data and crystal-chemical and thermal considerations, we explore the controls on trace element partitioning between coexisting garnet and biotite. We believe that the data we have obtained so far add significantly to the current body of knowledge concerning trace element partitioning between coexisting garnet and biotite.

## 3.2 Geologic setting

The Grenville Orogen in western Labrador comprises two lithotectonic terranes, Gagnon and Molson Lake terranes, that are structurally stacked from northwest to southeast on the Ashuanipi Metamorphic Complex foreland of the Superior Province (Fig. 3.1). Metasediments in Gagnon terrane, which are part of the Paleoproterozoic Knob Lake Group, experienced a single Barrovian-type regional metamorphism during the Grenvillian Orogeny at *ca.* 1000 Ma (Rivers 1983; Brown *et al.* 1992; van Gool 1992; Rivers *et al.* 1993). During this orogenic event, Gagnon terrane was incorporated into the base of a major thrust wedge and was overthrust by Molson Lake terrane, composed of Late Paleoproterozoic to Mesoproterozoic granitoid and gabbroic rocks, from the southeast (Fig. 3.1).

Rivers (1983) outlined a metamorphic field gradient from greenschist to upper amphibolite facies in the area, and defined several metamorphic zones on the basis of the following isograd mineral assemblages: *i.e.* garnet-biotite (low-T), staurolite-kyanite and kyanite-garnet-biotite (mid-T), and migmatite zones (high-T). Pressure-temperature estimates across the metamorphic field gradient in the Gagnon terrane indicate an increase in temperature and pressure from *ca.* 435°C and 5.5 kbar in the northwest to 670°C and 11 kbar in the southeast (van Gool, 1992), compatible with the variation in mineral assemblages. The presence of relict growth zoning in some garnets from the highest grade migmatite zone, together with the observation that the P-T paths are hairpin-shaped, suggests that the rocks were cooled and exhumed rapidly, shortly after attaining their peak metamorphic conditions (van Gool, 1992).

Normal patterns of growth zoning are preserved in garnet from garnet-biotite and staurolite-kyanite zones (van Gool, 1992). The pattern is characterized by $X_{sps}$ and $X_{Fe}$ (=Fe/(Fe+Mg) decreasing outward in typical bell-shaped profiles, with $X_{prp}$ and $X_{alm}$ increasing from core to rim. $X_{grs}$ slightly increases or remains nearly constant from core to rim in garnet from the garnet-biotite zone, and decreases or remains nearly constant in garnet from the higher grades. In the kyanite-garnet-biotite and migmatite zones, the pattern of growth zoning is perturbed near some garnet rims by an increase in $X_{sps}$ and $X_{Fe}$ in conjunction with a decrease in $X_{prp}$ and $X_{alm}$, reflecting the resorption of garnet (van Gool, 1992). Flat chemical profiles observed in some garnets from the granitic veins zone indicate homogenization of garnet composition due to intracrystalline diffusion. No breaks in major-element zoning were found, consistent with the interpretation of a single

prograde metamorphism in the area. Mineral assemblages, textures and reactions in metasedimentary rocks from Gagnon terrane are described in detail elsewhere (*e.g.* Rivers, 1983; van Gool, 1992).

## 3.3 Sample description and analytical methods

### 3.3.1 Samples

The thirteen quartzofeldspathic and metapelitic samples chosen for this study include five rocks from the garnet-biotite zone, two from the staurolite-kyanite zone, one from the kyanite-garnet-biotite zone, and five from the migmatite zone (Fig. 3.1). Samples from the low-T zone come from the upper Knob Lake Group, whereas those from mid- and high-T zones come from the lower Knob Lake Group. This distinction is significant because the metasediments of the upper Knob Lake Group are more Ca-rich than those from the lower Knob Lake Group. Three of the samples from the migmatite zone (88-80, 88-58 and 88-57) are located very close together and were selected to test for the effects of major element composition on trace element partitioning. All selected rocks are composed primarily of quartz, muscovite and biotite, with variable modal compositions of garnet (Table 3.1). Staurolite occurs only in sample 88-49 which is also characterized by the presence of gedrite. Zircon, apatite, rutile, ilmenite, magnetite, hematite, pyrite, tourmaline and graphite occur as accessory minerals in the sample suite.

Muscovite and chlorite occur as minor late-stage minerals indicating that water-rich fluids have infiltrated the samples. Biotite is typically fresh in appearance, with only local

minor chloritization. Garnet grains from the garnet-biotite and staurolite-kyanite zones form small (< ~1 mm in diameter) euhedral or subhedral porphyroblasts that commonly contain abundant inclusions of quartz, apatite, tourmaline, ilmenite and epidote. Garnet growth in the zones was largely synkinematic as grains commonly display sigmoidal internal fabrics. Although epidote occurs commonly in calcic metapelites in the biotite zone, its occurrence is restricted to inclusions in garnet in the higher temperature zones. At higher grade, the garnets are large (up to 10 mm in diameter), irregular anhedral porphyroblasts that exhibit evidence of partial resorption during retrograde metamorphism. For garnets showing evidence of resorption, efforts were made to analysis spots close to unresorbed rims which usually contact with quartz domains and have straight crystal outlines.

### 3.3.2 Bulk-rock analysis

For ten samples, concentrations of major elements and first-series transition elements of bulk rocks were determined using a Fisons/ARL® model 8420+ sequential wavelength-dispersion X-ray fluorescence spectrometer at the Department of Earth Sciences, Memorial University of Newfoundland, as described by Longerich (1995). Samples were prepared as pressed pellets using 5 g of rock powder mixed with 0.7 g of BRP-5933 Bakelite® phenolic resin. Bulk-rock concentrations of 14 rare-earth elements (REE) and six other trace-elements (Y, Zr, Nb, Ba, Hf, and Ta) were determined by solution inductively coupled plasma - mass spectrometry (ICP-MS; Perkin Elmer Sciex Elan® model 250) at Memorial University of Newfoundland, following a sodium peroxide

($Na_2O_2$) sinter digestion procedure (Longerich *et al.,* 1990). Synthetic solutions were used to calibrate the ICP-MS. Standard reference materials, MRG-1 and BR-688, and reagent blanks were analyzed for quality-control purposes. Further details of the sample preparation, precision and accuracy are given in Longerich *et al.* (1990).

### 3.3.3 Microanalysis

Quantitative analyses of garnet and biotite grains were carried out using a Cameca® SX-50 electron-microprobe analyzer (EMP) with EDS and WDS analyzers at the Department of Earth Sciences, Memorial University of Newfoundland. An accelerating voltage of 15 kV, a beam current of 10 nA and a beam diameter of about 1~5 μm were used. Instrument calibration was done on a cobalt standard for EDS analyses and on natural and synthetic standards for WDS analyses, with data reduction of raw counts performed with a Link® ZAF matrix-correction program.

Concentrations of trace elements were determined by LAM-ICP-MS at Memorial University of Newfoundland. Current instrumentation and procedures have been described by Taylor *et al.,* (1997). A laser sampler utilizing a frequency-quadrupled Nd:YAG laser source with a wavelength of 266 nm was coupled to a Fisons ®-VG PQII+"S" ICP-MS. The laser was operated in Q-switched mode, with pulse energy optically attenuated to between 0.2 and 0.5 mJ and a pulse-repetition rate of 10 Hz. Calibrations were made against the National Institute of Science and Technology (NIST) standard reference material (SRM) 610, which has a nominal abundance of 500 ppm of the trace elements concerned (Pearce *et al.,* 1997). Either Ca (for garnet) or Ti (for

biotite), whose concentration was previously determined by EMP analysis, was used as an internal standard to correct for differences in ablation yield between samples and the calibration standard. LAM-ICP-MS analyses were conducted separately for the light (Sc to Ba) and heavy (REE to Ta) elements to increase counting times. Data reduction was performed on an in-house spreadsheet program. From examination of graphical output, the presence of spikes potentially related to ablation of micro-inclusions was assessed and optimal background and signal time-intervals for integration were selected accordingly. Concentrations and detection limits were calculated using algorithms derived by Longerich *et al.* (1996b).

Given the inherent heterogeneity of minerals and the impossibility of doing repeated measurements on the same spot, the precision of the LAM-ICP-MS technique is difficult to measure on natural samples. However, precision was estimated by repeated analyses of BCR-2, a glass reference material obtained from the USGS, using operating conditions similar to those applied during routine analyses (Table 3.2). The analytical precision for most of the elements analyzed is within 10% relative standard deviation (RSD) except for Cr, Ni and Cu. For Cr and Ni, concentrations are close to their detection limits (DL; *i.e.* < 4×DL) as defined by 3σ counting statistic errors (Table 3.2). For the analyzed minerals, Ni, Cu, Sr, Nb, Ba, La and Ce in garnet, and Ca, Y, Zr, Cu and the heavy rare earth elements (HREE; Ho to Lu) in biotite are near or below detection limits.

Potential sources of error include: (1) inaccuracies in the determination and mismatch of the normalizing elements Ca and Ti by EMP and LAM; (2) contamination from previously ablated grains or micro-inclusions within grains; and (3) fractionation of

chalcophile elements such as Zn and Cu during sample ablation and plasma transportation (Longerich *et al.,* 1996a). Great efforts were made to spatially match the LAM-ICP-MS and EMP analysis spots to prevent the first error, especially for garnet. However, the two normalizing elements are not significantly zoned in the minerals. Detection of inclusions of minerals very different composition from the host (*e.g.*, apatite or zircon in a silicate) was done by examination of results. However, where silicates are included within silicates containing similar elements, detection of inclusions in the ablated spot is not easy, the only way being the internal consistency of the results. Ba and HREE were used as indicators of contamination of garnet and biotite by micro-inclusions and adjacent minerals, respectively. In order to reduce fractionation effects, a sample cell designed to lower the ablation temperature by directing the Ar carrier gas onto the ablation spot in a high velocity jet was used. The comparable reproducibility of Zn with other elements demonstrates the utility of the sample cell (Table 3.2). This sample cell also helped to reduce the contamination from adjacent analysis spots, by directing the ablated material away from them. To further reduce within-run fractionation, the laser was operated in defocused mode (*i.e.*, focused ~100 μm above the sample surface), thereby reducing the relative amount of defocusing of the laser beam during ablation. Despite these efforts, however, Cu shows strong fractionation effects as demonstrated by its low precision for both reference material and samples (Table 3.2). The pit sizes were generally about 30-60 μm in diameter, depending on target material, length of ablation, pulse energy and degree of defocusing.

## 3.4 Results

### 3.4.1 Major and trace element mineral chemistry

Representative major and trace element compositions of coexisting garnet and biotite from the metasedimentary rocks from Gagnon terrane are presented in Tables 3.3 and 3.4, respectively. Corresponding garnet and biotite stoichiometries are given in Tables 3.5 and 3.6, respectively, in which cation site-occupancies were assigned on the basis of ionic radii (from Shannon, 1976).

Garnet is predominantly an almandine-pyrope solid solution (Fig. 3.2) with $X_{alm}$ from 0.52 to 0.81 and $X_{prp}$ from 0.06 to 0.30. $X_{sps}$ ranges from 0.01 to 0.18; the lowest values are found in the garnet of samples 88-48 and 88-49. $X_{grs}$ ranges from 0.03 to 0.25, with low-Ca in high-T garnet except for sample 88-57 (Fig. 3.2). However, $X_{grs}$ appears to show no correlation with metamorphic temperature and pressure, and is controlled primarily by differences in bulk composition.

Biotite shows extensive Fe-Mg solid solution; $X_{Mg}$ of biotite ranges from 0.46 to 0.76, with the highest values from sample 88-49 which contains gedrite (Fig. 3.3). The Al content correlates weakly with the Mg content of biotite, indicating Mg-Tschermaks substitution (Fig. 3.3). $X_K$ ranges from 0.88 to 0.96 and is mainly controlled by bulk composition (Table 3.6). The chlorine and fluorine contents of biotite vary between 0.01 and 0.13 wt% and between 0.19 and 0.8 wt%, respectively (Table 3.4). Biotite Cl- and F-contents appear to be independent of the $Mg/(Mg+Fe_{Total})$ ratio. Biotite from the migmatite zone is relatively enriched in Ti (Table 3.6), reflecting the grade-related

increase of Ti-saturation in biotite coexisting with ilmenite.

Generally, the concentrations of trace elements in garnet exhibit much greater variation than those in biotite from the same sample (Fig. 3.4), suggesting that the compositional range in garnet is largely due to zoning and resorption. Garnet is rich in Sc, Mn, Y, Zr and HREE compared to coexisting biotite, but has extremely low concentrations of Ni, Cu, Sr, Nb, Ba, Ta and Hf (Fig. 3.4). The regular and consistent trace element distribution patterns, such as V, Cr, Mn, Co and Zn between coexisting garnet and biotite over a range of concentration and metamorphic grade, suggest equilibration of those elements (Figs. 3.4c, d, e, f, i). The distribution of Sc and Cr between coexisting garnet and biotite is not systematic and displays a large scattering in a sample (Fig. 3.4a, d). The abrupt decrease of Zn in garnet and biotite from sample 88-49 is consistent with the coexistence of staurolite in this sample, which is a major carrier of Zn (Fig. 3.4i). This sample, which is characterized by low Mn and Ca contents, also shows strong depletion in Sc and Y which are strongly partitioned into garnet (Figs. 3.4a, k). The whole-rock abundance of Sr, Zr, LREEs, Ta and Hf exceeds that measured in any of the analyzed phases (Figs. 3.4, 3.5), consistent with their concentration in trace element-enriched phases such as apatite, zircon, plagioclase, ilmenite and magnetite.

Most whole-rock REE patterns in the metasedimentary rocks are similar to those of pelitic sediments worldwide (Taylor and McLennan, 1985), being characterized by enriched levels of the LREE, depleted levels of HREE and negative Eu anomalies, except for samples 88-48 and 88-57 (Fig. 3.5a). The different REE patterns in samples 88-48 and 88-57 are not explained by an unusual mineral assemblage, modal abundance or

grain size, features in which they resemble other samples (Table 3.1). Chondrite-normalized patterns of garnet show a small negative Eu anomaly and marked enrichments in HREE relative to LREE throughout the metamorphic range (Fig. 3.5b). The HREE are known to be strongly partitioned into garnet during metamorphic crystallization because of their compatibility in the X-sites in garnet (Hickmott and Shimizu, 1990; Schwandt *et al.*, 1993; Ayres and Vance, 1994). This effect has resulted in enrichment of HREE in some of the garnet rims in samples 88-45, 88-85 and 88-74 during retrograde metamorphism.

Chondrite-normalized REE patterns for biotite show LREE-enriched profiles with negative Eu anomalies of variable magnitudes with the exception of sample 88-74 (Fig. 3.5c). Many low-abundance REEs in biotite have irregular chondrite-normalized patterns because their concentrations approach detection limits. However, most of REE patterns from La to Gd are consistent and regular.

In summary, the trace-element abundances among coexisting garnet and biotite are attributed primarily to: (1) bulk composition; (2) changing assemblages during prograde metamorphism, as can be seen from Zn concentrations in garnet and biotite from the staurolite-kyanite zone; and (3) retrograde metamorphism as shown by anomalously high Sc, Y and HREEs in high-T garnet with retrograde and resorbed rims. Thermal effects on the trace element concentrations or element ratios in either garnet or biotite were not found.

### 3.4.2 Partitioning of trace elements

The distribution ($D$) of trace-element $i$ is defined as the ppm concentration ($C$) ratio,

$$D_i = \frac{C_i^{garnet}}{C_i^{biotite}}, \tag{3.1}$$

which is equivalent to the Nernst distribution coefficient. However, a compositional dependence is partly created by the use of $D_i$, which has only limited thermodynamic significance. In an attempt to eliminate this compositional effect, the term $D_i^*$ was introduced (Nielsen, 1985 and 1988).

$$D_i^* = \frac{X_i^{garnet}}{X_i^{biotite}} \tag{3.2}$$

where $X$ is the mole fraction of component $i$ in a specific site in each mineral. Thus, $D_i^*$ depends on the site occupancies of the trace cation in the structures of garnet and biotite. Both $D_i$ and $D_i^*$ are employed in this study. Mole fractions were computed using the stoichiometric data in Tables 3.5 and 3.6 on the basis of three tetrahedral sites, two octahedral sites and three cubic sites for garnet and two interlayer sites, eight tetrahedral sites and six octahedral sites for biotite. Ti, V, Cr and Zr are commonly regarded as octahedrally coordinated cations in garnet and biotite, whereas Sc, Co, Zn and REE are considered to occupy X-sites in garnet (Meagher, 1982; Hickmott and Shimizu, 1990). In biotite, Sr, Ba and REE substitute in the interlayer sites (Dahl *et al.*, 1993), and the other trace elements are considered to substitute into the octahedrally coordinated sites on the basis of ionic radius and charges. Vanadium incorporation is dependent on its oxidation state ($V^{3+}$, $V^{4+}$ or $V^{5+}$), and the substitution of Ti in the tetrahedral site cannot definitely be excluded. Calculated $D_i^*$ are listed in Table 3.7 for representative garnet-biotite pairs

together with estimated metamorphic temperatures using the garnet-biotite geothermometer (Ferry and Spear, 1978).

Ti, V, Co, Zn and, to a lesser extent, Cr, are preferentially partitioned into the biotite, whereas Sc, Mn, and in most samples, Sm and Gd are preferentially incorporated into garnet (Figs. 3.6a-i). The analytical uncertainties shown in Fig. 3.6 are given as $1\sigma$ standard deviations measured from the counting statistics on the background, integrated signals of analyte and the elements used as an internal standard for sample and standard. The broad fan on the Sc correlation plot indicates a significant range in $D_{Sc}$ (Fig. 3.6a). The large scatter of Sc partitioning data in high-T samples indicates back diffusion of this 'garnet-compatible element' during garnet resorption. Ti distribution between coexisting garnet and biotite is irregular (Fig. 3.6b) and there is no thermal dependence, even if only Ti-saturated (ilmenite-bearing) samples are considered. The V distribution pattern between garnet and biotite appears to be linear, with different distribution patterns between low-T (slope = 0.21) and high-T (slope = 0.10) samples (Fig. 3.6c). The Cr correlation plot shows a broad scatter around a 2:1 line (Fig. 3.6d), which is not related to metamorphic grade. This suggests that Cr failed to achieve equilibrium distribution between coexisting garnet and biotite, consistent with 'overprint zoning' exhibited by Cr in garnet (see chapter 6). Unlike Cr, Co and Zn show good correlation between coexisting garnet and biotite, with different distribution coefficients at different metamorphic grades (Figs. 3.6e, f). There is a distinct difference in distribution coefficients between low- and high-T samples for the $D_{Zr}$, $D_{Sm}$ and $D_{Eu}$, despite their concentrations being close to detection limits in either garnet or biotite (Figs. 3.6g, h, i).

Mean Nernst distribution coefficients were calculated from low-, mid- and high-T samples for the trace elements (Table 3.8). The formulation of the distribution coefficient ($D_i$ or $D_i^*$) does not affect the relative order of trace element enrichment with metamorphic grade. The $D_i$ values for Sc, V, Cr and Co and the relative order of enrichments among them are similar to those of published data (Table 3.8). However, direct comparisons are problematic as most of the published analyses were determined by bulk-mineral methods which cannot be free from contamination and chemical zoning. Hickmott and Spear (1992) reported partitioning data for proton microprobe analyses of Zn in coexisting garnet and biotite from staurolite-bearing metapelitic rocks. Their Zn partition coefficient, $0.37 \pm 0.15$ ($1\sigma$; two anomalously high $D_{Zn}$ values were removed), is same as the value calculated in this study ($0.21 \pm 0.06$), within the permitted error (Table 3.8).

A close approach to equilibrium between coexisting minerals is suggested by the approximately linear distributions of V, Co and Zn (Figs. 3.6c, e, f) and by their intersections with the origin. This regularity also indicates that the distribution of these trace elements is controlled by crystal-chemical parameters and temperature which are discussed below. However, irregular distribution of Cr between coexisting garnet and biotite points to disequilibrum partitioning during greenschist- to upper amphibolite-facies metamorphism.

## 3.5 Discussion

### 3.5.1 Thermodynamic background

Trace element partitioning can be viewed in terms of simple exchange reactions for which the thermodynamic basis is well established (*e.g.* Kretz, 1961). For example, Co partitioning between garnet and biotite can be expressed by the reaction:

$KCo_3AlSi_3O_{10}(OH)_2 + (Mg, Fe)_3Al_2Si_3O_{12} =$

$K(Mg, Fe)_3AlSi_3O_{10}(OH)_2 + (Co)_3Al_2Si_3O_{12}$ (3.3)

The distribution coefficient for reaction (3.3) is approximately equal to $D_{Co}^*$. If the two phases are ideal crystalline solutions and follow Henry's law, at equilibrium

$$RTlnD_i^* = -\Delta H_R + T\Delta S_R - (P-1)\Delta V_R \quad (3.4)$$

where $R$ is the gas constant and $T$ is the temperature in Kelvins. $\Delta H_R$, $\Delta S_R$ and $\Delta V_R$ are the enthalpy, entropy and volume change of reaction, respectively. The effects of pressure are predicted to be small owing to the small change in volume for exchange reactions (McIntire, 1963). This prediction is reinforced by the results of Guo and Green (1989, 1990) who found that the net effects of pressure are relatively small over pressure ranges of 10-20 kbar for Ba partitioning between alkali feldspar and melt. Thus, in ideal solutions the distribution coefficients will be mainly controlled by temperature. If solid solution in garnet and biotite does not follow Henry's law and assuming that $\Delta V_R$ can be neglected, Eq. (3.4) is modified to:

$$RTlnD_i^* = -\Delta H_R + T\Delta S_R + W \quad (3.5)$$

where the $W$ term is composed of the product of the interaction parameters at each site in each phase. At constant temperature, the first two terms on the right-hand side of Eq. (3.5) are constants, and $lnD_i^*$ should be a function of compositions only. Compositional

effects on trace element partitioning are discussed in the following section.

### 3.5.2 Compositional effects

A successful way of representing the compositional dependencies of trace element partition coefficients is to compare the partitioning behaviour of a trace element with that of a major element. In examining such relationships, it is useful to consider atomic or molar proportions and cation site occupancies, rather than weight proportions (Beattie *et al.*, 1991; Beattie, 1993). In addition, by considering the parameter $RTlnD_i^*$ instead of $lnD_i^*$, we can simultaneously account for the effects of temperature on the trace element partitioning.

A negative correlation between Fe+Mg of garnet *vs.* Sc suggests that Sc substitutes into garnet X-sites (Fig. 3.7a). Incorporation of Sc in X-sites in garnet is considered to be charge-balanced by Al- and Si-substitutions. Sm and Eu contents of garnet increase with the $X_{Mg}$ ratio of garnet (Fig. 3.7b), contradicting the proposal of Caporuscio and Smyth (1990), that LREE concentrations in garnet should increase with Ca contents because of structural expansion of the 8-fold Y-sites incurred by the increasing Ca content. The substitution of REE into garnet X-sites involves vacancies or coupled substitutions in order to maintain charge balance. Jaffe (1951) suggested a mechanism involving Y substitution for divalent cations in 8-fold X-sites in garnet, with charge balance achieved by Al substitution for Si in the 4-fold site, yielding a YAG-type substitution. Enami *et al.* (1995) proposed a substitution involving Na, $Na(Y, Yb)Ca_{-2}$ on the X-sites. In this study Na was not detected by EMP in garnet, and substitutions involving vacancies were not

considered because the analyzed garnets commonly have total REE+Y concentrations greater than 100 ppm and up to 220 ppm, amounts far in excess of those possible for coupled vacancy defects (Beattie, 1993). In biotite, there is a broad negative correlation between Sc and Co contents and $Al^{vi}$ (Fig. 3.7c). This indicates that Sc and Co substitution involves a Tschermak-type substitution, $SiMgAl^{iv}_{-1}Al^{vi}_{-1}$, where Sc and Co replace $Al^{vi}$ and Mg, respectively. Concentrations of Sm, Eu and Gd in biotite decrease with increasing $X_{Mg}$ (Fig. 3.7d). REE incorporation in the 12-fold coordinated sites in biotite requires charge balance, but the mechanism cannot be determined with the data available. Fe (0.92 Å) and Mg (0.89 Å) contents of garnet and biotite have no effect on Co (0.9 Å) and Zn (0.9 Å) concentrations in both of the minerals, reflecting the similarity of ionic radii among them and the operation of exchange reactions, $R^{2+}Mg_{-1}$, where R indicates transitional element divalent cations. No correlation was found between $Fe^{3+}$ and trace elements in garnet, implying that all of the V may not occur as $V^{3+}$.

A plot of $RTlnD_{Sc}^{*}$ against $Al^{vi}$ of biotite (Fig. 3.8a) shows an overall positive correlation. This indicates that increasing octahedral Al through Tschermak substitution reduces the compatibility of Sc in biotite. Figure 3.8b shows a crystal chemical coupling between Ti and Ca substitution in garnet, as reported by Crawford (1974). Grossular has a larger unit-cell than almandine and pyrope (Novak and Gibbs, 1971), which may facilitate Ti substitution by expansion of the 6-fold Y-sites. There also is a bulk composition effect, as shown by the different trend for samples 88-49 and 88-45. $D_i$ values for Co and Zn show weak correlations with $X_{grs}$ (not shown). However, no correlations were found between Co and Zn with $X_{grs}$ in garnet when $RTlnD_i^{*}$ was plotted

against $X_{grs}$, indicating dependence of Co and Zn partitioning on metamorphic temperature. $D_{Zr}^{*}$ between garnet and biotite shows correlations with $X_{Mg}$ of biotite and garnet (Fig. 3.8c), indicating that Zr substitutes in the 6-fold Y-sites of garnet. The partitioning of Sm, Eu and Gd appears to be controlled essentially by the $X_{Mg}$ content of biotite (Fig. 3.8d) and garnet (not shown). Decreasing $X_{Mg}$ ratios are accompanied by increasing $X_K$ ratios in biotite, which leads to a secondary correlation of $D_{Sm}^{*}$, $D_{Eu}^{*}$ and $D_{Gd}^{*}$ with $X_K$ (not shown); however, these correlations are not so marked as that with $X_{Mg}$. The strong correlations of $D_{Sm}^{*}$ and $D_{Gd}^{*}$ with $X_{Mg}$ of both biotite and garnet across the entire compositional range indicate that the small crystal-chemical effects caused by the incorporation of Ca in garnet may have been masked by thermal effects. Among the trace elements studied here, Co and Zn show the least compositional effect on partitioning, implying ideal solid solution or the same amount of non-ideality in both of the phases.

### 3.5.3 Thermal effects

The implications of the thermal dependence of trace element partitioning between coexisting garnet and biotite are evident from Eq. (4). However, the effects of metamorphic temperature are difficult to predict for trace elements because enthalpy changes for exchange reactions are not available or cannot be calculated with sufficient precision using available calorimetric data. However, the thermal effects can be evaluated empirically if the temperature of equilibration can be determined for mineral pairs with known trace element contents.

In $lnD_i^*$ *vs.* $10^4/T$ diagrams, the slopes yield enthalpies which can be expressed as,

$$\Delta H_R = \Delta H_M + \Delta H_f \quad (3.6)$$

where $\Delta H_M$ is the heat of mixing, the change in enthalpy due to the change of chemical environment, and $\Delta H_f$ is heat of formation. These are the only possible contributions to $\Delta H_R$, and in a system where solid solutions are ideal, the heat of reaction will simply equal the heat of fusion. For compatible elements, $\Delta H_M$ is possibly negative; for incompatible elements $\Delta H_M$ is positive. In either case $\Delta H_f$ is negative and $\Delta H_R$ will be positive if $\Delta H_f < \Delta H_M$.

This study does not reveal the thermal effects of Sc partitioning between coexisting garnet and biotite suggested by Engel and Engel (1960) and Krylova *et al.* (1970) from the epidote-amphibolite facies to the granulite facies. This may be due to loss of equilibrium compositions of Sc at the rims of garnet by resorption during retrograde metamorphism, together with the compositional effects from $Al^{vi}$ of biotite on the distribution of Sc. The chemical potential of Ti in garnet (or any other phase) is buffered by phase relations with minerals such as rutile and ilmenite. Thus, in a Ti-buffered system, the distribution of Ti may reflect changes in P and T at equilibrium (Ghent and Stout, 1984; Hickmott and Spear, 1992). Ti-solubility in garnet is reported to increase with both P and T in Ti-buffered assemblages (Green and Sobolev, 1975; Hickmott *et al.*, 1987), contradicting the roughly decreasing Ti contents of garnet from low- to high-T (Fig. 3.4b). Thus, it can be concluded that crystal chemistry dominates the incorporation of Ti into garnet in the Labrador samples as shown by coupling of Ti and Ca (Fig. 3.8b). $lnD_V^*$ values become progressively more negative with increasing temperature (Fig.

3.9a), a result that is not compatible with the general thermodynamic requirement that the $D$ values for any element tends to approach unity with increasing temperature. In contrast, the $lnD_i^*$ values for Co and Zn tend toward zero with increasing temperature (Fig. 3.9b). $lnD_{Co}^*$ increases continuously from -1.69 at about 450 °C to -0.48 at about 700 °C, a factor of about 3. $lnD_{Zn}^*$ varies by a factor of 2 for the same temperature ranges (Fig. 3.9c). $lnD_i^*$ values for Zr, Sm, Eu and Gd show apparent positive correlations with metamorphic temperature and a systematic increase from Sm to Gd (Figs. 3.9d, e). This temperature dependence may be produced by the greater thermal expansion of the garnet structure relative to that of the biotite (Smyth and Bish, 1988), which would favour the incorporation of large cations at higher temperatures. While this may be a purely thermal effect it could also be due to the large analytical errors involved and the increasing Mg contents of both phases as temperature increases.

There is a positive correlation between $lnD_V^*$ and $10^4/T$, whereas negative correlations exist for Co, Zn, Zr, Sm, Eu and Gd (Fig. 3.9). For the latter trace elements, negative slopes on $lnD_i^*$ *vs.* $10^4/T$ diagrams imply that heats of reaction ($\Delta H_R$) are positive, indicating that Co, Zn, Zr, Sm, Eu and Gd partitioning between garnet and biotite is dominantly controlled by the heats of mixing. This is simply another way of saying that the partitioning process is not ideal as, if heats of mixing were small, the relations observed in Fig. 3.9b-e would not be possible.

### 3.5.4 Structural effects

The main crystal-chemical constraints in trace element partitioning are the charge

and the ionic radius of the trace-element, in relation to the nominal charge and volume of the incorporating polyhedron (*e.g.*, Nagasawa, 1966; Onuma *et al.*, 1968; Brice, 1975; Blundy and Wood, 1994; Beattie, 1994). Elastic and flexible crystal structures will most readily accommodate misfitting cations and therefore have the lowest interaction parameters.

Following the method of Blundy and Wood (1994), we have fitted our partitioning data for the X- and Y-sites, by weighted non-linear least-squares regression, to the relation:

$$D_i^* = D_o \exp\left[\frac{-4\pi E N_A}{RT}\left(\frac{r_o}{2}(r_i - r_o)^2 + \frac{1}{3}(r_i - r_o)^3\right)\right] \quad (3.7)$$

which relates the partition coefficients for some cation $i$ of ionic radius, $r_i$, to the partition coefficient $D_o$, for a cation whose radius equals the optimal site radius, $r_o$. In this relation, $E$ is the value of Young's modulus for the site, $N_A$ is Avogadro's number, $R$ is the gas constant and $T$ is in Kelvins. By fitting the determined $D_i^*$ values to Eq. (3.7), we can obtain best-fit values for $D_o$, $E$ and $r_o$ for each isovalent series. The results are listed in Table 3.9. For divalent cations, the calculated $r_o$ value for the X-sites, using the mean cation-oxygen distance for grossular (Smyth and Bish, 1988) and the size of $O^{2-}$ ion (Shannon, 1976), is consistent with the value of $r_o$ regressed from the partitioning data (Table 3.9). As only three trivalent cations (Sm, Eu and Gd) are used in the regression of trivalent cations substituting into garnet X-sites, we have set $r_o^{3+}$ equal to $r_o^{2+}$. For the same reason, we are forced to fix $r_o$ for garnet Y-sites: our chosen value (0.54 Å) is the ionic radius of Al in grossular which is a host cation on the Y-sites in grossular. The estimated Young's Modulus for trivalent cations substituting on the X-site is larger than

that of divalent cations, in keeping with the inferred higher elasticity when coupled substitutions are involved (Beattie, 1994).

Divalent and trivalent cations except for Sc show good agreement with the regression curves, with maxima corresponding to the size of 6- and 8-fold coordinated Y- and X-sites in garnet (Fig. 3.10). This suggests that all these elements are substituted into garnet Y- and X-sites and the partitioning of trivalent cations is charge balanced by coupled substitutions. The parabola-shaped cures also imply that the elastic strain is dominated by garnet. From ionic radius arguments alone, we anticipate that $Sc^{3+}$ substitutes into the garnet X-sites. However, Sc plots above the parabola that describes partitioning of trivalent cations into the X-sites, and Sc does not gain any crystal field stabilization energy (Schwarcz, 1967). The mismatch between the regression line for the parabola for trivalent cations in X-sites and Sc distribution coefficient may be caused by the large errors involved in the determinations of distribution coefficients of the REE, and hence significant error in the location and size of the parabola for trivalent cations.

According to the relationship between *P-T* and elasticity (Bass, 1995), the slope of the parabolas decrease with temperature and increase with pressure. Except for V, average trace element partition coefficients for high-T samples are higher than those of low-T (Fig. 3.6) supporting the relationship and indicating that temperature rather than pressure is a dominant factor in the partitioning of trace-elements between garnet and biotite. However, the high-T $D_i^*$ values for divalent and trivalent cations for most samples, although greater than those for low-T samples, do not allow definition of separate parabolas for high-T. Despite the larger errors in the estimations of the partition

coefficients of the REE, it appears from Fig. 3.10 that there is a greater thermal dependence of partitioning on trivalent compared to divalent cations in the X-sites. Furthermore, thermal dependence on partitioning of trace cations in the Y-sites appears negligible. It is worth noting that elements away from the peaks of each parabola such as Co, Zn, Sm, Eu and Gd exhibit stronger temperature dependence than elements in hinge areas, implying that elements whose ionic radii differ greatly from $r_o$ experience more severe change in thermal expansivity for a given $T$ change. However, these elements are also subject to higher interaction energies due to their larger misfit, resulting in stronger controls by crystal chemistry. The absence of compositional dependence of Co and Zn partitioning between coexisting garnet and biotite may be attributed to the similar degree of non-ideality in the two phases. The values of $D_o$, $E$ and $r_o$ regressed from garnet-biotite partitioning data can be used in conjunction with Eq. (3.6) to predict trace-element partition coefficients that were not examined in this study.

## 3.6 Conclusions

Detailed trace element analyses using LAM-ICP-MS, combined with results of major element analyses by electron microprobe of garnet and biotite from lower greenschist to upper amphibolite facies metamorphic rocks from western Labrador allow us to draw the following conclusions.

(1) Systematic distributions of some trace elements (*e.g.* V, Co and Zn) between garnet and biotite are consistent with equilibrium partitioning during metamorphism.

However, a large scattering in Cr distribution suggests different scale of equilibrium.

(2) The trace element compositions of garnet and biotite are mainly controlled by bulk composition and the coexisting mineral assemblage. For instance, garnet and biotite in the staurolite zone are strongly depleted in Zn due to the equilibration with staurolite. Such elemental signatures can contribute to deciphering reaction histories in favourable cases.

(3) Garnet and biotite studied here show correlations between trace and major elements, which support the existence of a major element control on incorporation of some trace elements. For other trace elements, temperature may be an important factor in partitioning. For example, the partitioning of Sc between garnet and biotite in the samples shows a dependence on octahedral Al content of biotite, but no dependence on *T*. Ti distribution is primarily controlled by the Ca content of garnet. On the other hand, $D_V^*$, $D_{Zr}^*$, $D_{Sm}^*$, $D_{Eu}^*$ and $D_{Gd}^*$ are controlled by both crystal-chemical factors and temperature. The partitioning of Co and Zn shows a *T* effect, with the least compositional effects; both elements partition preferentially into garnet at higher *T*.

(4) The partition coefficients between garnet and biotite exhibit dependence on ionic radius and charge. This suggests that trace element partitioning occurs by substitution onto specific crystallographic sites in crystalline phases and that the partitioning of trivalent cations in X-sites is charge balanced by coupled substitutions.

None of the elements promise simply applicable alternative 'trace element geothermometers' for greenschist- and amphibolite-facies metamorphic rocks. Scatter in

plots of $lnD_i^*$ versus $10^4/T$ is large, and in the case of V, Zr, Sm, Eu and Gd the composition effects cannot be separated from thermal effects. However, these data do provide a series of tests for equilibrium between phases in metapelitic samples, and hence can be used to improve the choice of appropriate samples for other studies. Compositional ranges of trace elements and partition coefficients between coexisting garnet and biotite provide useful information for qualitative and quantitative modelling of reaction histories of metamorphic assemblages. The relationships between distribution coefficients and ionic radius can be used to predict partition coefficients of trace elements which have not been studied in this paper and also to choose trace elements for a possible future 'trace element geothermometer'.

Table 3.1. Mineral assemblages and modal percentages of the metamorphic rocks from western Labrador.

| Spl. | Qtz | Ms | Bt | Chl | Ep | Pl | Ky | Grt | Ged | St | Tur | Ap | Rt | Zrn | Ilm | Hem | Mag | Py | Gr | Grt/Bt |
|---|---|---|---|---|---|---|---|---|---|---|---|---|---|---|---|---|---|---|---|---|
| 87-81 | 41 | 28 | 26 | | | <1 | | <1 | | | <1 | <1 | | <1 | <1 | | | | | 0.02 |
| 87-83 | 53 | 11 | 28 | <1 | <1* | <1 | | 4 | | | <1 | <1 | | <1 | <1 | | | | <1 | 0.13 |
| 87-86 | 40 | 11 | 43 | <1 | <1* | <1 | | <1 | | | <1 | <1 | | <1 | <1 | <1 | | | <1 | 0.01 |
| 87-283 | 43 | <1 | 45 | 2# | <1* | <1 | | <1 | | | <1 | <1 | | <1 | <1 | | | | <1 | 0.01 |
| 87-279 | 48 | 16 | 23 | 4# | | <1 | | 3 | | | | <1 | | <1 | <1 | | | <1 | <1 | 0.11 |
| 88-49 | 27 | | 37 | <1# | | | 5 | 19 | 2 | 9 | <1 | | <1* | <1 | | | | <1 | | 0.51 |
| 88-48 | 26 | 10- | 44 | 4 | | <1 | 2 | 10 | | | <1 | <1 | <1* | <1 | <1 | | | | | 0.24 |
| 88-45 | 44 | 27 | 11 | | | <1 | <1 | 11 | | | | | <1* | <1 | <1 | <1 | <1 | | | 1.02 |
| 88-85 | 62 | 29 | 6 | | | <1 | 2 | <1 | | | | | <1* | <1 | <1 | | <1 | <1 | | 0.12 |
| 88-74 | 34 | 26 | 23 | | | 2 | 9 | <1 | | | <1 | <1 | | <1 | <1 | | <1 | <1 | | 0.03 |
| 88-80 | 12 | 2# | 63 | 2 | | 9 | 2 | 4 | | | | <1 | | <1 | <1 | | | <1 | | 0.06 |
| 88-57 | 47 | <1 | 37.3 | 2 | | 6 | | 5 | | | | | | <1 | <1 | | | <1 | | 0.14 |
| 88-58 | 34 | 43 | 8 | | | | | 11 | | | | <1 | | <1 | | <1 | <1 | | | 1.49 |

* Minerals occur only as inclusions; and # secondary minerals. Mineral abbreviations after Kretz (1983).

Table 3.2. Mean value, precision and detection limits for BCR-2G and samples.

| Elements | BCR-2G | | Literature | Diff. | Detection limits (BCR-2G) | | | Detection limits (Sample) | | |
|---|---|---|---|---|---|---|---|---|---|---|
| | Mean | Std. dev. | Values* | (%) | min. | max. | avg. | min. | max. | avg. |
| Sc | 31.5 | 1.6 | 32.6 | 3.49 | 0.077 | 11.271 | 2.608 | 0.058 | 216.58 | 12.53 |
| $TiO_2$ | 2.04 | 0.06 | 2.24 | 8.99 | 0.00008 | 0.00192 | 0.00033 | 0.00003 | 0.05239 | 0.00216 |
| V | 398 | 16 | 407 | 2.16 | 0.032 | 1.207 | 0.233 | 0.026 | 22.75 | 1.64 |
| Cr | 15.6 | 2.3 | 16 | 2.29 | 0.906 | 25.647 | 5.058 | 0.947 | 416.22 | 35.00 |
| MnO | 0.18 | 0.01 | 0.177 | 3.15 | 0.000 | 0.001 | 0.000 | 0.000 | 0.01 | 0.00 |
| Co | 35.4 | 2.9 | 37 | 4.29 | 0.063 | 2.103 | 0.570 | 0.055 | 96.02 | 5.09 |
| Ni | 10.6 | 1.5 | 13 | 17.85 | 0.195 | 25.662 | 5.351 | 0.177 | 546.72 | 34.78 |
| Cu | 20.7 | 4.0 | 19 | 8.73 | 0.225 | 1.228 | 0.595 | 0.178 | 38.73 | 6.42 |
| Zn | 161 | 15 | 129.5 | 24.28 | 0.152 | 2.096 | 1.293 | 0.153 | 15.55 | 3.42 |
| Sr | 332 | 17 | 337 | 1.49 | 0.005 | 0.057 | 0.019 | 0.007 | 0.52 | 0.11 |
| Y | 31.4 | 2.6 | 32.51 | 3.29 | 0.003 | 0.133 | 0.025 | 0.003 | 2.21 | 0.18 |
| Zr | 171 | 12 | 184.4 | 7.53 | 0.003 | 0.232 | 0.046 | 0.004 | 7.01 | 0.31 |
| Nb | 9.9 | 0.9 | 13.14 | 24.07 | 0.002 | 0.021 | 0.009 | 0.003 | 0.23 | 0.05 |
| Ba | 652 | 41 | 681 | 4.28 | 0.002 | 0.480 | 0.070 | 0.005 | 7.89 | 0.48 |
| La | 25.4 | 1.5 | 25.3 | 0.55 | 0.001 | 0.039 | 0.008 | 0.001 | 0.86 | 0.07 |
| Ce | 54.8 | 3.7 | 53.6 | 2.22 | 0.001 | 0.044 | 0.007 | 0.002 | 0.96 | 0.06 |
| Pr | 7.2 | 0.4 | 6.83 | 4.74 | 0.001 | 0.006 | 0.003 | 0.001 | 0.08 | 0.01 |
| Nd | 29.1 | 1.8 | 28.63 | 1.62 | 0.008 | 0.252 | 0.067 | 0.011 | 5.62 | 0.70 |
| Sm | 6.7 | 0.5 | 6.67 | 0.71 | 0.006 | 0.180 | 0.042 | 0.008 | 3.96 | 0.38 |
| Eu | 2.0 | 0.2 | 2 | 0.59 | 0.001 | 0.049 | 0.011 | 0.002 | 0.96 | 0.11 |
| Gd | 6.5 | 0.5 | 6.8 | 5.04 | 0.006 | 0.135 | 0.044 | 0.008 | 4.48 | 0.37 |
| Tb | 1.07 | 0.08 | 1.04 | 2.61 | 0.001 | 0.004 | 0.002 | 0.001 | 0.06 | 0.01 |
| Dy | 6.6 | 0.5 | 6.38 | 3.89 | 0.005 | 0.128 | 0.026 | 0.004 | 2.18 | 0.22 |
| Ho | 1.4 | 0.1 | 1.29 | 6.59 | 0.001 | 0.006 | 0.003 | 0.001 | 0.07 | 0.01 |
| Er | 3.8 | 0.3 | 3.66 | 4.23 | 0.002 | 0.126 | 0.028 | 0.005 | 2.27 | 0.23 |
| Tm | 0.56 | 0.05 | 0.54 | 3.14 | 0.001 | 0.005 | 0.002 | 0.001 | 0.07 | 0.01 |
| Yb | 3.3 | 0.4 | 3.34 | 0.30 | 0.005 | 0.206 | 0.038 | 0.007 | 3.46 | 0.31 |
| Lu | 0.50 | 0.06 | 0.51 | 2.22 | 0.001 | 0.034 | 0.009 | 0.001 | 0.44 | 0.05 |
| Hf | 5.0 | 0.6 | 5.17 | 4.12 | 0.004 | 0.014 | 0.009 | 0.009 | 0.45 | 0.06 |
| Ta | 0.59 | 0.07 | 0.78 | 24.20 | 0.001 | 0.002 | 0.001 | 0.001 | 0.22 | 0.02 |

All results in ppm, except $TiO_2$ and MnO in wt% oxide. Based on 16 determinations over the period March 19, 1996 to April, 1997. Std. dev. = standard deviation; Diff. = percent difference between literature values and the values from this study for BCR2-G. * Literature values from Govindaraju (1994).

Table 3.3. Representative analyses of garnet determined by electron microprobe and LAM-ICP-MS.

| | 87-81 | | 87-83 | | 87-86 | | 87-283 | | 87-279 | | 88-49 | | 88-48 | | 88-45 | | 88-85 | | 88-74 | | 88-80 | | 88-57 | | 88-58 | |
|---|---|---|---|---|---|---|---|---|---|---|---|---|---|---|---|---|---|---|---|---|---|---|---|---|---|---|
| Spl. | F23 | G1 | C11 | C24 | C1 | C8 | C3 | D2 | D6 | D1 | A4 | A45 | D1 | D3 | E1 | E7 | C4 | D10 | C5 | D8 | B9 | B5 | A13 | A9 | B5 | C4 |
| (wt%) | | | | | | | | | | | | | | | | | | | | | | | | | | |
| $SiO_2$ | 37.50 | 37.50 | 37.30 | 37.10 | 37.20 | 37.10 | 37.10 | 37.40 | 37.80 | 37.80 | 37.44 | 37.44 | 37.20 | 37.70 | 37.70 | 38.00 | 38.10 | 38.10 | 37.30 | 37.90 | 39.10 | 38.90 | 38.50 | 38.20 | 37.90 | 37.80 |
| $TiO_2$ [#] | 0.055 | 0.048 | 0.047 | 0.059 | 0.031 | 0.034 | 0.030 | 0.063 | 0.030 | 0.027 | 0.010 | 0.010 | 0.044 | 0.065 | 0.004 | 0.006 | 0.005 | n.d. | 0.005 | 0.005 | 0.020 | 0.004 | 0.027 | 0.041 | 0.003 | 0.005 |
| $Al_2O_3$ | 21.00 | 20.80 | 20.80 | 21.00 | 20.70 | 20.60 | 20.70 | 20.90 | 21.00 | 21.00 | 21.48 | 21.48 | 21.00 | 21.10 | 21.20 | 21.40 | 21.30 | 21.60 | 21.10 | 21.20 | 22.00 | 22.00 | 21.30 | 21.40 | 21.50 | 21.30 |
| FeO | 30.30 | 31.60 | 30.00 | 30.80 | 30.10 | 29.00 | 27.90 | 26.90 | 30.30 | 30.30 | 35.94 | 35.94 | 35.20 | 35.40 | 35.10 | 35.20 | 34.90 | 35.10 | 35.90 | 35.30 | 27.60 | 28.30 | 27.20 | 28.40 | 38.00 | 38.30 |
| MgO | 1.70 | 1.90 | 1.80 | 1.80 | 1.70 | 1.70 | 1.80 | 1.60 | 2.40 | 2.40 | 5.70 | 5.70 | 4.30 | 4.20 | 4.30 | 4.50 | 4.40 | 4.30 | 3.80 | 4.00 | 7.00 | 6.70 | 3.40 | 3.90 | 3.70 | 3.70 |
| MnO | 3.50 | 2.70 | 3.70 | 4.00 | 4.30 | 4.70 | 3.50 | 5.10 | 2.90 | 2.90 | n.d. | n.d. | n.d. | n.d. | 0.30 | 0.30 | 0.40 | 0.40 | 1.90 | 2.00 | 3.30 | 4.90 | 3.60 | 2.00 | 0.40 | 0.30 |
| CaO | 7.30 | 6.80 | 7.00 | 6.40 | 6.50 | 6.80 | 8.70 | 8.70 | 6.70 | 6.70 | 0.58 | 0.58 | 2.30 | 2.40 | 2.70 | 2.80 | 3.00 | 3.30 | 1.60 | 1.60 | 3.50 | 2.10 | 8.40 | 7.80 | 1.60 | 1.50 |
| Total | 101 | 101 | 101 | 101 | 101 | 100 | 100 | 101 | 101 | 101 | 101 | 101 | 100 | 101 | 101 | 102 | 102 | 103 | 102 | 102 | 103 | 103 | 102 | 102 | 103 | 103 |
| (ppm) | | | | | | | | | | | | | | | | | | | | | | | | | | |
| Sc | 106 | 102 | 65 | 74 | 63 | 70 | 92 | 135 | 75 | | 23 | n.d. | 40 | 76 | 83 | 68 | 82 | 93 | 70 | 72 | 176 | 258 | 112 | 64 | 62 | 53 |
| V | 49 | 45 | 68 | 65 | 36 | 47 | 82 | 150 | 144 | | 27 | 34 | 44 | 46 | 19 | 22 | 22 | 30 | 17 | 16 | 23 | 25 | 71 | 47 | 19 | 21 |
| Cr | 153 | 33 | 34 | 135 | n.d. | 84 | 62 | 90 | 79 | | 130 | 117 | 305 | 300 | 121 | 164 | 113 | 127 | 85 | 88 | 42 | 239 | 781 | 156 | 209 | 172 |
| Co | 12.9 | 10.3 | 16.7 | 16.4 | 13.9 | 14.3 | 8.2 | 8.6 | 6.5 | | 29.6 | 25.8 | 20.7 | 21.5 | 12.2 | 10.8 | 18.5 | 18.3 | 37.7 | 36.4 | 18.4 | 16.2 | 24.3 | 23.3 | 19.8 | 18.7 |
| Ni | n.d. | n.d. | n.d. | n.d. | n.d. | n.d. | n.d. | n.d. | n.d. | | n.d. | n.d. | n.d. | 94 | n.d. | n.d. | n.d. | n.d. | n.d. | n.d. | n.d. | n.d. | n.d. | n.d. | n.d. | n.d. |
| Cu | n.d. | n.d. | n.d. | n.d. | n.d. | n.d. | n.d. | n.d. | n.d. | | n.d. | n.d. | n.d. | n.d. | n.d. | n.d. | n.d. | n.d. | n.d. | n.d. | 3 | 3 | n.d. | n.d. | n.d. | n.d. |
| Zn | 46 | 32 | 60 | 64 | 55 | 83 | 68 | 54 | 51 | | 6 | n.d. | 19 | 23 | 132 | 123 | 115 | 124 | 60 | 62 | 42 | 51 | 68 | 101 | 164 | 161 |
| Sr | n.d. | n.d. | n.d. | n.d. | n.d. | n.d. | n.d. | n.d. | n.d. | | n.d. | | n.d. | n.d. | n.d. | n.d. | n.d. | n.d. | n.d. | n.d. | n.d. | n.d. | | | 0.09 | n.d. |
| Y | 598 | 357 | 154 | 124 | 706 | 658 | 150 | 372 | 215 | | 7 | 4 | 29 | 13 | 450 | 314 | 89 | 103 | 166 | 192 | 95 | 140 | 24 | 58 | 72 | 66 |
| Zr | 2.2 | 1.4 | 1.8 | 2.1 | 1.3 | 1.8 | 1.0 | 1.4 | 1.3 | 0.9 | 2.6 | 2.0 | 8.1 | 9.0 | 1.1 | 1.7 | 2.1 | 2.4 | 6.0 | 4.1 | 16.0 | 11.4 | 3.0 | 2.4 | 1.0 | 1.3 |
| Nb | n.d. | n.d. | n.d. | n.d. | n.d. | n.d. | n.d. | n.d. | n.d. | | | | n.d. | n.d. | n.d. | n.d. | n.d. | n.d. | n.d. | n.d. | n.d. | n.d. | | | | |
| Ba | n.d. | 9.1 | 2.7 | n.d. | 0.5 | 0.2 | n.d. | 0.2 | n.d. | n.d. | n.d. | 0.0 | n.d. | n.d. | n.d. | n.d. | n.d. | n.d. | n.d. | n.d. | n.d. | n.d. | 0.1 | n.d. | n.d. | n.d. |
| La | | n.d. | n.d. | n.d. | n.d. | n.d. | 0.04 | 0.03 | | 0.01 | n.d. | n.d. | n.d. | 0.04 | n.d. | 0.00 | n.d. | | | | n.d. | n.d. | n.d. | n.d. | n.d. | n.d. |
| Ce | | 0.07 | 0.02 | 0.26 | n.d. | n.d. | 0.06 | 0.06 | | n.d. | n.d. | n.d. | 0.03 | 0.09 | n.d. | n.d. | 0.00 | | | | n.d. | 0.00 | n.d. | n.d. | | |
| Pr | | n.d. | n.d. | n.d. | n.d. | n.d. | 0.00 | 0.06 | | 0.00 | n.d. | n.d. | 0.01 | 0.04 | n.d. | 0.00 | 0.09 | | | | 0.01 | 0.00 | 0.01 | n.d. | n.d. | n.d. |
| Nd | | n.d. | n.d. | 0.24 | 0.03 | n.d. | n.d. | n.d. | | n.d. | n.d. | n.d. | 0.29 | 0.41 | n.d. | n.d. | n.d. | | | | 0.29 | 0.14 | 0.36 | 0.39 | n.d. | n.d. |
| Sm | | n.d. | 0.18 | n.d. | 0.21 | 0.43 | n.d. | n.d. | | 0.32 | 0.11 | 0.07 | 1.55 | 1.81 | 0.97 | 1.00 | 1.36 | | | | 1.79 | 0.95 | 0.88 | 0.54 | | |
| Eu | | 0.16 | 0.18 | 0.22 | 0.29 | 0.24 | n.d. | n.d. | | 0.24 | 0.08 | 0.06 | 0.73 | 0.43 | 0.51 | 0.71 | 1.05 | | | | 1.33 | 0.79 | 0.93 | 1.09 | 0.24 | 0.25 |
| Gd | | 1.56 | 3.02 | 1.68 | 3.26 | 4.39 | 1.11 | 1.04 | | 4.22 | 0.88 | 0.55 | 5.60 | 3.06 | 12.34 | 13.79 | 10.94 | | | | 11.20 | 11.63 | 4.87 | 5.90 | | |
| Tb | | 1.22 | 1.66 | 1.33 | 2.96 | 3.36 | 0.86 | 1.10 | | 3.16 | 0.24 | 0.13 | 0.91 | 0.36 | 6.82 | 6.13 | 2.77 | | | | 3.12 | 4.01 | 1.37 | 1.74 | 1.37 | 1.61 |
| Dy | | 33.9 | 20.1 | 15.7 | 59.0 | 65.9 | 16.1 | 23.3 | | 46.1 | 1.5 | 1.0 | 4.4 | 2.2 | 75.9 | 55.9 | 13.8 | | | | 18.9 | 30.1 | 7.1 | 11.3 | | |
| Ho | | 16.98 | 4.69 | 3.69 | 24.80 | 23.33 | 6.90 | 12.75 | | 11.77 | 0.24 | 0.19 | 0.97 | 0.47 | 20.81 | 11.16 | 1.75 | | | | 2.78 | 5.21 | 0.85 | 2.37 | 2.23 | 2.07 |
| Er | | 84.19 | 12.81 | 10.66 | 98.09 | 84.01 | 27.52 | 58.34 | | 28.28 | 0.47 | 0.43 | 2.96 | 1.40 | 57.33 | 21.71 | 3.05 | | | | 4.84 | 11.33 | 1.94 | 6.33 | | |
| Tm | | 18.10 | 1.66 | 1.48 | 15.80 | 12.68 | 4.26 | 10.06 | | 3.10 | 0.05 | 0.03 | 0.44 | 0.19 | 7.04 | 2.15 | 0.41 | | | | 0.43 | 1.51 | 0.22 | 0.94 | | |
| Yb | | 127.6 | 9.73 | 8.38 | 101.3 | 78.22 | 25.41 | 63.74 | | 14.77 | 0.54 | 0.23 | 2.33 | 1.43 | 35.77 | 10.67 | 2.46 | | | | 1.84 | 8.12 | 1.81 | 6.68 | 3.35 | 3.10 |
| Lu | | 18.02 | 1.16 | 1.17 | 15.20 | 11.50 | 3.50 | 7.98 | | 1.74 | 0.11 | 0.05 | 0.38 | 0.23 | 4.71 | 1.16 | 0.36 | | | | 0.28 | 1.03 | 0.28 | 1.05 | 0.39 | 0.52 |
| Hf | | n.d. | n.d. | n.d. | n.d. | 0.05 | n.d. | n.d. | | 0.02 | | | 0.11 | 0.19 | n.d. | 0.04 | 0.02 | | | | 0.24 | 0.20 | | | | |
| Ta | | n.d. | 0.02 | 0.03 | n.d. | n.d. | n.d. | n.d. | | n.d. | | | n.d. | 0.00 | n.d. | n.d. | n.d. | | | | n.d. | n.d. | | | | |

[#] Determined by LAM-ICP-MS. * Total Fe as FeO. n. d. = not detected. Blank = not determined.

Table 3.4. Representative analyses of biotite determined by electron microprobe and LAM-ICP-MS.

| | 87-81 | | 87-83 | | 87-86 | | 87-283 | | 87-279 | | 88-49 | | 88-48 | | 88-45 | | 88-85 | | 88-74 | | 88-80 | | 88-57 | | 88-58 | |
|---|---|---|---|---|---|---|---|---|---|---|---|---|---|---|---|---|---|---|---|---|---|---|---|---|---|---|
| Spl. | F8 | G12 | C23 | C9 | C34 | C4 | C5 | D5 | D3 | D3 | A5 | A1 | D2 | D4 | E2 | E4 | C5 | D11 | C6 | D9 | B4 | B6 | A12 | A12 | B3 | C3 |
| (wt%) | | | | | | | | | | | | | | | | | | | | | | | | | | |
| $SiO_2$ | 36.7 | 36.1 | 37.8 | 36.5 | 37.8 | 36.3 | 36.9 | 36.1 | 37.3 | 37.3 | 40.4 | 40.3 | 37.6 | 37.5 | 37.7 | 37.3 | 37.6 | 37.8 | 37.0 | 37.0 | 38.9 | 38.1 | 37.6 | 37.6 | 36.9 | 37.2 |
| $TiO_2$ | 1.70 | 1.60 | 1.80 | 1.70 | 1.70 | 1.70 | 1.80 | 1.80 | 1.70 | 1.70 | 1.40 | 1.20 | 1.40 | 1.40 | 1.70 | 1.60 | 1.70 | 2.00 | 2.10 | 2.20 | 1.30 | 1.40 | 2.00 | 2.00 | 2.30 | 2.20 |
| $Al_2O_3$ | 17.2 | 17.3 | 18.0 | 17.1 | 17.8 | 17.1 | 17.4 | 17.5 | 17.2 | 17.2 | 17.7 | 17.8 | 18.7 | 18.7 | 18.7 | 18.6 | 18.7 | 18.3 | 17.8 | 17.8 | 19.2 | 18.7 | 17.5 | 17.5 | 18.1 | 18.6 |
| FeO* | 20.1 | 19.7 | 19.1 | 20.0 | 18.8 | 19.0 | 19.7 | 19.7 | 18.4 | 18.4 | 11.6 | 11.4 | 15.0 | 14.6 | 16.1 | 16.4 | 16.4 | 16.6 | 17.7 | 18.0 | 12.6 | 12.8 | 16.9 | 16.9 | 20.4 | 20.5 |
| MgO | 10.0 | 10.0 | 11.0 | 10.5 | 11.2 | 10.5 | 10.7 | 10.4 | 11.3 | 11.3 | 17.5 | 17.7 | 13.4 | 13.3 | 12.3 | 12.3 | 12.6 | 12.4 | 11.7 | 11.7 | 15.7 | 14.9 | 12.2 | 12.2 | 9.7 | 10.4 |
| MnO# | 0.199 | 0.149 | 0.137 | | 0.141 | 0.138 | 0.108 | 0.104 | 0.176 | 0.176 | n.d. | n.d. | 0.005 | 0.005 | 0.005 | 0.005 | 0.005 | 0.006 | 0.030 | 0.033 | 0.114 | 0.095 | 0.136 | 0.136 | 0.023 | 0.023 |
| $Na_2O$ | n.d. | n.d. | 0.20 | n.d. | n.d. | n.d. | n.d. | 0.30 | 0.30 | 0.30 | 0.80 | 0.90 | 0.40 | 0.50 | 0.40 | 0.30 | 0.50 | 0.60 | 0.60 | 0.80 | 0.40 | 0.50 | n.d. | n.d. | n.d. | n.d. |
| $K_2O$ | 9.2 | 9.4 | 8.9 | 9.3 | 9.3 | 8.8 | 9.0 | 9.1 | 9.1 | 9.1 | 8.3 | 8.4 | 8.9 | 8.7 | 6.9 | 7.4 | 8.1 | 8.0 | 8.8 | 8.7 | 9.0 | 9.3 | 9.1 | 9.1 | 9.5 | 9.2 |
| F | | | 0.50 | | 0.50 | | 0.27 | | | | | 0.43 | 0.20 | | 0.45 | | 0.56 | | 0.33 | | 0.19 | | 0.22 | 0.22 | | 0.36 |
| Cl | | | 0.04 | | 0.05 | | 0.10 | | | | | 0.04 | 0.01 | | n.d. | | n.d. | | 0.02 | | 0.03 | | 0.02 | 0.02 | | 0.03 |
| Total | 95 | 94 | 95 | 95 | 93 | 93 | 95 | 95 | 95 | 95 | 98 | 97 | 95 | 95 | 94 | 94 | 95 | 96 | 96 | 96 | 96 | 96 | 97 | 97 | 97 | 96 |
| (ppm) | | | | | | | | | | | | | | | | | | | | | | | | | | |
| Sc | 18.5 | 16.5 | 12.3 | | 14.9 | 17.3 | 16.9 | 22.3 | 14.4 | 14.4 | n.d. | n.d. | 11.8 | 12.4 | 6.3 | 5.6 | 4.9 | 5.4 | 14.8 | 15.3 | 44.4 | 43.1 | 43.2 | 43.2 | 14.4 | 13.1 |
| V | 191 | 162 | 151 | | 174 | 195 | 523 | 550 | 655 | 655 | 305 | 283 | 136 | 125 | 253 | 223 | 261 | 273 | 249 | 261 | 281 | 273 | 485 | 485 | 114 | 108 |
| Cr | 173 | 162 | 184 | | 147 | 179 | 206 | 184 | 198 | 198 | 366 | 432 | 540 | 422 | 346 | 345 | 306 | 247 | 275 | 338 | 341 | 342 | 685 | 685 | 215 | 172 |
| Co | 49.6 | 39.8 | 52.4 | | 57.2 | 57.9 | 47.3 | 46.5 | 19.8 | 19.8 | 82.2 | 79.0 | 59.8 | 49.1 | 25.9 | 24.5 | 31.8 | 36.5 | 113.9 | 121.2 | 42.7 | 42.4 | 57.4 | 57.4 | 47.1 | 41.1 |
| Ni | 91 | 99 | 171 | | 127 | 132 | 91 | 76 | 39 | 39 | 363 | 352 | 99 | 112 | 72 | 57 | 45 | 44 | 269 | 282 | 143 | 129 | 218 | 218 | 118 | 113 |
| Cu | 8.4 | 7.2 | 7.2 | | 12.0 | 6.1 | 10.1 | 20.5 | 15.1 | 15.1 | n.d. | 5.9 | 5.2 | 4.2 | 22.7 | 10.4 | n.d. | n.d. | n.d. | n.d. | 6.2 | 11.6 | n.d. | n.d. | 11.9 | 6.3 |
| Zn | 437 | 278 | 452 | | 582 | 617 | 566 | 529 | 647 | 647 | 23 | 16 | 129 | 97 | 843 | 706 | 795 | 902 | 505 | 572 | 271 | 286 | 681 | 681 | 1196 | 1017 |
| Sr | 1.91 | 2.42 | 1.11 | | 1.39 | 1.50 | 1.39 | 1.13 | 2.00 | 2.00 | 22.47 | 20.65 | 2.63 | 2.50 | 3.15 | 1.96 | 4.41 | 5.89 | 1.93 | 2.70 | 7.99 | 3.75 | | | 4.37 | 3.70 |
| Y | 0.58 | 1.44 | 0.70 | | 1.87 | 0.27 | 0.92 | 2.49 | 1.98 | 1.98 | n.d. | n.d. | n.d. | 0.15 | 0.48 | 0.18 | n.d. | n.d. | n.d. | n.d. | 0.05 | 0.07 | n.d. | n.d. | 0.09 | 0.08 |
| Zr | 1.32 | 1.56 | 0.63 | 0.52 | n.d. | n.d. | 0.98 | 0.57 | 0.15 | 0.15 | n.d. | n.d. | 0.12 | n.d. | 0.34 | 0.10 | 0.14 | 0.62 | 0.10 | 0.16 | 0.14 | 0.14 | n.d. | n.d. | 0.09 | n.d. |
| Nb | 47.79 | 39.67 | 40.26 | | 49.07 | 44.84 | 28.80 | 23.83 | 35.28 | 35.28 | | | 26.01 | 23.03 | 0.82 | 0.82 | 1.01 | 1.54 | 17.53 | 18.63 | 13.91 | 12.25 | | | | |
| Ba | 1193 | 905 | 922 | 1151 | 1021 | 1106 | 1951 | 1845 | 1074 | 1074 | 364 | 304 | 451 | 169 | 637 | 696 | 1170 | 1361 | 541 | 665 | 3084 | 3046 | 2597 | 2597 | 415 | 402 |
| La | | 1.373 | 0.902 | 4.331 | 9.457 | | 9.523 | 3.890 | 3.597 | 3.597 | 0.020 | n.d. | 2.109 | 3.169 | 1.280 | 0.749 | 0.077 | 0.564 | 0.056 | 0.030 | 0.007 | 0.136 | 3.548 | 3.548 | 0.133 | 0.122 |
| Ce | | 5.21 | 2.04 | 5.16 | 7.69 | | 17.61 | 9.18 | 8.87 | 8.87 | n.d. | n.d. | 3.91 | 6.87 | 4.39 | 2.42 | 0.17 | 1.99 | 0.16 | 0.09 | n.d. | 0.08 | 4.75 | 4.75 | | |
| Pr | | 0.538 | 0.248 | 1.120 | 2.363 | | 2.055 | 1.046 | 1.508 | 1.508 | 0.020 | n.d. | 0.403 | 0.713 | 0.543 | 0.323 | 0.025 | 0.293 | 0.015 | 0.010 | 0.001 | 0.016 | 0.701 | 0.701 | n.d. | 0.037 |
| Nd | | 2.43 | 0.98 | 4.06 | 9.27 | | 7.73 | 4.46 | 6.28 | 6.28 | n.d. | n.d. | 1.33 | 2.20 | 2.56 | 1.27 | 0.19 | 1.38 | n.d. | 0.04 | n.d. | 0.08 | 2.71 | 2.71 | 0.26 | n.d. |
| Sm | | 0.45 | 0.29 | 0.49 | 1.85 | | 1.28 | 0.74 | 1.10 | 1.10 | n.d. | n.d. | 0.07 | 0.22 | 0.43 | 0.24 | 0.08 | 0.20 | 0.01 | 0.01 | n.d. | 0.01 | 0.21 | 0.21 | | |
| Eu | | 0.104 | 0.032 | 0.129 | 0.180 | | 0.237 | 0.135 | 0.186 | 0.186 | n.d. | 0.010 | 0.005 | 0.020 | 0.040 | 0.025 | 0.022 | 0.057 | 0.027 | 0.010 | 0.012 | 0.012 | 0.089 | 0.089 | n.d. | n.d. |
| Gd | | 0.139 | 0.254 | 0.425 | 0.916 | | 0.562 | 0.852 | 0.625 | 0.625 | n.d. | n.d. | n.d. | 0.086 | 0.287 | 0.166 | 0.109 | 0.078 | 0.048 | 0.010 | n.d. | 0.004 | n.d. | n.d. | | |
| Tb | | 0.032 | n.d. | 0.024 | 0.066 | | 0.085 | 0.071 | 0.080 | 0.080 | 0.030 | n.d. | n.d. | 0.006 | 0.033 | 0.019 | 0.007 | 0.062 | n.d. | n.d. | n.d. | n.d. | n.d. | n.d. | n.d. | n.d. |
| Dy | | 0.159 | n.d. | 0.171 | 0.233 | | 0.459 | 0.574 | 0.580 | 0.580 | n.d. | n.d. | 0.027 | n.d. | 0.088 | 0.054 | 0.070 | 0.033 | 0.030 | n.d. | n.d. | n.d. | n.d. | n.d. | | |
| Ho | | 0.046 | n.d. | 0.045 | 0.036 | | 0.054 | 0.096 | 0.074 | 0.074 | n.d. | n.d. | n.d. | n.d. | 0.008 | n.d. | 0.014 | 0.006 | n.d. | n.d. | n.d. | 0.001 | n.d. | n.d. | n.d. | n.d. |
| Er | | 0.106 | n.d. | 0.137 | n.d. | | 0.235 | 0.377 | 0.195 | 0.195 | n.d. | n.d. | n.d. | 0.020 | 0.021 | n.d. | n.d. | n.d. | 0.030 | n.d. | n.d. | 0.003 | n.d. | n.d. | | |
| Tm | | 0.004 | n.d. | 0.023 | n.d. | | 0.021 | 0.052 | 0.033 | 0.033 | n.d. | n.d. | 0.006 | n.d. | n.d. | n.d. | n.d. | n.d. | 0.001 | n.d. | n.d. | n.d. | 0.006 | 0.006 | | |
| Yb | | 0.186 | 0.057 | n.d. | n.d. | | n.d. | 0.185 | 0.139 | 0.139 | n.d. | n.d. | 0.013 | n.d. | n.d. | 0.019 | 0.009 | 0.026 | n.d. | n.d. | 0.004 | n.d. | n.d. | n.d. | n.d. | n.d. |
| Lu | | n.d. | 0.006 | n.d. | 0.011 | | n.d. | 0.038 | 0.025 | 0.025 | n.d. | n.d. | 0.002 | n.d. | n.d. | n.d. | n.d. | n.d. | n.d. | n.d. | 0.002 | 0.003 | n.d. | n.d. | n.d. | n.d. |
| Hf | | 0.056 | n.d. | n.d. | n.d. | | n.d. | 0.087 | 0.018 | 0.018 | | | n.d. | n.d. | n.d. | n.d. | 0.076 | n.d. | 0.011 | 0.010 | 0.020 | 0.038 | | | | |
| Ta | | 2.769 | 2.930 | 3.513 | 3.242 | | 1.093 | 0.776 | 2.414 | 2.414 | | | 1.054 | 0.585 | 0.020 | 0.024 | 0.055 | 0.051 | 0.970 | 0.970 | 0.298 | 0.242 | | | | |

# Determined by LAM-ICP-MS. * Total Fe as FeO. n. d. = not detected. Blank = not determined.

Table 3.5. Stoichiometries of representative garnet analyses (cations per 12 oxygens).

| | 87-81 | | 87-83 | | 87-86 | | 87-283 | | 87-279 | | 88-49 | | 88-48 |
|---|---|---|---|---|---|---|---|---|---|---|---|---|---|
| Spl. | F23 | G1 | C11 | C24 | C1 | C8 | C3 | D2 | D6 | D1 | A4 | A45 | D1 |
| Tetrahedral sites | | | | | | | | | | | | | |
| Si | 2.98 | 2.98 | 2.9 | 2.9 | 2.99 | 2.99 | 2.98 | 2.9 | 3.00 | 3.00 | 2.9 | 2.95 | 2.98 |
| Octahedral sites | | | | | | | | | | | | | |
| Ti[#] | 3.3E-03 | 2.9E-03 | 2.8E-0 | 3.5E-03 | 1.9E-03 | 2.1E-03 | 1.8E-03 | 3.8E-0 | 1.8E-03 | 1.6E-03 | 5.9E-04 | 5.9E-04 | 2.6E-03 |
| Al | 1.97 | 1.95 | 1.9 | 1.9 | 1.96 | 1.96 | 1.96 | 1.9 | 1.96 | 1.96 | 2.0 | 2.00 | 1.98 |
| $Fe^{3+}$ | 0.089 | 0.103 | 0.08 | 0.123 | 0.088 | 0.075 | 0.095 | 0.17 | 0.058 | 0.058 | 0.149 | 0.149 | 0.086 |
| V | 4.6E-04 | 4.2E-04 | 6.4E-0 | 6.1E-04 | 3.4E-04 | 4.4E-04 | 7.7E-04 | 1.4E-0 | 1.3E-03 | | 2.5E-04 | 3.2E-04 | 4.2E-04 |
| Cr | 1.4E-03 | 3.0E-04 | 3.1E-0 | 1.2E-03 | n.d | 7.8E-04 | 5.8E-04 | 8.3E-0 | 7.2E-04 | | 1.2E-03 | 1.1E-03 | 2.8E-03 |
| Zr | 1.1E-05 | 7.2E-06 | 9.3E-0 | 1.1E-05 | 7.0E-06 | 9.6E-06 | 5.0E-06 | 7.6E-0 | 7.0E-06 | 5.0E-06 | 1.4E-05 | 1.0E-05 | 4.3E-05 |
| Nb | n.d. | n.d. | n.d | n.d | n.d | n.d. | n.d | n.d | n.d. | | | | n.d. |
| Hf | | n.d. | n.d | n.d | n.d | 1.4E-07 | n.d | n.d | | 4.4E-08 | | | 3.1E-07 |
| Ta | | n.d. | 5.6E-0 | 6.8E-08 | n.d | n.d. | n.d | n.d | | n.d | | | n.d. |
| Total | 2.06 | 2.06 | 2.0 | 2.1 | 2.05 | 2.04 | 2.06 | 2.1 | 2.02 | 2.02 | 2.1 | 2.15 | 2.07 |
| Dodecahedral sites | | | | | | | | | | | | | |
| $Fe^{2+}$ | 1.92 | 2.00 | 1.9 | 1.9 | 1.93 | 1.88 | 1.78 | 1.6 | 1.95 | 1.95 | 2.3 | 2.37 | 2.27 |
| Mg | 0.201 | 0.225 | 0.21 | 0.214 | 0.203 | 0.204 | 0.216 | 0.19 | 0.284 | 0.284 | 0.670 | 0.670 | 0.513 |
| Mn | 0.236 | 0.182 | 0.25 | 0.271 | 0.292 | 0.321 | 0.238 | 0.34 | 0.195 | 0.195 | n.d | n.d | n.d. |
| Ca | 0.622 | 0.580 | 0.60 | 0.548 | 0.559 | 0.587 | 0.750 | 0.74 | 0.569 | 0.569 | 0.049 | 0.049 | 0.197 |
| Sc | 1.1E-03 | 1.1E-03 | 6.9E-0 | 7.9E-04 | 6.8E-04 | 7.6E-04 | 9.9E-04 | 1.4E-0 | 8.0E-04 | | 2.4E-04 | n.d | 4.2E-04 |
| Co | 1.0E-04 | 8.4E-05 | 1.4E-0 | 1.3E-04 | 1.1E-04 | 1.2E-04 | 6.7E-05 | 6.9E-0 | 5.3E-05 | | 2.4E-04 | 2.1E-04 | 1.7E-04 |
| Ni | n.d. | n.d. | n.d | n.d | n.d | n.d. | n.d | n.d | n.d. | | n.d | n.d | n.d. |
| Cu | n.d. | n.d. | n.d | n.d | n.d | n.d. | n.d | n.d | n.d. | | n.d | n.d | n.d. |
| Zn | 3.4E-04 | 2.4E-04 | 4.4E-0 | 4.7E-04 | 4.0E-04 | 6.1E-04 | 5.0E-04 | 3.9E-0 | 3.7E-04 | | 4.0E-05 | n.d | 1.4E-04 |
| Sr | n.d. | n.d. | n.d | n.d | n.d | n.d. | n.d | n.d | n.d. | | n.d | | n.d. |
| Y | 3.2E-03 | 1.9E-03 | 8.4E-0 | 6.7E-04 | 3.8E-03 | 3.6E-03 | 8.1E-04 | 2.0E-0 | 1.2E-03 | | 3.7E-05 | 2.0E-05 | 1.6E-04 |
| Ba | n.d. | 3.2E-05 | 9.5E-0 | n.d | 1.9E-06 | 6.5E-07 | n.d | 8.1E-0 | n.d. | n.d | n.d | 1.4E-07 | n.d. |
| La | | n.d. | n.d | n.d | n.d | n.d. | 1.5E-07 | 1.0E-0 | | 4.2E-08 | n.d | n.d | n.d. |
| Ce | | 2.5E-07 | 6.1E-0 | 9.0E-07 | n.d | n.d. | 2.2E-07 | 2.1E-0 | | n.d | n.d | n.d | 1.1E-07 |
| Pr | | n.d. | n.d | n.d | n.d | n.d. | 1.5E-08 | 2.1E-0 | | 5.7E-09 | n.d | n.d | 2.7E-08 |
| Nd | | n.d. | n.d | 8.1E-07 | 1.1E-07 | n.d. | n.d | n.d | | n.d | n.d | n.d | 9.7E-07 |
| Sm | | n.d. | 5.7E-0 | n.d | 6.7E-07 | 1.4E-06 | n.d | n.d | | 1.0E-06 | 3.5E-07 | 2.2E-07 | 5.0E-06 |
| Eu | | 5.1E-07 | 5.7E-0 | 7.0E-07 | 9.1E-07 | 7.7E-07 | n.d | n.d | | 7.5E-07 | 2.5E-07 | 1.9E-07 | 2.3E-06 |
| Gd | | 4.7E-06 | 9.2E-0 | 5.1E-06 | 1.0E-05 | 1.4E-05 | 3.4E-06 | 3.1E-0 | | 1.3E-05 | 2.7E-06 | 1.7E-06 | 1.7E-05 |
| Tb | | 3.7E-06 | 5.0E-0 | 4.0E-06 | 9.0E-06 | 1.0E-05 | 2.6E-06 | 3.3E-0 | | 9.5E-06 | 7.2E-07 | 3.9E-07 | 2.8E-06 |
| Dy | | 1.0E-04 | 6.0E-0 | 4.6E-05 | 1.8E-04 | 2.0E-04 | 4.8E-05 | 6.8E-0 | | 1.4E-04 | 4.4E-06 | 2.9E-06 | 1.3E-05 |
| Ho | | 4.9E-05 | 1.4E-0 | 1.1E-05 | 7.3E-05 | 6.9E-05 | 2.0E-05 | 3.7E-0 | | 3.4E-05 | 6.9E-07 | 5.5E-07 | 2.8E-06 |
| Er | | 2.4E-04 | 3.7E-0 | 3.1E-05 | 2.8E-04 | 2.4E-04 | 8.0E-05 | 1.7E-0 | | 8.1E-05 | 1.3E-06 | 1.2E-06 | 8.5E-06 |
| Tm | | 5.1E-05 | 4.7E-0 | 4.2E-06 | 4.5E-05 | 3.6E-05 | 1.2E-05 | 2.8E-0 | | 8.7E-06 | 1.4E-07 | 8.4E-08 | 1.3E-06 |
| Yb | | 3.5E-04 | 2.7E-0 | 2.3E-05 | 2.8E-04 | 2.2E-04 | 7.1E-05 | 1.8E-0 | | 4.1E-05 | 1.5E-06 | 6.3E-07 | 6.5E-06 |
| Lu | | 4.9E-05 | 3.2E-0 | 3.2E-06 | 4.2E-05 | 3.2E-05 | 9.7E-06 | 2.2E-0 | | 4.7E-06 | 3.0E-07 | 1.4E-07 | 1.1E-06 |
| Total | 2.99 | 2.99 | 2.9 | 2.9 | 2.99 | 3.00 | 2.99 | 2.8 | 3.00 | 3.00 | 3.0 | 3.09 | 2.98 |
| $X_{Mg}$ | 0.09 | 0.10 | 0.1 | 0.1 | 0.10 | 0.10 | 0.11 | 0.1 | 0.13 | 0.13 | 0.2 | 0.22 | 0.18 |
| $X_{Alm}$ | 0.65 | 0.67 | 0.6 | 0.6 | 0.65 | 0.63 | 0.60 | 0.5 | 0.65 | 0.65 | 0.7 | 0.77 | 0.76 |
| $X_{Prp}$ | 0.07 | 0.08 | 0.0 | 0.0 | 0.07 | 0.07 | 0.07 | 0.0 | 0.09 | 0.09 | 0.2 | 0.22 | 0.17 |
| $X_{Sps}$ | 0.08 | 0.06 | 0.0 | 0.0 | 0.10 | 0.11 | 0.08 | 0.1 | 0.06 | 0.06 | 0.0 | 0.00 | 0.00 |
| $X_{Grs}$ | 0.21 | 0.19 | 0.2 | 0.1 | 0.19 | 0.20 | 0.25 | 0.2 | 0.19 | 0.19 | 0.0 | 0.02 | 0.07 |

Notes: Site occupancies were assigned on the basis of ionic radii and charges (Shannon 1976). [#] Determined by LAM-ICP-MS. n.d. = not detected. Blank = not determined. $X_{Mg}$=Mg/(Mg+Fe); $X_{Alm}$=Fe/(Fe+Mg+Mn+Ca); $X_{Prp}$=Mg/(Fe+Mg+Mn+Ca); $X_{Sps}$=Mn/(Fe+Mg+Mn+Ca); $X_{Grs}$=Ca/(Fe+Mg+Mn+Ca).

Table 3-5. Continued.

| Spl. | 88-48 | 88-45 | | 88-85 | | 88-74 | | 88-80 | | 88-57 | | 88-58 | |
|---|---|---|---|---|---|---|---|---|---|---|---|---|---|
| | D3 | E1 | E7 | C4 | D10 | C5 | D8 | B9 | B5 | A13 | A9 | B5 | C4 |
| Tetrahedral sites | | | | | | | | | | | | | |
| Si | 2.99 | 2.98 | 2.97 | 2.98 | 2.97 | 2.96 | 2.99 | 2.98 | 2.98 | 2.99 | 2.98 | 2.97 | 2.97 |
| Octahedral sites | | | | | | | | | | | | | |
| Ti[#] | 3.9E-03 | 2.2E-04 | 3.3E-04 | 3.0E-04 | n.d. | 3.1E-04 | 2.9E-0 | 1.1E-0 | 2.2E-04 | 1.6E-03 | 2.4E-0 | 1.9E-0 | 2.7E-04 |
| Al | 1.97 | 1.97 | 1.97 | 1.97 | 1.98 | 1.98 | 1.97 | 1.98 | 1.98 | 1.95 | 1.97 | 1.98 | 1.97 |
| $Fe^{3+}$ | 0.056 | 0.096 | 0.110 | 0.094 | 0.120 | 0.136 | 0.078 | 0.072 | 0.088 | 0.105 | 0.108 | 0.114 | 0.127 |
| V | 4.3E-04 | 1.8E-04 | 2.0E-04 | 2.0E-04 | 2.8E-04 | 1.6E-04 | 1.5E-0 | 2.1E-0 | 2.2E-04 | 6.5E-04 | 4.3E-0 | 1.7E-0 | 1.9E-04 |
| Cr | 2.7E-03 | 1.1E-03 | 1.5E-03 | 1.0E-03 | 1.1E-03 | 7.8E-04 | 8.0E-0 | 3.7E-0 | 2.1E-03 | 7.0E-03 | 1.4E-0 | 1.9E-0 | 1.6E-03 |
| Zr | 4.7E-05 | 5.5E-06 | 8.8E-06 | 1.1E-05 | 1.2E-05 | 3.2E-05 | 2.1E-0 | 8.0E-0 | 5.7E-05 | 1.5E-05 | 1.2E-0 | 5.1E-0 | 6.8E-06 |
| Nb | n.d. | n.d. | n.d | n.d | n.d. | n.d. | n.d | n.d | n.d. | | | | |
| Hf | 5.2E-07 | n.d. | 9.4E-08 | 4.9E-08 | | | | 6.2E-0 | 5.3E-07 | | | | |
| Ta | 5.9E-09 | n.d. | n.d | n.d | | | | n.d | n.d. | | | | |
| Total | 2.03 | 2.07 | 2.09 | 2.06 | 2.10 | 2.11 | 2.05 | 2.05 | 2.07 | 2.06 | 2.08 | 2.10 | 2.10 |
| Dodecahedral sites | | | | | | | | | | | | | |
| $Fe^{2+}$ | 2.29 | 2.22 | 2.19 | 2.19 | 2.17 | 2.25 | 2.25 | 1.69 | 1.72 | 1.66 | 1.74 | 2.37 | 2.39 |
| Mg | 0.496 | 0.506 | 0.525 | 0.514 | 0.499 | 0.450 | 0.470 | 0.796 | 0.764 | 0.393 | 0.453 | 0.432 | 0.433 |
| Mn | n.d. | 0.020 | 0.020 | 0.027 | 0.026 | 0.128 | 0.134 | 0.213 | 0.317 | 0.236 | 0.132 | 0.027 | 0.020 |
| Ca | 0.204 | 0.229 | 0.235 | 0.252 | 0.275 | 0.136 | 0.135 | 0.286 | 0.172 | 0.698 | 0.651 | 0.134 | 0.126 |
| Sc | 8.1E-04 | 8.8E-04 | 7.1E-04 | 8.6E-04 | 9.7E-04 | 7.5E-04 | 7.6E-0 | 1.8E-0 | 2.6E-03 | 1.2E-03 | 6.7E-0 | 6.5E-0 | 5.5E-04 |
| Co | 1.7E-04 | 9.8E-05 | 8.6E-05 | 1.5E-04 | 1.5E-04 | 3.1E-04 | 2.9E-0 | 1.4E-0 | 1.3E-04 | 1.9E-04 | 1.8E-0 | 1.6E-0 | 1.5E-04 |
| Ni | 7.6E-04 | n.d. | n.d | n.d | n.d. | n.d. | n.d | n.d | n.d. | n.d. | n.d | n.d | n.d. |
| Cu | n.d. | n.d. | n.d | n.d | n.d. | n.d. | n.d | 2.4E-0 | 2.1E-05 | n.d. | n.d | n.d | n.d. |
| Zn | 1.7E-04 | 9.6E-04 | 8.8E-04 | 8.3E-04 | 8.9E-04 | 4.4E-04 | 4.5E-0 | 3.0E-0 | 3.6E-04 | 4.8E-04 | 7.3E-0 | 1.2E-0 | 1.2E-03 |
| Sr | n.d. | n.d. | n.d | n.d | n.d. | n.d. | n.d | n.d | n.d. | | | 5.0E-0 | n.d. |
| Y | 7.1E-05 | 2.4E-03 | 1.7E-03 | 4.7E-04 | 5.4E-04 | 8.9E-04 | 1.0E-0 | 4.9E-0 | 7.2E-04 | 1.2E-04 | 3.1E-0 | 3.8E-0 | 3.5E-04 |
| Ba | n.d. | n.d. | n.d | n.d | n.d. | n.d. | n.d | n.d | n.d. | 1.9E-07 | n.d | n.d | n.d. |
| La | 1.3E-07 | n.d. | 1.2E-08 | n.d | | | | n.d | n.d. | n.d. | n.d | n.d | n.d. |
| Ce | 3.0E-07 | n.d. | n.d | 9.8E-09 | | | | n.d | 6.0E-09 | n.d. | n.d | | |
| Pr | 1.4E-07 | n.d. | 1.6E-08 | 2.9E-07 | | | | 3.3E-0 | 4.9E-09 | 3.9E-08 | n.d | n.d | n.d. |
| Nd | 1.4E-06 | n.d. | n.d | n.d | | | | 9.2E-0 | 4.5E-07 | 1.2E-06 | 1.3E-0 | n.d | n.d. |
| Sm | 5.7E-06 | 3.1E-06 | 3.1E-06 | 4.3E-06 | | | | 5.5E-0 | 2.9E-06 | 2.7E-06 | 1.7E-0 | | |
| Eu | 1.4E-06 | 1.6E-06 | 2.2E-06 | 3.3E-06 | | | | 4.0E-0 | 2.4E-06 | 2.8E-06 | 3.4E-0 | 7.5E-0 | 7.6E-07 |
| Gd | 9.3E-06 | 3.7E-05 | 4.1E-05 | 3.3E-05 | | | | 3.3E-0 | 3.4E-05 | 1.4E-05 | 1.8E-0 | | |
| Tb | 1.1E-06 | 2.0E-05 | 1.8E-05 | 8.2E-06 | | | | 9.0E-0 | 1.2E-05 | 4.0E-06 | 5.1E-0 | 4.0E-0 | 4.8E-06 |
| Dy | 6.4E-06 | 2.2E-04 | 1.6E-04 | 4.0E-05 | | | | 5.3E-0 | 8.5E-05 | 2.0E-05 | 3.3E-0 | | |
| Ho | 1.4E-06 | 6.0E-05 | 3.2E-05 | 5.0E-06 | | | | 7.7E-0 | 1.5E-05 | 2.4E-06 | 6.7E-0 | 6.4E-0 | 5.9E-06 |
| Er | 4.0E-06 | 1.6E-04 | 6.1E-05 | 8.6E-06 | | | | 1.3E-0 | 3.1E-05 | 5.4E-06 | 1.8E-0 | | |
| Tm | 5.4E-07 | 2.0E-05 | 6.0E-06 | 1.1E-06 | | | | 1.2E-0 | 4.1E-06 | 6.0E-07 | 2.6E-0 | | |
| Yb | 3.9E-06 | 9.8E-05 | 2.9E-05 | 6.7E-06 | | | | 4.9E-0 | 2.2E-05 | 4.9E-06 | 1.8E-0 | 9.1E-0 | 8.5E-06 |
| Lu | 6.2E-07 | 1.3E-05 | 3.1E-06 | 9.8E-07 | | | | 7.3E-0 | 2.7E-06 | 7.4E-07 | 2.8E-0 | 1.1E-0 | 1.4E-06 |
| Total | 2.99 | 2.98 | 2.98 | 2.99 | 2.97 | 2.97 | 2.99 | 2.99 | 2.98 | 2.99 | 2.98 | 2.97 | 2.97 |
| $X_{Mg}$ | 0.18 | 0.19 | 0.19 | 0.19 | 0.19 | 0.17 | 0.17 | 0.32 | 0.31 | 0.19 | 0.21 | 0.15 | 0.15 |
| $X_{Alm}$ | 0.77 | 0.75 | 0.74 | 0.73 | 0.73 | 0.76 | 0.75 | 0.57 | 0.58 | 0.56 | 0.58 | 0.80 | 0.80 |
| $X_{Prp}$ | 0.17 | 0.17 | 0.18 | 0.17 | 0.17 | 0.15 | 0.16 | 0.27 | 0.26 | 0.13 | 0.15 | 0.15 | 0.15 |
| $X_{Sps}$ | 0.00 | 0.01 | 0.01 | 0.01 | 0.01 | 0.04 | 0.04 | 0.07 | 0.11 | 0.08 | 0.04 | 0.01 | 0.01 |
| $X_{Grs}$ | 0.07 | 0.08 | 0.08 | 0.08 | 0.09 | 0.05 | 0.05 | 0.10 | 0.06 | 0.23 | 0.22 | 0.05 | 0.04 |

Notes: Site occupancies were assigned on the basis of ionic radii and charges (Shannon 1976). [#] Determined by LAM-ICP-MS. n.d. = not detected. Blank = not determined. $X_{Mg}$=Mg/(Mg+Fe); $X_{Alm}$=Fe/(Fe+Mg+Mn+Ca); $X_{Prp}$=Mg/(Fe+Mg+Mn+Ca); $X_{Sps}$=Mn/(Fe+Mg+Mn+Ca); $X_{Grs}$=Ca/(Fe+Mg+Mn+Ca).

Table 3.6. Stoichiometries of representative biotite analyses (cations per 22 oxygens).

| | 87-81 | | 87-83 | | 87-86 | | 87-283 | | 87-279 | | 88-49 | | 88-48 |
|---|---|---|---|---|---|---|---|---|---|---|---|---|---|
| Spl. | F8 | G12 | C23 | C9 | C34 | C4 | C5 | D5 | D3 | D3 | A5 | A1 | D2 |
| Tetrahedral sites | | | | | | | | | | | | | |
| Si | 5.6 | 5.5 | 5.62 | 5.57 | 5.65 | 5.5 | 5.57 | 5.50 | 5.61 | 5.61 | 5.6 | 5.71 | 5.55 |
| $Al^{iv}$ | 2.4 | 2.4 | 2.38 | 2.43 | 2.35 | 2.4 | 2.43 | 2.50 | 2.39 | 2.39 | 2.3 | 2.29 | 2.45 |
| Octahedral sites | | | | | | | | | | | | | |
| Ti | 0.195 | 0.185 | 0.201 | 0.195 | 0.191 | 0.197 | 0.204 | 0.206 | 0.192 | 0.192 | 0.148 | 0.128 | 0.155 |
| $Al^{vi}$ | 0.686 | 0.700 | 0.782 | 0.646 | 0.788 | 0.694 | 0.661 | 0.649 | 0.656 | 0.656 | 0.626 | 0.680 | 0.798 |
| Fe | 2.5 | 2.5 | 2.38 | 2.55 | 2.35 | 2.4 | 2.49 | 2.51 | 2.31 | 2.31 | 1.3 | 1.35 | 1.85 |
| Mg | 2.2 | 2.3 | 2.44 | 2.39 | 2.50 | 2.4 | 2.41 | 2.36 | 2.53 | 2.53 | 3.6 | 3.74 | 2.95 |
| $Mn^{\#}$ | 2.6E-02 | 1.9E-02 | 2.5E-02 | n.d. | n.d. | 1.8E-02 | 1.4E-02 | 1.3E-02 | 2.2E-02 | 2.2E-02 | n.d. | n.d. | 5.7E-04 |
| Sc | 3.8E-04 | 3.4E-04 | 2.5E-04 | | 3.1E-04 | 3.6E-04 | 3.4E-04 | 4.5E-04 | 2.9E-04 | 2.9E-04 | n.d. | n.d. | 2.3E-04 |
| V | 3.4E-03 | 2.9E-03 | 2.7E-03 | | 3.2E-03 | 3.5E-03 | 9.3E-03 | 9.9E-03 | 1.2E-02 | 1.2E-02 | 5.1E-03 | 4.7E-03 | 2.4E-03 |
| Cr | 3.0E-03 | 2.9E-03 | 3.2E-03 | | 2.6E-03 | 3.2E-03 | 3.6E-03 | 3.2E-03 | 3.4E-03 | 3.4E-03 | 6.0E-03 | 7.1E-03 | 9.2E-03 |
| Co | 7.7E-04 | 6.2E-04 | 8.1E-04 | | 9.0E-04 | 9.1E-04 | 7.3E-04 | 7.2E-04 | 3.0E-04 | 3.0E-04 | 1.2E-03 | 1.1E-03 | 9.0E-04 |
| Ni | 1.4E-03 | 1.6E-03 | 2.6E-03 | | 2.0E-03 | 2.1E-03 | 1.4E-03 | 1.2E-03 | 6.1E-04 | 6.1E-04 | 5.2E-03 | 5.1E-03 | 1.5E-03 |
| Cu | 1.2E-04 | 1.1E-04 | 1.0E-04 | | 1.8E-04 | 8.9E-05 | 1.4E-04 | 3.0E-04 | 2.1E-04 | 2.1E-04 | n.d. | 8.0E-05 | 7.3E-05 |
| Zn | 6.1E-03 | 3.9E-03 | 6.3E-03 | | 8.2E-03 | 8.7E-03 | 7.8E-03 | 7.4E-03 | 8.9E-03 | 8.9E-03 | 3.0E-04 | 2.1E-04 | 1.7E-03 |
| Y | 5.9E-06 | 1.5E-05 | 7.1E-06 | | 1.9E-05 | 2.8E-06 | 9.4E-06 | 2.6E-05 | 2.0E-05 | 2.0E-05 | n.d. | n.d. | n.d. |
| Zr | 1.3E-05 | 1.6E-05 | 6.3E-06 | 5.3E-06 | n.d. | n.d. | 9.8E-06 | 5.8E-06 | 1.5E-06 | 1.5E-06 | n.d. | n.d. | 1.2E-06 |
| Nb | 4.7E-04 | 4.0E-04 | 3.9E-04 | | 4.9E-04 | 4.5E-04 | 2.8E-04 | 2.4E-04 | 3.4E-04 | 3.4E-04 | | | 2.5E-04 |
| Hf | | 2.9E-07 | n.d. | n.d. | n.d. | | n.d. | 4.5E-07 | 9.0E-08 | 9.0E-08 | | | n.d. |
| Ta | | 1.4E-05 | 1.5E-05 | 1.8E-05 | 1.7E-05 | | 5.5E-06 | 3.9E-06 | 1.2E-05 | 1.2E-05 | | | 5.2E-06 |
| Total | 5.7 | 5.7 | 5.84 | 5.78 | 5.84 | 5.7 | 5.80 | 5.77 | 5.74 | 5.74 | 5.8 | 5.91 | 5.77 |
| $X_{Mg}$ | 0.4 | 0.4 | 0.51 | 0.48 | 0.52 | 0.5 | 0.49 | 0.48 | 0.52 | 0.52 | 0.7 | 0.73 | 0.61 |
| Interlayer sites | | | | | | | | | | | | | |
| Na | n.d. | n.d. | 0.058 | n.d. | n.d. | n.d. | n.d. | 0.089 | 0.087 | 0.087 | 0.218 | 0.247 | 0.114 |
| K | 1.7 | 1.8 | 1.69 | 1.81 | 1.77 | 1.7 | 1.73 | 1.77 | 1.75 | 1.75 | 1.4 | 1.52 | 1.68 |
| F | | | 0.235 | | 0.236 | | | | | | | 0.193 | |
| Cl | | | 0.010 | | 0.013 | | | | | | | 0.010 | |
| Sr | 2.0E-05 | 2.6E-05 | 1.1E-05 | | 1.5E-05 | 1.6E-05 | 1.4E-05 | 1.2E-05 | 2.1E-05 | 2.1E-05 | 2.2E-04 | 2.0E-04 | 2.7E-05 |
| Ba | 8.0E-03 | 6.1E-03 | 6.1E-03 | 7.7E-03 | 6.9E-03 | 7.5E-03 | 1.3E-02 | 1.2E-02 | 7.1E-03 | 7.1E-03 | 2.2E-03 | 1.9E-03 | 2.9E-03 |
| La | | 9.1E-06 | 5.9E-06 | 2.9E-05 | 6.3E-05 | | 6.2E-05 | 2.6E-05 | 2.3E-05 | 2.3E-05 | 1.2E-07 | n.d. | 1.3E-05 |
| Ce | | 3.4E-05 | 1.3E-05 | 3.4E-05 | 5.1E-05 | | 1.1E-04 | 6.0E-05 | 5.7E-05 | 5.7E-05 | n.d. | n.d. | 2.5E-05 |
| Pr | | 3.5E-06 | 1.6E-06 | 7.3E-06 | 1.6E-05 | | 1.3E-05 | 6.8E-06 | 9.7E-06 | 9.7E-06 | 1.2E-07 | n.d. | 2.5E-06 |
| Nd | | 1.6E-05 | 6.2E-06 | 2.6E-05 | 6.0E-05 | | 4.9E-05 | 2.8E-05 | 3.9E-05 | 3.9E-05 | n.d. | n.d. | 8.2E-06 |
| Sm | | 2.8E-06 | 1.8E-06 | 3.0E-06 | 1.1E-05 | | 7.7E-06 | 4.5E-06 | 6.6E-06 | 6.6E-06 | n.d. | n.d. | 4.0E-07 |
| Eu | | 6.4E-07 | 1.9E-07 | 7.8E-07 | 1.1E-06 | | 1.4E-06 | 8.1E-07 | 1.1E-06 | 1.1E-06 | n.d. | 5.6E-08 | 2.8E-08 |
| Gd | | 8.2E-07 | 1.5E-06 | 2.5E-06 | 5.4E-06 | | 3.2E-06 | 5.0E-06 | 3.6E-06 | 3.6E-06 | n.d. | n.d. | n.d. |
| Tb | | 1.8E-07 | n.d. | 1.4E-07 | 3.8E-07 | | 4.8E-07 | 4.1E-07 | 4.5E-07 | 4.5E-07 | 1.6E-07 | n.d. | n.d. |
| Dy | | 9.0E-07 | n.d. | 9.6E-07 | 1.3E-06 | | 2.6E-06 | 3.2E-06 | 3.2E-06 | 3.2E-06 | n.d. | n.d. | 1.5E-07 |
| Ho | | 2.6E-07 | n.d. | 2.5E-07 | 2.0E-07 | | 3.0E-07 | 5.4E-07 | 4.1E-07 | 4.1E-07 | n.d. | n.d. | n.d. |
| Er | | 5.9E-07 | n.d. | 7.5E-07 | n.d. | | 1.3E-06 | 2.1E-06 | 1.1E-06 | 1.1E-06 | n.d. | n.d. | n.d. |
| Tm | | 2.1E-08 | n.d. | 1.2E-07 | n.d. | | 1.1E-07 | 2.8E-07 | 1.8E-07 | 1.8E-07 | n.d. | n.d. | 3.4E-08 |
| Yb | | 1.0E-06 | 3.0E-07 | n.d. | n.d. | | n.d. | 9.8E-07 | 7.2E-07 | 7.2E-07 | n.d. | n.d. | 6.9E-08 |
| Lu | | n.d. | 3.2E-08 | n.d. | 5.9E-08 | | n.d. | 2.0E-07 | 1.3E-07 | 1.3E-07 | n.d. | n.d. | 1.2E-08 |
| Total | 1.8 | 1.8 | 2.00 | 1.82 | 2.03 | 1.7 | 1.75 | 1.87 | 1.84 | 1.84 | 1.7 | 1.97 | 1.79 |
| $X_K$ | 1.0 | 1.0 | 0.97 | 1.00 | 1.00 | 1.0 | 1.00 | 0.95 | 0.95 | 0.95 | 0.8 | 0.86 | 0.94 |

Site occupancies were assigned on the basis of ionic radii and charges (Shannon 1976). # determined by LAM-ICP-MS. n.d. = not detected. Blank = not determined. $X_{Mg}$=Mg/(Mg+Fe); $X_K$=K/(K+Na).

Table 6. Continued.

| | 88-48 | 88-45 | | 88-85 | | 88-74 | | 88-80 | | 88-57 | | 88-58 | |
|---|---|---|---|---|---|---|---|---|---|---|---|---|---|
| Spl. | D4 | E2 | E4 | C5 | D11 | C6 | D9 | B4 | B6 | A12 | A12 | B3 | C3 |
| Tetrahedral sites | | | | | | | | | | | | | |
| Si | 5.56 | 5.61 | 5.5 | 5.5 | 5.57 | 5.53 | 5.5 | 5.5 | 5.55 | 5.63 | 5.63 | 5.5 | 5.50 |
| $Al^{iv}$ | 2.44 | 2.39 | 2.4 | 2.4 | 2.43 | 2.47 | 2.4 | 2.4 | 2.45 | 2.37 | 2.37 | 2.4 | 2.50 |
| Octahedral sites | | | | | | | | | | | | | |
| Ti | 0.156 | 0.190 | 0.180 | 0.189 | 0.222 | 0.236 | 0.246 | 0.14 | 0.153 | 0.225 | 0.225 | 0.259 | 0.245 |
| $Al^{vi}$ | 0.828 | 0.890 | 0.853 | 0.794 | 0.750 | 0.660 | 0.627 | 0.82 | 0.758 | 0.720 | 0.720 | 0.71 | 0.735 |
| Fe | 1.81 | 2.00 | 2.0 | 2.0 | 2.05 | 2.21 | 2.2 | 1.5 | 1.56 | 2.12 | 2.12 | 2.5 | 2.53 |
| Mg | 2.94 | 2.73 | 2.7 | 2.7 | 2.72 | 2.60 | 2.5 | 3.3 | 3.23 | 2.72 | 2.72 | 2.1 | 2.29 |
| Mn[#] | 6.6E-04 | 5.7E-04 | 6.1E-04 | 6.6E-04 | 7.6E-04 | 3.7E-03 | 4.2E-03 | n.d | 1.2E-02 | n.d. | n.d | 3.0E-0 | n.d. |
| Sc | 2.5E-04 | 1.3E-04 | 1.1E-04 | 9.6E-05 | 1.1E-04 | 3.0E-04 | 3.0E-04 | 8.6E-0 | 8.4E-04 | 8.6E-04 | 8.6E-04 | 2.9E-0 | 2.7E-04 |
| V | 2.2E-03 | 4.4E-03 | 3.9E-03 | 4.5E-03 | 4.7E-03 | 4.4E-03 | 4.6E-03 | 4.8E-0 | 4.7E-03 | 8.5E-03 | 8.5E-03 | 2.0E-0 | 1.9E-03 |
| Cr | 7.2E-03 | 5.9E-03 | 6.0E-03 | 5.2E-03 | 4.2E-03 | 4.7E-03 | 5.8E-03 | 5.7E-0 | 5.8E-03 | 1.2E-02 | 1.2E-02 | 3.7E-0 | 3.0E-03 |
| Co | 7.4E-04 | 3.9E-04 | 3.7E-04 | 4.8E-04 | 5.5E-04 | 1.7E-03 | 1.8E-03 | 6.3E-0 | 6.3E-04 | 8.7E-04 | 8.7E-04 | 7.2E-0 | 6.3E-04 |
| Ni | 1.7E-03 | 1.1E-03 | 8.7E-04 | 6.7E-04 | 6.7E-04 | 4.1E-03 | 4.3E-03 | 2.1E-0 | 1.9E-03 | 3.3E-03 | 3.3E-03 | 1.8E-0 | 1.7E-03 |
| Cu | 5.9E-05 | 3.2E-04 | 1.5E-04 | n.d | n.d. | n.d. | n.d | 8.5E-0 | 1.6E-04 | n.d. | n.d | 1.7E-0 | 9.0E-05 |
| Zn | 1.3E-03 | 1.2E-02 | 9.7E-03 | 1.1E-02 | 1.2E-02 | 6.9E-03 | 7.8E-03 | 3.6E-0 | 3.8E-03 | 9.3E-03 | 9.3E-03 | 1.6E-0 | 1.4E-02 |
| Y | 1.5E-06 | 4.8E-06 | 1.8E-06 | n.d | n.d. | n.d. | n.d | 4.9E-0 | 7.3E-07 | n.d. | n.d | 9.1E-0 | 8.3E-07 |
| Zr | n.d. | 3.3E-06 | 1.0E-06 | 1.4E-06 | 6.0E-06 | 1.0E-06 | 1.6E-06 | 1.4E-0 | 1.4E-06 | n.d. | n.d | 8.7E-0 | n.d. |
| Nb | 2.2E-04 | 7.9E-06 | 7.9E-06 | 9.6E-06 | 1.5E-05 | 1.7E-04 | 1.8E-04 | 1.3E-0 | 1.2E-04 | | | | |
| Hf | n.d. | n.d. | n.d | 3.8E-07 | n.d. | 5.7E-08 | 5.0E-08 | 9.7E-0 | 1.9E-07 | | | | |
| Ta | 2.9E-06 | 9.7E-08 | 1.2E-07 | 2.7E-07 | 2.5E-07 | 4.8E-06 | 4.8E-06 | 1.4E-0 | 1.2E-06 | | | | |
| Total | 5.75 | 5.84 | 5.8 | 5.8 | 5.77 | 5.74 | 5.7 | 5.8 | 5.73 | 5.82 | 5.82 | 5.7 | 5.83 |
| $X_{Mg}$ | 0.62 | 0.58 | 0.5 | 0.5 | 0.57 | 0.54 | 0.5 | 0.6 | 0.67 | 0.56 | 0.56 | 0.4 | 0.47 |
| Interlayer sites | | | | | | | | | | | | | |
| Na | 0.144 | 0.115 | 0.087 | 0.143 | 0.171 | 0.174 | 0.231 | 0.11 | 0.141 | n.d. | n.d | n.d | n.d. |
| K | 1.65 | 1.31 | 1.4 | 1.5 | 1.50 | 1.68 | 1.6 | 1.6 | 1.73 | 1.74 | 1.74 | 1.8 | 1.73 |
| F | | | | | | | | 0.08 | | 0.104 | 0.104 | | 0.168 |
| Cl | | | | | | | | 0.00 | | 0.005 | 0.005 | | 0.008 |
| Sr | 2.5E-05 | 3.2E-05 | 2.0E-05 | 4.5E-05 | 6.0E-05 | 2.0E-05 | 2.8E-05 | 7.9E-0 | 3.7E-05 | n.d. | n.d | 4.5E-0 | 3.8E-05 |
| Ba | 1.1E-03 | 4.1E-03 | 4.6E-03 | 7.5E-03 | 8.8E-03 | 3.5E-03 | 4.3E-03 | 2.0E-0 | 1.9E-02 | 1.7E-02 | 1.7E-02 | 2.7E-0 | 2.7E-03 |
| La | 2.0E-05 | 8.2E-06 | 4.8E-06 | 4.9E-07 | 3.6E-06 | 3.6E-07 | 1.9E-07 | 4.5E-0 | 8.6E-07 | 2.3E-05 | 2.3E-05 | 8.6E-0 | 7.9E-07 |
| Ce | 4.4E-05 | 2.8E-05 | 1.6E-05 | 1.1E-06 | 1.3E-05 | 1.1E-06 | 5.7E-07 | n.d | 5.3E-07 | 3.0E-05 | 3.0E-05 | | |
| Pr | 4.5E-06 | 3.4E-06 | 2.1E-06 | 1.6E-07 | 1.8E-06 | 9.2E-08 | 6.3E-08 | 3.7E-0 | 1.0E-07 | 4.4E-06 | 4.4E-06 | n.d | 2.4E-07 |
| Nd | 1.4E-05 | 1.6E-05 | 7.9E-06 | 1.2E-06 | 8.5E-06 | n.d. | 2.5E-07 | n.d | 5.1E-07 | 1.7E-05 | 1.7E-05 | 1.6E-0 | n.d. |
| Sm | 1.3E-06 | 2.5E-06 | 1.4E-06 | 4.5E-07 | 1.2E-06 | 3.3E-08 | 5.9E-08 | n.d | 7.0E-08 | 1.2E-06 | 1.2E-06 | | |
| Eu | 1.2E-07 | 2.3E-07 | 1.5E-07 | 1.3E-07 | 3.3E-07 | 1.6E-07 | 5.9E-08 | 6.9E-0 | 6.6E-08 | 5.2E-07 | 5.2E-07 | n.d | n.d. |
| Gd | 4.9E-07 | 1.6E-06 | 9.5E-07 | 6.1E-07 | 4.4E-07 | 2.8E-07 | 5.7E-08 | n.d | 2.2E-08 | n.d. | n.d | | |
| Tb | 3.3E-08 | 1.9E-07 | 1.1E-07 | 4.0E-08 | 3.4E-07 | n.d. | n.d | n.d | n.d. | n.d. | n.d | n.d | n.d. |
| Dy | n.d. | 4.9E-07 | 3.0E-07 | 3.8E-07 | 1.8E-07 | 1.7E-07 | n.d | n.d | n.d. | n.d. | n.d | | |
| Ho | n.d. | 4.1E-08 | n.d | 7.7E-08 | 3.4E-08 | n.d. | n.d | n.d | 7.2E-09 | n.d. | n.d | n.d | n.d. |
| Er | 1.1E-07 | 1.1E-07 | n.d | n.d | n.d. | 1.6E-07 | n.d | n.d | 1.6E-08 | n.d. | n.d | | |
| Tm | n.d. | n.d. | n.d | n.d | n.d. | 4.8E-09 | n.d | n.d | n.d. | 3.0E-08 | 3.0E-08 | | |
| Yb | n.d. | n.d. | 1.0E-07 | 4.4E-08 | 1.3E-07 | n.d. | n.d | 2.2E-0 | n.d. | n.d. | n.d | n.d | n.d. |
| Lu | n.d. | n.d. | n.d | n.d | n.d. | n.d. | n.d | 1.1E-0 | 1.8E-08 | n.d. | n.d | n.d | n.d. |
| Total | 1.79 | 1.43 | 1.5 | 1.6 | 1.68 | 1.85 | 1.8 | 1.8 | 1.89 | 1.86 | 1.86 | 1.8 | 1.91 |
| $X_K$ | 0.92 | 0.92 | 0.9 | 0.9 | 0.90 | 0.91 | 0.8 | 0.9 | 0.92 | 1.00 | 1.00 | 1.0 | 1.00 |

Site occupancies were assigned on the basis of ionic radii and charges (Shannon 1976). [#] determined by LAM-ICP-MS. n.d. = not detected. Blank = not determined. $X_{Mg}$=Mg/(Mg+Fe); $X_K$=K/(K+Na).

Table 3.7. Representative values of $D_i^*$ between coexisting garnet and biotite and estimated metamorphic temperature (Ferry & Spear 1978).

| Spl. | 87-81 | | 87-83 | | 87-86 | | 87-283 | | 87-279 | | 88-49 | | 88-48 | | 88-45 | | 88-85 | | 88-74 | | 88-80 | | 88-57 | | 88-58 | |
|---|---|---|---|---|---|---|---|---|---|---|---|---|---|---|---|---|---|---|---|---|---|---|---|---|---|---|
| Grt | F23 | G1 | C11 | C24 | C1 | C8 | C3 | D2 | D6 | D1 | A4 | A45 | D1 | D3 | E1 | E7 | C4 | D10 | C5 | D8 | B9 | B5 | A13 | A9 | B5 | C4 |
| Bt | F8 | G12 | C23 | C9 | C34 | C4 | C5 | D5 | D3 | D3 | A5 | A1 | D2 | D4 | E2 | E4 | C5 | D11 | C6 | D9 | B4 | B6 | A12 | A12 | B3 | C3 |
| Sc | 6.0 | 6.4 | 5.6 | | 4.4 | 4.3 | 5.8 | 6.3 | 5.5 | | | | 3.6 | 6.6 | 14.0 | 12.6 | 17.8 | 18.3 | 5.1 | 5.0 | 4.2 | 6.3 | 2.7 | 1.6 | 4.5 | 4.2 |
| Ti | 0.05 | 0.05 | 0.05 | 0.05 | 0.03 | 0.03 | 0.03 | 0.05 | 0.03 | 0.03 | 0.01 | 0.01 | 0.05 | 0.07 | | 0.01 | | | | | 0.02 | | 0.02 | 0.03 | | |
| V | 0.40 | 0.43 | 0.72 | | 0.33 | 0.38 | 0.25 | 0.43 | 0.35 | | 0.15 | 0.20 | 0.53 | 0.59 | 0.12 | 0.15 | 0.13 | 0.18 | 0.11 | 0.10 | 0.13 | 0.14 | 0.23 | 0.15 | 0.26 | 0.30 |
| Cr | 1.38 | 0.31 | 0.29 | | | 0.73 | 0.48 | 0.77 | 0.63 | | 0.60 | 0.45 | 0.92 | 1.14 | 0.56 | 0.75 | 0.59 | 0.82 | 0.50 | 0.41 | 0.19 | 1.10 | 1.79 | 0.36 | 1.52 | 1.56 |
| Mn | 18 | 19 | 29 | | 32 | 36 | 34 | 51 | 17 | 17 | | | | | 70 | 65 | 80 | 69 | 68 | 64 | 31 | 54 | 28 | 15 | 18 | 14 |
| Co | 0.27 | 0.27 | 0.34 | | 0.25 | 0.26 | 0.18 | 0.19 | 0.35 | | 0.40 | 0.36 | 0.38 | 0.47 | 0.50 | 0.46 | 0.62 | 0.53 | 0.35 | 0.32 | 0.45 | 0.40 | 0.44 | 0.43 | 0.44 | 0.47 |
| Ni | | | | | | | | | | | | | | 0.90 | | | | | | | | | | | | |
| Cu | | | | | | | | | | | | | | | | | | | | | 0.56 | 0.26 | | | | |
| Zn | 0.11 | 0.12 | 0.14 | | 0.10 | 0.14 | 0.13 | 0.11 | 0.08 | | 0.27 | | 0.16 | 0.26 | 0.17 | 0.18 | 0.15 | 0.15 | 0.13 | 0.12 | 0.16 | 0.19 | 0.10 | 0.16 | 0.14 | 0.16 |
| Sr | | | | | | | | | | | | | | | | | | | | | | | | | 0.01 | |
| Y | 1082 | 257 | 235 | | 394 | 2586 | 174 | 156 | 115 | | | | | 95 | 993 | 1797 | | | | | 2019 | 1977 | | | 836 | 845 |
| Zr | 3 | 1 | 4 | 6 | | | 2 | 4 | 14 | 10 | | | 106 | | 5 | 26 | 24 | 6 | 95 | 41 | 177 | 125 | | | 18 | |
| Nb | | | | | | | | | | | | | | | | | | | | | | | | | | |
| Ba | | | | | | | | | | | | | | | | | | | | | | | | | | |
| La | | | | | | | | | | | | | | | | | | | | | | | | | | |
| Ce | | | | 0.02 | | | | | | | | | | | | | 0.01 | | | | | 0.01 | | | | |
| Pr | | | | | | | | 0.02 | | | | | 0.01 | 0.02 | | 0.01 | 1.23 | | | | 5.81 | 0.03 | 0.01 | | | |
| Nd | | | | 0.02 | | | | | | | | | 0.08 | 0.07 | | | | | | | | 0.58 | 0.05 | 0.05 | | |
| Sm | | | 0.65 | | 0.12 | | | | | 0.31 | | | 24.78 | 8.97 | 2.40 | 4.47 | 18.98 | | | | | 82.37 | 4.48 | 2.74 | | |
| Eu | | 2 | 6 | 2 | 2 | | | | | 1 | | 7 | 163 | 23 | 14 | 30 | 51 | | | | 116 | 72 | 11 | 13 | | |
| Gd | | 12 | 13 | 4 | 4 | | 2 | 1 | | 7 | | | | 38 | 46 | 87 | 107 | | | | | 3064 | | | | |
| Tb | | 40 | | 57 | 47 | | 11 | 16 | | 42 | 9 | | | 64 | 217 | 331 | 407 | | | | | | | | | |
| Dy | | 221 | | 96 | 264 | | 37 | 42 | | 84 | | | 175 | | 911 | 1075 | 211 | | | | | | | | | |
| Ho | | 383 | | 86 | 711 | | 136 | 138 | | 167 | | | | | 2938 | | 129 | | | | | 4027 | | | | |
| Er | | 822 | | 81 | | | 125 | 161 | | 153 | | | | 75 | 2903 | | | | | | | 3953 | | | | |
| Tm | | 4988 | | 69 | | | 214 | 200 | | 98 | | | 74 | | | | | | | | | | 40 | 173 | | |
| Yb | | 709 | 180 | | | | | 359 | | 112 | | | 188 | | | 576 | 306 | | | | 452 | | | | | |
| Lu | | | 200 | | 1411 | | | 216 | | 73 | | | 181 | | | | | | | | 137 | 296 | | | | |
| Hf | | | | | | | | | | 1.46 | | | | | | | 0.39 | | | | 19.04 | 8.42 | | | | |
| Ta | | | 0.01 | 0.01 | | | | | | | | | | 0.01 | | | | | | | | | | | | |
| T(°C) | 464 | 478 | 442 | 463 | 419 | 444 | 481 | 481 | 493 | 493 | 441 | 434 | 519 | 501 | 570 | 593 | 576 | 580 | 571 | 592 | 668 | 671 | 602 | 636 | 660 | 634 |

Table 3.8. Mean Nernst distribution coefficients for selected trace elements between coexisting garnet and biotite, for low-, mid- and high-T samples, compared with literature data.

| Elements | Low-T | Mid-T | High-T | Amphibolite facies[#] | Granulite facies[§] |
|---|---|---|---|---|---|
| Zn | 0.11 ± 0.02 | 0.21 ± 0.06 | 0.15 ± 0.03 | 0.37 ± 0.15[*] | - |
| V | 0.25 ± 0.08 | 0.22 ± 0.13 | 0.11 ± 0.04 | 0.19 ± 0.13 | 0.15 ± 0.11 |
| Co | 0.26 ± 0.06 | 0.42 ± 0.05 | 0.44 ± 0.08 | 0.39 ± 0.20 | 0.56 ± 0.14 |
| Cr | 0.53 ± 0.34 | 0.63 ± 0.20 | 0.56 ± 0.36 | 0.76 ± 0.30 | 0.45 ± 0.49 |
| Sc | 4.91 ± 0.99 | 7.16 ± 4.35 | 8.49 ± 6.66 | 4.02 ± 2.15 | 6.51 ± 5.32 |

[#] Data from DeVore (1955), Turekian & Phinney (1962), Albee (1965) and Hietenan (1969); [§] Data from Kretz (1959) and Engel & Engel (1960); [*] Data determined using proton microprobe by Hickmott & Spear (1992). Sample standard deviations are calculated at 1σ level.

Table 3.9. Lattice site parameters obtained by regression of garnet/biotite partitioning data.

| Sites | Charge | *E* (kbar) | $r_0$ (Å) | $D_0$ |
|---|---|---|---|---|
| X | 2+ | 7249 ± 101 | 1.02 ± 0.06 | 107 ± 2 |
| | | | 1.02[#] | |
| | 3+ | 18029 ± 29 | 1.02[**] | 23 ± 1 |
| Y | 3+ | 13644 ± 50 | 0.54[#] | 7.8 ± 1.1 |
| Bulk | | 1628[*] | | |

*E* is Young's modulus for the site. $r_0$ is optimal site radius. $D_0$ is partition coefficient for a cation with the optimum radius. [#] $r_0$ is obtained by subtracting the ionic radius of the $O^{2-}$ ion, 1.38 Å, (Shannon 1976) from the observed average cation-oxygen bond length (Smyth & Bish 1988). [**] $r_0$ obtained from the regression for divalent cations in X-sites. [*] Measured Young's Modulus for the bulk crystals calculated at 740 K and 7 kbar (Bass, 1995).

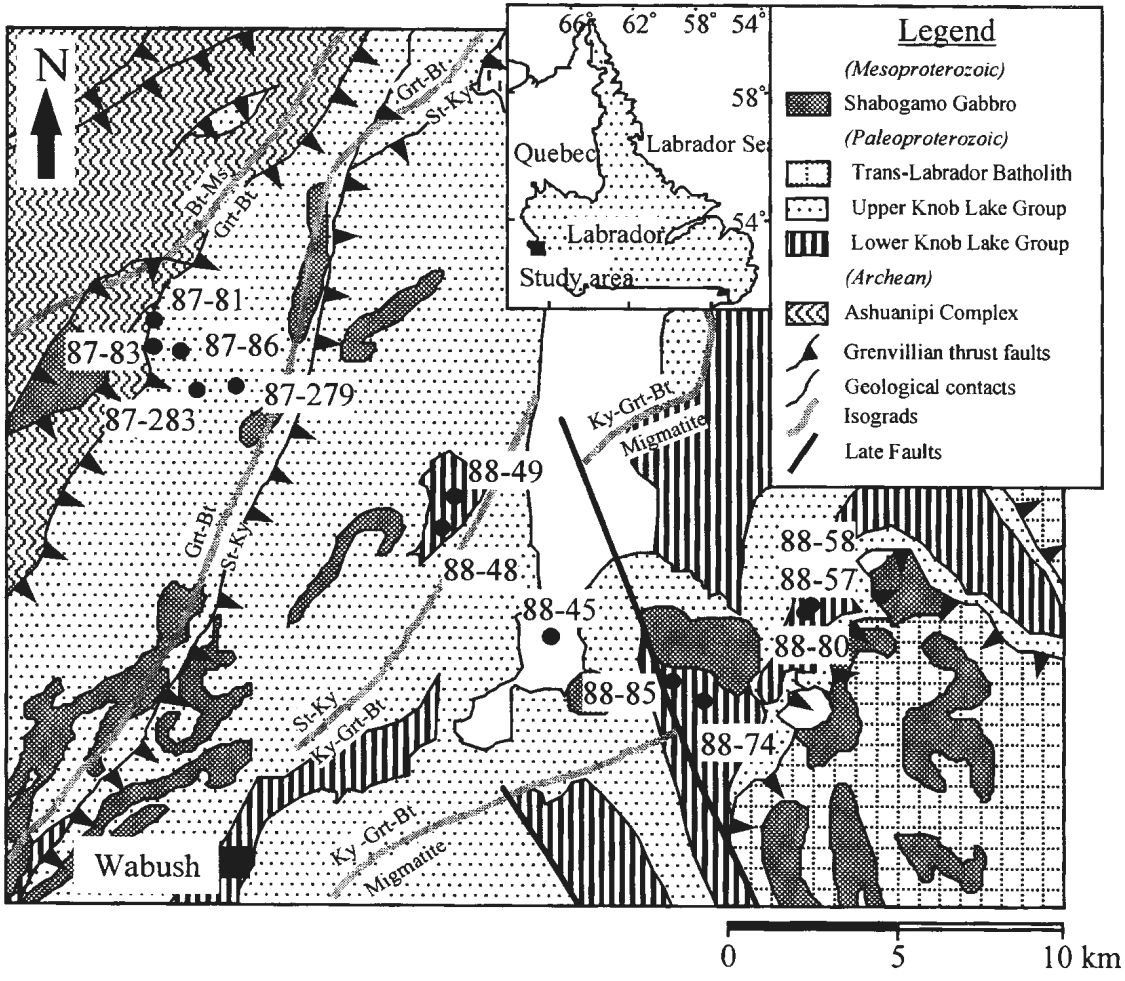


Fig. 3.1. Generalized geological map of the northern Grenville province in western Labrador showing metamorphic isograds and locations of the thirteen samples. Geologic map from Connelly *et al.* (1996) and metamorphic isograds and *P-T* conditions from Rivers (1983) and van Gool (1992), respectively.

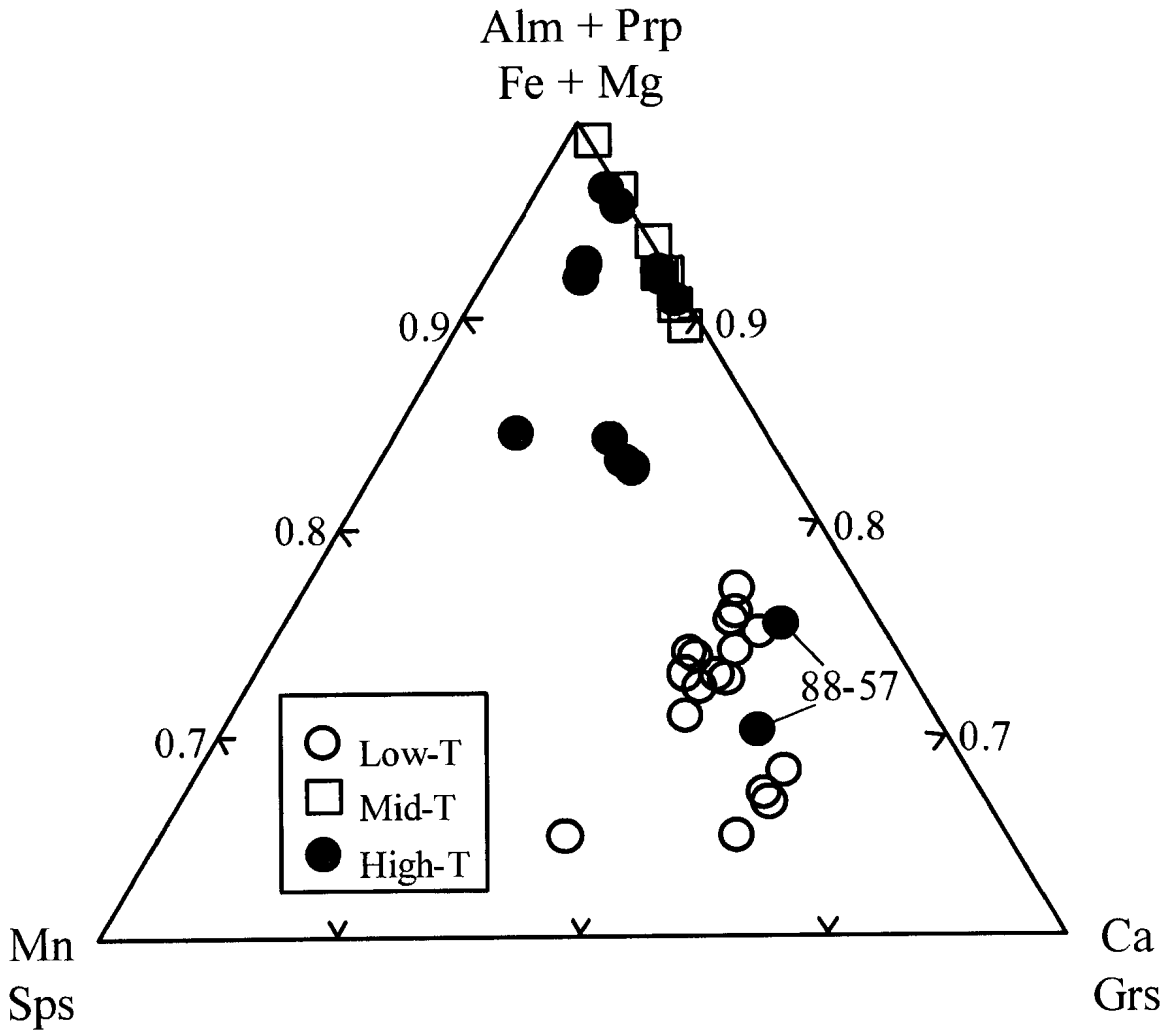


Fig. 3.2. Garnet compositions on the basis of dodecahedrally coordinated Fe, Mg, Mn and Ca. Note that low-T samples are more Ca-rich.

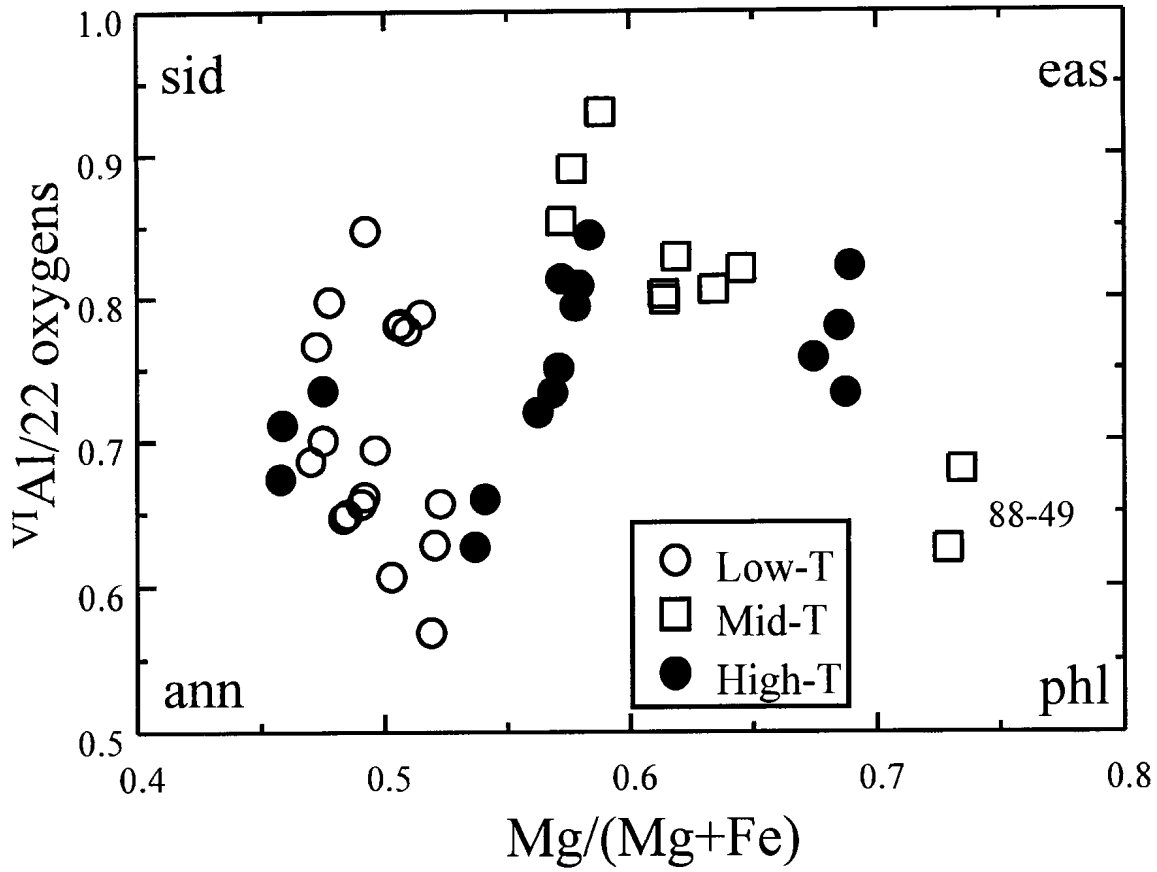


Fig. 3.3. Biotite compositions in the idealized annite-phlogopite-siderophyllite-eastonite plane assuming all iron as ferous. Sample 88-49 containing gedrite shows the highest value of $X_{Mg}$. Sid-siderophyllite, eas-eastonite, ann-annite, phl-phlogopite.

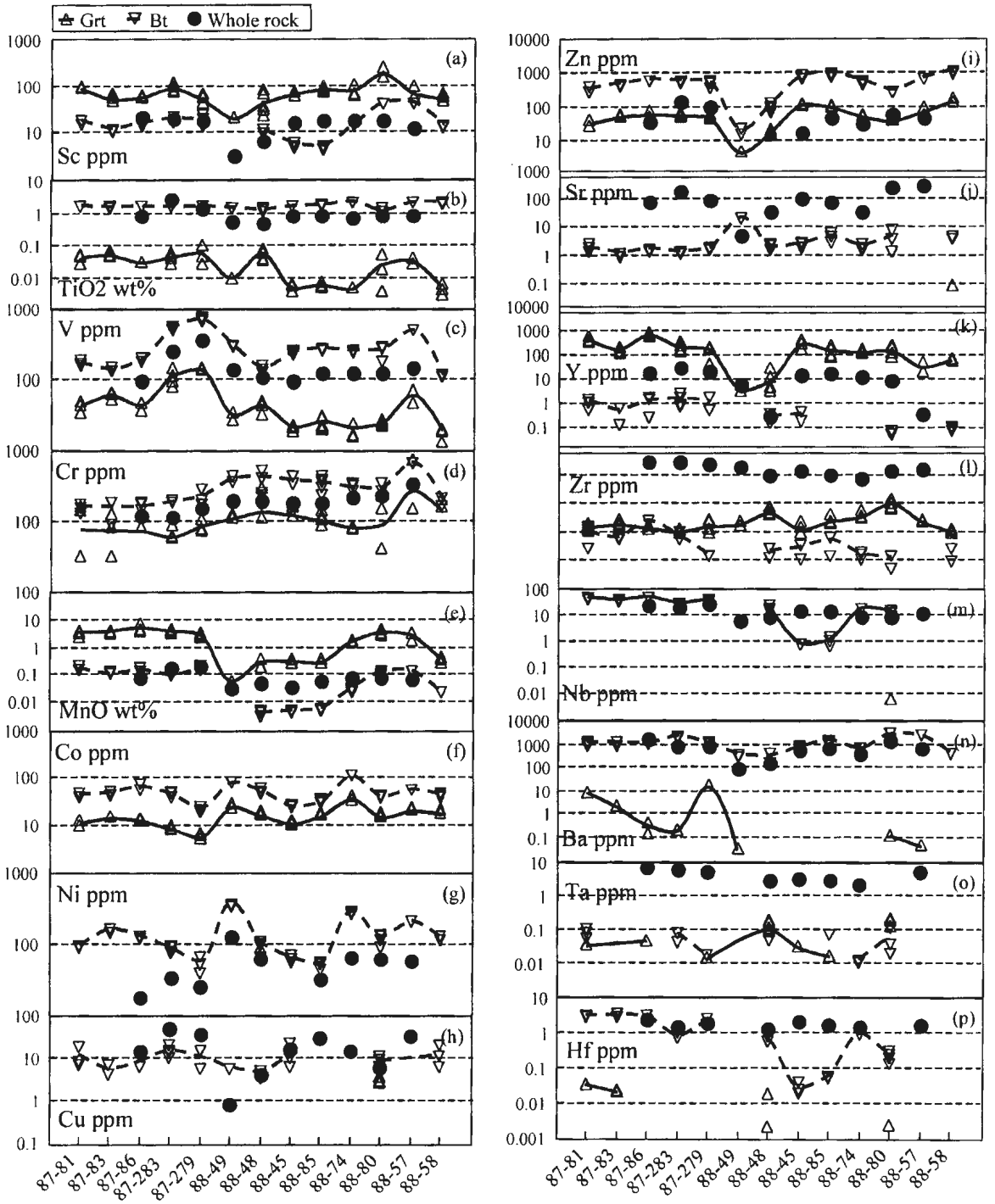


Fig. 3.4. Trace-element compositions in garnet, biotite and whole rock. Samples are arranged in the order of increasing metamorphic grade. Solid and dotted lines represent garnet and biotite, respectively. The within-sample compositional change of garnet and biotite is shown by multiple symbols, each representing a single analysis. Note systematic variations of V, Cr, Mn, Co and Zn concentrations in garnet and biotite over the range of temperature and bulk composition and abrupt depletion of Zn concentration in sample 88-49 from the staurolite zone.

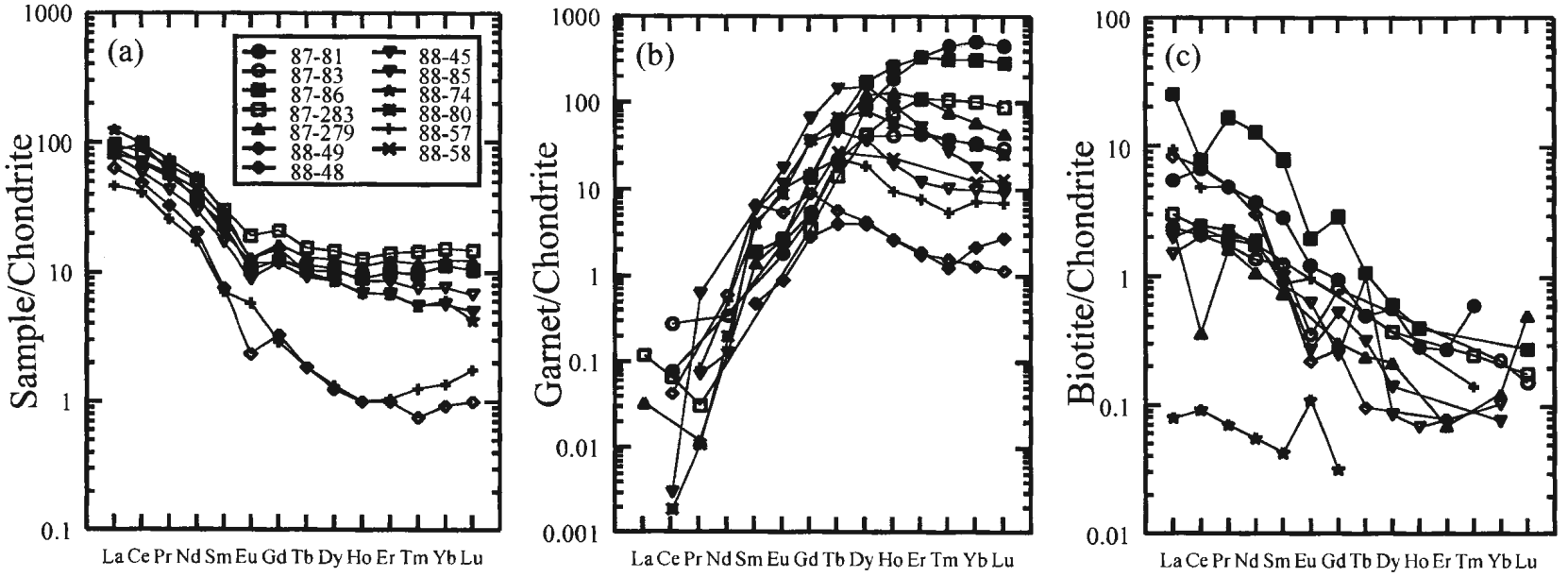


Fig. 3.5. Chondrite-normalized REE diagrams for representative bulk-rock (a), garnet (b) and biotite (c) analysis. Chondrite-normalization factors from Taylor & McLennan (1985).

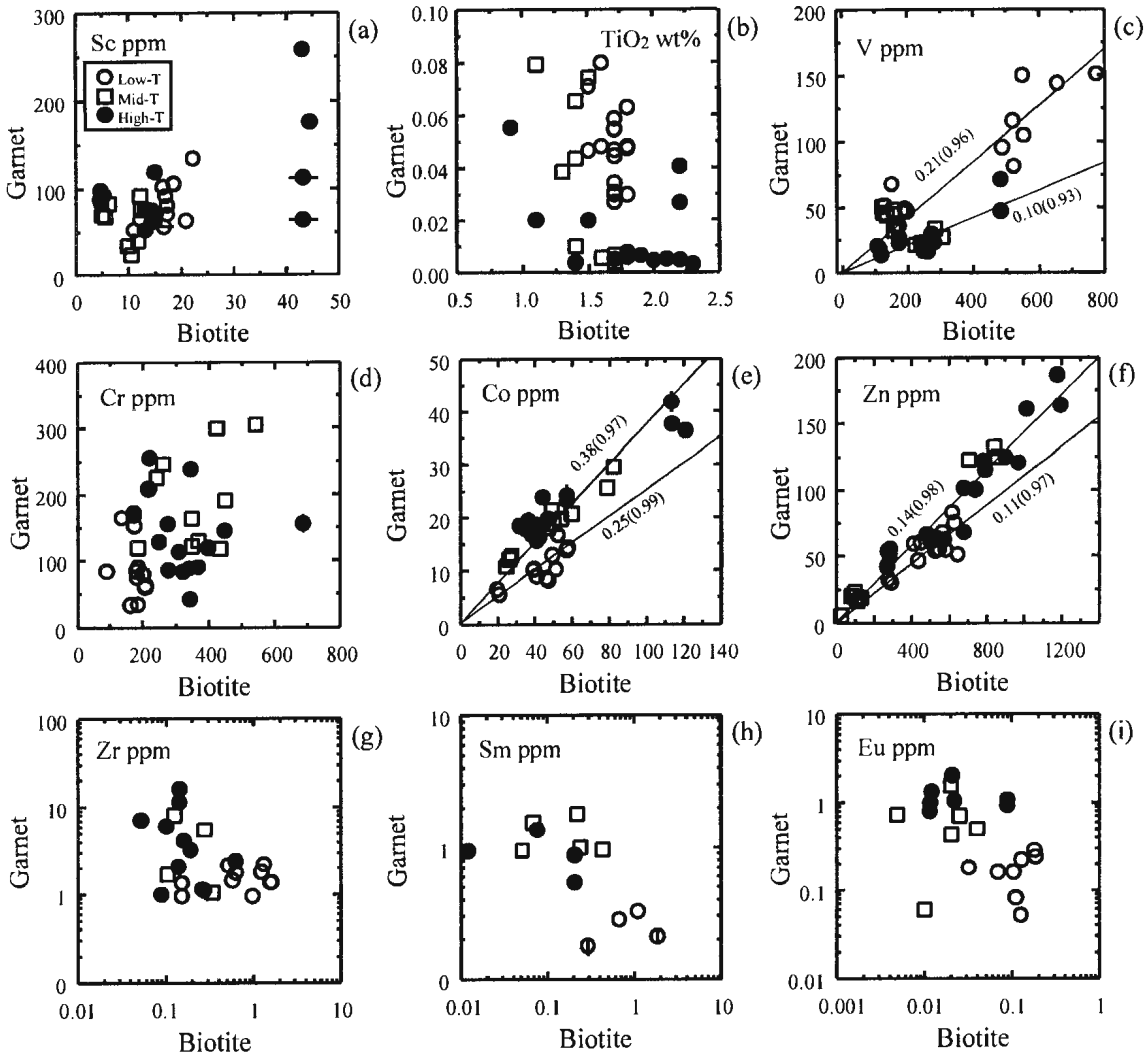


Fig. 3.6. Distribution diagrams illustrating the partitioning of Sc, $TiO_2$, V, Cr, Co, Zn, Zr, Sm and Eu between coexisting garnet and biotite. Diagonal lines represent least-square regression lines for low- and high-T samples. The values in parentheses represent $r^2$ of the regressions. One standard deviation analytical error bars are smaller than the symbols except where shown.

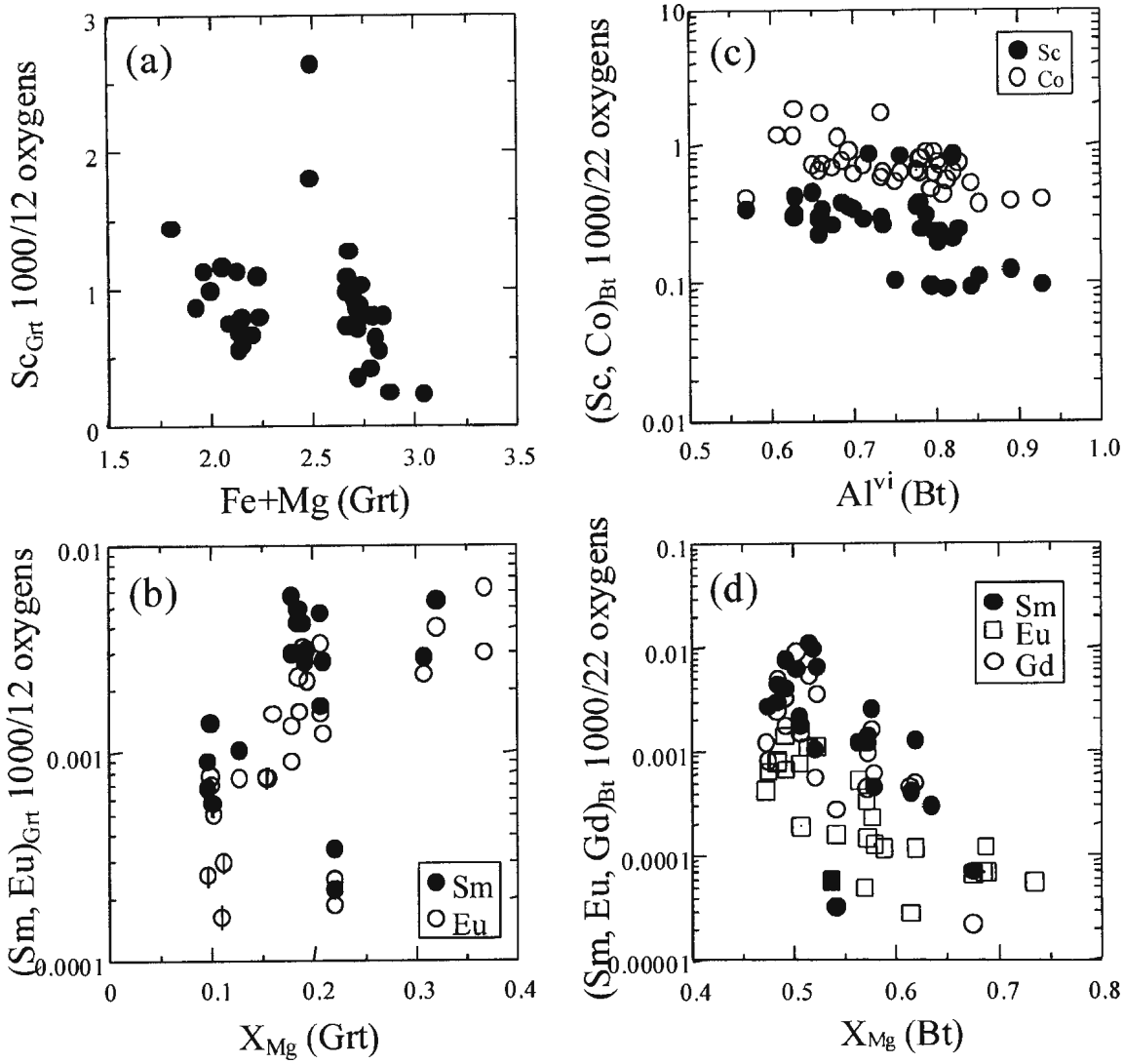


Fig. 3.7. Graphs showing trace-element concentrations *vs.* major element concentrations of garnet and biotite. One standard deviation analytical error bars are smaller than the symbols except where shown.

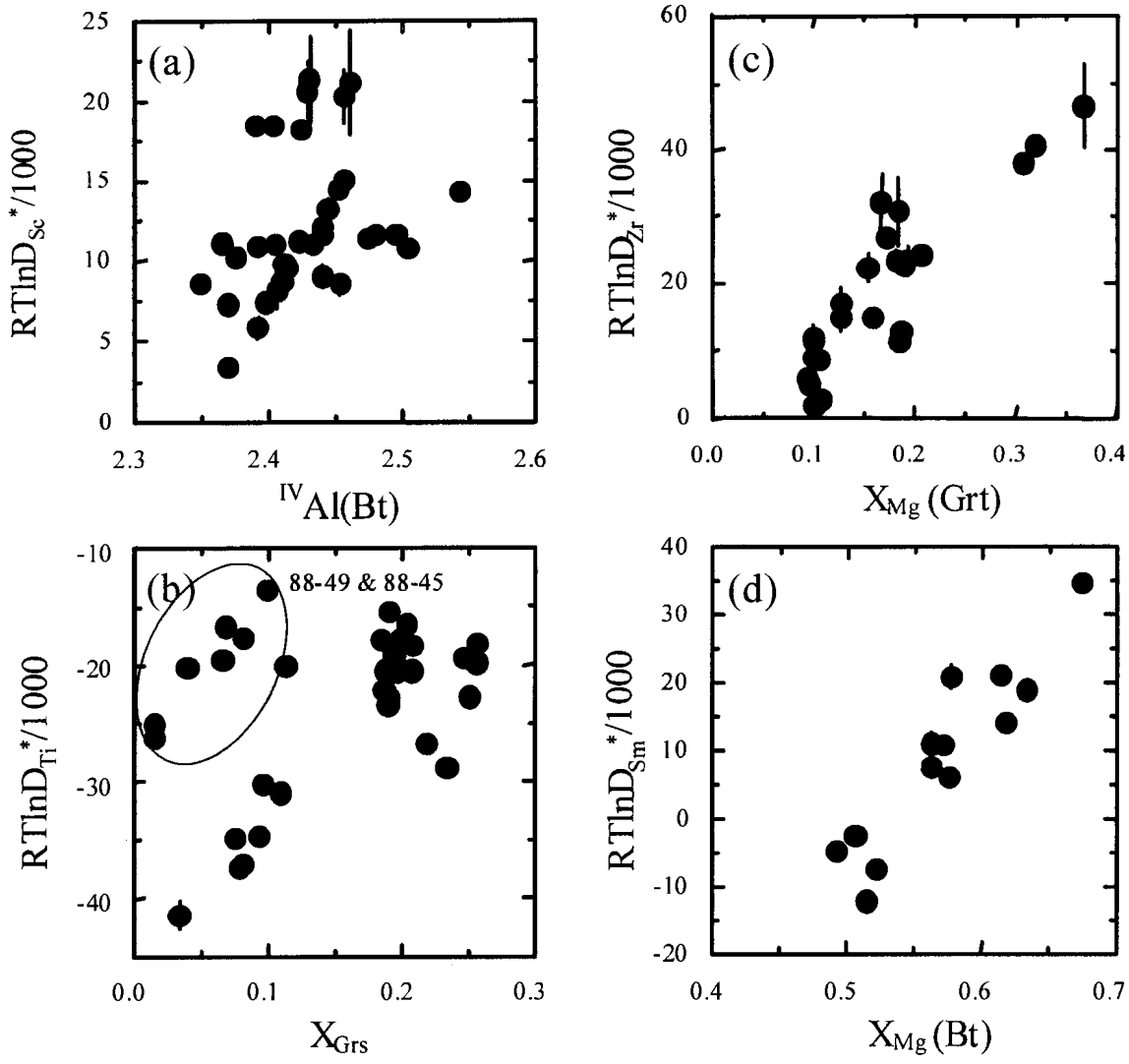


Fig. 3.8. RTlnD$_i^*$ values of Sc, Ti, Zr and Sm plotted against various major element parameters of garnet and biotite. One standard deviation analytical error bars in the estimate of RTlnD$_i^*$/1000 are smaller than the symbols except where shown. The standard deviations of the estimates of $D_i^*$ were calculated by propagating the error associated with counting statistics of each element in each phase; the relative standard deviations range from 1-15%, depending upon the element.

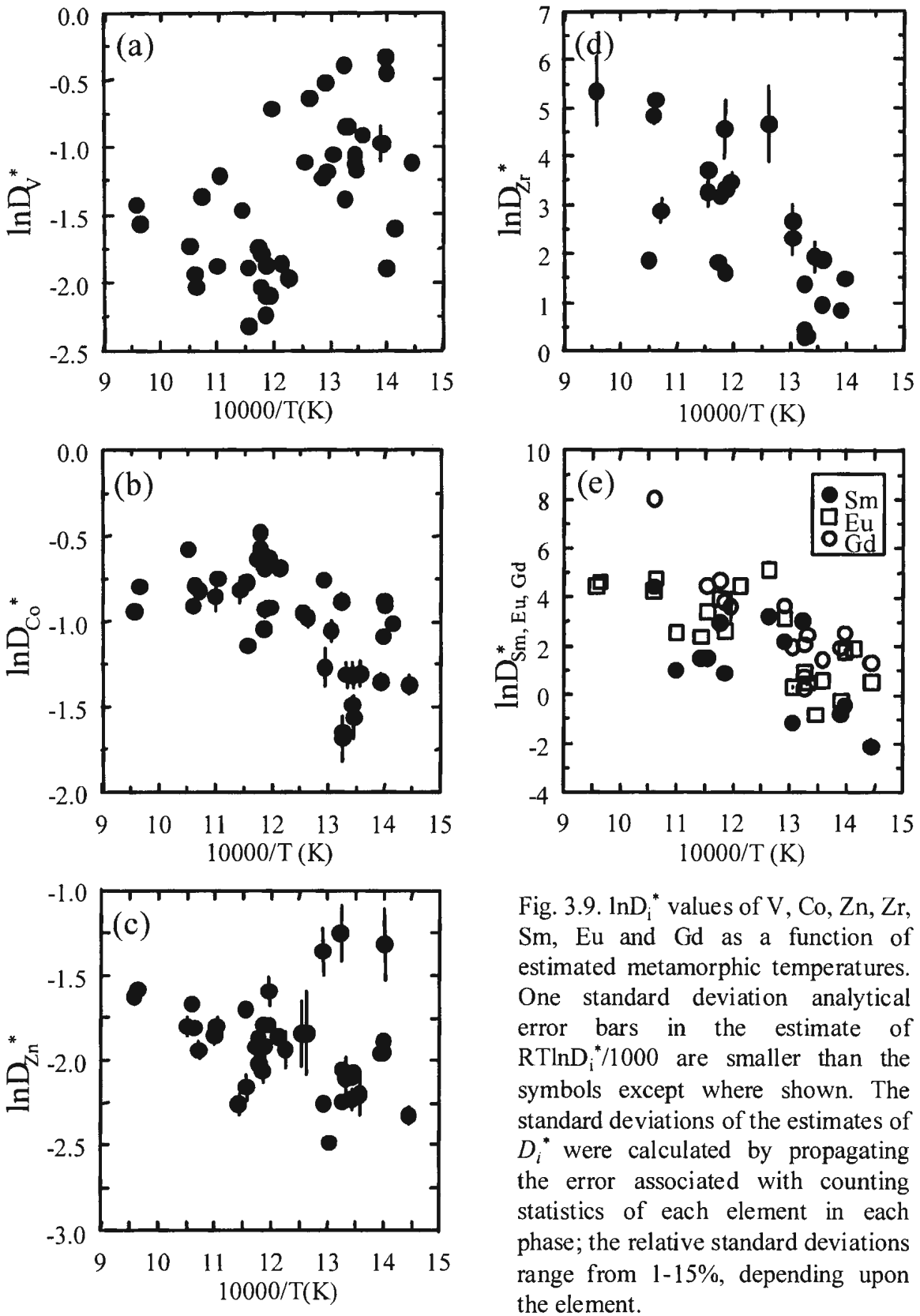


Fig. 3.9. $\ln D_i^*$ values of V, Co, Zn, Zr, Sm, Eu and Gd as a function of estimated metamorphic temperatures. One standard deviation analytical error bars in the estimate of $RT\ln D_i^*/1000$ are smaller than the symbols except where shown. The standard deviations of the estimates of $D_i^*$ were calculated by propagating the error associated with counting statistics of each element in each phase; the relative standard deviations range from 1-15%, depending upon the element.

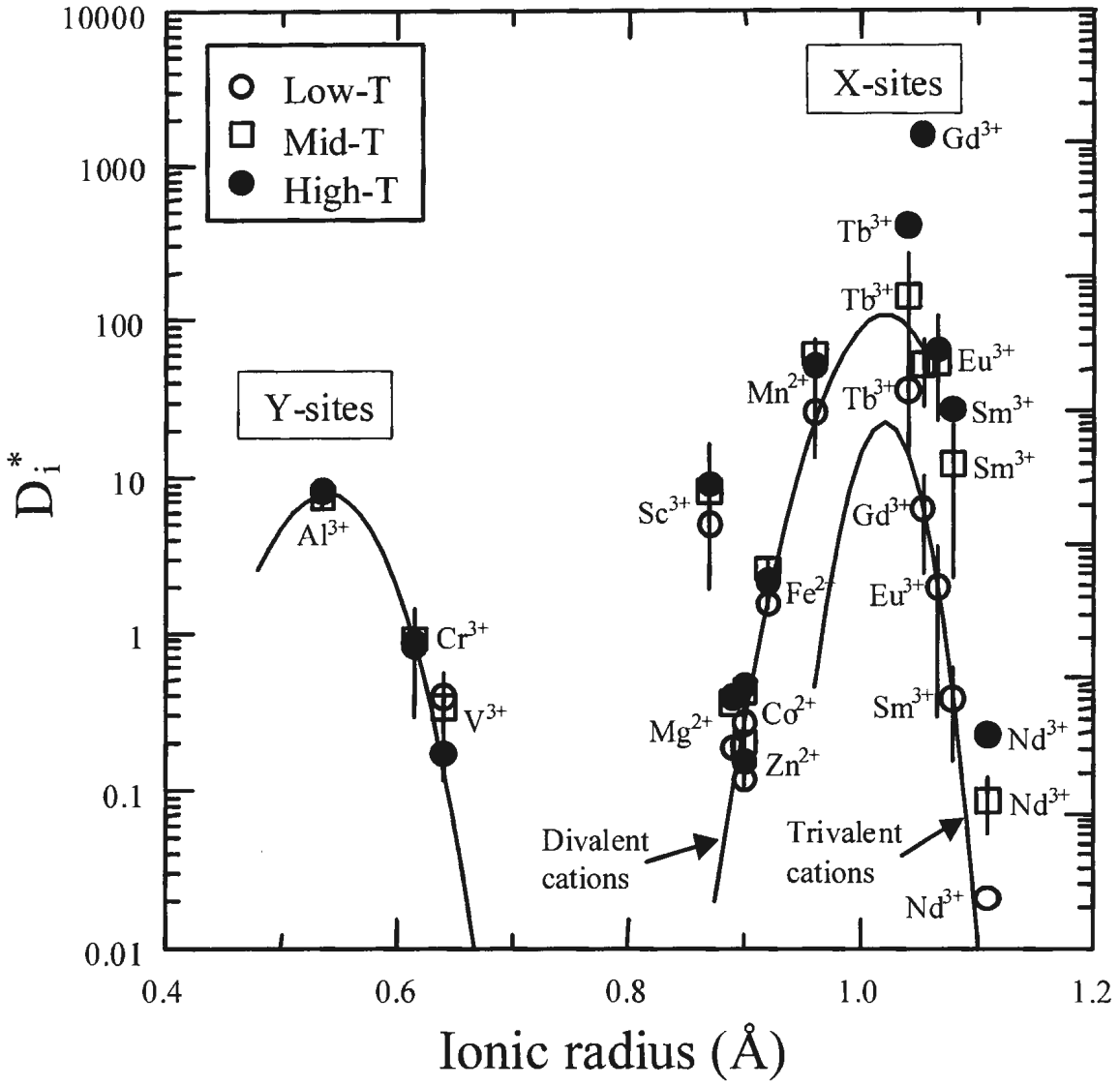


Fig. 3.10. An Onuma diagram showing the estimated partition coefficients plotted against ionic radius (Å) for the X- and Y-sites in garnet. The graph shows that the variation in trace-element partition coefficients is controlled by ionic radius and charge. The curves represent weighted non-linear regression fits for the garnet/biotite partitioning data. Standard deviations (1σ) are shown by vertical lines. Points for REE with no error bars represent single determinations.

# Chapter 4: Trace element partitioning between coexisting biotite and muscovite from metamorphic rocks, western Labrador: Structural, compositional and thermal controls

## 4.1 Introduction

Major element partitioning between coexisting phases is an important aspect of the characterization of phase equilibrium relationships as a function of pressure ($P$), temperature ($T$) and compositional variables ($X$) and is the basis for classical geothermobarometry (Kretz, 1961). In principle, the concept should also extend to trace element partitioning which should therefore also be useful to estimate P-T conditions during metamorphism (*e.g.*, Heinrich *et al.*, 1997; Bea *et al.*, 1997). In addition to thermobarometry, studies of the partitioning of trace elements among coexisting metamorphic minerals can provide valuable information about equilibrium and petrogenesis (*e.g.*, Haack *et al.*, 1984; Dahl *et al.*, 1993; Hickmott *et al.*, 1987; Hickmott and Spear, 1992; Jonhon, 1994; Kretz *et al.*, 1999; Yang *et al.*, 1999). However, the subject has been relatively little investigated because of the difficulty in obtaining uncontaminated trace element analyses and due to complications resulting from crystal chemistry and the composition of host minerals.

Micas are petrogenetically very useful minerals because of their high abundance in many metamorphic rocks, their wide range of stability, their relatively simple mineralogy and their potential to provide information about *P-T* conditions. To extract meaningful petrogenetic information, accurate measurement of the trace element partition coefficients for a wide range of trace elements in various metamorphic environments is essential. At present, there are relatively few published trace element partitioning studies for biotite-muscovite pairs in metamorphic systems (Butler, 1967; Moorbath, 1968; Dutrow *et al.*, 1986; Shearer *et al.*, 1986; Hervig and Peacock, 1989; Dahl *et al.*, 1993; Domanik *et al.*, 1993). Moreover, very little is known about the dependence of the biotite/muscovite distribution coefficients on the intensive and extensive variables, constraining geochemists to adopt a largely empirical approach using constant average distribution values in their modeling (*e.g.*, Haack *et al.*, 1984; Johnson, 1994). In addition, most trace element data in the earlier publications were obtained from bulk analyses of mineral separates, which have commonly proved to be contaminated with micro-inclusions of accessory minerals (Michael, 1988). The use of mineral separates also does not take mineral zoning into account, so the results may not yield equilibrium partition coefficients. These problems are especially acute in medium grade metamorphic rocks where micro-inclusions are ubiquitous. In this study, we have determined partition coefficients for selected trace elements in coexisting biotite and muscovite from ten metapelitic and quartzofeldspathic rocks from western Labrador using a microbeam technique and have examined the variation of biotite/muscovite partition coefficients as a function of crystal structure, variations in major element composition and metamorphic

temperature.

## 4.2. Geology and samples

The ten analyzed samples come from Gagnon terrane in the Grenville Province of western Labrador (Fig. 4.1). Gagnon terrane comprises a metamorphic foreland fold-and-thrust belt (Rivers, 1983a; Rivers, 1983b; van Gool, 1992), that is separated from the Superior province foreland in the northwest by the Grenville Front, and is tectonically overlain by Molson Lake terrane to the southeast. Metasediments in Gagnon terrane, which are part of the Paleoproterozoic Knob Lake Group, were deposited on the passive continental margin of the Superior Craton and experienced a single Barrovian-type regional metamorphism during the Grenvillian Orogeny at *ca.* 1000 Ma (Rivers, 1983b; Brown *et al.,* 1992; van Gool, 1992; Rivers *et al.,* 1993; Schwarz, 1998). During this orogenic event, Gagnon terrane was overthrust by Molson Lake terrane, composed of late Paleoproterozoic to Mesoproterozoic granitoid and gabbroic rocks, and incorporated into the base of a major thrust wedge. Metamorphic grade increases from greenschist facies in the north, at the Grenville Front, to upper amphibolite facies in the southeast, near Molson Lake terrane. Six metamorphic zones have been outlined by Rivers (1983b) based on the diagnostic mineral assemblages: chlorite-muscovite (*zone 1*), biotite-muscovite (*zone 2*), garnet-biotite (*zone 3*), staurolite-kyanite (*zone 4*), biotite-kyanite-garnet (*zone 5*) and migmatite (*zone 6*) in order of increasing metamorphic grade (Fig. 4.1). The isograds were telescoped during thrusting (van Gool, 1992), and the apparent absence of a staurolite-biotite zone between the garnet-biotite and staurolite-kyanite

zones may be due either to telescoping and/or to poor exposure. The samples chosen for this study include five from the garnet-biotite zone (referred to as low-T samples) and another five from staurolite-kyanite, biotite-kyanite-garnet and migmatite zones (referred to as high-T samples). Micas from the lowest grade zone are very fine grained, presenting difficulties for the LAM-ICP-MS technique, and were not included in this study.

All selected rocks are foliated and are composed principally of quartz (26-62 modal %), micas (35-54 modal %) and lesser amounts of garnet, kyanite, chlorite, epidote and plagioclase, with accessory minerals constituting the remainder (Table 4.1). All of the samples have at least one Ti-saturating phases such as ilmenite and rutile in the matrix. Plagioclase occurs in all samples except 88-58. Accessory minerals in the samples include pyrite, ilmenite, rutile, monazite, apatite, tourmaline, graphite and zircon. Both biotite and muscovite show little sign of retrogression and secondary muscovite rarely occurs in these rocks. Inclusions of apatite, zircon and ilmenite are common in the biotite crystals, and, to a lesser extent, in the white mica. A marked coarsening of the grain size of the micas occurs within the staurolite-kyanite zone and coincides with the disappearance of primary chlorite from the assemblage (Table 4.1). Mineral assemblages, textures and reactions in metapelitic rocks of the Gagnon terrane in western Labrador are described in detail elsewhere (*e.g.,* Rivers, 1983b; van Gool, 1992).

## 4.3 Analytical methods

### 4.3.1 Electron microprobe analysis

Major and minor element analyses were performed using the Cameca® SX-50 electron microprobe at Memorial University of Newfoundland using energy dispersive (ED) and wavelength dispersive (WD) methods simultaneously. Analyses were carried out using a 15 kV accelerating voltage, 10 nA current and a 5 micron beam diameter. ED analyses used a cobalt gain calibration. Ti, F and Cl were determined by WD analysis using ilmenite, apatite and tugtupite ($Na_4AlBeSi_4O_{12}Cl$) as standards, respectively. Analyses were obtained on three or more crystals of biotite and muscovite in each of the ten samples. Precision at the $1\sigma$ level for Ti (used for calibration of LAM-ICP-MS results, see below) was better than 6 relative % in both biotite and muscovite.

### 4.3.2 LAM-ICP-MS analysis

Trace element compositions in micas were determined by a laser ablation system coupled to an ICP-MS (Fisons VG PQII +S®) at Memorial University of Newfoundland. The LAM system incorporates a Nd:YAG laser (266 nm wavelength), a custom built sample cell and an Ar carrier gas system. Details of the system are described in Jackson *et al.* (1992), Jenner *et al.* (1994) and Taylor *et al.* (1997).

Data acquisition was performed by peak jumping in pulse counting mode, acquiring individual intensity data for each analyte isotope during each mass spectrometer sweep (~ 1 sec). A total of about 480 sweeps, comprising a gas background interval of about 200 sweeps followed by an ablation interval of about 280 sweeps was performed for each analysis. Calibration was conducted on the NIST SRM-610 glass standard, and BCR-2

was used to check the data quality during each run. Ti was routinely employed as the internal standard, based on electron microprobe measurement of the $TiO_2$ contents in the micas.

Data reduction followed the protocol outlined by Longerich *et al.* (1996a). Limit of detection for BCR-2 for a ~50 μm beam size and ~0.5 mJ/pulse was typically in the range 3-35 ppb for most high-mass elements (Rb to Ta), and between 68 and 6000 ppb for lower-mass elements (Li to Zn) (Table 4.2). However, detection limits for samples are different from the glass standard because of different beam diameters, counting times and ablation energy used for each single analysis. For high-T micas, we used a ~70 μm beam size and ~0.7 mJ/pulse of laser energy. For low-T micas, we had to reduce the beam size and pulse energy by almost half because of their smaller size. According to Longerich *et al.* (1996a), the difference in beam size between low- and high-T micas results in at least a fourfold increase in the detection limit.

Repeated measurements of BCR-2 glass at the same ablation conditions yielded a precision ($1\sigma$) of better than 5 and 10 % relative for absolute concentrations above and below 1 ppm, respectively, except for Cr and Ni. The poor precision obtained for Cr and Ni is attributed to their concentrations approaching detection limits in the glass. Zn analyses clearly show the effects of fractionation during the laser ablation, as indicated by increasing signals over time, invariably resulting in higher concentrations compared to the literature values (Table 4.2). Because of the fractionation effect observed, the lowest measured value of Zn for each sample was used.

The time-resolved analysis of the LAM allows detection of zoning and inclusions in

the analyzed mineral grain during ablation, which is a great advantage over other microbeam techniques such as PIXE and SIMS. However, the presence of submicroscopic inclusions below the resolution of the time-resolved signal (a few microns) cannot be ruled out. Indeed, Zr, La and Ce analyses of micas are highly variable on a thin-section scale. Since micro-inclusion phases enriched in Zr, La and Ce, such as zircon, monazite and apatite, were found in the analyzed micas, we consider the most reliable data to be those with the lowest concentrations of these elements. Zn, Zr, La and Ce data therefore should be considered as only semi-quantitative.

Electron microprobe and LAM-ICP-MS analyses of biotite and muscovite are presented in Tables 4.3-4.4 as averages and standard deviations ($1\sigma$) of 2-3 analyses performed for each mineral from two to three domains in a thin-section, except for sample 87-86, in which all analyses come from a single domain. Most analyses of Ca, Y, Zr, La, Ce and Hf in biotite and Ca, Ni, Cu, Y, Zr, La, Ce and Hf in muscovite are close to their respective lower limits of detection (< 3 times detection limit) and these elements are italicized in the Tables 4.3-4.4. Mica stoichiometries are given in Tables 4.5-4.6. Cation site-occupancies were assigned on the basis of ionic radii (Shannon, 1976).

Establishing the presence or absence of zoning is important for an evaluation of chemical equilibrium. Each mineral, therefore, was analyzed close to its rim and at the core for representative samples. The analyzed micas are virtually unzoned both in major and trace element concentrations. Care was taken to avoid obvious cleavages during laser ablation, but cleavage does not appear to affect analytical results.

## 4.4 Major element compositions

Structural formulae for both biotite and muscovite are based on 22 oxygen atoms (Tables 4.5-4.6). Both biotite and muscovite show no significant variation in Si and thus $Al^{IV}$ content, which is defined as the difference between 8.0 and the number of Si atoms. All of our micas are saturated with respect to Ti because of their coexistence with either ilmenite or rutile. In the case of Al, micas from high-T samples, except for sample 88-58, are saturated in Al because of the presence of kyanite in the matrix (Tables 4.5-4.6). However, there are no Al-saturating phases in the low-T samples. $Fe^{3+}/Fe^{2+}$ ratios in biotite and muscovite were not determined, precluding full evaluation of the variation of trace element distributions involving iron.

### 4.4.1 Biotite

The majority of the VI-fold sites are filled by Mg (2.04-3.01 atoms per formula unit, p.f.u.) and $Fe^{TOT}$ (1.77-2.80 atoms p.f.u.) (Table 4.5). $X_{Mg}$ of biotite, ranging from 0.42 to 0.64, reflects variation both in the bulk composition and T. Octahedral Al in biotite, defined as the difference between $Al^{TOT}$ and $^{IV}Al$, is between 0.63 and 0.83 atoms p.f.u. Most of the $Al^{IV}$ is balanced by $Al^{VI}$, suggesting operation of the Al-Tschermaks substitution, $(Fe, Mg)SiAl^{VI}_{-1}Al^{IV}_{-1}$. Biotite coexisting with kyanite is relatively enriched in $Al^{TOT}$ (3.18-3.28) compared to low-T biotite (3.09-3.17), presumably due to Al saturation in the former samples (Table 4.5). Ti contents in biotite range from 0.13 to 0.24 atoms p.f.u. with no clear correlation with the contents of Fe and Mg and metamorphic grade (Table 4.5). Concentrations of Mn are typically low, but vary widely

(31-1,541 ppm). In all of the biotites studied, the sum of the octahedral cations is below the theoretical value of six atoms p.f.u., but is always above 5.61, implying no significant amount of $Fe^{3+}$ in the biotites.

Theoretically, two atoms p.f.u. are allocated to the XII-interlayer site in biotite. The XII- site in the analyzed biotites is dominated by K (1.46-1.89 atoms p.f.u.) with small amounts of Na (0.10-0.15 atoms p.f.u.) and Ca (< 0.01 atoms p.f.u.) (Table 4.5). The amount of interlayer site vacancy, ranging from 0.02 to 0.41 atoms p.f.u., is surprising given the almost complete analyses. Concentrations of F in biotite range between 0.10 and 0.28 atoms p.f.u. Cl contents are uniformly low (< 0.04 atoms p.f.u.).

### 4.4.2 Muscovite

$Al^{VI}$ of muscovite varies from 3.46 to 3.61 atoms p.f.u. with the lowest value from the high grade sample 88-58. Al comprises 88% of the ions on average in the octahedral sites, the remainder being mostly Mg (0.21-0.28 atoms p.f.u.) and $Fe^{TOT}$ (0.14-0.28 atoms p.f.u.). The muscovite compositions deviate slightly from the ideal Al-Tschermak substitution when defined in terms of Si and $Al^{TOT}$. However, the linear distribution of analyses parallel to the Al-Tschermak substitution (not shown) indicates no significant variations in $Fe^{3+}$ contents among the analyzed muscovites. With the exception of sample 88-58 (which does not contain kyanite), the content of $Al^{TOT}$ of muscovite from high-T samples is similar to that of low-T samples, indicating pseudo-saturation of Al in low-T samples. The Ti contents of muscovite range from 0.04 to 0.09 cations p.f.u., and correlate positively with the Mg content. The Mn content of all muscovites studied is

extremely low (1.3-76.7 ppm) and appears to decrease with metamorphic grade. The total octahedral occupancy of analyzed muscovites (ideally 4.00 atoms p.f.u.) varies from 4.02 to 4.11 atoms p.f.u., indicating slight deviation from dioctahedral micas in all analyses.

The XII interlayer site in white mica is filled predominantly by K (1.48-1.82 atoms p.f.u.) and by lesser amounts of Na (0.17-0.35 atoms p.f.u.). The Ca content determined by LAM-ICP-MS is negligible (mostly below detection limits, occasionally up to 0.02 atoms p.f.u.). The total occupancy of the interlayer site ranges from 1.80 to 2.02 and is not related to metamorphic grade. Deficiencies in the XII-sites in muscovite, even when trace elements are included in the analyses, may be partially explained by the $H_3OK_{-1}$ and $NH_4K_{-1}$ substitutions and by vacancies in XII-sites due to charge balance constraints caused by other substitutions in IV, VI and XII-sites (Guidotti and Sassi, 1998a, b). The analyzed muscovites have less than 0.06 atoms of F p.f.u. with a strong positive dependence on Mg content. Most Cl concentrations are below detection limits.

## 4.5 Thermodynamics of trace element distribution

The partitioning behaviour of trace elements can be considered in terms of exchange reactions involving major element cations for which the thermodynamic basis is well established (*e.g.*, Kretz, 1961). For example, partitioning of the trace element Cs and the major element K between coexisting biotite and muscovite may be expressed by the exchange reaction:

$$\underset{Cs\text{-}Bt}{Cs_2^{XII}Mg_6^{VI}Al_2^{IV}Si_6^{IV}O_{20}(OH)_4} + \underset{K\text{-}Ms}{K_2^{XII}Al_4^{VI}Al_2^{IV}Si_6^{IV}O_{20}(OH)_4} = \underset{K-Bt}{K_2^{XII}Mg_6^{VI}Al_2^{IV}Si_6^{IV}O_{20}(OH)_4} + \underset{Cs-Ms}{Cs_2^{XII}Al_4^{VI}Al_2^{IV}Si_6^{IV}O_{20}(OH)_4} \quad (4.1)$$

At equilibrium,

$$\mu_{Cs-Bt} + \mu_{K-Ms} = \mu_{K-Bt} + \mu_{Cs-Ms} \quad (4.2)$$

where $\mu_{Cs\text{-}Bt}$ is the chemical potential of endmember *Cs-Bt*, which is related to the concentration by

$$\mu_{Cs\text{-}Bt} = G_{Cs\text{-}Bt} + RTlnX_{Cs\text{-}Bt}\gamma_{Cs\text{-}Bt} \quad (4.3)$$

Here $G_{Cs\text{-}Ba}$ is the molar Gibbs energy of pure endmember *Cs-Bt*, *R* is the gas constant, $\gamma_{Cs\text{-}Bt}$ is an activity coefficient, and $X_{Cs\text{-}Bt}$ is the mole fraction, Cs/(Cs+K) in biotite. By introducing three additional equations analogous to Eq. (4.3) and substituting them into Eq. (4.2), we obtain

$$K_D^{Cs-K} = \left[\frac{X_{Cs}}{X_K}\right]^{Bt} \Big/ \left[\frac{X_{Cs}}{X_K}\right]^{Ms} = \left[\frac{\gamma_K}{\gamma_{Cs}}\right]^{Bt}\left[\frac{\gamma_{Cs}}{\gamma_K}\right]^{Ms}\left\{\exp\left(\frac{-\Delta G^\circ}{RT}\right)\right\} \quad (4.4)$$

where $K_D^{Cs-K}$ is the distribution coefficient for Cs in K-biotite/K-muscovite, and $\Delta G^\circ$ is the Gibbs energy difference in reaction (4.1) with all components pure. In dilute solutions, the activity coefficients are expected to remain constant following Henry's Law. Therefore, the concentration ratio will also remain constant by the Gibbs-Duhem equation. $\Delta G^\circ$ is thus mainly dependent on variations in *T*. The effects of *P* are predicted to be small owing to very small changes in the volume of reaction as a result of the exchange reactions. Because $X_{K\text{-}Bt}$ and $X_{K\text{-}Ms}$ are very nearly 1.0, the distribution

coefficient on the left may be written $X_{Cs\text{-}Bt}/X_{Cs\text{-}Ms}$. Hence, for a very low concentration of Cs, we would expect a linear relation between $X_{Cs\text{-}Bt}$ and $X_{Cs\text{-}Ms}$ at constant temperature.

## 4.6 The distribution of trace elements

The abundance ranges and partitioning behaviour of the trace elements among the 22 biotite-muscovite pairs are presented in Figs. 4.2a-u. Also included for comparison in these plots are data from Dahl *et al.* (1993) who reported ICP solution analyses of separates from 49 coexisting biotite-muscovite pairs from the staurolite and sillimanite zones in the Black Hills of South Dakota. The partition coefficients are presented here both as ppm concentration ratios

$$D_i = \frac{ppm\ Bt}{ppm\ Ms} \tag{4.5}$$

equivalent to Nernst distribution coefficients, and as atomic or molar partition coefficients

$$D_i^* = \frac{X_i^{Bt}}{X_i^{Ms}} \tag{4.6}$$

following the terminology of Beattie *et al.* (1993). In these relationships, *i* refers to a specific element and $X_i$ is the mole fraction of component *i* in biotite or muscovite, calculated on the basis of two interlayer sites, eight tetrahedral sites, and either six or four octahedral sites for biotite and muscovite, respectively. $D_i^*$ values between coexisting biotite and muscovite determined in this study are listed in Table 4.7, with their

corresponding standard deviations (1σ). Metamorphic *P-T* were estimated using garnet-plagioclase-biotite-muscovite and garnet-kyanite-quartz-plagioclase geobarometers of Hodges and Crowley (1985) and garnet-biotite geothermometry of Holdaway *et al.* (1997) (Table 4.7). Garnet-biotite geothermometers incorporating significant corrections for calcium in garnet, such as those of Hoinkes (1986), Williams and Grambling (1990) and the TWQ program, version 2.02 (Berman, 1991) invariably yield unreasonably high temperatures for low-T samples which contain garnet enriched in calcium (~0.2 mole fraction) compared to high-T garnets (< 0.1 mole fraction). There is a temperature gap between low- and high-T samples, which may correspond to the missing staurolite-biotite zone noted above. As discussed above, distribution coefficients of Ni, Cu, Y, Zr, La, Ce and Hf involve relatively high analytical errors because of their concentrations in either biotite or muscovite or both approach detection limits. The distribution coefficients for these elements, therefore, should be considered as only rough estimates.

### 4.6.1 Trace element distribution

For the trace elements, it is evident from Fig. 4.2 that: (1) Li, Mn, Co, Ni, Cu, Zn, Rb, Nb, Cs, La, Ce and Ta prefer biotite over muscovite regardless of metamorphic grade; (2) at low-T, Cr and Y partition coefficients are nearly equal between the micas; and (3) Sc, V, Cr (high-T), Sr, Zr, Ba and Hf favour muscovite. The distributions of Li, Sc, V, Cr, Nb and Ba show systematic differences between low- and high-T micas (Figs. 4.2a, b, d, e, o, q). The factors governing these differences are discussed in a later section. The decreasing concentrations of Sc, Mn and Y in micas with metamorphic grade (Figs.

4.2b, f, m) indicate that the matrix is progressively depleted in these elements, probably because of the increasing modal abundance of garnet, which is known to strongly sequester them. The distribution of Ti between biotite and muscovite is strongly controlled by $X_{Mg}$ of muscovite (not shown).

As indicated by the thermodynamic considerations above, the systematic linear distributions of most trace elements at similar metamorphic grade, together with the measured distributions intersecting at the origin (Fig. 4.2), suggest a close approach to chemical equilibrium between coexisting biotite and muscovite across the range of bulk-rock composition and metamorphic grade. In addition, there is no evidence that any of the trace elements departs from Henry's Law behaviour.

However, it is noteworthy that biotite and muscovite from sample 87-279 show variations in Sc ranging from 14 to 22 and from 55 to 74 ppm, respectively, but with similar distribution coefficients (Fig. 4.2b). Analytical errors can be ruled out, because they are especially low for Sc due to its abundance well above the detection limits in both biotite and muscovite, and the absence of spectral interferences. The variability in Sc concentrations at the thin-section scale may be attributed to mosaic equilibrium (initially defined by Zen, 1963), which is caused by limited diffusion ranges of the element under the metamorphic conditions. Kretz *et al.* (1999) also reported evidence for different domains of equilibrium for specific trace elements, which they attributed to variations in the magnitudes of deformation and recrystallization, together with different diffusion rates.

### 4.6.2 Contamination

Most trace elements in the micas show similar abundance ranges when compared to the data of Dahl *et al.* (1993), but Zr, La and Ce are much lower in our analyses (Fig. 4.2n, r, s). This result is clearly due to contamination from zircons and monazite in their samples, which are difficult to remove from mineral separates. Moreover, consistently lower contents of Mn and Co in muscovite and higher Ca and Sr contents in biotite from our data (Figs. 4.2f, g, l; Table 4.3) indicate that there may have been other important sources of contamination in Dahl *et al.*'s data. High Mn and Co in muscovite analyses of Dahl *et al.* (1993) may be attributed to contamination by ilmenite, despite their efforts to remove it using a high strength magnetic field. They reported that Sr data of their muscovite were contaminated by oligoclase and applied corrections using Sr contents in oligoclase. However, significantly higher Sr contents in biotite, together with high Ca contents in the biotites of Dahl *et al.* (1993), indicate that their biotite analyses were also probably contaminated by oligoclase (Fig. 4.2l). Bea *et al.* (1993) reported a similar difference between LAM-ICP-MS and mineral separate analyses for biotite. Their solution ICP-MS analyses for REE, Th, U, Y, Sr, Zr, Cu and Zn were consistently higher, by almost two orders of magnitude, than results from analyzing the same crystals in thin section with a LAM-ICP-MS.

### 4.6.3 Comparison

The measured distribution coefficients from this study are compared with other data from pelitic rocks, most of which represent amphibolite facies conditions, except for

those of Butler (1967) which are for greenschist facies conditions (Table 4.8). In Table 4.8, the data of Dahl *et al.* (1993) and Butler (1967) are averages of their staurolite- and sillimanite-zones samples, and samples with no epidote, respectively. Overall, the trace element distributions and relative enrichment patterns are consistent with published analyses of coexisting biotite and muscovite (*e.g.*, Butler, 1967; Moorbath *et al.*, 1968; Dutrow *et al.*, 1986; Hervig and Peacock, 1989; Dahl *et al.*, 1993; Domanik *et al.*, 1993). However, there are important differences between this and previous studies.

The average $D_{Li}$, $D_V$ and $D_{Ba}$ values of high-T samples show good agreement with those of Dahl *et al.* (1993) (Table 4.8). The average $D_{Li}$ value of high-T samples also shows excellent agreement with that of Dutrow *et al.* (1986). The measured $D_{Ba}$ value from high-T samples is similar to values reported for epidote-bearing blueschists from the Franciscan Complex by Domanik *et al.* (1993) within permitted errors, implying no significant pressure or bulk composition dependence on Ba distribution (Table 4.8). However, the $D_{Ba}$ value of Butler (1967), which was obtained from an upper greenschist facies pelite, is higher than that of our low-T samples (Table 4.8). Distribution coefficients of Li, V and Ba between biotite and muscovite increase with metamorphic grade (Table 4.8).

For Sc and Cr, the distribution coefficients of Dahl *et al.* (1993), which are from a metamorphic grade equivalent to our high-T samples, are close to our low-T samples (Table 4.8). A close examination of the plots for Sc and Cr from Dahl *et al.* (1993) reveals that their staurolite-zone data are close to our high-T data, but their sillimanite zone data overlap with the low-T data from this study (Fig. 4.2b, e). In addition, on the

basis of the observed trend for V partitioning between biotite and muscovite in this study, the partitioning of Sc and Cr are expected to increase with *T*. However, the opposite trends in the data of Dahl *et al.* (1993) may indicate that their Sc and Cr compositions from the sillimanite-zone micas were re-equilibrated at lower temperatures, or that their data were influenced by an increasing amount of secondary (retrograde) micas in the sillimanite-zone.

Our distribution coefficients for Ca, Co and Sr differ significantly from those Dahl *et al.* (1993), probably because of contamination in either biotite or muscovite in their analyses as mentioned above. In support of this assertion, $D_{Sr}$ of Domanik *et al.* (1993), which was determined by the SIMS technique, shows a good agreement with our high-T results (Table 4.8). On the other hand, $D_{Sr}$ values determined by a bulk mineral analysis method such as employed by Dahl *et al.* (1993) and Moorbath *et al.* (1968) are 10 times higher.

Partitioning of Rb between biotite and muscovite is within the range of values reported in the literature and shows little variation through the entire range of bulk composition and metamorphic grade. Mn, Ni, Cu and Zn data from Dahl *et al.* (1993) plot on or very close to our trends (Fig. 4.2). For the distribution of Nb, Hf, Ta and Cs between coexisting micas, no published data from pelitic micas are available for comparison.

The comparison of data given above enables us to conclude that our partition coefficients are more reliable than the results from several previous studies which were obtained by means of bulk analysis of mineral separates. Assuming an equilibrium

distribution of trace elements, as is suggested by our data, we now discuss the distribution behaviour of trace elements in terms of various structural, compositional or thermal controls on element partitioning.

## 4.7 Factors influencing the distribution coefficients

### 4.7.1 Crystal structural effects

Crystal-melt partitioning behaviour of trace elements for various minerals has been modeled in terms of the lattice strain associated with placing a cation on a particular crystallographic site when the radius of the cation differs from the optimal radius for that site (*e.g.*, Onuma *et al.,* 1968; Möller, 1988; Blundy and Wood, 1991, 1994; Beattie, 1994; Brenan *et al.,* 1995). Trace element partitioning in mica-melt and mica-fluid systems also shows that the incorporation of a trace element into the crystal lattice is controlled by the size mismatch between the trace and host cations in the mica structures (Jensen, 1973; Matsui *et al.*, 1977; Iiyama, 1979; Volfinger and Robert, 1980; LaTourrette *et al.*, 1995). Using the phlogopite-fluid and muscovite-fluid partition coefficients experimentally measured by Volfinger (1976) at 500 and 600 °C at a constant pressure of 1 kbar, we test the model in order to develop analogous relations that describe biotite/muscovite partition coefficients in terms of the ionic radius of the substituting trace elements.

We assume, for example for reaction (4.1), that $\Delta G_{exchange}$ can be approximated by the energy required to remove a $Cs^+$ ion from the biotite and insert it into the crystal

lattice of muscovite while simultaneously transferring a $K^+$ ion from muscovite to biotite. The structural work required to incorporate a $Cs^+$ into the muscovite is the sum of $\Delta G_{strain}$, the lattice strain due to size mismatch between the radius of $Cs^+$ and the optimum radius ($r_o$) of the XII-site in muscovite, and $\Delta G_{relaxation}$, the energy liberated when a $Cs^+$ ion is removed from the lattice site in biotite, assuming major element substitution contributes a negligible amount of $\Delta G_{strain}$ and $\Delta G_{relaxation}$ because of its similarity in ionic radius to the optimum size of the crystallographic site.

Following the method of Blundy and Wood (1994), we have fitted the partitioning data of Volfinger (1976) by non-linear least-squares regression to the relation:

$$D(P,T,X) = D_o(P,T,X)\exp\left[\frac{-4\pi E N_A}{RT}\left\{\frac{r_o}{2}(r_i - r_o)^2 + \frac{1}{3}(r_i - r_o)^3\right\}\right] \qquad (4.7)$$

which relates the partition coefficient, $D(P,T,X)$, for a given cation of ionic radius $r_i$, at a particular condition of P, T and bulk composition, to the partition coefficient, $D_o(P,T,X)$, for a cation whose radius equals the optimal site radius, $r_o$. In this relation, $E$ is the value of Young's modulus for the site, $N_A$ is Avogadro's number, $R$ is the gas constant and $T$ is in Kelvins. The data and associated fits using Eq. (4.7) are shown in Fig. 4.3 in which the slope of the parabola is a function of $E$. Partition coefficients for elements substituting into XII-sites in biotite and muscovite decrease as the cation size misfit increases, consistent with incorporation of the trace element becoming less favourable with increasing lattice strain. Variations in $D_i^{Ms-fluid}$ with $T$ are greater for Na and Cs than for Rb (Fig. 4.3a), consistent with the ionic radius of Rb being close to the ideal radius for the site (Fig. 4.3b). For $D_i^{Bt-fluid}$, in contrast, the pattern is different, with Cs partitioning

showing the least effect of $T$. This is not in accord with expections, since the ionic radius of Rb is close to the ideal radius for the site, suggesting that it should show the least variation with $T$. Although we are unable to unambiguously explain this result, we suspect that it may be due to poor quality analytical data for Cs for the biotite experiments.

It is noteworthy that the derived peak value for $r_o$ for 1+ cations in biotite is slightly larger than that for muscovite. In biotite, the peak $r_o$ coincides with the radius of $Rb^+$ ion. In contrast, in muscovite the peak closely corresponds to the radius of the $K^+$ ion. This difference in optimum ionic radius of XII-sites between biotite and muscovite is compatible with the fact that ideal trioctahedral biotite has a completely filled octahedral sheet (filled by the relatively large $Fe^{2+}$ and $Mg^{2+}$ cations), whereas ideal muscovite has smaller and fewer octahedral sites as a result of the tetrahedral rotation necessary to accommodate the size mismatch between the IV- and VI-sheets (Guidotti and Sassi, 1998b). The decreasing slopes of the curve for +1 cations in XII-sites of muscovite, as the temperature increases from 500 to 600 °C, may indicate variations in thermal expansivity with $T$ (Fig. 4.3). If this is true, we would expect more significant thermal effects for elements away from the optimum ionic radius. The slopes of parabolas for XII-sites in biotite do not appear to change with $T$.

On the basis of biotite-fluid and muscovite-fluid partitioning, the distributions of trace elements between coexisting biotite and muscovite would be expected to vary systematically with ionic radius, if lattice strain were a major controlling factor. Fig. 4.4a shows the curve for $D_i^{Bt\text{-}Ms}$, derived by dividing the values for $D_i^{Bt\text{-}fluid}$ by those for $D_i^{Ms\text{-}}$

$^{fluid}$ in Fig. 4.3, together with our data. Overall, our partitioning data for Na, K, Rb and Cs fit the modeled biotite-muscovite partitioning curves very well, demonstrating controls of ionic radius on solid-solid partitioning. It is evident from Fig. 4.4a that cations $Ba^{2+}$ (1.61 Å), $Sr^{2+}$ (1.44 Å) and $Na^{+}$ (1.39 Å) favour muscovite with its smaller interlayer site, whereas $K^{+}$ (1.64 Å) is equally partitioned between biotite and muscovite. In contrast, $Rb^{+}$ (1.72 Å) and $Cs^{+}$ (1.88 Å) which are larger than $K^{+}$, favour the more open structure of biotite. In octahedral sites, distribution coefficients exhibit the sequence $Cr^{3+}$ (0.615 Å) > $V^{3+}$ (0.64 Å) > $Sc^{3+}$ (0.745 Å) for 3+ cations, implying that biotite has the smaller optimum ionic radius for 3+ cations in octahedral sites (Fig. 4.4b). This is consistent with the smaller mean octahedral metal-oxygen bond length of the M1-M2 site of 1M biotite (2.093 ± 0.027 Å) compared to the M2 site of 2M1 muscovite (2.236 ± 0.021 Å) (Bailey, 1984). We can also infer that octahedral $Fe^{3+}$ is probably slightly favoured in muscovite over biotite on the basis of the ionic radius argument (Fig. 4.4). For the distribution of divalent transition elements in the VI-sites, it is difficult to evaluate the effects of ionic radius or crystal-field stabilization energy because of the high analytical errors involved in the determination of distribution coefficients for Ni, Cu and Zn.

### 4.7.2 Compositional effects

$Li^{+}$ contents of biotite correlate positively with $\Sigma(Al^{IV}+Al^{VI})$ contents of biotite (Fig. 4.5a). There is a similar, but less evident, relationship between $Li^{+}$ and $\Sigma(Al^{IV}+Al^{VI})$ of muscovite (Fig. 4.5g). The Li contents of biotite and muscovite also show weak negative correlations with $\Sigma(Fe^{TOT}+Mg)$ contents (not shown), indicating that the main atomic

substitution in the micas is $Li_3Al_{-1}\square_{-2}$ in octahedral sites with $Li_2(Fe, Mg)_{-1}9_{-1}$ being subordinate. The incorporation of Cr, V, and Sc into biotite is controlled by the content of $Al^{TOT}$, with the slope and its sign depending on ionic radius (Fig. 4.5b, c, d). Cr shows a stronger positive correlation with $Al^{TOT}$ of biotite, than V. On the other hand, Sc shows a negative correlation with $Al^{TOT}$, indicating that the presence of Al does not promote the incorporation of Sc into the biotite structure. Such correlations, however, are not observed in coexisting muscovite, because of the relatively small variations of $Al^{TOT}$. The concentrations of $Rb^+$ and $Cs^+$ in biotite show negative correlations with $K^+$, suggesting that the incorporation of the smaller $K^+$ cations reduces the optimum ionic radius of the interlayer sites (Figs. 4.5e, f). A positive correlation between the Co content and $\Sigma(Fe^{TOT}+Mg)$ in muscovite (Fig. 4.5h) indicates that Co incorporation is facilitated by higher contents of the larger $Fe^{2+}$ and $Mg^{2+}$ cations replacing $Al^{VI}$. Increased amounts of phengite components in muscovite are expected to produce a larger XII-site, due to a smaller tetrahedral rotation angle ($\alpha$) being required for articulation of the IV- and VI-sheets (Harlow, 1995; Guidotti and Sassi, 1998b). Indeed, Volfinger (1974) found that Mg in VI-sites correlated positively with the replacement of $K^+$ by $Rb^+$ and $Cs^+$. However, Rb, Sr, and Cs contents of our muscovites show negative correlations with $\Sigma(Fe^{TOT}+Mg)$, which more likely controls the substitution of these elements rather than $Mg^{2+}$ alone. Thus, the relationships between $\Sigma$ $(Fe^{TOT}+Mg)$ and the contents of Rb, Sr, and Cs in muscovite cannot be attributed to the expansion of interlayer sites by the phengite substitution in muscovite. Instead, it may reflect pressure dependence, because $\Sigma(Fe^{TOT}+Mg)$ in muscovite increases strongly as a function of pressure (Guidotti and

Sassi, 1998b). Substitution of $Sr^{2+}$ and $Ba^{2+}$ into XII-sites of micas must involve a coupled substitution or vacancies to maintain charge balance, but our data do not allow us to identify the mechanism.

Compositional effects on trace element partitioning are evident if solid solution is not ideal and there are interactions between the constituent molecules, so that the excess chemical potentials of these molecules contribute to the equilibrium constant in Eq. (4.4). In examining compositional dependence, molar proportions, rather than weight proportions, are used. In general, biotite favours divalent transition elements in VI-sites due to the higher abundance of appropriately sized sites compared to coexisting muscovite (Dahl *et al.*, 1993). Based on the same argument, strong affinities of $V^{3+}$ and $Sc^{3+}$ for muscovite can be explained by appropriate sites for these elements in muscovite.

$D_{Li}^{*}$ and $D_{Sc}^{*}$ show negative dependence on $Al^{VI}$ contents of biotite with two different trends depending on metamorphic grade (Figs. 4.6a, b). The possibility of an effect due to the difference in Al-saturation level between the two groups can be ruled out because sample 88-58, which is the only Al-undersaturated sample from high-*T* group, shows the same trend as other high-*T* samples with respect to the distribution of Li and Sc. The reason for the high distribution coefficient of Li in sample 88-32, which belongs to low-*T* group, is not known. Fig. 4.6c shows that the distribution of Rb between biotite and muscovite is governed by the $\Sigma(Fe^{TOT}+Mg^{2+})$ content of muscovite. Sr and Ba distributions between biotite and muscovite are strongly controlled both by metamorphic grade and the K contents of biotite (Fig. 4.6d, e). Fig. 4.6 also shows that the distributions of Li, Sc, Sr and Ba are dependent both on major element composition and metamorphic

temperature, making the separation of the two competing factors difficult.

### 4.7.3 Temperature effects

The equilibrium constant $K_D$ in Eq. (4.4) should vary with T according to the relation

$$LnK_{D} = -\frac{\Delta H^{\circ}}{RT} + \frac{\Delta S^{\circ}}{R} \tag{4.8}$$

if the constant $K_D$ is solely determined by $\Delta G^{\circ}_{exchange}$ of a reaction such as (4.1). To evaluate thermal effects, $D_i^*$ values for Li, Sc, V, Sr, Ba and Zr are plotted against metamorphic temperature estimated using the garnet-biotite geothermometer (Fig. 4.7a-f). Positive correlations between $D_i^*$ and $T$ are seen for Li, Sc, V, Sr and Ba, whereas a negative correlation exists for Zr. $D_i^*$ values for Sc, V, Sr, Cs and Ba have a tendency toward equal partitioning as temperature increases (Fig. 4.7), as predicted from fundamental thermodynamic considerations. However, all of these trace element partitionings except for V are also controlled by major element compositions. Recall that V concentrations in biotite show the least major element compositional effects among the 3+ cations in VI-sites (Fig. 4.5c).

Despite the occurrence of $Zr^{4+}$ in biotite and muscovite at trace levels, the chemical potential of Zr is buffered by phase relations with zircon in the rocks. Thus, at equilibrium, partitioning of Zr may reveal changes in P-T. Zr is preferentially incorporated into muscovite over the temperature range of the studied samples (450 to 650 °C), resulting in a four-fold decrease in the distribution coefficients (Fig. 4.7f). Major element compositions are not correlated with the distribution of Zr between biotite and

muscovite.

The ratio of $D_{Cs}^{*}/D_{Rb}^{*}$ shows good correlation with metamorphic temperature (Fig. 4.7g). This may be explained by the relationship between the elasticity of interlayer sites and temperature, as shown in Figs. 4.3 and 4.4. In this scenario, the distribution line for 1+ cations in XII-sites would rotate clockwise around an axis of at $K^{+}$ as the temperature increases, to approach equal partitioning, resulting in the decrease of $D_{Cs}^{*}/D_{Rb}^{*}$ ratios. Elements whose ionic radii are close to the optimum ionic radii for specific sites in the micas do not show significant variation in distribution coefficients with temperature. In addition, as mentioned earlier, $D_i^{*}$ ratios are also controlled by the phengite contents of muscovite which are correlated with pressure.

Among the trace elements showing thermal dependence, distributions of V and Zr show significant thermal effects with no major element compositional effects. However, for the distribution of Li, Sc, Sr and Ba between biotite and muscovite, it is difficult to separate thermal dependence from major element compositional and structural effects, because $X_{Mg}$ ratios of both biotite and muscovite are dependent on metamorphic temperature, which in turn affects the structure of interlayer sites of micas.

## 4.8 Conclusions

The systematic distribution of trace elements in coexisting biotite and muscovite indicates that equilibrium was achieved between these minerals in the analyzed metamorphic rocks. Distribution behaviour between biotite and muscovite for many

elements is compatible with lattice strain theory, especially in interlayer sites of micas. Unfortunately, none of the trace elements investigated promises simply applicable alternative geothermometers for the metamorphic environment. The thermal dependences derived here for Li, Sc, Sr and Ba partitioning between biotite and muscovite are not strong enough, and it was not possible to separate them from major element compositional and structural effects. However, the trace element partitioning data for V and Zr may be used to cross-check conventional geothermometers for samples from a similar range of P-T and bulk composition, especially when conventional geothermometers suffer from retrograde resetting and/or high $Fe^{3+}$ contents. The ranges and dependences of distribution coefficients on major element compositions established here, for quartzofeldspathic and metapelitic rocks from upper greenschist to upper amphibolite facies, also provide important constraints on the values that can be used in modeling trace element zoning of garnet, because biotite and muscovite participate in many prograde metamorphic reactions.

Table 4.1. Mineral assemblages and modal percentages of the ten metapelitic samples from western Labrador.

| Sample | Zones | Qtz | Ms | Bt | Chl | Ep | Pl | Ky | Grt | Tur | Ap | Rt | Zrn | Ilm | Py | Mo | Gr |
|---|---|---|---|---|---|---|---|---|---|---|---|---|---|---|---|---|---|
| 87-81 | 3 | 41 | 28 | 26 | | | <1 | | <1 | <1 | <1 | <1 | <1 | <1 | <1 | | |
| 87-83 | 3 | 53 | 11 | 28 | <1 | <1* | <1 | | 4 | <1 | <1 | | <1 | <1 | | | <1 |
| 87-86 | 3 | 40 | 11 | 43 | <1 | <1* | <1 | | <1 | <1 | <1 | | <1 | <1 | | | <1 |
| 87-279 | 3 | 48 | 16 | 23 | 4# | <1 | <1 | | 3 | | <1 | <1 | <1 | <1 | <1 | | <1 |
| 88-32 | 3 | 30 | 19 | 35 | <1 | <1* | <1 | | 10 | <1 | <1 | | <1 | <1 | | | |
| 88-48 | 4 | 26 | 10 | 44 | 4# | | <1 | 2 | 10 | <1 | | <1 | <1 | <1* | <1 | | |
| 88-45 | 5 | 44 | 27 | 11 | | | <1 | <1 | 11 | | | <1 | <1 | | <1 | <1 | |
| 88-85 | 5 | 62 | 29 | 6 | | | <1 | 2 | <1 | | <1 | <1 | <1 | <1 | <1 | <1* | |
| 88-74 | 6 | 34 | 26 | 23 | | | 5 | 9 | <1 | <1 | <1 | <1* | <1 | <1 | <1 | <1 | |
| 88-58 | 6 | 34 | 43 | 8 | | | | | 11 | | <1 | <1 | <1 | <1 | | <1 | |

* Minerals occur only as inclusions in garnet; # secondary minerals. Characteristic mineral assemblages of metamorphic zone are: zone 3; Grt-Bt, zone 4; St-Ky; zone 5; Bt-Ky-Grt and zone 6; Bt-Ky-Grt migmatite. Mineral abbreviations after Kretz (1983).

Table 4.2. Precision and mean values for a glass standard BCR-2 determined by LAM-ICP-MS.

| Elements | AVG | STD | RSD | DL | No | Known | AVG/known |
|---|---|---|---|---|---|---|---|
| Li | 8.4 | | | 5.955 | 1 | 9.98 | 0.84 |
| Sc | 31.4 | 0.8 | 2% | 0.653 | 5 | 32.6 | 0.96 |
| $TiO_2$ | 2.05 | 0.04 | 2% | 0.000 | 10 | 2.24 | 0.91 |
| V | 402 | 11 | 3% | 0.068 | 7 | 407 | 0.99 |
| Cr | 15.0 | 2.5 | 16% | 2.501 | 6 | 16 | 0.94 |
| MnO | 0.18 | 0.01 | 4% | 0.000 | 7 | 0.177 | 1.03 |
| Co | 36.4 | 1.7 | 5% | 0.325 | 7 | 37 | 0.98 |
| Ni | 11.3 | 1.4 | 12% | 1.041 | 7 | 13 | 0.87 |
| Cu | 20.5 | 1.0 | 5% | 0.356 | 5 | 19 | 1.08 |
| Zn | 173 | 12 | 7% | 0.581 | 5 | 129.5 | 1.33 |
| Rb | 54 | | | 0.018 | 2 | 47.51 | 1.14 |
| Sr | 337.2 | 7.6 | 2% | 0.006 | 5 | 337 | 1.00 |
| Y | 31.9 | 1.7 | 5% | 0.007 | 7 | 32.51 | 0.98 |
| Zr | 170.5 | 6.3 | 4% | 0.021 | 10 | 184.4 | 0.92 |
| Nb | 10.8 | 1.0 | 9% | 0.006 | 5 | 13.14 | 0.82 |
| Cs | 1.3 | | | 0.014 | 2 | 1.19 | 1.09 |
| Ba | 644 | 21 | 3% | 0.035 | 10 | 681 | 0.95 |
| La | 25.5 | 1.1 | 4% | 0.005 | 7 | 25.3 | 1.01 |
| Ce | 54.3 | 1.7 | 3% | 0.003 | 9 | 53.6 | 1.01 |
| Hf | 4.8 | 0.3 | 5% | 0.021 | 7 | 5.17 | 0.94 |
| Ta | 0.6 | 0.1 | 9% | 0.004 | 7 | 0.78 | 0.77 |

Based on 10 determinations over the period March 19, 1996 to April 5, 1997. AVG = average; STD = standard deviation; RSD = relative standard deviation; DL = detection limits; No = number of observations; and Known = literature values from Govindaraju (1994).

Table 4.3. Averages and standard deviations (1σ) of biotite analyses.

| | 87-81F | 87-81I | 87-81K | 87-83C | 87-83D | 87-86F | 88-32A | 88-32B | 87-279D | 87-279F | 87-279G |
|---|---|---|---|---|---|---|---|---|---|---|---|
| (wt. %) | | | | | | | | | | | |
| $SiO_2$ | 36.93(0.16) | 36.93(0.16) | 36.93(0.16) | 36.98(0.18) | 36.98(0.18) | 37.23(0.26) | 35.92(0.38) | 35.92(0.38) | 37.16(0.62) | 37.16(0.62) | 37.16(0.62) |
| $TiO_2$ | 1.56(0.05) | 1.56(0.05) | 1.56(0.05) | 1.57(0.02) | 1.57(0.02) | 1.62(0.07) | 1.54(0.08) | 1.54(0.08) | 1.65(0.06) | 1.65(0.06) | 1.65(0.06) |
| $Al_2O_3$ | 17.35(0.16) | 17.35(0.16) | 17.35(0.16) | 17.67(0.10) | 17.67(0.10) | 17.75(0.19) | 17.58(0.27) | 17.58(0.27) | 17.64(0.33) | 17.64(0.33) | 17.64(0.33) |
| $FeO^{\#}$ | 19.92(0.27) | 19.92(0.27) | 19.92(0.27) | 19.57(0.32) | 19.57(0.32) | 19.23(0.26) | 21.91(0.27) | 21.91(0.27) | 17.93(0.08) | 17.93(0.08) | 17.93(0.08) |
| MgO | 10.08(0.18) | 10.08(0.18) | 10.08(0.18) | 10.58(0.14) | 10.58(0.14) | 10.74(0.13) | 8.97(0.14) | 8.97(0.14) | 11.25(0.19) | 11.25(0.19) | 11.25(0.19) |
| $Na_2O$ | D.L. | D.L. | D.L. | 0.35 | 0.35 | D.L. | D.L. | D.L. | D.L. | D.L. | D.L. |
| $K_2O$ | 9.26(0.20) | 9.26(0.20) | 9.26(0.20) | 9.61(0.10) | 9.61(0.10) | 9.64(0.15) | 9.24(0.23) | 9.24(0.23) | 9.94(0.16) | 9.94(0.16) | 9.94(0.16) |
| F | 0.363(0.042) | 0.363(0.042) | 0.363(0.042) | 0.510(0.050) | 0.510(0.050) | 0.540(0.071) | 0.500(0.009) | 0.500(0.009) | 0.590(0.025) | 0.590(0.025) | 0.590(0.025) |
| Cl | 0.138(0.025) | 0.138(0.025) | 0.138(0.025) | 0.058(0.010) | 0.058(0.010) | 0.061(0.013) | 0.108(0.011) | 0.108(0.011) | 0.069(0.007) | 0.069(0.007) | 0.069(0.007) |
| Total | 95.43 | 95.43 | 95.43 | 96.68 | 96.68 | 96.56 | 95.53 | 95.53 | 95.97 | 95.97 | 95.97 |
| (ppm) | | | | | | | | | | | |
| Li | | 103 | 101(19) | 132(13) | 99(16) | 168 | 91(5) | | 125 | 123(12) | 127 |
| *Ca* | D.L. | 321 | 415(128) | D.L. | 275(98) | 323 | 244(48) | D.L. | D.L. | 272 | D.L. |
| Sc | 18.5 | 15.4 | 12.9(0.9) | 11.7(0.8) | 12.8(1.3) | 17.2 | 11.7(1.4) | 12.9 | 14.4 | 20.3(2.5) | 22.2(3.0) |
| V | 191 | 153 | 146(2) | 140(15) | 139(2) | 141 | 181(10) | 192 | 655 | 665(102) | 653(65) |
| Cr | 173 | 198 | 180 | 89 | 94(3) | 106 | 89(8) | 86 | 198 | 172(14) | 183 |
| Mn | 1541 | 1487 | 1325(48) | 974(123) | 957(20) | 948 | 530(30) | 539 | 1360 | 1050(162) | 986 |
| Co | 50 | 45 | 40(5) | 47(7) | 48(6) | 49 | 39(3) | 40 | 20 | 17(3) | 21(4) |
| Ni | 91 | 90 | 86(16) | 161(14) | 149(6) | 108 | 67(8) | 69 | 39 | 48(4) | 63(10) |
| Cu | 8.36 | 5.92 | 12.50 | 5.75(2.04) | 6.50(0.55) | D.L. | 4.51(0.49) | D.L. | D.L. | 5.64(0.28) | 5.50 |
| Zn* | 174 | 174 | 174 | 323 | 323 | 281 | 79 | 79 | 212 | 212 | 212 |
| Rb | | 396 | 448(15) | | 549(29) | 401 | 409(40) | | | 322(35) | 416(73) |
| Sr | 1.9 | 2.1 | 1.7(0.5) | 1.0(0.1) | 1.2(0.1) | 1.2 | 2.5(0.4) | D.L. | 2.0 | 1.5(0.1) | 1.9(0.4) |
| *Y** | 0.17 | 0.17 | 0.17 | 0.25 | 0.25 | 0.27 | 0.14 | 0.14 | 0.15 | 0.15 | 0.15 |
| *Zr** | 0.10 | 0.10 | 0.10 | D.L. | D.L. | D.L. | 0.08 | 0.08 | 0.10 | 0.10 | 0.10 |
| Nb | 47.8 | 53.6 | 55.9(1.6) | 38.3(2.7) | 58.5(3.1) | 45.8 | 39.1(2.2) | D.L. | 35.3 | 34.2(7.1) | 35.2 |
| Cs | | 18.8 | 19.7(0.4) | | 30.5(3.5) | 19.1 | 9.6(1.3) | | | 17.1(2.4) | 17.3 |
| Ba | 1193 | 1278 | 1282 | 1037(162) | 1190(42) | 873 | 1002(38) | 1275 | 1074 | 912(97) | 1118(265) |
| *La** | 0.2 | 0.2 | 0.2 | 0.4 | 0.4 | D.L. | 0.1 | 0.1 | 0.5 | 0.5 | 0.5 |
| *Ce** | 0.6 | 0.6 | 0.6 | 0.4 | 0.4 | D.L. | 0.2 | 0.2 | 1.0 | 1.0 | 1.0 |
| *Hf* | D.L. | 0.11 | D.L. | D.L. | D.L. | 0.07 | 0.06(0.03) | D.L. | D.L. | 0.05 | D.L. |
| Ta | D.L. | 3.766 | 3.839(0.079) | 3.063(0.400) | 4.004(0.026) | 2.935 | 0.946(0.048) | D.L. | 2.414 | 1.466(0.261) | 1.076 |

Notes Total Fe as FeO. For these elements the lowest value within a sample is reported because of fractionation during laser ablation (Zn) and contamination from micro-inclusions (Y, Zr and REE). D.L. and blank represent data below detection limits and elements not determined, respectively. Italicized elements are present in concentrations lower than 3 times detection limits in most analyses. Values in parentheses are standard deviations at 1σ level

Table 4.3. Continued.

| | 88-48C | 88-45D | 88-45E | 88-74C | 88-74D | 88-74E | 88-85C | 88-85D | 88-58A | 88-58B | 88-58C |
|---|---|---|---|---|---|---|---|---|---|---|---|
| (wt. %) | | | | | | | | | | | |
| $SiO_2$ | 37.81(0.37) | 37.58(0.56) | 37.58(0.56) | 37.08(0.09) | 37.08(0.09) | 37.08(0.09) | 37.40(0.31) | 37.40(0.31) | 36.38(0.31) | 36.38(0.31) | 36.38(0.31) |
| $TiO_2$ | 1.21(0.05) | 1.68(0.08) | 1.68(0.08) | 2.12(0.08) | 2.12(0.08) | 2.12(0.08) | 1.71(0.09) | 1.71(0.09) | 2.13(0.21) | 2.13(0.21) | 2.13(0.21) |
| $Al_2O_3$ | 19.09(0.18) | 18.58(0.33) | 18.58(0.33) | 18.34(0.15) | 18.34(0.15) | 18.34(0.15) | 18.92(0.33) | 18.92(0.33) | 18.01(0.08) | 18.01(0.08) | 18.01(0.08) |
| $FeO^{\#}$ | 14.57(0.34) | 16.27(0.30) | 16.27(0.30) | 17.27(0.12) | 17.27(0.12) | 17.27(0.12) | 16.40(0.48) | 16.40(0.48) | 20.87(0.67) | 20.87(0.67) | 20.87(0.67) |
| MgO | 13.89(0.25) | 12.01(0.46) | 12.01(0.46) | 11.83(0.15) | 11.83(0.15) | 11.83(0.15) | 12.49(0.25) | 12.49(0.25) | 9.54(0.36) | 9.54(0.36) | 9.54(0.36) |
| $Na_2O$ | 0.48(0.05) | 0.41 | 0.41 | 0.54(0.11) | 0.54(0.11) | 0.54(0.11) | 0.41(0.01) | 0.41(0.01) | 0.40 | 0.40 | 0.40 |
| $K_2O$ | 9.45(0.07) | 7.70(0.19) | 7.70(0.19) | 9.29(0.15) | 9.29(0.15) | 9.29(0.15) | 8.50(0.09) | 8.50(0.09) | 9.73(0.16) | 9.73(0.16) | 9.73(0.16) |
| F | 0.261(0.024) | 0.374(0.070) | 0.374(0.070) | 0.214(0.010) | 0.214(0.010) | 0.214(0.010) | 0.435(0.062) | 0.435(0.062) | 0.349(0.027) | 0.349(0.027) | 0.349(0.027) |
| Cl | 0.024(0.003) | D.L. | D.L. | D.L. | D.L. | D.L. | 0.010 | 0.010 | 0.032(0.013) | 0.032(0.013) | 0.032(0.013) |
| Total | 96.68 | 94.45 | 94.45 | 96.59 | 96.59 | 96.59 | 96.09 | 96.09 | 97.29 | 97.29 | 97.29 |
| (ppm) | | | | | | | | | | | |
| Li | | 315(25) | 305(21) | 198(70) | 222(1) | 206 | 346(15) | 313 | 186 | 193 | |
| *Ca* | D.L. | 293 | 301(93) | 233(38) | 218(25) | 254 | 234(43) | 243(95) | 295 | 209 | D.L. |
| Sc | 10.9(1.2) | 5.4(0.5) | 6.3(0.6) | 14.7(1.2) | 14.1(0.9) | 12.5 | 4.8(0.1) | 5.1(0.3) | 12.8 | 12.6(1.8) | 11.9(1.6) |
| V | 151(20) | 219(29) | 230(18) | 251(8) | 246(14) | 260(15) | 256(4) | 261(18) | 131 | 114(6) | 104(11) |
| Cr | D.L. | 379 | 343(4) | 338(37) | 328(42) | 296(49) | 345(29) | 366(42) | 174 | 194(21) | 172 |
| Mn | 31(3) | 34(2) | 39(4) | 227(22) | 229(18) | 216(8) | 42(2) | 44(5) | 156 | 160(20) | 164(30) |
| Co | 49(4) | 26(2) | 26(1) | 112(9) | 110(10) | 107(10) | 31(2) | 35(4) | 52 | 43(4) | 39(5) |
| Ni | 97(21) | 62(3) | 59(9) | 279(13) | 258(18) | 276(17) | 46(7) | 46(8) | 108 | 103(13) | 107(18) |
| Cu | 3.57(0.25) | 7.11(1.16) | 10.44(4.40) | 6.68(0.25) | 5.86(0.05) | 6.50 | 7.43(0.98) | 6.65 | 5.77 | 4.98(0.04) | 5.32(0.86) |
| Zn* | 77 | 570 | 570 | 251 | 251 | 251 | 408 | 408 | 475 | 475 | 475 |
| Rb | | 673 | 705 | 527(2) | 459(9) | 479 | 669(18) | 611 | 456 | 380 | |
| Sr | 2.0(0.2) | 2.4(0.2) | 1.9(0.2) | 1.9(0.3) | 2.5(0.3) | 1.8(0.3) | 4.7(0.3) | 5.4(0.5) | 4.8 | 5.4(1.1) | 3.8(0.4) |
| *Y** | D.L. | 0.08 | 0.08 | D.L. | D.L. | D.L. | 0.07 | 0.07 | 0.04 | 0.04 | 0.04 |
| *Zr** | 0.12 | 0.15 | 0.15 | 0.11 | 0.11 | 0.11 | 0.14 | 0.14 | 0.15 | 0.15 | 0.15 |
| Nb | 21.7(3.5) | 0.9(0.2) | 0.8 | 18.2(1.1) | 18.5(0.5) | 17.7(1.4) | 1.1(0.3) | 1.4(0.4) | 24.1 | 25.8 | D.L. |
| Cs | | 36.4 | 40.4 | 9.9(0.3) | 8.3(0.5) | 8.4 | 31.2(4.5) | 38.0(7.4) | 26.8 | 25.8 | |
| Ba | 409(27) | 810(25) | 680(38) | 576(57) | 605(59) | 615(37) | 1095(72) | 1203(208) | 396 | 401(14) | 366(42) |
| *La** | 0.6 | 0.1 | 0.1 | 0.0 | 0.0 | 0.0 | 0.1 | 0.1 | 0.2 | 0.2 | 0.2 |
| *Ce** | 1.0 | 0.3 | 0.3 | 0.0 | 0.0 | 0.0 | 0.2 | 0.2 | 0.2 | 0.2 | 0.2 |
| *Hf* | 0.02 | 0.05 | 0.02 | 0.01 | 0.01 | 0.02(0.01) | 0.08(0.01) | 0.08(0.02) | D.L. | D.L. | D.L. |
| Ta | 0.855(0.097) | 0.048(0.012) | 0.030(0.014) | 1.048(0.124) | 1.020(0.100) | 1.011(0.150) | 0.076(0.003) | 0.076(0.009) | 2.449 | 3.084 | D.L. |

Notes: # Total Fe as FeO. * For these elements the lowest value within a sample is reported because of fractionation during laser ablation (Zn) and contamination from micro-inclusions (Y, Zr and REE). D.L. and blank represent data below detection limits and elements not determined, respectively. Italicized elements are present in concentrations lower than 3 times detection limits in most analyses. Values in parentheses are standard deviations at 1σ level.

Table 4.4. Averages and standard deviations (1σ) of muscovite analyses.

| | 87-81F | 87-81I | 87-81K | 87-83C | 87-83D | 87-86F | 88-32A | 88-32B | 87-279D | 87-279F | 87-279G |
|---|---|---|---|---|---|---|---|---|---|---|---|
| (wt. %) | | | | | | | | | | | |
| $SiO_2$ | 47.02(0.40) | 47.02(0.40) | 47.02(0.40) | 46.47(0.07) | 46.47(0.07) | 47.17(0.32) | 46.83(0.18) | 46.83(0.18) | 46.92(0.19) | 46.92(0.19) | 46.92(0.19) |
| $TiO_2$ | 0.39(0.01) | 0.39(0.01) | 0.39(0.01) | 0.38(0.04) | 0.38(0.04) | 0.45(0.03) | 0.37(0.02) | 0.37(0.02) | 0.74(0.05) | 0.74(0.05) | 0.74(0.05) |
| $Al_2O_3$ | 34.44(0.30) | 34.44(0.30) | 34.44(0.30) | 34.14(1.04) | 34.14(1.04) | 33.85(0.43) | 33.87(0.72) | 33.87(0.72) | 33.53(0.26) | 33.53(0.26) | 33.53(0.26) |
| $FeO^{\#}$ | 1.76(0.09) | 1.76(0.09) | 1.76(0.09) | 1.67(0.32) | 1.67(0.32) | 1.79(0.17) | 2.10(0.17) | 2.10(0.17) | 1.59(0.09) | 1.59(0.09) | 1.59(0.09) |
| MgO | 1.09(0.15) | 1.09(0.15) | 1.09(0.15) | 1.14(0.27) | 1.14(0.27) | 1.26(0.07) | 1.16(0.06) | 1.16(0.06) | 1.29(0.05) | 1.29(0.05) | 1.29(0.05) |
| $Na_2O$ | 0.88(0.33) | 0.88(0.33) | 0.88(0.33) | 0.96(0.32) | 0.96(0.32) | 0.89(0.17) | 0.66(0.20) | 0.66(0.20) | 0.90(0.04) | 0.90(0.04) | 0.90(0.04) |
| $K_2O$ | 10.07(0.32) | 10.07(0.32) | 10.07(0.32) | 10.05(0.43) | 10.05(0.43) | 10.14(0.22) | 10.71(0.24) | 10.71(0.24) | 10.19(0.08) | 10.19(0.08) | 10.19(0.08) |
| | (0.003 | (0.003 | (0.003 | (0.046 | (0.046 | (0.021 | (0.009 | (0.009 | (0.029 | (0.029 | (0.029 |
| F | 0.090) | 0.090) | 0.090) | 0.145) | 0.145) | 0.126) | 0.113) | 0.113) | 0.112) | 0.112) | 0.112) |
| Cl | D.L. | D.L. | D.L. | D.L. | D.L. | 0.031 | D.L. | D.L. | D.L. | D.L. | D.L. |
| Total | 95.70 | 95.70 | 95.70 | 94.91 | 94.91 | 95.65 | 95.79 | 95.79 | 95.22 | 95.22 | 95.22 |
| (ppm) | | | | | | | | | | | |
| Li | | 66(7) | 71 | 54 | 54(2) | 91 | 17(1) | | | 52(14) | 56 |
| *Ca* | D.L. | 710 | D.L. | D.L. | D.L. | 775 | 716(132) | D.L. | D.L. | 1055(523) | 571 |
| Sc | 53.0(4.2) | 45.8(5.9) | 38.4(2.6) | 31.7 | 52.3(0.7) | 53.3 | 47.3(6.7) | 44.2(12.7) | 54.9 | 66.5(12.2) | 74.4(13.7) |
| V | 289(14) | 346 | 301(66) | 312 | 293(11) | 309 | 372(30) | 350(25) | 1364 | 1336(173) | 1259(283) |
| Cr | D.L. | D.L. | 155(4) | 143 | 145 | 67 | 103(19) | D.L. | D.L. | 240 | 179(32) |
| Mn | 51.4 | 76.7 | 41.0 | 41.1 | 58.1(20.4) | 48.4 | 30.6(8.9) | 28.7(4.3) | 75.5 | 62.9(1.5) | 67.8(19.9) |
| Co | 3.07 | 3.69(0.19) | 3.31 | D.L. | 4.67(0.29) | 3.54 | 2.26(0.03) | D.L. | D.L. | 1.51(0.68) | 1.93(0.85) |
| *Ni* | D.L. | 11.81 | | 11.29 | 13.93(0.63) | 8.03 | 3.68(0.16) | | | 5.80(3.50) | 5.02 |
| *Cu* | 3.39 | 3.47(2.13) | | D.L. | 2.49 | 1.21 | 1.33(0.29) | | | 4.36(3.10) | 3.43(4.56) |
| Zn* | 13 | 13 | 13 | 22 | 22 | 28 | 9 | 9 | 16 | 16 | 16 |
| Rb | | 239(32) | | | 290(1) | 244 | 232(17) | | | 204(40) | 185(38) |
| Sr | 127 | 149(5) | | 151 | 204(20) | 161 | 333(64) | D.L. | 178 | 138(14) | 131(19) |
| *Y** | 0.33 | 0.33 | 0.33 | 0.28 | 0.28 | 0.17 | 0.27 | 0.27 | 0.09 | 0.09 | 0.09 |
| *Zr** | 0.12 | 0.12 | 0.12 | 0.53 | 0.53 | 0.19 | 0.17 | 0.17 | 0.23 | 0.23 | 0.23 |
| Nb | 25.2(3.9) | D.L. | 27.2(1.4) | 26.2 | 40.5(1.6) | 28.0 | 25.4(1.9) | D.L. | | 22.4(18.6) | 19.4(20.7) |
| Cs | | 1.18(0.16) | 0.74(0.14) | | 2.10(0.17) | 1.41 | 0.83(0.02) | | | 1.53(0.47) | 1.69(0.30) |
| Ba | 5712(382) | 7201(250) | 5842 | 3900 | 6176(447) | 4935 | 4367(572) | 4747(364) | 4216 | 4014(512) | 3938(702) |
| *La** | D.L. | D.L. | D.L. | D.L. | D.L. | 0.028 | 0.057 | 0.057 | 0.042 | 0.042 | 0.042 |
| *Ce** | 0.184 | 0.184 | 0.184 | 0.323 | 0.323 | 0.014 | 0.054 | 0.054 | D.L. | D.L. | D.L. |
| | | | | | | | (0.082 | | | | (0.051 |
| *Hf* | 0.271 | D.L. | D.L. | D.L. | 0.178 | 0.162 | 0.216) | D.L. | 0.114 | 0.057 | 0.140) |
| Ta | 1.01(0.06) | 0.99 | 0.91(0.01) | 0.89 | 1.57(0.01) | 1.06 | 0.35(0.02) | D.L. | D.L. | 0.33(0.10) | 0.30(0.20) |

Notes: Total Fe as FeO. For these elements the lowest value within a sample is reported because of fractionation during laser ablation (Zn) and contamination from micro-inclusions (Y, Zr and REE). D.L. and blank represent data below detection limits and elements not determined, respectively. Italicized elements are present in concentrations lower than 3 times detection limits in most analyses. Values in parentheses are standard deviations at 1σ level.

Table 4.4. Continued.

| | 88-48C | 88-45D | 88-45E | 88-74C | 88-74D | 88-74E | 88-85C | 88-85D | 88-58A | 88-58B | 88-58C |
|---|---|---|---|---|---|---|---|---|---|---|---|
| (wt. %) | | | | | | | | | | | |
| $SiO_2$ | 46.56 (0.45) | 47.02 (0.46) | 47.02 (0.46) | 46.73 (0.10) | 46.73 (0.10) | 46.73 (0.10) | 47.04 (0.58) | 47.04 (0.58) | 47.30 (0.48) | 47.30 (0.48) | 47.30 (0.48) |
| $TiO_2$ | 0.38 (0.01) | 0.78 (0.03) | 0.78 (0.03) | 0.75 (0.04) | 0.75 (0.04) | 0.75 (0.04) | 0.92 (0.06) | 0.92 (0.06) | 0.91 (0.09) | 0.91 (0.09) | 0.91 (0.09) |
| $Al_2O_3$ | 34.68 (0.08) | 34.84 (0.21) | 34.84 (0.21) | 33.57 (0.37) | 33.57 (0.37) | 33.57 (0.37) | 33.87 (0.53) | 33.87 (0.53) | 33.06 (0.36) | 33.06 (0.36) | 33.06 (0.36) |
| $FeO^{\#}$ | 1.56 (0.02) | 1.24 (0.27) | 1.24 (0.27) | 2.53 (0.05) | 2.53 (0.05) | 2.53 (0.05) | 1.27 (0.13) | 1.27 (0.13) | 1.63 (0.31) | 1.63 (0.31) | 1.63 (0.31) |
| MgO | 1.16 (0.01) | 1.13 (0.03) | 1.13 (0.03) | 1.06 (0.15) | 1.06 (0.15) | 1.06 (0.15) | 1.25 (0.08) | 1.25 (0.08) | 1.42 (0.19) | 1.42 (0.19) | 1.42 (0.19) |
| $Na_2O$ | 1.21 (0.07) | 1.38 (0.04) | 1.38 (0.04) | 1.18 (0.42) | 1.18 (0.42) | 1.18 (0.42) | 1.21 (0.21) | 1.21 (0.21) | 0.70 (0.11) | 0.70 (0.11) | 0.70 (0.11) |
| $K_2O$ | 9.89 (0.04) | 8.94 (0.16) | 8.94 (0.16) | 8.69 (0.76) | 8.69 (0.76) | 8.69 (0.76) | 9.26 (0.17) | 9.26 (0.17) | 10.46 (0.09) | 10.46 (0.09) | 10.46 (0.09) |
| F | D.L. | (0.013 0.102 ) | (0.013 0.102 ) | 0.070 | 0.070 | 0.070 | (0.012 0.134 ) | (0.012 0.134 ) | (0.029 0.150 ) | (0.029 0.150 ) | (0.029 0.150 ) |
| Cl | (0.008 0.006 ) | D.L. | D.L. | 0.010 | 0.010 | 0.010 | 0.010 | 0.010 | D.L. | D.L. | D.L. |
| Total | 95.44 | 95.38 | 95.38 | 94.56 | 94.56 | 94.56 | 94.90 | 94.90 | 95.58 | 95.58 | 95.58 |
| (ppm) | | | | | | | | | | | |
| Li | | 79 | 78 (2) | 36 (7) | 46 (6) | 46 | 89 (10) | 74 (14) | 37 | 43 (5) | |
| *Ca* | D.L | 344 | 374 | 295 (5) | 437 (72) | 357 | 565 (164) | 513 (56) | 339 (101) | 465 (4) | D.L |
| Sc | 15.7 (6.9) | D.L. | 14.4 (6.0) | 15.4 (3.3) | 25.1 | 17.1 | 8.2 | 7.2 (0.3) | 10.3 (1.2) | 17.0 (1.5) | 11.6 |
| V | 252 (41) | 280 | 294 (22) | 220 (32) | 274 (29) | 229 | 312 (22) | 252 (13) | 156 (2) | 177 (41) | 124 |
| Cr | 353 | 160 | 128 | 95 (7) | D.L. | 110 | 188 (3) | 160 (44) | 83 (15) | D.L. | 134 |
| Mn | 2.1 | D.L | 1.3 (0.1) | 12.3 (5.2) | 10.5 (1.8) | 9.7 | 3.4 (0.5) | 2.6 (0.2) | 3.6 (0.0) | 4.8 (1.2) | 5.8 |
| Co | 2.89 | 0.84 | 1.06 (0.24) | 5.19 (0.65) | 4.72 (0.72) | 4.22 | 1.94 (0.54) | 1.94 (0.49) | 3.22 (0.03) | 2.99 (0.15) | 2.29 |
| Ni | | 1.96 | 2.13 | 8.84 (1.06) | 10.09 (0.53) | 9.80 | 2.57 (0.46) | 2.05 (0.20) | 7.38 (0.61) | 8.39 (0.66) | 7.17 |
| Cu | | 2.77 | 2.77 | 0.99 (0.11) | 1.40 (0.08) | 0.79 | 1.35 (0.34) | 1.36 (0.04) | 1.31 (0.74) | 1.10 | |
| Zn* | 6 | 20 | 20 | 12 | 12 | 12 | 24 | 24 | 27 | 27 | 27 |
| Rb | | 280 | 312 | 197 (18) | 210 (4) | 215 | 322 | 376 (23) | 251 (8) | 275 (20) | |
| Sr | D.L. | 237 | 289 (13) | 69 (11) | 81 (17) | 67 | 303 (32) | 311 (8) | 143 (4) | 252 (9) | 120 |
| *Y** | D.L. | 0.07 | 0.07 | 0.08 | 0.08 | 0.08 | 0.14 | 0.14 | 0.03 | 0.03 | 0.03 |
| *Zr** | 0.25 | 1.15 | 1.15 | 0.85 | 0.85 | 0.85 | 1.14 | 1.14 | 2.06 | 2.06 | 2.06 |
| Nb | 18.8 (3.6) | 2.0 | 1.9 (0.3) | 12.8 (3.0) | 15.1 (2.5) | 15.0 | 4.0 (0.6) | 4.0 (0.1) | 18.6 (4.9) | 23.7 (0.8) | D.L. |
| Cs | | 2.46 | 3.64 | 0.89 (0.10) | 0.80 (0.21) | 0.92 | 3.33 | 4.93 (0.33) | 6.89 (0.73) | 4.79 (0.51) | |
| Ba | 832 (139) | 1966 (253) | 1828 | 900 (53) | 1155 (194) | 1050 (76) | 2331 (287) | 2131 (124) | 598 (10) | 784 (58) | 618 |
| *La** | 0.014 | 0.010 | 0.010 | 0.004 | 0.004 | 0.004 | 0.033 | 0.033 | 0.007 | 0.007 | 0.007 |
| *Ce** | 0.038 | 0.080 | 0.080 | 0.005 | 0.005 | 0.005 | 0.021 | 0.021 | D.L. | D.L. | D.L. |
| *Hf* | (0.001 0.077 ) | (0.007 0.075 ) | D.L. | (0.011 0.134 ) | (0.024 0.120 ) | 0.136 | (0.030 0.180 ) | (0.028 0.182 ) | (0.029 0.116 ) | (0.028 0.192 ) | D.L. |
| Ta | 0.34 (0.07) | 0.09 (0.04) | 0.03 | 0.35 (0.08) | 0.43 (0.09) | 0.46 (0.14) | 0.14 (0.05) | 0.12 (0.04) | 1.39 | 1.32 (0.08) | D.L. |

Notes: # Total Fe as FeO. * For these elements the lowest value within a sample is reported because of fractionation during laser ablation (Zn) and contamination from micro-inclusions (Y, Zr and REE). D.L. and blank represent data below detection limits and elements not determined, respectively. Italicized elements are present in concentrations lower than 3 times detection limits in most analyses. Values in parentheses are standard deviations at 1σ level.

Table 4.5. Stoichiometries of biotite.

| | 87-81F | 87-81I | 87-81K | 87-83C | 87-83D | 87-86F | 88-32A | 88-32B | 87-279D | 87-279F | 87-279G | 88-48C | 88-45D | 88-45E | 88-74C | 88-74D | 88-74E | 88-85C | 88-85D | 88-58A | 88-58B | 88-58C |
|---|---|---|---|---|---|---|---|---|---|---|---|---|---|---|---|---|---|---|---|---|---|---|
| Tetrahedral sites | | | | | | | | | | | | | | | | | | | | | | |
| Si | 5.584 | 5.583 | 5.584 | 5.523 | 5.523 | 5.591 | 5.492 | 5.492 | 5.543 | 5.544 | 5.544 | 5.506 | 5.578 | 5.579 | 5.478 | 5.479 | 5.479 | 5.488 | 5.488 | 5.451 | 5.451 | 5.452 |
| $^{IV}$Al | 2.416 | 2.417 | 2.416 | 2.477 | 2.477 | 2.409 | 2.508 | 2.508 | 2.457 | 2.456 | 2.456 | 2.494 | 2.422 | 2.421 | 2.522 | 2.521 | 2.521 | 2.512 | 2.512 | 2.549 | 2.549 | 2.548 |
| Octahedral sites | | | | | | | | | | | | | | | | | | | | | | |
| Ti | 0.177 | 0.177 | 0.177 | 0.177 | 0.177 | 0.183 | 0.177 | 0.177 | 0.185 | 0.185 | 0.185 | 0.133 | 0.188 | 0.188 | 0.236 | 0.236 | 0.236 | 0.188 | 0.188 | 0.240 | 0.240 | 0.240 |
| $^{VI}$Al | 0.676 | 0.675 | 0.676 | 0.635 | 0.633 | 0.731 | 0.660 | 0.660 | 0.645 | 0.647 | 0.647 | 0.782 | 0.830 | 0.830 | 0.673 | 0.673 | 0.674 | 0.761 | 0.760 | 0.631 | 0.632 | 0.634 |
| $Fe^{\#}$ | 2.519 | 2.519 | 2.520 | 2.445 | 2.445 | 2.415 | 2.801 | 2.802 | 2.237 | 2.237 | 2.237 | 1.775 | 2.019 | 2.020 | 2.134 | 2.134 | 2.134 | 2.012 | 2.012 | 2.615 | 2.615 | 2.616 |
| Mg | 2.272 | 2.272 | 2.272 | 2.355 | 2.355 | 2.405 | 2.044 | 2.045 | 2.502 | 2.503 | 2.502 | 3.015 | 2.659 | 2.659 | 2.605 | 2.605 | 2.605 | 2.733 | 2.733 | 2.131 | 2.131 | 2.132 |
| Mn | 2.6E-02 | 2.5E-02 | 2.2E-02 | 1.6E-02 | 1.6E-02 | 1.6E-02 | 8.8E-03 | 9.0E-03 | 2.2E-02 | 1.7E-02 | 1.6E-02 | 5.1E-04 | 5.5E-04 | 6.3E-04 | 3.7E-03 | 3.8E-03 | 3.5E-03 | 6.7E-04 | 7.0E-04 | 2.6E-03 | 2.6E-03 | 2.7E-03 |
| Li | | 2.6E-03 | 2.5E-03 | 3.3E-03 | 2.4E-03 | 4.2E-03 | 2.2E-03 | | 3.0E-03 | 3.0E-03 | 3.1E-03 | | 7.5E-03 | 7.3E-03 | 4.8E-03 | 5.4E-03 | 5.0E-03 | 8.3E-03 | 7.5E-03 | 4.5E-03 | 4.7E-03 | |
| Sc | 3.8E-04 | 3.2E-04 | 2.6E-04 | 2.4E-04 | 2.6E-04 | 3.5E-04 | 2.4E-04 | 2.6E-04 | 2.9E-04 | 4.1E-04 | 4.5E-04 | 2.2E-04 | 1.1E-04 | 1.2E-04 | 2.9E-04 | 2.8E-04 | 2.5E-04 | 9.4E-05 | 1.0E-04 | 2.6E-04 | 2.5E-04 | 2.4E-04 |
| V | 3.5E-03 | 2.8E-03 | 2.6E-03 | 2.5E-03 | 2.5E-03 | 2.6E-03 | 3.3E-03 | 3.5E-03 | 1.2E-02 | 1.2E-02 | 1.2E-02 | 2.6E-03 | 3.8E-03 | 4.0E-03 | 4.4E-03 | 4.3E-03 | 4.6E-03 | 4.5E-03 | 4.5E-03 | 2.3E-03 | 2.0E-03 | 1.8E-03 |
| Cr | 3.1E-03 | 3.5E-03 | 3.2E-03 | 1.6E-03 | 1.7E-03 | 1.9E-03 | 1.6E-03 | 1.5E-03 | 3.4E-03 | 3.0E-03 | 3.2E-03 | D.L. | 6.5E-03 | 5.8E-03 | 5.8E-03 | 5.7E-03 | 5.1E-03 | 5.9E-03 | 6.3E-03 | 3.0E-03 | 3.3E-03 | 3.0E-03 |
| Co | 7.8E-04 | 7.0E-04 | 6.3E-04 | 7.3E-04 | 7.5E-04 | 7.6E-04 | 6.1E-04 | 6.2E-04 | 3.0E-04 | 2.6E-04 | 3.3E-04 | 7.5E-04 | 3.9E-04 | 3.9E-04 | 1.7E-03 | 1.7E-03 | 1.6E-03 | 4.7E-04 | 5.3E-04 | 8.0E-04 | 6.6E-04 | 5.9E-04 |
| Ni | 1.4E-03 | 1.4E-03 | 1.4E-03 | 2.5E-03 | 2.3E-03 | 1.7E-03 | 1.0E-03 | 1.1E-03 | 6.1E-04 | 7.4E-04 | 9.7E-04 | 1.5E-03 | 9.4E-04 | 8.9E-04 | 4.3E-03 | 3.9E-03 | 4.2E-03 | 7.0E-04 | 7.0E-04 | 1.7E-03 | 1.6E-03 | 1.6E-03 |
| Cu | 1.2E-04 | 8.6E-05 | 1.8E-04 | 8.3E-05 | 9.4E-05 | D.L. | 6.5E-05 | D.L. | D.L. | 8.0E-05 | 7.8E-05 | 5.0E-05 | 9.9E-05 | 1.5E-04 | 9.4E-05 | 8.3E-05 | 9.2E-05 | 1.0E-04 | 9.3E-05 | 8.2E-05 | 7.1E-05 | 7.5E-05 |
| Zn | 2.5E-03 | 2.5E-03 | 2.5E-03 | 4.5E-03 | 4.5E-03 | 4.0E-03 | 1.1E-03 | 1.1E-03 | 2.9E-03 | 2.9E-03 | 2.9E-03 | 1.0E-03 | 7.7E-03 | 7.7E-03 | 3.5E-03 | 3.5E-03 | 3.5E-03 | 5.5E-03 | 5.5E-03 | 6.5E-03 | 6.5E-03 | 6.5E-03 |
| *Y* | 1.7E-06 | 1.7E-06 | 1.7E-06 | 2.6E-06 | 2.6E-06 | 2.8E-06 | 1.5E-06 | 1.5E-06 | 1.6E-06 | 1.6E-06 | 1.6E-06 | D.L. | 7.8E-07 | 7.8E-07 | D.L. | D.L. | D.L. | 6.8E-07 | 6.8E-07 | 3.9E-07 | 3.9E-07 | 3.9E-07 |
| *Zr* | 9.8E-07 | 9.8E-07 | 9.8E-07 | D.L. | D.L. | D.L. | 8.1E-07 | 8.1E-07 | 9.6E-07 | 9.6E-07 | 9.6E-07 | 1.2E-06 | 1.4E-06 | 1.4E-06 | 1.1E-06 | 1.1E-06 | 1.1E-06 | 1.3E-06 | 1.3E-06 | 1.5E-06 | 1.5E-06 | 1.5E-06 |
| Nb | 4.7E-04 | 5.3E-04 | 5.5E-04 | 3.8E-04 | 5.8E-04 | 4.5E-04 | 3.9E-04 | D.L. | 3.4E-04 | 3.3E-04 | 3.4E-04 | 2.1E-04 | 8.7E-06 | 7.7E-06 | 1.8E-04 | 1.8E-04 | 1.7E-04 | 1.1E-05 | 1.3E-05 | 2.3E-04 | 2.5E-04 | D.L. |
| *Hf* | | 5.8E-07 | | | | 3.4E-07 | 3.2E-07 | D.L. | D.L. | 2.7E-07 | D.L. | 8.1E-08 | 2.4E-07 | 1.2E-07 | 5.6E-08 | 5.0E-08 | 9.0E-08 | 3.8E-07 | 3.8E-07 | D.L. | D.L. | D.L. |
| Ta | | 1.9E-05 | 2.0E-05 | 1.5E-05 | 2.0E-05 | 1.5E-05 | 4.8E-06 | D.L. | 1.2E-05 | 7.3E-06 | 5.4E-06 | 4.2E-06 | 2.4E-07 | 1.5E-07 | 5.2E-06 | 5.1E-06 | 5.0E-06 | 3.8E-07 | 3.8E-07 | 1.2E-05 | 1.5E-05 | D.L. |
| $X_{Mg}$ | 0.474 | 0.474 | 0.474 | 0.491 | 0.491 | 0.499 | 0.422 | 0.422 | 0.528 | 0.528 | 0.528 | 0.629 | 0.568 | 0.568 | 0.550 | 0.550 | 0.550 | 0.576 | 0.576 | 0.449 | 0.449 | 0.449 |
| Total | 5.683 | 5.683 | 5.682 | 5.643 | 5.641 | 5.766 | 5.701 | 5.700 | 5.614 | 5.612 | 5.611 | 5.711 | 5.723 | 5.724 | 5.677 | 5.677 | 5.677 | 5.720 | 5.720 | 5.640 | 5.640 | 5.638 |
| $Al^{TOT}$ | 3.092 | 3.092 | 3.092 | 3.111 | 3.111 | 3.140 | 3.168 | 3.168 | 3.102 | 3.103 | 3.103 | 3.276 | 3.252 | 3.252 | 3.195 | 3.195 | 3.195 | 3.272 | 3.272 | 3.181 | 3.181 | 3.181 |
| Interlayer sites | | | | | | | | | | | | | | | | | | | | | | |
| *Ca* | D.L. | 7.4E-03 | 9.6E-03 | D.L. | 6.3E-03 | 7.4E-03 | 5.6E-03 | D.L. | D.L. | 6.2E-03 | D.L. | D.L. | 6.5E-03 | 6.7E-03 | 5.2E-03 | 4.9E-03 | 5.7E-03 | 5.2E-03 | 5.4E-03 | 6.6E-03 | 4.7E-03 | D.L. |
| Na | D.L. | D.L. | D.L. | 0.100 | 0.100 | D.L. | D.L. | D.L. | D.L. | D.L. | D.L. | 0.135 | 0.118 | 0.118 | 0.154 | 0.154 | 0.154 | 0.118 | 0.118 | 0.115 | 0.115 | 0.115 |
| K | 1.787 | 1.787 | 1.787 | 1.831 | 1.831 | 1.846 | 1.803 | 1.803 | 1.891 | 1.892 | 1.892 | 1.756 | 1.458 | 1.458 | 1.752 | 1.752 | 1.752 | 1.592 | 1.592 | 1.860 | 1.860 | 1.861 |
| Rb | D.L. | 2.5E-03 | 2.9E-03 | D.L. | 3.5E-03 | 2.6E-03 | 2.6E-03 | D.L. | D.L. | 2.0E-03 | 2.6E-03 | D.L. | 4.1E-03 | 4.3E-03 | 3.3E-03 | 2.9E-03 | 3.0E-03 | 4.1E-03 | 3.8E-03 | 2.8E-03 | 2.4E-03 | D.L. |
| Sr | 2.0E-05 | 2.2E-05 | 1.8E-05 | 1.1E-05 | 1.3E-05 | 1.3E-05 | 2.7E-05 | D.L. | 2.1E-05 | 1.5E-05 | 2.0E-05 | 2.0E-05 | 2.4E-05 | 1.9E-05 | 2.0E-05 | 2.6E-05 | 1.8E-05 | 4.7E-05 | 5.5E-05 | 5.0E-05 | 5.5E-05 | 3.9E-05 |
| Cs | D.L. | 1.6E-04 | 1.7E-04 | D.L. | 2.6E-04 | 1.6E-04 | 8.1E-05 | D.L. | D.L. | 1.4E-04 | 1.4E-04 | D.L. | 3.0E-04 | 3.3E-04 | 8.2E-05 | 6.9E-05 | 7.0E-05 | 2.6E-04 | 3.1E-04 | 2.2E-04 | 2.1E-04 | D.L. |
| Ba | 8.0E-03 | 8.6E-03 | 8.6E-03 | 6.9E-03 | 7.9E-03 | 5.8E-03 | 6.7E-03 | 8.5E-03 | 7.1E-03 | 6.0E-03 | 7.4E-03 | 2.7E-03 | 5.2E-03 | 4.4E-03 | 3.8E-03 | 4.0E-03 | 4.0E-03 | 7.1E-03 | 7.8E-03 | 2.6E-03 | 2.6E-03 | 2.4E-03 |
| *La* | 1.5E-06 | 1.5E-06 | 1.5E-06 | 2.5E-06 | 2.5E-06 | D.L. | 6.7E-07 | 6.7E-07 | 3.6E-06 | 3.6E-06 | 3.6E-06 | 3.8E-06 | 7.7E-07 | 7.7E-07 | 8.9E-08 | 8.9E-08 | 8.9E-08 | 4.9E-07 | 4.9E-07 | 9.9E-07 | 9.9E-07 | 9.9E-07 |
| *Ce* | 4.1E-06 | 4.1E-06 | 4.1E-06 | 2.4E-06 | 2.4E-06 | D.L. | 1.2E-06 | 1.2E-06 | 6.3E-06 | 6.3E-06 | 6.3E-06 | 6.1E-06 | 2.2E-06 | 2.2E-06 | 1.4E-07 | 1.4E-07 | 1.4E-07 | 1.1E-06 | 1.1E-06 | 1.2E-06 | 1.2E-06 | 1.2E-06 |
| $X_{Na}$ | | | | 0.052 | 0.052 | | | | | | | 0.071 | 0.075 | 0.075 | 0.081 | 0.081 | 0.081 | 0.069 | 0.069 | 0.058 | 0.058 | 0.058 |
| Total | 1.795 | 1.806 | 1.808 | 1.938 | 1.949 | 1.862 | 1.817 | 1.811 | 1.898 | 1.906 | 1.902 | 1.893 | 1.592 | 1.592 | 1.919 | 1.918 | 1.919 | 1.726 | 1.727 | 1.987 | 1.985 | 1.978 |

Notes: Stoichiometries are based upon 22 O and site occupancies are assigned on the basis of ionic radius arguments. # Total Fe as FeO. $X_{Mg}$=Mg/(Mg+$Fe^{TOT}$); $X_{Na}$=Na/(Na+K).

Table 4.6. Stoichiometries of muscovite.

| | 87-81F | 87-81I | 87-81K | 87-83C | 87-83D | 87-86F | 88-32A | 88-32B | 87-279D | 87-279F | 87-279G | 88-48C | 88-45D | 88-45E | 88-74C | 88-74D | 88-74E | 88-85C | 88-85D | 88-58A | 88-58B | 88-58C |
|---|---|---|---|---|---|---|---|---|---|---|---|---|---|---|---|---|---|---|---|---|---|---|
| Tetrahedral sites | | | | | | | | | | | | | | | | | | | | | | |
| Si | 6.218 | 6.215 | 6.217 | 6.202 | 6.198 | 6.268 | 6.222 | 6.223 | 6.237 | 6.236 | 6.237 | 6.183 | 6.197 | 6.197 | 6.248 | 6.247 | 6.247 | 6.241 | 6.242 | 6.284 | 6.283 | 6.284 |
| $^{IV}$Al | 1.782 | 1.785 | 1.783 | 1.798 | 1.802 | 1.732 | 1.778 | 1.777 | 1.763 | 1.764 | 1.763 | 1.817 | 1.803 | 1.803 | 1.752 | 1.753 | 1.753 | 1.759 | 1.758 | 1.716 | 1.717 | 1.716 |
| Octahedral sites | | | | | | | | | | | | | | | | | | | | | | |
| Ti | 0.039 | 0.039 | 0.039 | 0.038 | 0.038 | 0.045 | 0.037 | 0.037 | 0.074 | 0.074 | 0.074 | 0.038 | 0.077 | 0.077 | 0.075 | 0.075 | 0.075 | 0.091 | 0.091 | 0.091 | 0.091 | 0.091 |
| $^{VI}$Al | 3.586 | 3.580 | 3.584 | 3.574 | 3.565 | 3.569 | 3.527 | 3.529 | 3.491 | 3.488 | 3.490 | 3.611 | 3.610 | 3.610 | 3.538 | 3.537 | 3.537 | 3.539 | 3.541 | 3.461 | 3.461 | 3.462 |
| Fe | 0.194 | 0.194 | 0.194 | 0.187 | 0.187 | 0.199 | 0.234 | 0.234 | 0.177 | 0.177 | 0.177 | 0.174 | 0.136 | 0.136 | 0.283 | 0.283 | 0.283 | 0.141 | 0.141 | 0.182 | 0.182 | 0.182 |
| Mg | 0.215 | 0.215 | 0.215 | 0.227 | 0.226 | 0.249 | 0.230 | 0.230 | 0.256 | 0.256 | 0.256 | 0.229 | 0.221 | 0.221 | 0.210 | 0.210 | 0.210 | 0.248 | 0.248 | 0.282 | 0.282 | 0.282 |
| Mn | 7.5E-04 | 1.1E-03 | 6.0E-04 | 6.0E-04 | 8.5E-04 | 7.1E-04 | 4.4E-04 | 4.1E-04 | 1.1E-03 | 8.9E-04 | 9.6E-04 | 3.0E-05 | D.L. | 1.8E-05 | 1.8E-04 | 1.5E-04 | 1.4E-04 | 4.8E-05 | 3.7E-05 | 5.1E-05 | 6.8E-05 | 8.3E-05 |
| Li | | 1.4E-03 | 1.5E-03 | 1.2E-03 | 1.2E-03 | 2.0E-03 | 3.7E-04 | | | 1.1E-03 | 1.2E-03 | | 1.7E-03 | 1.6E-03 | 7.6E-04 | 9.7E-04 | 9.7E-04 | 1.8E-03 | 1.5E-03 | 7.7E-04 | 8.9E-04 | |
| Sc | 9.4E-04 | 8.1E-04 | 6.8E-04 | 5.6E-04 | 9.3E-04 | 9.5E-04 | 8.3E-04 | 7.8E-04 | 9.5E-04 | 1.2E-03 | 1.3E-03 | 2.8E-04 | D.L. | 2.5E-04 | 2.7E-04 | 4.4E-04 | 3.0E-04 | 1.4E-04 | 1.2E-04 | 1.8E-04 | 2.9E-04 | 2.0E-04 |
| V | 4.5E-03 | 5.4E-03 | 4.7E-03 | 4.9E-03 | 4.6E-03 | 4.8E-03 | 5.8E-03 | 5.4E-03 | 2.1E-02 | 2.0E-02 | 1.9E-02 | 3.9E-03 | 4.3E-03 | 4.5E-03 | 3.4E-03 | 4.2E-03 | 3.5E-03 | 4.7E-03 | 3.8E-03 | 2.4E-03 | 2.7E-03 | 1.9E-03 |
| Cr | D.L. | D.L. | 2.4E-03 | 2.2E-03 | 2.2E-03 | 1.0E-03 | 1.6E-03 | D.L. | D.L. | 3.6E-03 | 2.7E-03 | 5.4E-03 | 2.4E-03 | 1.9E-03 | 1.4E-03 | D.L. | 1.7E-03 | 2.8E-03 | 2.4E-03 | 1.2E-03 | D.L. | 2.0E-03 |
| Co | 4.2E-05 | 5.0E-05 | 4.5E-05 | | 6.3E-05 | 4.8E-05 | 3.0E-05 | D.L. | D.L. | 2.0E-05 | 2.5E-05 | 3.9E-05 | 1.1E-05 | 1.4E-05 | 6.9E-05 | 6.3E-05 | 5.6E-05 | 2.5E-05 | 2.5E-05 | 4.3E-05 | 3.9E-05 | 3.0E-05 |
| *Ni* | D.L. | 1.6E-04 | D.L. | 1.5E-04 | 1.9E-04 | 1.1E-04 | 4.9E-05 | D.L. | D.L. | 7.7E-05 | 6.7E-05 | D.L. | 2.6E-05 | 2.8E-05 | 1.2E-04 | 1.4E-04 | 1.3E-04 | 3.4E-05 | 2.7E-05 | 9.8E-05 | 1.1E-04 | 9.5E-05 |
| *Cu* | 4.3E-05 | 4.4E-05 | D.L. | | 3.1E-05 | 1.5E-05 | 1.7E-05 | D.L. | D.L. | 5.3E-05 | 4.2E-05 | D.L. | 3.4E-05 | 3.4E-05 | 1.2E-05 | 1.7E-05 | 9.7E-06 | 1.6E-05 | 1.7E-05 | 1.6E-05 | 1.3E-05 | D.L. |
| Zn | 1.5E-04 | 1.5E-04 | 1.5E-04 | 2.7E-04 | 2.7E-04 | 3.4E-04 | 1.0E-04 | 1.0E-04 | 1.9E-04 | 1.9E-04 | 1.9E-04 | 7.3E-05 | 2.4E-04 | 2.4E-04 | 1.5E-04 | 1.5E-04 | 1.5E-04 | 2.8E-04 | 2.8E-04 | 3.2E-04 | 3.2E-04 | 3.2E-04 |
| *Y* | 3.0E-06 | 3.0E-06 | 3.0E-06 | 2.5E-06 | 2.5E-06 | 1.5E-06 | 2.4E-06 | 2.4E-06 | 7.6E-07 | 7.6E-07 | 7.6E-07 | D.L. | 5.9E-07 | 5.9E-07 | 7.2E-07 | 7.2E-07 | 7.2E-07 | 1.2E-06 | 1.2E-06 | 2.4E-07 | 2.4E-07 | 2.4E-07 |
| *Zr* | 1.0E-06 | 1.0E-06 | 1.0E-06 | 4.6E-06 | 4.6E-06 | 1.6E-06 | 1.4E-06 | 1.4E-06 | 2.0E-06 | 2.0E-06 | 2.0E-06 | 2.1E-06 | 9.8E-06 | 9.8E-06 | 7.4E-06 | 7.4E-06 | 7.4E-06 | 9.6E-06 | 9.6E-06 | 1.8E-05 | 1.8E-05 | 1.8E-05 |
| Nb | 2.2E-04 | D.L. | 2.3E-04 | 2.3E-04 | 3.5E-04 | 2.4E-04 | 2.2E-04 | D.L. | D.L. | 1.9E-04 | 1.6E-04 | 1.6E-04 | 1.7E-05 | 1.6E-05 | 1.1E-04 | 1.3E-04 | 1.3E-04 | 3.3E-05 | 3.3E-05 | 1.6E-04 | 2.0E-04 | D.L. |
| *Hf* | 1.2E-06 | D.L. | D.L. | D.L. | 8.0E-07 | 7.3E-07 | 9.5E-07 | D.L. | 5.0E-07 | 2.5E-07 | 6.1E-07 | 3.4E-07 | 3.3E-07 | D.L. | 5.9E-07 | 5.3E-07 | 6.0E-07 | 7.8E-07 | 7.9E-07 | 5.0E-07 | 8.4E-07 | D.L. |
| Ta | 4.5E-06 | 4.4E-06 | 4.0E-06 | 3.9E-06 | 6.9E-06 | 4.7E-06 | 1.5E-06 | D.L. | D.L. | 1.4E-06 | 1.3E-06 | 1.5E-06 | 3.7E-07 | 1.5E-07 | 1.5E-06 | 1.9E-06 | 2.0E-06 | 5.8E-07 | 5.0E-07 | 6.0E-06 | 5.7E-06 | D.L. |
| $X_{Mg}$ | 0.526 | 0.526 | 0.526 | 0.548 | 0.548 | 0.556 | 0.496 | 0.496 | 0.591 | 0.591 | 0.591 | 0.569 | 0.619 | 0.619 | 0.426 | 0.426 | 0.426 | 0.637 | 0.637 | 0.609 | 0.609 | 0.609 |
| Total | 4.042 | 4.038 | 4.043 | 4.035 | 4.027 | 4.072 | 4.038 | 4.038 | 4.021 | 4.023 | 4.023 | 4.061 | 4.053 | 4.054 | 4.113 | 4.112 | 4.113 | 4.030 | 4.030 | 4.021 | 4.020 | 4.021 |
| $Al^{TOT}$ | 5.368 | 5.365 | 5.367 | 5.371 | 5.368 | 5.301 | 5.305 | 5.306 | 5.254 | 5.252 | 5.253 | 5.428 | 5.413 | 5.413 | 5.290 | 5.290 | 5.290 | 5.298 | 5.298 | 5.178 | 5.177 | 5.178 |
| Interlayer sites | | | | | | | | | | | | | | | | | | | | | | |
| *Ca* | D.L. | 1.4E-02 | D.L. | D.L. | D.L. | 1.5E-02 | 1.4E-02 | D.L. | D.L. | 2.0E-02 | 1.1E-02 | D.L. | 6.7E-03 | 7.2E-03 | 5.8E-03 | 8.6E-03 | 7.0E-03 | 1.1E-02 | 9.9E-03 | 6.6E-03 | 9.0E-03 | D.L |
| Na | 0.225 | 0.224 | 0.224 | 0.249 | 0.249 | 0.230 | 0.171 | 0.171 | 0.231 | 0.231 | 0.231 | 0.311 | 0.352 | 0.352 | 0.306 | 0.306 | 0.306 | 0.311 | 0.311 | 0.181 | 0.181 | 0.181 |
| K | 1.699 | 1.698 | 1.698 | 1.712 | 1.710 | 1.719 | 1.816 | 1.817 | 1.728 | 1.727 | 1.727 | 1.676 | 1.503 | 1.503 | 1.482 | 1.482 | 1.482 | 1.567 | 1.567 | 1.773 | 1.773 | 1.773 |
| Rb | D.L. | 1.3E-03 | D.L. | D.L. | 1.6E-03 | 1.4E-03 | 1.3E-03 | D.L. | D.L. | 1.1E-03 | 1.0E-03 | D.L. | 1.5E-03 | 1.7E-03 | 1.1E-03 | 1.1E-03 | 1.2E-03 | 1.7E-03 | 2.0E-03 | 1.4E-03 | 1.5E-03 | D.L. |
| Sr | 1.2E-03 | 1.4E-03 | D.L. | 1.4E-03 | 1.9E-03 | 1.5E-03 | 3.0E-03 | D.L. | 1.6E-03 | 1.2E-03 | 1.2E-03 | D.L. | 2.1E-03 | 2.6E-03 | 6.2E-04 | 7.2E-04 | 6.0E-04 | 2.7E-03 | 2.7E-03 | 1.3E-03 | 2.2E-03 | 1.1E-03 |
| Cs | D.L. | 8.7E-06 | 5.4E-06 | | 1.6E-05 | 1.0E-05 | 6.0E-06 | D.L. | D.L. | 1.1E-05 | 1.2E-05 | D.L. | 1.8E-05 | 2.6E-05 | 6.4E-06 | 5.8E-06 | 6.7E-06 | 2.4E-05 | 3.5E-05 | 5.0E-05 | 3.4E-05 | D.L. |
| Ba | 3.3E-02 | 4.2E-02 | 3.4E-02 | 2.3E-02 | 3.6E-02 | 2.9E-02 | 2.5E-02 | 2.7E-02 | 2.4E-02 | 2.3E-02 | 2.2E-02 | 4.8E-03 | 1.1E-02 | 1.0E-02 | 5.2E-03 | 6.6E-03 | 6.0E-03 | 1.3E-02 | 1.2E-02 | 3.4E-03 | 4.4E-03 | 3.5E-03 |
| *La* | D.L. | D.L. | D.L. | D.L. | D.L. | 1.6E-07 | 3.3E-07 | 3.3E-07 | 2.4E-07 | 2.4E-07 | 2.4E-07 | 7.8E-08 | 5.6E-08 | 5.6E-08 | 2.4E-08 | 2.4E-08 | 2.4E-08 | 1.8E-07 | 1.8E-07 | 4.1E-08 | 4.1E-08 | 4.1E-08 |
| *Ce* | 1.0E-06 | 1.0E-06 | 1.0E-06 | 1.8E-06 | 1.8E-06 | 8.1E-08 | 3.0E-07 | 3.0E-07 | D.L. | D.L. | D.L. | 2.2E-07 | 4.4E-07 | 4.4E-07 | 2.6E-08 | 2.6E-08 | 2.6E-08 | 1.2E-07 | 1.2E-07 | D.L. | D.L. | D.L. |
| $X_{Na}$ | 0.117 | 0.117 | 0.117 | 0.127 | 0.127 | 0.118 | 0.086 | 0.086 | 0.118 | 0.118 | 0.118 | 0.157 | 0.190 | 0.190 | 0.171 | 0.171 | 0.171 | 0.166 | 0.166 | 0.093 | 0.093 | 0.093 |
| Total | 1.958 | 1.981 | 1.957 | 1.985 | 1.999 | 1.996 | 2.030 | 2.015 | 1.984 | 2.004 | 1.994 | 1.992 | 1.876 | 1.877 | 1.801 | 1.805 | 1.803 | 1.906 | 1.905 | 1.967 | 1.971 | 1.959 |

Notes: Stoichiometries are based upon 22 O and site occupancies are assigned on the basis of ionic radius arguments. # Total Fe as FeO. $X_{Mg}$=Mg/(Mg+$Fe^{TOT}$); $X_{Na}$=Na/(Na+K).

Table 4.7. Molar partition coefficients (Di*) of coexisting biotite-muscovite pairs from metapelites, western Labrador.

| Elements | 87-81F | 87-81I | 87-81K | 87-83C | 87-83D | 87-86F | 88-32A | 88-32B | 87-279D | 87-279F | 87-279G |
|---|---|---|---|---|---|---|---|---|---|---|---|
| Octahedral sites | | | | | | | | | | | |
| Li | | 1.18 | 1.09 | 1.80 | 1.37(0.23) | 1.40 | 4.01(0.28) | | | 1.77(0.51) | 1.69 |
| Sc | 0.27 | 0.25 | 0.26(0.02) | 0.27 | 0.18(0.02) | 0.25 | 0.19(0.03) | 0.22 | 0.20 | 0.23(0.05) | 0.22(0.05) |
| V | 0.50 | 0.33 | 0.37(0.08) | 0.33 | 0.35(0.01) | 0.35 | 0.37(0.04) | 0.42 | 0.36 | 0.37(0.07) | 0.39(0.09) |
| Cr | | | 0.88 | 0.46 | 0.48 | 1.21 | 0.66(0.14) | | | 0.53 | 0.76 |
| Co | | | | | | 10.4 | | | | | |
| | 12.26 | 9.25 | 9.26 | | 7.67(1.01) | 3 | 13.22(0.95) | | | 8.41(4.12) | 8.29(3.98) |
| *Ni* | | | | | | 10.2 | | | | | |
| | | 5.77 | | 10.59 | 7.95(0.48) | 4 | 13.97(1.82) | | | 6.12(3.73) | 9.31 |
| *Cu* | 1.87 | 1.30 | | | 1.94 | | 2.59(0.64) | | | 0.96(0.68) | 1.19 |
| Zn | 10.46 | 10.46 | 10.46 | 10.89 | 10.89 | 7.73 | 7.02 | 7.01 | 10.18 | 10.12 | 10.12 |
| *Y* | 0.39 | 0.39 | 0.39 | 0.67 | 0.67 | 1.21 | 0.40 | 0.40 | 1.32 | 1.31 | 1.31 |
| *Zr* | 0.62 | 0.62 | 0.62 | | | | 0.37 | 0.37 | 0.31 | 0.31 | 0.31 |
| Nb | 1.44 | | 1.56(0.09) | 1.09 | 1.07(0.07) | 1.25 | 1.18(0.11) | | | 1.14 | 1.35 |
| *Hf* | | | | | | 0.31 | 0.22(0.12) | | | 0.70 | |
| Ta | | 2.88 | 3.21(0.08) | 2.56 | 1.89(0.01) | 2.10 | 2.04(0.14) | | | 3.31(1.15) | 2.65 |
| Interlayer sites | | | | | | | | | | | |
| Rb | | 1.89 | | | 2.11(0.11) | 1.88 | 2.02(0.25) | | | 1.76(0.40) | 2.51(0.68) |
| Sr | 0.02 | 0.02 | | 0.01 | 0.01(0.001) | 0.01 | 0.01(0.002) | | 0.01 | 0.01(0.002) | 0.02(0.004) |
| Cs | | | | | | 15.4 | | | | | |
| | | 18.12 | 30.50(5.93) | | 16.14(2.31) | 6 | 13.27(1.84) | | | 12.43(4.18) | 11.44 |
| Ba | 0.24 | 0.20 | 0.25 | 0.30 | 0.21(0.02) | 0.20 | 0.26(0.04) | 0.31 | 0.29 | 0.25(0.04) | 0.32(0.09) |
| *La* | | | | | | | 2.04 | 2.04 | 14.55 | 14.46 | 14.45 |
| *Ce* | 3.90 | 3.90 | 3.90 | 1.29 | 1.29 | | 3.86 | 3.86 | | | |
| T (°C) | 507 | 507 | 507 | 492 | 492 | 503 | 503 | 503 | 530 | 530 | 530 |
| P (kbar) | 7.6 | 7.6 | 7.6 | 7.7 | 7.7 | 7.4 | 8.8 | 8.8 | 8.8 | 8.8 | 8.8 |

Italicized elements are present in concentrations below or close to 3 times detection limits in either biotite or muscovite. Metamorphic temperatures and pressures were estimated using the garnet-biotite geothermometer of Holdaway et al., (1997) and Grt-Pl-Bt-Ms and Grt-Ky-Qtz-Pl geobarometers of Hodges and Crowley (1985).

Table 4.7. Continued.

| Elements | 88-48C | 88-45D | 88-45E | 88-74C | 88-74D | 88-74E | 88-85C | 88-85D | 88-58A | 88-58B | 88-58C |
|---|---|---|---|---|---|---|---|---|---|---|---|
| Octahedral sites | | | | | | | | | | | |
| Li | | 2.98 | 2.93(0.22) | 4.04(1.64) | 3.58(0.49) | 3.32 | 2.86(0.34) | 3.09 | 3.78 | 3.40 | |
| Sc | 0.51(0.23) | | 0.32(0.14) | 0.70(0.16) | 0.41 | 0.54 | 0.43 | 0.52(0.04) | 0.93 | 0.55(0.09) | 0.77 |
| V | 0.44(0.09) | 0.59 | 0.59(0.06) | 0.84(0.13) | 0.66(0.08) | 0.83 | 0.60(0.04) | 0.76(0.07) | 0.63 | 0.48(0.11) | 0.63 |
| Cr | | 1.78 | 2.01 | 2.62(0.34) | | 1.99 | 1.34(0.12) | 1.68(0.50) | 1.57 | | 0.96 |
| Co | 12.47 | 22.89 | 18.53(4.36) | 15.93(2.35) | 17.14(3.03) | 18.63 | 11.91(3.46) | 13.26(3.67) | 12.16 | 10.85(1.14) | 12.68 |
| *Ni* | | 23.73 | 20.73 | 23.23(2.99) | 18.81(1.65) | 20.69 | 13.15(3.16) | 16.51(3.16) | 11.02 | 9.17(1.38) | 11.16 |
| *Cu* | | 1.92 | 2.82 | 4.98(0.58) | 3.08(0.18) | 6.07 | 4.05(1.15) | 3.58 | 3.29 | 3.40 | |
| Zn | 9.37 | 21.31 | 21.31 | 15.31 | 15.31 | 15.31 | 12.53 | 12.52 | 13.43 | 13.43 | 13.44 |
| *Y* | | 0.86 | 0.86 | | | | 0.36 | 0.36 | 1.05 | 1.05 | 1.05 |
| *Zr* | 0.37 | 0.09 | 0.09 | 0.09 | 0.09 | 0.09 | 0.09 | 0.09 | 0.05 | 0.05 | 0.05 |
| Nb | 0.84(0.21) | 0.34 | 0.33(0.06) | 1.04(0.25) | 0.90(0.15) | 0.87 | 0.21(0.07) | 0.25(0.07) | 0.97 | 0.82 | |
| *Hf* | 0.15 | 0.48 | | 0.06(0.01) | 0.06 | 0.10 | 0.31(0.08) | 0.31(0.08) | | | |
| Ta | 1.83(0.41) | 0.42 (0.21) | 0.65 | 2.20(0.58) | 1.75(0.39) | 1.610.55 | 0.41(0.16) | 0.48(0.18) | 1.32 | 1.75 | |
| Interlayer sites | | | | | | | | | | | |
| Rb | | 2.70 | 2.54 | 2.95(0.28) | 2.41(0.07) | 2.46 | 2.29 | 1.79 | 2.04 | 1.55 | |
| Sr | | 0.01 | 0.01(.001) | 0.03(.007) | 0.03(.008) | 0.03 | 0.02(.002) | 0.02(.002) | 0.04 | 0.02(.005) | 0.04 |
| Cs | | 16.60 | 12.47 | 12.35(1.42) | 11.41(3.07) | 10.05 | 10.31 | 8.50(1.76) | 4.39 | 6.06 | |
| Ba | 0.54(0.10) | 0.46 (0.06) | 0.42 | 0.71(0.08) | 0.58(0.11) | 0.650.06 | 0.52(0.07) | 0.62(0.11) | 0.74 | 0.58(0.05) | 0.67 |
| *La* | 47.24 | 13.48 | 13.48 | 3.60 | 3.60 | 3.60 | 2.56 | 2.56 | 23.47 | 23.48 | 23.48 |
| *Ce* | 27.34 | 4.77 | 4.77 | 5.34 | 5.34 | 5.34 | 8.95 | 8.95 | | | |
| T (°C) | 622 | 643 | 643 | 658 | 658 | 658 | 656 | 656 | 680 | 680 | 680 |
| P (kbar) | 9.4 | 9.4 | 9.4 | 8.0 | 8.0 | 8.0 | 8.0 | 8.0 | 12.5 | 12.5 | 12.5 |

Italicized elements are present in concentrations below or close to 3 times detection limits in either biotite or muscovite.
Metamorphic temperatures and pressures were estimated using the garnet-biotite geothermometer of Holdaway et al., (1997) and Grt-Pl-Bt-Ms and Grt-Ky-Qtz-Pl geobarometers of Hodges and Crowley (1985).

Table 4.8. Comparison of the Nernst distribution coefficients ($D_i$) between biotite and muscovite with those of previous studies.

| | This study | | Dahl et al. (1993) | Domanik et al. (1993) | Dutrow et al. (1986) | Butler (1967) | Moorbath et al. (1968) |
|---|---|---|---|---|---|---|---|
| Facies | U. Greenschist | Amphibolite | Amphibolite | Ep. Blueschist | Amphibolite | U. Greenschist | Amphibolite |
| Methods | LAM-ICP-MS | | Solution ICP-MS | SIMS | AA | Spectrography | Isotope Dilution |
| Octahedral sites | | | | | | | |
| Mn | 20.62 (5.73) | 24.18 (9.64) | 16.96 (7.22) | | | | |
| Li | 2.38 (1.22) | 4.49 (0.56) | 5.31 (1.47) | | 4.57 (0.68) | | |
| Sc | 0.31 (0.04) | 0.77 (0.24) | 0.49 (0.12) | | | | |
| V | 0.50 (0.06) | 0.86 (0.18) | 0.88 (0.15) | | | | |
| Cr | 0.95 (0.34) | 2.35 (0.67) | 1.30 (0.32) | | | | |
| Co | 13.04 (2.51) | 20.41 (5.05) | 3.45 (2.15) | | | | |
| Ni | 12.15 (3.71) | 22.68 (7.30) | 18.03 (7.93) | | | | |
| Cu | 2.18 (0.79) | 4.98 (1.68) | 2.52 (1.53) | | | | |
| Zn | 12.73 (2.11) | 20.00 (4.76) | 17.77 (10.43) | | | | |
| Y | 1.02 (0.57) | 1.07 (0.41) | 1.94 (2.15) | | | | |
| Zr | 0.58 (0.19) | 0.15 (0.12) | 0.74 (0.25) | | | | |
| Nb | 1.67 (0.22) | 0.89 (0.45) | | | | | |
| Hf | 0.55 (0.34) | 0.28 (0.21) | | | | | |
| Ta | 3.43 (0.72) | 1.68 (0.93) | | | | | |
| Interlayer sites | | | | | | | |
| Na | 0.47 (0.11) | 0.28 (0.03) | 0.21 (0.11) | | | | |
| | | | | | | 1.85 (0.78) | |
| Rb | 1.80 (0.25) | 2.07 (0.40) | | 2.08 | | | 1.52 |
| Sr | 0.01 (0.00) | 0.02 (0.01) | 0.32 (0.33) | 0.03 | | | 0.40 |
| Cs | 14.81 (5.64) | 9.21 (3.26) | | | | | |
| | | | | | | 0.42 (0.05) | |
| Ba | 0.23 (0.04) | 0.53 (0.09) | 0.44 (0.34) | 0.57 | | | |
| La | 8.48 (6.12) | 13.11 (12.70) | 0.72 (0.55) | | | | |
| Ce | 2.76 (1.10) | 8.03 (7.04) | | | | | |
| | | | | | | 0.48 (0.08) | |
| Ca | 0.37 (0.09) | 0.65 (0.19) | 2.07 (1.09) | | | | |

The data of Dahl et al. (1993) represent an average of the St- and Sil-zones. Values in parentheses represent standard deviations at 1σ level. Abbreviations: SIMS; secondary ion mass spectrometry, AA: atomic absorption spectrophotometry.

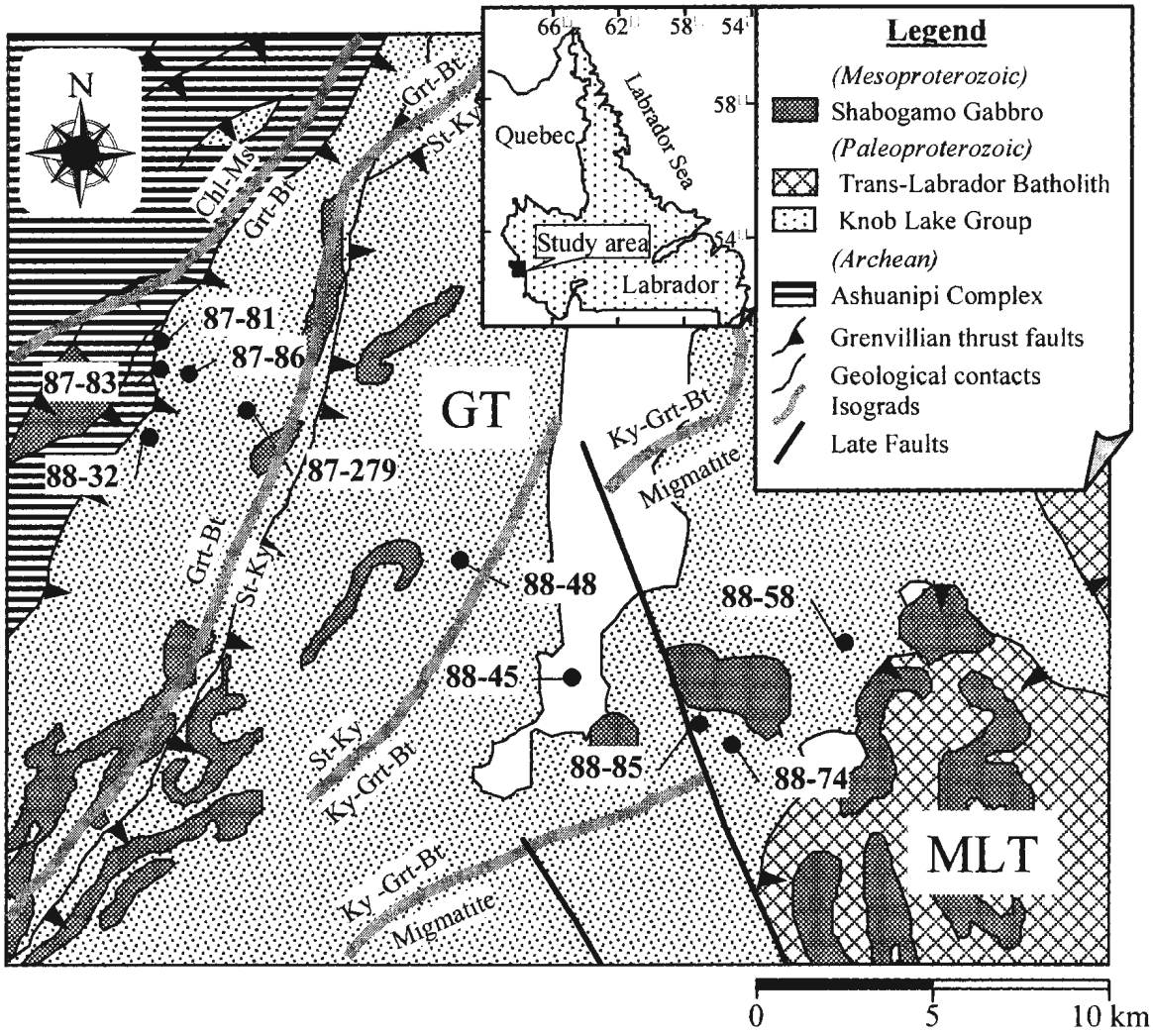


Fig. 4.1. Generalized geologic map of the northern Grenville province in western Labrador, Canada, showing metamorphic isograds and locations of the ten analyzed samples. Geologic map from Connelly *et al.* (1996) and metamorphic isograds from Rivers (1983b) and van Gool (1992).

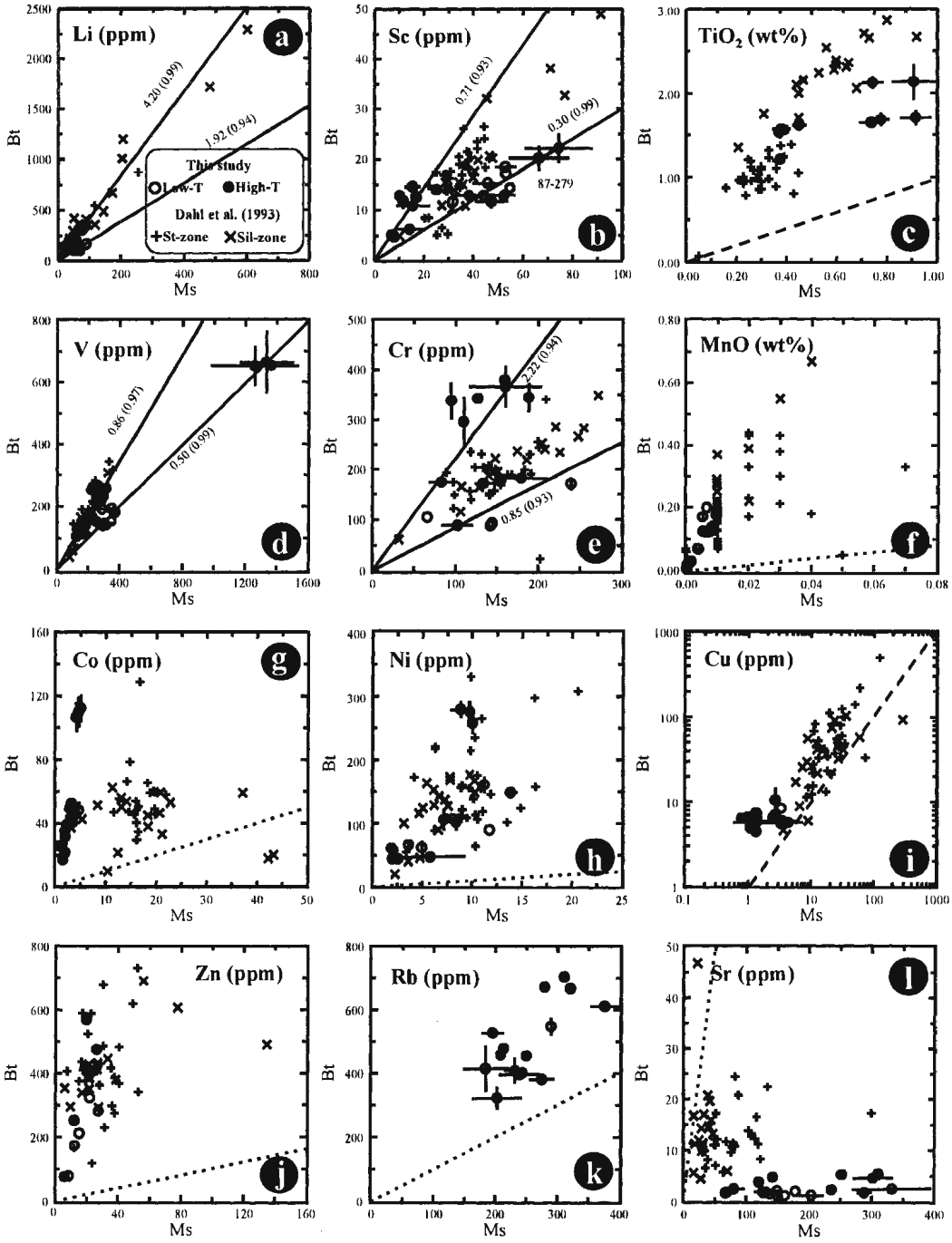


Fig. 4.2. Distribution diagrams showing the partitioning of elements between coexisting biotite (Bt) and muscovite (Ms). Open and closed circles represent low- and high-$T$ biotite-muscovite pairs, respectively. + and × represent mica pairs from St- and Sil-zone, reported by Dahl *et al.* (1993). Error bars represent the standard deviation at 1σ. Data are regressed where they show systematic differences between low- and high-$T$. The numbers are slopes of regression lines, with values in parentheses representing $r^2$. Dashed lines represent equal partitioning. Labelled data points are discussed in the text.

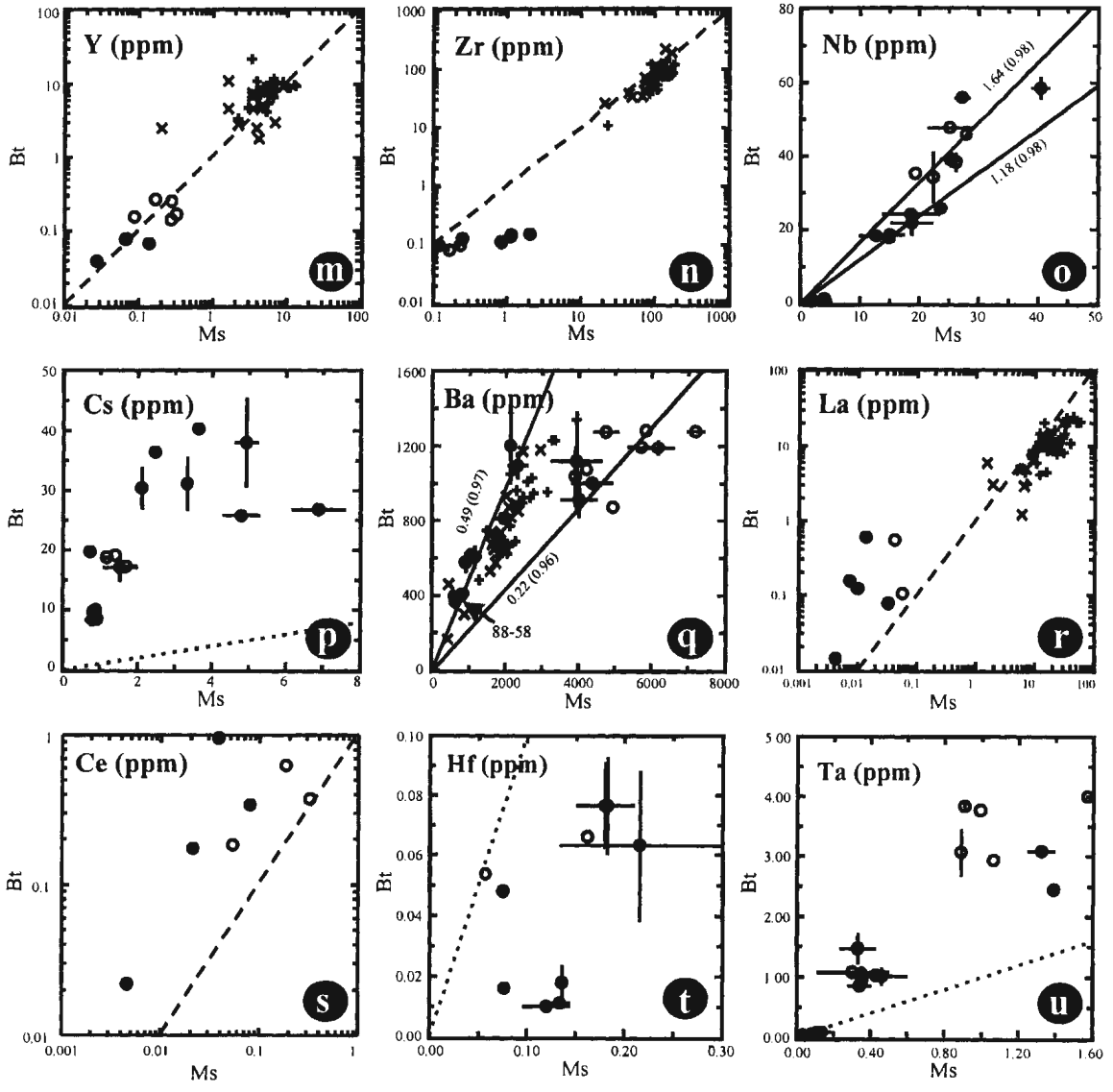


Fig.4.2. Continued.

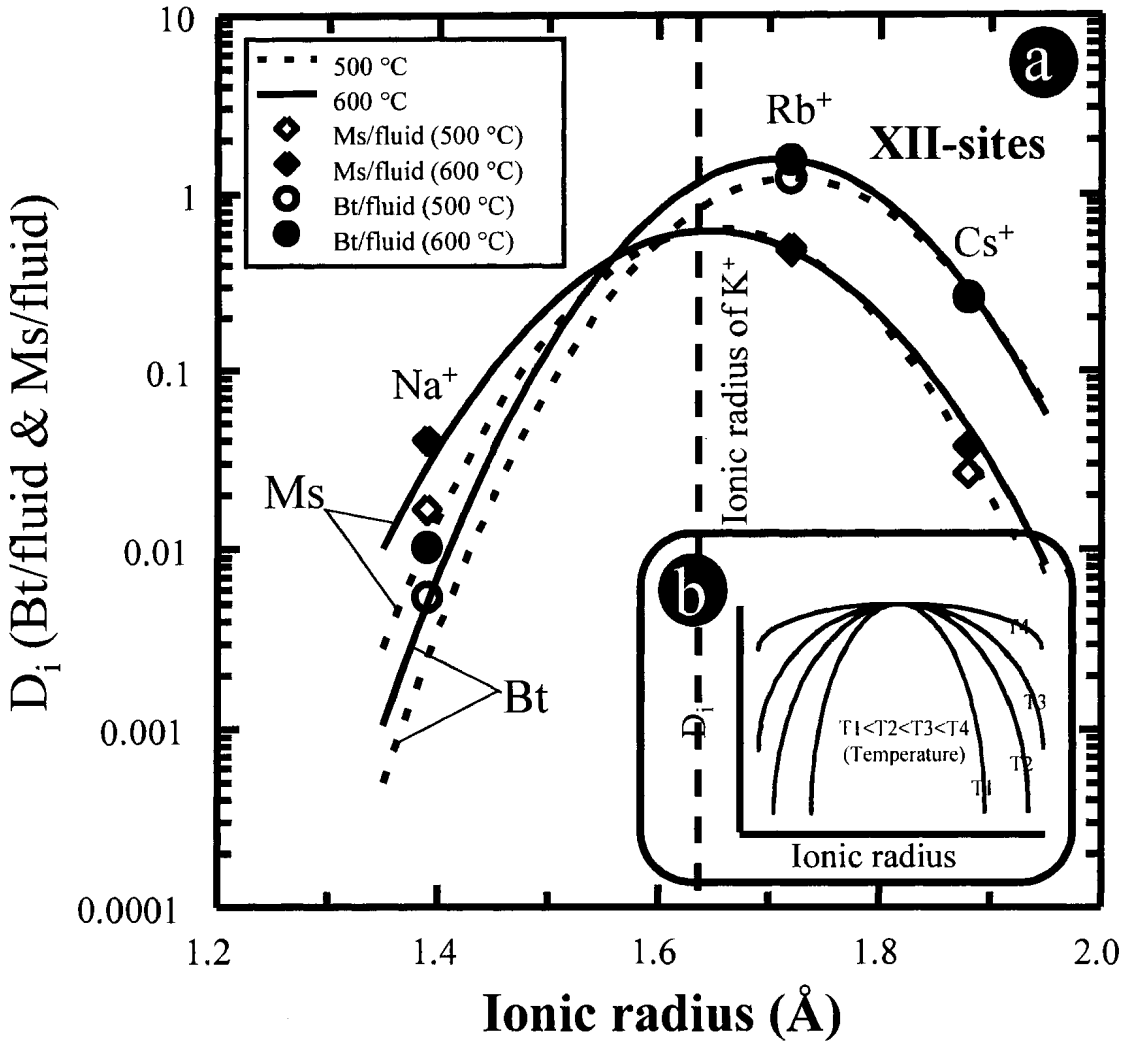


Fig. 4.3. (a) Crystal-fluid partition coefficient vs. ionic radius for interlayer cations in phlogopite and muscovite. Data are from Volfinger (1976). Curves are calculated from Eq. (4.5). Dotted line indicates ionic radius of $K^+$. (b) Schematic diagram showing the predicted decrease of slopes with increasing temperature.

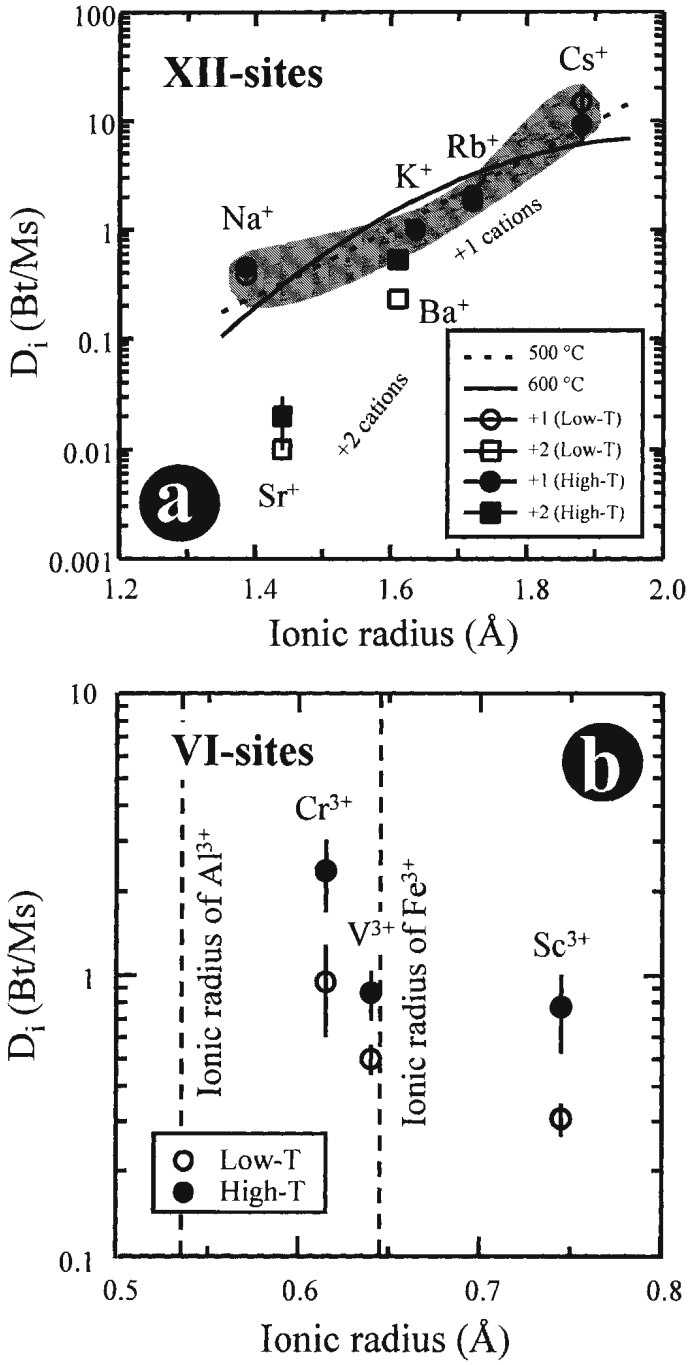


Fig. 4.4. Relationship between distribution coefficient and ionic radius. (a) $D_i$ values for low- and high-$T$ micas plotted against ionic radius for monovalent and divalent cations in XII-interlayer sites (shaded areas), along with distribution lines for 500 and 600 °C (solid and dashed lines) calculated from the data of Volfinger (1976). (b) $D_i$ values of 3+ cations in VI-sites plotted against corresponding ionic radius. For reference, ionic radii of $Al^{3+}$ and $Fe^{3+}$ ions are shown.

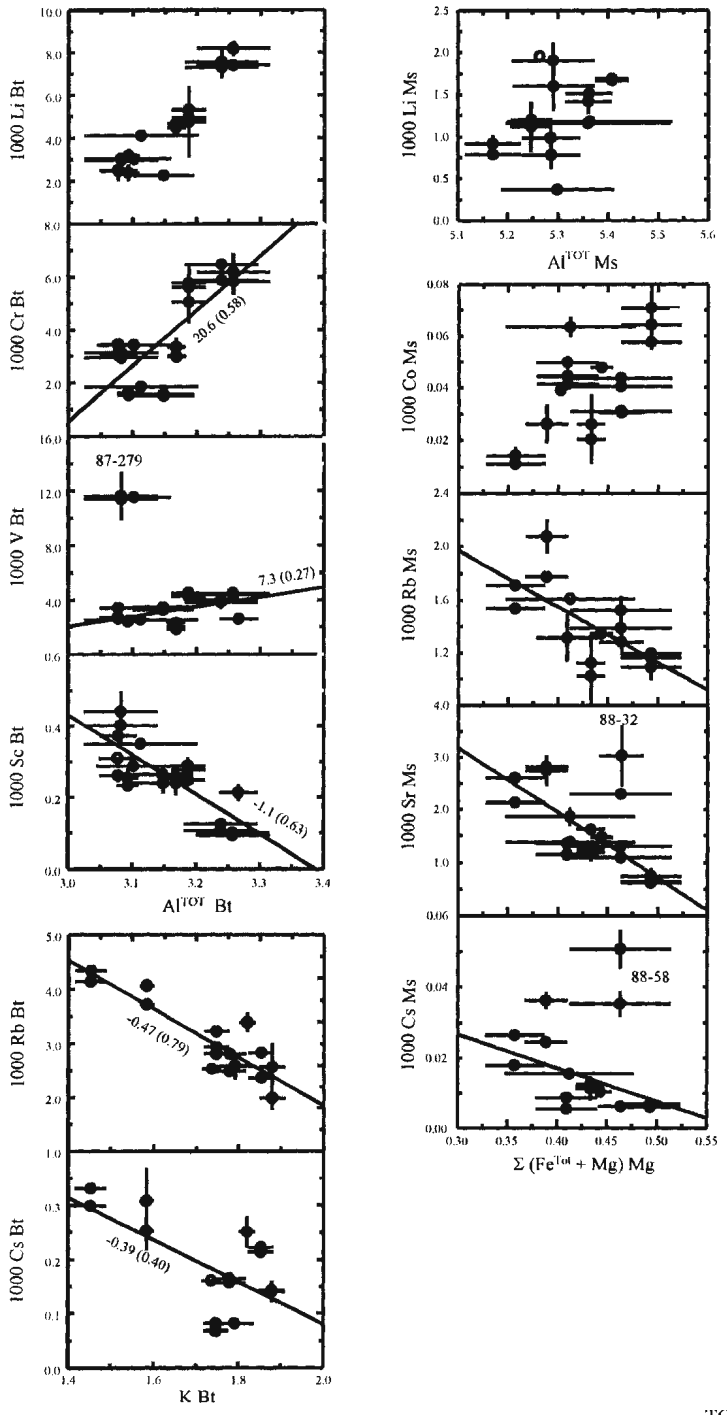


Fig. 4.5. (a-d) The concentrations of Li, Cr, V and Sc versus $Al^{TOT}$ in biotite. Note that the effects of $Al^{TOT}$ on the contents of Cr, V and Sc are different. (e-f) The concentrations of Rb and Cs in biotite versus K contents. (g) Li in muscovite versus $Al^{TOT}$. (h-k) Co, Rb, Sr and Cs versus $\Sigma(Fe^{TOT}+Mg)$ of muscovite. Open and closed circles represent low- and high-*T* samples, respectively. Regression lines are shown, and the numbers represents slopes of regression lines, with $r^2$ in parentheses, where these are significant.

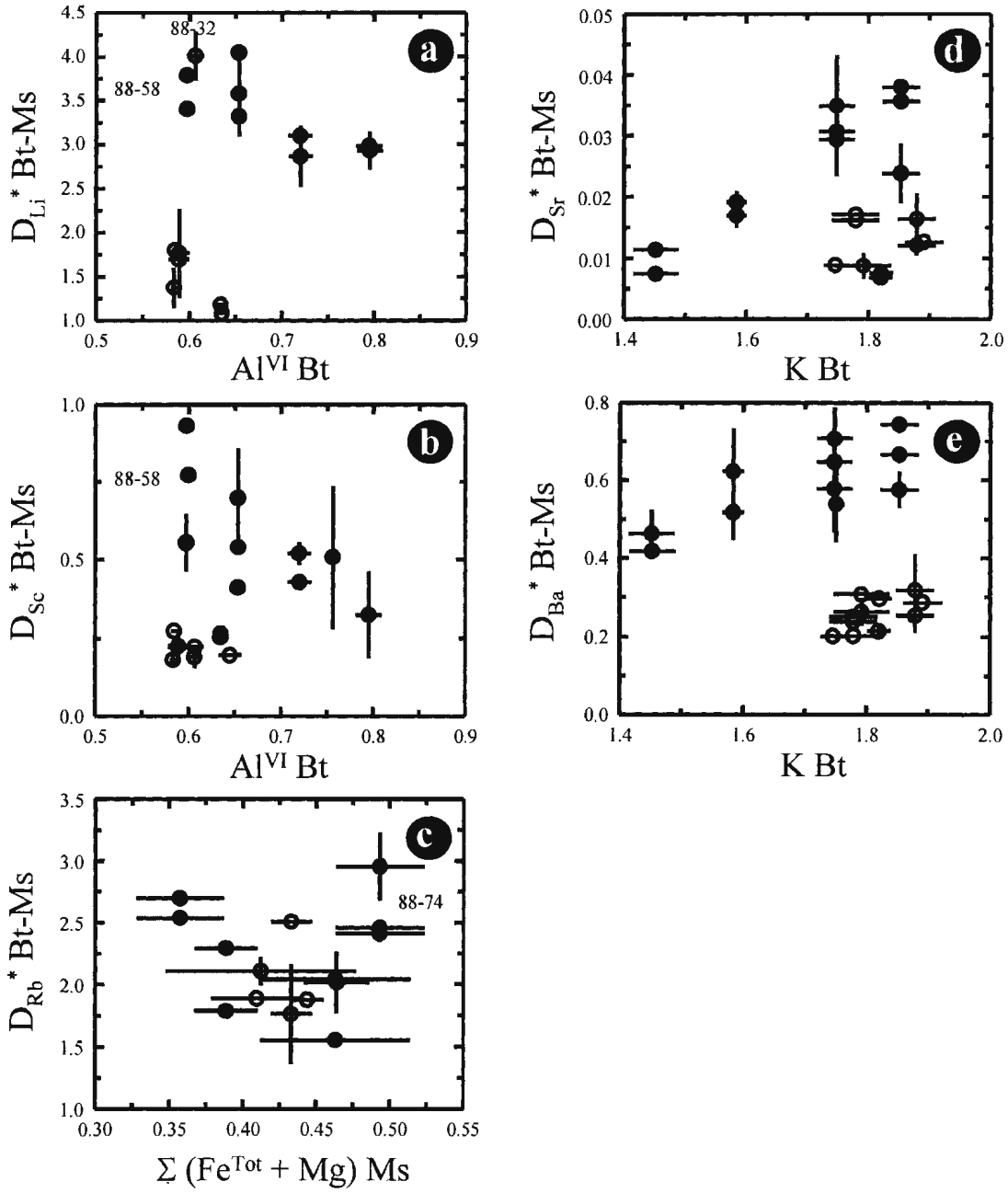


Fig. 4.6. (a-e) Major element compositional effects of $Al^{VI}$, $\Sigma(Fe^{TOT}+Mg)$ and K of either biotite or muscovite on the distribution of Li, Sc, Rb, Sr and Ba between biotite and muscovite. All of the trace elements except for Rb show two different trends with metamorphic grade. Open and closed circles represent low- and high-*T*, respectively

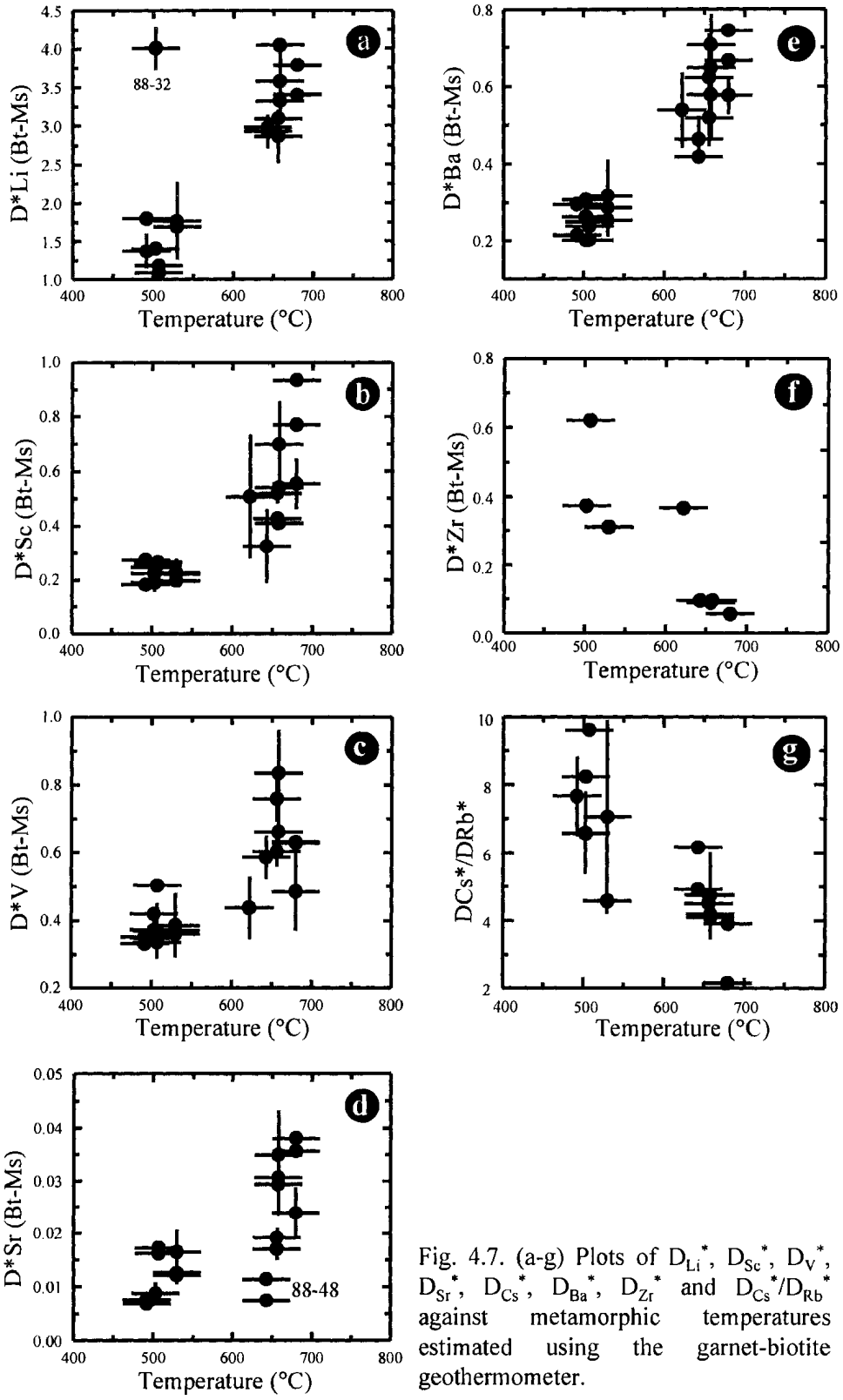


Fig. 4.7. (a-g) Plots of $D_{Li}^*$, $D_{Sc}^*$, $D_V^*$, $D_{Sr}^*$, $D_{Cs}^*$, $D_{Ba}^*$, $D_{Zr}^*$ and $D_{Cs}^*/D_{Rb}^*$ against metamorphic temperatures estimated using the garnet-biotite geothermometer.

# Chapter 5: Trace element zoning in metamorphic minerals

## 5.1 Introduction

Textures, inclusion zoning, and element zoning in porphyroblasts, particularly garnet, have commonly been used to infer information on both physicochemcial and kinetic aspects of metamorphism during prograde metamorphism (e.g., Hollister, 1966; Rosenfeld, 1970; Tracy et al., 1976; Spear and Selverstone, 1983; Spear et al., 1984; Spear and Rumble, 1986). Growth zoning provides information on changes in effective bulk composition (Hollister, 1966; Atherton, 1968), changes in assemblage (Thompson et al., 1977), and changes in pressure and temperature during garnet growth (Selverstone et al., 1984; Selverstone and Spear, 1985; Spear and Rumble, 1986; St-Onge, 1987). This information has been used to constrain the tectonic and chemical histories of metamorphic terranes (Spear et al., 1984).

However, textures, matrix and inclusion phase relationships and major element zoning cannot be interpreted uniquely in terms of metamorphic processes, and major element zoning is commonly modified by intracrystalline diffusion under amphibolite-facies conditions and above (Spear, 1988). More recently a number of studies have shown that, compared with major elements, the behaviour of trace elements may be a more sensitive indicator of metamorphic processes such as mineral breakdown or growth,

change in *P-T* conditions, the operation of disequilibrium processes, and open system behaviour (e.g. Hickmott et al., 1987; Hickmott and Shimizu, 1990; Hickmott and Spear, 1992; Dahl et al., 1993; Lanzirotti, 1995; Schwandt et al., 1996; Spear and Kohn, 1996; Bea et al., 1997; Chernoff and Carlson, 1999; Pyle and Spear, 1999; Pyle and Spear, 2000). In this study, trace element zoning is investigated by integrated electron microprobe and LAM-ICP-MS techniques to provide additional constraints on metamorphic processes in greenschist- to upper amphibolite-facies pelites and calc-pelites from Gagnon terrane.

Garnets from a wide range of bulk compositions and metamorphic grades are the most frequently studied zoned porphyroblasts (e.g., Tracy, 1982; Loomis, 1983; Spear and Selverstone, 1983). In this study, in addition to garnet, we analyzed trace element zoning in kyanite, epidote-group minerals, and apatite to provide constraints on the interpretation of trace element zoning in garnet. In Gagnon terrane, kyanite is a major refractory mineral in the St-Ky zone and above and contains significant amounts of Sc, V and Cr (see Chapter 2). In calc-pelitic rocks, epidote and clinozoisite are important sources of REE, Y, Zr and Sc (Hickmott and Spear, 1982; Chapter 2). In addition to these epidote-group minerals, Mn-rich epidote (piemontite) and allanite also occur in Gagnon terrane, where they are locally important reservoirs for Mn and Ce. It has been suggested that in metapelitic rocks, apatite may be the best trace phase for the study of REE distributions between minerals during metamorphism. For example, Bingen et al. (1996) reported that, for quartzofeldspathic gneiss, the contribution of apatite to the whole rock budget for most trace elements is higher than those of feldspar, biotite, and zircon except

for, U, Eu and La which are more abundant in zircon (U) and feldspars (Eu, La).

Because a number of trace minerals can be dated isotopically, especially monazite and zircon, the participation of trace minerals in metamorphic reactions has an important bearing on attempts to determine the age of metamorphism. An understanding of the petrology of trace minerals therefore holds promise, not just for dating an episode of metamorphism, but also for developing a chronology of specific chemical processes during metamorphism. However, the behaviour of trace phases during regional metamorphism, as well as the petrological relationships between trace phosphate minerals such as xenotime, monazite and apatite and the principal silicate minerals, are poorly documented in crustal conditions. In Chapter 7, the relationships between garnet, apatite and epidote-group minerals are investigated and the implications of P zoning in garnet and Y zoning in apatite are discussed.

## 5.2 The scale of equilibrium

Geothermometry, geobarometry, modelling of fluid-rock interactions, and modelling of garnet zoning all assume chemical equilibrium between rims of coexisting metamorphic minerals. However, equilibrium between coexisting minerals during prograde metamorphims is not a fully evaluated assumption in metamorphic petrology.

Attainment of local chemical equilibrium between grain rims during prograde metamorphism is indicated by the following: (1) phase equilibria studies of natural assemblages in restricted geologic regions that are commonly interpretable in a consistent

manner in terms of facies-series, particularly if the chemical potentials of fluid species are internally buffered (Rumble et al., 1982; Spear, 1982); (2) thermobarometric studies from restricted areas that yield internally consistent *P-T* conditions (Hodges and Spear, 1982; Bohlen et al, 1985; Hodges and McKenna, 1987); (3) isograds and calculated metamorphic temperatures are often progressively and regularly distributed within regional and contact metamorphic terranes; and (4) textural equilibrium is attained in many metamorphic samples (Zen, 1963). Metapelitic and quartzofeldspathic rocks from Gagnon terrane show all of the above equilibrium features (van Gool, 1992). However, these equilibrium features do not automatically guarantee equilibrium trace element partitioning between coexisting minerals if the behaviour of particular trace elements during metamorphic processes is sluggish.

Disequilibrium in metamorphic systems has been documented extensively in contact metamorphosed pelites (e.g., Chinner, 1962; Loomis, 1982; Loomis, 1983; Hickmott and Shimizu, 1990), carbonate rocks (Joesten, 1974) and in blueschists and coronitic eclogites (e.g., Tribuzio et al., 1995). Loomis (1982) related the inverse correlation between bulk rock Mn content and $X_{Sps}$ in garnet cores to a reaction-controlled growth model in which nucleation of garnet was delayed to a temperature higher than equilibrium growth conditions. Hickmott and Shimizu (1990) suggested that entrapment of trace elements could occur at the interface of garnet during episodes of rapid garnet growth on the basis of Ti and Na zoning. Documented occurrences of prograde chemical disequilibrium are few in regional metamorphic rocks, although Chernoff and Carlson (1997) and Chernoff and Carlson (1999) interpreted non-equilibrium behaviour of Ca and several trace

elements during prograde regional metamorphism.

It is also important to define the scale of equilibrium during metamorphism. The preservation of distinct sedimentary layering on the cm scale up to amphibolite-facies conditions (Carmichael, 1969) suggests that the distances of material transport are less than a few mm or cm. A much smaller scale of equilibrium is indicated by Chernoff and Carlson (1997) and Kretz et al. (1999). This scale problem is particularly acute for trace-element-enriched trace minerals such as zircon, xenotime and monazite because of their poorly known behaviour during metamorphism. The chemical system of interest is defined in this study as the effective bulk composition (EBC) that chemically communicates with the surface of a growing mineral over a specific time interval (Hickmott et al., 1987). Such a system does not necessarily equal the total mass of all elemental components in a hand sample if the interior of a zoned mineral is not part of the equilibrating metamorphic system, or if certain trace phases are shielded from reaction within porphyroblasts.

## 5.3 Processes controlling trace element zoning

Understanding trace element zoning in metamorphic systems is complicated by the number of variables to be considered. Element distributions between coexisting minerals are governed by thermodynamic, kinetic and system factors. Under equilibrium conditions, the trace element abundance (C) at the surface of growing garnet is given by

$$C = D_o \times C_o \qquad (5.1)$$

where $D_o$ is the bulk partition coefficient and $C_o$ is the EBC in equilibrium with the garnet rim, and

$$D_o = \Sigma X_i D_i \quad (5.2)$$

where $X_i$ is the weight mode of phase $i$ in equilibrium with garnet, and $D_i$ is the mineral-mineral partition coefficient. Eq. (5.2) implies that the bulk partition coefficient is a function of pressure, temperature, garnet composition, and the nature and abundance of minerals coexisting with garnet. Pressure effects on $D_i$ may be small because of the generally small variation in volume of trace element substitutions into silicates (McIntire, 1963). Changes in the distribution coefficients with temperature make useful thermometers (e.g., Kretz, 1961; McIntire, 1963, Heinrich et al., 1997: Pyle and Spear, 2000). However, additional complexity may arise in cases where major element solid solution occurs, such that the crystal chemical changes associated with major element substitution affect other major and trace element distribution coefficients. For example, Ca and Mn substitutions into Fe-Mg garnet change the activities of Fe and Mg, thereby changing the distribution coefficients and the calibration of the garnet-biotite geothermometer (Ganguly and Saxena, 1984; Williams and Grambling, 1990).

Both the $X_i$ and the EBC are difficult to define for a particular trace element in metamorphic rocks for kinetic reasons. Firstly, the $X_i$ for metamorphic minerals changes during metamorphism as product minerals grow and reactant minerals break down (Hollister, 1969). Furthermore, the effective $X_i$ increases with temperature because of the logarithmic dependence of diffusion coefficients on temperature. At low temperatures, a refractory mineral (defined as a phase in which volume diffusion is slow) may remain as

an inert phase because diffusion coefficients are low enough that virtually none of the mineral reacts with other minerals over reasonable metamorphic time scales. As temperature increases, however, a larger fraction of the refractory mineral can participate in the reacting metamorphic system.

Thus, in addition to thermodynamic considerations, there are kinetic factors to consider. These include the time available for growth, the diffusion rate, and crystal growth rates (Tracy, 1982). Time is important from the standpoint of its availability when considering reaction rates, diffusion rates, and equilibrium/re-equilibration. A disequilibrium zoning profile can be developed when the speed of crystal growth is faster than intercrystalline diffusion of certain elements, or vice versa.

The zoning of an element that exhibits smoothly decreasing, roughly flat, or increasing zoning profiles can probably be explained in terms of equilibrium partitioning models (Hollister, 1966; Cygan and Lasaga, 1982). Elements exhibiting annuli (concentric zones of enrichment or depletion in their profiles) require either: (1) large fluctuations in the bulk partition coefficient, or (2) strong metasomatic enrichment of the EBC, over a narrow growth interval.

These thermodynamic, kinetic and system factors are addressed below. It is important to note that these processes are not independent of each other; several may operate together, or in different samples, from the same metamorphic terranes.

### 5.3.1 Rayleigh fractionation

Rayleigh fractionation models assume equilibrium partitioning of elements between

a mineral rim and matrix minerals during mineral growth. Examples of such models include one-stage, isothermal, Rayleigh fractionation models (Hollister, 1966); multi-stage, polythermal, Rayleigh fractionation models (Atherton, 1968); fractionation models that allow bulk distribution coefficients to be a function of *P-T* and composition (Cygan and Lasaga, 1982), and equilibrium thermodynamic models such as those of Loomis and Nimick (1982) and Spear (1993).

Simple Rayleigh fractionation is an idealized process requiring constraints such as: (1) mass balance within a closed system, (2) constant partitioning during the modelled process, and (3) complete removal of the fractionating element from the reacting system by mineral growth processes. However, it has been widely used to model mineral zoning in metamorphic rocks (Hollister, 1966; Atherton, 1968; Tracy, 1982; Hickmott and Shimizu, 1990; Pyle and Spear, 1999). The simple Rayleigh fractionation equation is (Hollister, 1969):

$$C_i = \lambda C_o \left(1 - \frac{W_i}{W_o}\right)^{\lambda - 1} \tag{5.3}$$

where $W_i/W_o$ is the weight-fraction of the mineral grown, and the rest of symbols are as defined above.

Simple Rayleigh fractionation occurring in a closed system and constant *P-T* yields continuously decreasing core-to-rim profiles for compatible elements, flat profiles for elements with bulk distribution coefficients near unity, and profiles with a slight increase at the rims for incompatible elements (Fig. 5.1). Hickmott and Shimizu (1990) concluded that simple Rayleigh fractionation was not a valid model for trace element zoning in most

metamorphic environments. However, it may provide the best approximation available for modelling short periods of mineral growth because mineral assemblages, the scale of equilibrium, and bulk partition coefficients may not change greatly during such a small growth interval. This hypothesis is exercised in Chapter 7 for REE zoning in garnet. Rayleigh fractionation may be an important control on trace element zoning in garnets from Gagnon terrane, where refractory minerals such as epidote-group minerals, staurolite, kyanite, and ilmenite occur.

### 5.3.2 Breakdown/growth of trace element-enriched phases

Breakdown or growth of refractory minerals enrich or deplete the EBC in trace elements compatible in the refractory mineral; the effect can be complex, particularly if the refractory mineral is itself zoned in trace elements (Hollister, 1969; Kretz, 1973; Hickmott et al., 1987; Hickmott and Spear, 1992). Garnet, plagioclase, epidote-group minerals, ilmenite, staurolite, and trace phases such as zircon, monazite, xenotime and apatite are all refractory minerals in amphibolite facies rocks. Their breakdown or growth will provide distinctive trace element signatures to growing garnet. Applying these relative enrichments/depletions of trace elements between metamorphic minerals to garnet-forming reactions, Hickmott and Spear (1992) and Spear and Kohn (1996) predicted the trace element effects of garnet growth along specific *P-T* paths.

The behaviour of trace minerals during prograde metamorphism is not well known. If the trace minerals are inert, they do not interact with a reacting metamorphic system due to sluggish intra-mineral, surface kinetic, or intergranular kinetic effects. However,

mapped allanite-in and monazite-in isograds demonstrate that trace minerals are not necessarily inert during metamorphism, but may be active participants in prograde mineral reactions (Ferry, 2000). Progressive changes in the chemical composition of apatite and monazite with metamorphic grade also imply that reactions between these trace minerals and major minerals and, where present, a melt, took place under equilibrium conditions (Bea and Montero, 1999). Equilibrium participation of xenotime in garnet-forming reactions was demonstrated by Y activity in garnet buffered by coexisting xenotime (Pyle and Spear, 1999). However, large variations (>10 times) in the abundance of Zr in garnets correlated with the breakdown of clinozoisite (Hickmott et al., 1987) suggest that zoning for trace elements does not solely reflect equilibrium with trace-element saturating phases. If Zr activity in the garnet was buffered by zircon, a smaller range of Zr abundance would be expected.

### 5.3.3 Resorption and regrowth

Garnet-compatible elements can be enriched in garnet by either: (1) resorption of garnet followed by re-incorporation of garnet-compatible elements during a second garnet growth episode, or (2) passive enrichment when there are no phases capable of incorporating the garnet-compatible elements. These processes were used to explain Y annuli in metapelitic garnets (Pyle and Spear, 1999). They attributed the Y annuli in garnet to be a result of garnet resorption during staurolite-forming reactions, which is compatible with the occurrence of Y annuli in garnets from staurolite and higher zones in their samples. These processes should produce irregular and discontinuous annuli with a

steeper slope on the inner side of the zoning profile (Fig. 5.2), although the occurrence of resorption parallel to crystal outlines of garnet was indicated by Pyle and Spear (1999). In contrast to garnet-compatible elements, garnet-incompatible elements would be depleted during resorption.

### 5.3.4 Variations in *P-T*

Mineral/mineral distribution coefficients, and therefore bulk distribution coefficients, vary as a function of pressure and temperature for all trace elements (see Eq. 5.1 and 5.2), but are most easily interpreted for elements that are essential structural constituents of phases coexisting with garnet (Hickmott et al., 1987). For instance, in the case of a crystallizing igneous system containing rutile, zircon and apatite, the activities of Ti, Zr and P are buffered in evolved igneous melts (Harrison and Watson, 1985). Similarly, the activities of these elements and Y may be buffered in metamorphic systems by equilibria with phosphates (apatite, monazite, xenotime), Fe-Ti oxides (rutile and/or ilmenite) and zircon. Thus, equilibrium partitioning of these elements between garnet and matrix minerals has the potential to be a monitor of *P* and *T* but is also a function of whole-rock bulk composition. In addition, non-ideal solution effects associated with changes in the major element compositions of the minerals involved in buffering equilibria must be evaluated before they can be used as thermobarometers (Kretz, 1959). An additional complication is the poorly known nature of P, Ti, Zr and Y substitutions into metamorphic garnets.

Previous studies of trace element zoning in garnet have suggested that Ti-solubility

in garnet decreases with decreasing pressure and increasing temperature in ilmenite-bearing assemblages (Hickmott et al., 1987) and that Y activity in garnet decreases with increasing temperature (Pyle and Spear, 2000). Turning to P and Zr incorporation in garnet, it has been observed that apatite, in contrast to zircon, commonly displays a rounded habit indicating that grain boundary migration occurred during metamorphism and deformation (Rubatto et al., 2001), implying faster equilibration of apatite than zircon. Phosphorus-bearing garnets have mostly been reported from mantle xenoliths, and the P content in garnet has been considered to have potential as an indicator of pressure (Thompson, 1975). A coupled P substitution in garnet such as $PNaSi_{-1}Ca_{-1}$ has been proposed based on correlation between Na and P in garnets from high pressure rocks. However, high concentrations of P have also been reported in spessartine-rich garnets from pegmatite (Wise, 1994; Taylor et al., 1997b), and the absence of Na in these pegmatitic garnets indicates that P substitution in garnet under low pressure conditions is different from that under high pressure conditions.

The incorporation of other elements into garnet will also show temperature and pressure dependence; however, these will vary markedly from assemblage to assemblage. These potentially buffered elements can also be used to infer disequilibrium partitioning during garnet growth (Hickmott and Shimizu, 1990).

### 5.3.5 Disequilibrium partitioning

The processes involved in the nucleation and growth of porphyroblasts during metamorphism have been discussed in numerous studies (e.g., Kretz, 1973; Finlay and

Kerr, 1987; Cashman and Ferry, 1988; Carlson, 1989; Kretz, 1993; Carlson et al., 1995; Danison and Carlson, 1997; Daniel and Spear, 1999). Several processes are involved in the growth of a new mineral. Given some finite amount of reaction overstepping, the rate-limiting processes include: (1) the dissolution of reactant minerals, (2) the nucleation of the new phase, (3) transportation of materials to the nucleus and removal of excess materials, and (4) incorporation of the materials into the growing phase at the crystal-matrix interface. In addition to these, Fisher (1978) proposed heat flow as another possible rate-limiting process in porphyroblast growth.

Rates of dissolution or growth are not rate-limiting except under exceptional circumstances (Walther and Wood, 1984), and heat flow is more likely to control the total amount of garnet produced in a rock rather than controlling crystal growth rates (Daniel and Spear, 1999). There are three mechanisms by which material can move along grain boundaries to the site of mineral growth: (1) bulk flow of a grain boundary fluid containing dissolved solutes, the most effective way, (2) diffusion of solutes through a grain boundary film, and (3) grain boundary diffusion through the surfaces of the minerals constituting the matrix. Diffusion through a fluid film is controlled by the solubility of the solute in the bulk fluid and its diffusivity in that fluid. Grain boundary diffusion involves diffusion through the outermost disorganized layers of the solid minerals (~10 Å in thickness, Mistler and Coble, 1974) and does not require solution in the fluid phase.

Obvious deviations from homogeneous equilibrium in minerals such as overprint zoning (Ca in plagioclase, Menard and Spear, 1996; Mn in garnet, Spear and Daniel,

2000), Cr in garnet (this study, Chapter 6), oscillatory zoning (Cr in lawsonite, Sherlock and Okay, 1999) and sectoral zoning in staurolite, point to kinetic controls on element uptake. Two groups of disequilibrium partitioning models during transportation of materials to the growth sites are described below: diffusion-controlled partitioning models and interface-controlled partitioning models.

***Diffusion-controlled models:*** Relative to simple Rayleigh fractionation, matrix diffusion-controlled disequilibrium partitioning produces drop-offs in compatible elements in a growing porphyroblast due to near-rim solute depletion, and enrichments in incompatible elements due to solute rejection (Albarède and Bottinga, 1972). Thus, in this model, the concentration of an element in the matrix in equilibrium with the surface of the crystal differs from that in the bulk matrix. These enriched/depleted zones in the matrix, subsequently enlarge, impinge and ultimately coalesce. Under the diffusion-controlled growth model, the growth rate of a crystal will be limited by the rapidity with which material can diffuse across the depleted zone. When depleted zones coalesce, competition among adjacent porphyroblasts for available garnet-forming elements may lead to a decrease in the instantaneous and overall growth rates of closely adjacent crystals (Carlson, 1989).

A simple diffusion-controlled growth model was applied to garnets from contact metamorphic rocks (Hickmott and Shimizu, 1990) using the differential equation for concentration in a growing mineral as a function of grain size (Shimizu, 1983) and is reproduced here as Fig. 5.3. Their isothermal model assumes that transport of material to

the interface is matrix diffusion-limited, that the radius of curvature of a growing grain is large enough that a one-dimensional model can be used, that the matrix diffusion coefficient has a constant value that is much larger than the diffusion coefficient in the growing mineral, and that growth is at a constant velocity. This simple diffusion-controlled growth model implies that incompatible elements decrease and compatible elements increase with decreasing growth velocity to a degree larger than simple Rayleigh fractionation (Fig. 5.3). Elements which have very large, or very small, equilibrium partition coefficients will be more readily discernible. Compatible element are more sensitive (by a factor of 100) to slow growth velocities than incompatible elements. There is a paucity of data on the diffusion rates of trace elements in metamorphic systems, but published results (e.g., Spear and Kohn, 1996; Chernof and Carlson, 1999) suggest that the diffusion rates of highly charged, incompatible cations (e.g. REE) are relatively slow and so their distributions are the most likely to be affected by variations in mineral growth rates.

Garnet growth dominated by diffusion-controlled disequilibrium would show enrichment of compatible elements (Y, HREE) and concomitant depletion of incompatible elements (V, Co, LREE) during episodes of reduced mineral growth. The diffusion-controlled growth model indicates much more significant enrichments of compatible elements than depletions of incompatible elements at the grain margin as a result of reduced growth rate (Fig. 5.3).

Hickmott and Shimizu (1990) used a dimensionless number ($Vx/D_m$) to estimate the circumstances in which matrix diffusion-controlled partitioning could be significant

during the metamorphic processes. Using various reported values of grain boundary diffusion coefficients ($D_m$) and crystal growth rates (V) ranging from contact metamorphism to regional metamorphism, and a distance (x)of mineral growth at growth velocity V, they concluded that matrix transport-controlled, disequilibrium trace element zoning in garnets is unlikely to be an important process in prograde regional metamorphic environments unless growth rates are rapid or diffusional transport is as slow as anion transport under dry conditions.

***Solute trapping of interface segregants:*** Interface-controlled disequilibrium leads to enrichment of small highly-charged cations such as Ti and Zr in growing porphyroblasts (Hickmott et al., 1987). Grain-boundary enrichment is well documented in ceramics, metals, and semiconductors (Blakery, 1979; Kingery et al., 1976; Li and Kingery, 1984; Kingery, 1984), but geological systems are sufficiently complex in their chemical compositions and phase relations to make unambiguous identification of this phenomenon extremely difficult. Geologic evidence for grain boundary enrichment, although sparse, comes in both circumstantial and direct forms (Dowty, 1976; Shimizu, 1981; Hickmott and Shimizu, 1990; Reeder, 1991; Staudt et al., 1994; Watson and Liang, 1995). Sector zoning in metamorphic minerals such as staurolite, which grows in intimate contact with other crystalline phases, could be interpreted as circumstantial evidence for grain boundary enrichment (Dowty, 1976), as could the unusual trace element zoning patterns in garnets described by Hickmott and Spear (1990). Direct evidence for the process comes from the enrichment in Al at grain boundaries in dunite and lherzolite

nodules (Waff and Holdren, 1981).

The solute enriched/depleted region in grain interfaces is carried along with the interface during slow crystal growth (Tiller and Ahn, 1980). Beyond a critical growth velocity, impurity atoms located on a grain surface cannot equilibrate with their growth environment prior to attachment of a new lattice plane, resulting in entrapment of interface segregants. The potential geologic significance of the competition between crystal growth rate and lattice diffusion was recognized by Hollister (1970), who hypothesized that surface enrichment coupled with slow lattice diffusion might lead to sector zoning. Hickmott and Schimizu (1990) used the same growth/diffusion competition as a possible explanation for unusual REE zoning patterns in garnets from contact-metamorphic rocks.

Tiller and Ahn (1980) formulated a dimensionless parameter $V\delta/D$, in which V is the linear growth rate of the crystal, $\delta$ is the thickness of the interface layer, and D is the diffusivity of the element in the near-surface region of the crystal, to determine the metamorphic environments in which interface solute segregants will be entrapped in growing metamorphic minerals. To attain equilibrium, cations must be able to migrate through the interface region of thickness $\delta$ more rapidly than mineral growth traps the interface solute. Thus, there will a critical interface velocity at which communication between bulk matrix and growing solid is lost, and interface solute trapping becomes important.

Despite the paucity of information on V, $\delta$, and D, some generalizations were made concerning natural systems and the circumstances conducive to growth entrapment by

Hickmott and Shimizu (1990). They developed a plot for metamorphic processes (log Vδ/D vs. 1/T) from which they concluded that most contact metamorphic events result in trapping of interface-enriched elements, whereas regional metamorphism can lead to trapping only at relatively low temperatures (e.g. 400°C) or unusually high crystal growth rates. Watson (1996) improved the Hickmott-Shimizu diagram by taking into account the improved constraints on the value of Vδ/D required for growth entrapment to occur, and more recent diffusion data. He concluded that whenever surface enrichment occurs at relatively low temperature (below ~700°C), growth entrapment is likely, especially for sluggish diffusants like the REE. High-temperature growth of crystals from a melt (above ~1000°C) is generally immune to lattice entrapment.

***Summary:*** A number of investigators have examined the spatial distribution, compositional zoning profiles, and/or size distributions of porphyroblasts to reach conclusions about the processes involved in their crystallization. Kretz (1966, 1969) and Daniel and Spear (1999) found no statistically significant departure from randomness in the distribution of garnet in metamorphic rocks, and likewise found no significant correlation between crystal radii and nearest-neighbor distances, implying interface-controlled reaction mechanisms. Although Chernoff and Carlson (1997, 1999) inferred diffusion-controlled incorporation of Ca and trace elements into metapelitic garnets during prograde regional metamorphism, unequivocal evidence for diffusional controls on crystallization mechanisms is restricted to results from corona structures (e.g. Whitney and McLelland, 1973; Foster, 1981; Grant, 1988). Growth controlled by intergranular

diffusion or by interface reaction will display an exponential dependence of rate upon temperature, because both mechanisms are thermally activated, driven by variations in the chemical affinity of the reaction.

Given the diversity of metamorphic conditions in nature, it is not unreasonable to suppose that diffusional kinetic controls may be dominant in certain metamorphic environments, whereas interface-controlled or heat-flow-controlled kinetics are dominant in others. In fact, the suggestion has been made that both interface-controlled and diffusion-controlled mechanisms operate, for different reactions, during some crystallization episodes (e.g., Tracy and McLellan, 1985), and that the rate-controlling processes may be different in early, middle, and the late stages of a crystallization episode (Fisher, 1978; Ridley and Thompson, 1986). Fisher (1978) predicted that first interface, then diffusional, and finally heat-flow controls would be dominant. It is also possible that different models may apply to different elements. Thus, examining a wide variety of trace elements ranging from compatible to incompatible may allow evaluation of the most important controls on trace element distributions during garnet growth.

### 5.3.6 Open system behaviour

Understanding the zoning of trace elements in metamorphic systems is also dependent on the definition of the thermodynamic system, whether open or closed. In many studies of garnet zoning, metamorphism of pelites has been considered to be isochemical for major elements other than the volatile constituents $H_2O$ and $CO_2$ (e.g., Shaw, 1956), although a few studies (e.g., Ferry, 1983) demonstrate substantial alkali

metal mobility.

Major elements are not good indicators of open system behaviour during metamorphism of chemically complicated bulk compositions such as pelites. Infiltration of a cation-rich fluid merely changes the modal abundance of the minerals in the rock, and does not change the chemistry of the minerals. On the other hand, the abundance of trace elements is controlled by the EBC, which can be modified by the introduction of a pulse of trace element-enriched fluid or by the breakdown of a trace element-rich refractory mineral (Hickmott et al., 1987; Lanzirotti, 1995).

Hickmott et al. (1987) referred the latter process as internal metasomatism and the former process as external metasomatism. External metasomatism of a fluid out of trace element equilibrium with the mineral assemblage of the rock produces enrichments or depletions in major and trace elements in growing porphyroblasts (Hickmott et al., 1987; Young and Rumble, 1993; Chamberlain and Conrad, 1993; Jamtveit and Hervig, 1994). Such open-system behaviour may most strongly affect trace element zoning for alkali metals that probably have high solubilities in high temperature fluids (Eugster, 1981). Internal metasomatism, on the other hand, enriches the EBC in elements that are compatible in refractory minerals broken down during metamorphism. A refractory mineral that grew in a closed system prior to garnet would probably exhibit core to rim elemental depletions in garnet-compatible elements due to rim re-equilibration after growth, whereas a refractory mineral that grew during garnet growth would exhibit the same core to rim elemental depletions as garnet.

### 5.3.7 Crystal chemical effects

The incorporation of minor and trace elements into a mineral structure is, at least in part, dependent on the composition of the mineral, as this modifies the crystal structure (Novak and Gibbs, 1971). For example, the dodecahedral X-site in garnet is larger in grossular than in pyrope. The increase in the size of this 8-coordinated site with calcium content favours incorporation of the REE, especially the larger LREE, into the garnet structure (Schwandt et al., 1993). Similar correlations of REE content with Ca content have been observed in pyroxene (Shearer et al., 1989) and in pyroxene element-partitioning experiments (McKay, 1989). In Ca-rich rock compositions, however, Hickmott and Spear (1992) observed both positive and negative correlations of REE content with the grossular component of garnet, depending on the bulk-rock composition and the presence of trace element-rich phases such as clinozoisite.

Garnet-melt partition coefficients for a series of isovalent cations show a near-parabolic dependence on cation radius, demonstrating the influence of cation charges and ionic radii on trace element partitioning (Liu et al., 1992; van Westrenen et al., 1999). Van Westrenen et al. (1999) reported a strong dependence of distribution coefficients between garnet and melt with variation in $X_{Prp}$ (=Mg/Mg+Ca) in garnet. For example, distribution of La between garnet and melt changes from 0.004 to 0.2 as $X_{Prp}$ varies from 84 to 9. Harte and Kirkley (1997), in their study of eclogite xenoliths, provided data on garnet-clinopyroxene partition coefficients as a function of garnet composition in the range from $X_{Grs}$=8 to $X_{Grs}$=50. They observed an increase up to three orders of magnitude in the distribution coefficient of LREE with increasing grossular component while the

distribution coefficients of HREE remained approximately constant.

Crystal chemical effects can be expressed in the form of coupled substitutions, which may lead to complementary variations in trace elements that charge-balance each other's entry into a mineral structure. For example, if Na+Ti=Ca+Al (the Ti-plagioclase substitution) is the primary Ti-substitution in garnet (Ringwood and Major, 1971), then concomitant increases and decreases in Na and Ti abundance may be expected (Dowty, 1971).

### 5.3.8 Diffusional reequilibration

Element zoning can be modified by intracrystalline diffusion, or post-growth intercrystalline diffusion at sufficiently high temperature and with sufficient time (Spear, 1988). Tracy et al. (1992) inferred from garnet in amphibolite-facies rocks that Ca diffusion was slower than diffusion of Mg, Fe, and Mn. Schwandt et al. (1996) experimentally determined that Ca self-diffusion in grossular is about one and one-half orders of magnitude slower than Mg self-diffusion in pyrope. This demonstrates that mineral composition is an important parameter when considering diffusion and that larger cations tend to diffuse more slowly than smaller cations. Because the trivalent REE are larger than the divalent cations they substitute for (Shannon and Prewitt, 1969), their zoning profiles are unlikely to have been affected by diffusional homogenization.

Because of the complexity of the diffusion problem involved in re-equilibration of a retrograded garnet, we use a simple model that may provide insights into the diffusional re-equilibration of cooling garnets,

$$X = \sqrt{4Dt} \tag{5.4}$$

(Crank, 1975), to estimate the characteristic diffusion penetration distance ($X$) for a range of time scales ($t$) in retrograding environments. Using the Mg self-diffusion coefficients of Schwandt et al. (1995) and a temperature of 600°C, maximum diffusion distances range from 0.6 μm for $10^5$ year to 5.7 μm for $10^7$ year. Using the Ca self-diffusion data of Schwandt et al. (1996), the maximum diffusion distances are even smaller. Therefore, even with long periods of elevated temperature, the distances over which diffusional reequilibration may have taken place are probably small. The slow diffusion of trace elements in garnet is indicated by preserved sharp peaks in trace element zoning profiles near rims of garnets from upper amphibolite facies (e.g. Spear and Kohn, 1996).

The extent of re-equilibrium is strongly dependent on kinetic factors affecting the matrix around garnets, particularly the availability of fluids to drive retrograde net-transfer reactions, the ion flux during retrogradation, and the presence or absence of deformation.

The existence of strong REE variations in amphibolite- and granulite-facies garnets with unzoned major element profiles confirms the sluggish nature of self-diffusion of REE in garnet up to upper amphibolite facies (Hickmott et al., 1987; Hickmott and Spear, 1992; Lanzirotii, 1995; Pyle and Spear, 1999).

### 5.3.9 Polymetamorphism

Polymetamorphism involving multiple episodes of garnet growth in distinct *P-T* environments may impart abrupt breaks to garnet zoning profiles under mid-amphibolite

facies conditions (Rosenfeld, 1968; Thompson et al., 1977; Karabinos, 1984; Rumble and Finnerty, 1974). De Lima et al. (1995) investigated trace element zoning in garnets from polymetamorphosed pelites. Inflections in the zoning of Ti, V, Cr, Y and $Eu/Eu^*$ and a hump in Sc coincide with a second episode of garnet growth. If resorption follows initial garnet growth then characteristic annuli in garnet-compatible elements (Mn, Y, HREE) may be observed (Fig. 5.2). This suggests that the textural and major element profiles, together with trace element profiles, can be used to constraint episodes of polymetamorphism and/or renewed garnet growth.

## 5.4 Analytical techniques

Determination and resolution of chemical zonation in minerals requires microbeam analytical techniques. The samples were chosen on the basis of petrographic and preliminary electron microprobe study; maximum effort was focused on garnet-bearing, low variance assemblages containing Ca-rich phase inclusion suites within garnet porphyroblasts. In an attempt to obtain central-section zoning profiles and maps of garnets, the largest garnet in each thin section was analyzed; however, this method does not guarantee a garnet center section.

### 5.4.1 EMP analyses

Major element compositions (P, Si, Al, Fe, Mg, Mn, Ca) of garnet, kyanite, apatite and epidote-group minerals were determined by energy-dispersive X-ray analysis using a

Link ED detector. Analytical conditions included an accelerating potential of 15 kV and a beam current of 10-20 nA, focused to 1-5 μm in diameter. Counting times were 60-120 sec on the samples. The precision of the analyses was generally better than 3% RSD for the major elements.

Apparent element % of Ti, P, and Y in garnet and Y in apatite and epidote-group minerals were determined by wavelength-dispersive X-ray analysis using the Cameca SX-50 electron microprobe. Operating conditions for garnet analyses included an accelerating potential of 15 kV, a beam current of 300 nA, a beam size 3 μm in diameter, and 60 sec counting times for garnet and epidote-group mineral analyses, whereas for apatite analyses an accelerating potential of 15 kV, a beam current of 20 nA, a beam diameter of 10 μm, and counting times of 120 sec were used. Elemental peaks were measured and standardized using ilmenite (Ti), apatite (P), xenotime (Y) and spessartine (Mn) as standards. Although absolute concentrations of trace elements were not calculated, relative variability of elements across garnet and apatite porphyroblasts provides significant petrologic information. Repeated analyses of an almandine standard revealed that the precision was better than 10% RSD for Ti and 3 % RSD for P and Y.

Digital X-ray mapping of garnets in 10 samples for Fe, Mg, Mn, Ca, P, Cr and Y and of kyanite in two samples for Al, Fe and Cr was carried out with the automated mapping program *MAP* (for details of the program *MAP*, see Appendix). Operating conditions for X-ray mapping included an accelerating voltage of 15 kV and a beam current of 50~100 nA for major elements, and 20 kV and 500~700 nA respectively for trace elements, with dwell times of 0.2~0.7 sec/pixel, and a beam size of 18~56 μm. The trace minerals were

examined using a SEM in BSE mode. Chemical characterization was aided by qualitative energy dispersive X-ray microanalysis performed with a Link systems 860 X-ray microanalyser attached to the SEM.

### 5.4.2 LAM-ICP-MS

Absolute concentrations of Li, P, Sc, Ti, V, Cr, Co, Zn, Rb, Sr, Y, Zr, Nb, Cs, Ba, Hf, Ta and REE were analyzed in garnet, kyanite, biotite, epidote and apatite using the LAM-ICP-MS. A complete account of the characteristics and the optimization of this instrument is reported elsewhere (Taylor et al., 1997a; Yang et al., 1999; Yang and Rivers, 2000). The combination of a Q-switched UV laser and the optimization of the laser parameters provides a high spatial resolution (10 μm in diameter). However, in order to achieve a balance between spatial resolution and detection limits, the pit size was set at 30~40 μm. This permitted the determination of element concentrations down to few micrograms/gram (ppm) for light elements.

The LAM-ICP-MS concentration values for garnet zoning profiles were calculated using Si data obtained by electron microprobe as an internal standard, because of strong Ca zoning in several garnets. This results in slightly poorer accuracy (2-5% RSD at 1σ) in the determination of trace elements than using Ca as an internal standard. However, it provides more accurate patterns of zoning profiles because there is no zoning in the element used as an internal standard. The error bars on the LAM-ICP-MS analyses do not take into account the precision on the electron microprobe determination (estimated at 2% RSD for Si) by error propagation. Analysis spots along each laser traverse were

spaced from 30 to ≥100 μm apart because of time limitations and the presence of inclusions. Thus, WD profiles give more detailed zoning patterns for Y, Ti, and P. Analysis spots with high P, Ti, Zr or Si counts, presumably indicating the incorporation of inclusions, were eliminated from the data sets.

## 5.5 Sample description

### 5.5.1 Major minerals

Garnets from the staurolite+kyanite and higher zones commonly show inclusion zoning, with inclusion-rich cores enclosed by inclusion-poor rims. The inclusion-rich cores are euhedral, indicating that they are of growth origin. In contrast, some garnets from the migmatite zone are characterized by oscillatory textural zoning (i.e., alternating inclusion-rich and inclusion-free zones). In both cases, formation of the inclusion-rich zones was possibly due to a delay in the onset of garnet growth, followed by a period of very rapid growth with significant trapping of inclusions. As the compositions of the minerals approached their equilibrium compositions due to mass transport, the affinity of the reaction decreased, the garnet growth velocity slowed, and the incorporation of inclusions diminished. It is postulated that, at the second or subsequent inclusion-rich zones the affinity of the garnet growth reaction again increased abruptly, and rapid growth, accompanied by significant inclusion trapping reccurred. The nature of the event that initiated the second episode of rapid growth is not well constrained. This hypothesis, that changes in growth rates in garnet caused the oscillatory textural zoning, is discussed

further in Chapter 7 using information from major and trace element zoning.

Garnets from the garnet+biotite zone are generally small (< a few mm in diameter) and show euhedral crystal outlines with no significant resorption at their margins. In contrast, garnets occurring in the staurolite+kyanite zone and above are mostly larger than those of garnet+biotite zone (up to a few cm in diameter) and show variable degrees of resorption. In the migmatite zone, a retrograde reaction responsible for the partial resorption of most garnets is:

$$Grt + Ms + H_2O = Pl + Bt + Qtz \quad (5.5)$$

as indicated by muscovite depleted zones with randomly oriented biotite and plagioclase around garnet porphyroblasts. Resorption does not appear to be related to metamorphic grade. The resorption at the margins of garnets makes the estimation of peak metamorphic *P-T* and peak equilibrium trace element partitioning coefficients difficult. However, resorption of garnet is commonly incomplete around a single grain and in most cases, non-resorbed rims are partially preserved. The patterns of inclusion-rich cores, contacting minerals, the shapes of crystal outlines, and X-ray maps were used to identify relics of non-resorbed garnet rims. The locations of garnet zoning profiles were selected on the basis of these criteria. There is no apparent textural indication of resorption during the growth of the studied garnets despite some mineralogical evidence for such reactions (Chapter 6).

Staurolite occurs as inclusions in garnets in several of the investigated samples. Matrix staurolite in other samples and staurolite inclusions in the investigated garnets do not exhibit sector zoning. The staurolite-forming reaction in the area is not well defined

because of poor exposure and tectonic telescoping of the staurolite zone rocks (van Gool, 1992). Kyanite in the migmatite zone is of two textural types: an early coarse-grained $Ky_1$ and a younger finer grained $Ky_2$. $Ky_1$ appears to be similar to the kyanite occurring in garnet-biotite-kyanite zone, which suggests that $Ky_2$, which only appears in migmatite zone, is formed by the terminal staurolite-breakdown reaction.

### 5.5.2 Trace minerals

Trace minerals are known to play an important role in both garnet zoning and the overall trace element budget (Hickmott, 1987; Hickmott and Spear, 1992; Bea et al.,1994). Epidote-group minerals occurring in Gagnon terrane include epidote, clinozoisite, and allanite. Clinozoisite cores in epidote are observed in the biotite-muscovite zone. Allanite is observed as small (< 40 μm), cores in epidote in one sample from the migmatite zone. Some epidote and allanite are manganoan varieties. Both pistacite and piemontite contents of epidote are up to 13% (Table 5.1). Experimental (Keskinen and Liou, 1987) and petrographic studies (Fukuoka et al., 1990) on piemontite both indicate that, due to the incorporation of $Mn^{3+}$ into the structure, oxygen fugacity is the variable which most strongly determines its stability. For significant amounts of the piemontite component to remain in solid solution, oxygen fugacity should be above that of the haematite-magnetite buffer for the samples containing Mn-rich epidote.

Apatite and zircon are present in all samples. Apatite is the main P carrier in the Gagnon metapelites, with subsidiary xenotime and monazite. Apatite commonly coexists with monazite. Except for apatite occurring in sample 88-88, most apatite crystals are

resorbed. BSE imaging shows grey-level contrasts in apatite, implying a significant difference in composition between core and rim (Fig. 5.4a). Monazite occurs only in rocks above the staurolite-kyanite isograd. Monazite grains are round or irregular-shaped with unzoned rims (Fig. 5.4b). Monazite and allanite do not coexist, supporting the view that monazite is a metamorphic mineral produced by allanite-breakdown reactions (e.g. Smith and Barreiro, 1990; Ferry, 2000).

Zircon grains are rounded and show oscillatory zoning, indicating that they are relics of igneous grains. In addition to the trace minerals described above, graphite, sphene, pyrite, chalcopyrite, magnetite, and carbonate occur as trace minerals in the metapelitic and quartzofeldspathic rocks. These latter phases have not been investigated in detail in this study.

## 5.6 Trace element constraints on garnet growth reactions

Major element zoning provides first order constraints on metamorphic reaction histories, and trace element zoning provides additional constraints that may be used to refine these histories (e.g. Hickmott and Spear, 1992). Although the details of major element zoning in garnets from Gagnon terrane depend on the mineral assemblages and *P-T*, garnets porphyroblasts commonly have high-Mn and -Ca cores, and are zoned toward lower Fe/Fe+Mg from core to rim (van Gool, 1992). The common occurrence of high-Mn cores in the garnets reflects the high compatibility of Mn in garnets (Hollister, 1969) and the general absence of Mn-bearing minerals other than garnet. However, a

number of garnets are anomalous in terms of Mn zoning, with Mn increasing midway between core and rim. The origin of this Mn zoning pattern is discussed in Chapter 7. Most of the garnets investigated exhibit a variable degree of near-rim Mn enrichment, compatible with limited garnet resorption.

Decreasing Fe/Fe+Mg toward the rim represents the operation of garnet-biotite-chlorite reactions in most amphibolite facies rocks. Ca zoning is variable from sample to sample because of variable bulk CaO contents of the samples and the growth/breakdown of calcic phases such as epidote during garnet growth. Ca growth zoning patterns were divided into four types (van Gool, 1992): Type 1 - essentially unzoned Ca; Type 2 - unzoned core with slightly increasing Ca near the rim; Type 3 - weakly decreasing then weakly increasing Ca near the rim; Type 4 - unzoned core with decreasing Ca near the rim. Garnets in equilibrium with epidote are enriched in the grossular component (> 0.2) and the Ca content drops abruptly after breakdown of epidote, resulting in the type 4 Ca zoning pattern. Retrograde, near-rim low Ca re-equilibration is locally superimposed on the above growth zoning in the samples.

If reacting metamorphic minerals have different characteristic trace elements, variation in these elements can be used to interpret the reaction histories of metamorphic assemblages during metamorphism, and hence the *P-T* paths experienced by the rocks. Trace element compatibilities in metamorphic minerals relative to garnet were reviewed for each mineral in Chapter 1 on the basis of trace element determinations on mineral separates and published micro-beam analyses of single grains, and in Chapter 2 on the basis of LAM-ICP-MS analyses made during the course of this study. Some

generalizations about the trace elements in selected refractory minerals relevant to this study are: (1) epidote and clinozoisite contain slightly more Sc, V and Zr and significantly more LREE and MREE than coexisting metapelitic garnet (Gromet and Silver, 1984; Hickmott and Spear, 1992; Chapter 2); (2) Li and Zn zoning in garnet may reflect involvement of staurolite during garnet growth (Dutrow et al., 1986; Hickmott and Spear, 1992; Chapter 2); (3) vanadium and Co are highly enriched in ilmenite and magnetite respectively, compared to coexisting garnet (Schwarcz, 1966; Hickmott and Spear, 1992); (4) plagioclase develops strong positive Eu anomalies relative to coexisting garnet (Hickmott and Spear, 1992; Bea et al., 1994); (5) garnet fractionates more Sc, Y and HREE than any of the major minerals in pelites and calc-pelites, except for epidote (Hickmott et al., 1987; Hickmott and Spear, 1992; Chapter 2), (6) monazite, allanite and possibly apatite fractionate the REE, especially LREE (Bea et al., 1994); (7) zircon and xenotime fractionation, like that of garnet, produces a strong depletion in the HREE and a concomitant increase in the LREE/HREE ratio (Hickmott and Spear, 1992; Bea et al., 1994; Pyle and Spear, 1999); and (8) the role of biotite, muscovite, chlorite and kyanite in fractionating Y and the REE is insignificant.

Predicted trace element effects are summarized in Table 5.2 using the above criteria for metamorphic reactions used to define the metamorphic zones in Gagnon terrane. Reaction (1) may enrich the EBC in $Eu^*$, reaction (2) releases Sc, Y, Zr and HREE from epidote, reaction (3) will consume garnet to produce staurolite releasing a variable quantity of garnet-compatible trace elements (depending on the composition of the resorbed garnet), and reactions (4) and (5) release Li and Zn from staurolite. Garnet

growth by all the reactions in Table 5.2 fractionates Mn, Sc and the HREE from the EBC, except for reaction (2) where garnet grew by epidote consumption.

## 5.7 Summary

Factors controlling major and trace element zoning are reviewed. Rayleigh fractionation combined with breakdown/growth of trace element-enriched minerals and resorption during garnet growth are predicted to play important roles in trace element zoning in garnets from Gagnon terrane because of the ubiquity of trace element-enriched refractory minerals and the importance of the garnet-consuming as well as garnet-producing reactions defined in the area. All the listed factors controlling trace element zoning are discussed in chapters 6 and 7 except for external metasomatism and polymetamorphism, which are not known to be important controls in the study area. The scale of equilibrium, especially for trace elements, is investigated in chapters 6 and 7 using zoning in garnet and adjacent minerals. Using previously known garnet-mineral partitioning data, trace element zoning patterns in garnet are predicted.

Table 5.1 Epidote group analyses from Gagnon terrane.

| Samples | 87-283[1] | 87-279[2] | 87-279[2] | 87-279[1] | 87-287[1] | P-11[1] |
|---|---|---|---|---|---|---|
| $SiO_2$ | 38.30 | 36.76 | 36.67 | 38.30 | 37.70 | 37.33 |
| $TiO_2$ | 0.20 | <DL | <DL | <DL | 0.20 | <DL |
| $Al_2O_3$ | 28.10 | 21.14 | 20.89 | 27.60 | 26.40 | 26.92 |
| FeO | 6.30 | 26.83 | 27.17 | 7.20 | 8.10 | 7.64 |
| MgO | 0.10 | 1.44 | 1.53 | 0.20 | 0.20 | <DL |
| MnO | 0.30 | 5.55 | 6.25 | 0.20 | <DL | <DL |
| CaO | 23.60 | 8.72 | 7.97 | 23.20 | 23.00 | 23.93 |
| $Cr_2O_3$ | 0.20 | <DL | <DL | <DL | 0.20 | 0.23 |
| Total | 97.10 | 100.44 | 100.48 | 96.70 | 95.80 | 96.05 |
| | | | | | | |
| Numbers of ions on the basis of 12.5 O | | | | | | |
| Si | 3.160 | 3.069 | 3.074 | 3.054 | 3.053 | 3.019 |
| $Al^{iv}$ | 0.000 | 0.000 | 0.000 | 0.000 | 0.000 | 0.000 |
| Sum | 3.160 | 3.069 | 3.074 | 3.054 | 3.053 | 3.019 |
| | | | | | | |
| Ti | 0.012 | <DL | <DL | <DL | 0.012 | <DL |
| $Al^{vi}$ | 2.733 | 2.081 | 2.064 | 2.594 | 2.520 | 2.566 |
| $Fe^{3+}$ | 0.435 | 0.833 | 0.813 | 0.480 | 0.549 | 0.517 |
| $Mn^{3+}$ | 0.021 | 0.392 | 0.444 | 0.014 | <DL | <DL |
| $Cr^{3+}$ | | <DL | <DL | <DL | 0.013 | 0.015 |
| $X_{Fe3+}$ | 0.136 | 0.252 | 0.245 | 0.156 | 0.177 | 0.167 |
| $X_{Mn3+}$ | 0.007 | 0.119 | 0.134 | 0.004 | 0.000 | 0.000 |
| Sum | 3.201 | 3.306 | 3.321 | 3.088 | 3.094 | 3.098 |
| | | | | | | |
| $Fe^{2+}$ | | 1.041 | 1.092 | | | |
| Mg | 0.012 | 0.180 | 0.191 | 0.024 | 0.024 | <DL |
| Ca | 2.087 | 0.780 | 0.716 | 1.982 | 1.996 | 2.073 |
| Sum | 2.099 | 2.000 | 2.000 | 2.006 | 2.020 | 2.073 |

Note: [1] epidote and [2] Mn epidote. <DL represents below detection limits.

Table 5.2. Predicted trace element zoning in garnet

| Reactions | | Predicted trace element zoning |
|---|---|---|
| $Chl+Ms+Pl+Qtz=Grt+Bt+H_2O$ | (R1) | (Sc, Mn, Y, HREE) ↓, Eu* ↑ |
| $Chl+Ep+Qtz+Ms=Grt+Bt+Pl+H_2O$ | (R2) | (Sc, Mn, Y, HREE) ↑, Eu* ↓ |
| $Chl+Ms+Grt=St+Bt+Qtz+H_2O$ | (R3) | Resorption (release Sc, Mn, HREE) |
| $St+Qtz=Grt+Ky+H_2O$ | (R4) | (Sc, Mn, Y, HREE) ↓ (Li, Zn) ↑ |
| $St+Ms+Qtz=Grt+Bt+Ky+H_2O$ | (R5) | (Sc, Mn, Y, HREE) ↓ (Li, Zn) ↑ |

Notes: ↑ means element increases in garnet, ↓ means element decreases in garnet. Eu* is Eu anomaly.

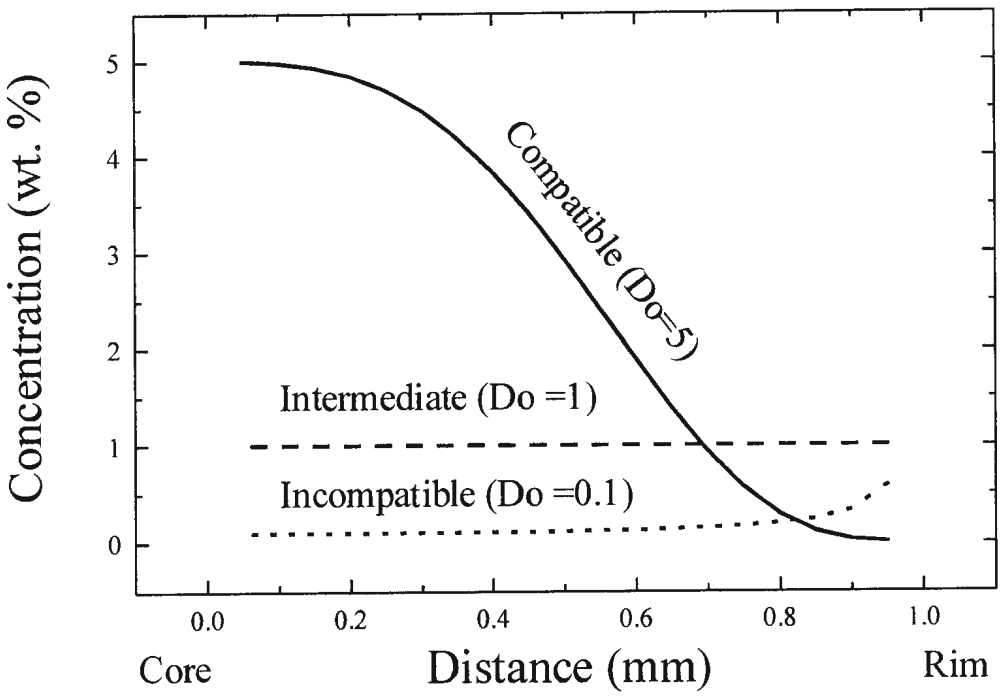


Fig. 5.1. Simple Rayleigh fractionation model showing the variations of compatible, intermediate and incompatible elements with crystal growth. Do is a bulk partition coefficient.

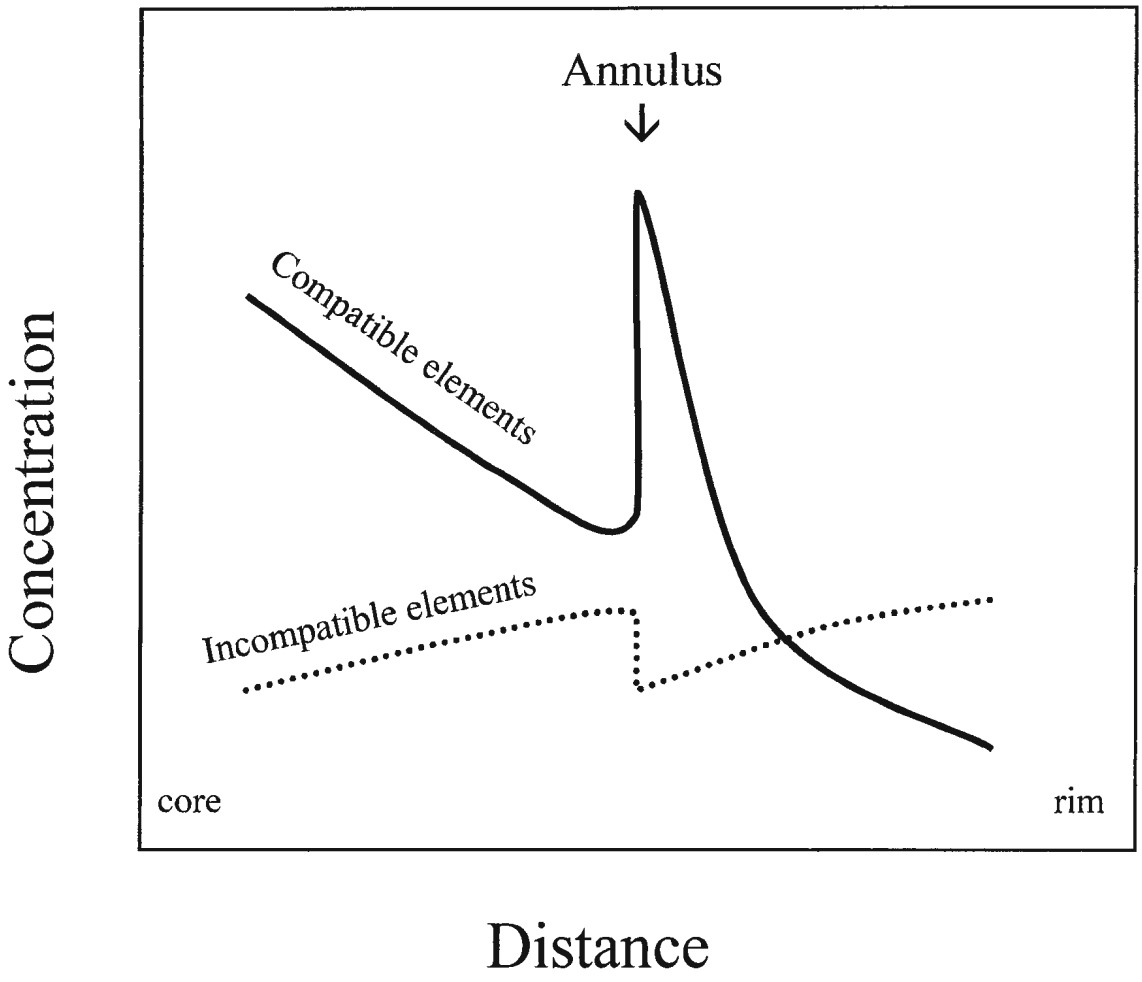


Fig. 5.2 A schematic diagram showing the variation of garnet-compatible and -incompatible elements at an Y annulus formed by garnet resorption and subsequent regrowth. This diagram is drawn on the assumption that both compatible and incompatible elements in the garnet rim become incorporated into trace phase(s) as a result of garnet resorption. Subsequently, on resorption of garnet growth, these elements again become partitioned into garnet as a function of their $D_i$ (garnet/trace phase) ratios.

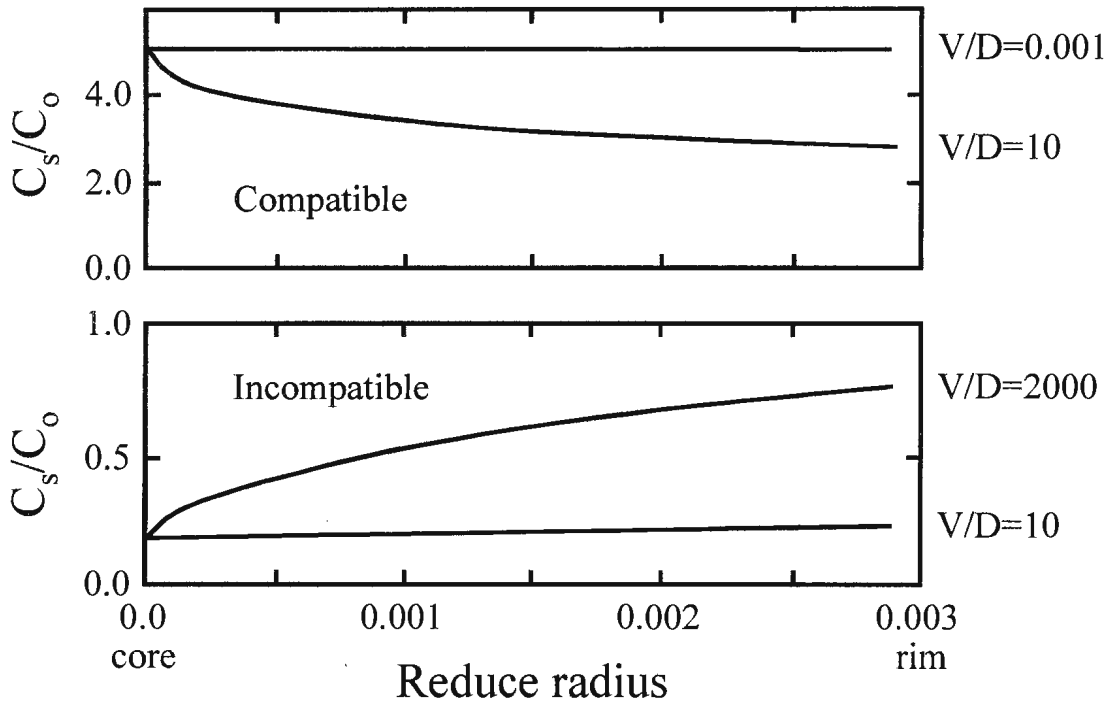


Fig. 5.3. Theoretical models of diffusion-controlled growth zoning in a solid phase (e.g., garnet) for compatible and incompatible elements versus reduced radius (normalized), from Hickmott and Shimizu (1990). $C_s$ is concentration in the solid and $C_o$ is initial bulk concentration in sample. V/D is a dimensionless ratio derived from the crystal growth rate (V) and the rate of grain boundary diffusion (D). A generalized compatible element is assigned a bulk partition coefficient of 5 and a generalized incompatible element is assigned a bulk partition coefficient of 0.2.

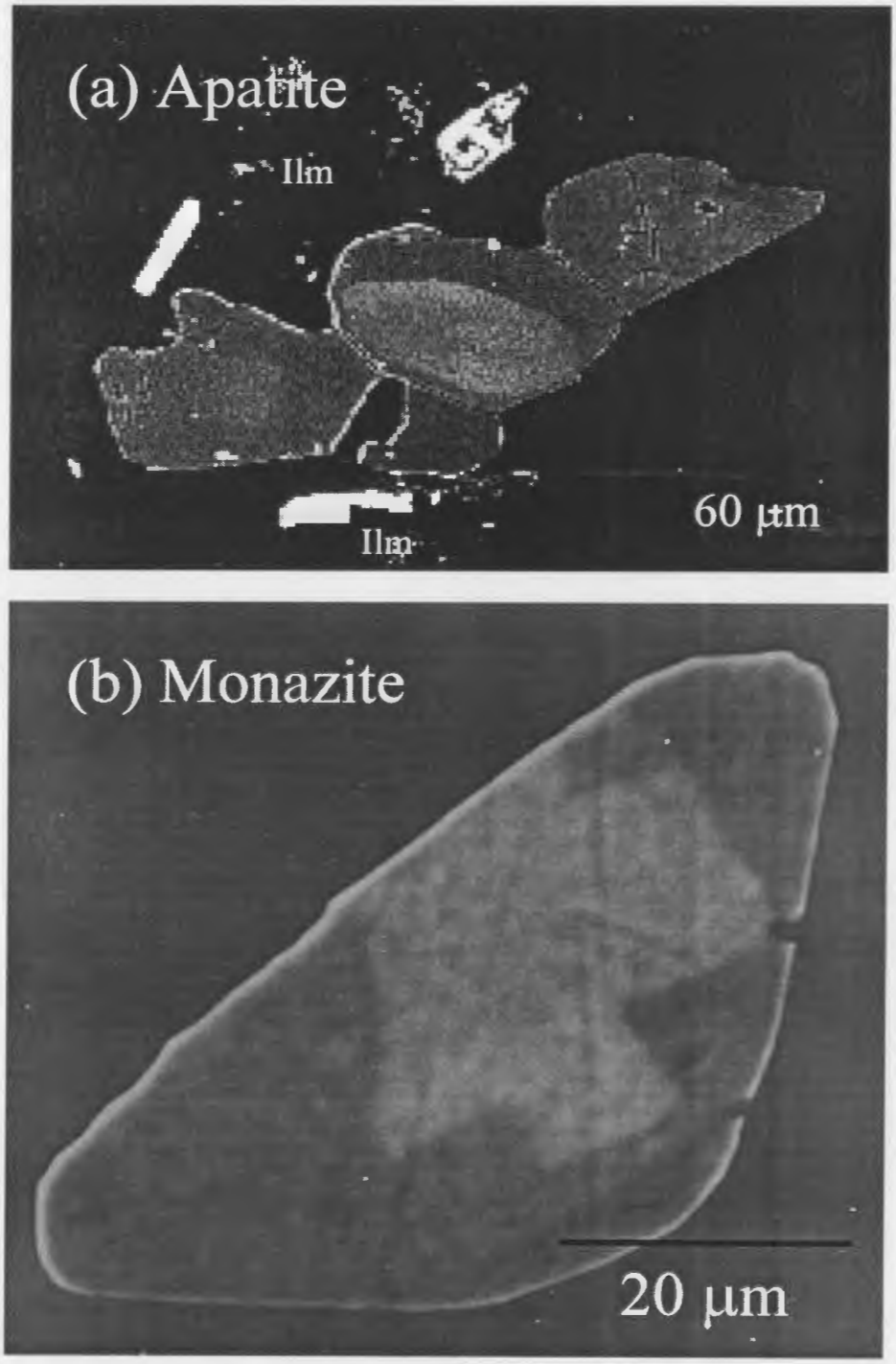


Fig. 5.4. Back scattered electron images of (a) apatite and (b) monazite showing internal zoning.

# Chapter 6: Chromium and manganese zoning in pelitic garnet and kyanite: Spiral, overprint, and oscillatory (?) zoning patterns and the role of growth rate

## 6.1 Introduction

Despite several studies that have demonstrated empirically that equilibrium partitioning of trace elements occurs in the metamorphic environment (*e.g.*, Hickmott and Spear, 1992; Dahl *et al.*, 1993; Bea *et al.*, 1997; Yang and Rivers, 2000), it remains unclear whether this is a widespread or common phenomenon. The major and trace element data from Mazzucchelli *et al.* (1992), Sánchez-Vízcaino *et al.* (1995), Messiga *et al.* (1995), Chernoff & Carlson (1997, 1999), and Kretz *et al.* (1999) indicate that diffusivities vary considerably among different elements and matrices. For example, in a trace element partitioning study between coexisting hornblende and Ca-pyroxene, Kretz *et al.* (1999) indicated that the degree of equilibrium decreases in the order of Zn > V > Cr > Sr > Ba > Ni. Thus, the possibility exists that, for specific trace elements in specific matrices, diffusion may be too slow to permit approach to an equilibrium distribution between coexisting phases over geologically reasonable time scales.

In this study, the behaviour of Cr in refractory minerals such as garnet and kyanite is investigated because these minerals can potentially preserve evidence of their growth history in the form of zoning. Under the relatively low-temperature conditions of the

amphibolite-facies, contrasts in inter-element diffusion rates and the role of kinetic factors are likely to impose important controls on element incorporation during mineral growth. We present X-ray maps and analyses for Mn, Ca, and Cr in garnet, and Al, Fe and Cr maps and analyses for kyanite, obtained using integrated electron microprobe and laser ablation microprobe-inductively coupled plasma-mass spectrometry (LAM-ICP-MS) techniques, for grains that show a range of textural relationships, in order to evaluate the role of textures on chemical growth zoning. We conclude that Cr was effectively immobile under amphibolite-facies metamorphism, a result which may explain previously reported irregular zoning of Cr in metamorphic garnets (Hickmott and Shimizu, 1989; Lanzirotti, 1995; Schwandt *et al.*, 1996) and the apparently non-equilibrium distribution of Cr between co-existing metamorphic mineral pairs (Yang *et al.*, 1999; Zack *et al.*, submitted).

## 6.2 Analytical techniques

Digital X-ray mapping of garnets in six samples for Mn, Ca, and Cr and of kyanite in two samples for Al, Fe and Cr was carried out with the automated mapping program *MAP*, coded by M. Piranian and the first author, on a Cameca SX-50 electron microprobe at the Department of Earth Sciences, Memorial University of Newfoundland (for details of the program MAP, see the appendix B). Operating conditions for X-ray mapping included an accelerating voltage of 15 kV, a beam current of 50~300 nA, dwell times of 0.2~0.7 sec/pixel, and a beam size of 18~56 μm. Accessory phases were located using back-scattered electron imaging and identified by EDS analyses.

X-ray mapping for Cr involved careful evaluation of the effect of interference of the Cr $K_\alpha$ peak with the V $K_\beta$ peak. Although the Cr concentration in ilmenite is lower than that in coexisting garnet (the Cr distribution coefficient (Ilm/Grt) is about 0.56, Hickmott and Spear, 1992), interference of the Cr $K_\alpha$ and V $K_\beta$ peaks leads to ilmenite having an apparently high concentration of Cr in Cr maps. Large ilmenite grains are readily recognized, but micro-inclusions of ilmenite, smaller than the step size used in the mapping, could potentially yield erroneously high apparent concentrations of Cr in the garnet host grain. We have evaluated this possibility by careful examination of areas of high apparent Cr concentration in garnet by high magnification BSE imaging. In all cases, we were unable to detect any micro-inclusions of ilmenite. Although the sampling depth of X-ray mapping is deeper than that of BSE imaging, the absence of micro-inclusions of ilmenite at the surface allows us to confidently assert that the Cr maps are indeed recording the Cr concentration in the garnet.

Quantitative analyses for Cr in garnet, kyanite, biotite, chlorite, epidote, and rutile were performed with a laser ablation system coupled to an ICP-MS (Fisons VG PQII +S) at the Department of Earth Sciences, Memorial University of Newfoundland. Laser sampling was performed in an Ar atmosphere using a 0.6-0.8 mJ/pulse laser energy, with the beam focused slightly above the sample, which produces a 50 to 70 μm spot size. Analyses were calibrated on NBS610 using Ca (for garnet and epidote), Ti (for biotite and rutile), and Si (for kyanite and chlorite) as internal standards. The average limit of detection for Cr from sample analyses is 2 ppm. The relative standard deviation for Cr concentration, derived from repeated analyses of BCR-2 (in which the Cr concentration is

reported as 16 ppm), is about 3%. Details of the laser system are described elsewhere (Jackson *et al.*, 1992; Longerich *et al.*, 1996; Taylor *et al.*, 1997).

## 6.3 Geology and sample descriptions

### 6.3.1 Regional geology

The seven investigated samples are pelites and calc-pelites from the Paleoproterozoic Knob Lake Group, in the Gagnon terrane of the Grenville Province of western Labrador, Canada (Fig. 6.1). Metamorphic grade in this part of Gagnon terrane increases from chlorite zone in the northwest near the Grenville Front, through the garnet, staurolite and kyanite zones, to migmatite zone (incipient partial melting) in the structurally highest part of the terrane over a distance of about 35 km (Rivers, 1983a). However, the migmatite zone samples investigated in this study do not show any textural evidence for partial melting as the first melting reactions take place in semi-pelitic compositions (Rivers, 1983a).

Metamorphism and deformation in Gagnon terrane are inferred to be a result of tectonic burial during northwest-directed overthrusting of Molson Lake terrane (van Gool, 1992; Rivers *et al.*, 1993). This part of the Gagnon terrane underwent two episodes of penetrative deformation during the overthrusting event (Rivers, 1983b; van Gool, 1992), with $S_1$ being recorded in the analysed samples as an internal foliation ($S_i$) within garnet porphyroblasts and $S_2$ being the external matrix foliation. On the basis of fabric relations, van Gool and Cawood (1994) concluded that garnet growth was synkinematic with the $D_1$ overthrusting. van Gool (1992) estimated that peak metamorphic conditions

in this part of the Gagnon terrane ranged from about 6 kbar/450 °C in the garnet zone to about 11 kbar/750 °C in the migmatite zone, and he inferred that the rocks followed "hair-pin" shaped *P-T-t* paths, implying rapid cooling and decompression after attainment of peak metamorphic conditions. Additional details concerning the geologic setting, phase relations, petrography, and *P-T* conditions can be found elsewhere (Rivers, 1983a, b; van Gool, 1992; Rivers *et al.*, 1993; van Gool and Cawood, 1994; Yang *et al.*, 1999).

### 6.3.2 Mineral assemblages

The mineral assemblages of the seven samples are given in Table 6.1 with their estimated peak *P-T* conditions from van Gool (1992). All seven samples contain garnet, biotite, plagioclase, and quartz with or without primary muscovite in the matrix. In samples 87-86, 87-271, P-11, and 88-80, epidote inclusions are restricted to the core of the garnet and do not occur in the matrix. Epidote inclusions occurring in 87-271 and 87-287 are Mn-rich (3.83 wt.% in 87-271 and 2.12 wt.% in 87-287). In addition to Mn-rich epidote inclusions, Mn-free epidote with allanite cores occurs both as a matrix mineral and as inclusions in garnet in sample 87-287. However, samples 87-83 and 88-74 contain no epidote. Apatite, zircon, rutile, and ilmenite commonly occur as minor phases with sparse occurrences of tourmaline, magnetite, allanite, monazite, and pyrite. Graphite occurs only in sample 87-83, and minor chlorite is a retrograde phase in all samples. K-feldspar was not found in any of the samples investigated in this study.

### 6.3.3 Internal fabrics and a textural unconformity in garnet

*Garnet zone* samples come from mica-rich pelitic layers, and the three analysed garnets contain an internal fabric ($S_i$). The garnets in 87-83 and 87-86 are subhedral and in both cases $S_i$ defines a spiral internal fabric with evidence for >360° and >180° of relative rotation, respectively (Figs. 6.2a, b). $S_i$ is defined by aligned inclusions, principally of quartz, ilmenite, plagioclase, and apatite in the two garnets. In contrast, the garnet in 87-271 is anhedral, $S_i$ is straight and principally defined by inclusions of quartz and ilmenite, and $S_i$ is at a high angle to $S_2$ outside the garnet (Fig. 6.2c).

Of the garnets in the three *migmatite zone* samples, those in 87-287 and 88-80 are anhedral and neither possesses an internal fabric, although both contain inclusions of quartz and plagioclase (Figs. 6.2d, e). The garnet in sample 87-287 is the only one situated in quartz- and plagioclase-rich layers. The garnets from samples 88-80 and P-11 come from mica-rich pelites (Figs. 6.2e, f). The core of the P-11 garnet contains abundant aligned inclusions that give rise to a straight internal fabric ($S_i$), defined mainly by quartz, biotite, and apatite, which is at a high angle to $S_2$ outside the garnet. The P-11 garnet, in addition, displays evidence for a textural unconformity, defined by the interface between the inclusion-rich core and an inclusion-free rim about 400 μm wide (TU in Fig. 6.2f).

In summary, we have examined garnets from both mica-rich and quartz-rich layers with a variety of inclusion species and with a range of textural relationships between $S_i$ and the external foliation ($S_2$). These textural relationships are representative of different garnet parageneses in Gagnon terrane and are typical of those involving garnets in pelites in many regional metamorphic terranes.

### 6.3.4 Garnet resorption and fracturing

All of the six analyzed garnets display variable degrees of resorption following growth. In the upper part of Fig. 6.2a, the spiral inclusion trails in garnet 87-83 are parallel to the euhedral crystal face, whereas in the lower part of the photomicrograph, the spiral inclusion trails are oblique to, and truncated at, the resorbed anhedral margin of the crystal. The ragged and embayed margins of garnets from samples 87-271 and 88-80 (Figs. 6.2c, e), and the incomplete rim outside the textural unconformity in P-11 (Fig. 6.2f) are also consistent with resorption. On the basis of textural relationships, garnet growth took place syn- or post-$D_1$, and resorption occurred syn- or post-$D_2$.

Sample P-11 also shows evidence for brittle fracturing of garnet. Fig. 6.2f (inset) shows four fragments of garnet that, on the basis of inclusion patterns, are inferred to have formerly been parts of a single large porphyroblast. The textural unconformity continues in the top left garnet fragment (not visible in Fig. 6.2f), but is absent along the upper margin of the largest fragment (Fig. 6.2f), consistent with the inference that this margin was not an original growth surface of the crystal, but developed subsequently as a result of fracturing. Fig. 6.2f (inset) also shows part of a symmetrical pressure shadow defined by the external $S_2$ foliation that is associated with the fragmented garnet as a whole, not with the individual parts of it, indicating the fracturing took place during the $D_2$ deformation. Quartz and biotite occupy the spaces between the garnet fragments (*e.g.*, at the top left side of Fig. 6.2f), and quartz occurs in the pressure shadow region adjacent to the porphyroblast. Elsewhere (*e.g.*, at the bottom left of Fig. 6.2f), garnet is in contact

with the $S_2$ foliation defined by biotite.

### 6.3.5 Kyanite petrography

Kyanite porphyroblasts in the migmatite zone have a bimodal size distribution, which is interpreted to represent two different stages of kyanite growth (van Gool, 1992). The older kyanite porphyroblasts ($Ky_1$) are coarse grained (up to a few cm long) and show subhedral crystal shapes and poikiloblastic textures. These kyanites are aligned with the foliation, suggesting growth during development of the regional $S_2$. The second type of kyanite porphyroblast ($Ky_2$) is much smaller (< 2 mm), randomly oriented, has idioblastic to subidioblastic crystal shapes and does not contain inclusions.

## 6.4 Results

The integrated X-ray maps and partial analyses for the six analysed garnets and two kyanites show a wide range of zoning features. These are qualitatively described in this section and the important features are summarized at the end.

### 6.4.1 Garnet zoning

***Sample 87-83 (garnet zone):*** Examination of the Mn map of this garnet (Fig. 6.3a) shows a well developed euhedral core with elevated $X_{Sps}$ (=Mn/Mn+Ca+Mg+Fe = 0.17) that declines outwards by a factor of about two to a rim about 0.4 mm wide. However, careful examination of Fig. 6.3a suggests that the zoning pattern was affected by inclusions captured during growth of the garnet. For example, growth on the upper side

of the garnet core was retarded by an inclusion-rich layer, whereas garnet growth on the opposing side in an inclusion-poor area was not, resulting in asymmetric zoning and a sharp compositional break at the inclusion-rich layer (Fig. 6.3a). This break appears as a cliff in a 3-D map of Mn zoning (Fig 6.3f), which was constructed on the basis of raw counts from the electron microprobe. Mn concentration along a radial traverse through the garnet, oriented perpendicular to the spiral inclusion pattern and away from the compositional break at the inclusion-rich layer, is shown in Fig 6.4a. The compositional profile shows a gradual decline outwards, compatible with preserved growth zoning, but there is a definite step in the profile, before a flattening out at the garnet rim. In contrast, Mn concentration varies gradually without sharp breaks when measured parallel to the spiral inclusion trails (Fig. 6.4b). We tentatively interpret this as evidence for spiral growth zoning in the core of the crystal and investigate it more fully below. In contrast to the core, the rim of the garnet has a homogeneous, low-Mn composition that we infer developed during a late stage of concentric growth. Part of the rim and the outer core were subsequently resorbed (dotted line, Fig. 6.3a).

Ca zoning is not strong in this garnet but a patchy distribution of Ca is evident (Fig. 6.3b). Apatite, which appears as small black dots in the Ca map, occurs in the matrix and as inclusions in the garnet. Lines of plagioclase inclusions (green) in the garnet define the spiral inclusion pattern locally, and larger, apparently unzoned plagioclase crystals are present in the matrix. The Cr map (Fig. 6.3c) defines a high Cr band (up to 207 ppm) that follows the spiral pattern, parallel to (but distinct from) the inclusion trails defined by ilmenite (red), and quartz (blue). Micro-inclusions of ilmenite smaller than the pixel size

used for the map (18μm) were not found (see Analytical Methods), so we attribute the spiral Cr zonation to real variations in Cr concentration in garnet. However, the spiral Cr banding has a different form to the spiral Mn zoning, in that bands of both high and low Cr concentration are present throughout the garnet and there is no overall trend in Cr concentration towards the margin of the grain.

***Sample 87-86 (garnet zone):*** The Mn map for the garnet in this sample shows a remarkable sigmoidal shape in the core, with the arms of the sigmoid being parallel to the spiral inclusion trails (Fig. 6.3d). We interpret this as another example of spiral growth zoning. In this case, there is a second smaller core in an inclusion-poor area above the main core, which also displays a similar, parallel sigmoidal pattern. As in 87-83, the core of this garnet was overgrown concentrically by a homogeneous, low Mn rim. It is interesting to note the presence of radially disposed, angular notches in the growth zoning patterns in the inner rims of the garnets in both 87-83 and 87-86 (red arrows in Figs. 6.3a, d). These patterns appear to be restricted to garnets with evidence of spiral growth, and we discuss their possible origin below.

The Ca map for garnet 87-86 (Fig. 6.3e) also shows a sigmoidal growth shape, parallel to the Mn zoning, and a similar pattern is also shown by the BSE map (Fig. 6.2b), where the mean atomic number contrast in the core is defined by enrichment in Y.

***Sample 87-271 (garnet zone):*** X-ray maps for Mn and Ca for this garnet (Figs. 6.5a, b) both show elevated concentrations in the lower right of the grain, suggesting that this

is the core region of a growth-zoned crystal. A partially preserved annulus of Mn enrichment near the rim (black arrows, Fig. 6.5a) is attributed to the breakdown of Mn-rich epidote during growth of the garnet. The core is not situated in the geometrical centre of the grain, implying either asymmetrical growth or asymmetrical resorption. Resorption is compatible with the indented shape of the garnet and with truncation of the outer Mn annulus. However, we point out that the garnet rim is also elevated in Ca and that the inner boundary of the high-Mn rim coincides with a subtle break in the Ca zoning pattern (thin green line near top right margin of grain in Fig. 6.5b), suggesting that the Mn rim is a growth feature. We therefore attribute it to garnet growth as a result of the final breakdown of Mn-rich epidote in the matrix (note preserved Mn-rich epidote inclusions in this garnet, Fig. 6.5a). The variable thickness and local absence of the high-Mn/Ca rim on this garnet suggests that growth of the rim was followed by a final stage of garnet resorption.

The Cr map for this sample (Fig. 6.5c) is unlike those for the other elements in that the area of highest Cr concentration shows no relation to the core or rim of the garnet. Instead, a diffuse band of high Cr concentration (up to 511 ppm), approximately parallel to the internal fabric defined by inclusions, passes across the upper right of the garnet. Cr is also present in matrix biotite, but the Cr content of biotite near garnet is much higher than that of biotite distal to garnet. For instance, there is a two-fold difference in the Cr concentrations in adjacent clusters of biotite crystals in the lower right corner of the map (580 versus 281 ppm, Fig. 6.5c). Noting that biotite replacing garnet in an embayment in the middle right side of the crystal has similar Cr content to the garnet it replaced (Fig.

6.5c), we infer that the sharp boundary between the matrix biotites with different Cr concentrations in the lower right hand side of Fig. 6.5c represents the original location of the garnet margin before resorption. The inferred location of the outline of the original garnet shown in Fig. 6.5c is based on this criterion.

***Sample 87-287 (migmatite zone):*** The Mn map (Fig. 6.5d) shows essentially flat Mn zoning in the core of the garnet with a 500 μm wide annulus of variously elevated $X_{Sps}$ concentration inboard from the garnet rim. The lack of Mn zoning in the core may be explained by an off-centred cut. Another possibility, that any growth zoning originally present was subsequently eliminated by diffusion, is not considered likely because we interpret the annulus of high Mn near the rim as a growth feature, probably associated with the breakdown of an Mn-rich phase. The presence of Mn-epidote inclusion within the annulus suggests that this mineral may be the source of the Mn. Resorption of this garnet appears to have been minor, despite its ragged shape (Fig. 6.5d). We infer that the shape is principally a growth feature resulting from growth surface impingement in a coarse-grained, quartz-plagioclase layer, an interpretation compatible with the presence of large quartz inclusions in the centre of the crystal.

The Ca map (Fig. 6.5e) shows that $X_{grs}$ is high (0.19 mol. %) in the core of the garnet, rising slightly in the Mn-rich annulus and declining at the rim. However, careful examination of the lower margin of the garnet shows that the lowest values of $X_{grs}$ occur in a narrow band just in from the rim. The absence of Mn enrichment at this low $X_{grs}$ band suggests that it is not a result of resorption. The Cr map for this garnet (Fig. 6.5f)

shows a core region with about 421 ppm Cr and that Cr concentration increases slightly at the Mn-rich annulus to about 447 ppm before decreasing at the thin band of low-Ca to about 182 ppm. The Cr rim shows a similar shape and width to the Mn annulus implying that it is a growth feature.

Summarizing these observations for 87-287, zoning for all measured elements appears to be essentially flat in the core, whereas in the annulus near the margin of the garnet, Mn and Cr increase together. The rise in Mn and Cr concentrations does not appear to be related to back-diffusion of Mn during dehydration melting of garnet (*e.g.*, Kohn *et al.*, 1997) as there is no evidence for resorption at the Mn annulus, which also involves changes in Ca and Cr zoning and preserves the euhedral former growth outline of the garnet. We therefore interpret the Mn and Cr annulus to be a growth feature, probably associated with the breakdown of Mn-epidote late in the growth history of the garnet. The thin low-Ca band, where Cr decreases significantly, may represent a change in the garnet-forming reaction.

***Sample 88-80 (migmatite zone)***. The analysed garnet in this sample is strongly resorbed, as indicated by its ragged appearance (Fig. 6.5g). However, it retains evidence of a large core, defined by enrichment in $X_{Sps}$ and $X_{Grs}$ with respect to the rim region (Figs. 6.5g, h). The Mn growth zoning pattern is truncated at the large quartz grain near the top right of the crystal, and was clearly also affected by the large quartz inclusion in the centre left of the crystal. We interpret these as growth features associated with impingement of matrix quartz on the garnet growth faces. We attribute to the thin

elevated Mn rim, which is superimposed on the growth zoning pattern, to minor back diffusion associated with resorption. The Ca map shows a core region with elevated Ca, but its shape is irregular, compatible with the suggestion above that grain impingement inhibited growth in certain directions during the formation of this crystal. Later modification of the Ca zoning pattern by subsequent diffusion is also possible, but may not be likely given its known slow diffusion in garnet (e.g., Ganguly and Chakraborty, 1991). Plagioclase (blue green) in the matrix is weakly zoned with Ca-rich rims.

The Cr map (Fig. 6.5i) shows that the garnet has a relatively homogeneous core (315 ppm Cr) with two partially preserved Cr-rich bands (up to 690 ppm Cr) located near the grain margin. The Cr-rich bands are approximately concentric, but the concentration of Cr along the bands is variable and two bands appear to merge near the bottom right of the garnet, implying that the origin of the zoning is different from the concentric zoning in 87-287. Note that Cr shows much narrower depletion zones around the quartz inclusions than Mn and Ca. The original boundary of the garnet is indicated by a white dotted line in Fig. 6.5i, on the basis of contrasts in the Cr composition of biotite.

***Sample P-11 (migmatite zone).*** The Mn map for this large garnet (Fig. 6.6a) shows a well-defined core, which is embayed around inclusions and partly modified by subsequent diffusion adjacent to the inferred fracture surface at the upper left margin of the grain. $X_{grs}$ decreases slightly from 0.17 in the core to 0.15 just inboard of the TU rising to 0.17 again at the TU. Outside the TU, it drops abruptly to 0.12, compatible with the disappearance of epidote at the TU noted above (Fig. 6.6b). Apatite and epidote

inclusions (black) are aligned with the internal fabric ($S_i$) in the core of the garnet. Plagioclase grains in the matrix adjacent to garnet are zoned with sodic cores and calcic rims.

The Cr map (Fig. 6.6c) shows a remarkable banded pattern, defined by Cr-rich and Cr-poor layers parallel to the included fabric ($S_i$), that is unrelated to the core of the garnet (as defined by Mn) or the inferred fracture surface along the upper margin of the grain. The textural unconformity in the garnet is well displayed in the lower right margin of the Cr map (Fig. 6.6c) where the Cr banding is truncated at a former dodecahedral growth face of the garnet. Figure 6.7 is a LAM-ICP-MS transect through the P-11 garnet, showing the Cr distribution. Cr concentration near the geometric centre of the grain varies from 2,303 ppm in Cr-rich layers to 18 ppm in Cr-poor layers, *i.e.*, concentration varies by a factor of about 128 times over a distance of 1.5 mm. In the garnet rim outboard of the textural unconformity, Cr abundance is relatively more homogeneous and drops to about 230 ppm at the rim.

Additional support for the contention that the analyzed garnet is one of several parts of a larger grain that was fragmented during the $D_2$ deformation comes from the Cr map (Fig. 6.6c). The garnet fragment in the upper left corner of the figure also shows Cr layering, with the $S_i$ layers having a width and spacing that conforms with, and is approximately parallel to, that in the main grain. Timing of the fragmentation is constrained to have been after the development of the TU and the growth of the rim, because both are truncated by quartz occupying the space between the garnet fragments.

Cr abundance in matrix biotite varies significantly from 260 to 1573 ppm, with

higher Cr concentration in biotite close to the garnet (Fig. 6.6c). Chlorite (retrograde) and epidote inclusions in the garnet contain about 1,438 and 1,269 ppm Cr, respectively. A rutile inclusion in the garnet contains about 1,053 ppm Cr. No Cr was detected in analyses of quartz, plagioclase and apatite.

### 6.4.2 Kyanite zoning

The Al X-ray map for kyanite from sample 88-74 (Fig. 6.6d) shows that Al concentration decreases slightly towards the rims. However, the zoning pattern is not concentric in the large ($Ky_1$) kyanite grains. Fe is depleted in the cores of the grains, and shows a sharply delineated zone of enrichment near the rims of the grains (Fig. 6.6e). Assuming kyanite growth during constant or increasing temperature, this may indicate an increase in $f_{O2}$ during growth if there were no other sources of $Fe^{3+}$ such as epidote present. Epidote was not observed in this rock and the low Ca concentration in the garnet ($X_{grs} < 0.05$) does not support the involvement of epidote during kyanite growth. The Cr map for the kyanite (Fig. 6.6f) shows two distinct, partial annuli of Cr enrichment in the two larger grains, but there is no Cr annulus in the small grains. The positions of the Cr annuli in the large grains correspond closely with the increase in Fe in the kyanite rims, but the Cr annuli are narrower than the zones of Fe enrichment. The bifurcating arrangement of the Cr annulus in the largest kyanite grain suggests either that it may have formed by the coalescence of two crystals or that it is preserving the Cr distribution of matrix minerals (*e.g.* micas). The correlation between Cr and Fe zoning in the large kyanite ($Ky_1$), but not in small kyanites ($Ky_2$), suggests that Cr was derived locally.

In the kyanites in 88-80, Al is not zoned significantly and Fe increases gradually towards the rims (Figs. 6.6g, h). The Cr map for the larger kyanite grain in sample 88-80 (Fig. 6.6i) shows at least three concentric Cr annuli, with measured concentrations up to 823 ppm, and Cr concentration varies at least by a factor of about 2 throughout the grain as a whole. The smaller kyanite grain has a single thin incomplete Cr annulus with a considerably lower maximum Cr concentration. Unlike kyanite in sample 88-74, the positions of Cr annuli are not correlated with Fe zonation. We note that, as in sample 88-74, the Cr annuli in both kyanites are discontinuous around the crystals, being better developed on the long axes of the prismatic grains. Kyanite shows more complex Cr zoning than coexisting garnet, suggesting that there is not a 1:1 correlation between individual annuli in the two minerals. In addition, the number of annuli in garnet and kyanite does not appear to correlate with metamorphic grade.

### 6.4.3 Summary of observations

Figure 6.8 is a summary of the inclusion and zoning observations discussed above. In the text below, the principal conclusions from these observations are organized into those related to growth mechanisms and diffusion phenomena (1-7 below, derived from both major and trace element data), and those related to metamorphic reactions (8-12 below, derived principally from major element data).

1. On the basis of Mn and to a lesser extent Ca zoning, garnets with straight inclusion trails or randomly oriented inclusions grew concentrically, whereas garnets with spiral inclusion trails grew in a spiral pattern *(spiral zoning)*.

2. Garnet growth around large inclusions may be greatly retarded and produce a depleted region in the growth zoning pattern, which may be difficult to distinguish from subsequent diffusional modifications (87-83, 87-83, 88-80, and P-11).
3. In three of the six garnets analysed (87-83, 87-271, core of P-11), Cr zoning is not related to major element zoning and is parallel to the internal fabric ($S_i$) within the garnet. We refer to this as *overprint zoning*. Although an internal fabric is not developed in the garnet of 88-80, bifurcating Cr zoning at the rim is also compatible with an origin by overprinting of Cr-rich minerals such as micas during growth. Overprint zoning suggests that Cr was essentially immobile during garnet growth.
4. In contrast, garnets in 87-287 and the rim of P-11 show concentric Cr zoning which is associated with enrichments and/or depletions in major elements. The concentric zoning indicates that the mobility of Cr was enhanced during the upper amphibolite- facies growth of these garnets.
5. Cr zoning in kyanite in 88-80 forms concentric annuli of variable width, concentration and continuity. We tentatively refer to this as *oscillatory zoning*, although we acknowledge that it is less regular than oscillatory zoning in many igneous minerals.
6. Cr zoning in kyanite in 88-74 shows a bifurcating pattern, similar to that in the garnet in 88-80 (Fig. 6.5i), which we likewise interpret as a result of overprinting of mica-rich layers (i.e. overprint zoning).
7. Fe zoning in kyanite is minor, but there is a significant, well-defined increase in Fe

towards the margins in the analysed grains in 88-74. Cr annuli in kyanite coincide with the zones of $Fe^{3+}$ enrichment in some, but not all grains, indicating that the Cr was locally derived.

8. $X_{sps}$ declines continuously from core to rim in most garnets with minor Mn enrichment at the rim due to garnet resorption locally. The source of Mn in the garnet cores is inferred to have been another ferromagnesian phase in which Mn was less compatible than garnet (*e.g.*, chlorite). The exceptions to this pattern are the garnets in 87-271 and 87-287. 87-287 lacks Mn zoning in the core, and both samples show elevated Mn at the rim that are associated with growth resulting from the breakdown of Mn-epidote.

9. For calc-pelite garnets, $X_{grs}$ is generally high in the core (up to 0.25 mol %), decreasing slightly towards the rims and plummeting after breakdown of epidote (P-11).

10. Matrix plagioclase shows An enrichment from core to rim in three samples. This zonation is typically associated with progressive breakdown of a Ca-rich phase such as epidote during garnet growth (Menard and Spear, 1993). Matrix plagioclase from the other two samples is unzoned.

11. The textural unconformity in the P-11 garnet is the site of both textural (inclusion-rich core / inclusion-free rim) and compositional contrasts in the garnet.

12. All garnets, from both the garnet and the migmatite zones, show variable degrees of resorption with the least from sample 87-287. The degree of resorption does not appear to be correlated with metamorphic grade.

## 6.5 Garnet- and kyanite-forming reactions

Mineral growth reactions can, in principle, be constrained from major and trace element zoning and inclusion relationships amongst coexisting phases. In this section, we use major element garnet zoning and textural relationships to qualitatively infer garnet- and kyanite-forming reactions in the model CNKFMASH system, and then consider their application to the interpretation of Cr zoning.

On the basis of major element zoning, we infer that the continuous reaction that accounts for the first appearance of garnet in pelitic samples (87-83 and 87-271) was:

$$Chl + Pl + Ms + Qtz \Rightarrow Grt + Bt + H_2O \quad (6.1)$$

(Rivers, 1983a; van Gool, 1992). This reaction is compatible with the major element garnet zoning, *i.e.*, a decrease in $X_{sps}$ and an increase in $X_{prp}$ from core to rim. $X_{grs}$ in the cores of these garnets varies from 0.08 and 0.19 and decreases slightly towards the rims, and $X_{an}$ in matrix plagioclase is not significantly zoned. In the calc-pelite samples, which contain epidote either as a matrix mineral (87-287) or as inclusions in garnet (87-86, 88-80 and P-11), the garnet-forming reaction involved epidote as a reactant instead of Ca-plagioclase:

$$Chl + Ep + Ms + Qtz \Rightarrow Grt + Bt + Pl + H_2O \quad (6.2)$$

High $X_{grs}$ in the cores of these garnets (up to 0.25 mol % in 87-287) is compatible with garnet growth buffered by a Ca-rich phase such as epidote, and plagioclase in the matrix is zoned with An-rich rims, also compatible with epidote breakdown (Menard and Spear, 1993).

Reactions 6.1 and 6.2 proceeded until chlorite was exhausted in the rocks examined.

For samples with remaining epidote, the next reaction was:

$$Grt + Ms + Ep + Qtz \Rightarrow Bt + Pl + H_2O \quad (6.3)$$

accounting for removal of epidote and for An enrichment in the rims of matrix plagioclase, in accord with observations. Possible staurolite- and kyanite-forming reactions in the area were:

$$Grt + Chl + Ms + Qtz \Rightarrow St + Bt + H_2O \quad (6.4)$$

$$Grt + Chl + Ms + Qtz \Rightarrow Ky + Bt + H_2O \quad (6.5)$$

(Rivers, 1983a; van Gool, 1992). Both reactions are compatible with evidence for garnet resorption in most amphibolite-facies samples. These reactions also apparently resulted in the removal of muscovite from several of the analysed samples (Table 6.1). Reaction 6.5 leads to the formation of kyanite, but several other kyanite-forming reactions are also possible in pelites of intermediate Fe/Mg ratio such as those examined here. For instance, kyanite may form from staurolite by the continuous reaction

$$St + Qtz \Rightarrow Grt + Ky + H_2O \quad (6.6)$$

or the discontinuous reaction

$$St + Ms + Qtz \Rightarrow Bt + Grt + Ky + H_2O \quad (6.7)$$

(Rivers, 1983a; van Gool, 1992). Either of reactions (6.5) or (6.6) could account for the earlier coarse-grained kyanite, with reaction (6.7) being responsible for the later fine-grained kyanite. Reactions 6.6 and 6.7 imply resumption of garnet growth. Dehydration melting reactions are not considered to be responsible for garnet growth in this area, in which melting is restricted to Al-poor lithologies lacking kyanite (i.e., semi-pelitic compositions, Rivers, 1983a).

Attempts to derive information on the garnet- and kyanite-forming reactions from the Cr zoning patterns were less successful. This is because Cr is dispersed among several abundant phases in pelites, *e.g.*, chlorite, micas, epidote, ilmenite (DeVore, 1955; Hickmott and Spear, 1992; Sánchez-Vízcaino *et al.*, 1995; Yang *et al.*, 1999), so that Cr zoning does not provide a unique signature for the involvement of a particular phase in the garnet- or kyanite-forming reactions. Multiple trace element signatures may be necessary to characterize individual reactants in this case. Although conclusions with respect to the source of Cr in the garnet- and kyanite-forming reactions remain enigmatic, Cr zoning can potentially be coupled with textural information to yield unique information about growth mechanism and reaction rates, as is discussed below.

## 6.6 Discussion

The X-ray maps and analyses described above reveal a wide range of growth zoning patterns in garnet and kyanite. Concentric bell- and saddle-shaped zoning profiles have been widely reported in the literature on garnet, but spiral zoning has not been described previously except for a brief report of asymmetrical zoning in garnets in pelitic schist from Gassetts, Vermont (Thompson *et al.*, 1977). Overprint zoning is indicated by Menard and Spear (1996) and Spear and Daniel (2000) for plagioclase and garnet, respectively, but was not explicitly named or discussed in detail. Oscillatory zoning is apparently not common in metamorphic minerals occurring in isochemical environments. These three types of zoning and changes in Cr mobility during the metamorphism are considered in more detail below.

### 6.6.1 Spiral zoning

Spiral growth zoning is most apparent in the Mn maps in 87-83 and 87-86 (Figs. 6.3a, d), but subtle evidence for spiral zoning is also present in the BSE image (Y zoning) and the Ca map for the garnet in 87-86 (Figs. 6.2b, 3e). The spiral growth zoning is parallel to the spiral pattern of inclusions, implying that garnets with this type of zoning grew in a different manner to normal, concentrically zoned crystals. This is also indicated by Fig. 6.4, in which Mn analyses from along a radial transect across the garnet exhibit a break between the inner and outer spirals (Fig. 6.4a), whereas those taken along the spiral decrease monotonically up to the concentrically-grown rim (Fig. 6.4b). In order to examine the spiral growth history of the garnets in samples 87-83 and 87-86 in more detail, garnet growth has been simulated by applying sequential thresholding to the Mn X-ray maps. Representative slices for the two garnets are presented in Fig. 6.8, and full animation is available on the web site of JMG at http://www.gly.bris.ac.uk/www/jmg/JMG.html.

The garnet in 87-83 started to grow in the vicinity of a large quartz grain (stage 1 in Fig. 6.8a), and careful examination of stage 2 reveals that at least three small garnet nuclei crystallized initially. The garnet maintained a euhedral shape up to stage 5 when growth at the upper surface became severely retarded because of quartz crystals aligned along the top of the garnet which acted as a 'growth barrier' (see the inset of stage 5 in Fig. 6.8a). A simple comparison of crystal size between stages 3 and 5 shows that the garnet grew approximately 2 times faster in a SW direction compared to NW and SE

directions. At stages 5 and 6, the garnet started to surround the large quartz crystal by growth in SE and then NE directions, at high angles to the former principal growth direction, implying a dominant rotational force. A small garnet crystallized at the right hand side of the main garnet crystal at stage 7. Continued SW-ward growth between stages 7 and 8 suggests that the notch was produced by rotational growth of the garnet, not by resorption of the crystal. A sketch of the spiral pattern is depicted at stage 10, which shows that most of the lower arm was removed by resorption along the bottom of the crystal.

The garnet growth history for 87-86 is similar to that of 87-83. This garnet grew in a N-S direction from stage 1 to 2 and started to rotate at stage 3. At stage 4, the garnet rotated symmetrically with relative rotation of about 90° between stages 3 and 4. It is important to note that the garnet did not grow around the quartz inclusion (Qtz1, for location see Fig. 6.8b) even though there was inclusion-free space around the crystal. Instead, it principally grew towards the west forming the left arm of the sigmoid. Another garnet nucleated above the major core at this stage. Continued spiral growth of the second garnet, even in what is near a relatively inclusion-free area, indicates that the spiral growth was not an artifact resulting from a series of spirally aligned inclusions. Growth of the lower arm of the second garnet appears to have been arrested by the elongate quartz inclusion lying perpendicular to the growth path (stage 5 in Fig. 6.8b). By stage 6, Qtz1 was completely surrounded by the upper spiral and Qtz2 was partially surrounded by the lower spiral and the two garnets merged into a single grain. At stage 7, the upper spiral continued to grow downwards whereas the lower spiral grew upwards,

producing a notch at the end of the spiral growth face. However, growth of the lower arm was retarded by contacting quartz inclusions. At stage 8, the garnet stopped growing spirally and started to grow concentrically. The pattern of spiral growth in this garnet is shown in stage 10.

The postulated garnet growth mechanism is schematically shown in Fig. 6.9. Two radial growth faces or notches are located in the pressure shadow regions of the garnet. From the widespread evidence of neo-crystallized phases in pressure shadow regions in many deformed rocks, we infer that these regions are the foci for enhanced diffusion and as such are favourable locations for active growth faces in 'snowball' garnets such as this. If this assumption is correct, it implies that the positions of the growth notches remain approximately static as they track the pressure shadow regions which lie in the plane of foliation at each side of the garnet. This in turn implies relative rotation of the growing garnet with respect to the matrix foliation during growth, so as to maintain the growth face in the pressure shadow region. In the case of garnets in 87-83 and 87-86, subsequent concentric growth after rotation ceased, preserved the growth notches defined by Mn concentration in the interior of the garnets. The spiral zoning pattern for Cr is different to that for Mn, in that both Cr-rich and Cr-poor spirals are present throughout the garnet. We interpret this to be a result of the incorporation of Cr-rich and Cr-poor layers in the growing garnet, as schematically illustrated in Fig. 6.10, so that, in contrast to Mn, there is no overall change in Cr concentration form core to rim.

Rotation of snowball garnets during growth has been proposed by many authors (*e.g.*, Zwart, 1960; Powell and Treagus, 1970; Rosenfeld, 1970; Schoneveld, 1977;

Powell and Vernon, 1979; Passchier *et al.*, 1992; Miyake, 1993; Williams & Jiang, 1999). However, the rotation hypothesis has not been universally accepted and other authors have argued that the snowball patterns result from strain partitioning and overprinting (*e.g.*, Bell, 1985; Bell *et al.*, 1992; Bell and Johnson, 1992; Bell and Hickey, 1999; Hickey and Bell, 1999). While it is not the purpose of this communication to comment on the general merits of rotation versus non-rotation of snowball garnets during growth, we note that the presence or absence of spiral growth zoning provides a new technique to test the rotation hypothesis and has the potential to contribute to resolution of the argument in specific cases. Furthermore, with respect to the papers in which porphyroblast rotation is proposed, all the authors noted above inferred, either implicitly or explicitly, that the garnet porphyroblasts grew concentrically. The finding from this study that, at least in some cases, growth takes place in a spiral manner has important implications for the modeling of snowball garnets, which are beyond the scope of this paper.

### 6.6.2 Overprint zoning

The spiral and straight Cr zoning patterns, parallel to $S_i$ as defined by inclusions, are not explicable by any of the processes usually invoked to explain garnet zoning, *e.g.*, elemental fractionation (Hollister, 1966); disequilibrium partitioning in the interface region (Hickmott and Schimizu, 1989); internal or external metasomatism (Hickmott and Spear, 1992; Jamtveit *et al.*, 1993); or changes in garnet-mineral partition coefficients as a result of changes in intensive variables during metamorphism. Instead, Cr zoning in the

garnets in 87-83, 87-271 and the core of P-11 appears to have been inherited from the Cr distribution present in the pre-existing fabric ($S_i$) that was overprinted during garnet growth. Menard and Spear (1996) and Spear and Daniel (2000) reported similar zoning patterns produced by Ca in plagioclase overgrowing a heterogeneous matrix of crenulated muscovite and biotite, and by Mn in garnet overprinting crenulation folds, respectively. In our case, we infer that the Cr-rich layers in the garnet are the sites of former mica ± chlorite ± epidote-rich layers, whereas the Cr-poor layers represent former quartz ± plagioclase-rich layers. This overprint process also occurred during retrograde metamorphism. For example, sample 87-271 contains resorbed garnet that has been replaced by retrograde biotite. The Cr concentration of biotite replacing the garnet is apparently identical to that in the former garnet, but different (by a factor of >2) from that in adjacent matrix biotite in sample (Fig. 6.5c), as noted above.

There is some evidence from the mineralogical literature to suggest that Cr may be inherently a relatively insoluble element. As a result, Cr tends to become enriched in remnant reactant phases, in rather the same way that Carmichael (1969) suggested that Al was a relatively immobile element in amphibolite-facies pelites, while the more mobile cations redistributed themselves more evenly into the product minerals. In this context, our observations that garnet preserved pre-existing variations in Cr content are not unexpected, although the scale of the compositional gradients is surprising. Brady (1983) suggested that differential transport of cations along grain boundaries is controlled by cation solubilities, either in the grain boundaries themselves or in an intergranular fluid. In metapelitic rocks Cr is known to be resistant to substitution reactions (Burns, 1993),

and may be less soluble in the grain boundary fluid than many other trace elements, potentially leading to very limited transport. Thus, the irregular Cr concentrations from single garnet and biotite crystals over short distances (Yang *et al.*, 1999) reflect both the original precursor distribution and the fact that Cr was insufficiently mobile to achieve even short-range equilibrium.

### 6.6.3 Oscillatory zoning in kyanite (?)

Oscillatory zoning in metamorphic minerals is not common except in fluid-dominated environments such as skarns and mineralized hydrothermal systems. Examples of oscillatory zoning in metamorphic systems produced by fluctuations in either fluid supply or fluid composition include the studies of Yardley (1991), Jamtveit (1991), Jamtveit *et al.* (1993), and Stowell *et al.* (1996). Sherlock and Okay (1999) suggested fluctuating redox conditions during subduction as a possible reason for oscillatory Cr zoning in lawsonite. In contrast, Schumacher *et al.* (1999) proposed that oscillatory Fe, Mn, and Ca zoning in pelitic garnet was produced by small-scale variations in the rate of decompression of the host rocks.

The Cr zoning patterns in kyanite in this study show several features in common with oscillatory zoning described in the studies noted above. In particular, some crystals show one or more concentric zones of Cr enrichment that can reasonably be correlated with former growth faces in the crystals. From this perspective, it could be argued that the Cr zoning represents a record of minor oscillations in physico-chemical parameters such as pressure, temperature, fluid or kyanite composition or $f_{O_2}$ during metamorphism.

On the other hand, however, it is clear that the Cr zoning is not continuous and symmetric in a single crystal, it tends to be better developed on the long axes of the crystals than the terminations, and in at least one case a single Cr band clearly bifurcates into two nonparallel bands. Furthermore, the Cr zoning patterns in coexisting kyanite and garnet cannot be correlated in a straightforward manner and the number of Cr annuli is not simply related to metamorphic grade (i.e., reaction history). These observations, coupled with the recognition of overprint zoning in garnet above, lead us to suggest an alternative explanation, *i.e.*, that the Cr zoning in kyanite is due to overprint zoning of Cr-rich matrix phases such as biotite and muscovite. This would provide a ready explanation for the better preserved Cr zoning parallel to the long axes of the crystals, which lie in the main $S_2$ foliation, and for the locally bifurcating Cr zoning.

In summary, although we are unable to come to a definite conclusion, we prefer the interpretation that at least part of the Cr zoning pattern in kyanite is due to overprinting of Cr-rich zones in a domainal fabric. However, we acknowledge that sporadic release of Cr from the breakdown of Cr-rich minerals such as epidote, ilmenite and micas can potentially provide a significant amount of Cr to growing minerals if it can be efficiently transported to the growth surfaces (Hickmott and Spear, 1992; Sánchez-Vízcaino *et al.*, 1995; Carlson and Chernoff, 1999). With respect to the latter mechanism, if diffusion of such locally-derived Cr in the interface region between growing kyanite and matrix is slow, and its concentration in either the grain boundary region or the metamorphic fluid is limited, discontinuous Cr zoning and different numbers and/or widths of Cr annuli could develop around a single kyanite crystal. In this model, the observation that Cr

zoning is poorly developed at the crystal terminations that lie at high angle to the matrix foliation could be used to infer that grain-boundary diffusion was faster parallel to the matrix foliation than perpendicular to it, and the variable number of Cr annuli may simply be a function of the local density of Cr-rich mineral phases such as micas, ilmenite and epidote on opposite sides of the growing kyanite crystal. However, we have been unable to come up with a ready explanation for the bifurcating zoning using this model. In the limit, both the overprint and oscillatory zoning hypotheses require that Cr is a relatively immobile element and that its distribution in kyanite is a reflection in some more or less direct way of the previous Cr distribution in the precursor mineralogy.

We conclude that the zoning in kyanite in our samples is best explained by sporadic release of Cr from Cr-rich minerals such as micas, ilmenite, and epidote, combined with sluggish diffusion of Cr in the matrix and interface region. In this context, the recent report of oscillatory Cr zoning in lawsonite from a blueschist terrane (Sherlock and Okay, 1999) is of interest. Their lawsonite shows a similar pattern of oscillatory zoning to our kyanite in that some annuli are discontinuous around an individual crystal, although overall the Cr annuli in their lawsonite are much more regular and numerous than in our kyanites. They suggested that the Cr zoning may be a result of changing $f_{O2}$ conditions, with the $Cr^{3+} = Al^{3+}$ substitution taking place preferentially under elevated $f_{O2}$ conditions. However, the present of some discontinuous Cr annuli leads us to suggest that sporadic release of Cr (due to breakdown of matrix chromite?) coupled with slow Cr diffusion during the growth of lawsonite may also have been a contributory factor.

These interpretations also imply that the crystal-chemical effects considered by

Ghera *et al.* (1986) on the partitioning of trace elements into kyanite are of secondary importance. They attributed the homogeneous distribution of Cr and the inhomogeneous distribution of Fe and Ti in kyanite from various metamorphic environments to cation size misfit in octahedral sites, with the smallest $Cr^{3+}$ ion being more easily substituted into the kyanite structure and the larger cations being clustered into local crystal defects. However, the different zoning patterns in this study indicate that the kinetics of element diffusion were more important than crystal-chemical effects.

### 6.3.4 Changes in Cr mobility

Non-systematic partitioning behaviour of Cr between coexisting phases in metapelites during amphibolite-facies metamorphism (*e.g.,* Treloar, 1987; Sánchez-Vízcaino *et al.*, 1995; Yang *et al.,* 1999) is consistent with the inference that Cr was less mobile than other analyzed elements. However, this is the first study in which Cr overprint zoning has been unequivocally demonstrated. The overprint zoning in the garnet zone (87-83, 87-271, and core of P-11) gives way to concentric zoning at higher metamorphic grade (garnet in 87-287 and rim of P-11), indicating either enhanced mobility at higher temperature or garnet growth in a homogeneous matrix in terms of Cr. The latter possibility is not considered here because garnets growing in quartz-plagioclase-rich layers (87-287) and in mica-rich layers (P-11) both show concentric Cr zoning. The enhanced Cr mobility indicates that interface-controlled partitioning becomes important with increasing metamorphic grade.

This transition in Cr mobility is caught in the P-11 garnet. The textural unconformity

in this garnet, defined by a sharp boundary between the inclusion-rich core and the inclusion-free rim, coincides with the change from Cr overprint zoning in the core to a relatively homogeneous distribution of Cr at the rim (Fig. 6.6c). Increased metamorphic temperature during the growth of the garnet rim ($X_{prp}$ increases, not shown) could have contributed to the enhanced mobility of Cr because diffusion is a first order function of temperature. However, an abrupt increase in temperature at the TU is not consistent with the inferred gradual change of metamorphic temperature assumed from the reaction history which is dominated by continuous reactions in the CNKFMASH model system. Furthermore, there is no independent evidence to support the addition of advected (*e.g.*, magmatic) heat that could possibly have caused a sharp rise in T during the garnet growth. We are therefore left with the observations that the growing garnet incorporated inclusions during a period of relatively low T and slow temperature rise when Cr was immobile, but excluded inclusions at the metamorphic peak when Cr was relatively mobile. This warrants further consideration.

Possible explanations for the contrasting behaviour of Cr at TU include a change in (1) fluid activity, (2) growth of the garnet rim in equilibrium with anatectic melts, or (3) a change in the rate of garnet growth triggered by change in the garnet-forming reaction. Cr is known to be mobile in some low grade, $CO_2$-dominated metamorphic systems, *e.g.*, Tracy (1991) reported chromian muscovite in veins and in the matrix of a calcite-dolomite marble. Thus a change in fluid composition from an $H_2O$-rich fluid during growth of the garnet core to a $CO_2$-rich fluid at the TU could potentially have changed the solubility, and hence transport of Cr (*e.g.*, Walther and Orville, 1983). However, there

is no field or geochemical evidence supporting the infiltration of large volumes of $CO_2$-rich fluid during growth of the garnet in sample P-11. No calcite or graphite were found in or adjacent to the garnet and $f_{O2}$ apparently did not change significantly at the textural unconformity (the calculated concentration of $Fe^{3+}$ in garnet decreases gradually from the core to the rim with no break at the TU, Fig. 6.11). Thus we do not attribute the TU to a change in the activity of any component in the metamorphic fluid.

The mobility of Cr is inferred to increase dramatically during muscovite or biotite dehydration melting (Spear and Kohn, 1996). These authors have shown that the muscovite dehydration melting reaction causes release of Cr into the matrix and that there is a concomitant decrease in the P concentration in garnet in equilibrium with melt because of the high solubility of P in the melt. In our case, however, we do not believe that this was the origin of the relatively homogeneous Cr rim in the P-11 garnet because there is no marked enrichment of Cr at the TU, apatite is abundant in the matrix, and there is no break in P zoning in the garnet at the TU (not shown). Furthermore, all existing petrologic interpretations from this area of Gagnon terrane have concluded that the migmatites resulted from the granite minimum melting reaction in Al-poor rocks rather than dehydration melting reactions in Al-rich rocks (Rivers 1983a, van Gool 1992). On the basis of these observations, we conclude that the textural unconformity in the garnet was caused mainly by a change in the rate of garnet growth. Possible relationships between the crystal growth rate (G) and the matrix diffusion coefficient (D) are depicted in Fig. 6.12. A dimensionless ratio defined by,

$$Crystal\ growth\ rate\,(G) \times Length\ scale\,(L) \Big/ Matrix\ diffusion\ coefficient\,(D)$$

is referred to as the *GL:D* ratio, where *L* is the length scale on which mineral growth occurs at growth rate (*G*). With respect to the P-11 garnet, we infer that nucleation of the garnet was delayed and significant overstepping of the garnet-forming reaction occurred at the beginning of the garnet growth, subsequently resulting in rapid growth and entrapment of abundant inclusions. During this stage, diffusion of Cr ions in the grain boundary region/pore fluid was slower than the rate of garnet growth and the pre-existing Cr distribution in matrix minerals was largely preserved intact ($GL:D > 1$). These growth conditions must have persisted from nucleation up to the TU. At the TU, we infer that the rate of garnet growth slowed abruptly, because of the relatively small amount of garnet produced by the new garnet-forming reaction, resulting in sufficient time for the elimination of matrix material from the growth face of the garnet. At this stage, Cr diffusion became faster than the rate of garnet growth, leading to the relatively homogeneous Cr distribution in the garnet rim ($GL:D < 1$). The TU thus records a crossover between the rates of garnet growth and Cr diffusion ($GL:D = 1$).

Although there are some preliminary estimates of the relative rates of volume diffusion for different elements in garnet (*e.g.*, Griffin *et al.*, 1996) and Cr grain boundary diffusion coefficients have been determined in a NiO-NiO matrix (Atkinson and Taylor, 1986), they are not directly applicable to the relatively low temperatures at which garnets grew in this study. Furthermore, growth rates for the garnets in this study are not known, so we are not able to provide quantitative values of the *GL:D* ratios to evaluate the qualitative conclusions shown in Fig. 6.12. However, using the garnet growth rate

calculated from Rb/Sr analyses of large garnets from Vermont ($1.4 \times 10^{-7}$ cm/year; Christensen *et al.*, 1989) and the Tauern Window ($0.67 \times 10^{-7}$ cm/year; Christensen *et al.*, 1991) and a length scale appropriate to an early stage of garnet growth (10 μm; Hickmott and Shimizu, 1990), the matrix diffusion coefficient for Cr at the TU where the *GL:D* ratio becomes unity can be roughly estimated as $4.43 \times 10^{-16}$ cm$^2$/sec. This estimated Cr matrix diffusion coefficient is two orders of magnitude slower than that determined from the NiO-NiO grain boundary diffusion experiments extrapolated from 700 to 600 °C ($1.9 \times 10^{-14}$ cm$^2$/sec; calculated from data of Atkinson and Taylor, 1986) and one order of magnitude slower than Joesten's (1983) dry grain-boundary diffusion coefficient estimate for oxygen ($5.2 \times 10^{-15}$ cm$^2$/sec).

However, the estimated grain boundary diffusion coefficient at the TU is comparable with that inferred from differences between rates of volume and grain boundary diffusion, and between estimated volume diffusion rates for Mn and Cr. Pyle and Spear (2000) estimated that volume diffusion of Cr in metapelitic garnet equilibrated at 560 °C was at least four orders of magnitude slower than volume diffusion of Mn, which has been estimated as $4.3 \times 10^{-20}$ cm$^2$/sec (Charkraborty and Ganguly, 1992). In addition, if we follow Joesten (1991) in assuming that grain boundary diffusion is roughly four orders of magnitude faster than volume diffusion during regional metamorphism, the resulting grain boundary diffusion coefficient for Cr can be roughly estimated as equal to the volume diffusion coefficient for Mn, *i.e.*, $4.3 \times 10^{-20}$ cm$^2$/sec, indicating that Cr partitioning in garnet will be controlled by grain boundary diffusion under amphibolite-facies metamorphism.

Increased $T$ would undoubtedly have caused an increase in the absolute rate of Cr diffusion in the garnet rim, but the discontinuous Cr annuli of variable concentration in both garnet and kyanite from the migmatite zone suggest that Cr diffusion was limited even at the highest grades examined here, so we consider the change in garnet growth rate to be the more critical factor.

## 6.7 Conclusions

This study has provided evidence for two and possibly three types of growth zoning in metamorphic garnets, referred to as *spiral, overprint,* and *oscillatory zoning. Spiral growth zoning* is displayed by both major and trace elements in garnet and the growth is restricted to the pressure shadow regions of a rotating garnet. Two forms of spiral zoning have been identified which are distinguished on the basis of the core to rim compositional change measured parallel to the spirals. Recognition of spiral growth zoning provides a new tool to resolve the controversy over rotation versus non-rotation of snowball garnet porphyroblasts. *Overprint growth zoning,* which is exhibited by Cr zoning patterns that are parallel to straight and/or spiral internal fabrics ($S_i$) in the garnet, indicates limited mobility of Cr during growth, and is reported here from amphibolite-facies assemblages. The existence of overprint growth zoning in several of the garnets examined indicates that Cr partitioning was far from equilibrium and provides a simple explanation of the irregular Cr distribution coefficients between garnet and coexisting minerals determined by previous workers. Cr zoning in kyanite displayed by crystals with Cr zoning of variable width, continuity, and Cr concentration in individual annuli, may be a result of

oscillatory or overprint zoning or both. In all three cases, it implies limited mobility of Cr during kyanite growth, even under upper amphibolite-facies conditions. Despite this negative conclusion concerning the attainment of equilibrium with respect to Cr, it is possible to derive qualitative information on the relative rates of Cr diffusion and garnet growth in many samples. We have derived a dimensionless ratio (*GL:D*) to qualitatively explain the differences in texture and Cr behaviour in our analysed garnets. Examined samples exhibit evidence of a range of *GL:D* from >1 to <1. One sample displays a textural unconformity coincident with a change in the behaviour of Cr, which we interpret to represent a crossover in the rates of growth and Cr diffusion, *i.e.*, where *GL:D* changes from >1 through unity to <1. The results from this study emphasize the importance of element diffusion and crystal growth rates in controlling the incorporation of trace elements and inclusions within porphyroblasts.

Table 6.1. Mineral assemblages of the seven samples from western Labrador.

| *Samples* | | *Ms* | *Chl* | *Ep* | *Ky* | *Accessory minerals* | *Inclusions in Grt* | *P / T* |
|---|---|---|---|---|---|---|---|---|
| 87-83 | Qtz, Bt, Pl, Grt | × | R | | | Ap, Zrn, Ilm, Tur | Qtz, Pl, Ap, Zrn, Ilm, Tur, Gr | 5.9 / 435 |
| 87-86 | Qtz, Bt, Pl, Grt | × | R | | | Ap, Zrn, Ilm, Tur | Qtz, Pl, Ap, Zrn, Ilm, Tur, Ep | 5.5/442 |
| 87-271 | Qtz, Bt, Pl, Grt | R | R | | | Ap, Zrn, Ilm, Py, Tur | Qtz, Bt, Zrn, Ilm, Ap, Py, Mag, Ep | 6.0 / 482 |
| 87-287 | Qtz, Bt, Pl, Grt | × | R | × | | Ap, Zrn, Rt, Aln | Qtz, Bt, Pl, Ap, Zrn, Aln, Ep | 10.0 / 665 |
| 88-74 | Qtz, Bt, Pl, Grt | × | R | | × | Ap, Zrn, Rt, Py, Mnz | Qtz, Ilm, Ap, Rt, Mag, Zrn | 10.0 / 670 |
| P-11 | Qtz, Bt, Pl, Grt | R | R | | | Ap, Zrn, Rt, Py | Qtz, Ap, Zrn, Ilm, Rt, Py, Mag, Ep | 11.0 / 702 |
| 88-80 | Qtz, Bt, Pl, Grt | R | R | | × | Ap, Zrn, Ilm, Py | Qtz, Ap, Zrn, Rt, Ilm, Mnz, Ep | 9.0 / 645 |

Mineral abbreviations from Kretz (1983). ×-present, blank-absent, R-retrograde minerals. P (kbar) and T (°C) estimated by van Gool (1992).

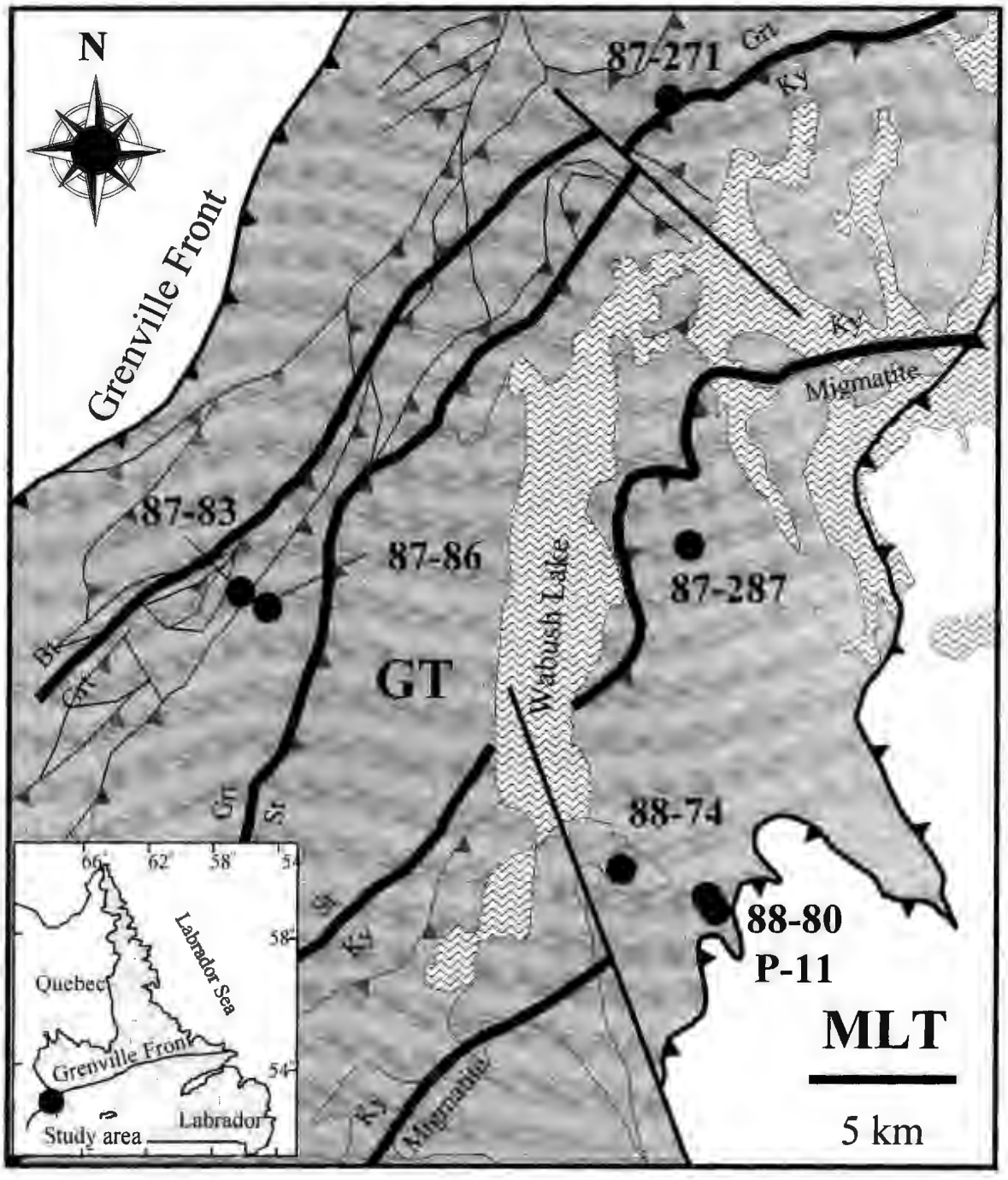


Fig. 6.1. Generalized geologic map of the northern Grenville Province in western Labrador, Canada, showing metamorphic isograds and locations of the seven analyzed samples. GT, Gagnon terrane; MLT, Molson Lake terrane. Geologic map and metamorphic isograds from van Gool (1992).

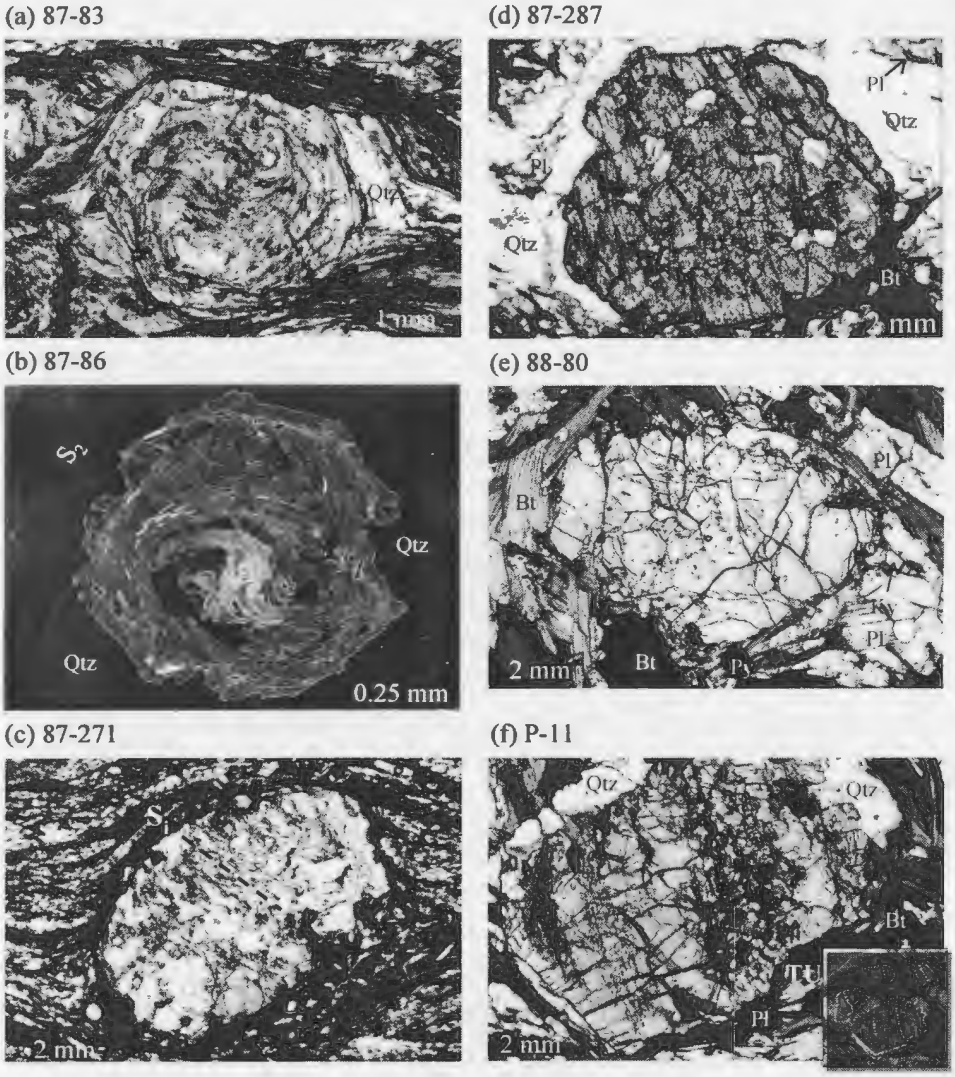


Fig. 6.2. (a-f) Photomicrographs and a BSE image of the six metapelitic samples from western Labrador. (a) Garnet porphyroblast from sample 87-83 showing spiral fabric mainly defined by inclusions of ilmenite, graphite, and quartz. (b) A BSE image of sample 87-86; white core is due to high Y concentration; small white rectangular inclusions are ilmenite. (c) Anhedral garnet from sample 87-271 showing a straight internal fabric and significantly resorbed rims. Subhedral and anhedral garnet porphyroblasts from sample 87-287 (d) and 88-80 (e) showing no preferred orientation of inclusions. (f) Garnet from sample P-11 showing two generations of growth (inclusion-rich core and inclusion-free rim), separated by a textural unconformity (TU). Inset in (f) shows the four fragments of the former large garnet grain and the surrounding microstructures. Note that garnets from samples 87-287 and 88-80 grew mainly on quartz and plagioclase rich layers whereas garnets in other samples grew on alternating quartz-plagioclase and mica-rich layers.

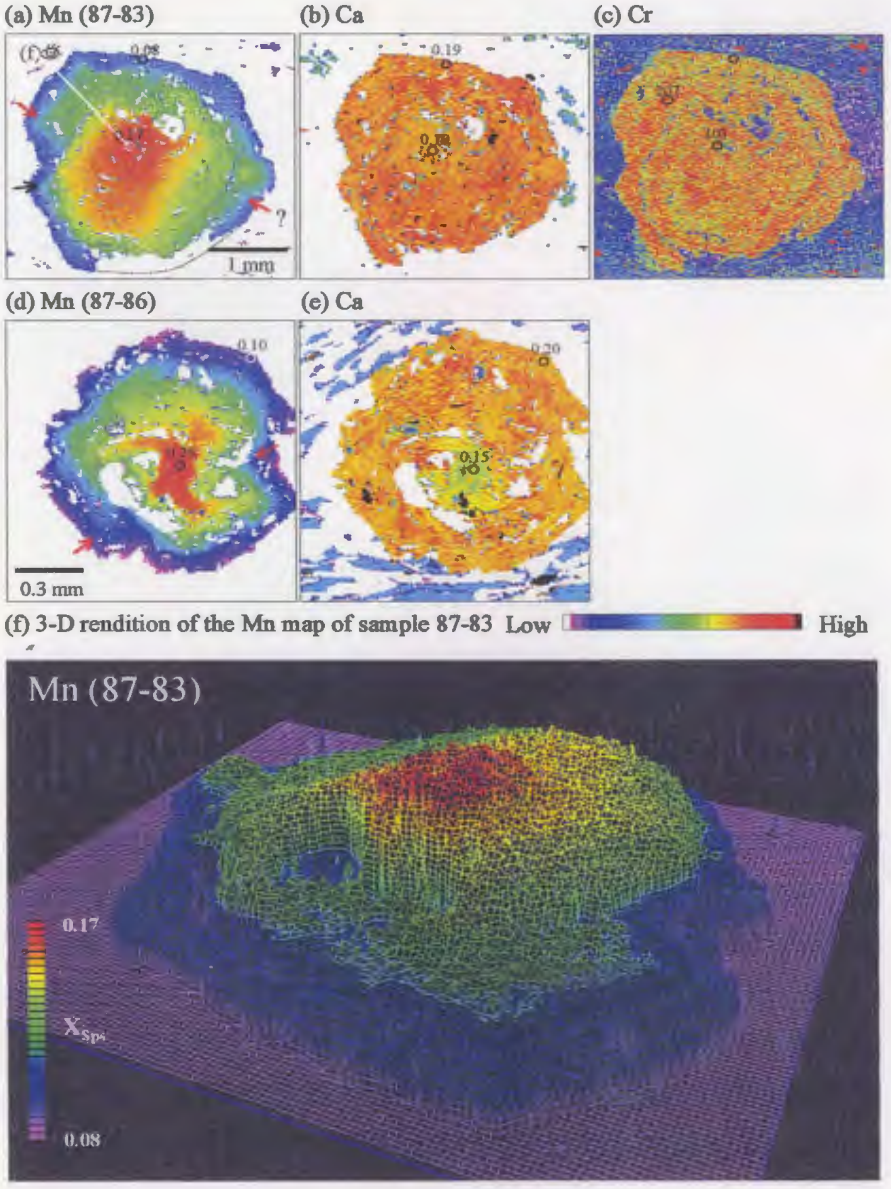


Fig. 6.3. (a-c) X-ray composition maps for Mn, Ca, and Cr of the garnet from sample 87-83 (garnet-zone). Red arrows in the Mn map indicate growth faces produced by spiral growth of the garnet. The small garnet that was incorporated during the growth is situated in the right margin of the large garnet. Black arrow represents the euhedral growth faces cross-cutting the inclusion trails. A white line represents zoning profile in Fig. 6.4a. (d-e) X-ray composition maps for Mn and Ca of the garnet from sample 87-86 (garnet-zone). Red arrows in the Mn map indicate growth faces. (f) A 3-D rendition of the Mn map of sample 87-83 produced by plotting raw Mn X-ray counts, showing the spiral growth pattern. See (a) for viewing direction. In all figures, selected Mn, Ca, and Cr concentrations from electron microprobe and laser analyses are given in mol% (Mn, Ca) and ppm (Cr).

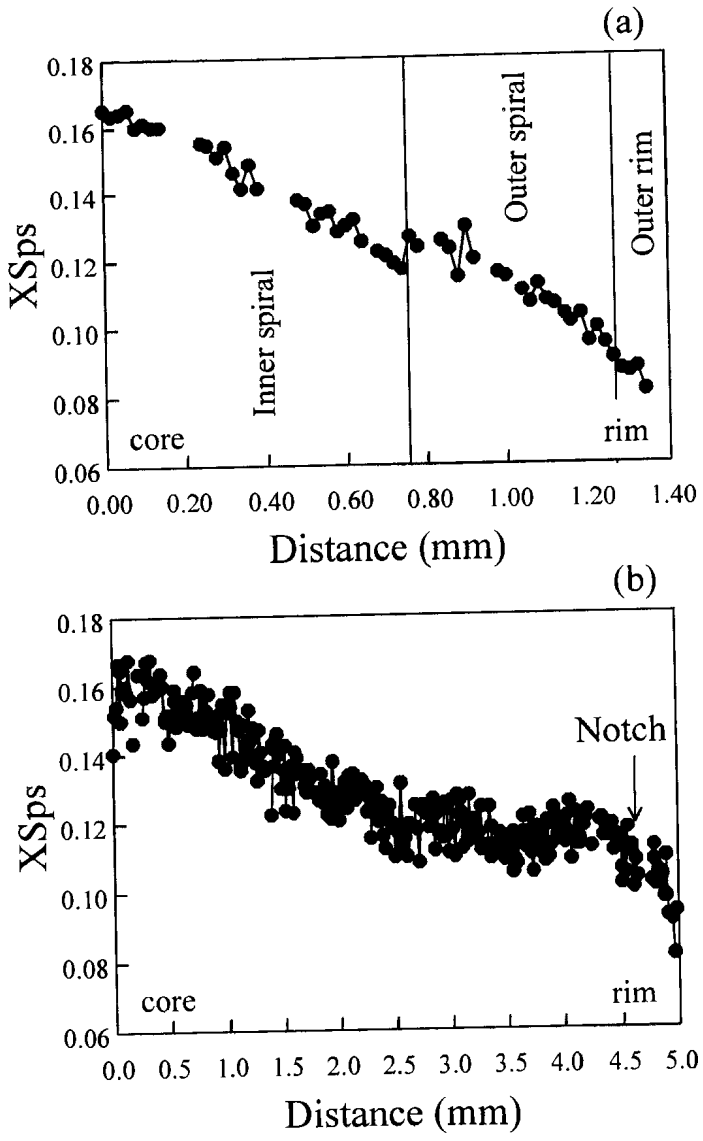


Fig. 6.4. Electron microprobe traverses of garnet in sample 87-83 along a radial transect across the garnet (a) and parallel to the spiral inclusion trails (b). Note the compositional break between inner and outer spirals in (a).

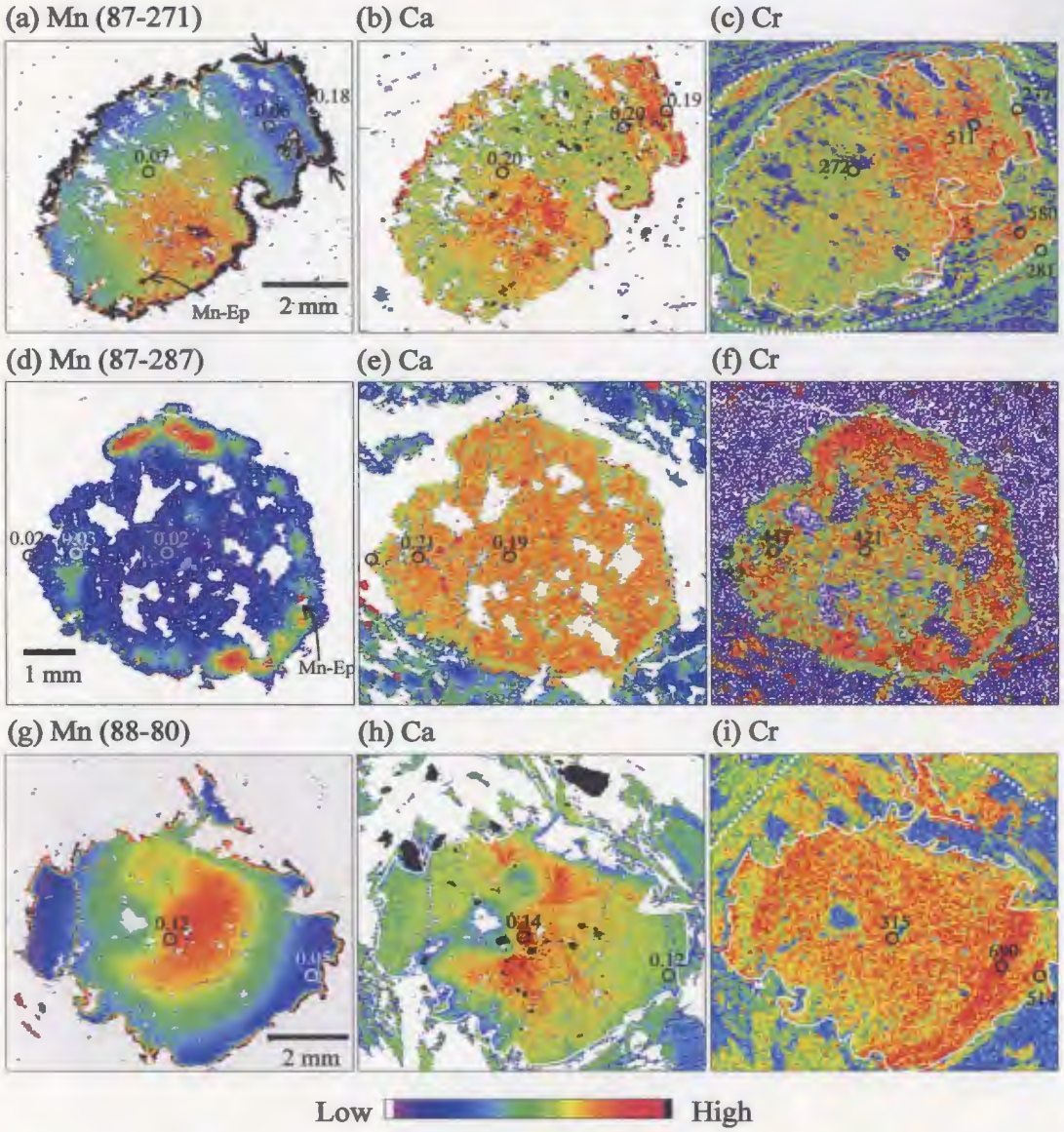


Fig. 6.5. (a-c) X-ray composition maps for Mn, Ca, and Cr for the garnet from sample 87-271 (garnet-zone). The outline of the garnet in the Cr map has been enhanced for clarity. Note the wide range in Cr concentrations in matrix biotite in the lower right corner of the map. The postulated original size of the garnet is outlined with white dotted lines in Cr map. (d-f) X-ray composition maps for Mn, Ca, and Cr for the garnet from sample 87-287 (migmatite-zone). (g-i) X-ray composition maps for Mn, Ca, and Cr for the garnet from sample 88-80 (migmatite-zone). The outlines of the garnet in the Ca and Cr maps have been enhanced for clarity. White dotted lines in Cr map represent original size of the garnet. In all cases, selected Mn, Ca, and Cr concentrations of garnet from electron microprobe and laser analyses are given in mole % (Mn, Ca) and ppm (Cr).

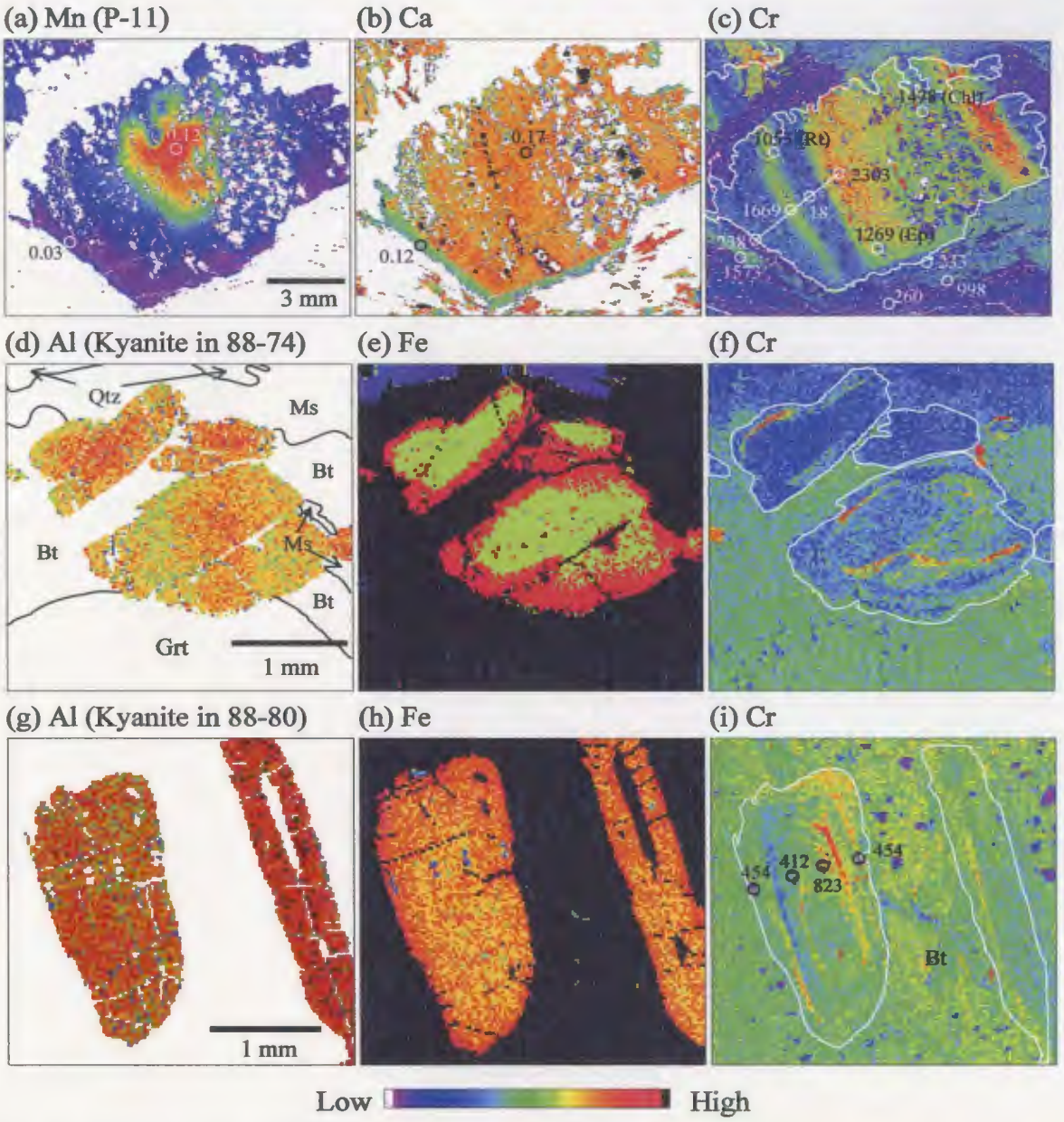


Fig. 6.6. (a-c) X-ray composition maps for Mn, Ca, and Cr for the garnet from sample P-11 (migmatite zone). Apatite and epidote inclusions appear black in the Ca map. Cr displays overprint zoning in the core which extends to the other fragment of the garnet grain in the upper left corner. Note the sharp decrease of Ca and Cr contents at the textural unconformity, especially at the lower margin of the garnet. Representative Cr concentrations of garnet, biotite, chlorite, epidote, and rutile from laser spot analyses are given in ppm. a-a′ is location of the traverse shown in Fig. 6.6. (d-i) X-ray composition maps for Al, Fe and Cr in kyanite from samples 88-74 and 88-80. Cr concentration of kyanite in sample 88-80 is given in ppm.

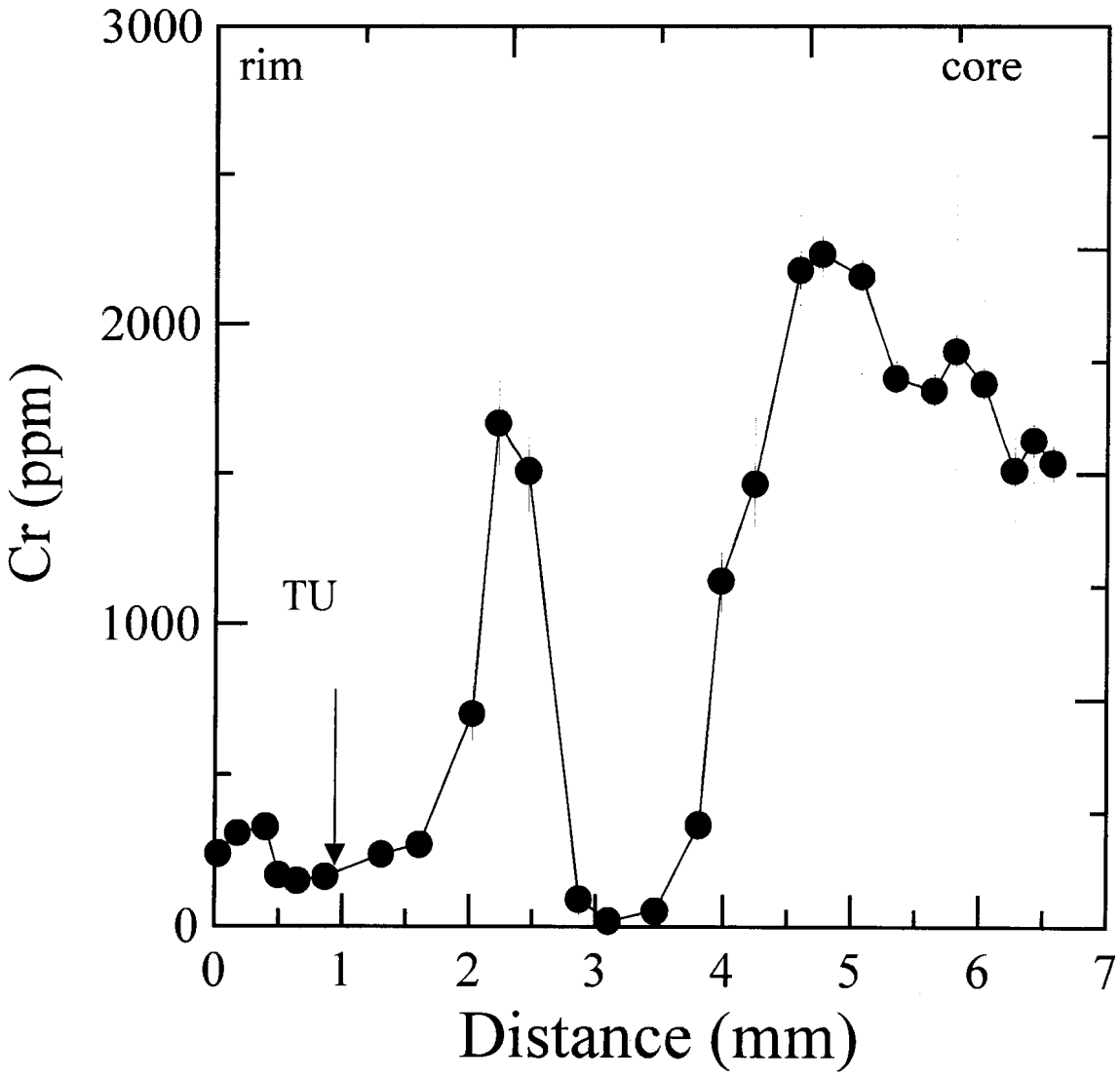


Fig. 6.7. A LAM-ICP-MS traverse of garnet in sample P-11 from core to rim.

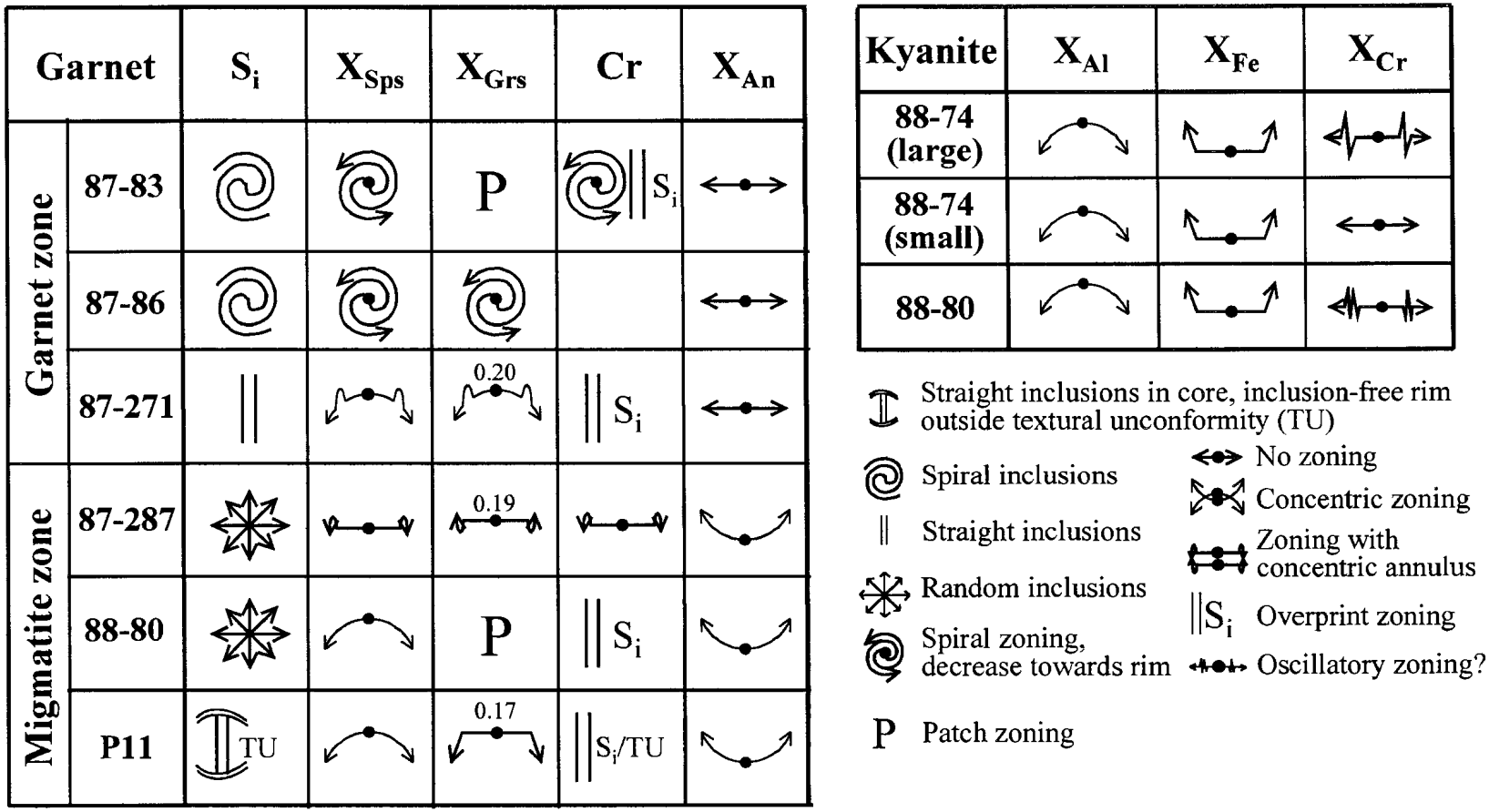


Fig. 6.8. Summary of inclusion and zoning relationships of the analyzed garnet and kyanite grains.

(a) Mn map of 87-83

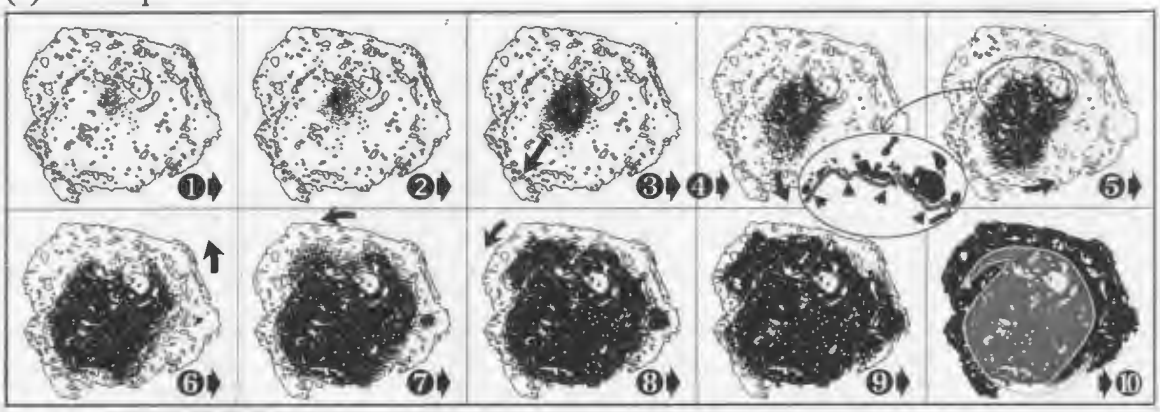


(b) Mn map of 87-86

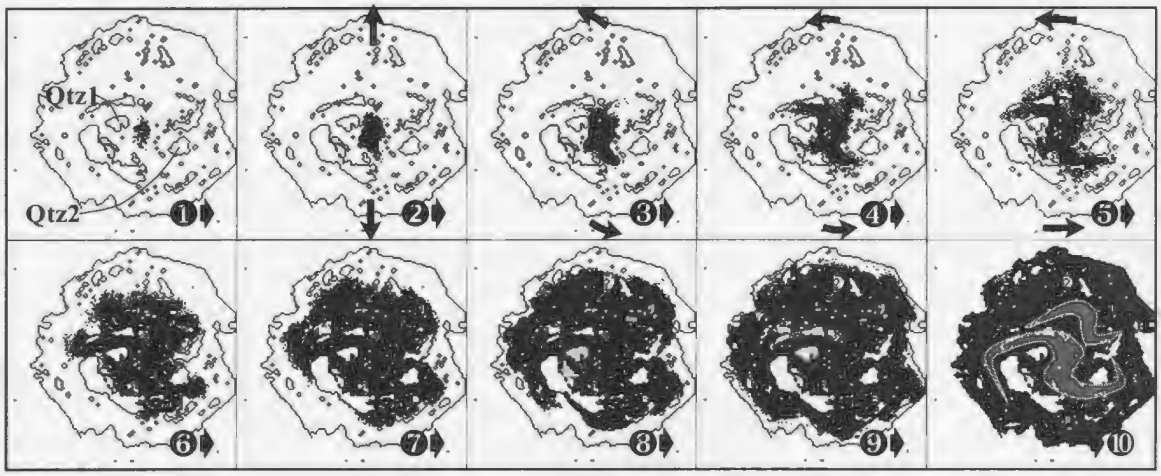


Fig. 6.9. (a-b) A series of Mn X-ray maps of samples 87-83 and 87-86 produced by applying sequential threshold to the original images. The postulated spiral patterns are overlayed in the last stage of each sample.

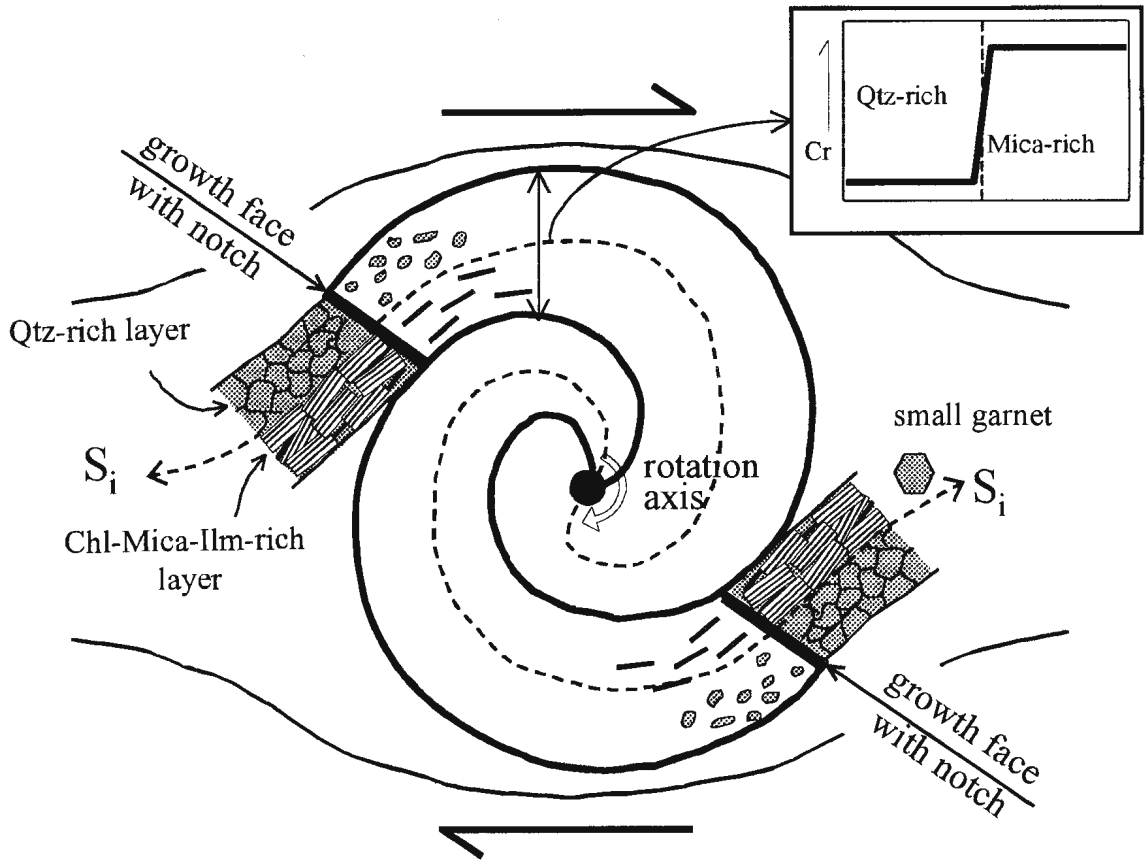


Fig. 6.10. Schematic 2-D illustration of a section through a garnet undergoing spiral growth, with active growth faces illustrated. In 3-D, each growth face would extend across the diameter of the garnet and taper to a point where the external foliations converge. Cr zoning profile for garnet overgrowing quartz- and mica-rich layers is depicted schematically.

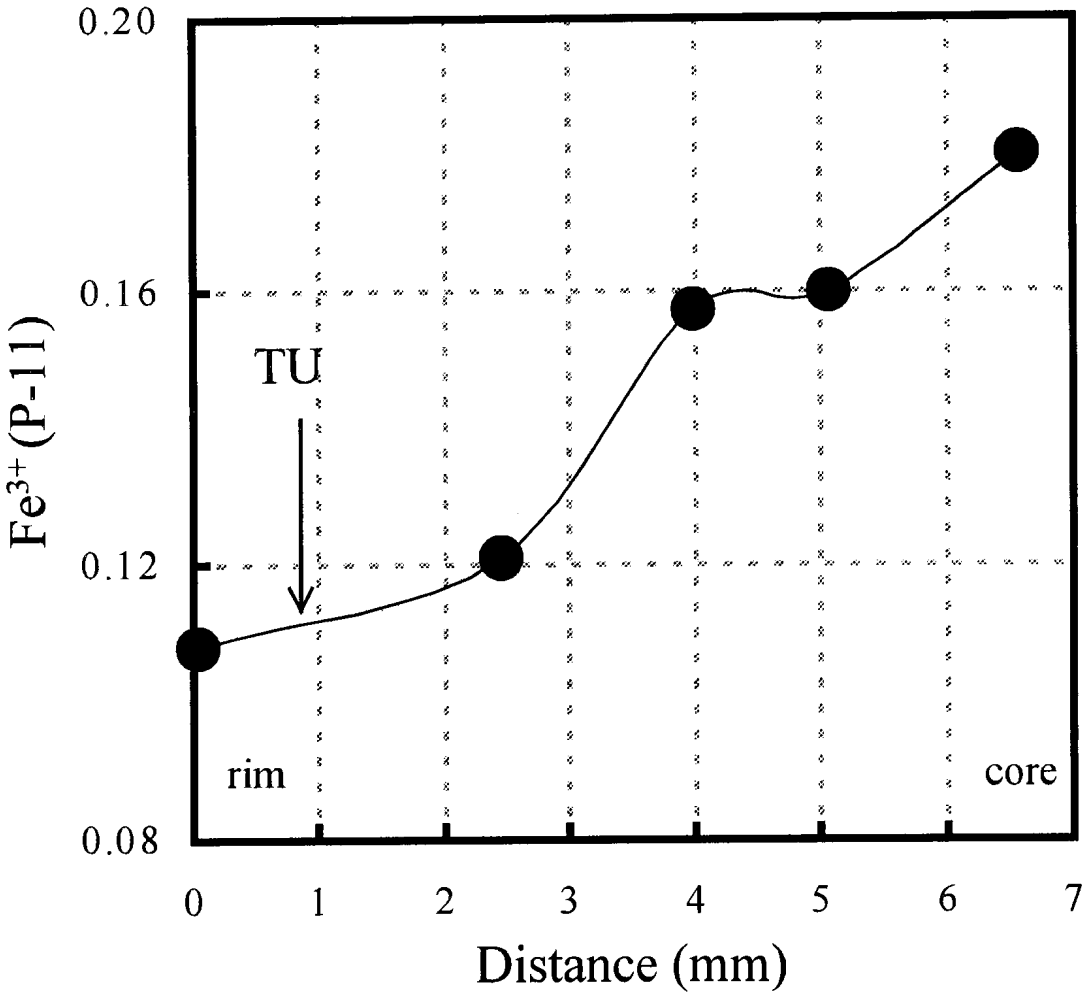


Fig. 6.11. Rim-to-core $Fe^{3+}$ zoning for the garnet from sample P-11. $Fe^{3+}$ concentrations are estimated on the basis of cationic charge balance. TU represents textural unconformity defined by inclusion-rich core and inclusion-free rim.

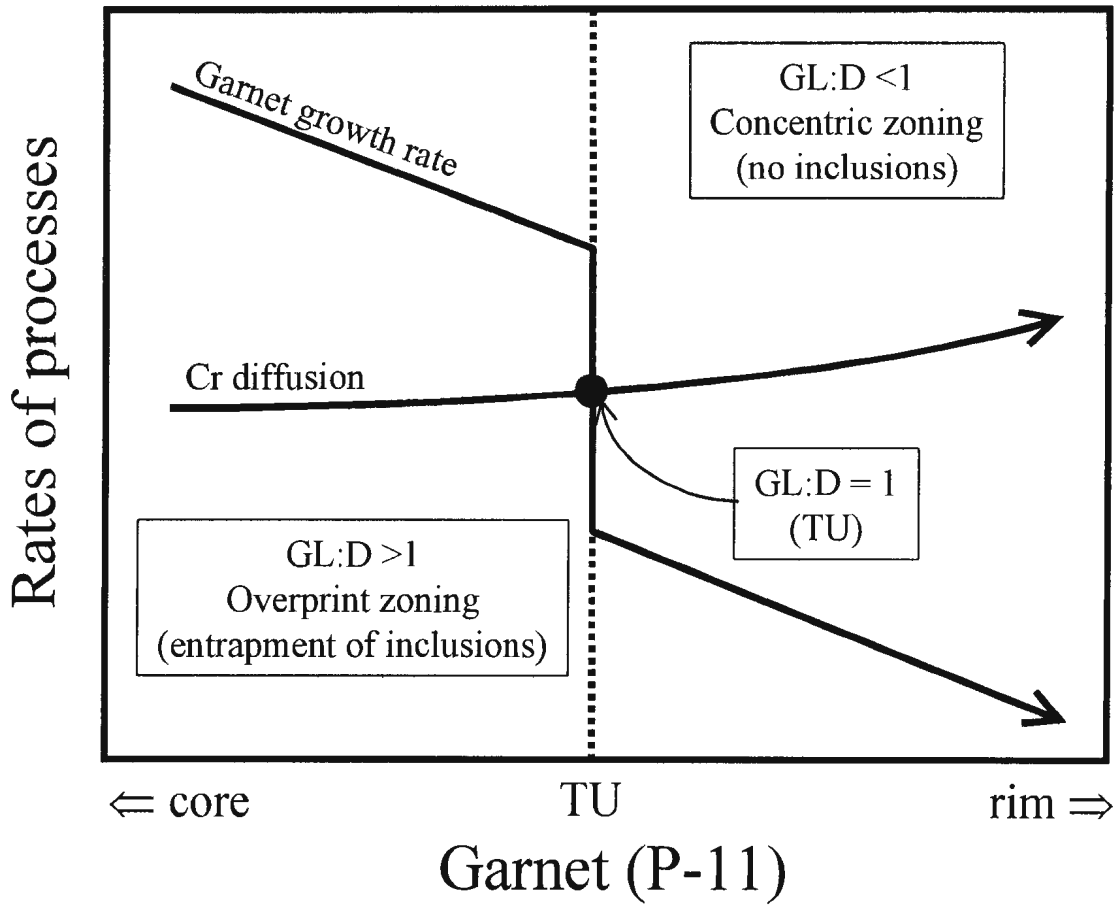


Fig. 6.12. Schematic diagram illustrating the crossover between rates of Cr diffusion and garnet growth (in garnet P-11), with $S_i$ and Cr overprint zoning in the core separated by a textural unconformity (TU) from an inclusion-free rim with concentric Cr zoning. Note that although the rate of Cr diffusion increases slightly from core to rim in the garnet due to increasing T, the reduction in garnet growth rate is inferred to be a more significant factor in determining whether inclusions are entrapped and Cr behaves as a mobile species.

# Chapter 7: The origin of Mn and Y annuli in garnet and the thermal dependence of P in garnet and Y in apatite in calc-pelite and pelite, Gagnon terrane, western Labrador

## 7.1 Introduction

Major and trace mineral reaction histories of samples from metamorphic terranes are key to deciphering P-T paths of metamorphism, understanding the composition of metamorphic fluids, and interpreting the ages of metamorphism. Reaction histories have been traditionally interpreted by examination of major element zoning in metamorphic minerals and the study of inclusion suites in porphyroblasts. However, major element zoning commonly does not yield unique results in terms of metamorphic processes and also does not provide information on the involvement of trace minerals. This is especially important with respect to trace minerals that are used for age dating because potentially they may provide an opportunity to date reaction processes. Recently, trace element zoning in garnet has been shown to be a potentially useful monitor of metamorphic processes (Hickmott et al., 1987; Hickmott and Shimizu, 1989; Hickmott and Spear, 1992; Lanzirotti, 1995; Schwandt et al., 1996; Spear and Kohn, 1996; Bea et al., 1997; Chernoff and Carlson, 1999; Pyle and Spear, 1999; Pyle and Spear, 2000), and this

subject is explored further in this paper.

Several trace element zoning studies of garnet porphyroblasts have reported individual or multiple Y annuli of variable shape and width in pelitic garnets from greenschist to granulite facies (e.g. Lanzirotti, 1995; Schwandt et al., 1996; Chernoff and Carlson, 1999; Pyle and Spear, 1999). Understanding the origin of these features is important because they may reflect a wide range of metamorphic processes such as resorption of garnet, breakdown of Y-enriched trace minerals, kinetic effects such as growth rate, and/or metasomatic infiltration of Y-enriched metamorphic fluids. Phosphorus and Y are major elements in the minerals apatite $(Ca_5PO_4)_3(F,OH)$ and xenotime ($YPO_4$). The chemical potentials of P- and Y-components in garnet and apatite are potentially buffered by phase relations with these minerals and other silicates in a rock. Thus, at equilibrium, P and Y zoning in garnet may reveal changes in pressure, temperature, and phase relations of P- and Y-rich minerals during garnet growth.

In this study, the zoning patterns and trace element contents of garnet, apatite and epidote-group minerals are used to investigate the dependence of trace element substitution on metamorphic grade, to decipher various metamorphic processes during growth of the minerals and to identify the former presence of trace minerals that are no longer present in the stable mineral assemblage.

## 7.2 Geological setting and sample description

The seven samples investigated are calc-pelites and pelites from the Paleoproterozoic

Knob Lake Group, in the Gagnon terrane of the Grenville Province of western Labrador, Canada (Fig. 7.1). Metamorphic grade in this part of Gagnon terrane increases from chlorite-zone in the northwest near the Grenville Front, through the garnet-, staurolite- and kyanite-zones, to migmatite-zone (incipient partial melting) in the structurally highest part of the terrane over a distance of about 30 km (Rivers, 1983a). However, the migmatite-zone samples investigated in this study do not show any textural evidence for partial melting because they are pelites and the first $H_2O$-saturated melting reactions take place in semi-pelitic compositions (Rivers, 1983a). In pelitic rocks, the upper limit of the metamorphic field gradient occurs below the vapor-absent muscovite-melting reaction, since the assemblage muscovite-plagioclase-quartz is still stable and the assemblage kyanite-potassic feldspar (± secondary muscovite) has not been observed (Rivers 1983a).

Metamorphism and deformation in Gagnon terrane are inferred to be a result of northwest-directed understacking of the Gagnon terrane beneath the Molson Lake terrane (Brown et al., 1992; van Gool, 1992; Rivers et al., 1993). This part of the Gagnon terrane underwent two episodes of penetrative deformation during the understacking event (Rivers, 1983b; van Gool, 1992), with $S_1$ being recorded in the analyzed samples as an internal foliation ($S_i$) within garnet porphyroblasts and $S_2$ being the external matrix foliation. The peak of regional metamorphism coincided with the second phase of deformation. Estimates of the peak temperature and pressure conditions during metamorphism were determined with garnet-rim and matrix-mineral compositions (van Gool, 1992). Temperature variation across the metamorphic gradient, calculated using the Ferry and Spear (1978) geothermometer equation, ranges from 450 to 750°C, and

associated pressures determined using the garnet + plagioclase + kyanite + quartz and garnet + plagioclase + biotite + muscovite geobarometers of Newton and Haselton (1981) and Hodges and Spear (1982), range from 6 to 11 kbar. van Gool (1992) and Indares (1995) inferred that the rocks followed "hair-pin" shaped *P-T-t* paths with an average slope of 1kbar/50°C for both prograde and retrograde paths, implying a short period of isobaric heating and decompression after attainment of peak pressure conditions. Additional details concerning the geologic setting, phase relations, petrography, and *P-T* conditions can be found elsewhere (Rivers, 1983a; Rivers, 1983b; van Gool, 1992; Rivers et al., 1993; van Gool and Cawood, 1994; Indares, 1995; Yang and Rivers, 2001).

The mineral assemblages of the seven analyzed samples are given in Table 7.1. All seven samples contain garnet, biotite, plagioclase, and quartz with or without primary muscovite in the matrix. Garnet nucleated before the development of the $S_2$ foliation, and asymmetric pressure shadows around garnet associated with that foliation are common. Garnet porphyroblasts from the garnet- and staurolite-zones are rich in inclusions. Most garnet porphyroblasts from the migmatite-zone are characterized by inclusion-rich cores and inclusion-free rims. Two garnet porphyroblasts (samples 88-74 and 88-88) show an oscillatory textural zoning pattern defined by alternating inclusion-rich and inclusion-free zones. Most garnets investigated in this study are variably resorbed as a result of reaction to form biotite and plagioclase, and show evidence of minor late retrogression to chlorite.

The bulk compositions of all samples except for 88-74 are sufficiently calcic to stabilize epidote-group minerals. Epidote occurs in the matrix as well as in the cores of garnets in sample 87-271 and 87-287, whereas in samples 87-86, 87-271, 88-88, and 88-

80 epidote occurs only as inclusions in garnet. Epidote in samples 87-271 and 87-287 is Mn-rich, containing 12 and 7 mol% piemontite respectively. In addition to Mn-rich epidote inclusions, Mn-free epidote with allanite cores occurs both as a matrix mineral and as inclusions in garnet in sample 87-287. Calcite occurs as a minor phase in other samples from the lower grade rocks, but no matrix carbonate or carbonate inclusions in garnet were observed in the samples examined in this study. Apatite, zircon, rutile, and ilmenite commonly occur as minor phases with sparse occurrences of tourmaline, magnetite, allanite, monazite, and pyrite. Ilmenite predominates over rutile in the lower grade samples, with the reverse distribution occurring in the higher-grade rocks, compatible with the inferred *P-T-t* path. Magnetite is found in the most Fe-rich samples such as 87-279, 87-271, and 87-287. Graphite occurs only in sample 87-83, and minor chlorite is a retrograde phase in many samples. Neither K-feldspar nor xenotime were found in any of the samples investigated in this study.

## 7.3 Analytical techniques

Major element compositions (Si, Al, Fe, Mg, Mn, Ca) of garnet were determined by energy-dispersive (ED) X-ray analysis using a LINK ED detector. ED analyses used a cobalt gain calibration and were refined using the LINK ZAF correction program. Analytical conditions included an accelerating potential of 15 kV and a beam current of 20 nA, focused to 1 μm in diameter. Counting times were 60 sec on the samples. The precision of the analyses was generally better than 3% RSD for the major elements.

Apparent concentrations of Ti, P, and Y in garnet and Y in apatite and epidote-group minerals were determined by wavelength-dispersive (WD) X-ray analysis using the Cameca SX-50 electron microprobe at Memorial University of Newfoundland. Operating conditions for garnet analyses included an accelerating potential of 15 kV, a beam current of 300 nA, a beam size 3 μm in diameter, and 60 sec counting times for garnet and epidote-group mineral analyses, whereas for apatite analyses an accelerating potential of 15 kV, a beam current of 20 nA, a beam diameter of 10 μm, and counting times of 120 sec were used. Elemental peaks with no background measurements were standardized using ilmenite (Ti), apatite (P) and xenotime (Y) as standards, resulting in *apparent ppm* which is not ZAF corrected. Although quantitative concentrations of trace elements were not calculated, relative variability of elements across garnet and apatite porphyroblasts provides significant petrologic information. Repeated analyses of an almandine standard revealed that the precision was better than 10% RSD for Ti and 3 % RSD for P and Y. Abnormally high Ti concentrations near Fe-Ti oxides are attributed to fluorescence of Ti X-rays by Fe X-rays (Feenstra and Engi, 1998).

The trace minerals were examined using a SEM in BSE mode. Chemical characterization was aided by qualitative energy dispersive X-ray microanalysis performed with a Link systems 860 X-ray microanalyser attached to the SEM. In an attempt to obtain central-section zoning profiles and maps of garnets, the largest garnet in each thin section was analyzed; however, this method does not guarantee a garnet center section. X-ray maps were obtained in WD spectrometry mode, with an accelerating potential of 15 kV and a beam current of 50~100 nA for major elements and 20 kV and

500~700 nA for trace elements using the method described in Yang and Rivers (2001).

Absolute concentrations of P, Sc, Ti, V, Co, Zr, Y, and REE were analyzed in garnet using the LAM-ICP-MS at Memorial University. A complete account of the characteristics and the optimization of this instrument is reported elsewhere (Taylor et al., 1997a; Yang et al., 1999; Yang and Rivers, 2000), and only the key specifications relevant to the present work are given here. The combination of a Q-switched UV laser and optimization of the laser parameters provide a high spatial resolution (10 μm in diameter). However, in order to achieve a balance between spatial resolution and detection limits, the pit size was set at 30~40 μm. Repeated analyses of a glass standard (BCR -2) were used to estimate the precision of the LAM-ICP-MS analyses. This was typically in the range of 6-25 % RSD, depending on the element and its concentration. The LAM-ICP-MS concentration values were calculated using Si concentration obtained by electron microprobe as an internal standard. However, the error bars do not take into account the precision on the electron microprobe determination (estimated at 2% RSD for Si) by error propagation. Analysis spots along each laser traverse were spaced from 30 to ≥100 μm apart because of time limitations and the presence of inclusions. Thus, WD profiles give more detailed zoning patterns for Y, Ti, and P. However, LAM-ICP-MS profiles are used when trace element concentrations are below detection limits of WD analysis (~ 100 ppm).

## 7.4 Results

### 7.4.1 Major and trace element zoning in garnet and reaction histories

Major and trace element zoning patterns in representative garnets from seven samples were examined using X-ray mapping (Mn, Ca, Y, P), quantitative (Fe, Mg, Mn, Ca) and qualitative (Ti, P, Y) electron microprobe zoning profiles, and laser ICP-MS zoning profiles (Sc, V, Co, Y, Zr, REE). Details of Mn and Cr zoning in garnet from samples 87-86, 87-271, 87-287, 88-74, and 88-88 are discussed in Yang and Rivers (2001). Due to abundant ilmenite and rutile inclusions in most of the examined garnets, interpretation of fine-scale zoning for Ti is difficult. In this study, Sm is considered as a representative for the LREE (Nd, Sm), Gd as a representative for the MREE (Eu, Gd, Tb, Dy), and Yb as a representative for the HREE (Ho, Er, Tm, Yb, Lu). Points labeled A and B in the zoning profiles represent the locations of compositional breaks defined by one or more elements.

### 7.4.2 Regional metamorphic isograd reactions

Since detailed discussions of the metamorphic reactions among major phases in metapelitic rocks from the Gagnon terrane have been presented by Rivers (1983a), van Gool (1992) and Yang and Rivers (2001), only metamorphic reactions in calc-pelites are discussed here. For details of staurolite-, kyanite-, and melt-forming reactions, the reader is referred to Rivers (1983a), van Gool (1992), and Yang and Rivers (2001). The changes of mineral compositions and volumes (modes) of minerals in calc-pelites with changing *P-T* were modeled using the Gibbs method by Menard and Spear (1993). In this study, we use their method to infer compositional zoning and the trend of mineral growth and

consumption along the *P-T* path estimated by van Gool (1992). We examine two ways by which the observed zoning could have been achieved, i.e., on the prograde compression-heating path and or by a combination involving isobaric heating or decompression. The results are summarized in Table 7.2.

A common mineral assemblage in calc-pelites in the garnet zone in Gagnon terrane is garnet + biotite + plagioclase + quartz + muscovite, with chlorite and epidote occurring as inclusions in garnet. Along the initial compression-heating path, the net reaction is:

$$Chl + Ms + Ep = Grt + Bt + Pl + H_2O \quad (7.1)$$

For this reaction, both the compression-heating and isobaric heating/decompression paths result in the same sense of compositional changes in garnet; i.e., $X_{Mg}$ (Mg/Mg+Fe) increases and $X_{Sps}$ (Mn/Fe+Mg+Mn+Ca) and $X_{Grs}$ decrease with the growth of garnet. $X_{An}$ of plagioclase is nearly constant during the compression-heating path, but increases slightly during isobaric heating or decompression. Reaction (7.1) would result in the release of Sc, Y, Zr and REE from epidote (Hickmott and Spear, 1992). The exact nature of enrichment of these elements in garnet would depend on the type, abundance and degree of zoning of the epidote-group mineral that was consumed.

The subsequent evolution depends on whether chlorite or epidote reacts out first (Menard and Spear, 1993). If chlorite is removed from the assemblage first, the net reaction along the compression-heating path becomes:

$$Ep + Bt = Grt + Pl + Ms + Qtz + H_2O \quad (7.2a)$$

Garnet and plagioclase continue to grow with no variation in $X_{Sps}$ and with increasing $X_{Grs}$ and $X_{An}$ along the compression-heating path. (Table 7.2). However, along the

isobaric heating or decompression paths garnet is consumed in the reaction:

$$Grt + Ms + Ep + Qtz = Bt + Pl + H_2O \quad (7.2b)$$

(see Fig. 7.12d of Menard and Spear, 1993). Thus, evidence of garnet resorption by reaction 7.2b indicates a change in the prograde *P-T* path from compression-heating to isobaric heating. On the other hand, if epidote is consumed first, the assemblage becomes a simple pelite and the net reaction becomes:

$$Chl + Pl + Ms + Qtz = Grt + Bt + H_2O. \quad (7.3)$$

The directions of compositional changes in garnet and plagioclase as a result of reaction (7.3) are independent of the two different *P-T* paths; in both cases, $X_{Mg}$ of garnet increases and $X_{Sps}$, $X_{Grs}$ and $X_{An}$ all decrease. The transition from reaction (7.1) to (7.3) is characterized by a sharp decrease in Ca in garnet due to the removal of epidote from the assemblage (Menard and Spear, 1993). Garnet growing by reaction (7.3) is expected to fractionate garnet-compatible elements such as Sc, Y, and HREE originally present in epidote. After both chlorite and epidote are removed, reaction (7.4) comes into play:

$$Grt + Ms = Bt + Pl \quad (7.4)$$

For this reaction, Menard and Spear's model predicts that garnet will be consumed along an isobaric heating path, but will continue to grow along a compression-heating path (reaction goes from right to left), with increasing $X_{Mg}$ and decreasing $X_{Sps}$ and $X_{Grs}$. Coexisting plagioclase becomes more enriched in the anorthite component.

This prediction of compositional changes of garnet and plagioclase and associated growth or consumption of garnet, together with measured major and trace element zoning patterns and inclusion assemblages, were integrated to infer the reactions that occurred

during the growth of garnet in Gagnon terrane.

### 7.4.3 Analyzed Samples

***87-86 (Garnet-zone).*** The analyzed garnet from sample 87-86 (0.8 mm in diameter) has an euhedral crystal shape with the left side partly resorbed, as indicated by non-concentric Mn and Y zoning (Figs. 7.2a, c). $X_{Sps}$ in the garnet decreases monotonically from 0.22 in the core to 0.1 in the rim (Fig. 7.2e). Both almandine and pyrope components increase continuously toward the rims, and $X_{Mg}$, although showing a short wavelength periodicity, remains approximately constant (~ 0.09) from core to rim (Fig. 7.2e), suggesting only minor change in temperature during growth. Calcium concentration in the garnet shows a step function; $X_{Grs}$ is 0.164 in the core and 0.185 in the rim with a slight discontinuity in the zoning midway between core and rim. The position of the Ca break does not coincide with the point labeled A defined by a marked inflection in Y zoning; on the left side, the Ca break is located just outside the point A, whereas on the right side break is just inside the point A (Fig. 7.2f), indicating that the Ca discontinuity is not related to the formation of the Y annulus. Epidote inclusions are absent in the garnet core and the matrix, but occur in the outer part of the garnet where $X_{Grs}$ increases (Fig. 7.2b).

In contrast to the smooth, nearly monotonic changes in the Mn, Mg, and Fe profiles, Y and Yb (HREE) zoning profiles (Figs. 7.2f, j) display prominent spikes in concentration between core and rim that correspond to the hexagonal-shaped annuli of high-Y concentration seen in the X-ray map (Fig. 7.2c). Yttrium concentration in the core

of this garnet (1,871 ppm) is the highest among the investigated garnets. In addition to the major peaks, there are a few minor Y-peaks on the profiles that are not apparent on the yttrium X-ray map. Based on the X-ray map and zoning profile, we note that the shapes of the Y annuli are euhedral and symmetrical and infer that they are growth features. Gadolinium (MREE) zoning is decoupled from Y and Yb zoning, and Sm (LREE) increases slightly before decreasing at the rim (Fig. 7.2j). Ti in this garnet decreases continuously from 629 app. ppm in the core to 320 app. ppm in the rim (Fig. 7.2f). P decreases slightly from 128 app. ppm in the core to 118 app. ppm in the rim (Fig. 7.2g). Scandium decreases from 215 ppm in the core to 72 ppm in the rim with an inflection that is correlated with the break in Ca and a slight increase in Zr (Figs. 7.2h, i). Cobalt increases gradually from core to rim (Fig. 7.2i) and V concentrations do not change significantly from core to rim (Figs. 7.2h).

Apatite, which appears red in the P map (Fig. 7.2d), occurs as a matrix mineral, as inclusions in the garnet, and as a cluster of tiny grains along the left resorbed margin of the garnet. The Y concentration of apatite inclusions in garnet is higher than that of matrix apatite, consistent with the observed decreasing Y concentration towards the garnet rim. Secondary apatite in the garnet resorption area has a slightly higher Y concentration than other matrix apatite, implying that this apatite incorporated Y released from the garnet.

The initial growth of garnet in 87-86 is attributed to an epidote-absent reaction such as reaction (7.3) because the garnet shows low-Ca and continuously decreasing Y and HREE inward of the point A. A period of epidote growth during which garnet did not

grow or was slightly resorbed may have followed reaction (7.3). Addition of epidote to the assemblage in reaction (7.3) led to the growth of garnet by reaction (7.1), consistent with the observed increases in Ca, Sc and Zr released from epidote. Major element zoning profiles after the Ca break are compatible with the predicted change of garnet and plagioclase compositions along the compression-heating *P-T* path; $X_{Grs}$ and $X_{An}$ (~0.21) are constant (Fig. 7.2b). The absence of chlorite in the matrix and the evidence that Ca concentration remained high to the rim suggests that chlorite was consumed during growth of the rim outward of the Ca break and that the garnet continued to grow by reaction (7.2a) along the compression-heating *P-T* path. Resorption of garnet is restricted to grains adjacent to mica-rich layers, indicating consumption by the reverse of reaction (7.3) during retrograde metamorphism.

The occurrence of Y and HREE peaks inside the Ca break suggests that at least the first Y and HREE peaks are not related to the breakdown of epidote, although the minor Y and HREE spikes outside the Ca break may have been produced by breakdown of epidote.

***87-279 (Garnet-zone).*** The peak metamorphic assemblage in this sample was garnet + epidote + biotite + plagioclase + muscovite + quartz, with minor tourmaline, apatite, rutile and ilmenite. The garnet grains contain inclusions of epidote, apatite, quartz, ilmenite and rutile. X-ray maps and zoning profiles for a representative garnet in sample 87-279 are shown in Fig. 7.3. BSE images and zoning profiles of the four major elements, plus Y and Ti profiles for sixteen other garnet grains from the same thin-section

are included in the Appendix B. The garnet in Fig. 7.3 has a spessartine-enriched core (0.13) and displays a moderate decrease in $X_{Sps}$ towards the rim with two distinct annuli (Figs. 7.3a, e). These annuli generally conform to the euhedral outline of the garnet. However, careful examination of the outer annulus reveals that the inner side is embayed in several places (see red arrows in Fig. 7.3a), whereas the outer side is straight. The locations of embayments on the inner side of the outer annulus are not related to inclusions. Furthermore, the shapes of Mn zoning profiles across the inner and outer annuli are different; the inner annulus is broad and symmetric, whereas the outer annulus is narrower and asymmetric with a steeper slope on the inner side (see Fig. 7.3e and Appendix B). The increase in spessartine content is correlated with an antithetic change in $X_{Alm}$ and $X_{Grs}$ in the outer annulus, but not in the inner annulus (Fig. 7.3e and Appendix B). Finally, Y concentration in the outer annulus varies significantly from 339 to 1100 app. ppm (Figs. .i and k in Appendix B). All the above features indicate that the inner Mn annulus is a growth feature, whereas the outer Mn annulus was produced by garnet resorption. Ilmenite is common in the garnet porphyroblasts and in the matrix (Fig. 7.3a). Analyses of ilmenite inclusions in garnet show that the Mn content of ilmenite varies sympathetically with that of garnet, implying that ilmenite was not the source of Mn in the annuli. However, ilmenite crystals in the matrix are significantly enriched in MnO (3.0 wt%), even higher than those in the garnet rim (2.32 wt%). Matrix ilmenite is not zoned in Mn. We speculate that manganese in matrix ilmenite may have been enriched by garnet-consuming reactions associated with formation of sulphide minerals. Sulphide minerals locally replace the rim of the garnet (Fig. 7.3b), but do not occur as

inclusions within garnet, implying they were probably formed during retrograde metamorphism. As in garnet 87-86, $X_{Grs}$ of this garnet is slightly lower in the core (0.204) than the rim (0.238), and is correlated with an increase in Sc (Figs. 7.3e, h). $X_{Grs}$ remains high throughout the garnet, compatible with the presence of epidote in the matrix. However, $X_{Grs}$ increases slightly from point B outward to the outermost rim.

Yttrium is high (1,009 app. ppm) in the core and plummets to about 450 app. ppm toward the rim with a major Y annulus (Figs. 7.3d, f). The dramatic decrease in Y in the core is similar to Y zoning in garnet produced by breakdown of xenotime in the Bronson Hill Anticlinorium and Merrimack Synclinorium, west-central New Hampshire (Pyle and Spear, 2000). It is interesting to note that in detail the inner annulus may consist of a single peak, or two or more separated peaks, implying a discontinuous supply of Y during the growth of garnet. Although the position of the inner Y annulus coincides with the inner Mn annulus in the garnet in Fig. 7.3, Y annuli in other garnets in this sample are not always accompanied by an inner Mn annulus, indicating Y may have different sources from Mn (e.g. Figs. a, d, e, i, m, k in Appendix B). On the other hand, the outer Mn annulus is correlated with a small increase in Y in several places, supporting the inference that the outer Mn annulus is of resorption origin.

Tiny inclusions (~10 μm) of compositionally zoned, REE-rich epidote in the garnet grains occur outside the low-Ca core (Fig. 7.4a). In the BSE images of epidote inclusions, light gray zones (1-2 μm wide) have higher Ce concentrations than the darker areas of the grains, and the zoning pattern appears to reflect a multi-stage growth history prior to partial epidote consumption. Y concentrations also vary greatly across the epidote

inclusions, with higher Y contents in the light gray zones, and epidote is not resorbed concentrically, implying that there would have been a discontinuous and irregular supply of Y to the matrix during epidote breakdown. This may explain the observed multiple peaks on the major Y annulus. Growth zoning in other samples can be further complicated by release of epidote-group minerals such as piemontite, clinozoisite, and allanite which were enclosed in epidote (Figs. 7.4b, c, d).

Ytterbium and Gd in the garnet in 87-279 exhibit similar behaviour to Y, but Sm shows no significant variation (Fig. 7.3j). Ti and P decrease continuously toward the rim in the garnet (Figs. 7.3f, g), although Ti zoning is disrupted by ilmenite and rutile inclusions. Scandium shows an initial increase in the core and another increase at point A then follows Y, implying that it was derived from the breakdown of epidote (Fig. 7.3h). Vanadium concentration increases gradually toward the rim before decreasing at the outermost rim. Unlike garnet 87-86, Co abundance in this garnet decreases toward the rim with no compositional breaks at points A or B.

The core of garnet 87-279 shows the same major and trace element patterns as garnet 87-86; low-Ca and Sc and declines in the abundances of garnet-compatible elements such as Y and HREE, suggesting that initial growth of the garnet was by reaction (7.3). The garnet subsequently grew by reaction (7.1) as indicated by increases in Ca and Sc from breakdown of epidote. At the point B, chlorite was removed from the rock and the garnet was resorbed by reaction (7.2b), indicating a change of *P-T* path from compression-heating to isobaric heating or decompression. The identity of the reaction that caused renewed growth of garnet outboard of the outer Mn annulus is problematic because both

reactions (7.2b) and (7.4) consume garnet along the isobaric heating or decompression paths. Renewed growth in the absence of chlorite (reaction 7.2a) requires an additional period of increasing pressure. This resorption-regrowth of garnet produced the asymmetric Mn and Y zoning profiles with a steeper slope on inner side, which is different from back-diffusion profiles.

***87-271 (Staurolite-zone)***. Sample 87-271 is a staurolite-zone calc-pelite collected from the lowest part of the staurolite-zone (Fig. 7.1). The matrix assemblage is garnet + biotite + plagioclase + quartz, with no muscovite and staurolite in the matrix. The absence of staurolite in this rock is probably because of either low bulk Al and Fe contents or poor definition of the staurolite isograd in the area. The core, represented by high-Mn ($X_{Sps}$ = 0.05) in the garnet, is not situated in the geometrical center of the grain, implying either asymmetrical growth or that a significant amount of resorption has taken place (Fig. 7.5a). Resorption is compatible with the corroded appearance of the rim and also with the traditional interpretation of the high-Mn rim ($X_{Sps}$ = 0.18). In addition to the high Mn at the outermost rim, this garnet shows partial preservation of a Mn annulus (red arrows at A, Fig. 7.5a). It is inferred that most of this Mn annulus was removed by later resorption. A Mn-rich epidote inclusion (~3.83 wt% Mn) was found inside the partial Mn annulus but inclusions of this composition were not found outside the Mn annulus or in the matrix. Severe resorption of the garnet is also indicated by non-concentric Ca zoning and by a thin resorption rim with low Ca (red arrows, Fig. 7.5b). Grossular is low in the core and increases, then decreases toward the rim. Almandine, which behaves roughly

antithetically to grossular in this garnet, decreases sharply at the resorbed rim.

Yttrium and Lu in garnet 87-271 are weakly zoned in the core (Figs. 7.5f, j) and display an inflection at the point A where Mn exhibits an annulus. Unlike garnets 87-86 and 87-279, the zone of Y enrichment at the rim of garnet 87-271 is very thin, irregular and discontinuous along the crystal outline and coincides with the low Ca rim zone, consistent with a resorption origin. Gadolinium decreases from 10 ppm in the core to 2 ppm at the point A then increases to 7 ppm at the resorbed rim. Samarium is not zoned in the core of the garnet and decreases outboard of point A.

Garnet in sample 87-271 exhibits a continuous decrease in Ti toward the rim with a significant decrease at the resorbed rim. The abundance of P in the garnet is nearly constant (120 app. ppm). Scandium abundance decreases from the core outward, but increases abruptly outboard of point A. Vanadium is flat in the core and decreases slightly at the rim. Cobalt and Zr increase gradually before decreasing abruptly at the rim.

Most apatite in sample 87-271 occurs inside the original outline of the garnet postulated by Yang and Rivers (2001) on the basis of Cr distribution (see Fig. 7.5d), implying that apatite was consumed during garnet growth. Apatite crystals occurring in the garnet resorption area have higher Y than apatite inclusions in garnet (Fig. 7.5d), consistent with growth of apatite at the expense of garnet during resorption.

Major and trace element zoning patterns of garnet 87-271 are similar to those of garnet 87-279; low Ca and decreasing Y and HREE in the core, a Mn annulus and resorption and regrowth of the garnet at the rim, as represented by significant increases in Mn, Sc, Y and HREE and a decrease in Ca at the rim. These features suggest that initial

growth of the garnet was by reaction (7.3), followed by reaction (7.1) with the addition of epidote in the assemblage. The second increase in Ca can be explained by garnet growth by reaction (7.2a) along a heating-compression path after chlorite was removed from the assemblage (Table 7.2). When the *P-T* path changed to isobaric heating, the garnet was consumed by reaction (7.2b) producing the observed Mn, Sc, Y and HREE enrichments at the rim. Small amounts of garnet grew again by reaction (7.4) during an inferred second period of compression.

***87-287 (Migmatite-zone).*** In this sample, epidote occurs both as a matrix mineral and as inclusions throughout the garnet. Mn zoning in the core of the garnet from this sample is essentially flat, but there is a 500 μm wide incomplete annulus of elevated spessartine inboard from the garnet rim, labeled A in the profile (Figs. 7.6a, e). The presence of inclusions of Mn-epidote (2.83 wt% MnO) within the annulus suggests that this mineral may be the source of the excess Mn and thus that the annulus is a growth feature, although the Mn annulus is discontinuous. The absence of corresponding Y peaks at the point A support the interpretation that the Mn annulus is not of resorption origin. The absence of Mn and Y enrichment at the outermost rim also suggests that resorption did not occur in this garnet, despite its ragged shape (Fig. 7.6a), which we therefore infer to be principally a growth feature resulting from pinning of the garnet grain boundary adjacent to quartz and plagioclase, an interpretation compatible with the presence of large quartz inclusions in the centre of the crystal. The grossular component is high (~ 0.20) in the core of the garnet and declines slightly outwards, increasing locally at the rim where

garnet is in contact with a plagioclase-rich layer (Figs. 7.6b, e). The Ca X-ray map shows that $X_{An}$ of plagioclase in the matrix increases from 0.17 in the core to 0.32 in the rim. Neither almandine nor pyrope is significantly zoned.

LAM-ICP-MS analyses of Y and Lu zoning in garnet 87-287 show a slightly enriched core and a sharp increase near the rim to form a narrow annulus with a steeper slope on the outer side, which is different pattern to those produced by back-diffusion or resorption-regrowth (Figs. 7.6f, j). Terbium displays similar zoning patterns to Y and Lu, except that there is no enrichment in the core (Fig. 7.6j). Samarium concentration is low in the core (0.1 ppm), but increases by a factor 4 at the rim (0.4 ppm). Ti zoning roughly parallels that of Y (Figs. 7.6d, f), and the P content of this garnet is below the detection limit of electron microprobe analysis. Scandium and V in this garnet are essentially unzoned (Fig. 7.6h), Co decreases toward the rim and Zr shows irregular zoning (Fig. 7.6i).

There was no change in the mineral assemblage during the garnet growth (Table 7.1). Numerous inclusions of epidote in the garnet and absence of chlorite in both garnet and matrix indicate that the entire garnet grew by reaction (7.2a) during a compression-heating *P-T* path. Garnet growth by reaction (7.2a) along the compression-heating path is compatible with the increasing anorthite component in the matrix plagioclase, and the lack of Mn zoning in the core occurs because the isopleths of $X_{Sps}$ are almost parallel to the *P-T* path for Gagnon terrane (see Fig. 12 of Menard and Spear, 1992).

***88-74 (Migmatite-zone).*** This sample is the only pelitic rock investigated in this

study. The garnet in 88-74 displays an oscillatory textural zoning defined by alternating euhedral inclusion-free and inclusion-rich zones (Fig. 7.7). Parts of this inclusion zonation are truncated at the rim by resorption, especially in the upper right of the garnet. Alternation of inclusion-rich and inclusion-free zones may be explained by a change in the rate of garnet growth (Yang and Rivers, 2001), i.e., garnet growth in the inclusion-rich zones must have been sufficiently rapid to allow entrapment of abundant inclusions. Inclusion phases include ilmenite, apatite, zircon, and rutile (Table 7.1); xenotime, monazite, and clinozoisite were sought but not found. The matrix surrounding the garnet contains kyanite, biotite, muscovite, apatite, monazite, zircon, and ilmenite. The spessartine component in this garnet is unzoned in the inclusion-rich core, then decreases monotonically towards the rim before rising at the outermost rim on the left side of the garnet (Figs. 7.8a, e). Grossular content in the garnet is low (<0.05), compatible with the absence of epidote in this rock, but increases slightly toward the rim before decreasing at the outer rim. Almandine and pyrope are not significantly zoned in the core and are their concentrations change antithetically at the rim. A significant amount of resorption is indicated by truncation of high-Ca and -Y bands (Figs. 7.8b, c).

Yttrium zoning determined by LAM-ICP-MS in the poikiloblastic, inclusion-rich core increases slightly toward the inner inclusion-free zone (Fig. 7.8f). Yttrium abundance increases at the beginning of the two inclusion-free zones, and Yb and Gd show similar, but less pronounced variations (Fig. 7.8j). In contrast to MREE and HREE, Sm and Zr are low (0.34 and 1 ppm, respectively) in the inclusion-rich core and increase in the outer inclusion-rich zone before decreasing again at the outer inclusion-free zone.

Titanium zoning is difficult to interpret because many data are contaminated by minute inclusions of Fe-Ti oxides. In this garnet, P increases from 44 app. ppm in the core to 150 app. ppm in the rim, which is almost same as the entire P variation shown by the other six garnets (Fig. 7.8g). The P increase at the rim is correlated with a decrease in Y, compatible with growth of monazite which occurs in the matrix. Scandium shows a similar zoning pattern to Mn, being high in the core and decreasing toward the rim (Fig. 7.8h). Vanadium decreases gradually toward the rim, whereas Co and Zr increase continuously toward the rim. In summary, zoning patterns of Zr, Y and REE are correlated with inclusion zoning, and the behaviour of garnet-compatible elements (Y and HREE) is decoupled from garnet-incompatible elements (Sm and Zr) across the oscillatory textural zoning. However, zoning of transition elements (Sc, V, Co) is not correlated with the textural zoning.

***88-88 (Migmatite-zone).*** This garnet also shows an oscillatory textural zoning defined by a euhedral poikiloblastic core, primarily containing inclusions of quartz, apatite, zircon, ilmenite, and rutile, a relatively inclusion-free zone (~300 μm wide), an outer inclusion-rich zone and an inclusion-free rim (Fig. 7.9). Staurolite, chlorite, epidote, biotite, ilmenite, rutile, apatite and quartz occur as inclusions in this garnet. However, epidote inclusions do not occur rimward of the inner inclusion-free zone. Spessartine is high in the core and decreases toward the rim, with a narrow zone of high Mn at the extreme rim (Fig. 7.10e). However, Mn zoning in the core of the garnet is not concentric (Fig. 7.10a). This garnet maintains high grossular values (> 0.19) in its core, which fall to

below 0.12 at the inner inclusion-free zone, defining the point A in the zoning profiles (Figs. 7.10b, e). This Ca zoning pattern indicates breakdown of epidote at the point A (Menard and Spear, 1993). $X_{An}$ is high in the core of plagioclase (0.42) and decreases at the rim (0.37), compatible with the disappearance of epidote at the point A. Almandine and pyrope components show inflections at the inner inclusion-free zone and are decoupled at the outermost rim. $X_{Mg}$ increases sharply at the point A, implying a significant increase in temperature. The presence of staurolite inclusions in the garnet suggests that some consumption of garnet occurred during staurolite formation by a reaction such as:

$$Grt + Chl + Ms = St + Bt + Qtz + H_2O \qquad (7.5)$$

Reaction (7.5) may explain the non-concentric Mn and Ca zoning in the core of the garnet (Figs. 7.10a, b).

X-ray maps for sample 88-88 display a hexagonal annulus of high-Y that is correlated with the narrow inclusion-free zone and the location of the decline in Ca concentration (Figs. 7.10c, f). Y concentration increases gradually from the core toward the rim and increases sharply at the point A followed by an immediate decrease. The Y zoning profile shows that the Y concentration along the Y annulus varies from 193 ppm on the left side to 132 ppm on the right side of the profile. Yb and Lu also show peaks coincident with the Y annulus, but unlike Y, REE larger than Tm in ionic radius show initial increases in their abundance in the core (e.g. Yb in Fig. 7.10j). Thulium zoning in the core of this garnet is approximately flat (not shown). The shapes of the Y and Yb peaks at the point A are asymmetric, with steeper slopes on their outer sides. Gadolinium

also appears to show a similar pattern to Y (Fig. 7.10j). Samarium is not strongly zoned in the core (0.4 ppm) and increases slightly at the rim (0.8 ppm).

Titanium is high in the core and decreases gradually outward before increasing again at the outer inclusion-rich zone (Fig. 7.10f). Phosphorus abundance is high in the core (~150 app. ppm) and decreases to ~100 app. ppm at point A, where Ca drops and $X_{Mg}$ increases sharply. Scandium zoning is parallel to that of Ca; i.e., high in the core of the garnet, decreasing abruptly at A (Fig. 7.10h). Vanadium gradually decreases toward the rim, whereas Co and Zr increase toward the rim with no major breaks in their zoning patterns (Figs. 7.10h, i). Apatite occurs as inclusions in grains of biotite that replace garnet at the retrograde rim (Fig. 7.10d). The Y concentrations of some of this apatite are higher than those of apatite elsewhere in the matrix.

***88-80 (Migmatite-zone).*** The analyzed garnet in this sample (8 mm in diameter) is strongly resorbed, as indicated by its ragged appearance (Fig. 7.11a), and it is mantled by biotite and plagioclase with no muscovite. However, it retains evidence of a large core, defined by enrichment in $X_{Sps}$ and Y with respect to the rim region (Figs. 7.11a, c). The Mn growth zoning pattern is truncated by several large quartz grains in and adjacent to the crystal. Yang and Rivers (2001) interpreted these as growth features associated with impingement of matrix quartz on the garnet during growth. The thin elevated Mn rim, which is superimposed on the growth zoning pattern, was caused by minor back diffusion associated with resorption. The Ca map shows an irregular core region with elevated Ca that may also have been affected by the quartz inclusions (Fig. 7.11b). The grossular

component decreases sharply at the rim, and low $X_{An}$ in the core (0.11) of plagioclase is followed by a sharp increase (0.20) at the rim, indicating garnet resorption by reaction (7.4) during isobaric heating or decompression.

Although this garnet contains epidote inclusions, Y and Lu display typical bell-shaped zoning profiles except adjacent to the large quartz inclusions (Figs. 7.11f, j). However, slopes of Y and Lu zoning profiles change at the point defined by an inflection in Gd zoning. In contrast, Gd and Sm initially decrease in the core, then increase slightly at point A toward rim (Fig. 7.11j). The variation of Sm and Gd is also coupled with increases in Sc and Zr, implying breakdown of epidote at point A.

The Ti zoning pattern in garnet 88-80 is difficult to interpret because of numerous minute (< 2 μm in width) rutile and ilmenite inclusions, but it appears to show a gradual increase toward the rim (Fig. 7.11f). Phosphorus in 88-80 decreases from the core toward point B, then rises steeply towards the rim (Fig. 7.11g), although no sharp features are preserved in the X-ray map for P (Fig. 7.11d). This increase in P is correlated with a sharp decrease in Y. Cobalt in the garnet increases from the core to point B, then decreases at the rim (Fig. 7.11 i). In contrast, V decreases continuously from 60 ppm at the core to 25 ppm at the rim (Fig. 7.11h).

### 7.4.4 Summary of garnet zoning

The patterns of selected major and trace element zoning are schematically depicted in Fig. 7.12 and preliminary interpretations are summarized below. A more complete discussion of the interpretations follows this section.

(a) Typically, Mn is zoned toward lower values outward from garnet cores (samples 87-86, 88-74, 88-88, and 88-80), consistent with depletion of this garnet-compatible element in the matrix during growth of garnet. Samples 87-279, 87-271, and 87-287 are special cases, with several euhedral annuli, a partially preserved Mn annulus near the rim, and a wide Mn-enriched annulus respectively. The inner Mn annulus in 87-279 does not always correlate with increases in Y and HREE, but Mn annuli in 87-271 and 87-287 are correlated with increases in Y and Zr, respectively. These annuli are interpreted to be growth features because of their euhedral shapes, straight boundaries and the absence of Y annuli produced by resorption. The source of the excess Mn is inferred to be Mn-rich epidote (piemontite), probably enclosed in clinozoisite or other matrix minerals.

(b) Garnet porphyroblasts from calc-pelites have high grossular contents, ranging from 0.15 to 0.23 mole fraction, that remained high until epidote breakdown. Constant or slightly decreasing $X_{Grs}$ in most garnets indicates increasing *P-T* during the growth. Slight increases in Ca in the cores of garnets 87-86, 87-279 and 87-271 mark the breakdown of epidote, which is also supported by increases in epidote-compatible elements such as Sc, Y, Zr and REE.

(c) Resorption and regrowth of garnet occurred in samples 87-279 and 87-271 by reaction (7.2b) along an isobaric heating path, and by reaction (7.2a) along a compression-heating path. The zoning profiles produced by resorption-regrowth are characterized by asymmetric Mn and Y annuli with steeper slopes and embayed and irregular shapes on their inner sides.

(d) All the garnets examined, except for sample 88-80, are characterized by Y annuli of variable width (20-300 μm) that result from the breakdown of epidote. Sample 88-80 has possibly lost its original Y annulus as a result of subsequent resorption. However, not all Y annuli are produced by breakdown of epidote as discussed below. For example, garnet 87-86 shows Y annuli that formed before the breakdown of epidote, and the breakdown of epidote is not indicated by increases in Y and HREE, but MREE in garnet 88-80. The shapes of Y annuli vary from sharp and euhedral (87-86, 87-279, and 88-88) to anhedral (87-287). The compositional gradient at the Y-peaks may be steeper on the inner side of the peak (outer Y annulus of 87-279, outermost rim of 87-271), or on the outer side of the peak, or be symmetrical (87-86, inner annuli of 87-279, 87-287, 88-74, and 88-88), implying that they have different origins. Most investigated garnets display bell-shaped Y and HREE profiles in their cores (i.e., elements are compatible in garnet), implying garnet growth was not associated with epidote breakdown. However, Y concentrations increase slightly in inclusion-rich zones in samples 88-74 and 88-88 (i.e., indicating control by garnet growth rate).

(e) Phosphorus generally shows convex upward profiles, except in samples 88-74 and 88-80, which display sharp increases in P at the rims (Fig. 7.12). The gradual decrease in P from core to rim in most garnets is correlated with increasing temperature as represented by increases in $X_{Mg}$ toward rims, especially in garnet 88-88. The sharp increases in P at the rims of garnets 88-74 and 88-80 are accompanied by abrupt decreases in Y concentration, implying growth of Y-

enriched phosphates such as monazite at the expense of apatite.

(f) Scandium profiles from pelitic garnet 88-74 roughly mimic the Mn profiles, implying Sc, like Mn, is compatible in garnet. However, garnet coexisting with epidote shows flat (87-287) or increasing Sc concentration profiles (core of 88-88, 88-80), indicating that Sc is more compatible in epidote than garnet. Scandium peaks coincide with those for Y in epidote-bearing garnets such as 87-86, 87-279, and 87-271, indicating both elements were derived from the breakdown of epidote.

(g) Where analyses are not disrupted by the presence of micro-inclusions, titanium concentration decreases from core to rim in all samples except 88-80. The increasing Ti concentration towards the rim in garnet 88-80 may be a result of changes in the Ti-bearing minor phase assemblage from ilmenite-rutile in the garnet core to rutile in the rim of the garnet, for which there is evidence from the inclusion assemblages (Table 7.1).

(h) Zirconium increases gradually in abundance from core to rim in all samples except 87-287, implying that Zr is an incompatible element in garnet. In 87-287, the zoning pattern is less regular and difficult to interpret. Zr is compatible in epidote (Hickmott and Spear, 1992) and Zr profiles show small peaks coincident with Ca or Mn breaks or annuli (e.g., garnet 87-279 and 87-287), implying Zr is a good indicator element for reactions involving epidote.

### 7.4.5 Distribution of REE in epidote and apatite

It is known that chondrite-normalized REE patterns in epidote-group minerals

commonly show a marked enrichment of LREE over HREE (Grauch, 1989). On the other hand, it has been reported that epidote and clinozoisite grown from HREE-rich hydrothermal veins show marked enrichment of HREE over LREE (Pan and Fleet, 1996), implying that REE contents in epidote-group minerals may vary greatly depending on external factors such as pressure, temperature, the composition of the coexisting fluid, and phase equilibria with other REE-rich minerals. In this study, an epidote inclusion in garnet from sample P-11 described by Yang and Rivers (2001, see Fig. 7.1 for location), has a chondrite-normalized REE pattern with a maximum at Tb (MREE) and a slight positive Eu anomaly (Fig. 7.13). Epidote is also commonly moderately enriched in Sc and V, and strongly enriched in Y and Zr relative to coexisting garnet (Hickmott and Spear 1992; this study). Representative analyses of apatite crystals performed during the course of this study show LREE-enriched, chondrite-normalized patterns with negative Eu anomalies and variable abundances (Fig. 7.13).

### 7.4.6 Distribution of phosphate minerals and Y zoning in apatite

Apatite commonly occurs as subhedral to anhedral grains in our samples, except in sample 88-88 in which it is euhedral to subhedral (Fig. 7.14). The majority of apatite grains found in the samples are shielded in garnet, especially in the migmatite zone. These features suggest that a significant portion of the apatite was consumed during the growth of the garnet porphyroblasts.

Yttrium zoning in apatite from samples 87-86, 87-287, and 88-88 is flat with similar ranges of Y abundance (~220 app. ppm) in the first two samples and slightly higher

(~270 app. ppm) in 88-88 (Figs. 7.14a, d, f). These Y contents are much lower than in apatite coexisting with xenotime (1,096-1,803 ppm Y) reported from mid-amphibolite-facies metapelite elsewhere (Bea and Montero, 1999). The flat Y zoning and low Y concentrations of apatite from samples 87-86, 87-287, and 88-88, together the absence of high-Y cores in the coexisting garnets, indicate that xenotime was not present in these rocks and suggest that breakdown of apatite in these samples was not responsible for the observed Y annuli in garnet. In contrast, apatite crystals from samples 87-279, 87-271, and 88-80 are strongly zoned in Y with high Y cores (Figs. 7.14b, c, g). In addition, LAM-ICP-MS analysis of the core of another apatite in 88-80 indicated a concentration of 997 ppm Y, which is much higher than that shown in Fig. 7.14g, suggesting that it is a non-center cut through the grain. The Y-rich cores of these apatite crystals are partially exposed to the matrix, indicating that their breakdown could potentially produce Y annuli in growing garnet, depending on the degree of zoning and the modal abundances of apatite and garnet.

The euhedral shape of the high-Y core in apatite from 87-279 (Fig. 7.14b) indicates that it is a growth feature rather than a detrital core overgrown by a metamorphic apatite. In contrast, the high Y cores in apatite crystals from 87-271 and 88-80 (Figs. 7.14c, g) are rounded, and it is possible on textural grounds that they are detrital. However, similar ranges of Y concentrations in the cores of all analyzed apatite crystals from the same thin-section, and the absence of a discontinuity in the Y zoning profile of apatite from 88-80 (Fig. 7.14g), suggest that the high-Y cores in the two apatite crystals are more likely of growth origin. The rounded habit of the apatite cores may have formed by grain

boundary migration during metamorphism and deformation. In detail, Y zoning in the cores of apatite crystals from samples 87-279, 87-271, and 88-74 is different from that of sample 88-80; i.e., Y shows a slight increase in the core region in samples 87-279, 88-74, and 87-271, but a continuous decrease in sample 88-80.

The high-Y cores of apatite grains 87-279, 87-271, and 88-74 require breakdown of Y-enriched minerals such as xenotime, monazite, zircon, or garnet during their growth. Among these Y-bearing minerals, xenotime is the only one that can buffer the activity of the Y component in metapelitic apatite (Bea and Montero, 1999; Pyle and Spear, 2000). Xenotime is present in other samples in the area, but not in those examined in this study. Xenotime is consumed in garnet-forming reactions and is the source of the elevated Y and HREE contents of garnet (Bea and Montero, 1999; Pyle and Spear, 2000). Monazite, another possible source of Y in apatite, does not occur in rocks from the garnet- and staurolite-zones in the study area, which is consistent with observations by Kingsbury et al. (1993), and Rubatto et al. (2001). Monazite and allanite do not coexist in the analyzed samples (Table 7.1), implying that monazite present as inclusions in metamorphic minerals in the migmatite-zone was produced by the breakdown of allanite and/or apatite (as also documented by others, e.g., Smith and Barreiro, 1990; Ferry, 2000). Monazite can also be produced by reactions involving apatite and LREE-oxides (Akers et al., 1993; Kingsbury et al., 1993; Bingen et al. 1996) or by dissolution-reprecipitation (Rubatto et al., 2001).

Zircon is another possible source of Y in apatite. Zircon is abundant in all analyzed samples, and its grain size is approximately constant. Zircons are usually idiomorphic and

display oscillatory zoning. Recent age determinations on detrital zircon from metapelite in Gagnon terrane indicate that most grains retain igneous zoning and yield Archean ages characteristic of their source region (Cox et al. 2001). Only very limited evidence for growth or consumption of zircon during the Grenvillian metamorphism was reported, suggesting that zircon is not likely an important for Y in apatite.

Summarizing the above observations, the high-Y core in apatite in samples 87-279, 87-271, and 88-74 is attributed to crystallization in equilibrium with xenotime, and increasing activity of the Y component in garnet with metamorphic temperature.

The activity of the Y component ($Y_3Al_2Al_3O_{12}$ or YAG) in metapelitic garnet coexisting with xenotime is a function of metamorphic temperature (Pyle and Spear, 2000). This empirical geothermometer can also be used to infer the presence of xenotime in the small Y-rich cores of garnets 87-86 and 87-279. Assuming, *a priori*, the presence of xenotime during the growth of the cores of the two garnets, metamorphic temperatures estimated by the YAG-xenotime thermometer (Pyle and Spear, 2000) for the cores of garnets 87-86 and 87-279 are about 500 and 522°C, respectively. The former temperature is approximately 100°C higher than the estimated garnet core temperature, whereas the latter is in good agreement with the garnet core temperature (both estimates by the garnet-biotite Fe-Mg exchange thermometer). An examination of Y zoning in apatite from these two samples may explain why the result for 87-86 is not in accord with that from Mg-Fe exchange thermometry. Apatite in sample 87-86 has a low Y concentration and flat Y zoning, whereas apatite in 87-279 has a high Y core. This suggests that garnet 87-86 crystallized in a xenotime-absent assemblage, compatible with the spurious

temperature estimate with the YAG-xenotime thermometer, whereas xenotime may have been present at the initial stages of garnet growth in sample 87-279. Similarly, the absence of high-Y cores in garnets in samples 87-271 and 88-80, in which apatite shows high-Y cores, may thus indicate that garnet crystallized after the breakdown of xenotime, or that xenotime was armored by other minerals and was not available during the growth of the garnet.

## 7.5 Discussion

Discontinuities in major and trace element zoning in garnet are generally ascribed to some change in the physicochemical environment during garnet growth: e.g., a change in *P-T* conditions, a change in the garnet-forming reaction, a change in the garnet growth rate, a change in garnet major-element composition, or a change in the composition of the coexisting fluid (Hickmott et al., 1987; Hickmott and Shimizu, 1989; Hickmott and Spear, 1992; Lanzirotti, 1995; Schwandt et al., 1996; Spear and Kohn, 1996; Bea et al., 1997; Chernoff and Carlson, 1999; Pyle and Spear, 1999). Specific processes that may have influenced the development of P zoning in garnet, Y zoning in apatite and the formation of Mn and Y annuli in the Gagnon garnets are considered below.

### 7.5.1 Variations of P in garnet and Y in apatite with metamorphic grade

As discussed above, phosphate minerals are not inert during metamorphism, but are active participants in prograde mineral reactions. For example, the decrease in modal

abundance of apatite with the crystallization of garnet, the presence of trace levels of P in garnet, and the resorbed crystal outlines of apatite crystals, all indicate consumption of apatite during the growth of garnet. On the other hand, small apatite crystals in a garnet resorption area have higher Y concentrations than other matrix apatite, indicating growth of apatite from P, Ca and Y derived from garnet. The involvement of apatite in major mineral reactions is also indicated by Y contents in apatite that were controlled by the breakdown of former xenotime. The appearance and disappearance of trace phases may also reflect changes in metamorphic grade. For example, xenotime starts to break down in the garnet zone (Bea and Montero, 1999; Pyle and Spear, 2000) and allanite-in and monazite-in isograds were recently mapped in a contact aureole (Ferry, 2000).

Although P and Y occur in garnet and apatite at trace levels, P and both P and Y are major structural constituents of apatite and xenotime, respectively. At equilibrium, the chemical potentials of the P-component in garnet and the Y-component in apatite may be buffered by phase relations among phosphates and other silicates, providing the potential to reveal changes in temperature and/or pressure during garnet and apatite growth. However, phase equilibria buffering the activities of the P-component in garnet and the Y-component in apatite are not well known because of poorly understood P and Y substitutions in amphibolite-facies pelitic garnet and apatite.

The substitution of a trivalent species, like $Y^{3+}$, for $Ca^{2+}$ in the apatite structure must be coupled with another substitution to maintain charge balance. Several such substitutions have been proposed for Y and trivalent REE (Rønsbo, 1989). These include $Y^{3+} + Si^{4+} = Ca^{2+} + P^{5+}$, $Y^{3+} + Na^{+} = 2Ca^{2+}$, $Y^{3+} + O^{2-} = Ca^{2+} + X^{-}$, and $2Y^{3+} + \square = 3Ca^{2+}$

where X is an anion, and □ represents a vacancy. Many studies have shown that the first two coupled substitutions dominate in natural apatite (e.g., Rønsbo, 1989; Fleet and Pan, 1995), and an experimental investigation by Ito (1968) demonstrated the existence of complete solid solution between apatite [$Ca_5(PO_4)_3(F,OH)$] and yttrium-lessingite [$Ca_2Y_3(SiO_4)_3(F,OH)$] under experimental hydrothermal conditions (500-700°C, 2 kbar).

The analytical techniques used in this study are not capable of detecting the dominant substitution. Assuming the first substitution noted above for apatite in Gagnon terrane, the xenotime ($YPO_4$)-apatite [$Ca_5(PO_4)_3(F,OH)$] equilibrium may be described by the equation:

$$3YPO_4 + 3SiO_2 + 7CaO \text{ (in Pl)} + (F_2, H_2O) =$$

$$Ca_5(PO_4)_3(F,OH) + Ca_2Y_3(SiO_4)_3(F,OH) \qquad (7.6)$$

Although the substitution of Y into the apatite structure and a phase equilibrium accounting for the buffering of the Y-component in apatite are not defined, considerations of the Y zoning pattern of apatite and variation of Y concentration in apatite with metamorphic grade are informative. If the high-Y cores of apatite crystals from samples 87-279, 87-271, and 88-80 were a result of buffering of the Y-component by xenotime, the concentrations of Y in the cores of coexisting apatite could be expected to show temperature dependence in the same way that the Y concentration in monazite or garnet coexisting with xenotime shows a thermal dependence (Pyle and Spear, 2000). Y concentrations in the high-Y cores of apatite vary from ~300 app. ppm in the garnet zone (87-279), through ~440 app. ppm in the staurolite zone (87-271), to 997 ppm in the migmatite zone (88-80). Increasing activity of the Y-component in apatite with

metamorphic grade is also consistent with the initial increase in Y concentration in the cores of the apatite in 87-279 and 87-271.

Phosphorus concentration varies smoothly from core to rim in most analyzed garnets. Apparent deviations from this trend are observed in garnets 88-74 and 88-80, where P and Y zoning are decoupled (Fig. 7.12). In these two samples, monazite was found in the matrix but not in garnet, indicating changes in the coexisting phosphate assemblage from apatite in the garnet cores to apatite + monazite in the garnet rims during garnet growth. Crystallization of monazite at the rims of the two garnets is also compatible with the observed abrupt decreases in Y at the point where P increases. Considering garnet that equilibrated with apatite only, P concentrations at the rims of garnets investigated in this study decrease systematically from a concentration of 122 app. ppm in the garnet zone to about 44 app. ppm in the migmatite zone, except for garnet 87-271, which is significantly resorbed. This systematic variation in P abundance with metamorphic grade and the smooth P zoning with no breaks imply that the activity of the P-component in garnet was buffered by phase equilibria involving apatite and silicates in Gagnon terrane. However, it is difficult to separate the thermal and pressure effects because they vary together, although a significant increase in $X_{Mg}$ in garnet 88-88, accompanied by a sharp decrease in P concentration, indicates that temperature was more likely the dominant factor in controlling P incorporation into garnet.

The substitution mechanism whereby P enters the tetrahedral Z-site in pelitic garnets is not well-known. For pegmatitic garnets, Wise (1994) and Taylor et al. (1997b) proposed the coupled substitution $2Si^{4+} = P^{5+} + Al^{3+}$ on the basis of strong correlation

between tetrahedral silicon deficiency, excess octahedral aluminum, and no appreciable Na in the garnet. For mantle garnet, Sobolev and Lavrent'ev (1971), Thompson (1975), and Bishop et al. (1978) proposed the substitution $Ca^{2+} + Si^{4+} = Na^{+} + P^{5+}$. Since the sum of the atomic radii of Na + P is less than that of Ca + Si, this substitution would cause a shortening of the unit cell edge and a reduction in the unit cell volume, leading Thompson (1975) and Meagher (1982) to propose that it should be sensitive to pressure.

Representative LAM-ICP-MS spot analyses of garnets 87-86 and 88-88 show around 94 and 48 ppm Na, respectively, which are similar to their P abundances, indicating the coupled Na+P substitution is also possible in pelitic garnets. If we consider the P zoning patterns as monitors for the coupled Na+P substitution, we would expect to see increasing P concentrations towards the rims of individual garnets, compatible with the preservation of growth zoning profiles (except where resorption or retrograde reactions occur), and also higher concentrations of P in the garnets from the highest metamorphic grades. However, the opposite is observed. P concentrations decrease slightly toward the rims of individual garnets, and there is an overall decrease in P content in garnet with metamorphic grade. We therefore infer that either the temperature effect on P incorporation in garnet was greater than the pressure effect in the analyzed samples, or that the Na + P substitution did not operate in the Gagnon terrane garnets.

Another way of deciphering the relative role of pressure and temperature in P incorporation in garnet is to compare the concentrations of P in garnet that formed under similar temperature, but different pressure conditions. Chernoff and Carlson (1999) reported P zoning in pelitic garnets from the Picuris Range, New Mexico, that

equilibrated at about 3.7 kbar and 525 ± 25°C. We can compare their data with garnet 87-279 (garnet zone), for which estimated conditions of formation are 6 kbar and 550°C. Phosphorus zoning in their garnets is flat in the cores (~100 ppm) then decreases before increasing abruptly to about 200 ppm at a point where Ca shows a spike. Apatite and monazite occur outside the Ca spike but no phosphates were found inside the Ca spike. Assuming that the cores of these garnets grew in equilibrium with former apatite, P concentrations in the garnet cores may be compared to the P concentration in the rim of our garnet 87-279. The similar range of P concentration in garnets from the two areas indicates that temperature may be the factor controlling P incorporation in garnet and that pressure may have a negligible effect.

The apparent P and Y variation in garnet and apatite with pressure and temperature cannot be effectively quantified at this time. However, the decoupling of P and Ca at the rims of garnets 88-74 and 88-80 suggests that crystal chemistry does not dominate the incorporation of P into garnet. If crystal chemical effects and disequilibrium partitioning can be ruled out, then decreasing P in garnet coexisting with apatite may indicate increasing metamorphic temperature, which is compatible with the observed significant decrease in P concentration with increasing $X_{Mg}$ at the rim of garnet 88-88.

### 7.5.2 The origin of Mn annuli

We suggested above that breakdown of Mn-rich epidote or allanite was the source of the Mn annuli in garnets 87-271 and 87-287. Enrichment in Mn in the two garnets is correlated with increases in Sc, Zr, Y and M-HREE, which are characteristic signatures

of epidote breakdown. Mn from Mn-rich epidote or allanite enclosed in the core of epidote or other matrix minerals was probably released to the matrix at the end of the epidote-breakdown episode (by reactions 7.1, 2a or 2b), resulting in the formation of Mn annuli near the rims of the two garnets.

The origin of the inner Mn-annulus in sample 87-279, however, is problematic since no Mn-rich mineral was found in this sample. Schumacher et al. (1999) proposed that oscillatory zoning of Mn, decoupled with Fe in their garnet, was due to slight fluctuations in the decompression rate that caused a perturbation of the *P-T* path and concomitant changes in Fe-Mn exchange between garnet and ilmenite. Although matrix ilmenite has a high Mn content (~3.0 wt% MnO) in sample 87-279, Mn in ilmenite inclusions in the garnet varies sympathetically with Mn in the host garnet, and the Mn annulus is not correlated with a decrease in Fe, implying that ilmenite was not the source of the Mn enrichments.

$X_{Sps}$ values at the peak of the inner annulus in sixteen garnets from sample 87-279 are plotted in Fig. 7.15. The $X_{Sps}$ is exceptionally high in grain e (0.148), with the rest of the garnets analyzed having $X_{Sps}$ between 0.087 and 0.112, with an average of 0.103 ± 0.015 (RSD = 15%). $X_{Sps}$ at the inner annulus also varies within a single garnet grain. For example, garnet grain c shows $X_{Sps}$ values of 0.092 on one side of the annulus and 0.109 on the other side of the same annulus, a variation of 17%. $X_{Sps}$ values at the inner annulus are low (0.087-0.100) in the upper quartz-rich layer and at the bottom of the thin-section, intermediate (0.100-0.112) in the middle of the garnet-rich area, and very high (0.148) in garnet grain e. This pattern of peak $X_{Sps}$ distribution in the annuli suggests that external

infiltration of an Mn-rich fluid or changes in *P-T* are not likely explanations for the Mn annuli in this sample. Instead, the thin-section scale differences between $X_{Sps}$ values in the annuli suggest that localized breakdown of Mn-rich minerals occurred, either simultaneously or sporadically. Epidote inclusions in garnet 87-279 have very low Mn contents. However, the possibility of Mn-rich epidote in the cores of some of the epidote grains, as in samples 87-271 and 87-287, or in other minerals, appears likely on the basis of the range of Mn concentrations at the inner Mn-annuli.

The range of $X_{Sps}$ values around an individual annulus also suggests that Mn incorporation into growing garnet rims is controlled by rates of intergranular transport and by local reactions in the immediate vicinity of each garnet porphyroblast. This interpretation is also compatible with the nonsystematic correlation between Mn and Y annuli and with the variable Mn concentrations in the broad annulus in 87-287 (Fig. 7.6a). Thus, in samples such as this, the use of MnO concentration as an index of the relative time of garnet nucleation (Carlson, 1989; Spear and Daniel, 1998) is questionable, especially where garnet grew at low temperature and in an inhomogeneous matrix with other Mn-rich minerals present.

### 7.5.3 The origin of Y annuli

High-Y annuli in garnet interiors occur in all the analyzed samples except 88-80, which may have lost its original Y annulus as a result of later resorption. We now consider the origin of this feature, which has the potential to provide important information about the mechanism and history of garnet growth. As noted in the

introduction, discontinuous changes in Y and other trace element concentrations in garnet have previously been attributed to: (1) garnet resorption and renewed growth (Pyle and Spear, 1999); (2) disequilibrium partitioning during growth due to kinetic factors such as acceleration of the garnet growth rate (Hickmott and Shimizu, 1990; Chernoff and Carlson, 1999); (3) changes in the garnet-forming reaction due to the breakdown of Y-enriched phases (Hickmott et al., 1987; Hickmott and Spear, 1992; Schwandt et al., 1996; Spear and Kohn, 1996); and (4) infiltration of trace element-enriched fluids during garnet growth (Hickmott et al., 1992; Schwandt et al., 1996, Stowell et al., 1996). Fluid infiltration was suggested by Stowell et al. (1996) to explain oscillatory Y zoning in garnets from contact aureoles surrounding plutons in the Grand Island diorite complex, Alaska. However, it was not considered in this study because indications of an open-system environment as the cause for the Y annuli were not found in the analyzed samples. The single Y annulus observed in most samples is morphologically different from the zoning patterns in garnets that grew in an open-system environment, which tend to show highly variable and irregular patterns of oscillatory zoning, even within a single sample. The three other possible mechanisms are evaluated below.

***Resorption and renewed growth (87-271).*** As discussed above, the presence of staurolite and epidote in some of these rocks suggests that a significant amount of garnet may have been consumed as a result of reaction (2b) during isobaric heating and reaction (5) along any prograde *P-T* path. During garnet resorption, release of garnet-compatible elements such as Mn, Y, Sc, HREE, and MREE elevates the activity levels of these

elements in the matrix and can even stabilize REE-rich minerals such as xenotime (Pyle and Spear, 1999). When garnet begins to grow again, the garnet-compatible elements would again become strongly fractionated into garnet, resulting in an asymmetric annulus with steeper slope on the inner side. On the other hand, garnet-incompatible elements such as Ti, P, V, Co, Zr, and LREE, would enter matrix phases and decline abruptly at the resorbed rim, and then increase gradually during renewed growth if it was diffusion-controlled. These relationships between garnet-compatible and garnet-incompatible elements are schematically illustrated in Fig. 7.16. In summary, we predict that resorption and regrowth of garnet would produce a jagged, embayed margin in the garnet with a steeper slope on the inner side of the annulus, as in the garnet rims of samples 87-279 and 87-271 (Figs. 7.5c, f). However, resorption of garnet may not necessarily produce embayments all around the crystal, as in garnet 87-271 (Fig. 7.5a); in other cases, embayments appear to have been localized on crystal defects, as in the outer Mn annulus of garnet 87-279 (Fig. 7.3a).

In contrast, Y annuli produced by growth are characterized by symmetric or asymmetric annuli with a steeper slope on the outer side. If Y zoning is diffusion-controlled, progressive breakdown of an Y-rich trace phase over a temperature or pressure interval will result in an initial gradual increase in Y, as a result of competition for available Y between garnet and the trace phase as the latter breaks down, followed by a sharp decrease in Y after the trace phase is finally consumed (Lanzirotti, 1995). Thus a sudden decrease in Y may mark the final breakdown of epidote.

Another possible mechanism for the gradual increase in Y during breakdown of Y-

enriched trace phases that have no significant zoning is an increase in the effective weight fraction of reactants with increasing metamorphic grade. If the effective weight fraction of matrix minerals increases with temperature due to the logarithmic dependence of diffusion coefficients on temperature, it may produce a gradually increasing concentration of Y toward the rim of garnet even when matrix minerals are not zoned.

Using these criteria, we conclude that the Y annuli in garnets such as 87-86, 87-279 (inner annulus), and 88-88 are not compatible with a resorption model; they display sharp euhedral and straight outlines, the annuli have symmetric profiles or a steeper slope on the outer side of the peak, and there is non-systematic variation between garnet-compatible and garnet-incompatible elements at the annulus, indicating no garnet resorption or hiatus during the garnet growth.

***Kinetic factors - garnet growth rate (88-74 and 88-88).*** Garnets 88-74 and 88-88 are characterized by oscillatory textural zoning defined by alternating inclusion-rich and inclusion-free zones (Figs. 7.7, 7.9). However, the breakdown of epidote across the oscillatory textural zoning in garnet 88-88 makes the detection of trace element signatures produced by changing garnet growth rates difficult because both processes control Y, Zr and REE zoning. On the other hand, Y and HREE variation in garnet 88-74 can be interpreted largely in terms of changing garnet growth rate because there are no known Y- and HREE-rich minerals in the rock.

For the inclusion-rich zones, it is likely that nucleation of garnet was delayed and significant overstepping of the garnet-forming reactions occurred, resulting in rapid

garnet growth with significant trapping of inclusions (Yang and Rivers, 2001). A corollary of the overstepping model is that as the compositions of the reacting minerals approached their equilibrium compositions, the affinity of the reaction would decrease, resulting in slower growth velocity with diminished entrapment of inclusions. However, this would not explain the sharp boundaries between inclusion-rich and inclusion-free zones.

We now consider the effect of rapid growth rate on the incorporation of garnet-compatible elements such as Y and HREE and garnet incompatible element such as Sm and Zr. Trace element concentrations are known to be enriched in the interfacial regions of polycrystalline aggregates (Kingery, 1984; Watson, 1996). Upon significant increase in growth rate, trace elements bound in the surface layer can be buried and trapped in the newly-formed lattice, resulting in lattice concentrations that deviate substantially from those predicted by equilibrium partitioning between the crystal and its growth medium. The effectiveness of this growth entrapment process depends on the interplay between the growth rate of the crystal and the diffusivity in the near-surface region of the crystal. Hickmott and Shimizu (1989) used this argument to explain Ti zoning in garnet from a contact aureole in the Kwoiek area, British Columbia. However, if Y were subjected to such an interface process, its concentration would be expected to decrease, rather than increase at the inclusion-free zones, as is seen in garnets 88-74 and 88-88.

An alternative mechanism was proposed by Lanzirotti (1995), who suggested that if the supply of elements to the growing garnet interface is diffusion-limited in the matrix, then a decrease in the garnet growth rate will result in an increase in the supply of garnet-

compatible elements and a corresponding decrease in garnet-incompatible elements. In garnet 88-74, systematic increases in garnet-compatible elements (Y, HREE, and MREE) at the beginning of each inclusion-free zone and corresponding increases in garnet-incompatible elements (Sm and Zr) at the outer inclusion-rich zone provide a robust fingerprint for diffusion-controlled incorporation of these elements (Figs. 7.8f, 10f).

***Breakdown of Y-enriched phases.*** Breakdown of refractory trace minerals changes the effective bulk composition (EBC) and imparts a characteristic trace element signature on garnet. The signatures can be predicted on the basis of garnet-trace mineral partition data and an understanding of the identity and amount (mode) of the refractory minerals. Refractory minerals containing significant amounts of Y and REE found in the analyzed Gagnon calc-pelitic and pelitic rocks include epidote, apatite, monazite, allanite and zircon, with plagioclase as a reservoir for Eu. In this section, we attempt to identify the reactant minerals that produced the Y annuli using REE ratios measured in garnet. The advantage of REE ratios is that they are not greatly affected by the amount of the refractory minerals present, zoning in the refractory minerals, or their dissolution patterns during regional metamorphism, which are all difficult to quantify. The parameters used to define the REE ratios are shown in Fig. 7.17a. Ratios of individual REE in the core and annulus (A) regions of the garnet are referred to as the core and A ratios, respectively. The sampling intervals (a-b, c-d), are chosen to be as short as possible to fulfill the conditions of a simple Rayleigh fractionation model.

Simple Rayleigh fractionation of REE in a finite reservoir, closed system during

garnet growth would yield the REE core ratio pattern shown in Fig. 7.17b, with depleted HREE and slightly enriched LREE ratios. Perturbations to this pattern would occur if a REE-enriched phase broke down during garnet growth, changing the effective bulk composition. For instance, breakdown of LREE-enriched minerals such as allanite and monazite should increase all REE, but especially LREE, in the EBC and therefore the growing garnet (Fig. 7.17b). Epidote is expected to provide Y, REE (especially MREE), Sc and Zr to the EBC during its breakdown (Hickmott and Spear, 1992; this study), resulting in a peak in the MREE ratios (Fig. 7.17b). Finally, breakdown of HREE-enriched minerals such as xenotime and zircon should produce REE ratio peaks in the HREE (Fig. 7.17b).

Before we apply these principles to our samples, it is also necessary to consider the relative timing of growth of the garnet and the REE- and Y-enriched refractory phase. In general, a refractory REE- and Y-enriched mineral that grew in a closed system *prior to* garnet growth would probably exhibit core to rim depletion in elements highly compatible in that mineral. On the other hand, any refractory mineral that grew *at the same time as garnet* would exhibit the same core to rim elemental depletions as garnet. Finally, if garnet grew *during the breakdown* of the REE- and Y-rich core of the refractory mineral, then an enrichment of these elements would be observed in the garnet zoning profile. The extent of these effects depends on mass balance constraints and the degree of zoning in the reactant minerals.

Applying these principles to our samples yields the following conclusions. Firstly, with respect to the early stages of garnet growth, core regions of garnets 87-86, 87-287

and 88-88 have peaks in the MREE, Gd, Tb and Dy, respectively, in their core ratio plots, compatible with the breakdown of epidote during the initial growth of these garnets (Fig. 7.17). Initial growth of garnets 87-279, 87-271 and 88-80 was not accompanied by epidote breakdown as indicated by all core REE ratios below unity, consistent with the observed initial decrease in Y in the cores of these garnets (Fig. 7.12 and Figs. 7.17d, e, i). In garnet 88-74, both MREE and HREE increase slightly during initial garnet growth (Fig. 7.17g), probably because of reduced garnet growth rate toward the inclusion-free zone. Variation in the core Eu ratio is controlled by growth or consumption of plagioclase during the initial growth of the garnets. Positive change of Eu in the core ratio in garnet 87-279 is compatible with the initial growth of the garnet by reaction (3) in which plagioclase is a reactant, and negative change of Eu in the core ratio of garnet 87-287 is consistent with growth by reaction (1), in which plagioclase and garnet grow at the expense of epidote.

Having discussed the core ratios, we now turn to the A ratios that are expected to fingerprint the refractory phase that broke down during formation of the Y annuli or inflections in Y concentration in garnet. A-ratio peaks can be classified into four types: (1) peaks at HREE (87-86, 87-279, 88-74), (2) peaks at LREE (87-287), (3) peaks at MREE (88-80) and (4) composite peaks at MREE and HREE (87-271, 88-88). The breakdown of xenotime is the most effective method by which the supply of Y and HREE to garnet could have been increased. A-ratio peaks at HREE in garnets such as 87-279, 87-271, 88-88 are compatible with the former presence of xenotime, as also indicated by the high Y cores in coexisting apatite noted above. In addition, the

reasonable estimation of temperature using the YAG-xenotime geothermometer (Pyle and Spear, 2000) for the core of garnet 87-279, as discussed above, is also compatible with the former presence of xenotime in this sample. However, the Y annulus of garnet 87-86 may have been produced by the breakdown of zircon because Y zoning in apatite does not indicate the presence of xenotime in this rock and the Y annulus in garnet started to form before breakdown of epidote. A-ratios for Gd and Tb below unity are also consistent with the REE signature of zircon. HREE-enriched REE ratios of garnet 88-74 indicate compatibility differences among REE during a decrease in garnet growth rate.

A-ratios at the Y annulus in garnet 87-287 show a peak at LREE, indicating breakdown of allanite, apatite or monazite. Apatite in this rock has a low Y concentration (217 ppm) and is not zoned in Y and monazite was not found in this sample. Thus allanite is believed to be the source of LREE enrichment in this case, consistent with remnants of matrix epidote with exposed allanite cores (Fig. 7.4d). A significant increase in the Eu ratio suggests breakdown of plagioclase occurred during formation of theY annulus in this garnet.

An A ratio peak in the LREE to MREE in garnet 88-80 (Fig. 7.17i) suggests breakdown of epidote at point A, compatible with enrichments in Gd, Sc and Zr. Across the inflection, Y and HREE change slopes in the zoning profiles but the lack of enrichments in these elements suggests that breakdown of epidote does not always increase the level of Y and HREE in the matrix. This may indicate that early epidote, which crystallized before garnet growth, was strongly zoned in Y, and that the Y-poor rims of epidote were involved in garnet formation at point A. Subsequently, with the

progress of the epidote breakdown reaction, the cores of epidote became exposed and released more Y to the EBC.

The two peaks of A ratio in garnet 87-271 indicate breakdown of Mn-rich epidote and xenotime at the same time. The presence of xenotime before the crystallization of garnet is indicated by the high-Y core in coexisting apatite, as already noted. The Y annulus in 88-88 is related to the epidote-out reaction, as epidote is restricted to the garnet core inward from the Y annulus. REE variation at the Y-annulus of this sample shows two peaks at MREE and HREE, implying that breakdown of epidote was associated with a breakdown of HREE-enriched mineral such as xenotime and zircon in this sample as well. In summary, the breakdown of Y-enriched cores of epidote or exposure of piemontite or clinozoisite cores in epidote, or the release of epidote group minerals included in other reactant minerals produced the sharp increases in Y concentration in garnets 87-271, 88-88 and 88-80.

## 7.6 Conclusions

Apatite appears to participate with the major silicate phases in metamorphic reactions in (calc) pelites at all grades. This inference is supported by a decrease in the modal abundance of apatite with garnet growth, the presence of a few hundred ppm P in garnet, and the embayed and resorbed outlines of remaining apatite crystals. Garnet coexisting with apatite shows smooth zoning profiles in P and the concentrations of P decrease systematically with metamorphic grade. High Y cores in apatite point to the former existence of xenotime that is inferred to have buffered activity of the Y-

component in apatite. In these buffered samples, the Y concentrations in the core increase with metamorphic grade. However, the effects of other phosphates such as monazite and xenotime on P zoning in garnet, P and Y substitutions in garnet and apatite, crystal-chemical effects on Y incorporation in garnet, and the scale of equilibrium all require further evaluation.

Mn annuli are inferred to result from the breakdown of Mn-rich phases such as piemontite (Mn-epidote) during garnet growth. Piemontite-rich inclusions in several of the analyzed garnets support this interpretation. The concentration of Mn in the Mn annuli is shown to vary by over 15% among garnets in a single thin section, suggesting that the effective Mn concentration varied significantly across the area of a thin section. This result suggests that the uncritical use of Mn concentration as a time marker during garnet growth may be inappropriate.

Yttrium annuli in the analyzed garnet porphyroblasts are shown to result from three processes: garnet resorption, diffusion-controlled garnet growth, and breakdown of Y-enriched trace phases during garnet growth. These processes are fingerprinted as follows. (1) Yttrium annuli produced by *garnet resorption* are characterized by irregular, locally embayed shapes on the inner side of the annulus, and by systematic variations between garnet-compatible and garnet-incompatible elements at the Y annulus. (2) Where the Y annulus coincides with inclusion-free zones in a garnet poikiloblast, the concentration of Y in garnet is *diffusion-controlled* and inversely related in some complex manner to the rate of garnet growth. Diffusion control on the incorporation of Y in garnet is compatible with significant measured differences in Y concentration around an individual annulus

and implies that the activity of the Y-component in the matrix also varied locally around the growing garnet porphyroblast. (3) REE ratio variations in garnet are shown to be sensitive indicators of the identity of the *trace minerals involved in garnet formation*. For instance, increases in MREE in garnet accompany the breakdown of epidote. Breakdown of allanite in the garnet-forming reaction is indicated by an increase in LREE in garnet, whereas involvement of xenotime and/or zircon is indicated by an increase in HREE in garnet.

Table 7.1. Mineral assemblages of the seven samples from western Labrador.

| Samples | Ky | Ep | Ms | Ilm | Rt | Py | Mag | Mnz | Aln | Tur | Inclusions in garnet | P (kbar)/T (°C) |
|---|---|---|---|---|---|---|---|---|---|---|---|---|
| 87-86 | | | × | × | | | | | | × | Qtz, Bt, Pl, Ap, Zrn, Ilm, Tur, Ep | 5.5/442 |
| 87-279 | | × | × | × | × | × | × | | | | Qtz, Pl, Ap, Zrn, Ilm, Tur, Ep | 6.0/570 |
| 87-271 | | | R | × | | × | × | | | × | Qtz, (Chl), Bt, Zrn, Ilm, Ap, Py, Ep | 6.0/418 |
| 87-287 | | × | × | | × | × | | | × | | Qtz, (Chl), Bt, Pl, Ap, Zrn, Aln, Ep | 10.0/665 |
| 88-74 | × | | × | × | × | × | | × | | × | Qtz, Pl, Ilm, Ap, Rt, Mag, Zrn, Tur | 7.1/601 |
| 88-88 | × | | × | | × | | | R | × | × | Qtz, St, Ep, (Chl), Ap, Zrn, Ilm, Rt, Tur | 8.0/618 |
| 88-80 | × | | R | R | | × | | × | | | Qtz, Ap, Zrn, Rt, Ilm, Mnz, Ep | 11.0/650 |

Qtz, Bt, Pl, Grt, Zr, Ap, and retrograde Chl are common in all samples. Retrograde phases in brackets. Mineral abbreviations after Kretz (1983). ×-present, blank-absent, R-retrograde minerals. P-T estimated by van Gool (1992).

Table 7.2. Predicted changes of compositions and volume of minerals from calc-pelite in Gagnon terrane using the models of Menard and Spear (1993) along the P-T path estimated by van Gool (1992).

| Reactions | $X_{Mg}$ | $X_{Sps}$ | $X_{Grs}$ | $X_{An}$ | $M_{Grt}$ |
|---|---|---|---|---|---|
| 1 | ↑ / ↑ | ↓ / ↓ | ↓ / ↓ | ↔ / ↑ | (+) / (+) |
| 2a, b | ↑ / ↑ | ↔ / ↑ | ↑ / ↓ | ↑ / ↑ | (+) / (−) |
| 3 | ↑ / ↑ | ↓ / ↓ | ↓ / ↓ | ↓ / ↓ | (+) / (+) |
| 4 | ↑ / ↑ | ↓ / ↓ | ↓ / ↓ | ↑ / ↑ | (+) / (−) |

Symbols on the left and right side represent direction of compositional changes and change of volume of garnet ($M_{Grt}$) along the compression-heating and isobaric heating and/or decompression paths, respectively.

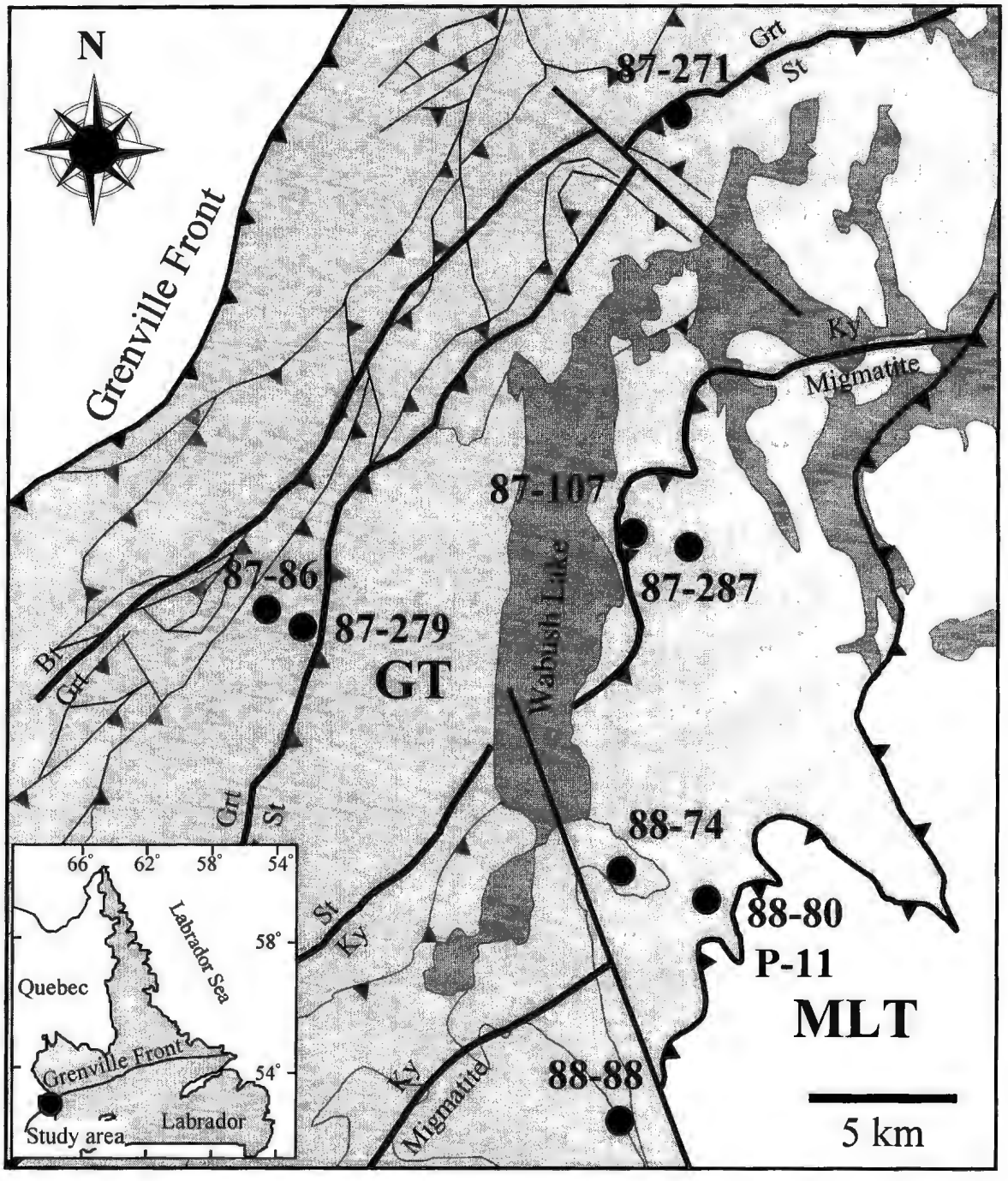


Fig. 7.1. Simplified map of Gagnon terrane, Grenville Province, western Labrador, showing locations of samples used in this study. Metamorphic isograds are from Rivers (1983a) and van Gool (1992). Inset shows the location of the study area with respect to Grenville Front in Labrador. GT: Gagnon terrane; MLT: Molson Lake terrane.

Fig. 7.2. X-ray compositional maps and zoning profiles in garnet from sample 87-86 (garnet zone). (a) Mn map; white lines indicate location of EMP and LAM-ICP-MS profiles. (b) Ca map: circles represent the locations of epidote inclusions in garnet. (c) Y map: representative concentrations of Y determined by LAM-ICP-MS are given in ppm. (d) P map: representative Y analyses of apatite grains determined by electron microprobe are given in app. ppm (italicized numbers). Note that the Y concentrations of apatite grains in the garnet resorption area are higher than those of apatite inclusions in the garnet and matrix apatite. The location of the apatite crystal imaged in Fig. 14a is indicated by the box. In the X-ray maps, warm colors indicate higher concentrations with black for the highest and white is for the lowest concentration. (e-g) Rim-core-rim compositional profiles of $X_{Mg}$ (=Mg/Mg+Fe), pyrope, grossular, spessartine, almandine, Y, Ti, and P along the line shown in (a). Note that Y, Ti, and P are in app. ppm. (h-j) Core-to-rim laser ICP-MS zoning profiles for Sc, V, Co, Zr, Sm, Gd and Yb. The letter A represents a compositional break defined by a peak in the Y profile.

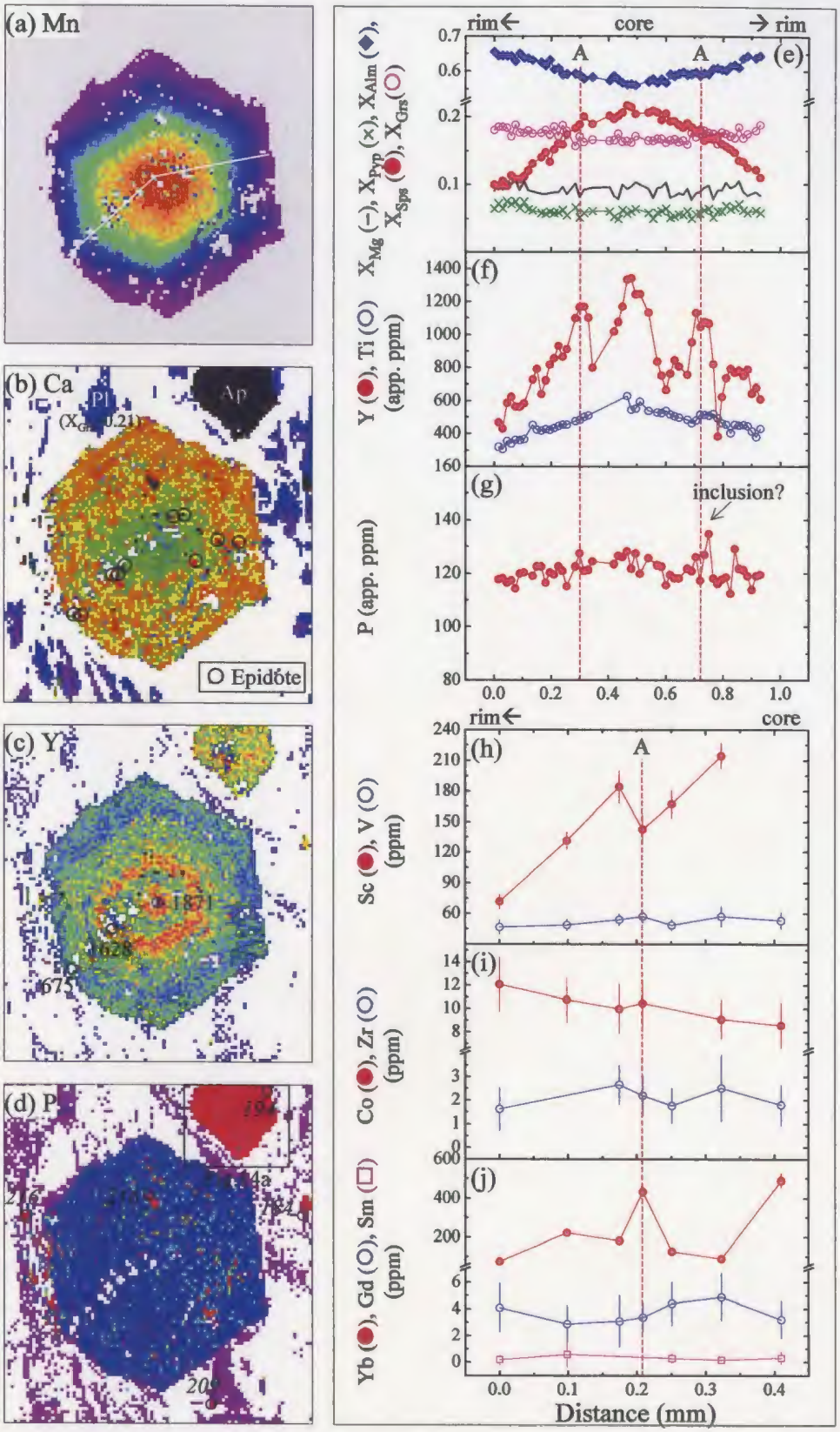
(a) Mn
(b) Ca
Pl
Ap
O Epidote
(c) Y
1871
1628
675
(d) P
194
216
204
(e)
rim←
core
→ rim
A
A
$X_{Mg}$ (–), $X_{Pyp}$ (×), $X_{Alm}$ (◆), $X_{Sps}$ (●), $X_{Grs}$ (○)
(f)
Y (●), Ti (○) (app. ppm)
(g)
inclusion?
P (app. ppm)
(h)
rim←
core
A
Sc (●), V (○) (ppm)
(i)
Co (●), Zr (○) (ppm)
(j)
Yb (●), Gd (○), Sm (□) (ppm)
Distance (mm)

Fig. 7.3. X-ray compositional maps and zoning profiles in garnet from sample 87-279 (garnet zone). (a) Mn map; white lines indicate location of EMP and LAM-ICP-MS profiles. Numbers in Mn map indicate concentrations of MnO (wt. %) in ilmenite. Note that the inner side of the outer Mn annulus is locally embayed as indicated by red arrows. (b) Fe map: note that Fe decreases at the outer Mn annulus, indicating resorption. (c) Ca map: the location of the apatite analyzed in Fig. 14b is indicated by a box. (d) Y map: representative concentrations of Y determined by laser ICP-MS are given in ppm. In the X-ray maps, warm colors indicate higher concentration with black for the highest and white for the lowest concentrations. (e-g) Rim-core-rim compositional profiles of $X_{Mg}$ (=Mg/Mg+Fe), pyrope, grossular, spessartine, almandine, Y, Ti, and P along the line shown in (a). Note that Y, Ti, and P are in app. ppm. (h-j) Core-to-rim laser ICP-MS zoning profiles for Sc, V, Co, Sm, Gd and Yb. The letters A and B represent compositional breaks defined by peaks in the Mn profile.

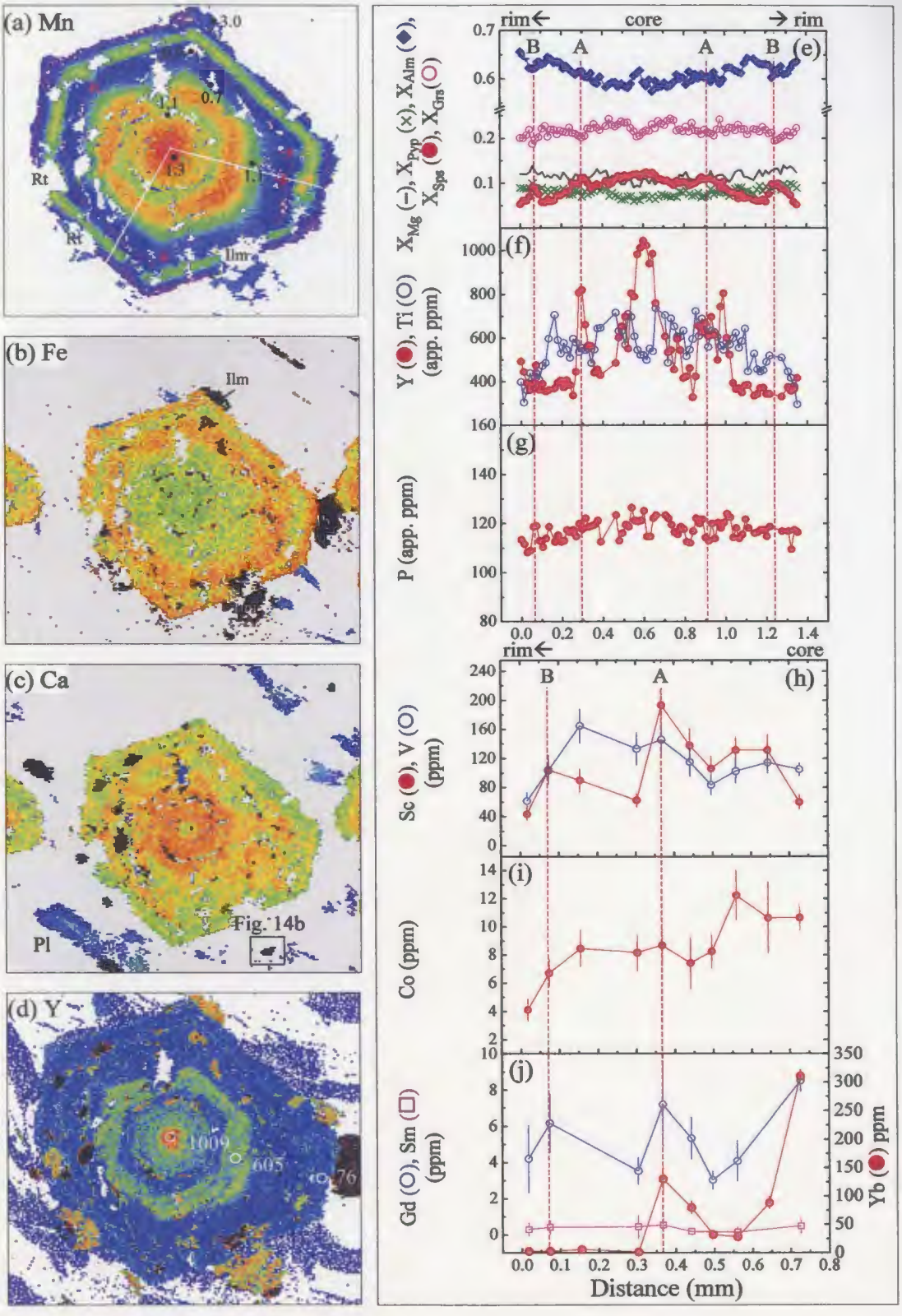
(a) Mn
3.0
1.1
0.7
1.3
1.1
Rt
Rt
Ilm
(b) Fe
Ilm
(c) Ca
Fig. 14b
Pl
(d) Y
1009
605
76
rim←
core
→ rim
B
A
A
B
(e)
$X_{Mg}$ (–), $X_{Pyp}$ (×), $X_{Alm}$ (◆), $X_{Sps}$ (●), $X_{Grs}$ (○)
(f)
Y (●), Ti (○) (app. ppm)
(g)
P (app. ppm)
rim←
core
B
A
(h)
Sc (●), V (○) (ppm)
(i)
Co (ppm)
(j)
Gd (○), Sm (□) (ppm)
Yb (●) ppm
Distance (mm)

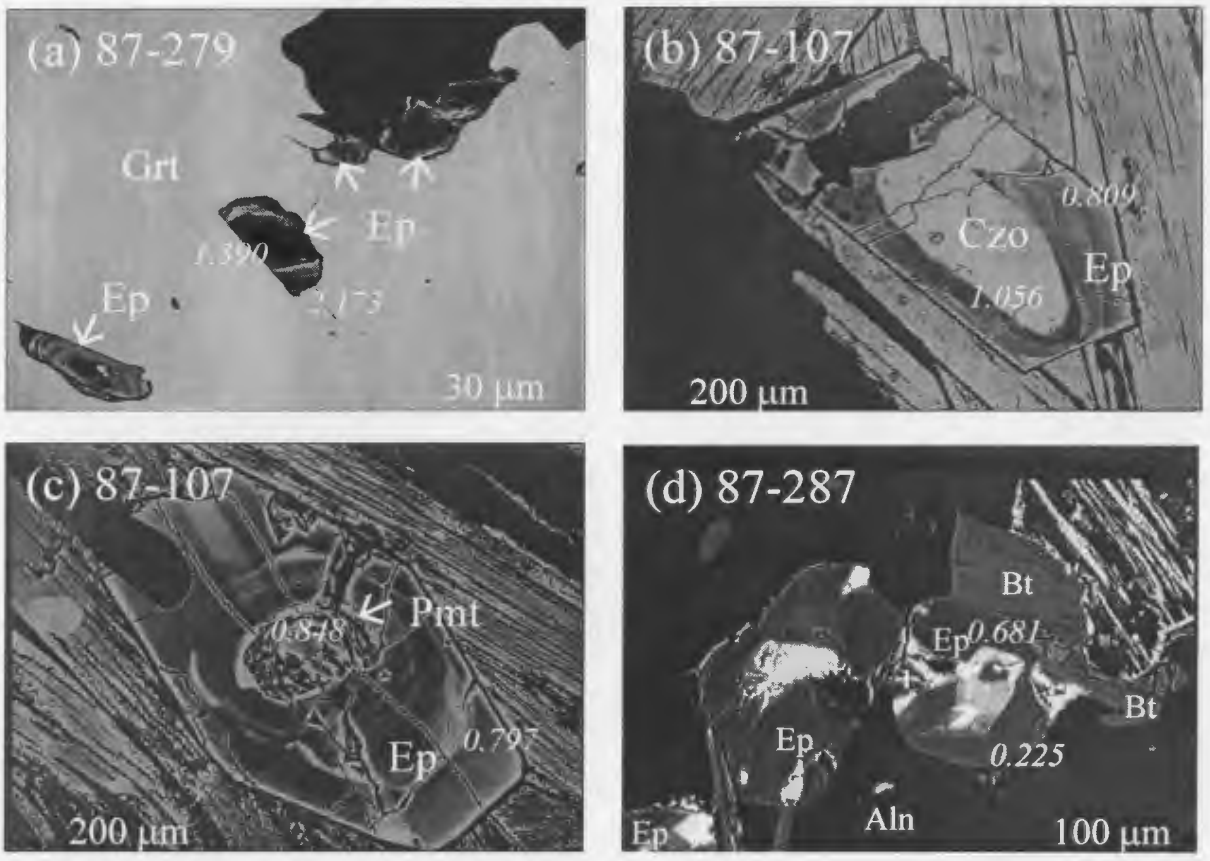


Fig. 7.4. BSE (back-scattered electron) images of epidote-group minerals in Gagnon terrane. The bright areas correspond to high-REE contents. (a) Epidote inclusions in garnet 87-279. (b) Epidote with piemontite core and (c) epidote with clinozosite core in sample 87-107 from the chlorite-zone. (d) Epidote with allanite core in sample 87-287 from the migmatite zone. Numbers in the BSE images indicate Y concentrations in app. wt%.

Fig. 7.5. X-ray compositional maps and zoning profiles in garnet from sample 87-271 (staurolite zone). (a) Mn map; white lines indicate locations of EMP and LAM-ICP-MS profiles. Manganoan epidote with 3.83 wt.% MnO occurs in the garnet porphyroblast. The position of a partially preserved Mn annulus is indicated by two red arrows in the upper right corner of the garnet (b) Ca map: the location of a thin Ca depleted zone is indicated by red arrows. (c) Y map: representative Y concentrations determined by the laser ICP-MS are given in ppm. (d) P map: representative Y analyses of apatite grains are given in app. ppm in the P map. Note that the Y concentrations of apatite grains in the garnet resorption area are slightly higher than those of apatite inclusions within the garnet. The location of the apatite shown in Fig. 14c is indicated by a box. Dotted lines represent the postulated former outline of the garnet on the basis of Cr zoning. In the X-ray maps, warm colors indicate higher concentrations with black for the highest and white for the lowest concentrations. (e-g) Rim-core-rim compositional profiles of $X_{Mg}$ (=Mg/Mg+Fe), pyrope, grossular, spessartine, almandine, Y, Ti, and P along the line shown in (a). Note that Y is in ppm and Ti, and P are in app. ppm. (h-j) Core-to-rim laser ICP-MS zoning profiles for Sc, V, Co, Sm, Gd and Lu. The letter A represents a compositional break defined by the partial Mn annulus.

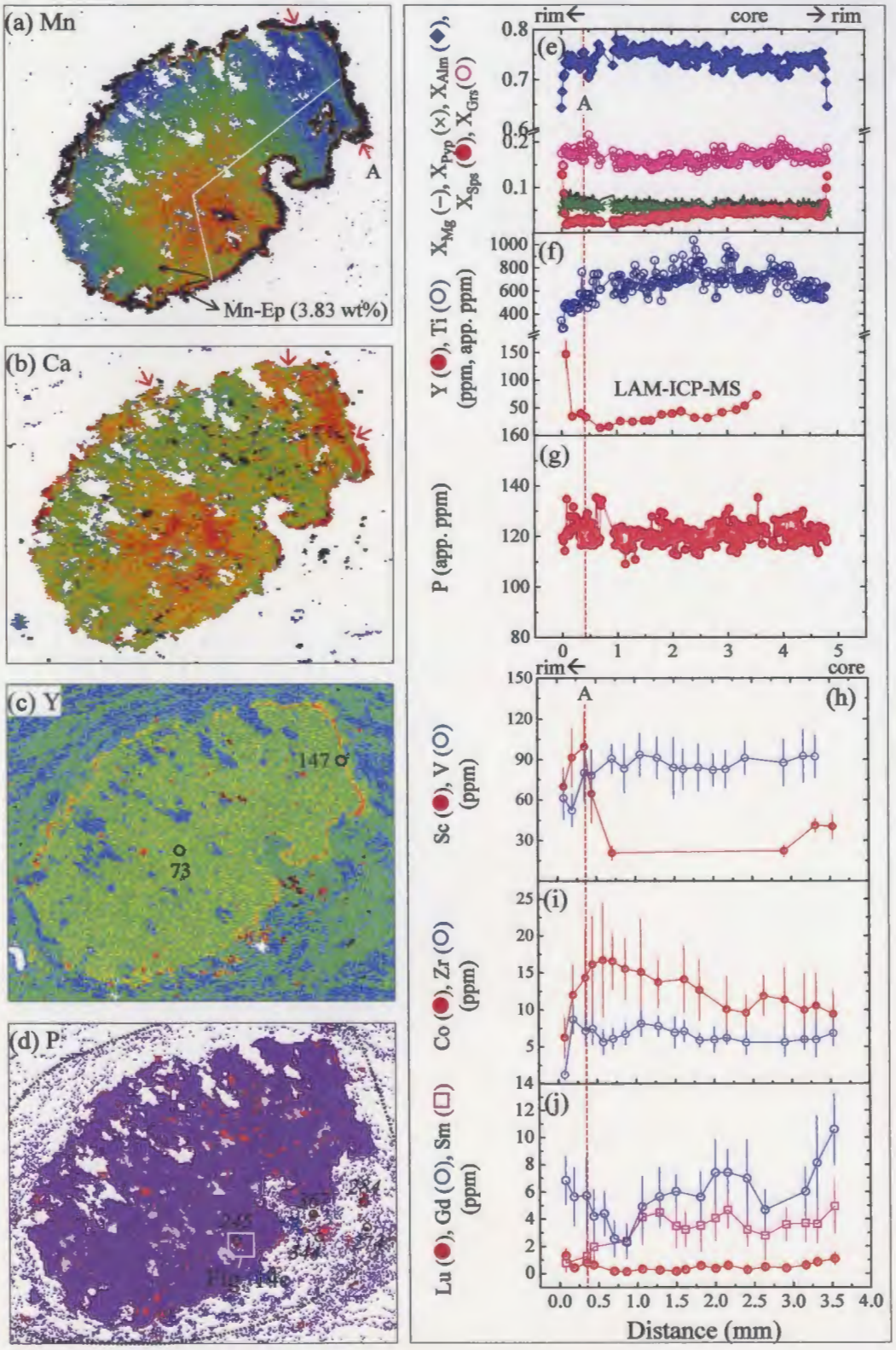
(a) Mn
A
Mn-Ep (3.83 wt%)
(b) Ca
(c) Y
147
73
(d) P
rim←
core
→ rim
(e)
A
$X_{Mg}$ (–), $X_{Pyp}$ (×), $X_{Alm}$ (◆), $X_{Sps}$ (●), $X_{Grs}$ (○)
(f)
Y (●), Ti (○) (ppm, app. ppm)
LAM-ICP-MS
(g)
P (app. ppm)
Distance (mm)
(h)
Sc (●), V (○) (ppm)
(i)
Co (●), Zr (○) (ppm)
(j)
Lu (●), Gd (○), Sm (□) (ppm)

Fig. 7.6. X-ray compositional maps and zoning profiles in garnet from sample 87-287 (migmatite-zone). (a) Mn map; white line indicates location of EMP and LAM-ICP-MS profiles. Manganoan epidote with 2.12 wt.% MnO occurs within the Mn annulus. (b) Ca map: location of the apatite shown in Figure 14d is indicated by a box. (c) Y map: representative Y concentrations determined by laser ICP-MS are given in ppm. (d) Ti map. In the X-ray maps, warm colors indicate higher concentrations with black for the highest and white for the lowest concentrations. (e-g) Rim-core-rim compositional profiles of $X_{Mg}$ (=Mg/Mg+Fe), pyrope, grossular, spessartine, almandine, Y, Ti, and P along the line shown in (a). Note that Y and Ti are in ppm and P is below the detection limit of electron microprobe analyses. (h-j) Core-to-rim laser ICP-MS zoning profiles for Sc, V, Co, Sm, Tb and Lu. The letter A marks the peak in the Mn profile.

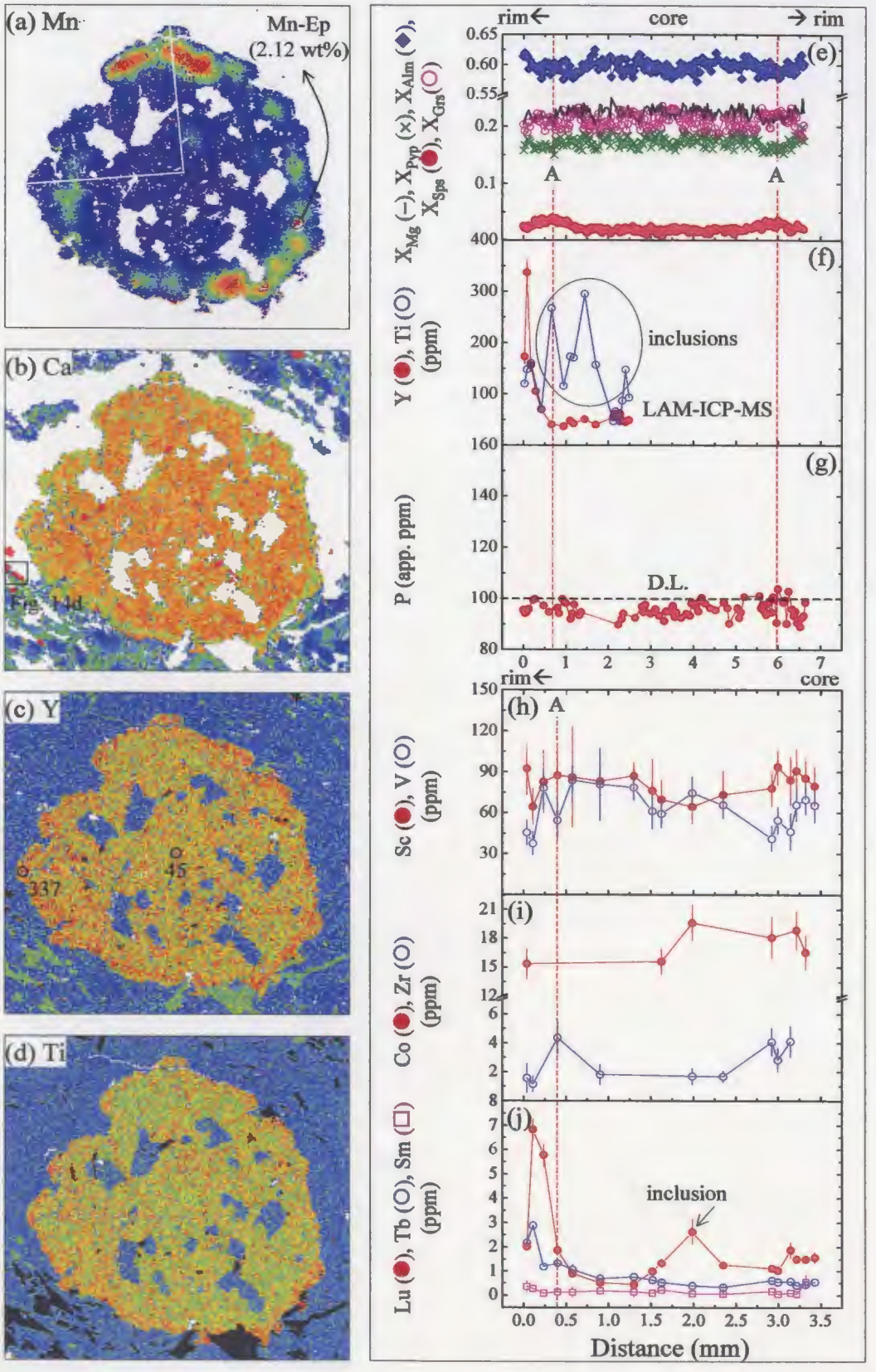
(a) Mn
Mn-Ep
(2.12 wt%)
(b) Ca
Fig. 14d
(c) Y
337
45
(d) Ti
rim←
core
→ rim
(e)
A
A
$X_{Mg}$ (–), $X_{Pyp}$ (×), $X_{Alm}$ (◆), $X_{Sps}$ (●), $X_{Grs}$ (○)
(f)
Y (●), Ti (○) (ppm)
inclusions
LAM-ICP-MS
(g)
P (app. ppm)
D.L.
rim←
core
(h) A
Sc (●), V (○) (ppm)
(i)
Co (●), Zr (○) (ppm)
(j)
Lu (●), Tb (○), Sm (□) (ppm)
inclusion
Distance (mm)

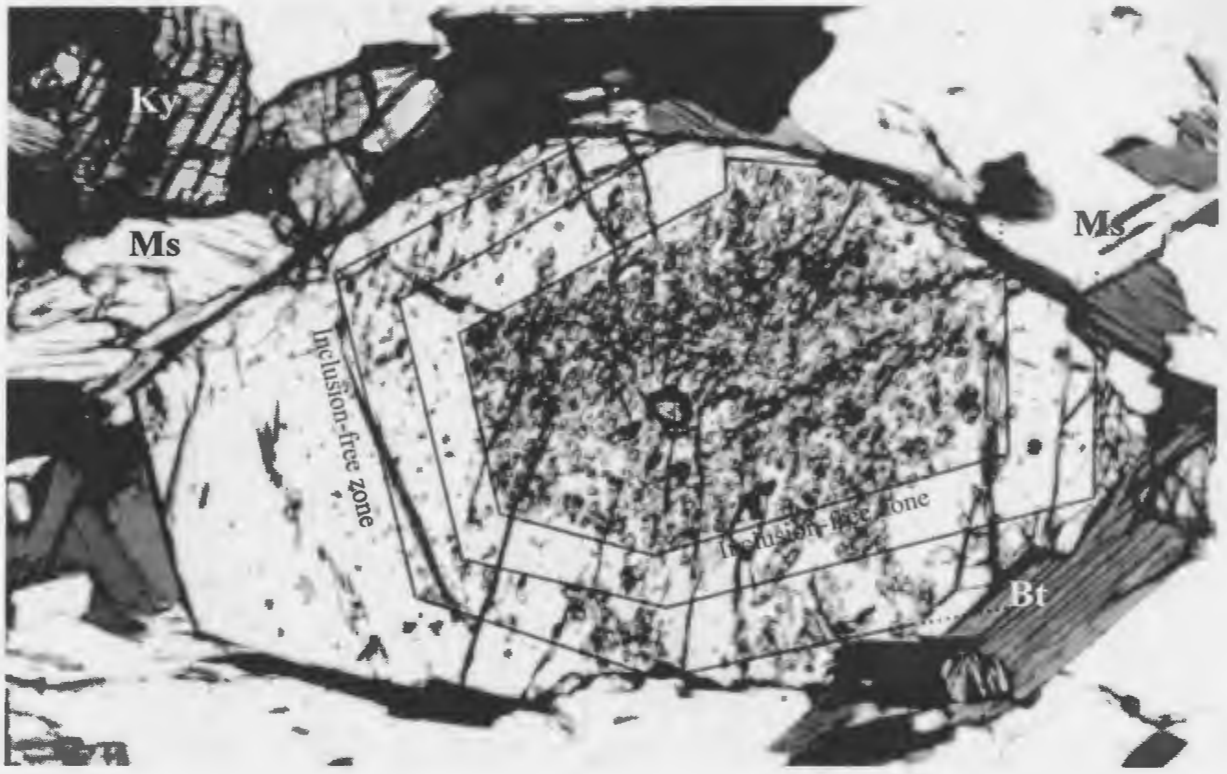


Fig. 7.7. Photomicrograph of sample 88-74 showing the oscillatory textural zoning in garnet defined by alternating inclusion-rich and inclusion-free zones.

Fig. 7.8. X-ray compositional maps and zoning profiles in garnet from sample 88-74 (migmatite-zone). (a) Mn map; white lines indicate locations of EMP and LAM-ICP-MS zoning profiles. (b) Ca map. (c) Y map: representative concentrations of Y are given in ppm. (d) P map: The location of the apatite in Figure 14e is indicated by a box. In the X-ray maps, warm colors indicate higher concentrations with black for the highest and white for the lowest concentrations. (e-g) Rim-core-rim compositional profiles of $X_{Mg}$ (=Mg/Mg+Fe), pyrope, grossular, spessartine, almandine, Y, Ti, and P along the line shown in (a). Note that Y and Ti are in ppm and P is in app. ppm. (h-j) Core-to-rim laser ICP-MS zoning profiles for Sc, V, Co, Zr, Sm, Gd and Yb. The letter A represents a compositional break defined by an abrupt increase in Y. Inclusion-free zones on profiles e-j are shown as vertical yellow bars.

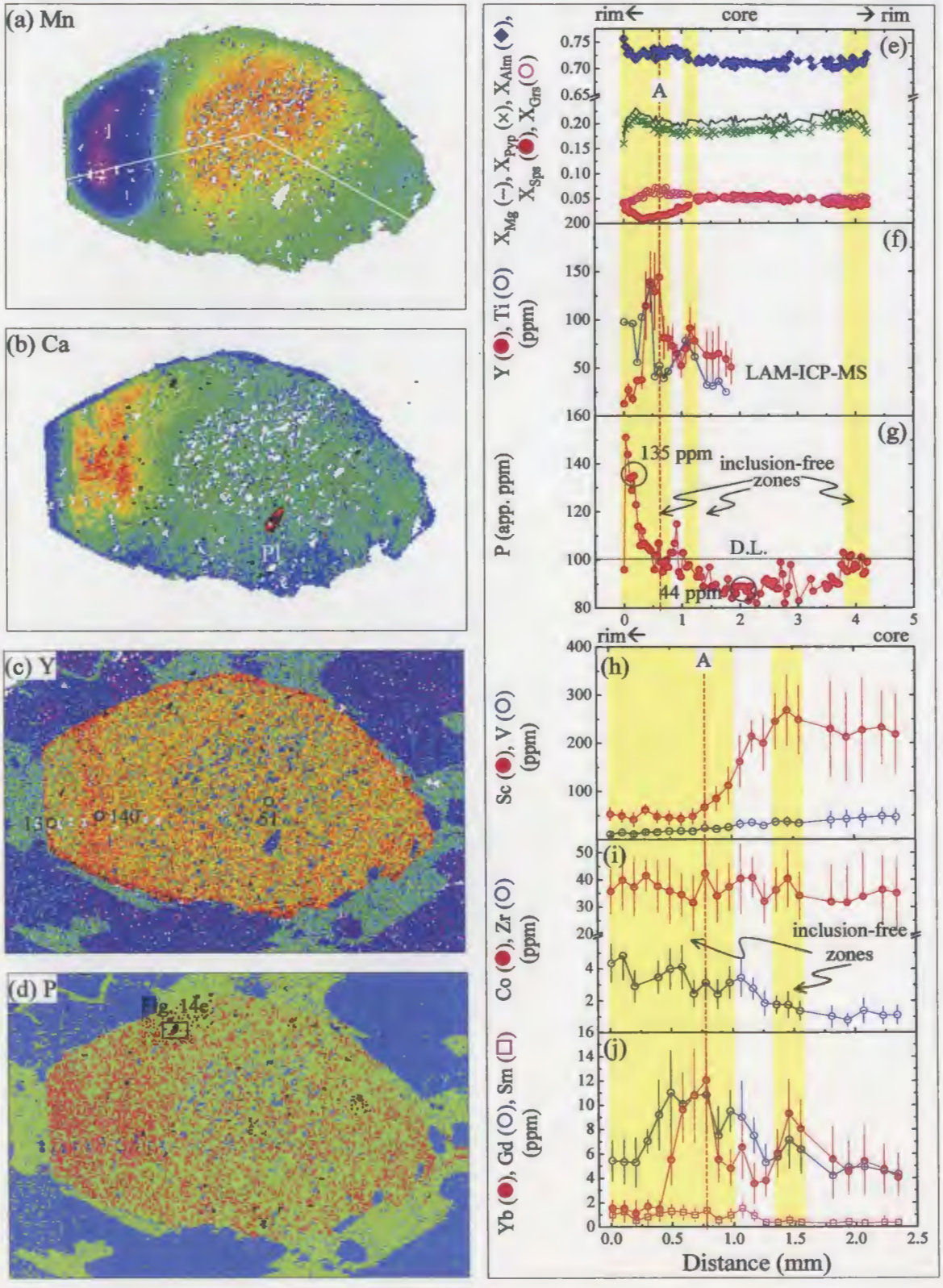
(a) Mn
(b) Ca
Pl
(c) Y
130
140
51
(d) P
Fig. 14e
rim←
core
→ rim
(e)
A
(f)
LAM-ICP-MS
(g)
135 ppm
inclusion-free zones
D.L.
44 ppm
rim←
core
(h)
A
(i)
inclusion-free zones
(j)
Distance (mm)


Fig. 7.9. Photomicrograph of sample 88-88 showing the oscillatory textural zoning in garnet defined by alternating inclusion-rich and inclusion-free zones. Bt-biotite, Chl-chlorite, Ky-kyanite, St-staurolite and Ms-muscovite.

Fig. 7.10. X-ray compositional maps and zoning profiles in garnet from sample 88-88 (migmatite-zone). (a) Mn map; white lines indicate locations of EMP and LAM-ICP-MS profiles. (b) Ca map. (c) Y map: representative Y concentrations are given in ppm. (d) P map: representative Y analyses of apatite grains are given in app. ppm. Note that the Y concentration of apatite in the garnet resorption area (see a red arrow) is higher than that of apatite in the matrix. Apatite illustrated in Figure 14f is indicated by box. In the X-ray maps, warm colors indicate higher concentrations with black for the highest and white for the lowest concentrations. (e-g) Rim-core-rim compositional profiles of $X_{Mg}$ (=Mg/Mg+Fe), pyrope, grossular, spessartine, almandine, Y, Ti, and P along the line shown in (a). Note that Y is in ppm and Ti and P are in app. ppm. (h-j) Core-to-rim laser ICP-MS zoning profiles for Sc, V, Co, Zr, Sm, Gd and Yb. The letter A represents a compositional break defined by a peak in the Y profile. Inclusion-free zones on profiles e-j are shown as yellow bars.

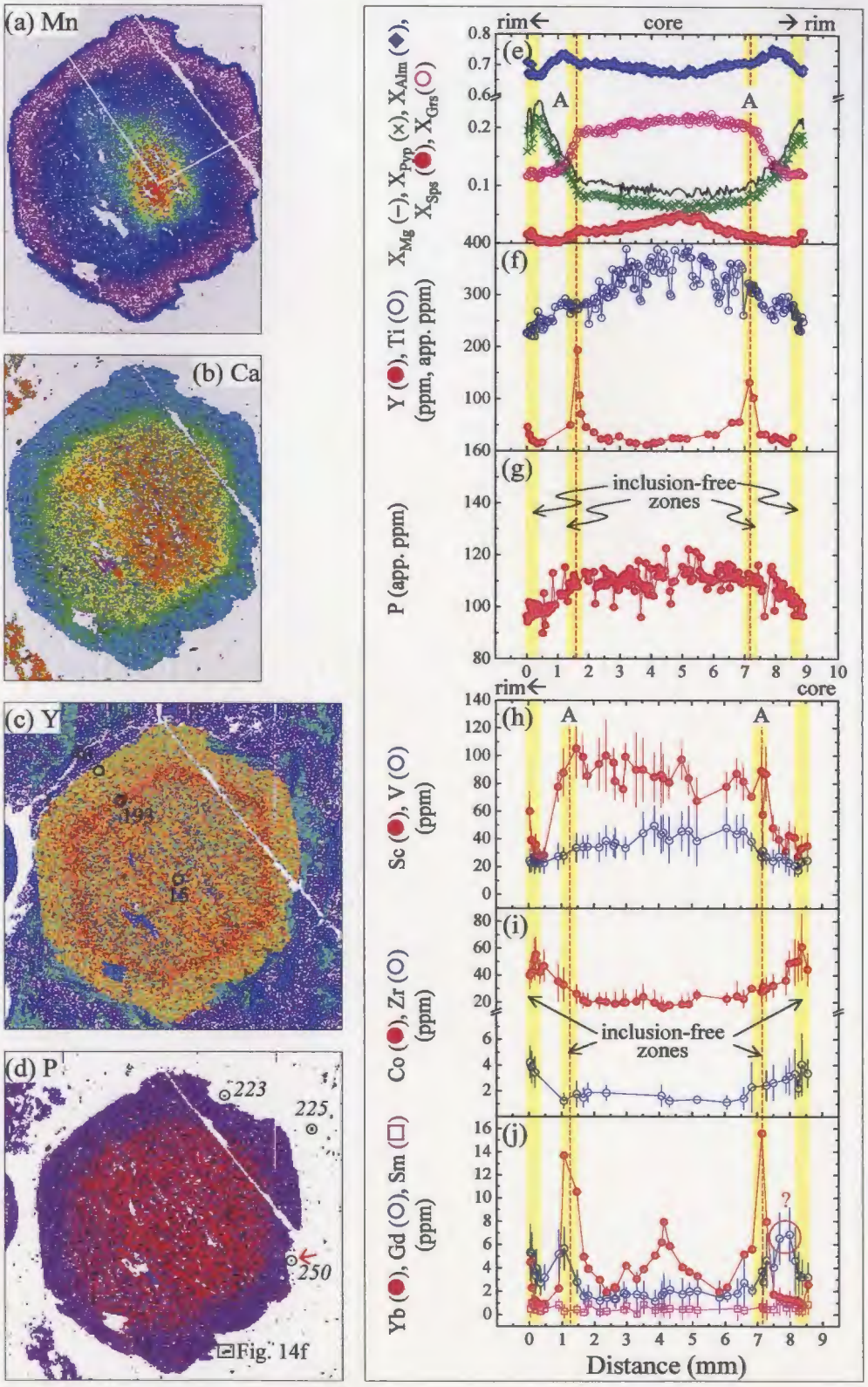
(a) Mn
(b) Ca
(c) Y
193
15
(d) P
223
225
250
Fig. 14f
rim←
core
→ rim
(e)
A
A
$X_{Mg}$ (–), $X_{Pyp}$ (×), $X_{Alm}$ (◆),
$X_{Sps}$ (●), $X_{Grs}$ (○)
(f)
Y (●), Ti (○)
(ppm, app. ppm)
(g)
inclusion-free
zones
P (app. ppm)
rim←
core
(h)
A
A
Sc (●), V (○)
(ppm)
(i)
inclusion-free
zones
Co (●), Zr (○)
(ppm)
(j)
?
Yb (●), Gd (○), Sm (□)
(ppm)
Distance (mm)

Fig. 7.11. X-ray compositional maps and zoning profiles in garnet from sample 88-80 (migmatite-zone). (a) Mn map; white lines indicate locations of EMP and LAM-ICP-MS profiles. (b) Ca map. (c) Y map: representative concentrations of Y are given in ppm. (d) P map: The location of apatite in Figure 14f is indicated by box. Dotted lines represent the postulated former outline of the garnet on the basis of Cr zoning. In the X-ray maps, warm colors indicate higher concentrations with black for the highest and white for the lowest concentrations. (e-g) Rim-core-rim compositional profiles of $X_{Mg}$ (=Mg/Mg+Fe), pyrope, grossular, spessartine, almandine, Y, Ti, and P along the line shown in (a). Note that Y, Ti, and P are in app. ppm. (h-j) Core-to-rim laser ICP-MS zoning profiles for Sc, V, Co, Zr, Sm, Gd and Lu. Letters A and B represent compositional breaks defined by inflections in the Gd and P zoning profiles, respectively.

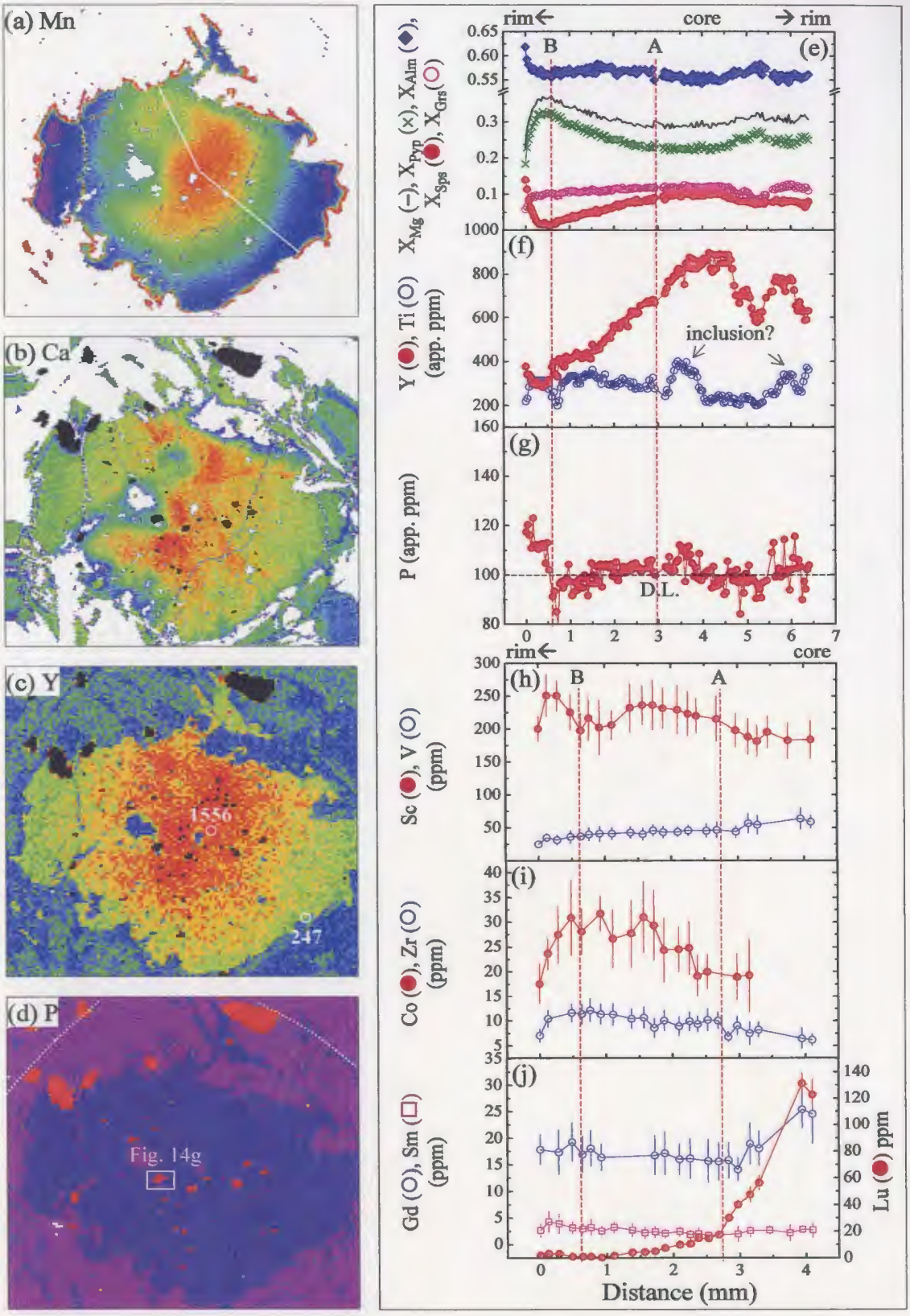
(a) Mn
(b) Ca
(c) Y
1556
247
(d) P
Fig. 14g
rim←
core
→ rim
B
A
(e)
$X_{Mg}$ (–), $X_{Pyp}$ (×), $X_{Alm}$ (◆), $X_{Sps}$ (●), $X_{Grs}$ (○)
(f)
Y (●), Ti (○) (app. ppm)
inclusion?
(g)
P (app. ppm)
D.L.
rim←
core
(h)
Sc (●), V (○) (ppm)
(i)
Co (●), Zr (○) (ppm)
(j)
Gd (○), Sm (□) (ppm)
Lu (●) ppm
Distance (mm)

| | $X_{Sps}$ | $X_{Grs}$ | Y | Gd | Sm | P | Sc | Ti | V | Co | Zr |
|---|---|---|---|---|---|---|---|---|---|---|---|
| 87-86 | | 0.19 / 0.16 | | | | 127 / 122 | | 540 / 240 | | | 1.62 |
| 87-279 | | 0.23 / 0.19 | | | | 122 / 113 | | 797 / 216 | | | 1.36 |
| 87-271 | | 0.20 / 0.18 | | | | 122 / 118 | | 959 / 241 | | | 8.68 / 5.96 |
| 87-287 | | 0.21 | | | | < 100 | | 138 / 47 | | | 4.37 / 1.57 |
| 88-74 | | 0.05 | | | | 153 / 44 | | 96 / 25 | | | 4.84 / 1.11 |
| 88-88 | | 0.22 / 0.12 | | | | 113 / < 100 | | 348 / 84 | | | 4.21 / 1.34 |
| 88-80 | | 0.15 | | | | 122 / 105 | | 372 / 228 | | | 11.61 / 6.17 |

Fig. 7.12. Schematic summary of rim-core-rim zoning relationships of the analyzed garnets. Numbers in P zoning are in app. ppm. Ti and Zr concentrations for core and rim are given in ppm.

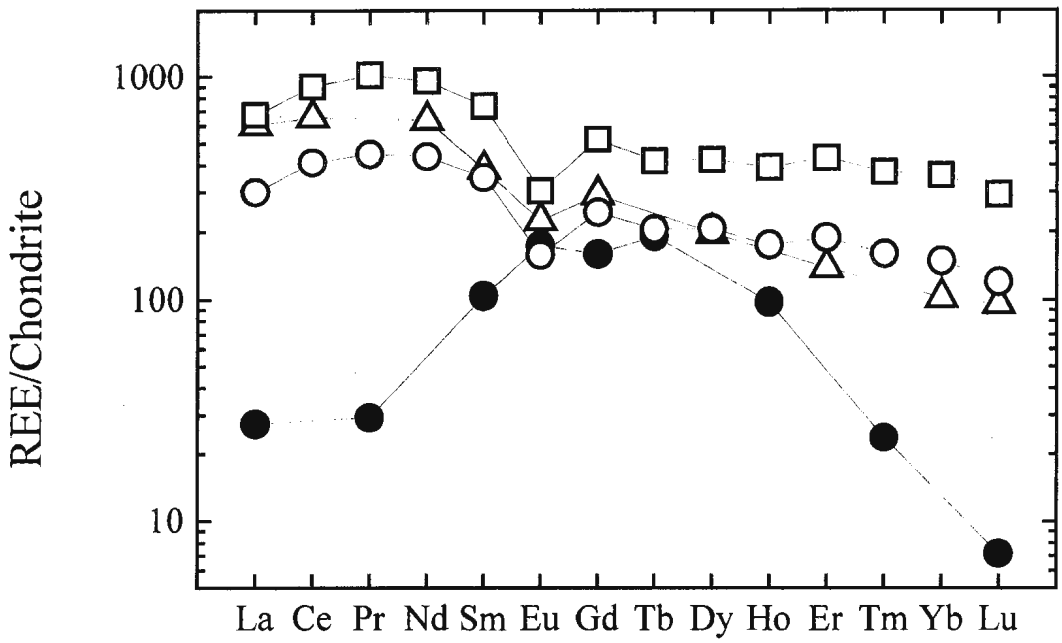


Fig. 7.13. Chondrite-normalized REE patterns of epidote from P-11 (migmatite zone, see Figure 1 and Yang and Rivers, 2001) and apatite from samples 87-86, 87-287 and P-11. Chondrite normalization factors from Taylor and McLennan (1985).

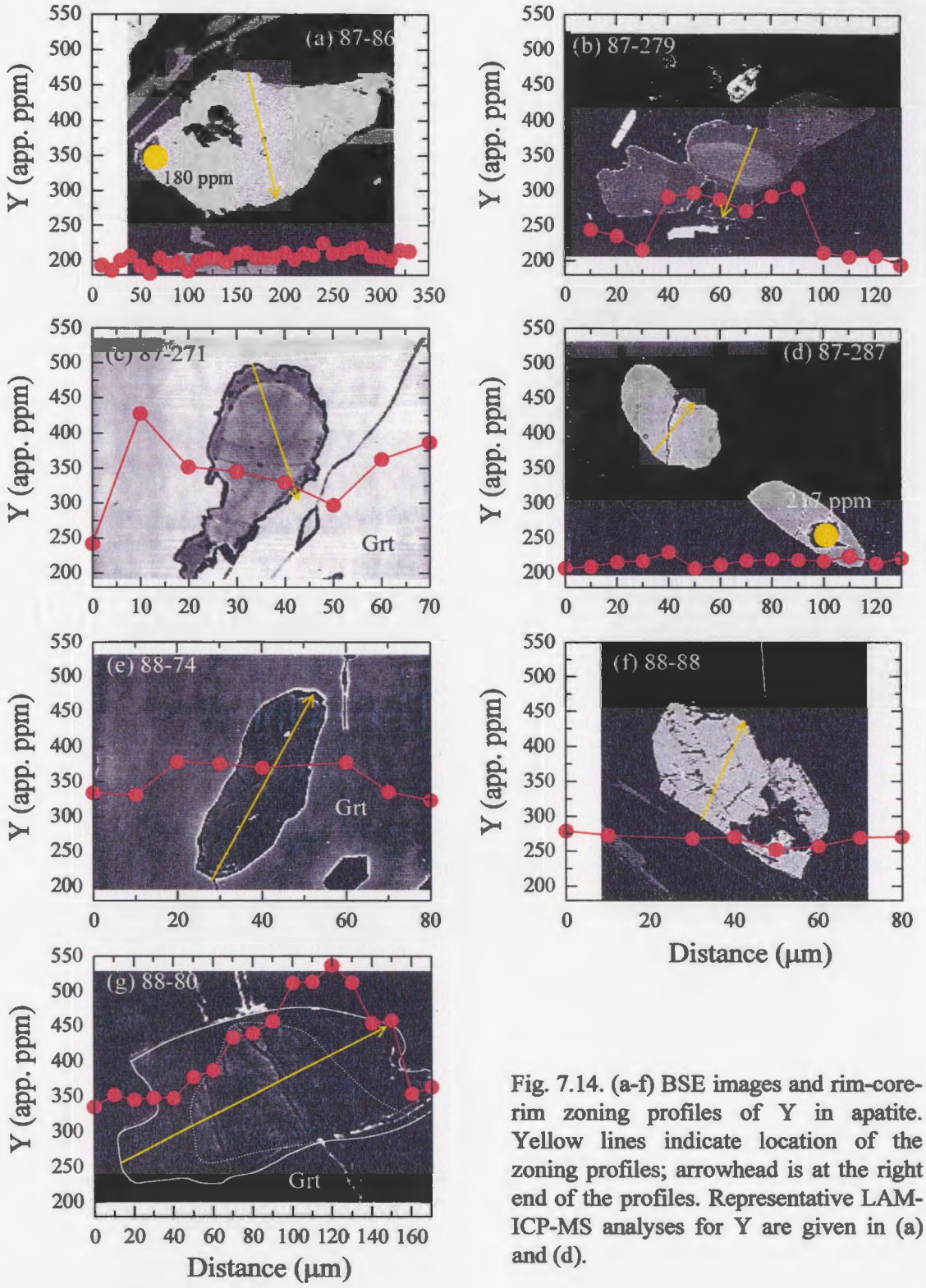


Fig. 7.14. (a-f) BSE images and rim-core-rim zoning profiles of Y in apatite. Yellow lines indicate location of the zoning profiles; arrowhead is at the right end of the profiles. Representative LAM-ICP-MS analyses for Y are given in (a) and (d).

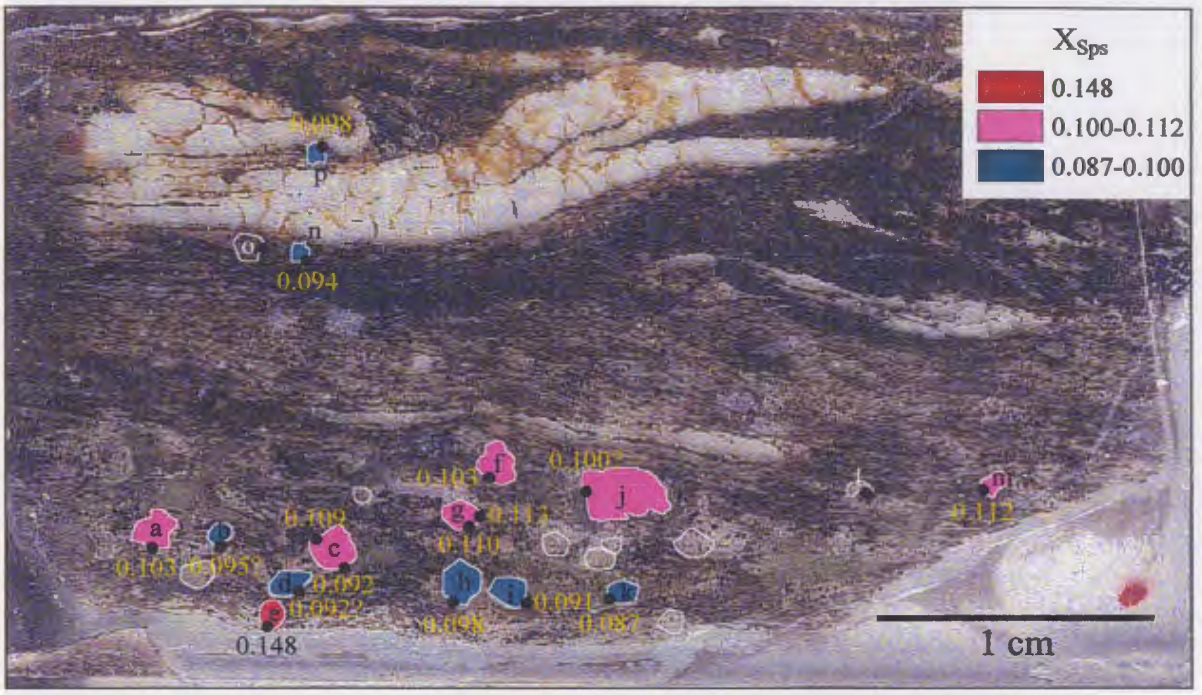


Fig. 7.15. Photomicrograph of sample 87-279 (garnet zone), with 16 garnets colored on the basis of their values of $X_{Sps}$ at the inner annulus.

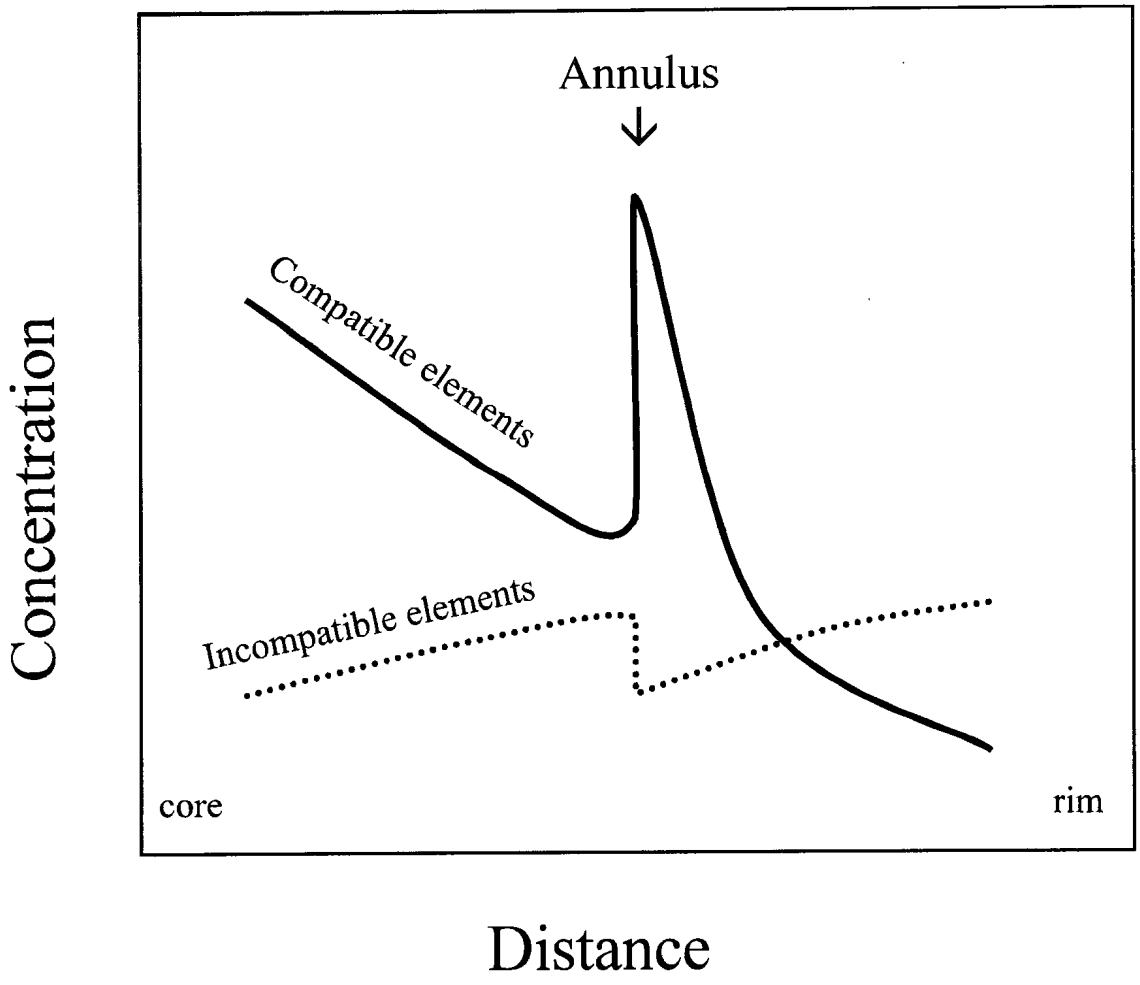


Fig. 7.16. A schematic diagram showing the variation of garnet-compatible and -incompatible elements at an Y annulus formed by garnet resorption and subsequent regrowth.

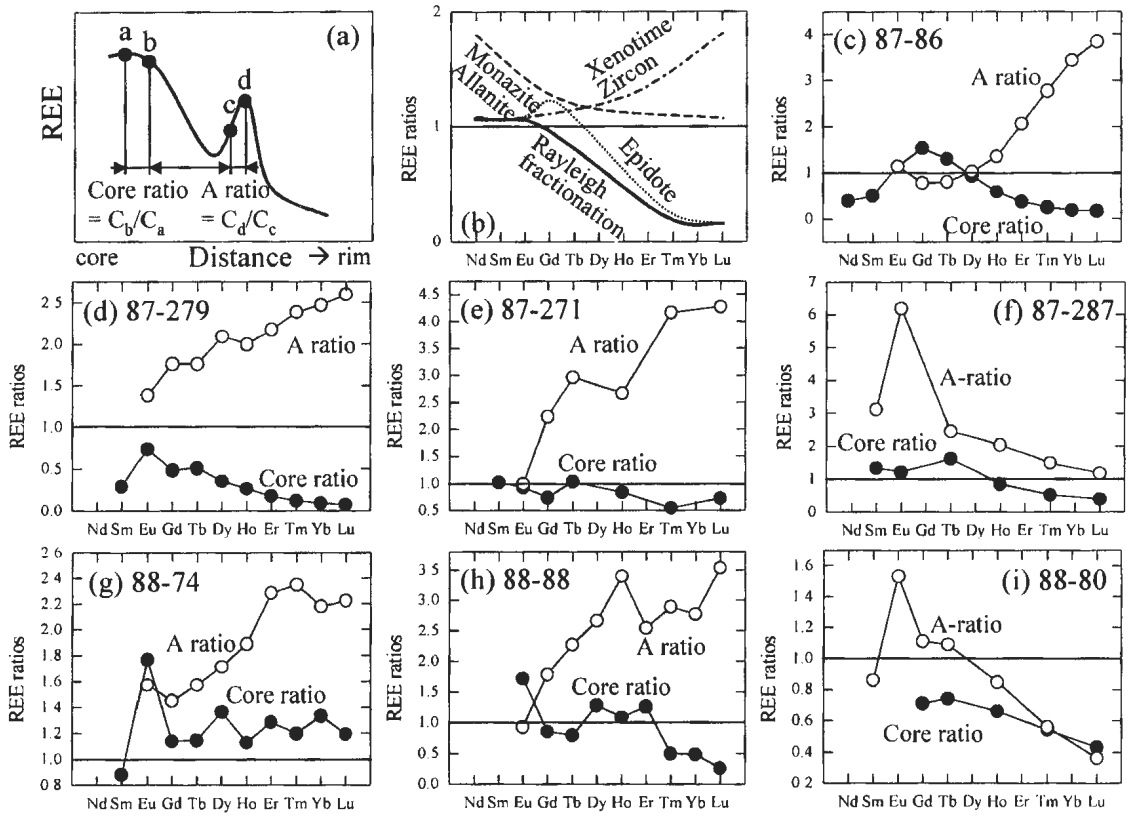


Fig. 7.17. (a) Definition of core and annulus (A) REE ratios. [Note: core ratio in garnet 87-86 is defined by Cc/Ca because only a single point was determined in the core]. (b) Solid line - expected REE pattern in garnet assuming Rayleigh fractionation; labeled dashed and dotted lines - expected perturbations to Rayleigh fractionation pattern as a result of breakdown of allanite and monazite (enrichment in LREE), epidote (enrichment in MREE), and xenotime and zircon (enrichment in HREE). (c-i) Changes in REE ratios for core and A regions, in analyzed garnets.

# Chapter 8: Summary

This study demonstrates that integrated micro-beam techniques, such as EMP and LAM-ICP-MS are required to resolve the major and trace element information contained in metamorphic minerals. In this study, detailed trace element analyses using LAM-ICP-MS, combined with results of major element analyses by electron microprobe, of coexisting metamorphic minerals from lower greenschist to upper amphibolite facies metamorphic rocks from western Labrador allow us to draw the following conclusions.

The trace element compositions of garnet, biotite and muscovite are mainly controlled by crystal-chemical factors, bulk composition and the coexisting mineral assemblage. As an example of the role of coexisting mineral assemblage, garnet, biotite and muscovite in the staurolite zone are strongly depleted in Zn due to equilibration with staurolite. Such elemental signatures can contribute to deciphering reaction histories in favourable cases.

Systematic distributions of some trace elements between garnet and biotite (e.g. V, Co and Zn) and biotite and muscovite (e.g. Sc, V, Ba) are consistent with equilibrium partitioning during metamorphism, indicating that irregular partitioning of trace elements suggested by several previous studies utilizing whole-mineral digestion techniques, may have been due at least in part to impurities and trace-element zoning, which are avoided with the in situ measurements by LAM-ICP-MS. However, large variations in the partitioning of other elements (e.g., Cr partitioning between garnet and biotite) indicate that different elements may achieve different scales of equilibrium during greenschist- to

upper amphibolite-facies metamorphism.

Trace element partitioning between coexisting garnet and biotite shows correlation between trace and major elements, which supports the existence of a major element control on incorporation of some trace elements. For example, the partitioning of Sc and Ti between garnet and biotite in the analyzed samples shows a dependence on the octahedral Al content of biotite and the Ca content of garnet, respectively. The partitioning of Co and Zn show a moderate *T* effect, with the least compositional effects; both elements partition preferentially into garnet at higher *T*. Partitioning of V, Zr, Sm, Eu and Gd between garnet and biotite is more complicated and controlled by both crystal-chemical factors and temperature. The partition coefficients between garnet and biotite also exhibit dependence on ionic radius and charge, resulting in parabola-shaped curves in an 'Onuma' diagram. This suggests that trace element partitioning occurs by substitution into specific crystallographic sites in crystalline phases and that the partitioning of trivalent cations in garnet X-sites is charge balanced by coupled substitutions.

Distribution behaviour between biotite and muscovite for many elements is compatible with lattice strain theory, especially in interlayer sites of micas. Partitioning of Li, Sc, Sr and Ba between biotite and muscovite shows moderate thermal dependence, but it was not possible to separate this effect from major element compositional and structural effects.

None of the analyzed elements promise a simply applicable, 'trace-element geothermometer' for greenschist- and amphibolite-facies metamorphic rocks. Scatter in

plots of $\ln D_i^*$ versus $10^4/T$ is large, and the composition effects cannot be readily separated from thermal effects. However, these data do provide a series of tests for equilibrium between phases in metapelitic samples, and hence can be used to improve the choice of appropriate samples for other studies. For example, the trace element partitioning data for V and Zr between biotite and muscovite may be used to cross-check conventional geothermometers for samples from a similar range of *P-T* and bulk composition, especially when conventional geothermometers suffer from retrograde resetting and/or high $Fe^{3+}$ contents. The ranges and dependences of distribution coefficients on major element compositions established here, for quartzofeldspathic and metapelitic rocks from upper greenschist to upper amphibolite facies, also provide important constraints on the values that can be used in modeling trace element zoning of garnet, because biotite and muscovite participate in many prograde metamorphic reactions.

This study has provided evidence for two and possibly three types of growth zoning in metamorphic garnets, referred to as spiral, overprint, and oscillatory (?) zoning. Spiral growth zoning is displayed by both major and trace elements in garnet and the growth is restricted to the pressure shadow regions of a rotating garnet. Recognition of spiral growth zoning provides a new tool to resolve the controversy over rotation versus non-rotation of snowball garnet porphyroblasts. Overprint growth zoning, which is exhibited by Cr zoning patterns that are parallel to straight and/or spiral internal fabrics ($S_i$) in the garnet, indicates limited mobility of Cr during growth, and is reported here from amphibolite facies assemblages. The existence of overprint growth zoning in several of

the garnets examined indicates that Cr partitioning was far from equilibrium and provides a simple explanation for the irregular Cr distribution coefficients between garnet and coexisting minerals determined by previous workers. Cr zoning in kyanite, characterized by zones with variable width, continuity, and Cr concentration in individual annuli, may be a result of oscillatory or overprint zoning or both. In all three cases, it implies limited mobility of Cr during the growth of the kyanite, even under upper amphibolite facies conditions. Despite this negative conclusion concerning the attainment of equilibrium with respect to Cr, it is possible to derive qualitative information on the relative rates of Cr diffusion and garnet growth in many samples. We have derived a dimensionless ratio (GL:D) to qualitatively explain the differences in texture and Cr behaviour in our analysed garnets. Examined samples exhibit evidence of a range of GL:D from >1 to <1. One sample displays a textural unconformity coincident with a change in the behaviour of Cr, which we interpret to represent a crossover in the rates of growth and Cr diffusion, i.e., where GL:D changes from >1 through unity to <1. The results from this study emphasize the importance of crystal growth rates in controlling the incorporation of trace elements and inclusions within porphyroblasts.

P, Ti and Zr occur in garnet in trace levels. Where the garnet grew in equilibrium with a saturating phase such as apatite, ilmenite or zircon respectively, the activities of P, Ti and Zr should be buffered at constant values, and incorporation of these elements into garnet has the potential to reflect the *P-T* conditions. However, the effects of other phosphates (e.g., monazite, xenotime), Ti-oxides (e.g., rutile, ilmenite) and Zr-bearing phases (e.g., zircon, xenotime) on the buffered activities may be important, and

substitution mechanisms, crystal-chemical effects and scale of equilibrium require evaluation. Mn annuli of growth origin are described in several of the analyzed garnets. They are inferred to result from breakdown of Mn-enriched phases such as piemontite during garnet growth. Piemontite-rich inclusions in several of the analyzed garnets support this interpretation. The concentration of Mn in the Mn annuli is shown to vary by over 50% among garnets in a single thin section, suggesting that the Mn activity varied significantly across the area of a thin section. This result suggests that the uncritical use of Mn annuli as time markers may be inappropriate, at least in low grade rocks.

Yttrium annuli in the analyzed garnet porphyroblasts are shown to result from three processes: garnet resorption, diffusion-controlled garnet growth, and breakdown of Y-enriched trace phases during garnet growth. These processes can be distinguished as follows. (1) Yttrium annuli produced by garnet resorption are characterized by irregular, locally embayed shapes on the inner side of the annulus, and by systematic variations between garnet-compatible and -incompatible elements at the Y annulus. (2) Where the Y annulus coincides with inclusion-free zones in a garnet poikiloblast, the concentration of Y in garnet is diffusion-controlled and inversely related in some complex manner to the rate of garnet growth. Diffusion control on the incorporation of Y in garnet is compatible with significant measured differences in Y concentration around an individual annulus and implies that the activity of Y also varied locally around the growing garnet porphyroblast. (3) REE ratio variations in garnet are shown to be sensitive indicators of the identity of the trace minerals involved in garnet formation. For instance, increases in Sc, Y, and MREE in garnet accompany the breakdown of epidote, and an increase in Mn

in association with the above elements indicates involvement of piemontite. Breakdown of allanite and/or monazite in the garnet-forming reaction is indicated by an increase in LREE in garnet, whereas involvement of xenotime is indicated by an increase in HREE in garnet and by high Y cores in coexisting apatite.

Apatite appears to participate in the major-phase reactions in (calc) pelites at all metamorphic grades. This inference is supported by a decrease in the modal abundance of apatite with garnet growth, the presence of a few hundred ppm P in garnet, and the embayed and resorbed outlines of remaining matrix apatite crystals. High Y cores in apatite point to the former existence of xenotime that is inferred to have buffered the Y activity in apatite. In these buffered samples, the Y content of apatite may be useful as a geothermometer. Future research into metamorphic trace element behaviour in a variety of well-constrained metamorphic systems should permit greater insight into the specific controlling factors considered in this study.

# References

Akers, W. T., Grove, M., Harrison, T. M., and Ryerson, F. J., 1993. The instability of rhabdophane and its unimportance in monazite paragenesis. Chemical Geology, 110, 169-176.

Albarede, F. and Botinga, Y., 1972. Kinetic disequilibrium in trace element partitioning between pheocrysts and host lavas. Geochimica et Cosmochimica Acta, 36, 141-156.

Albee, A. L., 1965. Phase equilibria in three assemblages of kyanite-zone pelitic schists, Lincoln mountain quadrangle, central Vermont. Journal of Petrology, 6, 246-301.

Andrehs, G. and Heinrich, W., 1998. Experimental determination of REE distributions between monazite and xenotime: potential for temperature-calibrated geochronology. Chemical Geology, 149, 83-96.

Annersten, H. and Eckström, T., 1971. Distribution of major and minor elements in coexisting minerals from a metamorphosed iron formation. Lithos, 4, 185-204.

Atherton, M. P., 1968. The variation in garnet, biotite, and chlorite composition in medium grade pelitic rocks from the Dalradian, Scotland, with particular reference to the zonation in garnet. Contribution to Mineralogy and Petrology, 18, 347-371.

Atkinson, A. and Taylor, R. I., 1986. Impurity diffusion in NiO grain boundaries. Journal of Physics and Chemistry of Solids, 47, 315-323.

Ayres, M. and Vance, D., 1994. Constraints on the thermal evolution of the Indian

Himalaya from manganese and erbium distributions in metapelitic garnets. Mineralogical Magazine, 58A, 34-35.

Baadsgaard, H., Krupicka, J. and Lambert, R. St. J., 1976. Mineral isotopic age relationships in the polymetamorphic Amistsoq gneiss, Godthaab district, West Greenland. Geochimica et Cosmochimica Acta, 40, 513-527.

Bailey, S. W., 1984. Crystal chemistry of the true micas. In Micas (ed. S. W. Bailey). Mineralogical Society of America. Reviews in Mineralogy, 13, 13-57.

Bass, J. D., 1995. Elasticity of minerals, glasses and melts. Handbook of Physical Constants. AGU Ref, Shelf, 2, 45-63.

Bea, F. and Montero, P., 1999. Behavior of accessory phases and redistribution of Zr, REE, Y, Th, and U during metamorphism and partial melting of metapelites in the lower crust: An example from the Kinzigite Formation of Iverea-Verbano, NW Italy. Geochimica et Cosmochimica Acta, 63, 1133-1153.

Bea F., Cámara F., Soler J. M. F., Pugnaire M. T. G., Pereira M. D., and Stroh A., 1993. Trace element determination in minerals: Analyses of concentrates versus laser ablation techniques-Case study: biotites from granitic rocks. European Winter Conference Plasma Spectrometry, 40.

Bea, F., Pereira, M. D., and Stroh, A., 1994. Mineral/leucosome trace-element partitioning in a peraluminous migmatite (a laser ablation-ICP-MS study). Chemical Geology, 117, 291-312.

Bea, F., Montero, P., Garut, G. and Zacharini, F., 1997. Pressure-dependence of rare earth element distribution in amphibolite- and granulite-grade garnets. A LA-ICP-MS study. Geostandards Newsletters, 21, 253-270.

Beattie, P., 1993. On the occurrence of apparent non-Henry's law behaviour in experimental partitioning studies. Geochimica et Cosmochimica Acta, 57, 47-55.

Beattie, P., Ford, C. and Russell, D., 1991. Partition coefficients for olivine-melt and orthopyroxene-melt systems. Contribution to Mineralogy and Petrology, 109, 212-224.

Beattie, P., 1994. What determines the values of mineral/melt partition coefficients? Mineralogical Magazine, 58A, 63-64.

Beattie, P., 1994. Systematics and energetics of trace-element partitioning between olivine and silicate melts: Implications for the nature of mineral/melt partitioning. Chemical Geology, 117, 57-71.

Beattie, P., Drake, M., Jones, J., Leeman, W., Longhi, J., McKay, G., Nielsen, R., Palme, H., Shaw, D., Takahashi, E., and Watson, B., 1993. Terminology for trace-element partitioning. Geochimica et Cosmochimica Acta, 57, 1605-1606.

Bell, T. H., 1985. Deformation partitioning and porphyroblast rotation in metamorphic rocks: a radical reinterpretation. Journal of Metamorphic Geology, 3, 109-118.

Bell, T. H. and Hickey, K. A., 1999. Complex microstructures preserved in rocks with a simple matrix: significance for deformation and metamorphic processes. Journal of Metamorphic Geology, 17, 521-535.

Bell, T. H. and Johnson, S. E., 1992. Shear sense: a new approach that resolves conflicts between criteria in metamorphic rocks. Journal of Metamorphic Geology, 10, 99-124.

Bell, T. H., Johnson, S. E., Davis, D., Forde, A., Hayward, N., and Wilkins, C., 1992. Porphyroblast inclusion-trail orientation data: eppure non son girate. Journal of Metamorphic Geology, 10, 295-307.

Berman, R. G., 1991. Thermobarometry using multi-equilibrium calculations: a new technique, with petrological applications. Canadian Mineralogist, 29, 833-855.

Bingen, B., Demaiffe, D., and Hertogen, J., 1996. Redistribution of rare earth elements, thorium, and uranium over accessory minerals in the course of amphibolite to granulite facies metamorphism: The role of apatite and monazite in orthogneisses from southwestern Norway. Geochimica et Cosmochimica Acta, 60, 1341-1354.

Bishop, F. C., Smith, J. V, and Dawson, J. B., 1978. Na, K, P and Ti in garnet, pyroxene and olivine from peridotite and eclogite xenoliths from African kimberlites. Lithos, 11, 155-173.

Blakery, 1979. Segregation to surfaces: dilute alloys of the transition metals. In Chemistry and Physics of Solid Surfaces, II (ed. R. Vanselow), 253-276. CRC press.

Blundy, J. D. and Wood, B. J., 1991. Crystal-chemical controls on the partitioning of Sr and Ba between plagioclase feldspar, silicate melts, and hydrothermal solutions. Geochimica et Cosmochimica Acta, 55, 193-209.

Blundy, J. and Wood B., 1994. Prediction of crystal-melt partition coefficients from

elastic moduli. Nature, 372, 452-454.

Bohlen, S. R., Valley, J. W., and Essene, E. J., 1985. Metamorhism in the Adirondacks. I. Petrology, temperature and pressure. Journal of Petrology, 26, 971-992.

Bollingberg, H. J. and Brynhi, I., 1972. Minor element zonation in an eclogite garnet. Contribution to Mineralogy and Petrology, 36, 113-122.

Brady, J. B., 1983. Intergranular diffusion in metamorphic rocks. American Journal of Science, 283-A, 181-200.

Brenan, J. M., Shaw, H. F., Ryerson, F. J., and Phinney, D. L., 1995. Mineral-aqueous fluid partitioning of trace elements at 900 °C and 2.0 GPa: constraints on the trace element chemistry of mantle and deep crustal fluids. Geochimica et Cosmochimica Acta, 59, 3331-3350.

Brice, J. C., 1975. Some thermodynamic aspects of the growth of strained crystals. Journal of Crystal Growth, 28, 249-253.

Brown, D., Rivers, T., and Calon, T., 1992. A structural analysis of a metamorphic fold-thrust belt, northeast Gagnon terrane, Grenville Province. Canadian Journal of Earth Science, 29, 1915-1927.

Burns, R. G., 1993. Mineralogical applications of crystal field theory. Cambridge University Press, p. 551.

Butler, B. C. M., 1967. Chemical study of minerals from the Moine schists of the Ardnamurchan area, Argyllshire, Scotland. Journal of Petrology, 8, 233-267.

Caporuscio, F. A. and Smyth, J. R., 1990. Trace element crystal chemistry of mantle eclogites. Contribution to Mineralogy and Petrology, 105, 550-561.

Carbonin, S., Salviulo, G., Munno, R., Desiderio, M., and Dal, N. A., 1989. Crystal-chemical examination of natural diopsides; some geometrical indications of Si-Ti tetrahedral substitution. Mineralogy and Petrology. 41; 1-10.

Carlson, W. D., 1989. The significance of intergranular diffusion to the mechanisms and kinetics of porphyroblast crystallization. Contributions to Mineralogy and Petrology, 103, 1-24.

Carlson, W. D., Denison, C., and Ketcham, R. A., 1995. Controls on the nucleation and growth of porphyroblasts; kinetics from natural textures and numerical models. Geological Journal, 30, 207-225.

Carmichael, D. M., 1969. On the mechanism of prograde metamorphic reactions in quartz-bearing pelitic rocks. Contributions to Mineralogy and Petrology, 20, 244-267.

Cashman, K. V. and Ferry, J. M., 1988. Crystal size distribution (CDS) in rocks and the kinetics and dynamics of crystallization. Contributions to Mineralogy and Petrology, 99, 401-415.

Chakraborty, S. and Ganguly, J., 1992. Cation diffusion in aluminosilicate garnets; experimental determination in spessartine-almandine diffusion couples, evaluation of effective binary, diffusion coefficients, and applications. Contributions to Mineralogy and Petrology, 111, 74-86.

Chamberlain, C. P. and Conrad, M. E., 1993. Oxygen isotope zoning in garnet: a record of volatile transport. Geochimica et Cosmochimica Acta, 57, 2613-2629.

Chernoff, C. B. and Carlson, W. D., 1997. Disequilibrium for Ca during growth of pelitic garnet. Journal of Metamorphic Geology, 15, 421-438.

Chernoff, C. B. and Carlson, W. D., 1999. Trace element zoning as a record of chemical disequilibrium during garnet growth. Geology, 27. 555-558.

Chinner, G. A., 1962. Almandine in thermal aureoles. Journal of Petrology, 3, 316-339.

Christensen, J. N., Rosenfeld, J. L., and DePaolo, D. J., 1989. Rates of tectonometamorphic processes from rubidium and strontium isotopes in garnet. Science, 244, 1465-1469.

Christensen, J. N., Rosenfeld, J. L., DePaolo, D. J., and Selverstone, J., 1991. The rate and timing of garnet growth in the upper Schieferhuelle, Tauern Window, Eastern Alps. EOS, 72, 313-314.

Cliff, R. A. and Droop, G. T. R., 1985. Alpine metamorphism in the south-east Tauern Window, Austria: 2. Rates of heating, cooling and uplift. Journal of Metamorphic Geology, 3, 403-415.

Connelly, J. N. and Heaman, L. M., 1993. U-Pb geochronological constraints on the tectonic evolution of the Grenville province western Labrador. Precambrian Research, 63, 123-142.

Connelly, J. N., Rivers, T., ad James, D. T., 1995.Thermotectonic evolution of the Grenville Province of western Labrador. Tectonics, 14, 202-217.

Connelly, J. N., van Gool J., Rivers T., and James D. T., 1996. Field guide to the geology of the Grenville province of western Labrador. Pre-conference field excursion; Proterozoic Evolution in the North Atlantic Realm, COPENA-ECSOOT-IBTA

Conference, Goose Bay, Labrador, July 29-August 2, 1996, Field excursion guide No. 1, 86 pp.

Cox, A., Rivers, T. and Tubrett, M., 2001. Laser-ablation microprobe (U-Pb) zircon ages from reworked basement gneiss and supracrustal metasediment, Gagnon terrane, Grenville province. 11th annual V. M. Goldschimidt Conference, 3792.

Crank, J., 1975. The mathematics of diffusion. Clarendon Press, Oxford.

Crawford, M. L., 1974. Calcium zoning in almandine: A model based on plagioclase equilibria. In The Feldspars (McKenzie, W. S. and Zussman, J. Eds.), Manchester University Press, New York, 629-644.

Cygan, R. T. and Lasaga, A. C., 1985. Self-diffusion of magnesium in garnet at 750° and 900°C. American Journal of Sciences, 285, 328-350.

Dahl, P. S., Wehn, D. C., and Feldmann, S. G., 1993. The systematics of trace-element partitioning between coexisting muscovite and biotite in metamorphic rocks from the Black Hills, South Dakota, USA. Geochimica et Cosmochimica Acta, 57, 2487-2505.

Daniel, C. G. and Spear, F. S., 1998. The influence of pre-existing deformational fabrics on porphyroblast growth. EOS, Transactions, American Geophysical Union, 79, 356.

Danison, C. and Carlson, W. D., 1997. Three-dimensional quantitative textural analysis of metamorphic rocks using high-resolution computed X-ray tomography: Part II. Applicaiton to natural samples. Journal of Metamorphic Geology, 15, 45-57.

Deer, W. A., Howie, R. A., and Zussman, J., 1982. Garnet group. In Rock-forming

Minerals, 2nd ed., vol. 1A, Orthosilicates. Longman, London, 467-698.

De Lima, E. S., Vannucci, R., Pottazzi, P., and Ottolini, L., 1995. Reconnaissance study of trace element zonation in garnet from the Central structural domain, Northeastern Brazil: an example of polymetamorphic growth. Journal of South American Science, 8, 315-324.

DeVore, G. W., 1955. The role of adsorption in the fractionation and distribution of elements. Journal of Geology, 63, 159-190.

Domanik, K. J., Hervig, R. L., and Peacock, S. M., 1993. Beryllium and boron in subduction zone minerals: an ion microprobe study. Geochimica et Cosmochimica Acta, 57, 4997-5010.

Dowty, E., 1976. Crystal structure and crystal growth: II Sector zoning in minerals. American Mineralogist, 61, 460-469.

Dupuy, C., Dostal, J., Liotard, J. M., and Leyreloup, A., 1980. Partitioning of transition elements between clinopyroxene and garnet. Earth and Planetary Science Letters, 48, 303-310.

Dutrow, B. L, Holdaway, M. J., and Hinton, R. W., 1986. Lithium in staurolite and its petrologic significance. Contribution to Mineralogy and Petrology, 94, 496-506.

Enami, M., Cong, B., Yoshida, T., and Kawabe, I., 1995. A mechanism for Na incorporation in garnet: an example from garnet in orthogneiss form the Su-Lu terrane, eastern China. American Mineralogist, 80, 475-482.

Ehlers, K., Powell, R., and Stüwe, K, 1994. Cooling rate histories from garnet + biotite equilibrium. American Mineralogist, 79, 737-744.

Engel, A. C. and Engel. C. G., 1960. Progressive metamorphism and granitization of major paragenesis, northwest Adirondack mountains, New York, Part II: Mineralogy. Bulletin of Geological Society of America, 71, 1-58.

Eugster, H. P., 1981. Metamorphic solutions and reactions. In: Chemistry and geochemistry of solutions at high temperatures and pressures. Physics and Chemistry of the Earth, 13-14, 461-507.

Fedorowich, J. S., Jain, J. C., and Kerrich, R., 1995. Trace-element analysis of garnet by laser-ablation microprobe ICP-MS. Canadian Mineralogist, 33, 469-480.

Feenstra, A. and Engi, M., 1998. An experimental study of the Fe-Mn exchange between garnet and ilmenite. Contributions to Mineralogy and Petrology, 131, 379-392.

Ferry, J. M., 1983. On the control of temperature, fluid composition, and reaction progress during metamorphism. American Journal of Science, 283-A, 201-232.

Ferry, J. M., 2000. Patterns of mineral occurrence in metamorphic rocks. American Mineralogist, 85, 1573-1588.

Ferry, J. M. and Spear, F. S., 1978. Experimental calibration of the partitioning of Fe and Mg between biotite and garnet. Contributions to Mineralogy and Petrology, 66, 113-117.

Finger, F., Broska, I., Roberts, M. P., and Schermaier, A., 1998. Replacement of primary monazite by apatite-allanite-epidote coronas in an amphibolite facies granite gneiss from the eastern Alps. American Mineralogist, 83, 248-258.

Finlay, C. A. and Kerr, A., 1987. Evidence for differences in growth rate among garnets in pelitic schists from northern Sutherland, Scotland. Mineralogical Magazine, 51, 569-576.

Fisher, G. W., 1978. Rate laws in metamorphism. Geochimica et Cosmochimica Acta, 42, 1035-1080.

Foster, C. T., 1981. A thermodynamic model of mineral segregation in the lower sillimanite zone near Rangeley, Maine. American Mineralogist, 66, 260-277.

Fleet, M. E. and Pan Y., 1995. Site preference of rare earth elements in fluorapatite. American. Mineralogist, 80, 329-335.

Fryer, B. J., Jackson, S. E., and Longerich, H. P., 1995. The design, operation and role of the Laser-ablation microprobe coupled with an inductively coupled plasma-mass spectrometer (LAM-ICP-MS) in the earth sciences. Canadian Mineralogist, 33, 303-312.

Fukuoka, M.; Mondal, A.; Guha, D., Chattopadhyay, G., 1990. Petrochemistry of piemontite-bearing assemblages in calc-silicate rocks from Sausar Group, India. Journal of the Geological Society of India, 36; 403-412.

Ganguly, J. and Saxena, S., 1984. Mixing properties of aluminosilicate garnets: Constraints form natural and experimental data, and applications to geothermo-barometry. American Mineralogist, 69, 8-97.

Ganguly, J. and Chakraborty, S., 1991. Compositional zoning and cation diffusion in garnets. In: Ganguly, J. (ed.) Diffusion, Atomic Ordering, and Mass Transport. Springer-Verlag, New York, 120-175.

Ghent, E. D., 1976. Plagioclase-garnet-$Al_2SiO_5$-quartz: a potential geobarometer-geothermometer. American Mineralogist, 61, 710-714.

Ghent, E. D. and Stout, M. Z., 1981. Geobarometry and geothermometry of plagioclase-biotite-garnet-muscovite assemblages. Contribution to Mineralogy and Petrology, 76, 92-97.

Ghent, E. D. and Stout, M. Z., 1984. $TiO_2$ activity in metamorphosed pelitic and basic rocks: principles and applications to metamorphism in southeastern Canadian Cordillera. Contrbutions to Mineralogy and Petrology, 86, 248-255.

Ghera, A., Graziani, G., and Lucchesi, S., 1986. Uneven distribution of blue colour in kyanite. Neues Jahrbuch fuer Mineralogie Abhandlungen, 155, 109-127.

Govindaraju K., 1994. Compilation of working values and sample description for 383 geostandards. Geostandards Newslett, 18, 331-331.

Gratz, R. and Heinrich, W., 1997. Monazite-xenotime thermobarometry: Experimental calibration of the miscibility gap in the binary system $CePO_4$-$YPO_4$. American Mineralogist, 82, 772-780.

Gratz, R. and Heinrich, W., 1998. Monazite-xenotime thermometry. III. Experimental calibration of the partitioning of gadolinium between monazite and xenotime. European Journal of Mineralogy, 10, 579-588.

Grant, S. M., 1988. Diffusion models for corona formation in metagabbros from the Western Grenville Province, Canada. Contributions to Mineralogy and Petrology, 98, 49-63.

Grauch, R., 1989. Rare earth elements in metamorphic rocks. In: Geochemistry and mineralogy of rare earth elements (Lipin, B. R. and McKay, G. A, eds). Mineralogical Society of America. Washington, DC, United States. Reviews in Mineralogy. 21; 147-167.

Green, D. H. and Sobolev, N. V., 1975. Coexisting garnet and ilmenite synthesized from pyrolite and olivine basanite and their significance for kimberlitic assemblages. Contributions to Mineralogy and Petrology, 50, 217-229.

Griffin, W. L., Smith, D., Ryan, C. G., O'Reilly, S. Y., and Win T. T., 1996. Trace-element zoning in mantle minerals: Metasomatism and thermal events in the upper mantle. Canadian Mineralogist, 34, 1179-1193.

Gromet, L. P. and Silver, L. T., 1983. Rare earth element distributions among minerals in a granodiorite and their petrogenetic implications. Geochimica et Cosmochimica Acta, 47, 925-939.

Guidotti, C. V., 1978. Compositional variation of muscovite in medium- to high-grade metapelites of northwestern Maine. American Mineralogist, 63, 878-884.

Guidotti, C. V. and Sassi, F. P., 1998a. Miscellaneous isomorphous substitutions in Na-K white micas: a review, with special emphasis to metamorphic micas. Rend. Fis. Acc. Lincei. 9, 57-78.

Guidotti, C. V. and Sassi, F. P., 1998b. Petrogenetic significance of Na-K white mica mineralogy: Recent advances for metamorphic rocks. European Journal of Mineralogy, 10, 815-854.

Guidotti, C. V., Yates, M. G., Dyar, M. D., and Taylor M. E., 1994. Petrogenetic implications of the $Fe^{3+}$ content of muscovite in pelitic schists. American Mineralogist, 79, 793-795.

Gulii, V. N. and Jarvis, K. E., 1998. Rare earth elements in coexisting minerals from apatite-bearing metamorphic rocks as indicators of their origin. Geochemistry International, 36, 734-741.

Günther, D., Longerich, H. P., Forsythe, and Jackson, S. E., 1995. Laser ablation microprobe-inductively coupled plasma-mass spectrometry. American Laboratory, June, 24-29.

Guo, J. and Green, T. H., 1989. Barium partitioning between alkali feldspar and silicate melts at high temperature and pressure. Contributions to Mineralogy and Petrology, 102, 328-335.

Guo, J. and Green, T. H., 1990. Experimental study of barium partitioning between phlogopite and silicate liquid at upper-mantle pressure and temperature. Lithos, 24, 83-96.

Haack, U., Heinrichs, H., Boneb, M., and Schneider, A., 1984. Loss of metals from pelites during regional metamorphism. Contributions to Mineralogy and Petrology, 85, 116-132.

Harlow, G. E., 1995. Crystal chemistry of barian enrichment in micas from metasomatized inclusions in serpentinite, Motagua Fault Zone, Guatemala. European Journal of Mineralogy, 7, 775-789.

Harrison, T. M., Armstrong, R. L., Naeser, C. W., and Harakal, J. E., 1979. Geochronology and thermal history of the Coast Plutonic Complex, near Prince Rupert, British Columbia. Canadian Journal of Earth Sciences, 16, 400-410.

Harrison, T. M. and Watson, E. B., 1983. Kinetics of zircon dissolution and zirconium diffusion in granitic melts of variable water content. Contributions to Mineralogy and Petrology, 84, 66-72.

Harte, B. and Kirkley, M. B., 1997. Partitioning of trace elements between clinopyroxene and garnet: data from mantle eclogites. Chemical Geology, 136, 1-24.

Heinrich, W., Andrehs, G., and Franz, G., 1997. Monazite-xenotime miscibility gap thermometry; 1, An empirical calibration. Journal of Metamorphic Geology, 15, 3-16.

Hendricks, R. C. and Dahl, P. S., 1987. Trace-element partitioning between coexisting metamorphic garnets and clinopyroxene: crystal-field, compositional and thermal controls. Geological Society of America Abstract with Programs, No. 140554.

Hervig, R. L. and Peacock, S. M., 1989. Water and trace elements in coexisting muscovite and biotite from metamorphic rocks. EOS, 70, 490.

Hickey, K. A. and Bell, T. H., 1999. Behaviour of rigid objects during deformation and metamorphism: a test using schists from the Bolton syncline, Connecticut, USA. Journal of Metamorphic Geology, 17, 211-228.

Hickmott, D. D. and Shimizu, N., 1990. Trace-element zoning in garnet from the Kwoiek area, British Columbia: disequilibrium partitioning during garnet growth? Contributions to Mineralogy and Petrology, 104, 619-630.

Hickmott, D. D. and Spear, F. S., 1992. Major- and trace-element zoning in garnets from calcareous pelites in the NW Shelburne Falls quadrangle, Massachusetts: Garnet growth histories in retrograded rocks. Journal of Petrology, 33, 965-1005.

Hickmott, D. D., Shimizu, N., Spear, F. S., and Selverstone, J., 1987. Trace-element zoning in a metamorphic garnet. Geology, 15, 573-576.

Hietanen, A., 1969. Distribution of Fe and Mg between garnet, staurolite, and biotite in aluminum-rich schist in various metamorphic zones north of the Idaho batholith. American Journal of Science, 267, 422-456.

Hodges, K. V. and Crowley, P. D., 1985. Error estimation and empirical geothermobarometry for pelitic systems. American Mineralogist, 70, 702-709.

Hodges, K. V. and McKenna, L. W, 1987. Realistic propagation of uncertainties in geologic thermobarometry. American Mineralogist, 72; 671-680. 1987.

Hodges, K. V. and Royden, L., 1984. Geological thermobarometry of retrograded metamorphic rocks: An indication of the uplift trajectory of a portion of the Northern Scandinavian Caledonides. Journal of Geophysical Research, 89, 7077-7090.

Hodges, K. V. and Spear, F. S., 1982. Geothermometry, geobarometry and the $Al_2SiO_5$ triple point at Mt. Moosilauke, New Hampshire. American Mineralogist, 67, 1118-1134.

Hoinkes, G., 1986. Effect of grossular-content in garnet on the partitioning of Fe and Mg between garnet and biotite. Contributions to Mineralogy and Petrology, 92, 393-399.

Holdaway, M. J., Mukhopadhyay B., Dyar M. D., Guidotti C. V., and Dutrow B. L., 1997. Garnet-biotite geothermometry revised; new Margules parameters and a natural specimen data set from Maine. American Mineralogist, 82, 582-595.

Hollister, L. S., 1966. Garnet zoning: an interpretation based on the Rayleigh fractionation model. Science, 154, 1647-1651.

Hollister, L. S., 1970. Origin, mechanism and consequences of compositional sector-zoning in staurolite. American Mineralogist, 55, 742-766.

Hollister, L. S., 1982. Metamorphic evidence for rapid (2mm/yr) uplift of a portion of the central gneiss complex, Coast Mountain, B. C. Canadian Mineralogist, 20, 319-332.

Horn, I., Foley, S. F., Jackson, S. E, and Jenner, G. A., 1994. Compositional dependencies of the partition coefficients for Zr, Nb, Ta, Hf and selected transition elements between spinel and melt. Mineralogical Magazine, 58A, 430-431.

Iiyama, J. T., 1979. Trace element distribution in rock-forming silicates. The alkali and alkaline earths: Origin and distribution of the elements. Physics and Chemistry of Earth, 2, 161-174.

Indares, A., 1995. Metamorphic interpretation of high-pressure-temperature metapelites with preserved growth zoning in garnet, eastern Grenville Province, Canadian Shield. Journal of Metamorphic Geology, 13, 475-486.

Ito, J. 1968. Silicate apatites and oxyapatites. American Mineralogist, 53, 890-907.

Jackson, S. E., Longerich, H. P. Dunning, G. R., and Fryer, B. J., 1992. The application of laser-ablation microprobe-inductively coupled plasma-mass spectrometry (LAM-ICP-MS) to in situ trace-element determinations in minerals. Canadian Mineralogist, 30, 1049-1064.

Jaffe, H. W., 1951. The role of yttrium and other minor elements in the garnet group. American Mineralogist, 70, 272-278.

Jamtveit, B., 1991. Oscillatory zonation patterns in hydrothermal grossular-andradite garnet: Nonlinear dynamics in regions of immiscibility. American Mineralogist, 76, 1319-1327.

Jamtveit, B. and Hervig, R. L., 1994. Constraints on transport and kinetics in hydrothermal systems from zoned garnet crystals. Science, 263. 505-508.

Jamtveit, B., Wogelius, R. A., and Fraser, D. G., 1993. Zonation patterns of skarn garnets: records of hydrothermal system evolution. Geology, 21, 113-116.

Jenner, G. A., Longerich, H. P., Jackson, S. E., and Fryer, B. J., 1990. ICP-MS-A powerful tool for high-precision trace-element analysis in Earth sciences: Evidence from analysis of selected U.S.G.S. reference samples. Chemical Geology, 83, 133-148.

Jenner, G. A., Foley, S. F., Jackson, S. E., Green, T. H., Fryer, B. J., and Longerich, H. P., 1994. Determination of partition coefficient for trace elements in high-pressure-temperature experimental run products by laser ablation microprobe-inductively coupled plasma-mass spectrometry (LAM-ICP-MS). Geochimica et Cosmochimica Acta, 58, 5099-5103.

Jensen, B. B., 1973. Patterns of trace element partitioning. Geochimica et Cosmochimica Acta, 37, 2227-2242.

Joesten, R., 1974. Pseudomorphic Replacement of Melilite by Idocrase in a Zoned Calc-Silicate Skarn, Christmas Mountains, Big Bend Region, Texas. American Mineralogist, 59, 694-699.

Joesten, R., 1983. Grain growth and grain-boundary diffusion in quartz from the Christmas Mountains (Texas) contact aureole. American Journal of Science, 283-A, 233-254.

Joesten, R., 1991. Grain-boundary diffusion kinetics in silicate and oxide minerals. In: Diffusion, atomic ordering, and mass transport; selected topics in geochemistry (ed. Ganguly, J.). Advances in Physical Geochemistry, 8, 345-395.

Johnson, C. A., 1994. Partitioning of zinc among common ferromagnesian minerals and implications for hydrothermal mobilization. Canadian Mineralogist, 32, 121-132.

Kean, S. D. and Essene, E. J., 1996. Trace element thermobarometry using Zr in garnet. Geological Society of America Abstract with Programs, 28, 7, 357.

Keskinen, M. and Liou, J. G., 1987. Stability relations of Mn-Fe-Al piemontite. Journal of Metamorphic Geology, 5, 495-507.

Kingery, W. D., 1984. Segregation phenomena at surfaces and at grain boundaries in oxides and carbides. Solid State Ionics, 12, 299-307.

Kingery, W. D., Bowen, H. K., and Uhlmann, D. R., 1976. Introduction to Ceramics, 2nd ed. Wiley.

Kingsbury, J. A., Miller, C. F., Wooden, J. L., and Harrison, T. M., 1993. Monazite paragenesis and U-Pb systematics in rocks of the eastern Mojave desert, California, USA: implications for thermochronometry. Chemical Geology, 110, 147-167.

Kohn, M. J., Orange, D. L., Spear, F. S., Rumble, D. III, and Harrison, T. M., 1992. Pressure, temperature, and structural evolution of west-central New Hampshire. Hot thrusts over cold basement. Journal of Petrology, 33, 521-556.

Kohn, M. J., Spear, F. S., Harrison, T. M., and Dalziel, W. D., 1995. $^{40}Ar/^{39}Ar$ geochronology and P-T-t paths from the Cordillera Darwin metamorphic complex, Tierra del Fuego, Chile. Journal of Metamorphic Geology, 13, 251-270.

Kohn, M. J., Spear, F. S., and Valley, J. W., 1997. Dehydration-melting and fluid recycling during metamorphism; Rangeley Formation, New Hampshire, USA. Journal of Petrology, 9, 1255-1277.

Korsman, K., 1975. Distribution of cobalt, vanadium, and chromium between coexisting biotite and garnet in granulites facies rock samples. Bulletin of Geological Society of Finland, 47, 13-17.

Kretz, R., 1959. Chemical study of garnet, biotite, and hornblende from gneisses of southwestern Quebec, coexisting minerals. Journal of Geology, 67, 371-402.

Kretz, R., 1961. Some applications of thermodynamics to coexisting minerals of variable composition. Examples: orthopyroxene-clinopyroxene and orthopyroxene -garnet. Journal of Geology, 69, 361-387.

Kretz, R., 1966. Grain-size distribution for certain metamorphic minerals in relation to

nucleation and growth. Journal of Geology, 74, 147-173.

Kretz, R., 1969. On the spatial distribution of crystals in rocks. Lithos, 2, 39-66.

Kretz, R, 1973. Kinetics of the crystallization of garnet at two localities near Yellownife. Canadian Mineralogist, 12, 1-20.

Kretz, R., 1983. Symbols for rock-forming minerals. American Mineralogist, 68, 277-279.

Kretz, R., 1993. A garnet population in Yellowknife schist, Canada. Journal of Metamorphic Geology, 11, 101-120.

Kretz, R., 1994. Metamorphic crystallization, Wiley, Chichester.

Kretz, R., Campbell, J. L., Hoffman, E. L., Hartree, R. and Teesdale, W. J., 1999. Approaches to equilibrium in the distribution of trace elements among the principal minerals in a high-grade metamorphic terrane. Journal of Metamorphic Geology, 17, 41-59.

Krylova, M. D., Dagelayskiy, V. B., and Orlovskaya, K. V., 1970. Distribution trends of scandium between the minerals of metamorphic rocks. Geokhimiya, 10, 1183-1193.

Lanzirotti, A., 1995. Yttrium zoning in metamorphic garnets. Geochimica et Cosmochimica Acta, 59, 4105-4110.

Lasaga, A. C., Richardson, S. M., and Holland, H. D., 1977. The mathematics of cation diffusion and exchange between silicate minerals during retrograde metamorphism. The Energetics of Geological Processes (Saxena, S. K. and Bhattacgarji, S. eds.), New York, Springer-Verlag, 353-388.

LaTourrette, T, Hervig, R. L., and Holloway, J. R., 1995. Trace element partitioning between amphibole, phlogopite, and basanite melt. Earth and Planetary Science Letters, 135, 13-30.

Li, C.-W. and Kingery, W. D., 1984. Solute segregation at grain boundaries in polycrystalline $Al_2O_3$. In Strucutre and Properties of MgO and $Al_2O_3$ Ceramics, American Ceramic Society, 368-378.

Liu, C.-Q., Masuda, A., Shimizu, H., Takahashi, K., and Xie, G.-H., 1992. Evidence for pressure dependence of the peak position in the REE mineral/melt partition patterns of clinopyroxene. Geochimica et Cosmochimica Acta, 56, 1523-1530.

Lonergan, A. J. and Dahl, P. S., 1989. Systematics of trace-element partitioning between coexisting garnet and biotite in high-grade metapelitic rocks. Geological Society of America Abstracts with Programs, A276.

Longerich, H. P., 1995. Analysis of pressed pellets of geological samples using wavelength-dispersive X-ray fluorescence spectrometry. X-ray Spectrometry, 24, 123-136.

Longerich, H. P., Jackson, S. E., and Günther, D., 1996a. Laser ablation inductively coupled plasma mass spectrometric transient signal data acquisition and analyte concentration calculation. Journal of Analytical Atomic Spectrometry, 11, 899-904.

Longerich, H. P., Günther, D., and Jackson, S. E., 1996b. Elemental fractionation in laser-ablation inductively-coupled mass-spectrometry. Fresenius Journal of Analytical Chemistry, 355, 538-542.

Longerich, H. P., Jenner, G. A., Fryer, B. J., and Jackson, S. E., 1990. Inductively coupled plasma-mass spectrometric analysis of geological samples: A critical evaluation based on case studies. Chemical Geology, 83, 105-118.

Loomis, T. P., 1982. Numerical simulation of the disequilibrium growth of garnet in chlorite-bearing aluminous pelitic rocks. Canadian Mineralogist, 20, 411-423.

Loomis, T. P., 1983. Compositional zoning of crystals: a record of growth and reaction history. In S. K. Saxena ed., Kinetics and Equilibrium in Mineral Reactions. Springer-Verlag, New York, 1-60.

Loomis, T. P. and Nimick, F. B., 1982. Equilibrium in Mn-Fe-Mg aluminous pelitic compositions and the equilibrium growth of garnet. Canadian Mineralogist, 20, 393-410.

Mason, R. A., 1982. Trace element distributions between the perthite phases of alkali feldspars from pegmatites. Mineralogical Magazine, 45, 101-106.

Massonne, H. J. and Schreyer, W., 1987. Phengite geobarometry based on the limiting assemblage with K-feldspar, phlogopite, and quartz. Contributions to Mineralogy and Petrology, 96; 212-224.

Matsui, Y., Onuma, N., Nagasawa, H., Higuchi, H., and Banno, S., 1977. Crystal structure control in trace element partition between crystal and magma. Bull. Soc. Fr. Mineral. Cristallogr, 100, 315-324.

Mazzucchelli, M., Rivalenti, G., Vannucci, R, Bottazzi, P., Ottolini, L., Hofmann, A. W., Sinigoi, S., and Demarchi, G., 1992. Trace element distribution between

clinopyroxene and garnet in gabbroic rocks of the deep crust: an ion microprobe study. Geochimica et Cosmochimica Acta, 56, 2371-2385.

McIntire, W. L., 1963. Trace element coefficients-a review of theory and applications to geology. Geochimica et Cosmochimica Acta, 27, 1209-1264.

McKay, G. A., 1989. Partitioning of rare earth elements between major silicate minerals and basaltic melts. In: Geochemistry and mineralogy of rare earth elements. Lipin, B. R. and McKay, G. A. (Eds.). Reviews in Mineralogy, 21; 45-77.

Meagher, E. P. ,1982. Silicate garnets. In: Ribbe P. H. (ed.), Orthosilicates, Mineralogical Society of America, Washington, D. C., volume 5, 25-67.

Menard, T. and Spear, F. S., 1993. Metamorphism of calcic pelitic schists, Strafford Dome, Vermont: Compositional zoning and reaction history. Journal of Petrology, 34, 977-1005.

Menard, T. and Spear, F. S., 1994. Metamorphic P-T paths from calcic pelitic schists from the Strafford Dome, Vermont, USA. Journal of Metamorphic Geology, 12, 811-826.

Menard, T. and Spear, F. S., 1996. Interpretation of plagioclase zonation in calcic pelitic schist, south Strafford, Vermont, and the effects on thermobarometry. Canadian Mineralogist, 34, 133-146.

Messiga, B., Tribuzio, R. T., Bottazzi, P., and Ottolini, L., 1995. An ion microprobe study on trace element composition of clinopyroxenes from blueschist and eclogitized Fe-Ti-gabbros, Ligurian Alps, northwestern Italy: some petrologic considerations. Geochimica et Cosmochimica Acta, 59, 59-75.

Michael, P., 1988. Partition coefficients for rare earth elements in mafic minerals of high silica rhyolites: The importance of accessory mineral inclusions. Geochimica et Cosmochimica Acta, 52, 275-282.

Miyake, A., 1993. Rotation of biotite porphyroblasts in pelitic schist from the Nukata area, central Japan. Journal of Structural Geology, 15, 1303-1313.

Miyashiro, A. and Shido, F., 1985. Tschermak substitution n low- and middle-grade pelitic schists. Journal of Petrology, 26, 449-487.

Möller, P., 1988. The dependence of partition coefficients on differences of ionic volumes in crystal-melt systems. Contributions to Mineralogy and Petrology, 99, 62-69.

Moorbath, S., Bell, K., Leake, B. E., and McKerrow, W. S., 1968. Geochronological studies in Connemara and Murrisk, Western Ireland. In Radiometric Dating for Geologists (eds. E. I. Hamilton and R. M. Farquhar). pp. 259-298. Interscience.

Moxham, R. L., 1965. Distribution of minor elements in coexisting hornblendes and biotites. Canadian Mineralogist, 8, 204-240.

Nagasawa, H., 1966. Trace element partition coefficient in ionic crystals. Science, 152, 767-769.

Newton, R. C. and Haselton, H. T., 1981, Thermodynamics of the garnet-plagioclase-$Al_2SiO_5$-quartz geobarometer. In: Newton R. C. (ed.), Thermodynamics of Minerals and Melts. Springer Verlag, New York, 131-147.

Nickel, E. H., 1954. The distribution of major and minor elements in coexisting ferro-magnesian silicates. American Mineralogist, 39, 486-493.

Nielsen, R. H., 1985. A method for the elimination of the compositional dependence of trace element distribution coefficient. Geochimica et Cosmochimica Acta, 49, 1775-1779.

Nielsen, R. H., 1988. A model for the simulation of the combined major and trace element liquid lines of descent. Geochimica et Cosmochimica Acta, 52, 27-38.

Novak, G. A. and Gibbs, G. V., 1971. The crystal chemistry of the silicate garnets. American Mineralogist, 56, 791-825.

Onuma, N., Higuchi, H., Wakita, H. and Nagasawa, H., 1968. Trace element partition between two pyroxenes and the host lava. Earth and Planetary Science Letters, 5, 47-51.

Pan, Y. and Fleet, M. E., 1996. Intrinsic and external controls on the incorporation of rare-earth elements in calc-silicate minerals. Canadian Mineralogist, 34, 147-159.

Passchier, C. W., Trouw, R. A. J., Zwart, H. J., and Vissers, R. L. M., 1992. Porphyroblast rotation: eppur si muove? Journal of Metamorphic Geology, 10, 283-294.

Pearce, N. J. G., Perkins, W. T., Westgate, J. A., Gordon, M. P., Jackson, S. E., Neal, C. R. and Chenery, S. P., 1997. A compilation of new and published major and trace-element data for NIST SRM-610 and NIST SRM-612 glass reference materials. Geostandards Newsletter, 21, 115-144.

Philpotts, J. A., 1978. The law of constant rejection. Geochimica et Cosmochimica Acta, 42, 909-920.

Powell, D. and Treagus, J. E., 1970. Rotational fabrics in metamorphic minerals. Mineralogical Magazine, 37, 801-814.

Powell, D. and Vernon, R. H., 1979. Growth and rotation history of garnet porphyroblasts with inclusion spirals in a Karakoram schist. Tectonophysics, 54, 25-43.

Pyle, J. M. and Spear, F. S., 1999a. Yttrium zoning in garnet: Coupling of major and accessory phases during metamorphic reactions. Geological Materials Research, 1, 1-49.

Pyle, J. M. and Spear, F. S., 1999b. Accessory-mineral and reaction-history controls on pelitic mineral trace-element partitioning: a combined EMP and LA-ICP-MS study. AGU spring meeting, S356.

Pyle, J. M. and Spear, F. S., 2000. An empirical garnet (YAG)-Xenotime thermometer. Contributions to Mineralogy and Petrology, 138, 51-58.

Rasband, W., 1998. Scion Image. http://www.scioncorp.com.

Reeder, R. J., 1991. Surfaces make a difference. Nature, 353, 797-798.

Reitan, P. H., Roelandts, I., and Brunfelt, A. O., 1980. Optimum ionic size for substitution in the M(2)-site in metamorphic diopside. N. Jahrb mineral. Monat., 4, 181-191.

Ridley, J. and Thompson, A. B., 1986. The role of mineral kinetics in the development of metamorphic microtextures. Advances in Physical Geochemistry, 5, 154-193.

Ringwood, A. E. and Major, A., 1971. Synthesis of majorite and other high pressure garnets and perovskites. Earth and Planetary Science Letters, 12, 411-418

Rivers, T., 1980. Revised stratigraphic nomenclature for Aphebian and other rock units, southern Labrador Trough, Grenville province. Canadian Journal of Earth Sciences, 17, 668-670.

Rivers, T., 1983a. The northern margin of the Grenville Province in western Labrador - Anatomy of an ancient orogenic front. Precambrian Research, 22, 41-73.

Rivers, T., 1983b. Progressive metamorphism of pelitic and quartzo-feldspathic rocks in the Grenville Province of western Labrador - tectonic implications of bathozone 6 assemblages. Canadian Journal of Earth Science, 20, 1791-1804.

Rivers, T., van Gool J. A. M., and Connelly, J. N., 1993. Contrasting tectonic styles in the northern Grenville province: implications for the dynamics of orogenic fronts. Geology 21, 1127-1130.

Roaldset, E., 1975. Rare earth distributions in some Precambrian rocks and their phyllosilicates, Numedal, Norway. Geochimica et Cosmochimica. Acta, 39, 455-469.

Rønsbo, J. G., 1989. Coupled substitutions involving REEs and Na and Si in apatites in alkaline rocks from the Ilimaussaq intrusion, South Greenland, and the petrological implications. American Mineralogist, 74, 896-901.

Rosenfeld, J. L., 1968. Garnet rotations due to the major Paleozoic deformations in Southeast Vermot. In Zen, E-An, White, W. S. Hadley,, J. B., and Thompson, J. B. Ed., Studies of Appalachian Geology: Northern and Maritime, Interscience Pubs., New York, 185-202.

Rosenfeld, J. L., 1970. Rotated garnets in metamorphic rocks. Geological Society of America Special Papers, 129, 102.

Rubatto, D., Williams, I. S., and Buick, I. S., 2001. Zircon and monazite response to prograde metamorphism in the Reynolds Range, central Australia. Contributions to Mineralogy and Petrology, 140, 458-468.

Rumble, D. III, Ferry, J. M., Hoering, T. C., and Boucot, A. J., 1982. Fluid flow during metamorphism at the Beaver Brook fossil locality, New Hampshire. American Journal of Science, 282; 886-919.

Sassi, P., Harte, B., Carswell, D. A., Yujing, H., 2000. Trace element distribution in central Dabie eclogites. Contributions to Mineralogy and Petrology, 139; 298-315.

Sánchez-Vizcaíno, L. V. A., Franz, G, and Gómez-Pugnaire, M. T., 1995. The behavior of Cr during metamorphism of carbonate rocks from the Nevado-Filabride complex, Betic Cordilleras, Spain. Canadian Mineralogist, 33, 85-104.

Schoneveld, C., 1977. A study of some typical inclusion patterns in strongly paracrystalline rotated growth. Tectonophysics, 39, 453-471.

Schumacher, R., Rötzler, K., and Maresch, W. V., 1999. Subtle oscillatory zoning in garnet from regional metamorphic phyllites and mica schists, western Erzgebirge, Germany. Canadian Mineralogist, 37, 381-402.

Schwandt, C. S., Papike, J. J., Shearer, C. K., and Brearley, A. J., 1993. A SIMS investigation of REE chemistry of garnet in garnetite associated with the Broken Hill Pb-Zn-Ag orebodies, Australia. Canadian Mineralogist, 31, 371-379.

Schwandt, C. S., Cygan, R. T., and Westrich, H. R., 1995. Mg self-diffusion in pyrope garnet. American Mineralogist, 80; 483-490.

Schwandt, C. S., Papike, J., and Shearer, C. K., 1996. Trace element zoning in pelitic garnet of the Black Hills, South Dakota. American Mineralogist, 81, 1195-1207.

Schwarcz, H. P., 1967. The effect of crystal field stabilization on the distribution of transition metals between metamorphic minerals. Geochimica et Cosmochimica Acta, 31, 503-517.

Schwarz, S. H., 1998. Structural, metamorphic and tectonic studies in central Gagnon terrane, Grenville Province. M. Sc. Thesis, Memorial University of Newfoundland.

Selverstone, J., 1985. Petrologic constraints on imbrication, metamorpism, and uplift in the S.W. Tauern Window, Eastern Alps. Tectonics, 4, 687-704.

Selverstone, J. and Spear, F. S., 1985. Metamorphic P-T path from pelitic schists and greenstones in the southwest Tauern Window, Eastern Alps. Journal of Metamorphic Geology, 3, 439-465.

Selverstone, J., Spear, F. S., Franz, G., and Morteani, G., 1984. High pressure metamorphism in the SW Tauren window, Austria: P-T paths from hornblende-kyanite-staurolite schists. Journal of Petrology, 25, 501-531.

Shannon, R. D., 1976. Revised effective ionic radii and systematic studies of interatomic distances in halides and chalcogenides. Acta Cyst., A32, 751-767.

Shaw, D. M., 1956. Geochemistry of pelitic rocks. Part III: major elements and general geochemistry. Geological Society of America Bulletin, 67, 919-934.

Shearer, C. K., Papike, J. J., Simon, S. B., and Laul, J. C., 1986. Pegmatite-wallrock interaction, Black Hills, South Dakota: Interaction between pegmatite-derived fluids and quartz-micas schist wallrock. American Mineralogist, 71, 518-539.

Shearer, C. K., Papike, J. J., Simon, S. B., and Shimizu, N., 1989. An ion microprobe study of the intra-crystalline behavior of REE and selected trace elements in pyroxene from mare basalts with different cooling and crystallization histories. Geochimica et Cosmochimica Acta, 53, 1041-1054.

Sherlock, S. C. and Okay, A. I., 1999. Oscillatory zoned chrome lawsonite in the Tavşanli Zone, northwest Turkey. Mineralogical Magazine, 63, 687-692.

Shimizu, N., 1981. Trace element incorporation into growing augite phenocryst. Nature, 289, 575-577.

Shimizu, N., 1983. Interface kinetics and trace element distribution between phenocrysts and magma. In Augustithis, S. S., Ed., The significance of trace elements in solving petrogenetic problems and controversies. Theophrastus Publications, Athens, Greece, 175-195.

Smith, H. A. and Barreiro, B., 1990. Monazite U-Pb dating of staurolite grade metamorphism in pelitic schists. Contributions to Mineralogy and Petrology, 105, 602-615.

Smyth, J. R. and Bish, D. L., 1988. Crystal structures and cation sites of the rock-forming minerals. Allen and Unwin, Boston-London-Sydney-Wellington, 332p.

Sorensen, S. S. and Grossman, J. N., 1989. Enrichment of trace elements in garnet amphibolites from a paleo-subduction zone: Catalinal Schist, southern California. Geochimica et Cosmochimica Acta, 53, 3155-3177.

Spear, F. S., 1988. Metamorphic fractional crystallization and internal metasomatism by diffusional homogenization of zoned garnets. Contributions to Mineralogy and Petrology, 99, 507-517.

Spear, F. S., 1993. Metamorphic phase equilibria and pressure-temperature-time paths. Mineralogical society of America monograph, Washington, D. C., p. 799.

Spear, F. S., 1982. Phase equilibria of amphibolites from the Post Pond Volcanics, Mt. Cube Quadrangle, Vermont. Journal of Petrology, 23; 383-426.

Spear, F. S. and Kohn, M. J., 1996. Trace element zoning in garnet as a monitor of crustal melting. Geology, 24, 1099-1102.

Spear, F. S., and Parrish, R. R., 1996. Petrology and cooling rates of the Valhalla complex, British Columbia, Canada. Journal of Petrology, 37, 733-765.

Spear, F. S. and Rumble, D., 1986. Pressure, temperature and structural evolution of the Orfordville Belt, West-Central New Hampshire. Journal of Petrology, 27, 1071-1093.

Spear, F. S. and Selverstone, J., 1983. Quantitative P-T paths from zoned minerals: Theory and tectonic applications. Contributions to Mineralogy and Petrology, 83, 348-357.

Spear, F. S., Selverstone, J., Hickmott, D., Crowley, P., and Hodges, K. V., 1984. P-T paths from garnet zoning: A new technique for deciphering tectonic processes in crystalline terrains. Geology, 12, 87-90.

Spry, A., 1969. Metamorphic textures. Pergamon Press, Oxford.

St-Onge, M. R., 1987. Zoned poikiloblastic garnets: P-T paths and syn-metamorphic uplift through 30 km of structural depth, Wopmay Orogen, Canada. Journal of Petrology, 28, 1-21.

Staudt, W. J., Reeder, R. J., and Schoonen, M. A. A., 1994. Surface structural controls on compositional zoning of $SO_4^{2-}$ and $SeO_4^{2-}$ in synthetic calcite single crystals. Geochimica et Cosmochimica Acta, 58, 2087-2098.

Stowell, H. H., Menard, T., and Ridgway, C. K., 1996. Ca-metasomatism and chemical zonation of garnet in contact-metamorphic aureoles, Juneau gold belt, southeastern Alaska. Canadian Mineralogist, 34, 1195-1209.

Taylor, R. P., Jackson, S. E., Longerich, H. P., and Webster, J. D., 1997a. In situ trace-element analysis of individual silicate melt inclusions by laser ablation microprobe-inductively coupled plasma-mass spectrometry (LAM-ICP-MS). Geochimica et Cosmochimica Acta, 61, 2559-2567.

Taylor, L., Wise, M. A., Simmons, W. B., and Falster, A. U., 1997. Occurrence of phosphorus in garnets from gem-bearing pegmatites. 23rd Rochester mineralogical symposium; abstracts. Rocks and Minerals, 72, 189-190.

Taylor, S. R. and McLennan, S. M., 1985. The continental crust: Its composition and evolution. Blackwell Scientific, Boston.

Thompson, R. N., 1975. Is upper-mantle phosphorus contained in sodic garnet?. Earth and Planetary Science Letters, 26; 417-424

Thompson, A. B., Tracy, R. J., Lyttle, P., and Thompson, Jr., J. B., 1977. Prograde reaction histories deduced from compositional zonation and mineral inclusions in garnet from the Gassetts schist, Vermont. American Journal of Science, 277, 1152-1167.

Tiller, W. A. and Ahn, K.-S., 1980. Interface field effects on solute redistribution during crystallization. Journal of Crystal Growth, 49, 483-501.

Tracy, R. J., 1982. Compositional zoning and inclusions in metamorphic minerals. Reviews in Mineralogy, 10, 355-397.

Tracy, R. J., 1991. Ba-rich micas from the Franklin Marble, Lime Crest and Sterling Hill, New Jersey. American Mineralogist, 76, 1683-1693.

Tracy, R. J. and Dietsch, C. W., 1982. High-temperature retrograde reactions in pelitic gneiss, Central Massachusetts. Canadian Mineralogist, 20, 425-437.

Tracy, R. J., Robinson, P., and Thompson, A. B., 1976. Garnet composition and zoning in the determination of temperature and pressure of metamorphism, central Massachusetts. American Mineralogist, 61, 762-775.

Tracy, R. J., Miller, S. J., Solberg, T. N., and Waldron, K. A., 1992. Documentation of diffusional modification of garnet growth zoning in amphibolite facies garnets. Geological Society of America, 24; 7, 219.

Treloar, P. J., 1987. The Cr-minerals of Outokumpu - Their chemistry and significance. Journal of Petrology, 28, 867-886.

Tribuzio, R., Riccardi, M. P., and Ottolini, L., 1995. Trace element redistribution in high-temperature deformed gabbros from East Ligurian ophiolites (Northern Apennines, Italy) constraints on the origin of syndeformation fluids. J. Metamorphic Geol. 13, 367-377.

Tuccillo, M. E., Essene, E. J., and van der Pluijm, B. A., 1990. Growth and retrograde zoning in garnets from high-grade metapelites: Implications for pressure-temperature paths. Geology, 18, 839-842.

Turekian, K. K. and Phinney, W. C., 1962. The distribution of Ni, Co, Cr, Cu, Ba, and Sr between biotite garnet pairs in a metamorphic sequence. American Mineralogist, 47, 1343-1441.

van Breemen, N., 1980. Magnesium-ferric iron replacement in smectite during aeration of pyritic sediments. Clay Minerals, 15, 101-110.

van Gool, J. A. M., 1992. The Grenville Front foreland fold-and-thrust belt in southwestern Labrador: mid-crustal structural and metamorphic configuration of a Proterozoic orogenic thrust wedge. Ph D Thesis, Memorial University of Newfoundland, St. John's, p. 372.

van Gool., J. A. M. and Cawood, P. A., 1994. Frontal vs. Basal accretion and contrasting particle paths in metamorphic thrust belts. Geology, 22, 51-54.

van Westrenen, W., Blundy, J., and Wood, B., 1999. Crystal-chemical controls on trace element partitioning between garnet and anhydrous silicate melt. American Mineralogist, 84, 838-847.

Viskupic, K. and Hodges, K. V., 2001. Monazite-xenotime thermochronometry; methodology and an example from the Nepalese Himalaya. Contributions to Mineralogy and Petrology, 141, 2, 233-247.

Volfinger, M., 1974. Effet de la composition des micas trioctaëdriques sur les distributions de Rb et Cs à l'état de traces. Earth and Planetary Science Letters, 24, 299-304.

Volfinger, M., 1976. Effet de la température sur les distributions de Na, Rb et Cs entre la sanidine, la muscovite, la phlogopite et une solution hydrothermale sous une pression de 1 kbar. Geochimica et Cosmochimica Acta, 40, 267-282.

Volfinger, M. and Robert J. L., 1980. Structural control of the distribution of trace elements between silicates and hydrothermal solutions. Geochimica et Cosmochimica Acta, 44, 1455-1461.

Waff, H. S. and Holdren, G. R., 1981. The nature of grain boundaries in dunite and iherzolite xenoliths: Implications for magma transport in refractory upper mantle material. Journal of Geophysical Reseraches, 86, 3677-3683.

Walther, J. V. and Orville, P. M., 1983. The extraction-quench technique for determination of the thermodynamic properties of solute complexes; application to quartz solubility in fluid mixtures. American Mineralogist, 68, 731-741.

Walther, J. V. and Wood, B. J., 1984. Rate and mechanism in prograde metamorphism. Contributions to Mineralogy and Petrology, 88, 246-259.

Watson, E. B., 1996. Surface enrichment and trace-element uptake during crystal growth. Geochimica et Cosmochimica Acta, 60, 5013-5020.

Watson, E. B. and Liang, Y., 1995. A simple model for sector zoning in slowly grown crystals: implications for growth rate and lattice diffusion, with emphasis on accessory minerals in crustal rocks. American Mineralogist, 80, 1179-1187.

Wedepohl, K. H., 1995. The composition of the continental crust. Geochim. Cosmochim. Acta 59, 1217-1232.

Whitney, P. R. and McLelland, J. M., 1973. Origin of coronas in metagabbros of the Adirondack Mts., N. Y. Contributions to Mineralogy and Petrology, 39, 81-98.

Williams, M. L. and Grambling, J. A., 1990. Manganese, ferric iron and the equilibrium between garnet and biotite. American Mineralogist, 75, 886-908.

Williams, P. F. and Jiang, D., 1999. Rotating garnets. Journal of Metamorphic Geology, 17, 367 - 378.

Winkler, H. G. F., 1979. Petrogenesis of metamorphic rocks. 5$^{th}$ ed. Springer Verlag, New York, 348p.

Wise, M. A., 1994. Phosphorus in pegmatitic garnets; examples from Maine. International Mineralogical Association, 16th general meeting; abstracts, 16; 441.

Yang, P, Rivers, T. and Jackson, S., 1999. Crystal chemical and thermal controls on trace-element partitioning between coexisting garnet and biotite in metamorphic rocks from western Labrador. Canadian Mineralogist 37, 443-468.

Yang, P. and Rivers, T., 2000. Trace element partitioning between coexisting biotite and muscovite from metamorphic rocks, western Labrador: Structural, compositional and thermal controls. Geochimica et Cosmochimica Acta 64, 1451-1472.

Yang, P. and Rivers, T., 2001. Chromium and manganese zoning in pelitic garnet and kyanite: spiral, overprint and oscillatory (?) zoning patterns and the role of growth rate. Journal of Metamorphic Geology 19. 455 - 474.

Yang, P. and Rivers, T. Trace element zoning in pelitic garnet, apatite and epidote-group minerals: The origin of Y annuli and P zoning in garnet. Geological Materials Research. Submitted.

Yardley, B. W. D., Rochelle, C. A., Barnicoat, A. C., and Lloyd, G. E., 1991. Oscillatory zoning in metamorphic minerals: an indicator of infiltration metasomatism. Mineralogical Magazine, 55, 357-365.

Young, E. D. and Rumble, D. III, 1993. The origin of correlated variations in in-situ ($\delta^{18}$) O/ ($\delta^{16}$) O and elemental concentrations in metamorphic garnet from southeastern Vermont, USA.. Geochimica et Cosmochimica Acta, 57; 2585-2597.

Zack, T., Foley, S. F., and Rivers, T. Evaluating hydrous eclogites from Trescolmen (Central Alps) for the derivation of trace element partitioning values relevant for subduction zone processes. Submitted to Journal of Petrology.

Zen E-an, 1963. Components, phases and criteria of chemical equilibrium in rocks. American Journal of Science, 261, 929-942.

Zwart, H. J., 1960. The chronological succession of folding and metamorphism in the central Pyrenees. Geologische Rundschau, 50, 203-218.

# Appendix A: X-ray mapping for major and trace elements with the Cameca SX-50 electron microprobe

The code is designed to acquire large wavelength dispersive (WD) X-ray maps on a Cameca SX-50 electron microprobe with no adequate stage mapping program incorporated in the system. X-ray maps are acquired by rastering the stage with pre-defined resolution and dwell time. For trace elements 15-20 kV accelerating voltage, 300-700 nA beam current, and counting times of 300-800 ms were routinely use to acquire maps of 128×128-256×256 pixels, which results in 4 to 10 hours analysis time.

The map area, defined by four points (labeled as N, S, E, and W) enclosing the mineral to be mapped, does not necessarily have to be square. The program defines new starting (lower left corner) and end (upper right corner) X-Y coordinates and automatically determines the direction of sample-stage movement. X-ray counts from three spectrometers are captured in a remote personal computer with the software Procomm, v. 1.02 (Datastorm Technologies, Inc.) and then converted to a comma separated format using a Qbasic® program for each element. X-ray maps were processed on an IBM compatible computer with the commercial image analysis program SigmaScan v. 3.02.035 (Jandel Scientific) and the public domain program Scion Image v. 3b (Rasband, 1998). The X-ray mapping code (map.tas) and the conversion program (convert.bas) can be downloaded at http://www.gly.bris.ac.uk/www/jmg/JMG.html.

## X-ray mapping code written by M. Piranian and P. Yang (1999)

```
   CL
  5 VAC
  6 VAC OFF
 10 PRINT LOCA "X-ray mapping starting"
 20 MOVE STAG W
 30 WMOV STAG
 40 DEFI WX [XPOS#]
 60 DEFI WZ [ZPOS#]
 70 MOVE STAG E
 80 WMOV STAG
 90 DEFI EX [XPOS#]
110 DEFI EZ [ZPOS#]
120 MOVE STAG S
130 WMOV STAG
140 DEFI SX [XPOS#]
150 DEFI SY [YPOS#]
160 DEFI SZ [ZPOS#]
170 MOVE STAG N
180 WMOV STAG
200 DEFI NY [YPOS#]
210 DEFI NZ [ZPOS#]
220 DEFI AVGZ [(WZ+EZ+SZ+NZ)/4]
230 AMOVE X WX
240 AMOVE Y SY
250 AMOVE Z AVGZ
260 WMOVE STAG
270 MOVE STAG START SAVE
330 INPUT "What resolution do you want? " RES
340 INPUT "What dwell time do you want? " DWELL
350 DEFI DELX [ABS(EX-WX)]
360 DEFI DELY [ABS(NY-SY)]
362 PRIN LOCA "X distance is, " DELX
364 PRIN LOCA "Y distance is, " DELY
366 INPUT "Speed is, " SPD
370 IF (DELX<DELY) THEN 410 ELSE 380
380 DEFI LENG [DELX]
390 DEFI STEP [DELX/RES]
400 GOTO 430
410 DEFI LENG [DELY]
420 DEFI STEP [DELY/RES]
430 DEFI XRES [DELX/STEP]
440 DEFI YRES [DELY/STEP]
500 INPUT "Spec #1 is, " SPC1$
510 INPUT "Spec #2 is, " SPC2$
520 INPUT "Spec #3 is, " SPC3$
530 INPUT "If this is the last run, type 0, if not, type 1 " LR
540 INPUT "Open a capture file now. When you finish, press 1 " P
550 IF (P=1) THEN 560 ELSE 980
560 prin loca "END OF JUNK"
570 PRIN LOCA SPC1$ ',' SPC2$ ',' SPC3$
580 PRIN LOCA "X RESOLUTION IS, " XRES
```

```
590 PRIN LOCA "Y RESOLUTION IS, " YRES
600 PRIN LOCA "PIXEL SIZE IS,    " STEP
610 PRIN LOCA "DWELL TIME IS,    " DWELL
620 DEFI CHAN [SQRT(LENG)]
630 PCOU , DWELL
640 SIZE STEP
650 MOVE STAG START
660 WMOV STAG
670 TIME 0 0 0
680 IF (DELX<DELY) THEN 820 ELSE 690
690 FOR R 1 YRES
700 PRIN LOCA "starting row, " R
710 SCAN X CHAN CHAN SPD
720 FOR N 1 XRES
730 COUN
740 WCOUN
750 PRIN LOCA N CNT#[1] CNT#[2] CNT#[3]
760 NEXT N
770 WMOV STAG
780 RMOV Y STEP
790 AMOV X WX
800 WMOV STAG
810 NEXT R
815 GOTO 950
820 FOR R 1 XRES
830 PRIN LOCA "starting row, " R
840 SCAN Y CHAN CHAN SPD
850 FOR N 1 YRES
860 COUN
870 WCOUN
880 PRIN LOCA N CNT#[1] CNT#[2] CNT#[3]
890 NEXT N
900 WMOV STAG
910 RMOV X STEP
920 AMOV Y SY
930 WMOV STAG
940 NEXT R
950 TIME
960 IF (LR=1) THEN 980 ELSE 970
970 BYE
980 STOP
```

# Appendix B: Garnet zoning profiles in sample 87-279

BSE images and core-to-rim quantitative zoning profiles of Fe, Mg, Mn and Ca and qualitative zoning profiles of Y and Ti determined by electron microprobe in sixteen garnets from sample 87-279. Light gray white areas in the BSE images are mainly defined by Y zoning. White lines in the BSE images represent the locations of zoning profiles. The contrast of BSE images is enhanced by using a high beam current (100 nA). Solid and dotted red lines in the profiles represent the locations of the inner and outer Mn annuli, respectively. The inner Mn annuli are characterized by broad and symmetrical shapes. In contrast, the outer Mn annuli are characterized by short wavelength, asymmetric profiles with steeper slopes on the inner side. Locations of these garnets and the Mn concentrations at the inner annuli are given in Fig. 15. Note that the Mn concentrations at the inner annuli are not always higher than those of outer annuli (h, i, k) and the inner Mn annuli are not always accompanied by Y annuli (e, i, k). In contrast, outer Mn annuli are correlated with enrichments in Y.

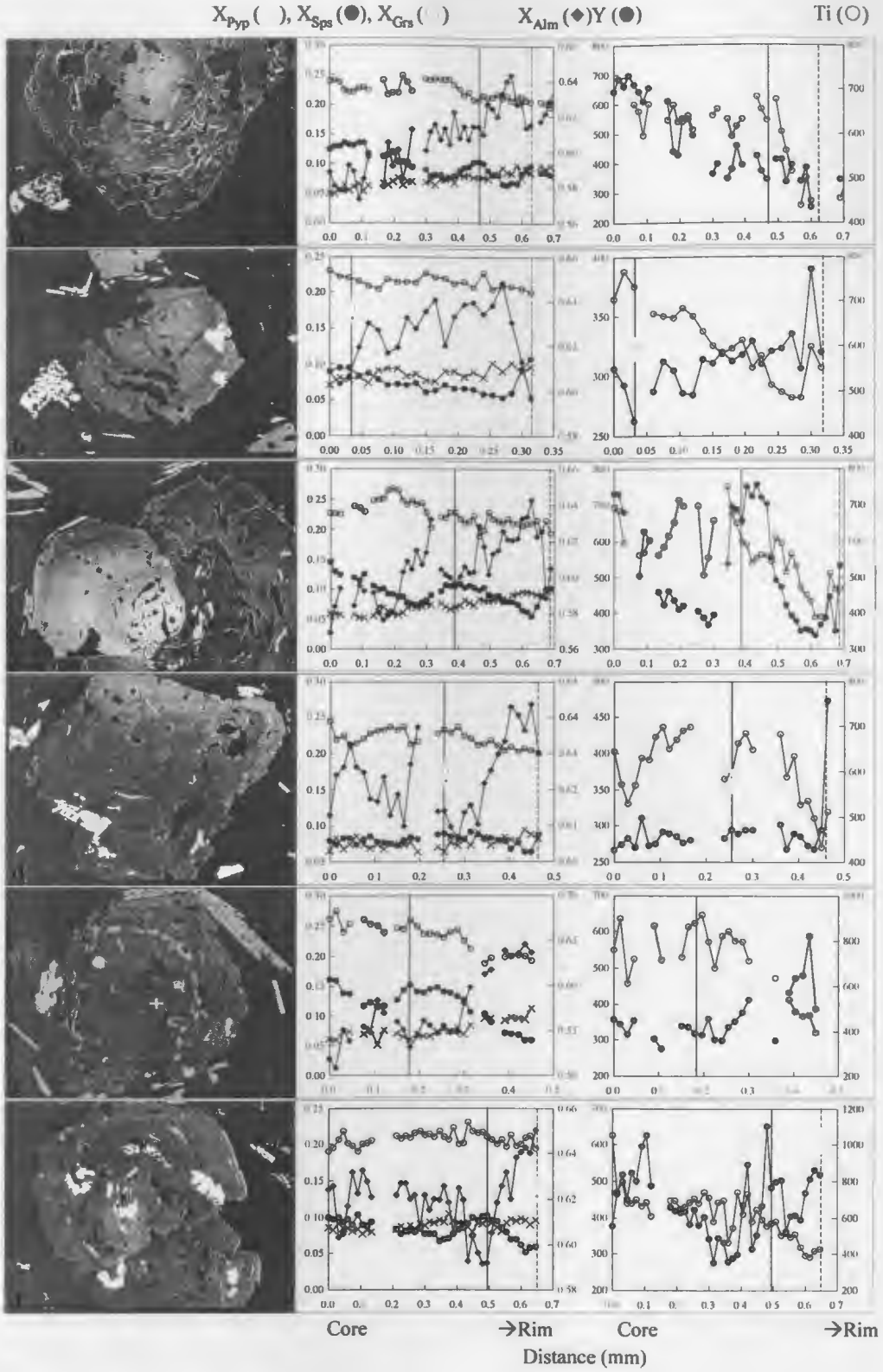
$X_{Pyp}$ ( ), $X_{Sps}$ (●), $X_{Grs}$ ( )
$X_{Alm}$ (◆)Y (●)
Ti (O)
Core
→Rim
Core
→Rim
Distance (mm)

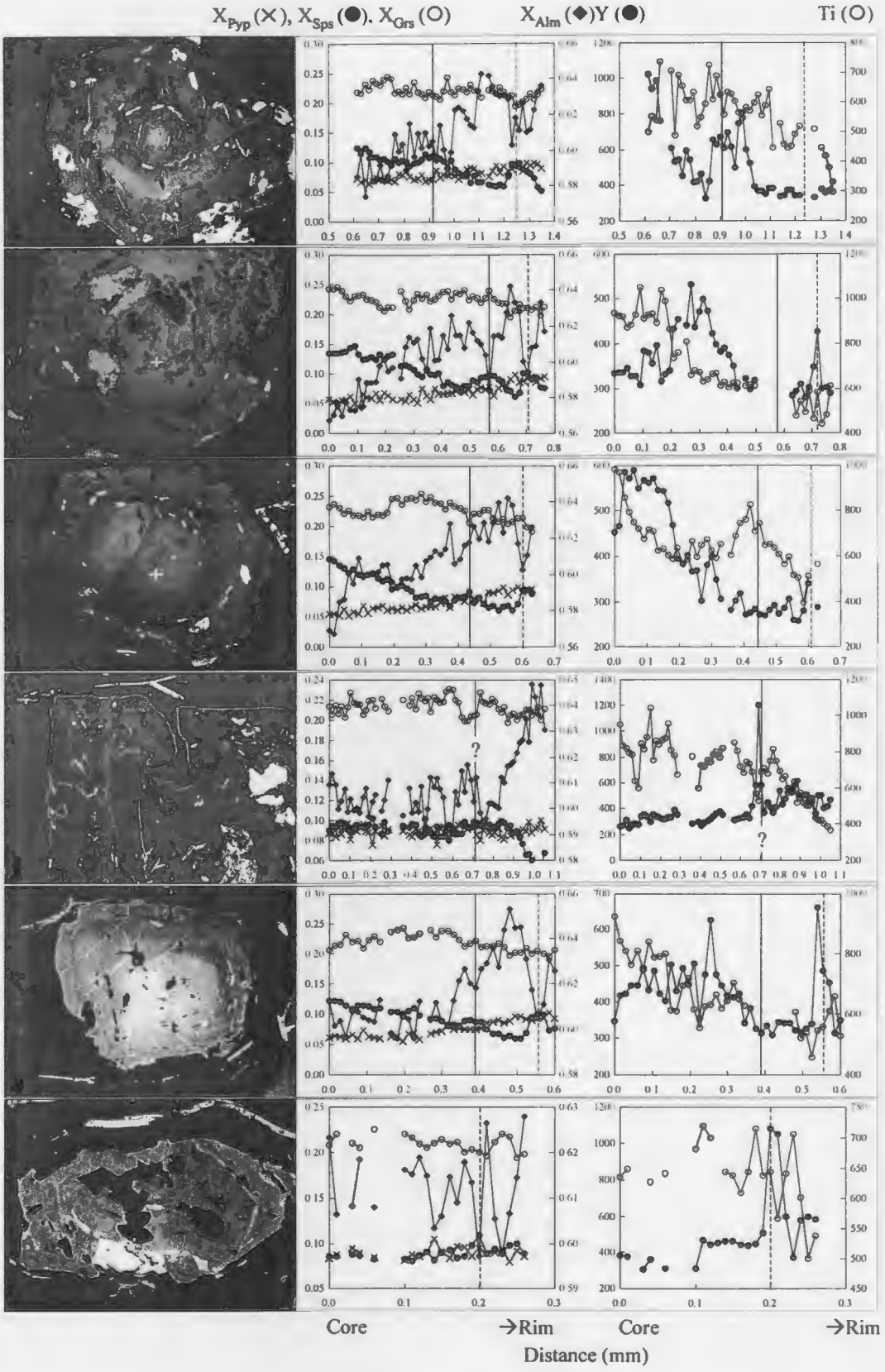
$X_{Pyp}$ (×), $X_{Sps}$ (●), $X_{Grs}$ (○)
$X_{Alm}$ (◆)Y (●)
Ti (○)
Core →Rim
Core →Rim
Distance (mm)

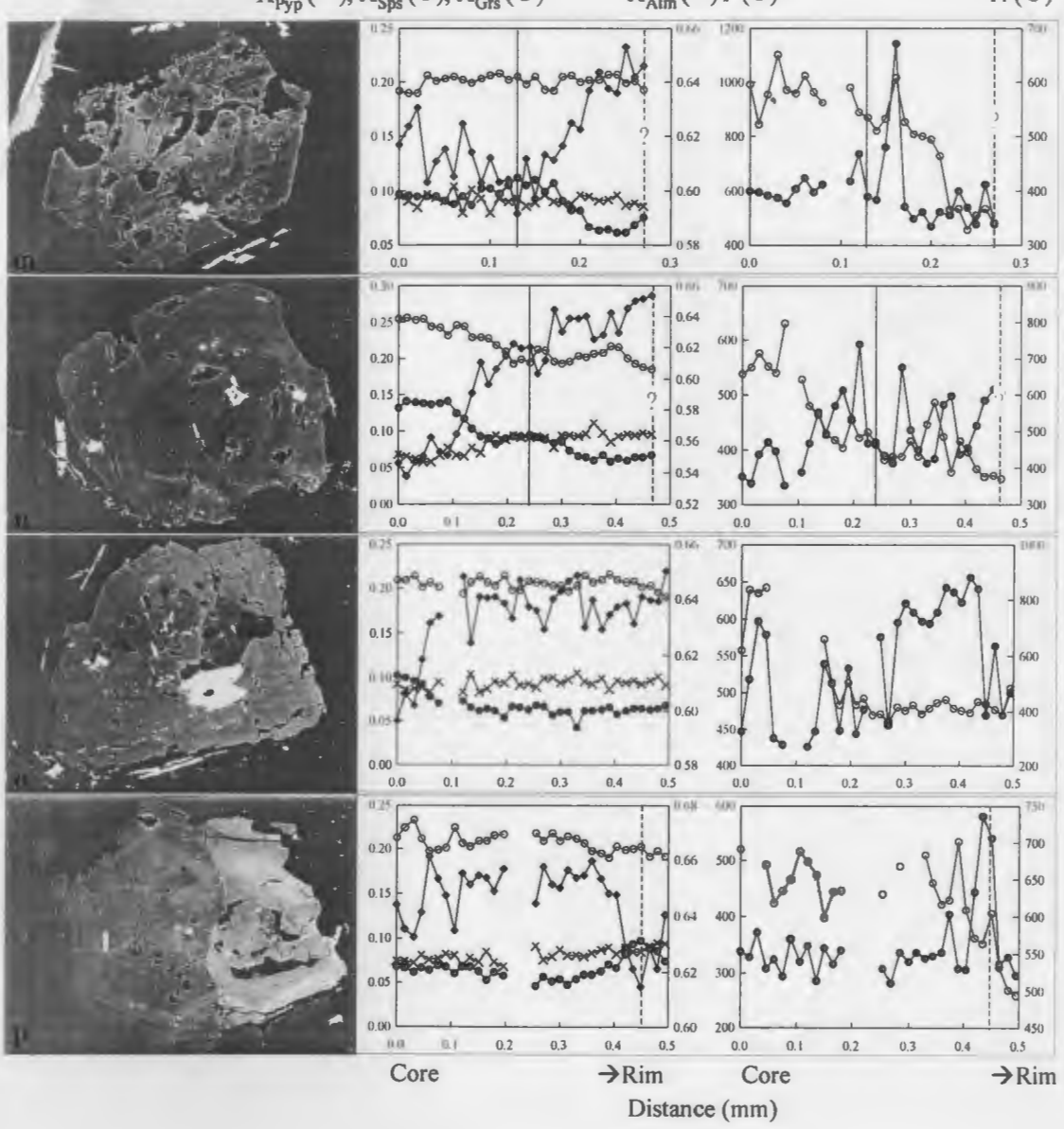
$X_{Pyp}$ ( ), $X_{Sps}$ (●), $X_{Grs}$ (○)
$X_{Alm}$ (◆)Y (●)
Ti (○)
Core
→Rim
Core
→Rim
Distance (mm)